Stress and Displacement Fields Around Magma Chambers and Fluid-driven Fractures in Volcanic Areas

Mohsen Bazargan

A thesis submitted for the degree of Doctor of Philosophy at the University of London

Rock Fractures and Fluid Flow Group
Department of Earth Sciences Royal Holloway,
University of London

January 2019

Declaration

I, Mohsen Bazargan, hereby declare that this thesis and the work presented in it is entirely my own, unless otherwise stated. The main body of thesis, Chapters 3-6, forms a collection of co-authored papers, which published, either in press or in prep for publication. I am responsible for the numerical modeling and partially with laboratory experiments data collection throughout this thesis, for primary authorship of all five of the included papers. Statements of my contribution are included on the cover page of each paper.

Signature: Mohsen Bazargan

Date: 23/01/2019

Declaration of Authorship for Co-Authored Work

If you are presenting partly co-authored work, please indicate below your individual contribution to the thesis.

Name of candidate: Mohsen Bazargan

Thesis title: Stress and Displacement Fields around Magma Chambers and Fluid-driven Fractures in Volcanic Areas

I confirm that the thesis that I am presenting has been co-authored with Agust Gudmundsson, Özgür Karaoğlu, John Browning and Alper baba

Within this partly co-authored work, I declare that the following contributions are entirely my own work:

(Here you should indicate, in précis style, the datasets that you gathered, interpreted and discussed; methods that you developed; complete first drafts that you wrote; content that is entirely your own work; etc. It is often appropriate to organise this statement by chapter)

Paper 1 (chapter 3) (MB & AG) 70%

The methodology of computation and creation of models were developed by MB. Field measurements conducted by AG. Writing a draft was made by MB and later critical review and commentary and changes from AG. All numerical-model illustrations were prepared by MB, with later adjustments and modifications from AG. Initial interpreted data and discussions were done by MB and specifically critical revision and changes from AG.

Paper 2 (chapter 4) (MB & AG) 70%

The methodology of computation and numerical modelling toolbox creation and development were done by MB as well as all analytical approach but they were both discussed in detail with AG. A draft of the paper and all numerical figures were prepared by MB with later critical revision and changes done by AG. Initial interpreted data along with conceptual model carried out by MB with substantial support and changes from AG. This work will have follow up of one or two papers later, because only fraction of modelling has been presented in this paper.

Paper 3 (chapter 5) (ÖK, JB, MB & AG) 40%

The origin idea, data collections, methodology and creation of 2-dimensional and 3-dimesional models were conducted by MB. Analysis and interpretation of numerical results were done by MB and specifically support input from JB and AG. Writing the initial draft was made by ÖK and JB and AG later revised the manuscript. Illustrations were prepared jointly by the authors.

Paper 4 (chapter 6) (ÖK, MB, AB & JB) 35%

The initial idea and creation of numerical models were conducted by ÖK and MB and support input from AB and JB. Analytical approach was developed by MB. Writing the initial draft was made by ÖK and AE and later revising the manuscript for important intellectual content from JB. Tomographic images and their analysis and interpretation were conducted by ÖK. Illustrations were prepared by MB and support input by ÖK.

Signed: Mohsen Bazargan (Candidate) Date: 23/01/2019

Signed: Agust Gudmundsson (Supervisor) Date:23/01/2019

This form should be signed by the candidate and the candidate's supervisor and returned to Student Administration, Royal Holloway, Egham, Surrey TW20 0EX with the copies of the thesis

Abstract

One of the fundamental unsolved problems in volcanology is assessing the probability of eruption during volcanic unrest periods. For interpreting surface deformation during unrest periods, most models assume an elastic half-space model. This means that the volcano and the hosting crustal segment assume that the elastic properties are uniform. It follows that not layering is taken into account. Here I use COMSOL Multiphysics software to develop new numerical models on stresses and displacements inside and at the surface of a volcano during unrest periods when realistic mechanical layering is taken into account. The models consider shallow magma chambers of various ideal geometries (prolate ellipsoids, oblate ellipsoids, spheres) located in crustal segments where the layers above the chamber have Young's modulus (stiffness) that varies from 20GPa (stiff) to 0.01GPa (very compliant or soft). Also considered are dike and inclined (cone) sheet emplacement in a layered crust and their effects on the internal and surface deformation of the hosting volcano. In most models the only loading is the magmatic pressure in the chamber/ dike. The results show that compliant or soft layers above magma chambers and dikes/sheets tend to suppress the surface stresses and displacements. Also, half-space models for surface deformation induced by dikes/sheets tend to underestimate (a) the depth to the top of the dike and (b) the dimensions, particularly the thickness, of the dike. In particular, the numerical models for dikes show that the surface-displacement peaks occur at widely different locations from the tensile and shear stress peaks. The boundary faults of a dike-induced graben should form at the stress peaks and not, as is commonly suggested, at the surface displacement peaks. The present results support the 'graben rule' which implies that any dike-induced graben is likely to be of a width about twice the depth to the tip/top of the arrested dike. Thus, for a dike tip arrested at 0.5 km depth, the surface width of a possible induced graben would be close to 1 km. Because of the suppression of stresses and displacement by typical compliant layers in volcanoes and rift zones, for typical dikes little or no dike-induced surface deformation is expected until the dike tip has propagated to depths below the surface of less than a kilometer.

Acknowledgements

Directly after my parents, my thanks go to Agust Gudmundsson, Philip Meredith as without their support and guidance this thesis certainly would not have been possible for me. I thank Agust for introducing me as engineer/physicists to the world of volcanotectonics and allowing me substantial academic freedom such that I was able to develop a project and research framework that matched my interests. He is thanked for supervising this work and for giving me the opportunity to delve into volcanology. I thank Philip for agreeing to be a part of this project and providing a positive enthusiasm to me. I also want to thank my mother and my father for the time devoted to helping me through this PhD abroad. I would also like to thank Ian Watkinson, for his encouragement and guidance throughout. Finally, I would like to thank my friends and colleagues like John Browning, Ozgur karaoglu, Pooyan Broumand, Reza Mohammadi, Mahdi Habibpour, Shahram Chamankhah, Elham joneidi, Mohammad reza Hirmand and Mohammad Vahab for their constant support and inspiration whom mostly we manage to publish an article or extended abstract with.

CONTENTS

List of figures:

List of Tables:

1. Introductions

1.1 Volcanotectonic structures and modelling

In almost all volcanic eruptions, magma is supplied by fluid driven fractures, whether they are dikes or inclined sheets. It is thus vital to have as complete understanding of the processes which govern the mechanisms of fracture-related magma transport as well as magma storage in volcanoes. This thesis investigates various volcano tectonic processes with the aim of increasing our understanding of the behavior of volcanoes. In this first chapter, I first provide a brief overview and introduction to the relevant studies and suggest areas that require further or better understanding. Then I discuss briefly the use of modelling, particularly the method of finite-element modelling, of volcanotectonic structures and processes. More details on modelling, including numerical modelling, are provided in Chapter 2.

1.1.1 Magma chambers

Magma normally accumulates at various depths in the crust below the surface of volcanically active areas (Marsh, 1989). Magma storage conditions are predominantly understood, as regards host-rock for chamber formation and their depths, derive primarily from structural geology and volcanotectonic field studies (e.g Gudmundsson, 1986a; Menand, 2011), analytical and numerical studies (Gudmundsson, 2011a,b; Gudmundsson, 2012; Barnett and Gudmundsson, 2014) fluid inclusions analyses of crystals (e.g Druitt et al., 2012; Walker, 1960), ground deformation studies (e.g Mogi, 1958), as well as geochemical and petrological studies such as degassing analyses (e.g Stevenson and Blake, 1998). Mechanisms that can control the formation of magma chambers are still not fully understood (Menand, 2011). However, field studies suggest that many of chambers form from the accumulation of horizontal intrusions, sills (Barnett and Gudmundsson, 2014; Gudmundsson, 2011a). Field and geodetic studies also suggest that that many and perhaps most magma chambers have approximately a sill-like geometry (Gudmundsson, 1986a, Burchardt and Gudmundsson, 2009; Camitz et al., 1995;

Gudmundsson, 2012; Yun et al., 2006). Other geometries such as spheres and oblate and prolate ellipsoids do, however, occur (Gudmundsson, 1986a; Hickey et al., 2013; Lipman, 1997; Menand, 2011; Parks et al., 2012). The shape of the shallow magma chamber and the regional tectonics and boundary condition) dictate the local stress field around the chamber and the associated volcanic system.

In volcanology, magma chambers are mostly approximated as spheres, or as small pressure points, when modelling volcano deformation (Anderson, 1937; Mogi, 1958; Parks et al., 2012; Sturkell et al., 2006b). These types of models are used to provide an estimation of the pressure and volume changes – and thus the amount of magma leaving the chamber - as well as constrain depth ranges of magma chambers (Manconi et al., 2007; Masterlark, 2007). These crude approximation models are considered useful partly because of the crust acts primarily with linear elasticity. Therefore, any significant pressure changes the stresses of the surrounding rocks, and these stresses are represented instantaneously as a surface ground deformation (Segall, 2013).

Many scientists challenge the notion that magma chambers exist as bulk magma volume reservoirs. Instead, they are more in favor of complex models (Cashman and Giordano, 2014). To form a large sustained eruption and a potential collapse caldera, however, magma chambers must exist in sufficient volume at shallow depth (Gudmundsson, 2012). The exact stress and mechanical conditions required to form an eruption are not known in exact detail; thermal degradation and thermal diffusion may play a role (Annen, 2011; Gregg et al., 2012) as well as mechanical anisotropy and heterogeneity (Gudmundsson and Philipp, 2006) of crustal host rocks.

1.1.2 Dikes, inclined sheets, and ring-faults/dikes

Rupture of a magma chamber can result in different types of fractures, primarily the injection of a dike, a sill, an inclined sheet, and a ring dike. Dikes, sills and inclined sheets are magma-driven fractures that propagate perpendicular to the minimum compressive (maximum tensile) principal stress σ_3. As the consequence, magma does not propagate vertically in many cases, instead favoring an inclined trajectory – as an inclined sheet - towards the surface (Gautneb and Gudmundsson, 1992; Figure 1.1) Sheet intrusions that dip less than around 75° are generally known in

volcanotectonics as the inclined sheets or cone sheets. It is possible in some cases to estimate crudely the location of the shallow magma chamber based on condition and measurement of collection of inclined cones (Gautneb and Gudmundsson, 1992), assuming that the attitude of magma driven propagation does not change significantly from its initiation direction (Gudmundsson and Phillip, 2006).

Most measured dikes are recorded are non-feeders. This means these intrusions did not reach the surface (Geshi et al., 2010; Gudmundsson, 2011a; Hooper et al., 2011; Pollard, 2010) but became arrested or stalled inside the volcanic zone/volcanic edifice to form a pure intrusions rather than providing magma for an eruption (Gudmundsson and Philipp, 2006). The dike propagation paths are much affected by the complexity of volcanic stratigraphy and tectonic relation so that numerical models on magma propagation in various settings are important to map out the possible paths.

Ring-faults are bound piston-like calderas The observed boundary of such calderas is a topographic boundary, with exposed fault walls of common height of tens to hundreds of metres (Hartley and Thordarson, 2012; Wilson et al., 1994). Therefore, caldera fault geometry at depth must be inferred from geophysical studies (e.g Saunders, 2001), or analogue (e.g Acocella, 2007) and numerical studies (e.g Gray and Monaghan, 2004) studies. In some cases the ring-fault is well exposed in deeply eroded fossil calderas. In fact, much understanding of caldera processes comes from studies of ancient and eroded systems in the United States of America (Lipman, 1984), Iceland (Gudmundsson, 1987a), and Scotland (Branney, 1995).

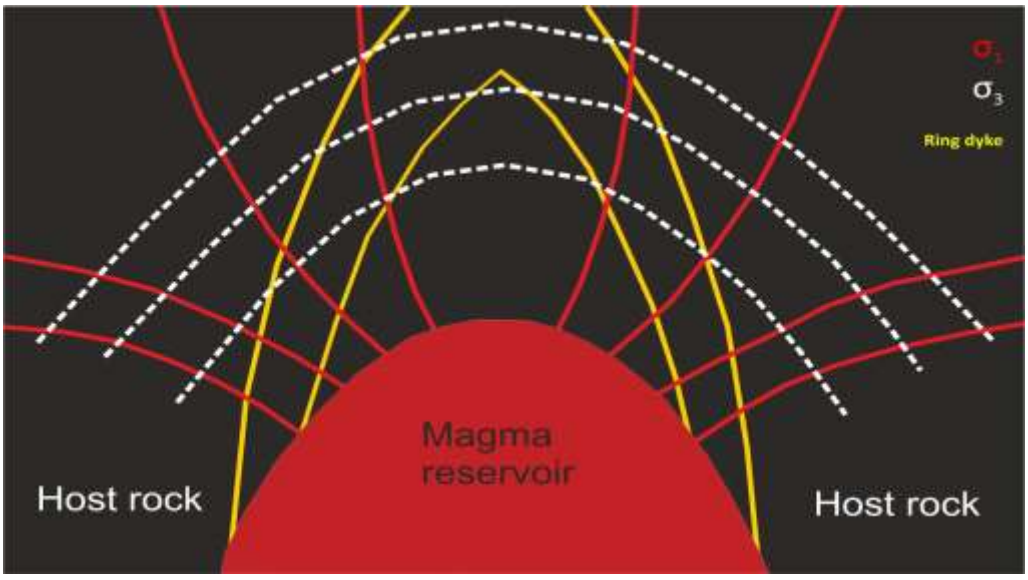

Figure 1.1: Traditional model for the formation of ring- dikes (outward-dipping, yellow lines) based on

Anderson's (1937) analytical solution. Trajectories of maximum tensile principal stress, σ_3, as dashed white lines, and maximum compressive principal stress, σ_1, as solid red lines. Those red lines indicate the likely direction of magma propagation in this simple example, modified after Gudmundsson and Nilsen, 2006.

Analogue model is one of the important ways of understanding the geological processes.. Analogue models suggest that collapse occurs mainly on reverse faults, with some contribution from normal faults (Acocella, 2007). However, the results depend of course on the boundary conditions. When the pressure change is only in the shallow chamber, then reverse faults normally form. When the pressure changes I also, or mostly, in a deep-seated reservoirs acting as source for the shallow chamber, then either normal faults or reverse faults may form. This is in agreement with numerical modelling which seem to suggest both reverse (Holohan et al., 2015) and normal (Gudmundsson and Nilsen, 2006) ring-fault faults, depending on the numerical and analytical modelling technique implemented (Geyer and Marti, 2014; Gudmundsson, 2016). As is well known however, dikes and inclined sheets are predominantly mode I fractures which require a magmatic overpressure in excess of the tensile strength of the host rock to propagate. The mechanics of dike formation was initially addressed by Anderson (1936) but has subsequently by discussed and analysed by many (e.g., Gudmundsson, 2011a, 2012)

1.1.3 Sills

Sills are relatively easy to interpret on seismic images, as they have a high acoustic contrast and thus show up as strong reflectors (Planke et al., 2005). Sill emplacement generates local stresses in the host rock. For example, Gudmundsson and Lotveit (2012) show how a saucer-shaped sill creates stresses in a sedimentary basin and select their paths depending on layering and local stresses (Fig. 1.2). This sill has caused the stress to concentrate in the upper layers, compared with a planar straight sill. If more stress is created during the growth of the sill, it will increase fracturing in the above layers. It thought that saucer-shaped sills tend to occur at shallow depths. Depth and timing of emplacement are factors that are investigated in detail in this study, which also show cooling joints as a main internal structure (Fig. 1.3).

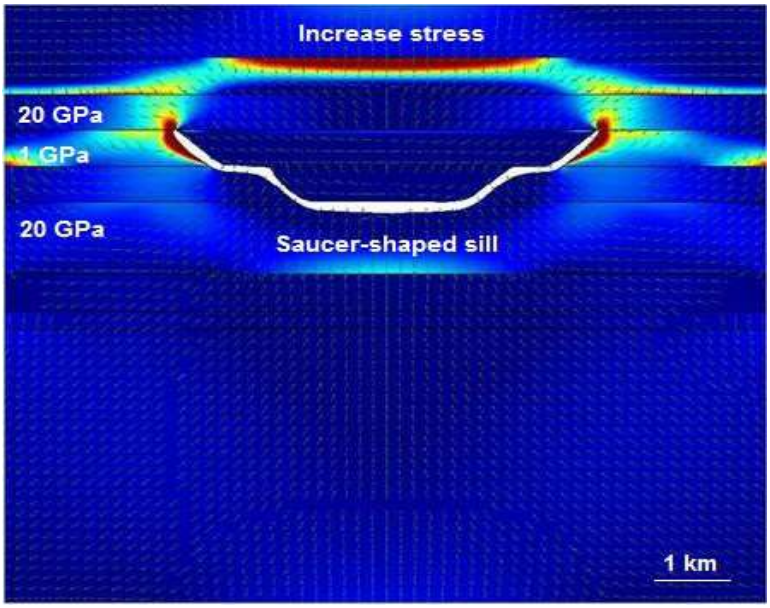

Figure 1.2 Multiphysics COMSOL model showing a saucer-shaped sill emplaced in various layers of stiffness 1GPa (soft) and 20GPa (stiff). Over pressure five MPa. (Modified from Gudmundsson and Løtveit, 2012).

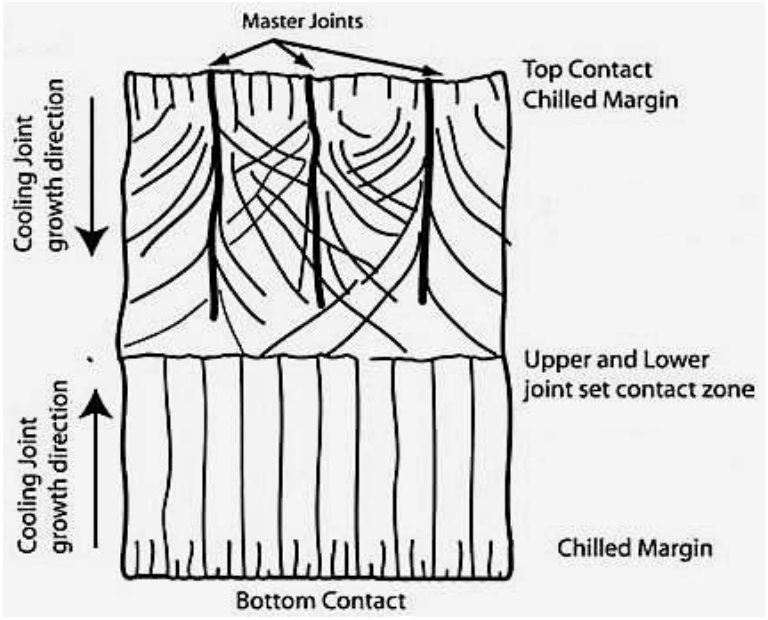

Figure 1.3 - Schematic showing the jointing inside cooling joint which their formation shows they have been from a horizontal intrusion or a sill (Modified from Rateau et al, 2013).

There are quite a few measurements missing in the collected data on sills, because some areas lack 2D/3D seismic data or any observations, meaning some basins do not have a recorded sill thicknesses or lateral dimensions. Sills are divided into small or large, depending on whether their lateral dimension is smaller or larger than their depth (Gudmundsson and Løtveit, 2012). When the diameter of sill is larger than its depth below the surface, it considered a large sill (Gudmundsson and Løtveit, 2012; Sydnes et al., 2018).

A common aspect of sills is that they change the geothermal gradient (Aarnes et al, 2010; Eide et al, 2016; Petford and McCaffrey, 2003; Syndes et al, 2018). This also

true when considering if a sill is part of a cluster of sills. The impact of clusters is presented in Chapter 2 through COMSOL models. Sydnes et al (2018) imply that sills over 50m in thickness will influence a sedimentary basin thermally. The sills can substantially influence maturation of organic matter, but timing is an important issue (Sydnes et al, 2018).

1.1.4 Fault zones

Our understanding of the physical properties of fault zones, especially permeability, heterogeneity, and local stresses is still very incomplete (Wimberley et al., 2008; Gudmundsson et al., 2010). Field studies of onshore fault systems and their internal architecture provide the basis for understanding of the fluid flow along and across fault zones. It is now well-established that fault zones have a complex internal structure, whose primary units are fault core and fault damage zone (Caine et al., 1996; Gudmundsson et al., 2010). Therefore, modelling faults as single cracks or dislocations is generally regarded as an oversimplification. The internal hydromechanical structure of the fault zone is known to affect permeability and fluid transmissivity across fault zones. However, it is also important to understand crack-to-crack interactions and the effects of segment linkages. Yet these pose limitations in understanding the local stresses around and within fault zones, which in turn determine displacement and fracture development and permeability along and traverse a fault plane.

General fault zone models show that fault zones are composed of two main hydromechanical units: low-permeability granular fault core, normally providing a barrier to across fault flow, and a higher-permeability fault damage zone adjacent to the core and providing a conduit for a long-fault flow (Caine et al. 1996). Whether or not each of these units are present at every location along the fault zone, and how important they are, depends upon various factors such as host lithology and displacement, which help to understand whether a given fault can act as a lateral barrier to fluid flow, a fault-parallel conduit, or both. A fault damage zone can commonly be divided into subzones because of its internal heterogeneities (Fig 1.4). More specifically, fault damage zones can be sub-divided into zones according to variations in fracture density or frequencies in the damage zone. Fig. 1.4 illustrates

three mains subzones within a 2D modelled normal fault. Increasing fracture density shows reduces rock strength of the fault zone rocks as well as effective permeability. Its intrinsic properties can be modelled according to fracture density and associated permeability. The core is the structural, lithological and morphological portion of the fault where much of the displacement is accommodated (Caine et al., 1996). The core usually found in the center and thicknesses may extend up to tens of meters in large fault complexes (Fig 1.5).

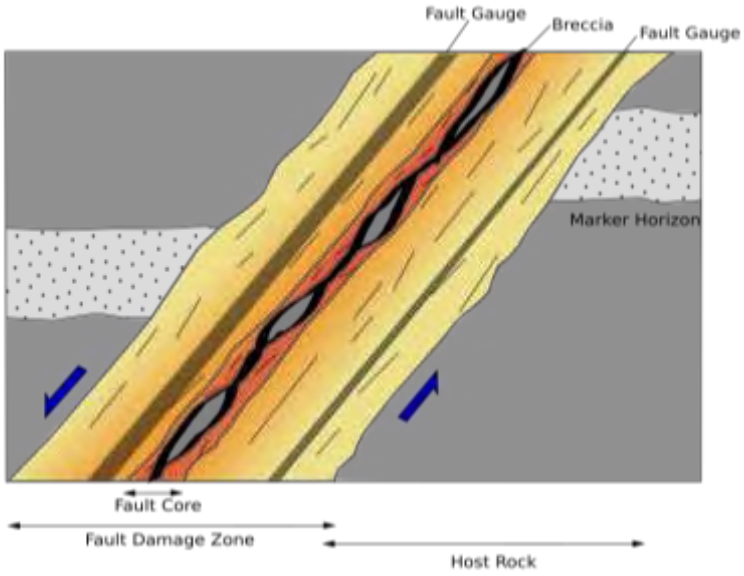

Figure 1.4: A conceptual 2D model of the hydromechanical units of a fault zone.

Figure 1.5 Field examples of fault cores (a) Clay smear taken from Miri, Malaysia (taken by Van der Zee & Urai, 1998) (b) Fault gouge from Jiaojia fault, China (taken by Monash University, 2015) (c) Fault breccia from Upper Kimmeridge Clay, UK (West, 2014)

Although phyllosilicates of rich cores is characterized by extremely low permeability during seismogenic slip (during high strain rates) the core act as brittle resulting in fracturing and increased permeability, which then gradually decreases (due to compaction and secondary mineralization). In the core there are thus commonly numerous mineral veins and amygdales spaced at mm to cm forming dense networks. Hydrothermal fluids precipitate within fault core cavities and internal fractures and lithify the core during interseismic period (Caine et al., 1996). The

granular media nature of the core is the reason of modelling core as a porous medium (Fig 1.6).

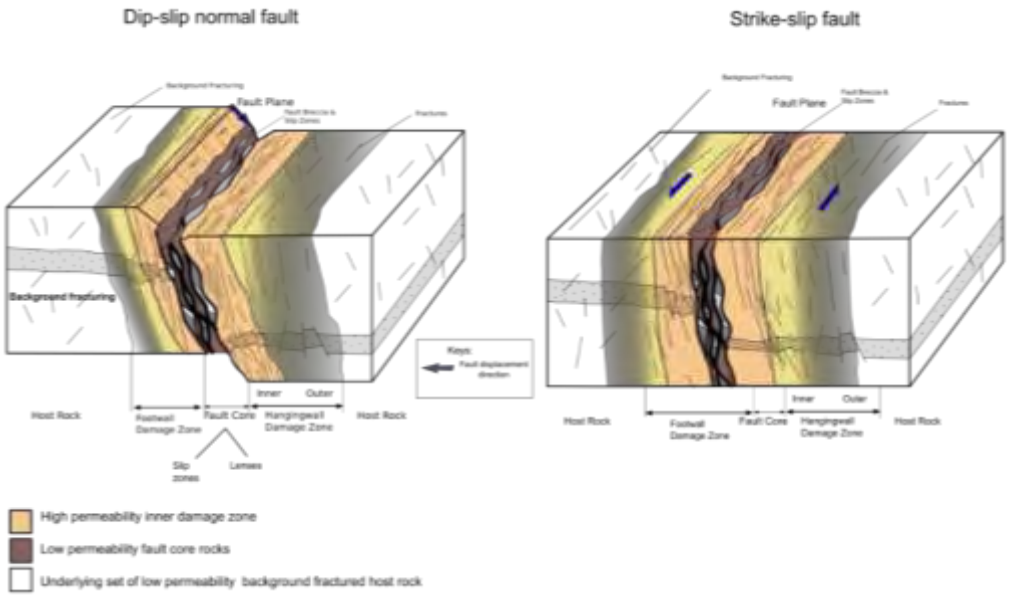

Figure 1.6: Schematic illustration of two fault zone models proposed according to its displacement attitude in siliclastic rocks (modified from Berg, 2011). Fault core includes the slip surfaces, intensely crushed and deformed rocks as well as lenses of undeformed rocks. The damage zone includes small faults and deformation bands. Note low permeability fault rocks within core and the high permeability host rock due to background fracturing.

Several models have been proposed for dynamic fault zones structures. Field observation shows differences in fracture frequencies across faults in different tectonic regimes. For dip-slip faults, there is damage zone asymmetry on either side of the fault plane (Fig. 1.6), but normally not for strike-slip faults (Fig. 1.7). The fault zone models investigated are symmetric strike slip and asymmetric dip slip faults. With continual growth and displacement, core and damage zone become thicker (Fig. 1.7). Thus increasing the volume core materials (with lower mechanical strength) as the process zone gradually becomes part of the core and damage zone (Gudmundsson, 2011a). Increased volume of core results in greater energy requirement to allow propagation of fractures through the fault zone.

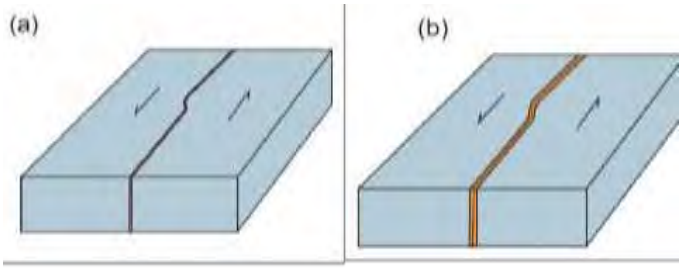

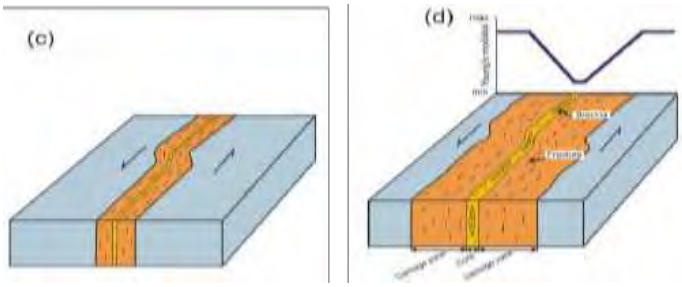

Figure 1.7 Evolution of the fault damage zone as a function of increasing displacement on the fault (Gudmundsson, 2011a). The damage zone becomes gradually thicker. If the damage zone mechanical properties vary linearly with distance from the core, the variation in Young's modulus may be as shown here.

(Figure 1.7). Increase in volume results in increase in energy dissipated through micro-cracking and/or plastic deformation before and during any major fault slip and thus increasing material toughness within the fault zone. Fracture development starts from mechanical interaction and linkage between smaller segments; once linked the faults gradually behave as a larger continuous structure up to tens, sometimes hundreds, of kilometres in length. The growth, linkage and propagation of fractures is influenced on a variety of parameters such as the mechanical properties of the rocks, the arrangement of the initial segments within the host rock, the velocity at which the fractures propagate, and the remote differential stress field (Gudmundsson, 2011a).

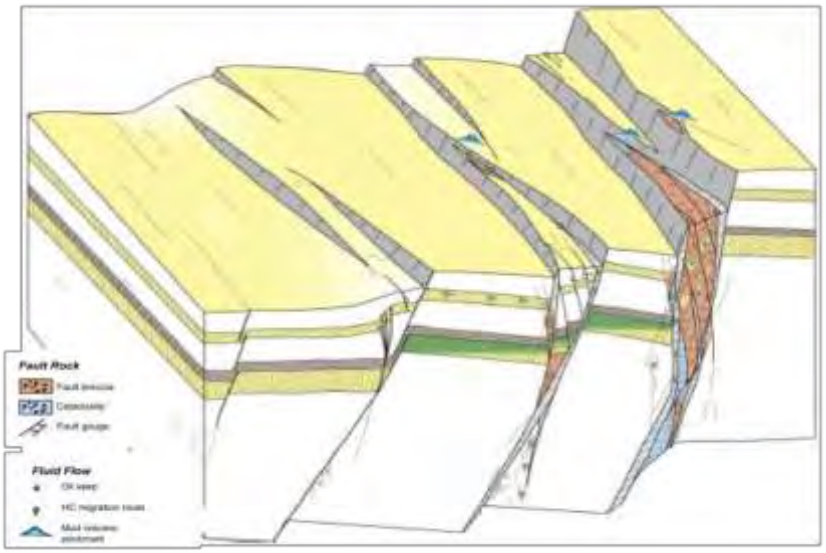

Figure 1.8: Conceptual model of a complex fault zone which shows complex interaction of mechanical, hydraulic and chemical processes and the permeability variation across fault zones (from Martel, 1990).

Material toughness may be higher for fracture propagation in fault zones with comparatively low Young modulus. This follows because more energy is commonly needed to propagate a fracture within a comparatively compliant fault zone than in a stiffer zone. The toughness, however, depends on discontinuities in the fault zone as

well (Gudmundsson et al., 2010). Generally, the fault zone has a greater toughness than the stiff protolith host rock. (Fig 1.8).

1.2 Numerical modelling

Numerical models are normally use for simulating physical problems and for solving complex equations when the analytical solutions cannot be obtained or are too complex. For example, commonly when these are nonlinear parts or terms in the equations, it is almost impossible to solve the associated problems with analytical methods. The numerical software used here (COMSOL Multiphysics versions 5.1) is a commercial software which is extremely well tested and benchmarked (e.g Hickey & Gottsmann, 2014) for solving problems in fluid and solid mechanics as well problems in heat transfer. These are problems that commonly occur in many fields of geology, in particular in volcanology and structural geology/tectonics.

In Chapter 2 I provide the constitutive equations that are used in the software to solve problems numerically and discuss their limitations and assumptions. Stress solution comparisons are also discussed with respect to previous published studies and field observation to show the consistency of results throughout the process. All numerical modelling in the thesis and the papers presented as part of this thesis were conducted using the commercial finite element code within COMSOL Multiphysics versions 5.1 (www.comsol.com). All the basic solid mechanics models in the thesis use the 'Structural Mechanics' module which solves the Navier-Cauchy equations. This set of equations provide linear elastic stresses and displacements as a result of pressure or displacement boundary conditions.

In this thesis, I used numerical modelling to investigate fracture formation, propagation, linkage, arrest, and fluid transport, as well as heat flow, heat transfer and material deformation, as discussed further in Chapter 2. Here I use geometries directly from field data which, together with well-tested theoretical models, can be used to explore the effects of fluid pressure and mechanical properties of rocks on local stresses induced by fluid-filled fractures such as dikes . All fractures modelled in this thesis are fluid-driven fractures opened by fluid overpressure (pressure above or over the normal stress on the fracture, which for mode I cracks or extension fractures, is σ_3, the minimum principal compressive, or the maximum tensile, stress).

1.2.1 Finite element method development and its applications in geosciences

The finite element method has been known as a very powerful and successful numerical softeware in modeling a variety of engineering phenomenon for many decades. Its applications is to fields such as general mechanical problems, fracture mechanics, fluid dynamics, nano-structures, electricity, chemistry, civil engineering, and material science. Despite of great capabilities of the classic finite element method, it has its limitations that initiate from the basic assumptions employed in the mathematical development of its framework: the continuity. This presumption includes any kind of variations, from property changes or external changes of boundary conditions.

Limitations of classic FEM are not generally critical. Many of these are handled by imposing the requirement of meshing alignment to the simulation process. This approach is useful for cases where no variation take place in time – where the modelling is not a function of time. However, interface evolution is quite common in wide group of problems. In classic finite element framework special algorithms are available for such cases, but they are cumbersome to develop and highly time-consuming to use. Issues involved in the classical finite element approach made researches look for replacement methods. A step forward was the introduction of partition of unity finite element method (PUFEM) devised based on research work by Melenk and Babuska (1996). In their work, the concept of partition of unity method is employed in order to omit the need for continuity by enhancing the solution field with discontinuous functions (Fig 1.9).

In the work of Belytschko and Black (1999) a minimal re-meshing finite element method for crack growth is presented, where discontinuous enrichment functions are added into the finite element approximation to account for the presence of the crack. This method allows for cracks of arbitrary align or orientation within the mesh. Yet for severely curved cracks, re-meshing is needed for zones away from the crack tip. Moës et al. (1999) presented an improvement of the previous methods for modeling the crack growth problem. In this study, the standard displacement-based approximation is used. It is enriched near a crack by incorporating both discontinuous fields and near tip asymptotic fields through a partition of unity method. This

technique successfully allows the entire crack to present independently of the mesh, resulting in re-meshing being unnecessary during crack growth. Dolbow (1999) developed the applications of the extended version in multiple aspects (Fig 1.9). In particular, Dolbow et al. (2000a, b) represented the specific examples of fixed cracks and crack growth in two-dimensional elasticity and Mindlin-Reissner plate theory. In their studies they used both a jump function and the asymptotic near tip field function. Dolbow et al. (2001) also presented an XFEM algorithm for modeling crack growth with frictional contact, the frictional contact being formulated as a non-smooth constitutive law on the interface formed by the crack faces, and the iterative scheme implemented in the LATIN method is applied to resolve the nonlinear boundary value problem. Also, Daux et al. (2000) presented arbitrary branched and intersecting cracks modeling with the extended finite element method.

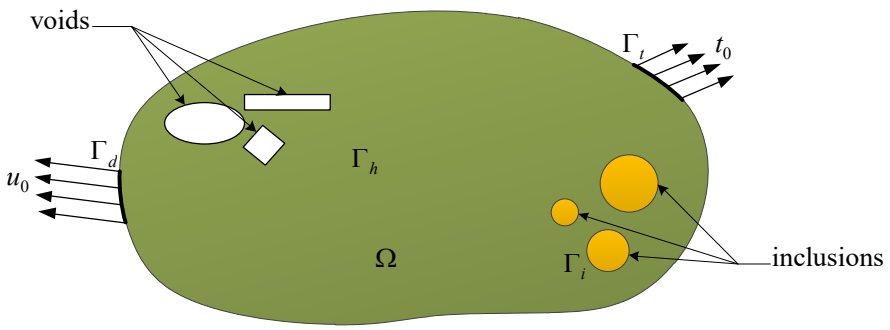

Figure 1.9 Rigid body with internal voids and inclusions.

An extended finite element, so named by Dolbow (2000), has been widely employed in various engineering applications. In what follows a comprehensive review of the extended finite element method is provided, with more extended discussion later in the thesis. Some reviews have been provided by Moës and Belytschko (2002a), Karihaloo and Xiao (2003), Bordas and Legay (2005), Rabczuk and Wall (2006), Belytschko et al. (2009), Fries and Belytschko (2010), and Natarajan (2011). Mohammadi (2008) published a book on extended finite element method for fracture analysis of structures, which was used as a reference for XFEM review until 2008. A more recently published XFEM book is also available by Mohammadi (2012) on fracture analysis of composites, which used as reference, too.

The extended finite element method was developed to ease modeling of weak or strong discontinuities. It is evident that the conFiguration of the interfaces, whether of material discontinuity type or domain discontinuity type, plays a decisive role in

numerical simulations by XFEM. A successive framework developed mainly for handling the interfaces is the Level Set Method (LSM) suggested by Osher and Sethian (1988). This method is well known as a simple and versatile method for computing and analyzing the motion along an interface. The important role of interfaces made XFEM researchers take advantages from this framework, namely LSM, in their simulations. Stolarska et al. (2001) presented first implementation of the LSM in extended finite element framework. In this study the modeling of crack propagation, which requires interface evolution, performed by employing the LSM (Fig 1.10).

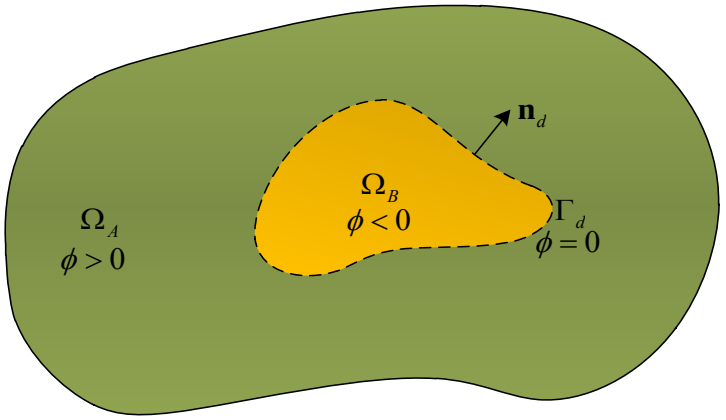

Figure 1.10 The level set method- definition and nomenclature.

Sukumar et al. (2001) utilized LSM in modeling of holes and inclusions. Ventura et al. (2002) introduced vector level sets for description of propagating crack in finite element. They modeled arbitrary discontinuities in space-time finite elements by level sets and XFEM (2004). Legay et al. (2006) proposed an Eulerian-Lagrangian method for fluid-structure interaction based on level sets. Zunino (2013) presented the analysis of backward Euler/extended finite element discretization of parabolic problems with moving interfaces. Stolarska and Chopp (2003) studied thermal fatigue cracking in integrated circuits by level sets in XFEM. These definitions were extensively used during my first year as a PhD student, but are now mostly a part of the published work and discussed in Appendix 1. The use of LSM is not limited to two-dimensional problems. Moës et al. (2002a) studied non-planar 3D crack growth by the extended finite element and level sets. In a similar research by the same team (2002b), level set updates studied (part II). The LSM utilized to model intersecting interfaces. Zie et al. (2004) employed the LSM for developing a method for modeling multiple crack growth with applications to fatigue cracks. Improvement to LSM is the fast-marching method (FMM) introduced by Sethian (1996) (Fig 1.11).

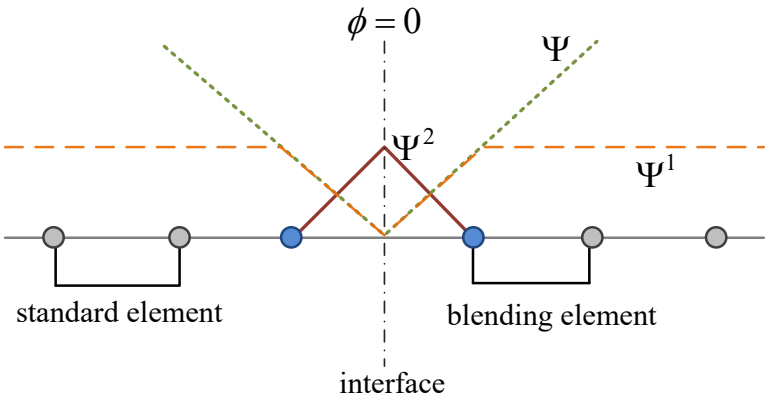

Figure 1.11 Various choices for Ramp enrichment function.

The main advantages of FMM to LSM are greater performance resulting from simplifications considered in implementation of the algorithm. First utilization of FMM in XFEM was by Sukumar et al. (2003) for modeling three-dimensional fatigue crack propagation.

1.2.2 Finite elements for linear elastic fracture mechanics (LEFM)

Elastic crack propagation has been the most common subject in XFEM research. Here I present a comprehensive review on research in this domain. Belytschko and Black (1999) presented a minimal re-meshing finite element method for crack growth, where discontinuous enrichment functions are added to the finite element approximation to account for the presence of the crack. Moës et al. (2000) developed an improvement of the previous method for modeling the crack growth problem, where the standard displacement-based approximation near a crack is enriched by incorporating both discontinuous fields and near-tip asymptotic fields through a partition of unity method. Stolarska et al. (2001) introduced an algorithm which couples the LSM with the extended finite element method to model crack growth. In this study, the LSM is used to represent the crack location, including the location of crack tips. Sukumar and Prevost (2003) described the implementation of the XFEM within a standard finite element package called Dynaflowe, which is used by Huang et al. (2003b) to present numerical solutions for the stress intensity factor for crack problems and conducting crack growth simulations. Stazi et al. (2003) presented a method for LEFM (Linear Elastic Fracture Mechanics) using enriched quadratic

interpolations, in which the geometry of the crack represented by a level set function interpolated on the same quadratic finite element discretization. Lee et al. (2004) represented a combination of the XFEM and the mesh superposition method (s-version FEM) for modelling of stationary and growing cracks. In this study, the near-tip field modeled by superimposed quarter-point elements on an overlaid mesh and the rest of the discontinuity described by a step function on partition of unity, where the two displacement fields are matched through a transition region.

Advanced issues in LEFM have been addressed by many. Réthoré et al. (2005) proposed an energy-conserving scheme of the XFEM to model dynamic fracture and time-dependent problems from a more general point of view, which gives a proof of the stability of the numerical scheme in the linear case. Later, Menouillard et al. (2006) introduced a lumped mass matrix for enriched elements, which enables one to use a pure explicit formulation in XFEM applications. Chahine et al. (2006) also presented a convergence result for a variant of the XFEM on cracked domains by using a cut-off function to localize the singular enrichment area. Moës et al. (2006) studied the imposition of Dirichlet-type conditions within the XFEM. In this research, a strategy to impose Dirichlet boundary conditions is introduced, while preserving the optimal rate of convergence. Rabinovich (2007) developed a new computational tool for the accurate detection and identification of cracks in structures, to use in conjunction with non-destructive testing of specimens. Xiao and Karihaloo (2007) implemented hybrid crack element (HCE) on a general FE mesh and incorporated it into commercial FE packages. Furthermore, they show how to couple the HCE with the extended/generalized finite element method.

Extension of XFEM to new cases has been the target of some other investigations. Asadpoure et al. (2006) proposed an extended finite element method for modeling cracks in orthotropic media. Next Asadpoure and Mohammadi (2007) developed new enrichment functions for crack simulation in orthotropic media by using the extended XFEM. Motamedi and Mohammadi (2010b) investigated dynamic crack propagation in composites based on development of orthotropic enrichment functions within the framework of partition of unity and the XFEM.

Three-dimensional fracture mechanics has been extensively studied. For example, in a study using an extended finite element method for three-dimensional crack modelling where a discontinuous function and the two-dimensional asymptotic crack-tip displacement fields added to the FEM Moës et al. (2002) represented

branch functions, which include asymptotic near-tip fields that improve the accuracy of the method. Also, Legrain et al. (2005) studied the application of the XFEM to large strain fracture mechanics for plane stress problems, specifically for rubber like materials. Furthermore, Ahyan (2007) presented a three-dimensional enriched finite-element methodology to compute stress intensity factors for cracks contained in functionally graded materials (FGMs).

Subsequently, Sukumar et al.(2008) proposed a numerical technique for non-planar three-dimensional linear elastic crack growth simulations. In this study, a technique of coupling the XFEM and the fast marching method (FMM) was used. Park et al. (2009) developed a mapping method to integrate weak singularities, which results from enrichment functions in the generalized/extended finite element method and is applicable to 2D and 3D problems including arbitrarily shaped triangles and tetrahedra. Fries and Baydoun (2012) presented a method for two-dimensional and three-dimensional crack propagation that combines the advantages of explicit and implicit crack descriptions. Later they extended this study to develop a propagation criterion for three-dimensional fracture mechanics. Minnebo (2012) presented three-dimensional integration strategies of singular functions introduced by the XFEM in the LEFM, where an adapted method proposed to treat these cases efficiently. Golewski et al. (2012) created a new 3D numerical model for compact shear specimens (CSS), used for experimental testing of the mode II fracture by using XFEM. This study investigates concrete samples containing siliceous fly-ash additive. Benvenuti (2012) represented the relationship between the Fourier transform of the weight functions and exploited the accuracy of the regularization procedure in 3D problems. González-Albuixech et al. (2013a) introduced the curvilinear gradient correction based only on the level set information used for the crack description and the local coordinate system definition. Pathak et al. (2013) presented a simple and efficient XFEM approach in which the crack front divided into a number of piecewise curve segments to avoid an iterative solution. Holl et al. (2013) presented a new multiscale technique to investigate advancing cracks in three-dimensional spaces. This technique is designed to take into account cracks of different lengths and is applicable, for example, to gas turbine blades. Multiple cracks and branching have been an attractive topics for some other researchers (Fig 1.12).

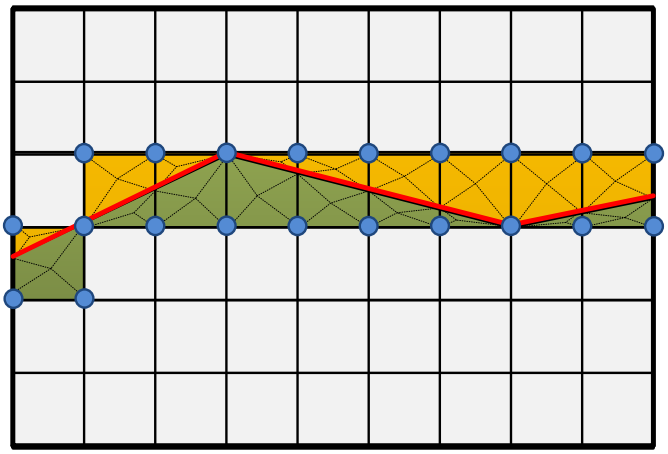

Figure 1.12 The triangular partition method show the diving one element into two after fracture had propagated in the element. The red line is the fracture, top and bottom sides are two new elements with new mesh after propagation.

Budyn et al. (2004) developed a method for multiple crack growth in brittle materials without re-meshing, which also treats the junction at the cracks. Zi et al. (2004) extended this study so as to analyze the growth and the coalescence of cracks in a quasi-brittle cell containing multiple cracks. Loehnert and Belytschko (2007) investigated the effect of crack shielding and amplification of various arrangements of microcracks on the stress intensity factors of a macrocrack, including large numbers of arbitrarily aligned microcracks. Mousavi et al. (2011a, b) presented a higher-order XFEM with harmonic enrichment functions for complex crack problems. Elguedj et al. (2009) represented a generalized mass lumping technique for explicit dynamic formulation in extended finite element framework. In a following work, Gravouil (2009) presented a general explicit time integration scheme for dynamics simulations using the XFEM with standard critical time step. Panetier et al. (2010) presented a method that leads to strict and high-quality local error bounds in the context of fracture mechanics.

Shen and Lew (2010a, b) introduced a variant of the XFEM rendering an optimally convergent scheme. They demonstrated the optimal convergence of a discontinuous-Galerkin-based XFEM for two-dimensional linear elastostatic problems of cracked domains (2010b). Menouillard and Belytschko (2010a, b) described a correction force to modify the forces smoothly release the tip element while the crack tip travels through the element. In another study by the same team, dynamic fracture with mesh-free enriched XFEM represented, where the mesh-free approximation used as enrichment in a cluster of nodes around the crack tip to improve accuracy (Fig 1.13).

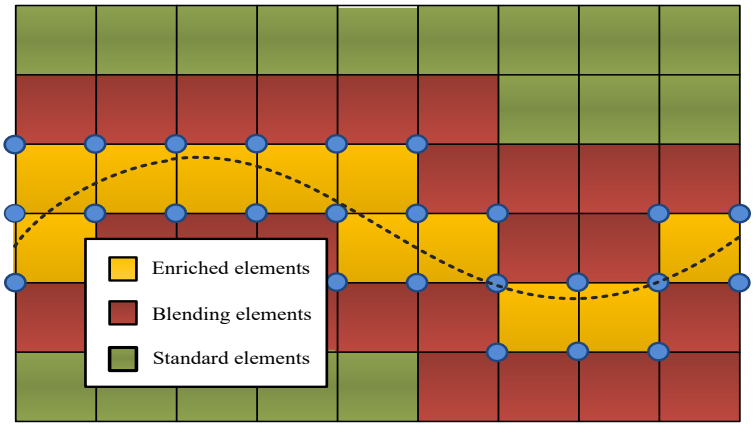

Figure 1.13 The blending element definition, the dotted line is the propagated fracture.

Dhia and Jamond (2010) used the Heaviside enrichment function within the Arlequin framework further reduce the costs of crack propagation simulations. Ródenas et al. (2010) introduced a recovery-type error estimator yielding upper bounds of the error in energy norm for LEFM problems. Mousavi and Sukumar (2010) presented new Gaussian integration scheme, which is efficient and accurate for the evaluation of weak-form integrals. Gauss-like quadrature rules constructed over arbitrarily shaped elements in two dimensions without the need for partitioning. Menouillard et al. (2010) proposed a new enrichment method with a time dependent enrichment function. Legrain et al. (2011) described the use of the XFEM in the context of quadtree/octree meshes, where attention have been paid to the enrichment of hanging nodes that inevitably arise with these meshes and an approach for enforcing displacement continuity along hanging edges and faces is proposed.

Bordas et al. (2011) extended strain smoothing to higher order elements and to investigate numerically in which condition strain smoothing is beneficial to accuracy and convergence of enriched finite element approximations. Shibanuma and Utsunomiya (2011) evaluated the reproductions of the prior knowledge in the original XFEM and the PUFEM-based XFEM for the crack analysis. They show that the method reproduced over the entire enrichment in the PUFEM- based XFEM. Liu et al. (2011) developed a higher-order XFEM based on the spectral element method for the simulation of dynamic fracture where the numerical oscillations suppressed, and the accuracy of computed SIF and crack path also improved. Prange et al. (2012) presented a simple recovery-based error estimator for the discretization error in XFEM-calculations for cracks, where enhanced smoothed stresses incorporating the discontinuities and singularities recovered to enable the error estimation (Fig 1.14).

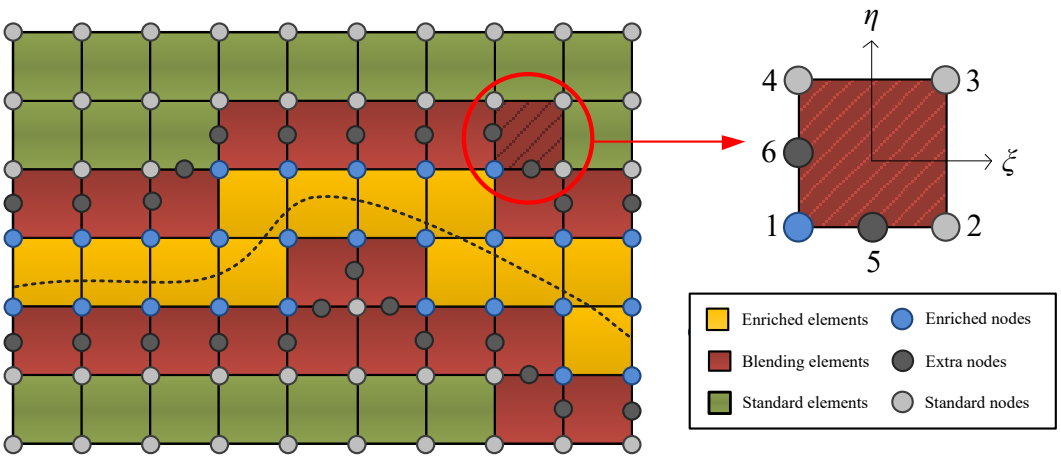

Figure 1.14 Hierarchical blending element approach. This element is between standard and blending elements condition, elements with three corners with standard nodes and one with enriched node is treated this way, there are common in bended fracture propagation paths.

Byfut and Schröder (2012) discussed higher-order XFEMs obtained from the combination of the standard XFEM with higher-order FEMs. Methodologies necessary for hp-adaptivity in XFEM, which allow for exponential convergence rates, are summarized. González-Albuixech et al. (2013b) studied the convergence rates achieved with domain energy integrals for the computation of the stress intensity factors (SIF) when solving 2-D curved crack problems with the XFEM. Ródenas et al. XFEM had developing and worked with other numerical methods, too. Legrain (2013) approach a NURBS as an enhanced XFEM for the unfitted simulation of structures which geometry has been defined by means of CAD parametric surfaces (mostly for complicated geometries and 3D, I have some CAD imported geometry modeling in COMSOL with XFEM in fluid flow section).

Blending issues have been of great interest in XFEM simulations. Gracie et al. (2008b) studied a patch-based version of the discontinuous Galerkin (DG) formulation, which decomposes the domain into enriched and unenriched subdomains. (2009) proposed enhancing the blending elements by adding hierarchical shape functions, which permits compensating for the unwanted terms in the interpolation. This method of processing is an extension to the study by Chessa et al. (2003a) to fracture mechanics problems. Chen et al. (2012) had illustrated employing the edge-based strain smoothing (ESm-XFEM) which works for linear elastic crack growth. Edge-based smoothing (ES) relies on some generalized smoothing operation over smoothing domains associated with edges of simplex meshes, and produces a softening effect leading to a close-to-exact stiffness, solutions. Fries (2007) shows that there would be no problems in blending elements by presenting the corrected XFEM approximation. The enrichment functions modified such that they are zero in the

standard elements, unchanged in the elements with all their nodes being norm using enriched and varying continuously in the blending elements (Fig 1.15).

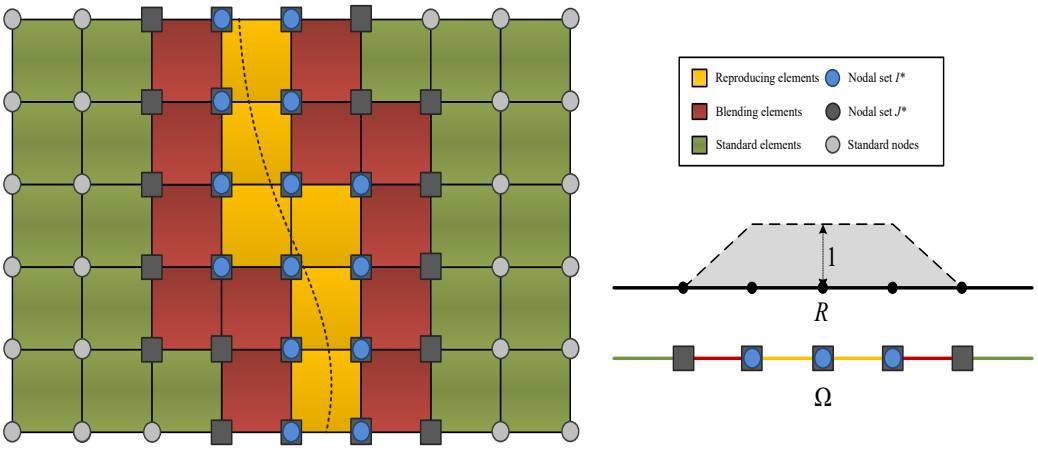

Figure 1.15 Weighted extended finite element method showing when there is a node that got enriched from three different elements during calculation, these nodes are happening when the cracks is start to curve its way to another direction

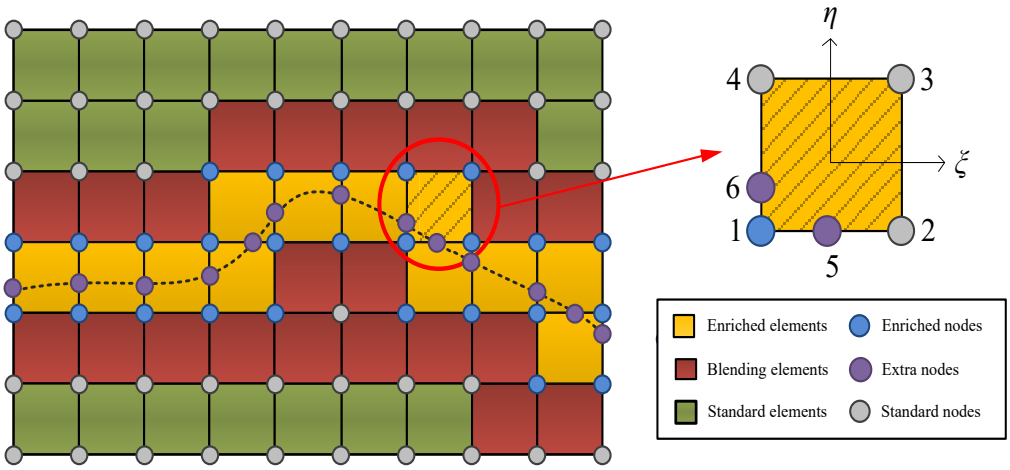

Figure 1.16 New intrinsic For elements between propagated crack and the new blending element

Ventura et al. (2009) introduced a weight function blending, where the enrichment function pre-multiplied by a smooth weight function with compact support to allow for a completely smooth transition between enriched and unenriched subdomains and a method for blending step function enrichment with singular enrichments described. Loehnert et al. (2011) presented 3D corrected XFEM approach and extension to finite deformation theory, which is a corrected version of XFEM originally presented in Fries (2008) for the 2D case, extended to 3D including different remedies. Chahine et al. (2013) replaced the transition layer of blending elements by an interface associated with an integral matching condition of mortar type for singular enrichment (Fig 1.16).

1.3 Thesis roadmap

Many of the results presented in this thesis are already published as papers, either in international journals or on conference proceedings. Other results are in preparation or in review for publication in international scientific journals. At the end there are two appendices, one of which is a publish paper which is not strictly part of my PhD thesis main topic. As 4 of the 7 results chapters have been published, I am presenting them as stand-alone works with independent page numbers. In Chapter 2 the main methodological and numerical frameworks that govern each part of the PhD study are presented. I first give an overview of analytical literature about the background of relevant to the study. Then after presenting the appropriate equations, illustrating common crack geometries and presenting the meshing.

Chapter 3, a published paper, is on dike emplacement, in particular on the effects of mechanical layering on dike-induced displacements and stresses. In the paper, I use solid mechanics and anisotropic geometry. The main idea is to understand better surface deformation and stresses induced by dikes – particularly those with upper tips at shallow depth – so as to estimate their geometries and likelihood of propagation to the surface (the hazard) better.

Chapter 4, a submitted paper, focuses on the displacements and stresses induced by inclined (cone) sheets arrested at shallow depth in a layered crustal segment. The focus is on the effects of layering, particularly one soft (compliant layer) and the variation in sheet dip.

Chapter 5 focuses on magma chamber and strike slip fault interaction in eastern Anatolia Turkey. Here the effects of fault movements on magma chamber stresses and potential dike propagation (and eventual eruption) are considered.

Chapter 6, a published paper, discusses geothermal water circulation and heat transfer in a fault zone. Basic principles of fluid dynamics and heat transfer are used in connection with permeability development of a fault zone.

Chapter 7 draws all the key findings together and evaluates in a critical manner the methods and techniques used in the thesis. I also discuss how the present work can expanded, refined and improved in the future.

2 Methodologies

2.1 Analytical models

2.1.1 Effective elastic constants

The two most commonly used elastic parameters for isotropic rocks are Poisson's ratio(v), which is negative of the ratio of transverse strain to longitudinal strain (lateral contraction to axial extension) and Young's modulus (E), which depends on rock stiffness – how much strain rock suffers for a given stress (loading) – and is the slope of the linear part of the stress-strain curve. Most rocks Poisson's ratio are within the range of 0.2 – 0.3. In this thesis, an average Poisson's ratio of 0.25 is used. Young's modulus, however, in common elastic materials, can vary by around six orders of magnitude (Gudmundsson, 2000). Note that the Young's modulus of rocks may also be different depending on the testing and geomechanical rating of rocks (Gudmundsson, 2000). The two principal methods for measuring Young's modulus (and Poisson's ratio) are dynamic and static, both of which can be made in the laboratory on small specimens and in the field tests. Several general statements made on the variation of Young's modulus of a given rock mass in the field (Gudmundsson, 2011):

- Increasing stress with increasing crustal depth increases stiffness, but this can vary a lot.
- Increasing temperature, porosity and water content all can decrease the modulus.
- Young's modulus, especially at shallow depths in seismologically active areas, tends to decrease with increasing is the fracture frequency in the rock mass.
- In-situ (field) Young's modulus (E) of rock mass is usually less than that of a laboratory sample of the same type of rock. This is due to presence of fractures and pores in the field rock.

Highly fractured rocks, like those in damage zones and cores of an active fault zones, tend to have smaller stiffness than normally fractured rocks of the same type. For a given loading, stresses within those layers with lower Young's modulus are less than the higher ones. Meaning, that the stiffer the layers are, more the loading tends to concentrate the stress in those layers while, softer layers take on very little stress. Stresses needed for propagating fractures and fault displacements depend on

stiffness variation and other factors such as layering and toughness. Rocks with many discontinuities cannot be strictly elastic; there is permanent deformation and irreversible damage after the load is removed. Fracture frequency within a host rock for effective Young's modulus of a rock mass is E_e and (Priest, 1993) is given it by:

$$E_e = \sigma_x \frac{x}{\Delta x} = (\frac{1}{E} + \frac{1}{\bar{s}k})^{-1} \quad (2.1)$$

Where σ_x is stress, E is young's modulus, K is bulk modulus, x is displacement.

2.1.2 Fracture modelling

There are several ways by which rock-fractures are described and classified (Price and Cosgrove, 1990; Twiss and Moores, 2007; Fossen, 2010;,Gudmundsson, 2011). One of the rock fractures modelling approach is to considering the ideal crack geometry, where the concept of a crack refers to the basic models in fracture mechanics. For analytical investigations, there are three ideal crack shapes or geometries (Fig. 2.1).

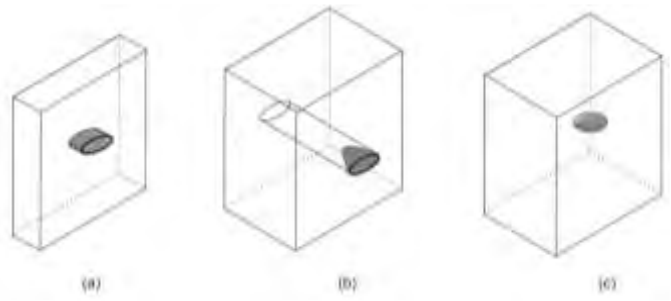

Figure 2.1 – Ideal crack geometries for fracture modelling. a) a through crack; b) a part-through crack; c) an interior crack. (Gudmundsson, 2011).

In Fig. 2.1 (a) This is through-the-thickness crack, which crack that go through the entire elastic body. The fracture then extends from one free surface or a surface in contact with a fluid to another free surface. This model is very commonly used in modeling of feeder dikes (Gudmundsson, 2011). (b) This is a part-through crack, which referred to it as a thumbnail crack also. This type of crack extends from a free surface into the elastic body. This type of crack is commonly used to model fluid driven fractures such as non-feeder dikes and induced hydraulic fractures. (c) This crack geometry is the penny-shaped crack. It also called interior crack because this crack does not terminate at any free surfaces and does not link to other cracks and entirely hosted within the elastic body with a general elliptical shape.

In addition, fractures are classified mechanically in fracture mechanics. This is according to the displacement of material, the rock walls, on the opposite sides of the fracture. There are three modes, sometimes a fourth mode is added to classification list but that is not very common. They referred to as Mode I, Mode II, Mode III and Mode IV. In civil engineering and mechanical engineering it is common to use the combination between them (Modes I and II or Modes III and I) which are called mixed-mode fractures. All fracture initiation, stress concentration, propagation and arrest for brittle materials follow the Griffith's theory (1924).

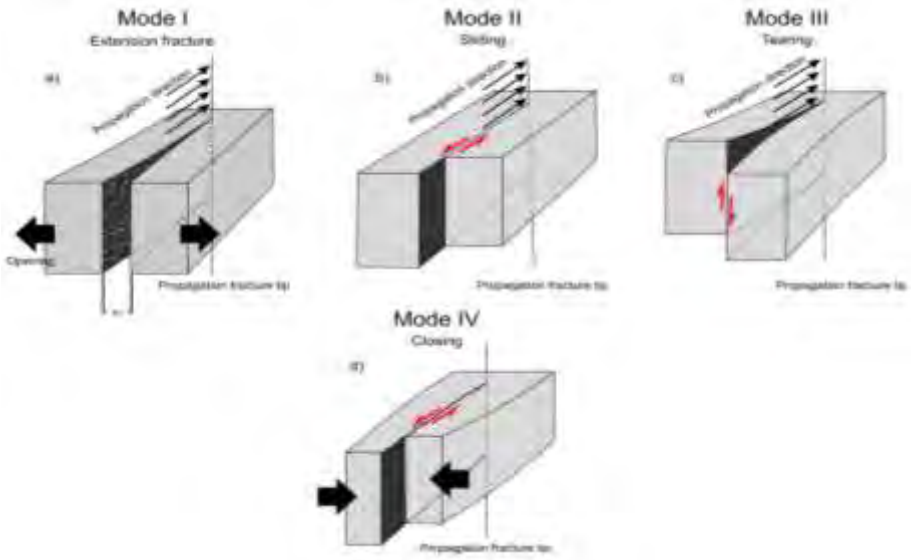

Figure 2.2 - Fracture displacement mode a) mode I fracture is an opening (extension) fracture where the displacement is perpendicular to the walls of the crack as it propagates in direction to the tip of the fracture. It is in generally used to model tension fractures and fluid driven fractures, including dikes, sills, and many mineral veins. B) Mode II is also called sliding fracture, in plane or forward shear mode. It occurs through the sliding of the walls or surfaces over one another in direction perpendicular to the tip or tip line of the crack (e.g. dip-slip fault.). c) Mode III is also called tearing or anti-plane or transverse shear crack. It is a shear fracture where the displacement occurs through relative movements of the crack walls one to another in direction parallel to the tip or the tip-line or edge of the fracture. (E.g. large strike-slip fault). d) Mode IV or closing mode crack sometimes used Adapted from (Twiss and Moores (2007); Fossen (2010); Gudmundsson (2011)).

2.1.3 Geometry of cracks

An elliptical crack within an elastic body can have three basic ideal shapes (Fig 2.3). First, through-the-thickness crack or crack goes through the entire elastic body. Second, part-through crack or thumbnail crack enters partly into the elastic body from the free surface. Third, elliptical interior crack or the circular penny-shaped crack is in the infinite elastic body.

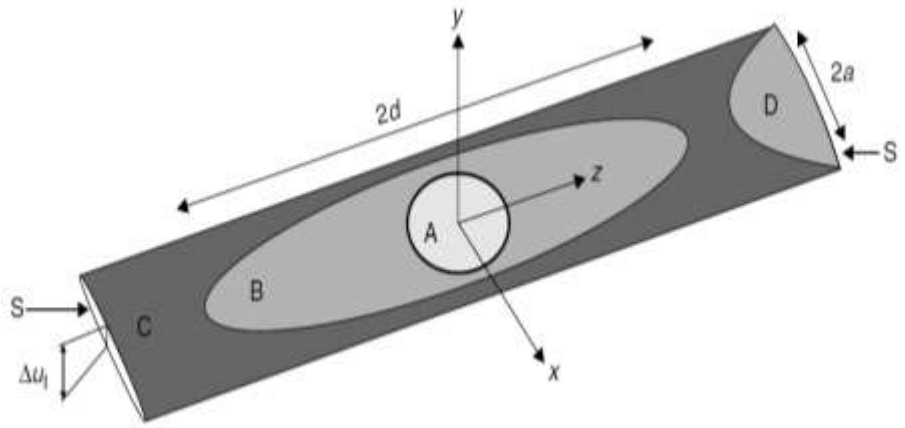

Figure 2.3. Crack geometry in three dimensions. The three basic shapes of ideal elliptical cracks in an elastic body: (A) and (B) a penny shaped interior crack, C) a through tunnel crack and D) a part-through crack, extending from one free surface(s) and partly into host rock. The circular interior crack A), with major axis 2a and minor axis 2b, is a special case of the general three-dimensional elliptical interior crack (B). Thickness through crack (C) extends from one free surface to another (O) where its maximum opening displacement is Δu.The part-through crack (D) extends from one free surface (O) partly into the elastic body. The attitude of the co-ordinate system, and thus the strike and dip of the cracks, are arbitrary. Interior cracks (A and B) are non-restricted as they develop, whereas the other two shapes are restricted (Gudmundsson (2000)).

In a case of circular interior crack, dip dimension 2α is equal to strike dimension $2b$. The crack opening which u estimated as (Gudmundsson et al., 2001)

$$u = \frac{-4\sigma(1-v^2)}{\pi E}(b^2 - r^2)^{\frac{1}{2}} \tag{2.2}$$

where E is, Young is modulus, v is Poisons ratio, r is radial coordinate of the circle with pinned center at origin and σ is extensional stress, which is tension in this case. Note that u here is the half aperture. In case the dip dimension is much larger than the other ,$a > b$, the strike dimension is controlling the aperture. 2D plane strain equation for elliptical through crack subject to constant opening-mode loading can be written as (Gudmundsson, 2000)

$$u = \frac{-2\sigma(1-v^2)}{E}(b^2 - y^2)^{\frac{1}{2}} \tag{2.3}$$

The maximum displacement,u_{max}, is assumed to occur in the central parts of the crack, which commonly is the case (Gudmundsson, 2000)

$$u_{max} = \frac{-2\sigma(1-v^2)}{EE\,(\varepsilon\,)} \tag{2.4}$$

Where ε is eccentricity of the crack and E (ε) complete elliptical integrals (Gudmundsson, 2000). This means, the smaller dimension has the greatest effect on the opening displacement of an elliptical crack. Particularly, when the ratio a/b is large smaller dimension is the controlling dimension. In a tensile regime, the differential stress cannot be more than the four times tensile strength , that i:,

$$\sigma_d < 4T_o \tag{2.5}$$

Where: σ_d = differential stress ($\sigma_1 - \sigma_3$), Pa; T_o = tensile strength of the rock, Pa;

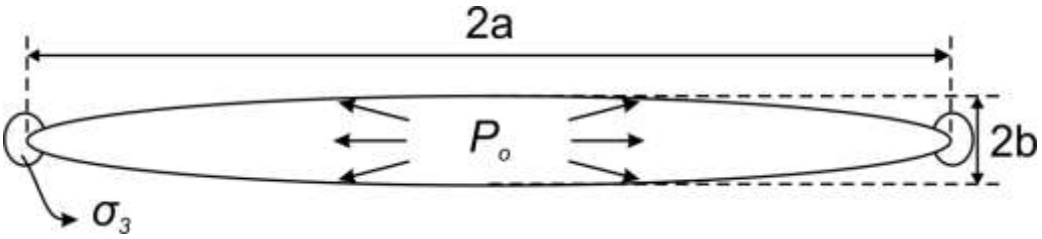

Figure 2.4 - Elliptical fracture with overpressure causing tensile stress concentration at its tip.

The condition for the initiation of a fluid-driven fracture, assuming that it hosted by an elastic medium, is given by,

$$P_l + P_e \geq \sigma_3 + T_0 \tag{2.6}$$

This says that the sum of lithostatic pressure (P_l) and fluid overpressure (P_e) must be equal to (or somewhat larger than) the minimum compressive principal stress (σ_3) plus the tensile strength (T_0) at the timing of fracturing. Therefore, once a fracture has been initiated, further propagation depends on the induced tensile stress concentration of stress intensity factor at the tip of the fracture (Fig 2.4). Moreover, this tensile stress is determined from fluid pressure in fracture as well as aperture and length of the fracture. When assuming the fracture as an elliptical empty scape, the maximum tensile stress at fracture tip given,

$$\sigma_3 = -P_o\left(\frac{2a}{b} - 1\right) \tag{2..7}$$

where: σ_3 = maximum tensile stress at fracture tip, Pa; p_0 = fluid overpressure in the fracture, Pa; a = half-length of elliptical fracture, m; b =half aperture of fracture, m;

2.2 Fracture arrest

2.2.1 Stress barrier and cook-gordon delamination

Fractures are propagating in steps (recorded by plumose structures and rib marks). Stresses absorbed by host elastic rock, suppressing a further propagation until enough potential energy is available (related to overpressure and length of the fracture) for further propagation. To make larger fractures more energy is needed (Gudmundsson, 2011). Rock offers resistance which is the material toughness and it

works again the fracture propagation or critical energy release for crack to propagate (G_c), explained in function of material toughness, is given by

$$\sigma = \left(\frac{EG_c}{\pi(1-\upsilon^2)\alpha}\right)^{\frac{1}{2}} \tag{2.8}$$

where: σ = tensile stress, Pa; E = Young's modulus, Pa; G_c = material toughness or critical energy release rate, Pa.m; α = Half-length of fracture, m; $(1-\upsilon^2)$ = Condition for plane strain; so, if the stress intensity factor is

$$K = \sigma\sqrt{\pi\alpha} \tag{2.9}$$

In addition, for a fracture to propagate K needs to reach a minimal critical value, which often referred as the fracture toughness K_c ($Pa.m^{\frac{1}{2}}$). By reformulating the equations for *G*, the critical energy release rate for mode I fracture (Extensional) propagate is given by,

$$G_c = \frac{(1-\upsilon^2)K^2}{E} \tag{2.10}$$

Stiffness has a high impact on the energy needed for fracture propagation, because a brittle material with higher stiffness needs less energy than less-brittle material for failure. As seen in the Fig 2.5, the softer materials such as shale, has a large area under stress-strain curve before the yield point compared to stiff material?

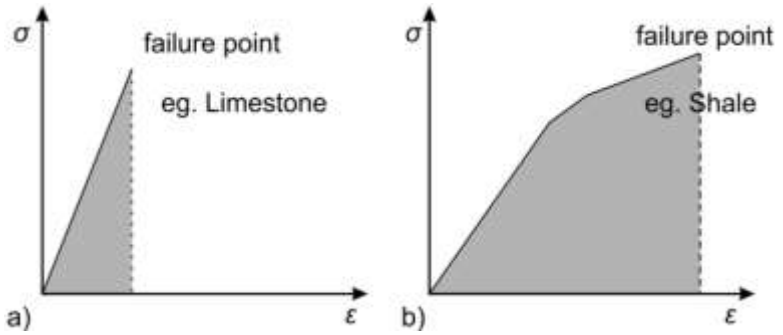

Figure 2.5 - Material toughness. It defined by the area under stress-strain curve before it reaches the failure point, a) brittle material b) tough material. (Gudmundsson, 2011).

From field observation, extension fractures can change into shear fractures, forming longer mixed-mode fracture. They theoretically need higher strain energy to propagate than mode I fracture. This follows

$$G_{total} = G_I + G_{II} + G_{III} = \frac{(1-v^2)K_I^2}{E} + \frac{(1-v^2)K_{II}^2}{E} + \frac{(1+v^2)K_{III}^2}{E} \tag{2.11}$$

where: G_{total} = total energy release rate, Pa.m; G_I, G_{II}, G_{III} = energy release rates

for the ideal fracture displacement modes I, II and III; v = Poisson's ratio; E = Young's modulus, Pa; K = stress intensity factor, ($Pa.m^{\frac{1}{2}}$);

In a homogeneous and isotropic medium, extensional fractures are propagating parallel to the maximum compressive stress (σ_1) trajectory. However, mechanical changes in a potential fracture path, like layers with different stiffness, will affect the direction of fracture propagation. Layering, interfaces or discontinuities can affect the stress, resulting in a stress barrier. This means the local stress is not favorable for vertical fracture propagation and causing deflection or arrest. There are three mechanisms for explaining a fracture will arrested, deflected or will penetrate at the contact of dissimilar adjacent layers (Fig 2.6) (Ming-Yuan and Hutchinson (1989) and described in Zhang et al. 2007, Larsen et al. 2010 and Gudmundsson, 2011). There is a rotation of principal stresses at the bed contact.

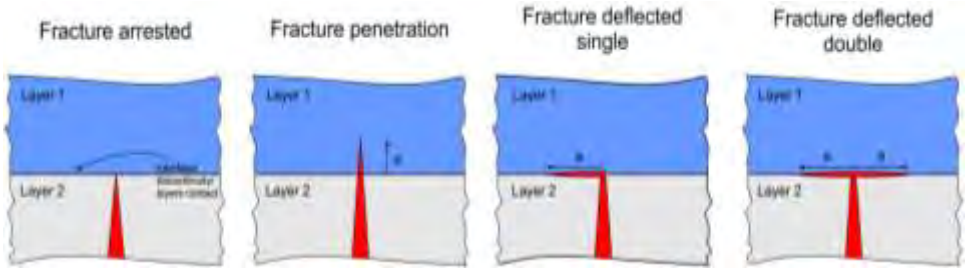

Figure 2.6 - Fracture termination possibilities when a fracture reaches a mechanical boundary. a) Fracture is arrested b) fracture penetration c) and d) fracture deflected. (Larsen et al., 2010 and Gudmundsson, 2011).

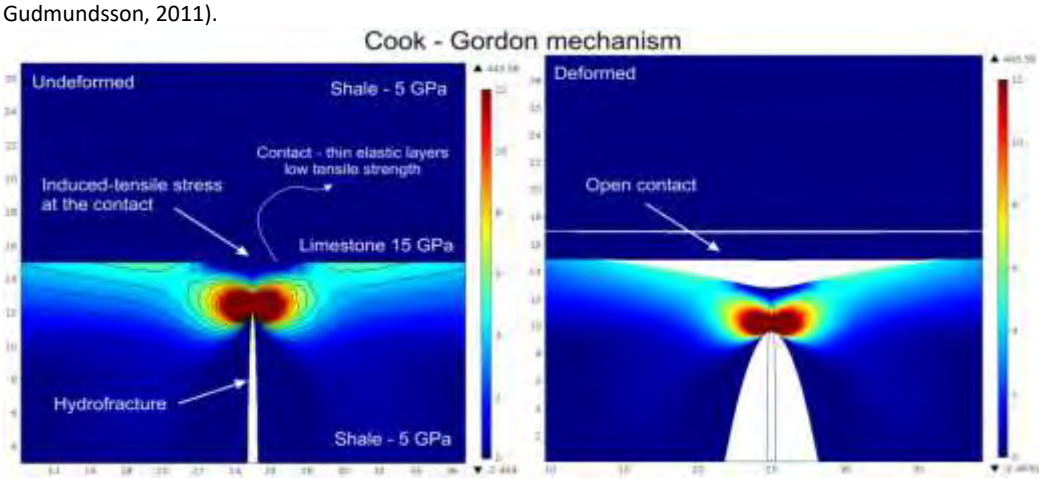

Figure 2.7 – Numerical model of the Cook-Gordon debonding or delamination mechanism. The induced-tensile stress parallel to the fracture in its tips is 20% of the tensile-induced stress perpendicular to that one. So, if the discontinuity has tensile strength 20% of the tensile strength of the rock around, a horizontal fracture would initiate and the hydrofracture will be deflected. Cf. Cook and Gordon (1964) and Gudmundsson (2011).

Induced tensil stress ahead of the fluid driven propagation, is called delamination mechanism or Cook-Gordon deboning (Fig 2.7); Elastic mismatch and material toughness.

2.2.2 Elastic mismatch

A propagating fracture arrested or deflected at a contact of materials with different stiffness is known as the elastic mismatch between layers. Then the geological layers on either side of the discontinuity have the different mechanical properties. However, when they have the same properties, a fluid driven fracture will penetrate when fracture energy release rate (G_p) reaches the layer's material toughness (Γ_{L}) and is given by,

$$G_p = \frac{(1-v^2)k_I^2}{E} = \Gamma_{\mathrm{L}} \tag{2.12}$$

Fracture will deflect when fracture energy release reaches material toughness of the discontinuity, given by,

$$G_d = \frac{(1-v^2)}{E}(k_I^2 + k_{II}^2) = \Gamma_{\mathrm{D}} \tag{2.13}$$

Fluid driven fracture penetrates the contact if this condition is satisfied,

$$\frac{G_d}{G_p} < \frac{\Gamma_D}{\Gamma_L} \tag{2.14}$$

While, fracture will deflect towards the discontinuity if,

$$\frac{G_d}{G_p} \geq \frac{\Gamma_D}{\Gamma_L} \tag{2.15}$$

where: G_d = Strain release rate for a fracture deflection into a discontinuity; G_p = strain energy release rate for a fracture penetration of a discontinuity; Γ_D = material toughness of discontinuity; Γ_L = material toughness of a layer;

Layered rocks commonly have contrasting mechanical properties especially in volcanic areas, so that the elastic mismatch parameter is an indication of potential fracture arrest (Dundurs (1969)) for dissimilar layers. fracture propagation or deflection is partly governed by relationship between Dundurs elastic mismatch parameterα and relative energy release rate (G_d/G_p) defined by,

$$\alpha = \frac{E_1^* - E_2^*}{E_1^* + E_2^*} \tag{2.16}$$

where: α = Dundur elastic mismatch parameter in extensional or uniaxial stiffness; E_1^* = plain strain tensile modulus in the layer the fracture is propagating into; E_2^* = plain strain tensile modulus in the layer that host the hydrofracture;

When α = zero it means that the mechanical properties are similar and the fluid driven fracture tends to penetrate the adjacent layer. If α is below zero, fracture is

propagating from a stiff layer into a soft one, therefore, fracture has smaller chance to be deflected. Finally, when α is above zero, the fracture is propagating from a soft layer into a stiff one, fracture have higher possibility to deflected in the discontinuity.

2.3 Fluid flow in fracture media

2.3.1 General theory

The fluid percolation within porous media is described through Darcy's law (Eq. 2.17). The Darcy's fluid velocity is proportional to the hydraulic gradient,

$$q = \frac{Q}{A} = -K\frac{\Delta h}{\Delta L} \tag{2.17}$$

where: q = fluid velocity, m.s^{-1}; Q = volumetric flow rate, m^3.s^{-1}; A = cross-sectional area normal to the fluid flow direction, m^2; K = hydraulic conductivity, m s^{-1}; negative sign indicates the direction of the flow; Δh = difference of water head (h1 - h2), m; ΔL = distance that the fluid is flowing, m; $\frac{\Delta h}{\Delta L}$ = hydraulic gradient, which indicates the total head drop for a unit length, dimensionless. Darcy's law was obtained for pipe flow and assumes that the flow is laminar, because in laminar flow, particles are moving parallel to each other. It can be written as function of the volumetric flow rate (2.18),

$$Q = KiA \tag{2.18}$$

Darcy's law describes fluid flow in porous medium rather than fracture media. Exceptions are cases in which rocks are intensively fractured and produce a complex interconnected fracture network that act similarly to a porous medium (eg. Gudmundsson, 2011). To modeling fluid flow in fracture medium, I used the Darcy law and cubic law (2.19), which is derived from the Navier-Stokes equation for viscous flow. The cubic law assumes that the fluid flows between parallel plates, such as smooth fracture walls. For smooth fracture walls the cubic law for horizontal flow parallel to the walls is given by:

$$Q = \frac{(P1 - P2)b^3}{12\mu_f}\frac{W}{L} \tag{2.19}$$

where: Q = volumetric flow rate, m^3.s^{-1}; $(P1 - P2)$ = pressure difference over the length (L); b = kinematic aperture of fracture, referred as Δu in solid mechanics, m;

W = width of the plate perpendicular to the flow, m; L = length of the plates parallel to the flow, m; μ_f = fluid viscosity, Pa.s;

The equation 2.19 is used for horizontal flow (Fig 2.8), with no gravity influence on flow, just pressure gradient. The cubic law is for describing a flow within fracture with any orientation (Gudmundsson (2011)),

$$Q = \frac{\rho_f g W b^3}{12\mu_f} i \tag{2.20}$$

In the equation above gravity (g) and fluid density (ρ_f) Unit vectors i are considered.

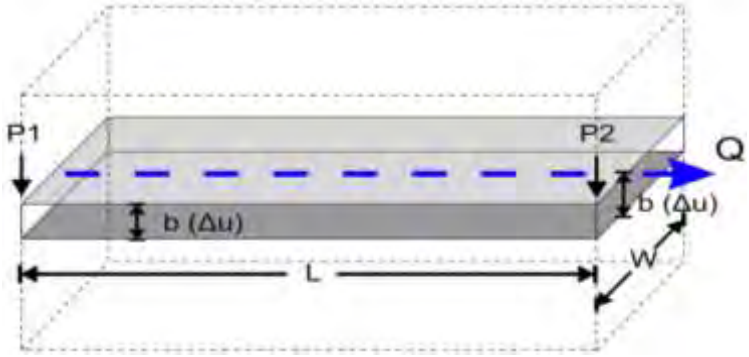

Figure 2.8 - Sketch of laminar flow between two plates, explaining the variables for cubic law equation. Modified from Gudmundsson (2011).

The cubic law could show that the volumetric flow rate (Q) is commonly proportional to the cubic of fracture aperture (b^3),

$$Q = Cb^3\Delta h \tag{2.21}$$

Where: C = Constant of cubic law for straight flow, defined by:

$$C = \frac{\rho_f g}{12\mu_f}\frac{W}{L} \tag{2.22}$$

where Δh = change in hydraulic head;

Small changes in the fracture aperture create a significant change in total volumetric flow rate. Fracture aperture is highly sensitive to surrounding stresses of the fracture. The rock rheology under stress variation has impact on fracture aperture. Some materials are more in favor of keeping higher due to applied stress.

Hydraulic conductivity *K,* often used in hydrogeology is, presenting the ability of a fracture transmit to fluid, given by

$$K = \frac{\rho_f g b^2}{12\mu_f} \tag{2.23}$$

The equations above related to a single fracture. These can also be generalized for

calculating volumetric flow rate for fractures, which belongs to set or network. If flow is parallel to the fracture length with no aperture variation between fracture walls the volumetric flow rate in length of (L) perpendicular to the fractures,

$$Q = \frac{\rho_f g m b^3}{12\mu_f} i \tag{2.24}$$

where: Q = Volumetric flow rate, $m^3.s$; ρ_f = fluid density, $kg.s^{-2}$; g = acceleration of gravity, $m.s^{-2}$; m = number of fractures dissect by the length; b^3 = cubic of fracture aperture, m^3; i = pressure gradient; μ_f = dynamic viscosity of the fluid, Pa.s;

The hydraulic conductivity for vertical fractures given by

$$K_f = \frac{\rho_f g m b^3}{12\mu_f L} \tag{2.25}$$

where: L = length of the profile where the fracture measurement taken m.

Fracture with variation of aperture rewritten followed by

$$Q = \frac{\rho_f g M}{12\mu_f}\left(\sum_{i=1}^{m} b_i^3\right) i \tag{2.26}$$

And,

$$K_f = \frac{\rho_f g}{12\mu_f L}\left(\sum_{i=1}^{m} b_i^3\right) \tag{2.27}$$

Then, m is height unit of the section, in order to simplifying the calculation, it assumed 1m, and however, for thicker layers we multiply the results by the thickness. The hydraulic conductivity or horizontal permeability for multiple layers averaged with,

$$K_h = \frac{\sum(mK_f)}{\sum m} \tag{2.28}$$

where: K_h = average horizontal hydraulic conductivity, $m.s^{-1}$; K_f = Hydraulic conductivity for an individual layer, $m.s^{-1}$; m = Thickness of the layer, m;

To average hydraulic conductivity which is perpendicular to bedding,

$$K_v = \frac{\sum m}{\sum\left(\frac{m}{K_f}\right)} \tag{2.29}$$

2.3.2 Fracture-related permeability factors

Among other important parameters for fluid transport in fractured rocks, one is the percolation threshold. Before threshold is reached there is no flow between two points through a fracture network unless fractures are interconnected and form a cluster or corridors (Fig 2.9).

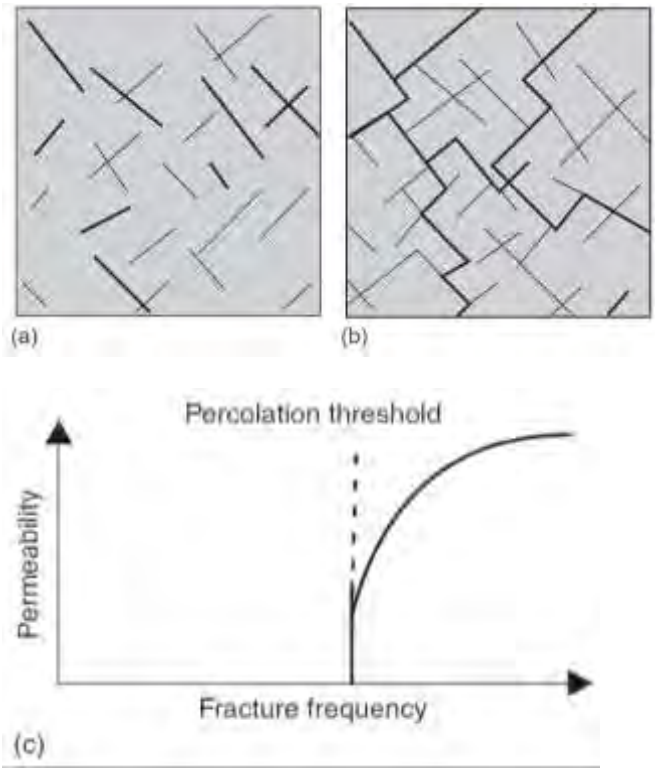

Figure 2.9 - Percolation threshold. It is a basic condition for fluid flow within a fracture network, assuming that there is no matrix permeability. a) Original fractures are non-connected; b) Fractures forming corridors or clusters that allow the fluid migration; c) Graph showing when percolation threshold reached, the permeability tend to increase with the fracture frequency. Extracted from Stauffer and Aharony (1994) (cf. Gudmundsson, 2011).

In nature, fractures confined by mechanical layers form stratabound or layerbound fractures. By contrast, fractures that penetrate more than one mechanical layer are called non-stratabound fractures. Whether fractures are stratabound or not, they directly influence the heterogeneity of the crustal segment or, say, a reservoir. As fractures are highly sensitive to stress and deform very easily compared to porous medium then fluid pressure that drives the pressure varies. For instance, when fracture is parallel to the maximum horizontal stress, the fracture prefers to increase its aperture and, therefore, the permeability. On the other hand, when maximum horizontal stress is perpendicular to fractures, it tends to decrease the aperture (Fig 2.10). The main effect of depth of the sedimentary basins on fractures is their permeability. Fracture intensity decreases gradually in the uppermost few hundreds

of meters, then keep it constant in the uppermost 1-2 km. Fracture aperture decreases sharply in the firsts few tens of meters, and then decrease far less with depth. Finally, fracture permeability or hydraulic conductivity is decreasing slowly first then keep constant in depth.

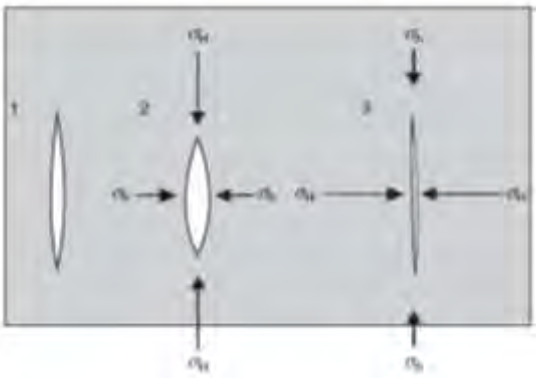

Figure 2.10 - Local stress field affecting fracture aperture. 1) Normal fracture geometry; 2) Fracture parallel to the SH_{max}, wider aperture; 3) Fracture perpendicular to the SH_{max}, Gudmundsson (2011).

2.4 Meshing

FEM method is so named because of the method of discretizing the problem into a series of elements or nodes called “finite elements” with process called meshing. These elements need to define by a series of assumptions made about the primary variables such as displacement (Deb, 2006) (Fig 2.11). Using computer modelling programs such as like BEASY (a boundary-element BEM software) semi-manually or COMSOL automatically, differential and partial differential equations can be solved for individual elements with solutions combined for the entire model.

The finer the mesh the smaller the element size becomes and therefore the greater the resolution. For this reason, in areas of interest, such as at fracture tips or between fracture tips, meshing is normally made much smaller than elsewhere in the model (Figs 2.12 and 2.13). The extended finite element modeling, a development of the standard FEM, is much used in engineering field on problems involving large deformations. When the geometry is deforming, it needs re-meshing so as to be able to sole the equation within the area of study.

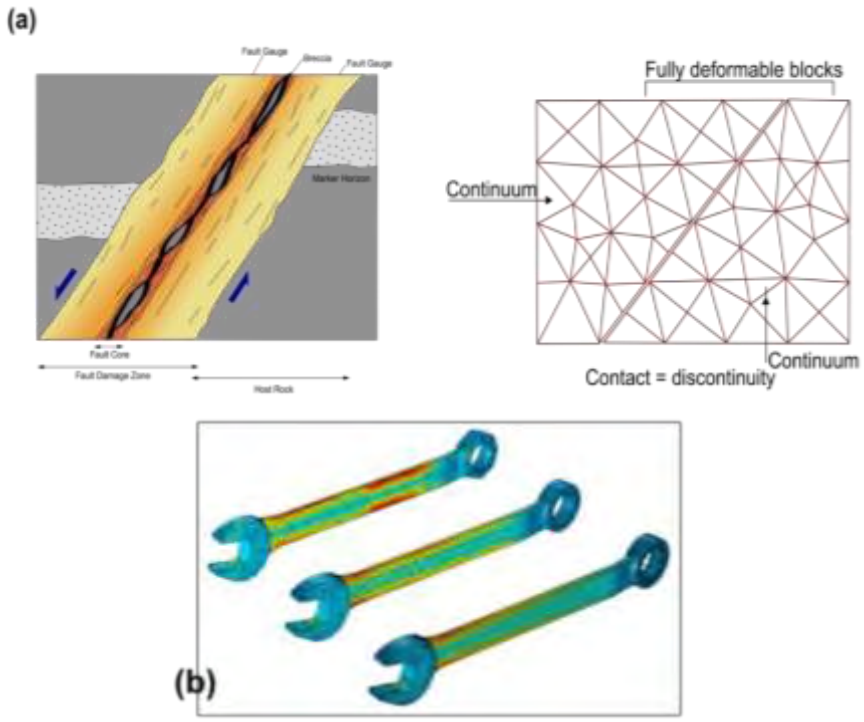

Figure 2.11: Example of a dip slip mesh. User-defined meshing applied to make mesh finer for more accurate modelling as seen in the a) fault zone and how meshing done for that area b) meshed geometry for a solid material with different mesh concentration to present the resolution better.

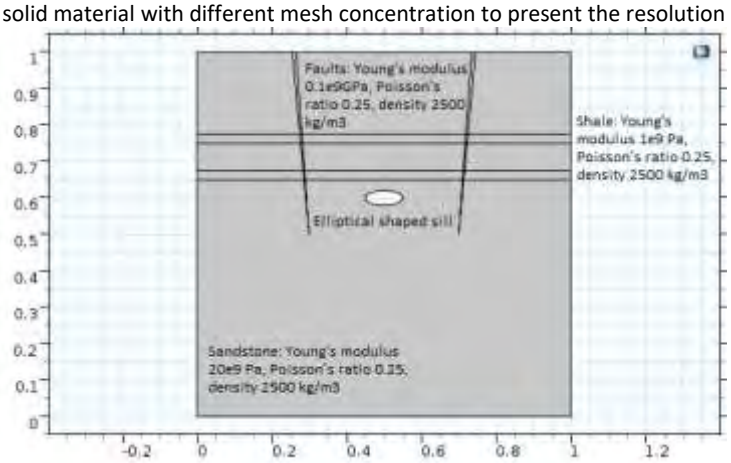

Figure 2.12 COMSOL model showing geometry and mechanical properties used in development mode.

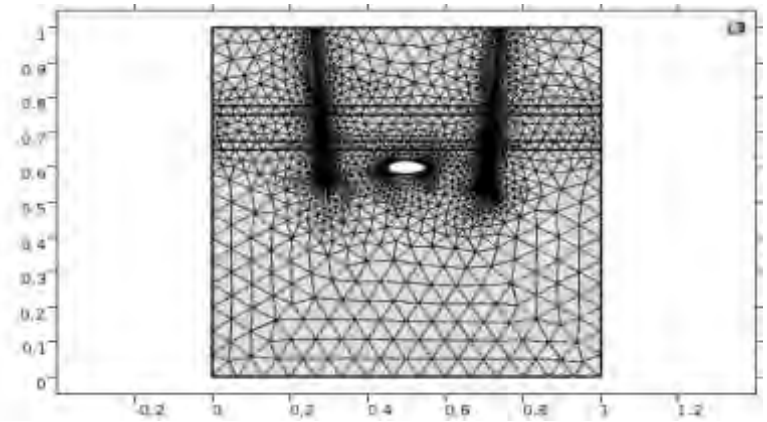

Figure 2.13 – COMSOL model showing mesh samples from my numerical models, added to model in development stage before run the model. Different mesh concentration in different area.

2.5 Finite elements for porous media

The first study on porous media in the Finite elements framework was performed by de'Borst et al. (2006). A finite element method that was proposed in this work can capture discontinuities in a two-phase media. Rethore et al. (2007) developed an approach named 'two-scale' for fluid flow in fractured porous medium. Lecampion (2009) presented a solution of hydraulic fracture problems by using an XFEM formulation where special tip functions for hydraulic fractures are introduced. Gracie and Craig (2010) applied XFEM to the layered sedimentary aquifer systems for the problem of predicting the steady-state leakage. In this work, multi-aquifer systems are modeled using a three-dimensional quasi model, where in each aquifer the hydraulic head distribution is assumed two-dimensional. Huang et al. (2011) proposed to model fractures and other conduits in porous media flow problems with a new enrichment scheme. The enrichment functions are capable of capturing effects of local heterogeneity. Watanabe et al. (2012) represent preexisting fractures in rocks by developing dimensional interface elements. This work focused on FE analysis of coupled hydro-mechanical problems in discrete fractured porous mediums. Gordeliy and Peirce (2013) solved for the elastic crack component of the elasto-hydrodynamic equations, which can described as coupled algorithms that eventually use the XFEM to govern hydraulic fracture propagation in an elastic media.

Khoei and Haghighat (2011) presented an enriched FEM for simulating the saturated porous medium, where the weak discontinuities like material interfaces or contacts between the layers encountered via the XFEM by enhancing the displacements. Khoei et al. (2012) also represented an XFEM idea for thermo-hydro-mechanical (THM) modeling discontinuities in saturated porous medium. Mohammadnejad and Khoei (2012) later developed a numerical model for fully coupled hydro-mechanical analysis of deformable media. Also, fracturing porous medium interacting with the flow of two immiscible, compressible wetting and non-wetting pore fluids. Mohammadnejad and Khoei (2013a) modelled the fully coupled analysis of deformable porous medium with existing weak discontinuities that interact with two immiscible fluids. Later, Mohammadnejad and Khoei (2013b) presented an approach with the cohesive crack to model hydraulic fracture propagation in porous medium using XFEM.

As an example of FEM approach, we consider here the flow of nitrogen in the

deformable porous media and its interaction with oil using a two-phase flow. We consider low velocity, immiscible, isothermal two-phase flow with no mass transfer and phase change inside an isotropic rigid porous media (Fig 2.14).

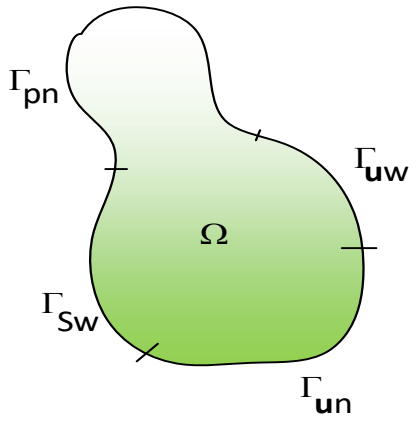

Figure 2.14. Generic porous media problem.

In this model oil and nitrogen, considered as Newtonian incompressible and compressible fluids, which constitute the non-wetting (n) and wetting (w) phases respectively. Consider a porous domain Ω with boundary Γ. The Darcy's law can express the motion of the phases in the porous media through the following:

$$u_n = -\frac{K_i k_{r,n}}{\mu_n}(\nabla p_n + \rho_n g) \quad (\text{non} - \text{wetting phase}) \tag{2.30}$$

$$u_w = -\frac{K_i k_{r,w}}{\mu_w}(\nabla p_w + \rho_w g) \quad (\text{wetting phase}) \tag{2.31}$$

where, u_α, p_α, ρ_α, μ_α and $k_{r,\alpha}$ are the average velocity vector, pressure, density, dynamic viscosity and relative permeability of the fluid phase and $\alpha = \{n, w\}$; K_i is the intrinsic permeability of the porous media and g is the vector of gravitational acceleration.

The continuity or mass conservation equations for wetting and non-wetting phases expressed as

$$\frac{\partial}{\partial t}(\phi S_n \rho_n) + \nabla.(\rho_n u_n) = 0 \quad (\text{non} - \text{wetting phase}) \tag{2.32}$$

$$\frac{\partial}{\partial t}(\phi S_w \rho_w) + \nabla.(\rho_w u_w) = 0 \quad (\text{wetting phase}) \tag{2.33}$$

where ϕ is the porosity and S_α is the saturation of phase α which varies between zero and 1. It assumed that the voids of the porous media are filled partly with oil and nitrogen; hence, the sum of the saturations of wetting and non-wetting phases is unity.

$$S_w + S_n = 1 \tag{2.34}$$

Substitution of the Darcy's laws in the continuity equations, assumption of constant ϕ, considering the compressibility of nitrogen and the incompressibility of oil and division by the respective densities, yields

$$\phi \frac{\partial S_n}{\partial t} + \phi S_n \frac{1}{\rho_n} \frac{\partial \rho_n}{\partial t} + \frac{1}{\rho_n} \nabla . \left[-\rho_n \frac{K_i k_{r,n}}{\mu_n} (\nabla p_n + \rho_n g) \right] = 0 \tag{2.35}$$

$$\phi \frac{\partial S_w}{\partial t} + \nabla . \left[-\frac{K_i k_{r,w}}{\mu_w} (\nabla p_w + \rho_w g) \right] = 0 \tag{2.36}$$

There are five unknowns S_w, p_w, S_n, p_n and ρ_n in these equations. In order to solve this system of equations we need some auxiliary equations, which come as follows.

The capillary pressure is define as the difference between the pressures of the two phases and plays a crucial role in determination of the states of the fluids in a multiphase problem.

$$p_c = p_n - p_w \tag{2.37}$$

There are several models in literature which relate the fluid saturation and relative permeability with capillary pressure; among them are Brooks-Corey and van-Genuchten laws. In this paper, we use van-Genuchten equations as following.

$$p_c(S_w) = \frac{1}{\beta} \left(\bar{S}_w^{\frac{1}{m}} - 1 \right)^{\frac{1}{n}} \tag{2.28}$$

$$k_{rn}(S_w) = \bar{S}_w^{\frac{1}{2}} \left(1 - \left(1 - \bar{S}_w^{\frac{n}{n-1}} \right)^{\frac{n-1}{n}} \right)^2 \tag{2.29}$$

$$k_{rw}(S_w) = \bar{S}_n^{\frac{1}{3}} \left(1 - (1 - \bar{S}_n)^{\frac{n}{n-1}} \right)^{\frac{2(n-1)}{n}} \tag{2.30}$$

where $\bar{S}_w$ is the effective saturation of wetting phase, which defined as?

$$\bar{S}_w = \frac{S_w - S_{wr}}{1 - S_{wr} - S_{nr}} \tag{2.31}$$

where S_{wr} and S_{nr} are residual saturations of wetting and non-wetting phases respectively. The logic behind this equation is that there is a saturation of wetting phase called residual saturation, below which is not physically feasible. In other

words, there is always some trapped oil, which cannot recovered by nitrogen injection. In addition, if nitrogen assumed an ideal gas, the relation between pressure and density expressed as

$$p_n = R_s T \rho_n \tag{2.32}$$

where R_s is specific gas constant and T is the gas temperature.

Now if, we express the continuity equation (4-a) in terms of S_w and p_n with the consideration of equations (5) to (8) and adding (4-a) with (4-b) we have,

$$\phi(1 - S_w)\frac{1}{p_n}\frac{\partial p_n}{\partial t} + \frac{1}{p_n}\nabla.\left[-p_n\frac{K_i k_{r,n}}{\mu_n}(\nabla p_n + \rho_n g)\right] + \nabla.\left[-\frac{K_i k_{r,w}}{\mu_w}(\nabla p_n - \nabla p_c + \rho_w g)\right] = 0 \tag{2.33}$$

In addition, equation (4-b) can be expressed in the terms of p_n and S_w as

$$\phi\frac{\partial S_w}{\partial t} + \nabla.\left[-\frac{K_i k_{r,w}}{\mu_w}(\nabla p_w + \rho_w g)\right] = 0 \tag{2.34}$$

Equations (2.33) and (2.34) form a system of nonlinear coupled equations in terms of p_n and S_w which are subject to below initial and boundary conditions (see Fig 2.27).

$$p_n(x, 0) = p_{n0}(x) \qquad \text{in } \Omega \tag{2.35}$$

$$S_w(x, 0) = S_{w0}(x) \qquad \text{in } \Omega \tag{2.36}$$

$$p_n(x, t) = \bar{p}_n(x, t) \qquad \text{on } \Gamma_{p_n} \tag{2.37}$$

$$S_w(x, t) = \bar{S}_w(x, t) \qquad \text{on } \Gamma_{S_w} \tag{2.38}$$

$$\rho_n u_n . n = \bar{\phi}_n(x, t) \qquad \text{on } \Gamma_{u_n} \tag{2.39}$$

$$\rho_w u_w . n = \bar{\phi}_w(x, t) \qquad \text{on } \Gamma_{u_w} \tag{2.40}$$

In this formulation the Drichlet's boundary conditions can be applied to p_n and S_w only. Numerical simulation, as Figure 2.28 shows, in the problem under investigation, the cylindrical core is initially saturated with oil with null Nitrogen; thus $S_w(x, 0) = 1$ and$p_n(x, t) = 0$. Due to small height of the core, the inertial term neglected. The perimeter surface of the cylinder is assumed to be impermeable to oil and nitrogen i.e. $\rho_n u_n . n = 0$ and$\rho_w u_w . n = 0$; the left surface is considered impermeable to oil. In the first stage of the experiment, the nitrogen pressure at left and right surfaces, known as

back-pressure, is increased linearly from 0 to 6.2 MPa In the second stage, the left surface pressure increased to 6.9 MPa while the pressure of the right surface held constant. Thus

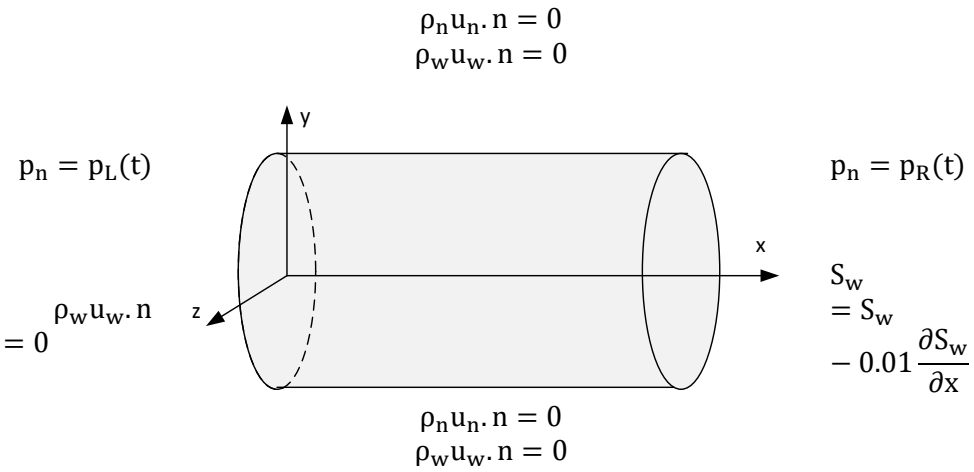

Figure 2.15 Problem boundary conditions.

The S_w boundary condition in the right surface is a bit difficult. In fact, the boundary condition depends on the current state of the system. This means that while the Nitrogen front has not reached the right surface the oil saturation remains constant i.e.$S_w = 1$; but when the nitrogen front arrives the Nitrogen saturation increases and oil saturation decreases. By use of directional derivative definition, we set the oil saturation as$S_w = S_w - 0.01 \frac{\partial S_w}{\partial x}$; where 0.01 is an arbitrary small number with the dimension of length.

$$p_n(x_L, t) = p_L(t) = \begin{cases} 900 \frac{t}{t_1} & t < t_1 \\ 900 + 100 \frac{t - t_1}{t_2 - t_1} & t_1 \le t \le t_2 \end{cases} \quad (2.41)$$

and

$$p_n(x_R, t) = p_R(t) = \begin{cases} 900 \frac{t}{t_1} & t < t_1 \\ 900 & t_1 \le t \le t_2 \end{cases} \quad (2.42)$$

In this study, a method described with the interface and free surfaces define by level sets. The fluid is treated by an Eulerian mesh whereas the solid or structure is treated by a Lagrangian mesh, in which the Lagrange multiplier method and penalty methods are used to couple the fluid and structure. Rabczuk et al. (2007) developed a simplified method for accounting for the effects of fluid-structure interaction in sandwich structures subjected to dynamic underwater loads. Wang et al. (2008) represented a weak form and an implementation for fluid-structure interaction by the immersed/fictitious element method for compressible fluids. This method has a

unique feature, which is using the Lagrangian description for treatment of the fictitious fluid, which is simplifying the interface conditions.

Gerstenberger and Wall (2008b) illustrated a new fixed grid fluid and solid interaction scheme that applied to the intact isotropic solid with incompressible flow. Gerstenberger and Wall (2008a) also explored two enhancements of fixed-grid methods that allow the improved solution of such complex FSI problems. The two enhancements are based on local adaptivity and a hybrid method that combines ideas from fixed-grid methods and arbitrary Lagrangian-Eulerian formulations. Mayer et al. (2009) extended these studies to provide a method for the localization of a higher-order interface finite element mesh in an underlying three-dimensional higher-order FE mesh. Mayer et al. (2010) presented a 3D fluid-structure-contact interaction based on a combined XFEM FSI and dual mortar contact approach. This combined method allows computing contact of arbitrarily moving and deforming structures embedded in an arbitrary flow field. Shahmiri et al. (2011) presented a finite element embedding mesh technique embed arbitrary fluid mesh patches into Cartesian or unstructured background fluid grids. An overview on recent research activities on a fixed grid fluid-structure interaction scheme that can be applied to the interaction of most general structures with incompressible flow, with special consideration given to Wall's group activities is provided by Wall et al. (2010).

Zilian and Legay (2008) introduced a weighted residual-based approach for the numerical investigation of the interaction of fluid flow and thin flexible structures, which enables one to treat strongly coupled systems involving large structural motion and deformation of multiple-flow-immersed solid objects. Massimi et al. (2008) extended the discontinuous enrichment method (DEM) to the solution of a class of three-dimensional evanescent wave problems in the frequency domain. New DEM elements for elastodynamic problems are first proposed, then these and other DEM elements are further enriched with free-space solutions of model evanescent wave problems, is technique is for higher accuracy in meshing for better resolution in case of fluid-fluid and fluid-solid applications. Legay (2013) introduced an XFEM approach for solid and acoustic problems involving immersed solids at arbitrary positions. The immersed solids supposed to be thin shells and localized in the fluid domain by a signed distance level-set, which implemented for a three-dimensional fluid and tested on academic examples. This part in advanced can be used to model the crystals in magma flow with acoustic waves. This detects the density of the crystals and with acoustic pressure; it move them by transferring its energy towards them.

One of the main cases of solid and fluid coupling in field of geoscience is Enhanced Oil Recovery (EOR). EOR by its nature always involves at least two fluid phases, which makes the problem multiphase by adding solid to the equation. It is commonly water injected into oil-saturated media, or sometimes gas injected into oil-saturated media and even gas injected into water-saturated media and so on. The mixture of this method is used in different industries for increasing the rate of production, rom hydrocarbon to geothermal and water wells. Modelling two-phase flow in numerically is generally very computationally complex for the mater of nonlinear cases and the calculations depends on number of parameters.

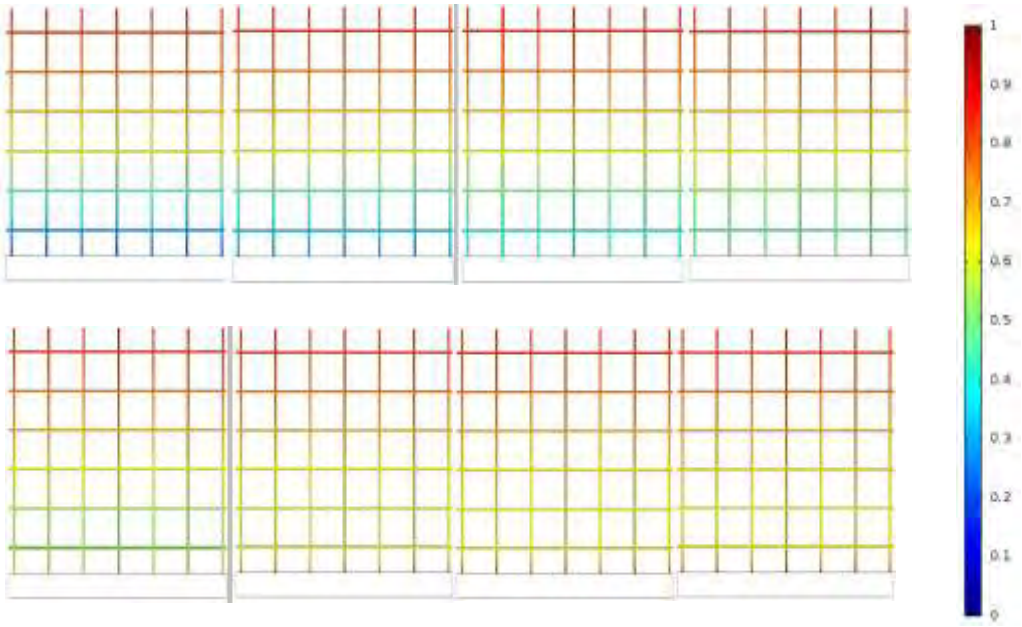

Figure 2.16: Basic 0.5 x 0.5 m fracture grid model initially saturated with oil. Nitrogen injection into tops of vertical fractures during time-dependant study. Colour scale shows nitrogen saturation. As time increases, nitrogen pushes the oil from the network and replaces it with nitrogen.

Numerical modelling can be used to study fracture network formation, crack propagation and fluid linkage. In next section, models will show how various fluids move through fracture networks and fractured reservoirs to show the dynamic of fluid flow in fractures. Enhanced oil recovery involves maintaining reservoir pressure during oil production. A fractured reservoir undergoing nitrogen injection modelled numerically as a realistic example of multiphase fluid flow. The model shows how fractures will perform as a smoother pathway for injecting phase to reach further parts of the reservoir (Fig 2.16). The first model uses fracture geometries taken directly from single limestone layer at Nash Point. Water injected with pressure 0.01 Pa into the fractures in the inlets on the left and a time-dependent model run to study the flow pattern. The results shown at regular intervals from 10s to 90s provide further information on gas injection into fractured reservoirs (Fig 2.17).

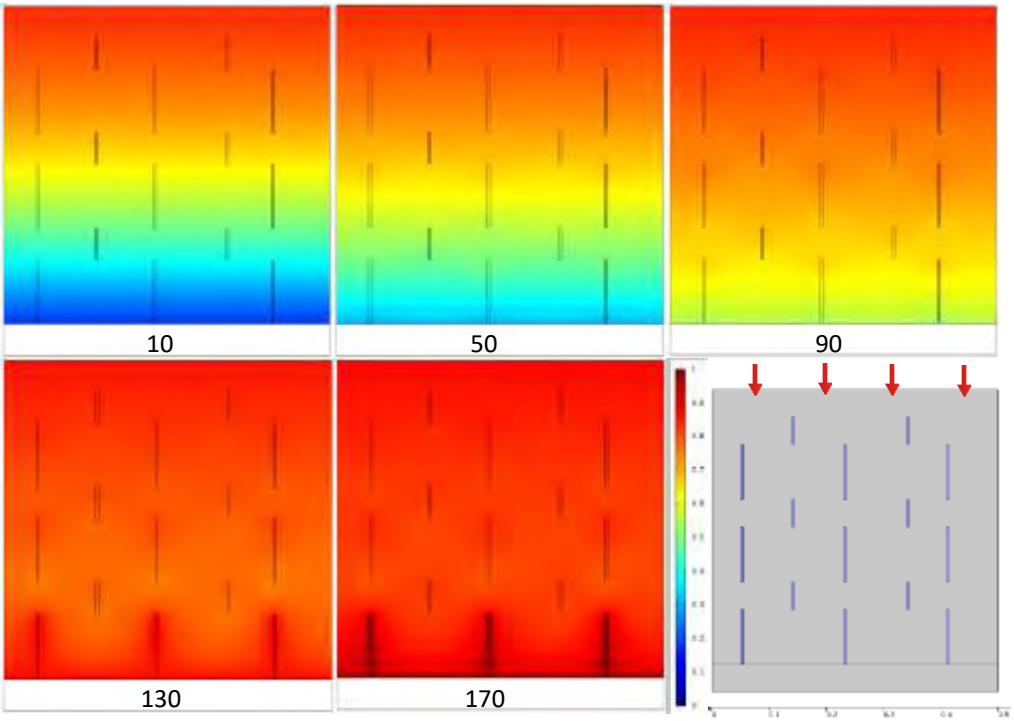

Figure 2.17: Synthetic unconnected fracture network surrounded by 20% porosity matrix, initially filled with reservoir oil and injected from the top with nitrogen. Colour scale shows nitrogen saturation. As time increases, nitrogen pushes the oil from the network and replaces it with nitrogen.

This is a naturally fractured reservoir with the permeability of the reservoir matrix ranges from zero to 12 mD, and for the fractured zone permeability increases to a wide range of 25-181 mD. The gas drive is a natural production mechanism, as well as gas cap drive, gravity drainage and water drive. This makes the zone an ideal candidate for gas injection for both pressure maintenance and EOR. The field is also located very closely to a large nitrogen reservoir. This is therefore the gas used for injecting operation. The same computational setup used to model nitrogen injection into an oil reservoir.

The first model geometry is a 0.5 x 0.5 meter basic grid network of open fractures with an aperture of 4 mm. They saturated with reservoir oil and nitrogen injected at the vertical fractures top boundaries. Because the same equations are used, the injection is using same pressure-time steps. Results shown in Figure 2.17 for the period from 10 and 150 hours in terms of nitrogen saturation. As expected, nitrogen saturation increases over time and has a uniform distribution across the grid network. For the following two-dimensional models two coupled Darcy's law, one for the wetting phase (w), and another for the non-wetting phase (nw) are used. Next model which incorporates the 20% porosity matrix with reservoir fractures present but not connected. Same nitrogen injection method is used. The unconnected fractures appear to have a small effect on the saturation of nitrogen throughout the

reservoir section, at the 90h and 130h. The explanation is, fractures act, as faster pathways for the nitrogen to flow than the matrix but to be more useful those fractures need to be connected.

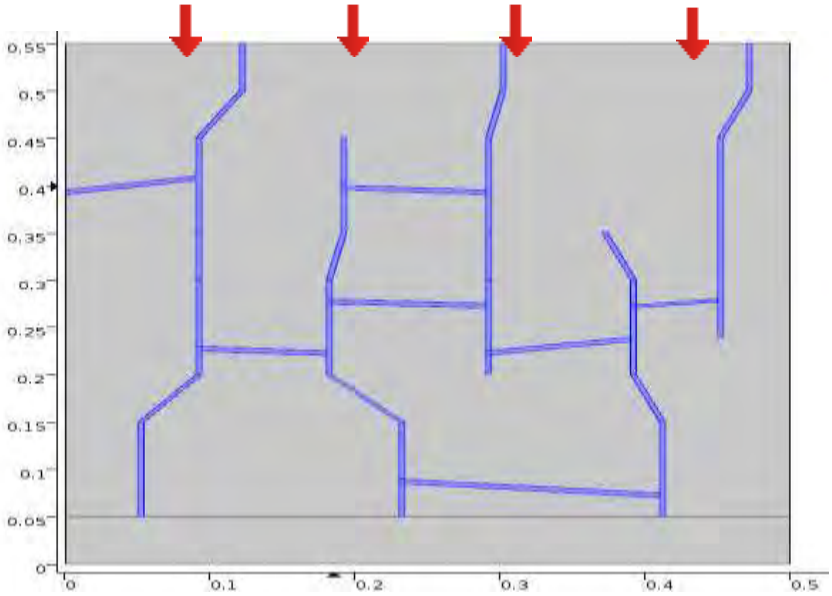

Figure 2.18: 0.5 x 0.5 m reservoir model with synthetic fracture network. Grey area is 20% porosity matrix, blue areas are fractures, red arrows show top boundary is location of nitrogen injection.

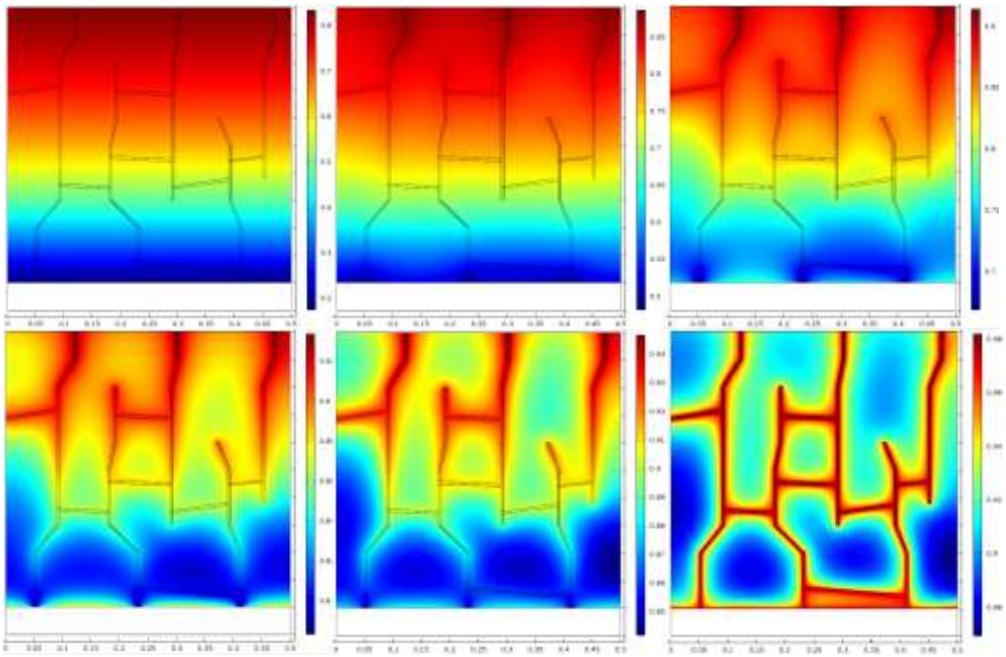

Figure 2.19: Synthetic interconnected fracture network surrounded by 20% porosity matrix. Initially filled with reservoir oil and injected from the top with nitrogen. Colour scale shows nitrogen saturation. As time increases, nitrogen pushes the oil from the network and replaces it with nitrogen. This happens fastest within the fractures and the matrix surrounding the fracture benefits from this. Matrix further away from a fracture takes a longer time for nitrogen to penetrate and displace the oil

Next, a reservoir model with a connected fracture network is used. Figure 2.18 where the geometries based on field observations from the reservoir analogue at Nash Point of the Bristol Channel in the UK. Figure 2.18 shows images from 10 to 170 h

after nitrogen injection begun. The injected fluid moves with higher velocity through the fractures than matrix. This allows nitrogen to reach matrix areas that are further away from injection well, quicker than there were no fractures network. The matrix surrounding the fractures benefits from the fractures as nitrogen confined to the fractures but spreads in surrounding matrix. This means that nitrogen transported from the injection well into reservoir at the greater rate and to the greater distance in the presents of a connected fracture network. In contrast, Figure 2.19 shows nitrogen injected into matrix containing individual, unconnected fractures. Comparing Figures 2.17 and 2.19 illustrates how fractures must be linked, not just existent, for the most effective penetration of injected nitrogen to occur.

2.6 Finite elements for thermo-mechanics

Stolrska and Chopp (2003) proposed an algorithm that couples the level set with XFEM to investigate the effects of multiple cracks, interconnect material, multiple interconnect lines and the crack propagation due to fatigue from heat cycling. Michlik and Berndt (2006) represented an image-based XFEM technique for thermal barrier coatings (TBC). This XFEM model incorporated in a developed program to analyzing the existing cracks in TBCs; for both heat transfer analysis as well as stress-strain analysis. Fagerstorm and Larsson (2008) investigated the possibility to model both mechanical and thermal incidents on the fracture process zone within the cohesive zone. Duflot (2008) applied XFEM for thermal stress simulation, cracked solids, where no only thermal but also mechanical fields enriched. Zamani et al. (2010) to enrich approximation of displacement and temperature near crack tips by implementing higher order thermoplastic asymptotic for the crack tip fields.

Table 2.1 - Table showing parameters used in modeling

Parameters	Sill	Shale	Sandstone
Young's Modulus	60GPa	1GPa	20GPa
Poisson's Ratio	0.25	0.25	0.25
Density	3300 kg/m^3	2500 kg/m^3	2500 kg/m^3
Thermal Conductivity	1.5 W/mK	1.5 W/mK	1.79 W/mK
Initial Temperature	1200°C	800°C	800°C

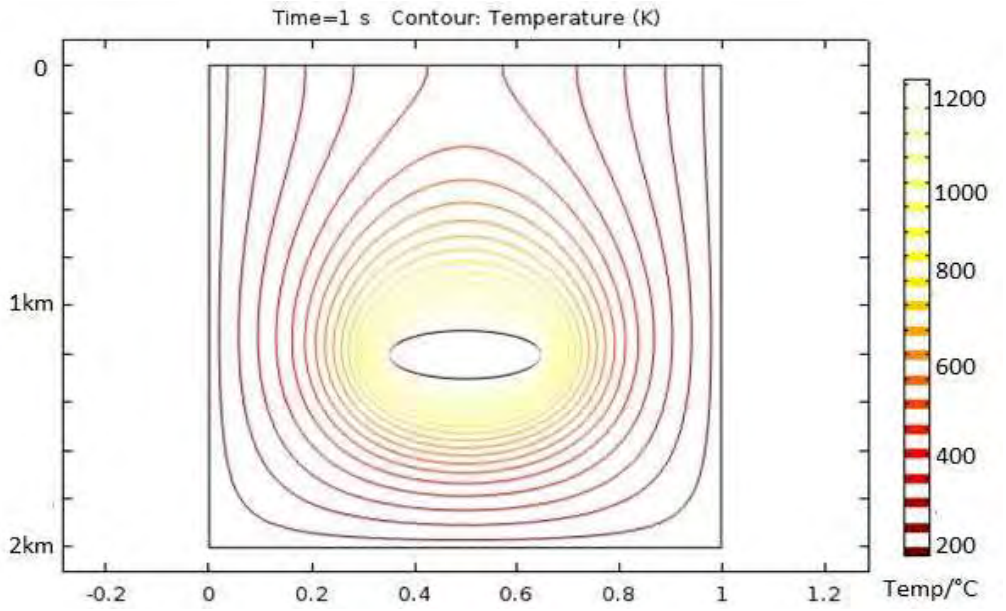

Figure 2.20 - FEM model showing temperature of sill with isotherms demonstrating gradual change in temperature further away. Initial temperature of sill at 1200°C (Gudmundsson, 1990).

Zamani and Eslami (2010) extended this study to dynamic fracture initiation in thermoplastic materials where Crank-Nicolson and Newmark integration of time integration use dynamically solve matrix equations obtained from elastic and thermal discretization. Lee et al. (2011) developed an XFEM approach for the analysis heat transfer. Yvonnet et al. (2011) proposed a method for modelling the Kapitza thermal resistance 'based on the XFEM in tandem with a level-set method'. Fan et al. (2012) worked on thermally grown oxide (TGO) for multiple surface crack propagation. Hosseini et al. (2013) introduced a technique based on the XFEM in functionally graded materials for analyzing fracture of isotropic and orthotropic (FGMs) under stationary and time dependent thermal loadings. YU and GONG (2013) investigated the computation methods for modeling temperature field in heterogeneous materials. Their elements were capable of containing material interfaces.

Here I use the heat equation for solids and fluids for some geological examples. The examples in this section for heat transfer were limited to sills and magma chambers. I also modelled heat transfer in the dikes during my PhD and I have tested them to verify their result. But these models are in my future work sections in Chapter 7. Therefore, here I am only presenting sill and magma chamber heat transfer. The thermal impacts of a sill modelled in COMSOL table 2.1. This is important to show how far a sill can thermally influence a basin. Sills commonly modelled as of an elliptical shape. The following parameters have been used (Gudmundsson, 2011). It is obvious that temperature will decrease in distance from the sill (Fig 2.20).

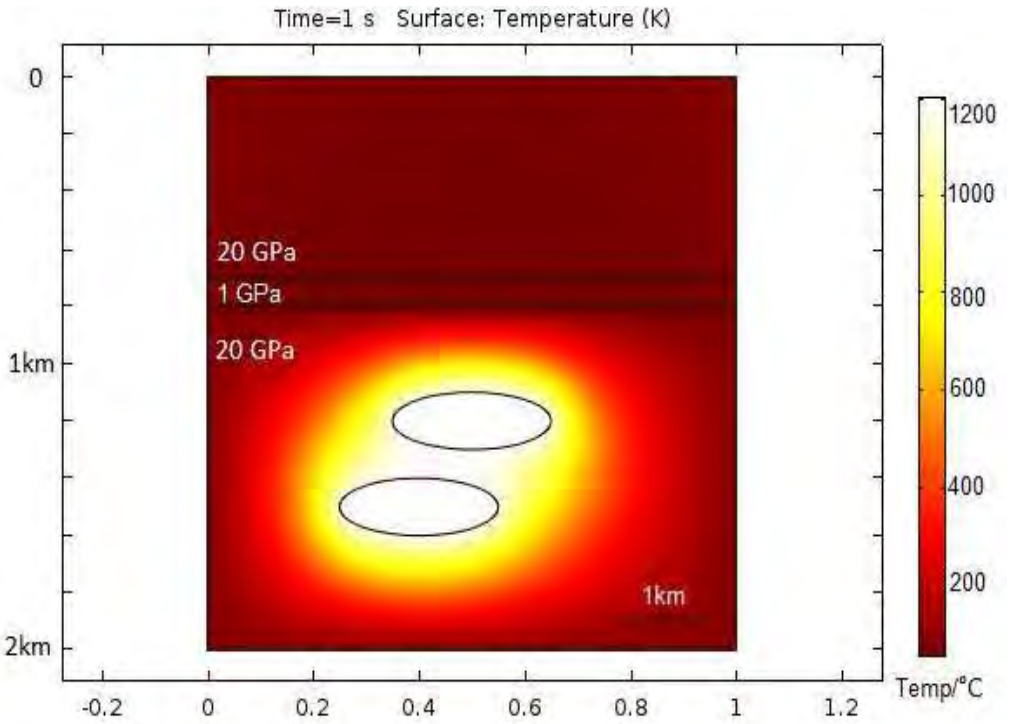

Figure 2.21 - Heat Transfer model showing two sills modelled as elliptical shape, emplaced within sandstone. Initial temperature of sills 1200°C (Gudmundsson, 1990). Alternative layers of rock sandstone 20GPa and Shale 1GPa. Overpressure 10MPa.

It is hard to know exactly what these temperatures should be, however. In addition, as noted before, thermal conductivity will vary between rocks. This model does take important factors into consideration such as magma density, magma heat capacity, sill composition, and crystallization heat. These parameters could potentially alter the thermal impact, as well depends on condition. These models showing single sill and two sills were the heat would intensify. Then, this would increase the temperature in the basin and possible cause over-maturation (Fig 2.20). Heat transfer needs to select when setting up model it is also time-dependent, so that impacts analyzed dynamically. Applying the boundary heat source to sill (elliptical shaped), which is 1200°C common temperature for basaltic magma (Gudmundsson, 1990). Apply an initial temperature to the host rock, which is in this section used 800°C (Far too high for host rock. 800 is the temperature when cooling joints form in an intrusion, but), as host rock tends to be cooler than intrusion (Barnett, 2014). Isotherm contours used to present heat provinces and their effects. This model (Fig 2.21) does consider that sills emplaced at the same time. If they developed at different stages, then multiple sills might not cause over- maturation. These sills may have different thickness, therefore their solidification time are will be different, and then their impact may differ from each other. To evaluate the heat transfer from different intrusions in three different host rock types a temperature profile was recorded as a function of time 200 m above the top of the intrusions, i.e. at 800 m depth in the

models. A geothermal gradient of 200°C/km exists in the top 1 km of the model and initial temperature of the host rock is 200°C below 1 km depth. Heat transfer caused by this geothermal gradient occurs in models and estimate the heat transfer caused only by the magmatic intrusions each model setup modeled twice. Convection-diffusion problems also investigated in FEM but as we neglected heat diffusion in this work, I do now present results or explain them in detail. Abgrall and Krust (2012) developed an adaptive enrichment algorithm for advection-dominated problems.

2.7 Finite elements for fluid mechanics

One application of multiple fluid mechanics in the context of XFEM is modeling of rigid particles in stokes flow, with geological and volanological application to rotating crystals in magma flow. This type of study first made by Wagner et al. (2001). A weak form of equations of motion used for simulating of freely moving particles with unknown velocities. Choi et al. (2010) developed an XFEM formulation to simulate of the flow of viscoelastic fluids numerically with suspended particles. For the problem of moving particle, a temporary arbitrary Lagrangian-Eulerian (ALE) defines field variables at previous time steps by the mapping FE mesh at the current time step. Later Choi et al. (2012) presented the simulation of viscoelastic fluid flowing around a stationary cylinder at XFEM framework. Sarhangi Fard et al. (2012b) analyzed non-Newtonian viscous flow in the complex geometries with parts were moving internally and small voids by investigating on two different techniques of fictitious domain method (FDM) and XFEM. Sarhangi Fard et al. (2012a) extended this study to three-dimensional modeling of Stokes flow within complex geometries and internal moving parts. Multiphase flow is new subfield of fluid mechanics and a great importance in engineering. Chessa and Belytschko (2003b) for two-phase immiscible flow problems illustrate an XFEM with internal discontinuous gradients. The discontinuity in the derivative of the velocity field introduced by an enrichment function with an extended basis whose gradient is discontinuous across the interface where the phase interfaces are tracked by level set functions. In a similar work by Chessa and Belytschko (2003b) a FEM for axisymmetric two-phase flow modeling was made where the surface tension effects were considere. Groß and Reusken (2007) provided an analysis that explains why some known standard methods for discretization of localized force term. In addition, for discretization of pressure variable often yields

velocities and introduced a new and accurate method for approximation of the surface tension force. Dolbow et al. (2008) examined the coupling of the patterned-interface-reconstruction (PIR) algorithm with XFEM for general multi-phase cases. This will helps to model the flowing fluid in fractured network, where we have air, fluid and solid phases, but the fracture network modeled in this section of the thesis as like as pipes with no frictional force and infinite permeability and porosity.

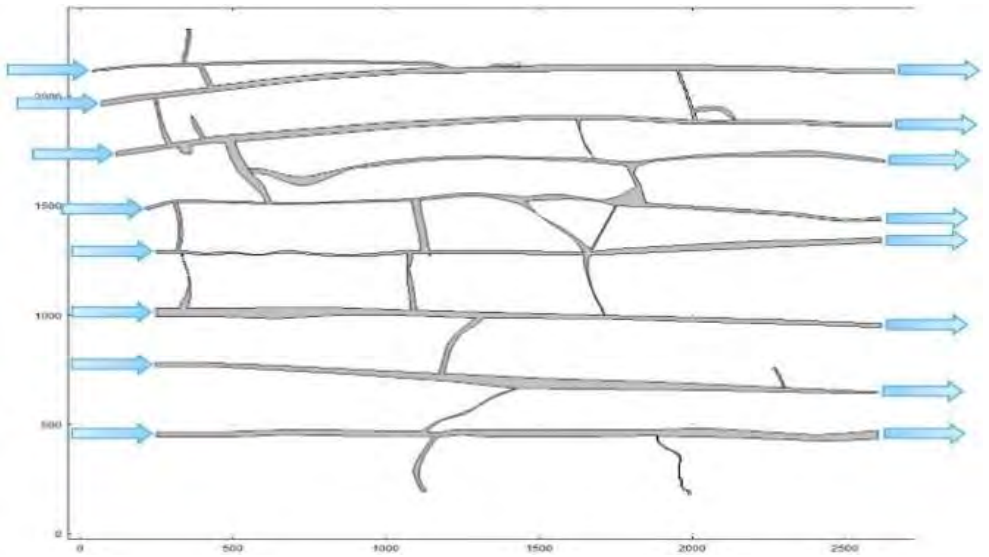

Figure 2.22: Open fracture network model based on Nash Point geometries. Blue arrows show fluid inlet points (left) and outlet points (right). Total width is ~2.5 m.

Fries (2009) employed the intrinsic XFEM technique for numerical simulation of incompressible two-phase fluid flows. Fries and Zilian (2009) focused also on time integration in XFEM framework, where the performance of the discontinuous Galerkin method in space-time FEs and time-stepping schemes analyzed by convergence studies for different models. Esser et al. (2010) introduced a standard model for incompressible fluid. Fluid is water and it consider to be incompressible for simplification, in some cases I used some other fluid for some problem where I define them as slightly compressible fluid by the volume changes were relatively small to take into the consideration two-phase flows where the effect of surface tension describing localized force at the interface describes. This approach however investigated for simple two-phase flows but with high accuracy in modeling the problems. It also applies to a physically realistic levitated droplet. Sauerland and Fries (2011) investigated time-integration schemes and different enrichment schemes using FEM. Cheng and Fries (2012) developed the h-version of the FEM as well as XFEM which applies to simulation of two-phase incompressible fluid flow in both two and three-dimensional modeling.

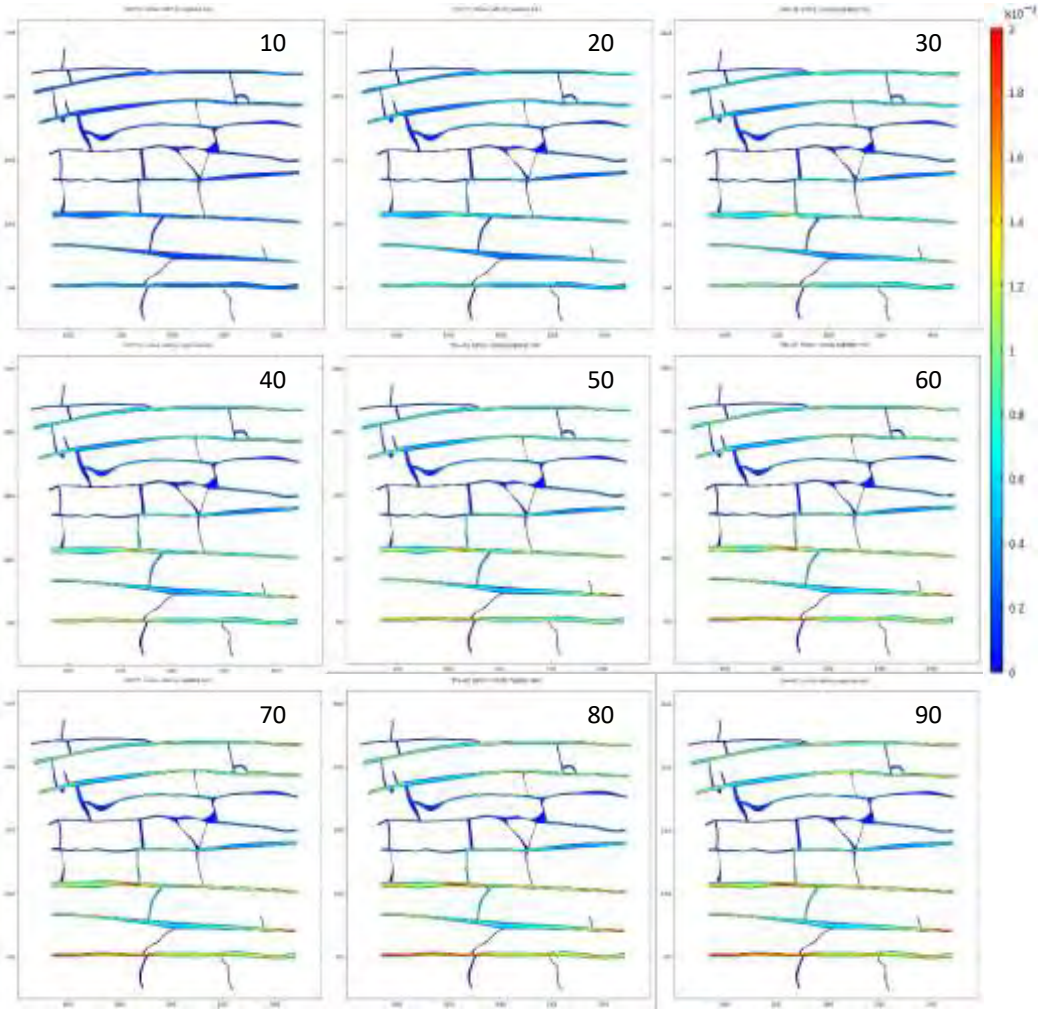

Figure 2.23: 2.5 m wide fracture network in limestone showing results of water injection on the left with outlets on the right. scale shows velocity (m s-1) magnitude of water where blue is 0 and red is 2e-4

A multilevel adaptive mesh refinement can also be used through hanging nodes on irregular meshes and has been employed near the two-phase fluid interface. For example, Liao and Zhuang (2012) presents consistent streamline based on projection upwind or pressure stabilizing Petrov-Galerkin (SUPG/PSPG) FEM to model incompressible immiscible two-phase flows. In addition, here projections of convection and pressure gradient terms are constructed and incorporated into the stabilization formulation. Sauerland and Fries (2013) introduced the stable XFEM technique for two-phase flows, in which introduces and studies few new approaches to circumvent of ill conditioning with the XFEM. Van der Bos and Gravemeier (2013) presented the numerical simulation method of premixed combustion by using an enriched FEM. This method uses the G-function (the fundamental function related to thermodynamic) approach to premixed combustion. In this technique, the domain divided into two separate parts, in which, one part containing the burned and another containing the unburned gases. Gases in this model defined as ideal gas. This

will be simplifying some non-ideal gases difficulties. In fluid mechanics there are number of cases that tested, from test cases with and without surface tension. Solving the problem on the moving or stationary meshes studied. The results compared to interface tracking when possible (Fig 2.24).

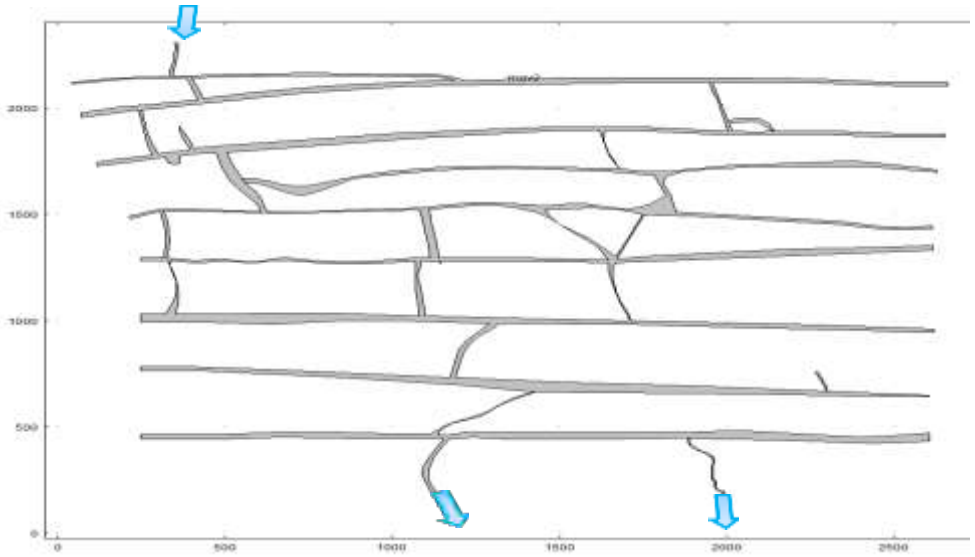

Figure 2.24: Open fracture network model based on Nash Point geometries. Blue arrows show fluid inlet points (top) and outlet points (bottom). Total height is ~2 m.

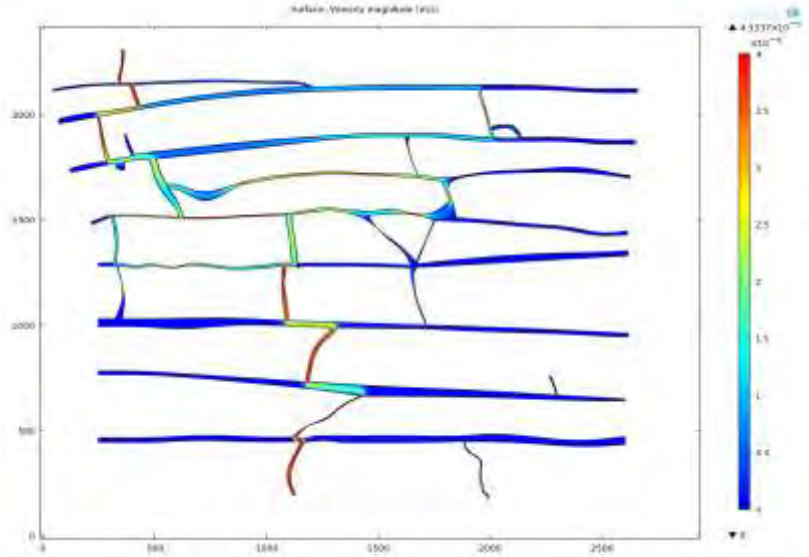

Figure 2.25: Results of numerical modelling of flowing water under a pressure gradient from the top to the bottom of the model. Scale shows velocity (m s^{-1}) magnitude of water where blue is 0, red is $4e^{-6}$.

Here I present the image-based FEM technique modeling results for fluid flow in fracture networks, also using the CAD software for importing geometries (Fig 2.22) and (Fig 2.24). These fracture geometries exist in sea cliffs in the Bristol Channel, UK, and are based on actual field measurements. Photos taken and fracture networks and the fracture apertures have been carefully measured. The results are then drawn in CAD and projected into COMSOL FEM software. Mesh fixed in these models and we observe the spring and thermal fluid traces in the fracture network, which were

exist in different directions, that bring the idea of modeling fluid flow in fracture network from X and Y direction. The plane view of fractures, neither X or Y direction need the gravity.

Flow has the greatest velocity in fractures with directions parallel to water pressure gradient (horizontal) fractures have the largest aperture (Fig 2.23). These results are a good demonstration of the cubic law and flow channeling. Using the same geometry again, fluid inlet and outlet points at the top and bottom of the model are tested. In this case, there is only one inlet as opposed to eight. It seen clearly that the flow favors fracture segments that are parallel to the pressure gradient (in this case vertical). Even if fractures have a much greater aperture, but are not optimally orientated, they contain much less flow. Therefore, orientation relative to fluid pressure gradient, perhaps more than fracture aperture, is the key control on fluid flow through a fracture network (Fig 2.25).

2.8 Finite elements for contact

The first implementation of contact in XFE framework was made by Dolbow et al. (2001). In this thesis, a new technique for FEM of crack propagation with frictional contact on the crack faces is investigated. In this work, we have many nonlinear problems where the acronym of LArge Time INcrement (LATIN) method applied to solve the problem of nonlinear boundary value. Vitali and Benson (2006) presented an XFEM formulation for contact in multi-phase ALE calculations. Khoei and Nikbakht (2006) were developed FEM and XFEM approaches for frictional contact. The classic FE approximation is enriched just by applying additional terms to simulate the contacts between the materials and their frictional behavior. The calculations are then made for enrichment of nodal displacements, which depend on the condition of the contact between two or multi surfaces. Later Khoei et al. (2006) illustrate a new computational technique based on FEM for pressure-sensitive plasticity of compaction the powder with considering frictional contact.

Khoei et al. (2009) also presented a Lagrangian-extended FEM for contact problems and large-plasticity deformations, which is used to model contact zones in two-dimensional or even three-dimensional single-phase large deformations. Vitali and Benson (2009) presented for classical kinetic friction laws to model an XFEM in a

multi-material arbitrary Lagrangian Eulerian (MMALE) formulation. Here, the velocities of the nodes are coming from more than one material calculated through the nodal accelerations to account for the kinetic friction effects. Liu and Borja (2010) employed a stabilized FE formulation governed pressure. This been used successfully for coupled solid-deformation-fluid-diffusion and Stokes equation in low-order mixed FE. Giner et al. (2008b) presented the numerical modelling of complete sliding contact and its associated singularity, which carried out using the partition of unity finite element method. Enriched functions derived from the analytical expression of the asymptotic displacement field near the contact corner.

Bechet et al. (2009a) introduced a new algorithm to define a stable Lagrange multiplier space to impose stiff interface conditions within the context of the XFEM. Becker et al. (2009) presented A Nitsche extended Finite Elements Method for incompressible elasticity with discontinuous modulus of elasticity, where the problem written on mixed form using P^1-continuous displacements and elementwise P^0 pressures, leading to the possibility of eliminating the pressure beforehand in the compressible case. Liu and Borja (2008) illustrated an algorithm based on an incremental quasi-static contact for path-dependent frictional crack propagation in FEM. Later Liu and Borja (2009) presented a FEM approach to simulate numerically a slow-rate frictional faulting in relatively close to real geology area. This is also incorporating variable friction and bulk plasticity by combining and considering the effects of bulk plasticity as well as variable friction in a two-dimensional plane strain condition (Fig 2.26).

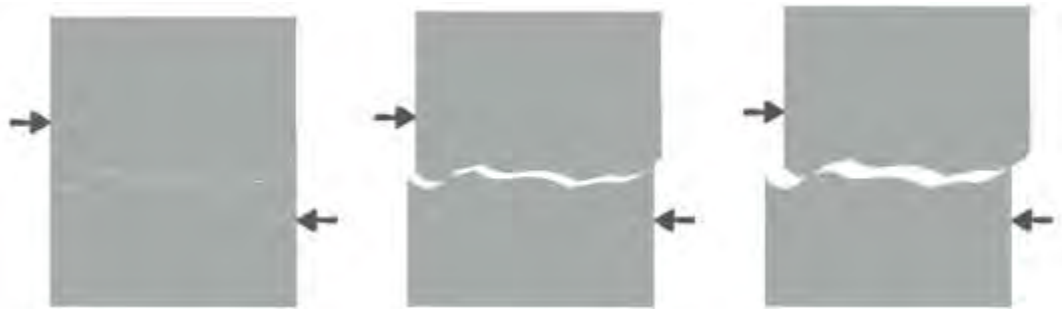

Figure 2.26: Illustration of shear slip and associated aperture increase.

The fracture frequency also influences the mechanical properties of the rocks especially Young's modulus. As fracture frequency increases Young's modulus decreases, thereby making highly fractured rock masses less stiff than unfractured rocks (Priest 1993). Additionally, gouge and breccia in the core and damage zone of an active fault decrease Young's modulus. Therefore, assumptions made that the Young's modulus of the core of the fault zone is relatively low, but increases with

decreasing fracture frequency. Internal fault core properties vary depending on the juxtaposition of stratigraphy during slip. During seismogenic slip, fault plane may smear against stratigraphic layering of different properties such as shale and sand sequences, with their own unique Young's modulus values. The amount of shale smearing, or clay smearing can be accounted by calculating Shale Gauge Ratio (SGR) which enables us to know the amount of shale smear along a fault plane and thus the core.

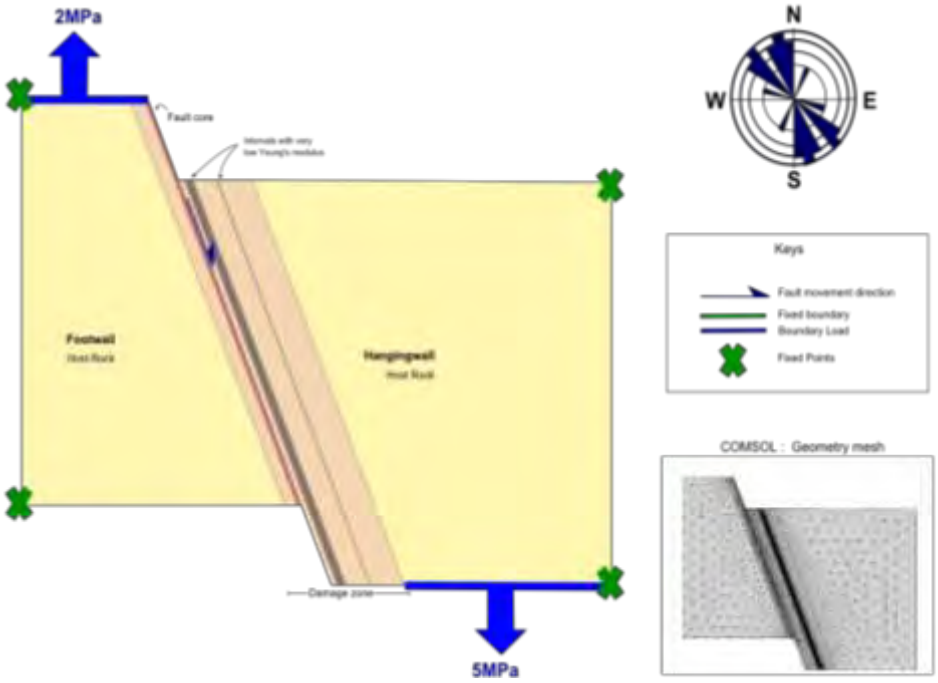

Figure 2.27 Set-up of the next numerical model based on the internal structure of the fault zone and the faults trends NW-SE normal dip-slip with 68° dip.

Shale forms an extremely effective capillary seal and permeability barrier due to its small pore throat and pore spaces. A high shale gouge ratio (SGR) value within a faulted region indicates that rock units with a high percentage of shale would have slipped past the fault therefore effective covering the plane with shale or clay smear. Shale or clay smear may have Young's modulus as low as 0.001GPa. Fault core may also consist of cataclasite (powdered rock due to intense abrasion between fault plane), fault gouge and breccia have relatively higher Young's modulus (E). As faults evolve over time, cores may stiffen due to hydrothermal crystallization or increased burial. Numerical model presented in Figure 2.27 shows von Mises shear stress and σ_1 stress trajectory of two Young's moduli extremes; between 0.001GPa and 2GPa. The model subjected to 5MPa stresses simulating normal faulting. Generally, the core has a lower shear stress concentration (stress suppression) compared to the surrounding zones. Shear stress concentration therefore decreases as E value

decreases towards the core. By contrast the outer most part of the fault zone (stiffer host rock) is highly stressed, therefore shear stress are mainly transferred into stiff outer damage zone and host rock, whereas the core and damage zone develop a stress shadow (suppression). Stress trajectories vary across the core centers with trajectories deflecting with exception of the center of the fault, meaning that fractures may not propagate or even get arrested. Regardless of favorable stress trajectories (homogenous or uniform stress trajectories going through fault core), the stress concentration would have been arguably low for fracture propagation. This numerical model based on the asymmetric damage zone (Fig 2.36). Intrinsic properties assigned to fault zone element of Sele fault zone. Young's modulus was estimated which relates fracture frequencies with Youngs modulus.

Table 2.2: mechanical properties of the fault zone

Fault Zone Elements	Intrinsic Properties (E)
Core	0.1GPa
Sub-zones with softer material (e.g. gouge or cataclasite)	5GPa
Damage Zone	10GPa
Host	40GPa

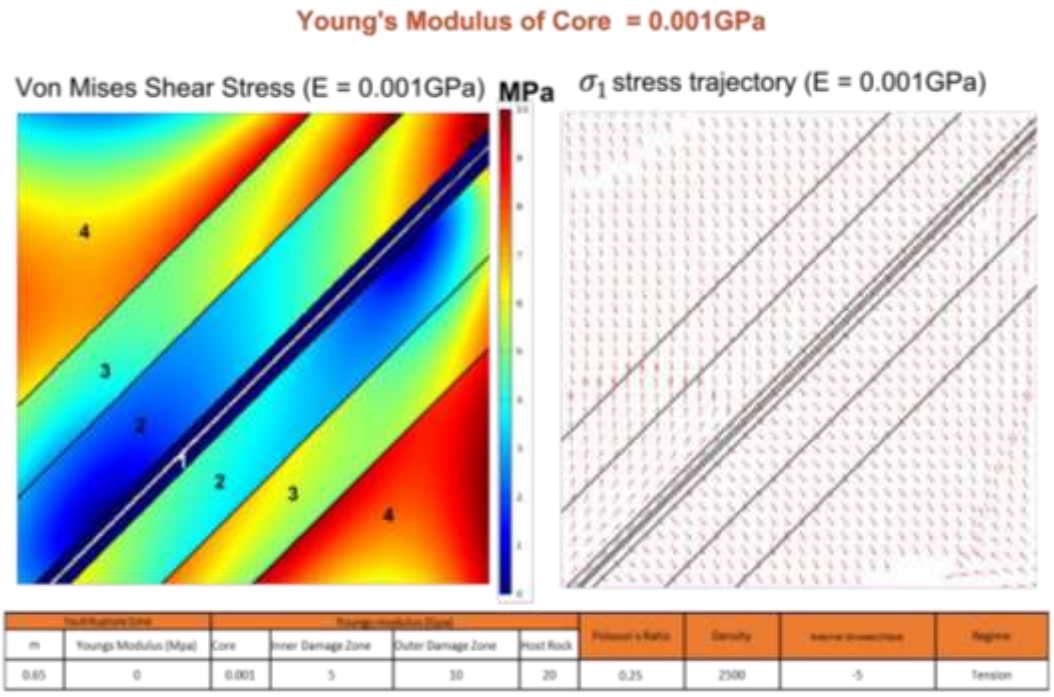

m	Youngs Modulus (Mpa)	Core	Inner Damage Zone	Outer Damage Zone	Host Rock				
0.65	0	0.001	5	10	20	0.25	2500	-5	Tension

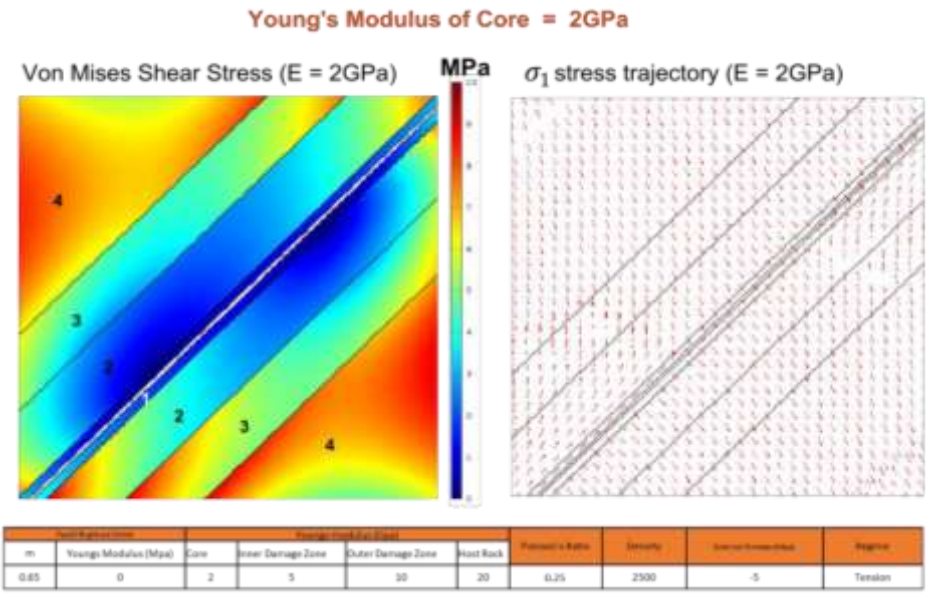

m	Young's Modulus (Mpa)	Core	Inner Damage Zone	Outer Damage Zone	Host Rock	Poisson's Ratio	Density	Gravity	Regime
0.85	0	2	5	10	20	0.25	2500	-5	Tension

Figure 2.28: Numerical model of a dip-slip fault showing the host rock and fault zone are modelled using different values for Young's modulus.

The loading is tensional shear stress of magnitude 5MPa downwards and 2MPa upwards, to simulate normal fault slip. The fault plane (the fracture represented by a red, thick line) has a stiffness of six MPa m^{-1}. The core has a Young's modulus of 0.1GPa, the sub-zones with softer materials (dark grey narrow zone 5GPa, the damage zone 10GPa, and the host rock 40GPa as shown in table 2.2 Dark grey zones are areas of the narrow stiff rock with slightly higher Young's modulus than surrounding damage zone rock. The model is fastened in the corners (indicated by crosses) to avoid rigid-body rotation and translation (Fig 2.28). The fault zone modelled as a high-angle normal fault, similar fault regime as seen on onshore and offshore Norway. Shear stress concentration vary within the zones of different Young's modulus (E), where generally higher shear stresses occurs within host rock and lower concentration of shear stresses within fault core.

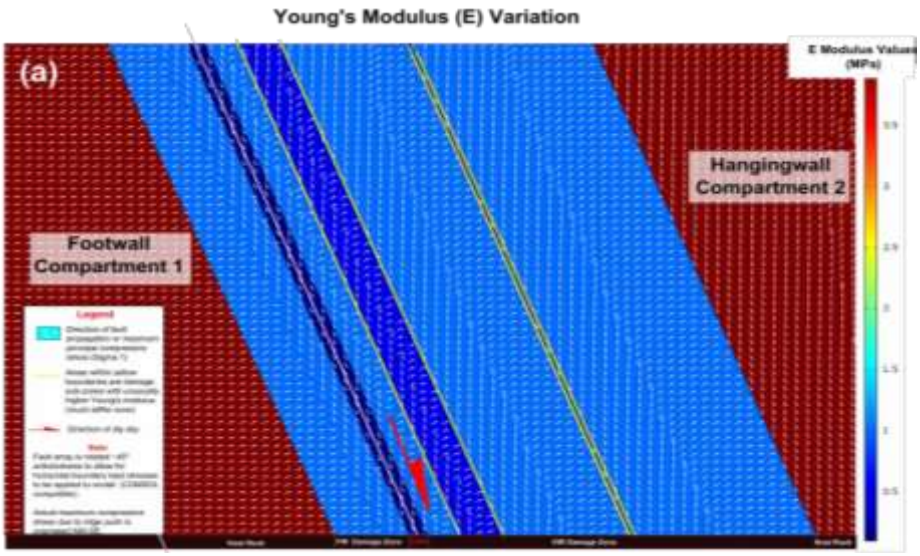

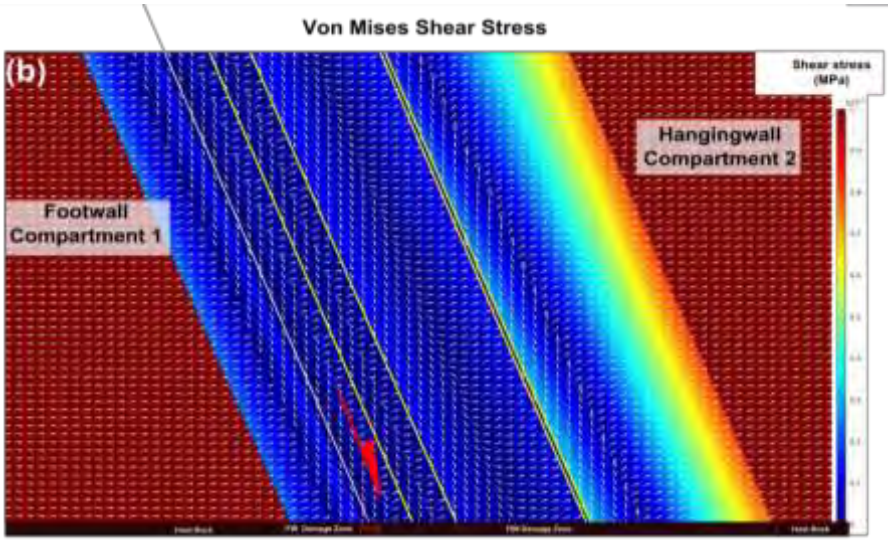

Figure 2.29: (a) Numerical model showing different values of E across each sub-zones of the fault zone. Darker blue denotes lower E modulus (softer properties) and red denotes E modulus (stiffer properties). Sub-zones outlined in light yellow lines are zones with unusually high fracture densities within damage zones showing internal heterogeneity. (b) Numerical model showing von Mises shear stress concentration across fault zone. Host rock tends to concentrate the highest shear stresses whereas the areas of lower E modulus shows a suppression of stress.

Trajectories of maximum principal stress σ_1 rotated. (a) This numerical model shows fault core with Young's modulus values of 0.001GPa (like that of some clay and shale smear properties) and (b)Numerical model below reveal the variation in the local stresses within fault zone as fault core Young's modulus value is increases to Young's modulus value of 2GPa. Young's modulus values may increase with progressive burial or diagenetic cementation. The numerical model (Fig 2.29) represent variation of Young's modulus, E. Dark blue areas are very low E values (relatively softer rock such as clay smear) and vibrant red areas shows high E values (stiffer rocks such as host rock with low fracture frequencies). Stress trajectories deflected upon contact with zones with relatively lower Young's modulus. Additionally, increased sub-zonation (with different E values) within a fault zone, would diminish the probability of fracture propagation through the fault zone as stress trajectories are deflected repeatedly in the orientation of main stress direction resulting in fracture arrest. This may develop unfavorable hydro-mechanical conditions allowing for fracture propagation and hydraulic lateral flow though the fault zone.

This may give rise to fault seal compartmentalization resulting in leakages and seeps but no lateral communication across fault zones. Fault zones anisotropy is also showing its effect on fluid transport within the fault zone, as the fault core is the softest material in the zone, we expect higher permeability, but this zone is impermeable. Meanwhile the damaged zones have different permeability and further they get from the fault core they get stiffer but more permeable. Fluid

transport through the fault zone is one of the main features of geothermal and groundwater fields (Fig 2.39). The basic of leakage from fault zone through the host rock investigated. This work will be important also in the field of enhancing the geothermal system, enhanced oil or gas recoveries and pressurizing the water wells and natural ideal gas reservoirs such as Nitrogen.

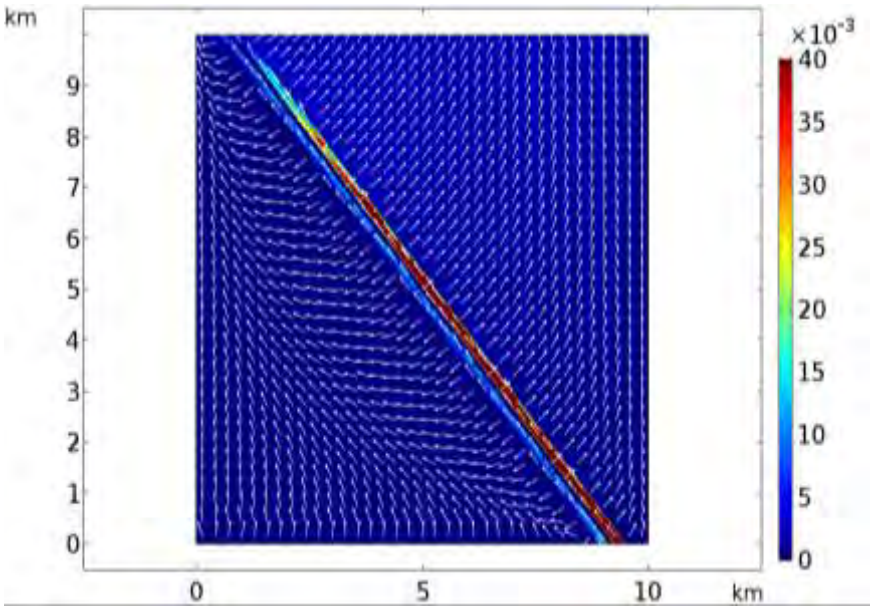

Figure 2.30 fluid leakage from fault zone to the host rock while transport through host rock

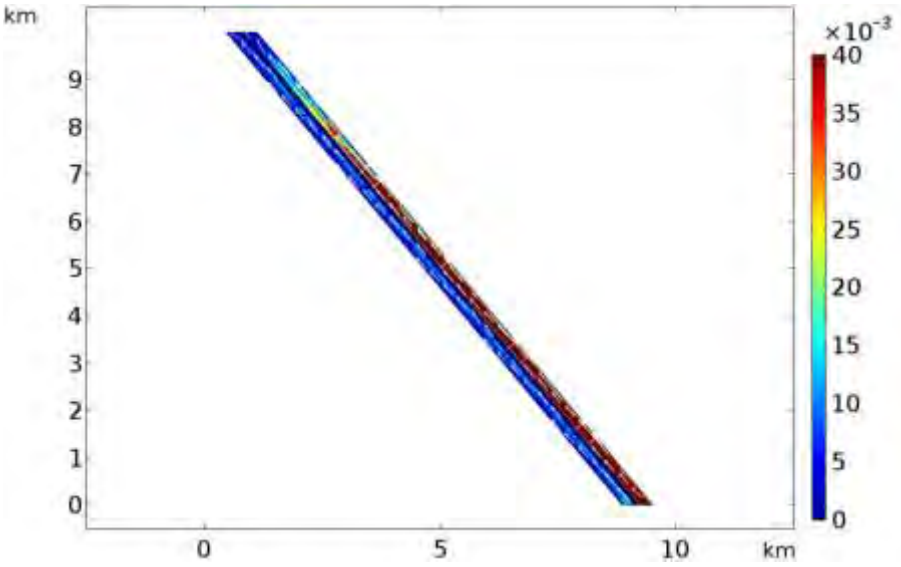

Figure 2.31 badly oriented fault can be a channel for fluid to flow though during and transfer to the places far from the source

In addition, this zone has before more important during the more regulatory era for hydraulic fracturing in hydrocarbon reservoirs. Because these faults can be oriented in the unfortunate, network hydraulic fracturing water can circulate through them and reach the surface or even underground water (Fig 2.30). This method is also can be used for many cased when new district heating proposals are coming through.

Just to use already drilled wells for geothermal purposes. Injecting water and gas to produce the reservoir heat can cause the fluid migration into other zone (Fig 2.31).

2.9 Finite element in three-dimensional (3D) modeling

In geology, modeling in 3D would be a step forward, particularly for structural geology and volcano tectonics. In this section of methodology, I present the models that presented in volcanology field before, unfortunately because of timing, these types of modeling are not in result section, but the very important plan is to publish these models and introduce them to the scientific community. Here I am illustrating how to model thrust fault, normal fault, strike slip fault, dike, inclines cone, sill, prelate magma chamber, oblate magma chamber and sphere magma chamber in inhomogeneous and anisotropic geometry. Pierrès et al. (2010) developed a method considering the three-dimensional fully or partially cracked solid geometry and the crack interface as two independent local and global parts, which characterized by different behaviors and different length scales. In this case, the interface linked to the global problem in a weak sense just for avoiding instabilities in contact solution. This method used for contact zone in 3D where, partially their idea for modeling the trust, normal and strike slip faults in 3D.

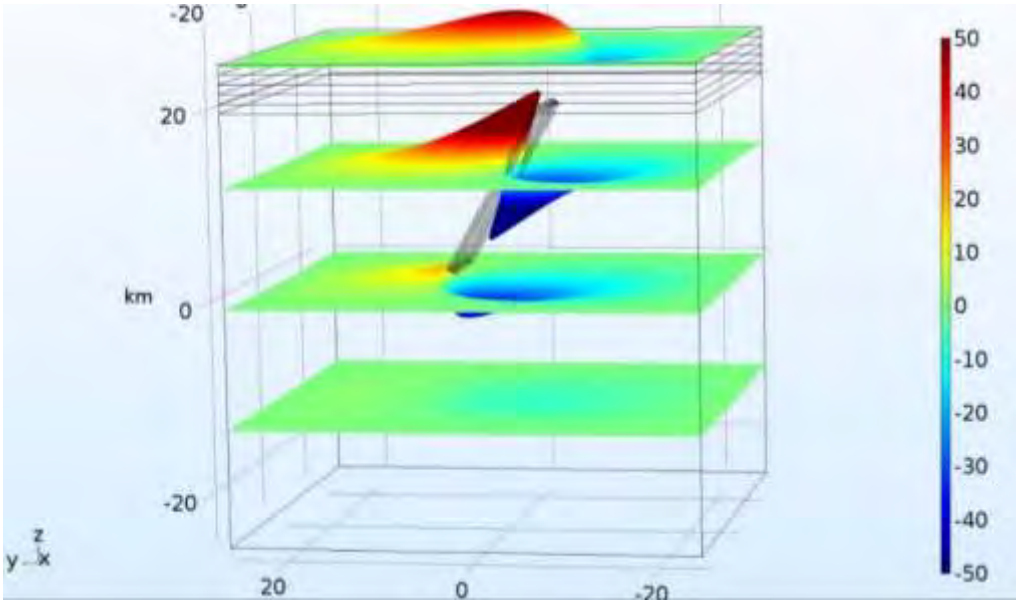

Figure 2.32 3D modeling of faulting and its effect on surface displacement

Using 3D modelling with 3D trajectories and understanding of the basic physics and

geollgy we can model some geological features in a much better and more realistic way. For instance, by modeling trust and nor fault in 3D we can see better how does and from which directly the horse and graben were form. In 3D modeling of dike, and inclined sheets we can study the feasibility of propagate through the layers and this time with two angles of reflection, to show from where in surface or next layer they might end up, this is one of the basic and fundamental way of understanding how dikes are turning to inclined sheets and vice versa. In 3D modeling of magma chamber, we have measured how much of the magma chamber displacement and shape can related to the surface displacement. Different shapes of magma chamber can have different mechanical deformation around them and this can affect the surface, which is the place we can measure the uplifting, and downgrading. In all these cases, the layering and their mechanics play an important role, which our model are showing them. To show them better I am introducing four 3D numerical models of trust fault, normal fault, inflating sphere magma chamber and deflating magma chamber all with layering and as close as it was possible to real geological and volcanological terms. All these three models have inhomogeneous with layering as the model anisotropy.

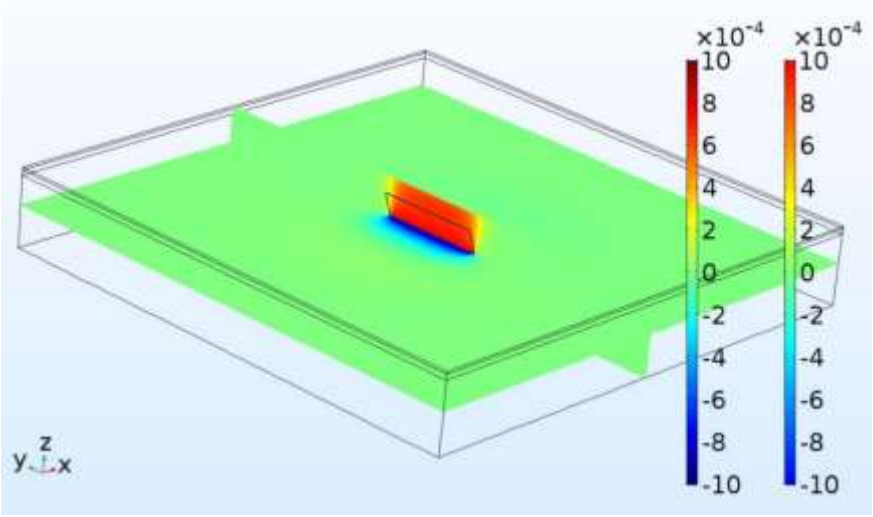

Figure 2.33 3D modeling of normal fault with layering of mixed stiff and soft materials

In fault model, we have 50 centimeters of uplifting and 50-centimeter of Deeping while the fault zone is also modeled 3D and realistic. In fault zone we have five layers, the central layer is the fault core, and four damage zones with each having stiffness and permeability. This model is not happening in geology or it might happen in some very rare incidents, we are here modeling 50 centimeters of movement of each side of the fault zone (Fig 2.32). This model has provided to show better the surface displacement and its relation to faulting. We can clearly observe and measure the

surface uplifting and downgrading during fault movement.

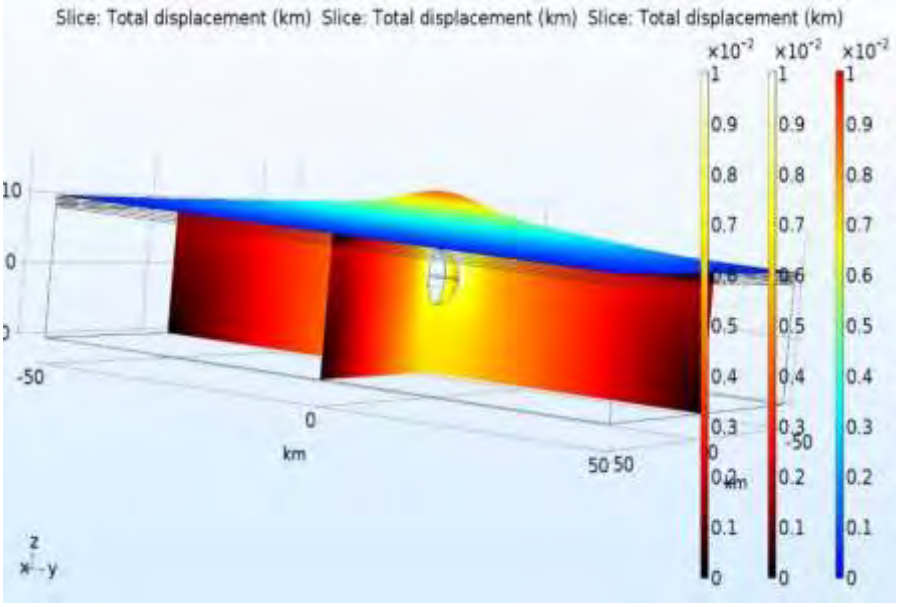

Figure 2.34 inflating magma chamber, displacement control model for 10 meters of volume change during the inflation

In the next model with the very same mechanical properties in geometry, I have increase the dimension. Therefore, we are having a larger area of investigation. While in this model, the fault movement is more realistic. Here we have 10 centimeters of moving upwards and 10 centimeters of moving downwards, this model is trying to illustrate normal fault and surface displacement regarding that tectonic feature (Fig 2.33). This model shows that the maximum displacement in around fault zone and it decreases throughout layer towards surface. Another interesting feature to investigate was the fault zone itself, in that zone as the stiffness in changing from the fault core to the farthest damaged zone.

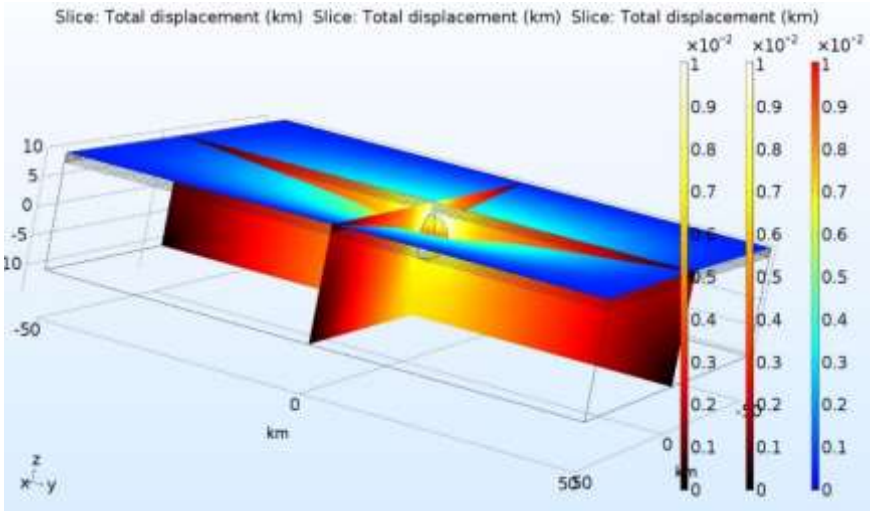

Figure 2.35 deflating magma chamber, displacement control model for 10 meters of volume change during the deflation

Therefore, the fault zone deformation is symmetric but not homogeneous. This also

can open a door for investigating the fluid path or mechanical behavior of fault zone after each tectonic event (Fig 2.34). Measuring the surface displacement is also very important and much related to magma chamber sizes in the volcanic areas. Two of the major incidents inside the magma chamber are inflation and deflation. During the inflation process, the magma chamber volume will increase and its pressure going to deform the geometry towards the free pressure zone, which is the surface (Fig 2.35).

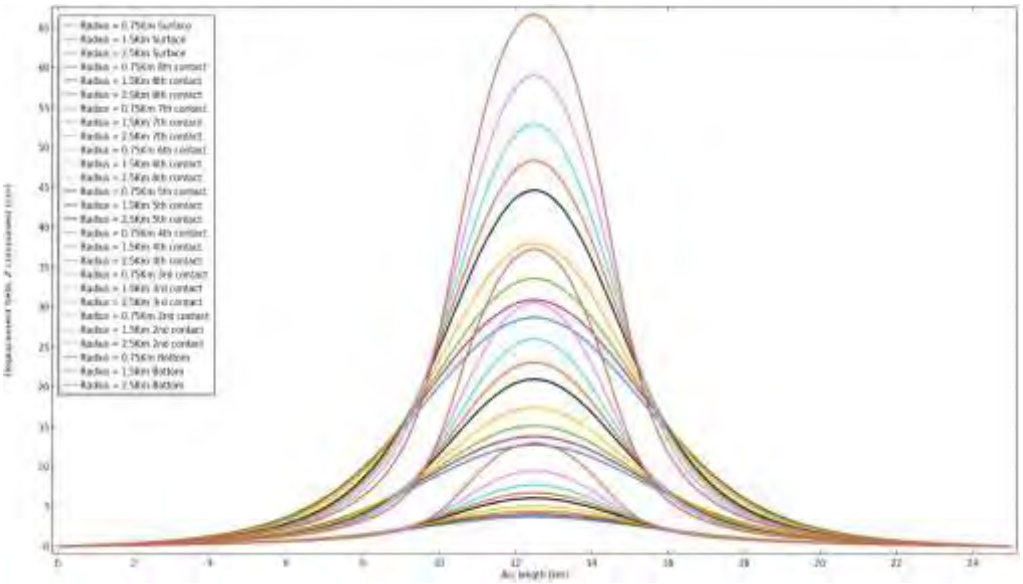

Figure 2.36: Vertical displacement of each contact between the layers through the surface. We are introducing eight layers therefore; we have nine contacts to present. In this model, we are changing the horizontal radius of the 3D magma chamber gradually, here were presenting only three steps of this transitional period. Horizontal radius is increasing from 0.75Km to 2.5km and this will change the 3D ellipsoid to oblate ellipsoid.

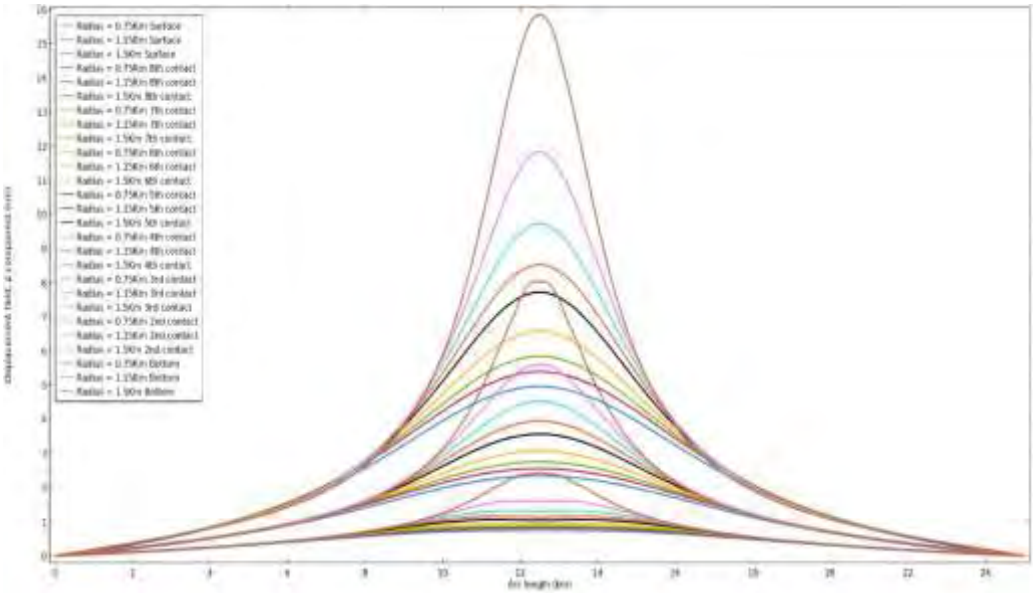

Figure 2.37: Vertical displacement of each contact between the layers through the surface. We are introducing eight layers therefore; we have nine contacts to present. In this model, we are changing the horizontal radius of the 3D magma chamber gradually, here were presenting only three steps of this transitional period. Horizontal radius is increasing from 0.75Km to 1.5km and this will change the 3D prolate ellipsoid to sphere.

In magma chamber inflation is when the chamber pressurized by arrival of new magma flow and it pressure is going to deform the northern hemisphere of the chamber and the materials around of it. The stress is going to compact the material that have nowhere to go and move the material that have possibilities to flow out of the high-pressure zone. These materials are mainly towards the surface and they will cause up lifting surface displacement. While magma chamber is inflating the bending stresses also increases, and this will cause eruptions. During the deflation, the magma chamber volume is decreasing and the suction effect for solid zone will happen. During this time because of lake of pressure and material within the magma chamber, then the solid zone must deform or bend downwards to bring back the thermodynamically stabilization to the zone. In deflation, we measure down grading on the surface while in inflation we were observing uplifting in the surface (Fig 2.34) and (Fig 2.35). This measurement is very important in the geology for dating the area and spot the incidents, therefore know how much of each displacement can be related to what tectonic events, is very important for eruption and earthquake estimations). In this model, I planned to connect the surface displacement effect to magma chamber shapes. In both sets of models, we are changing the one or the three radiuses of magma chamber to go from one magma chamber shape to another.

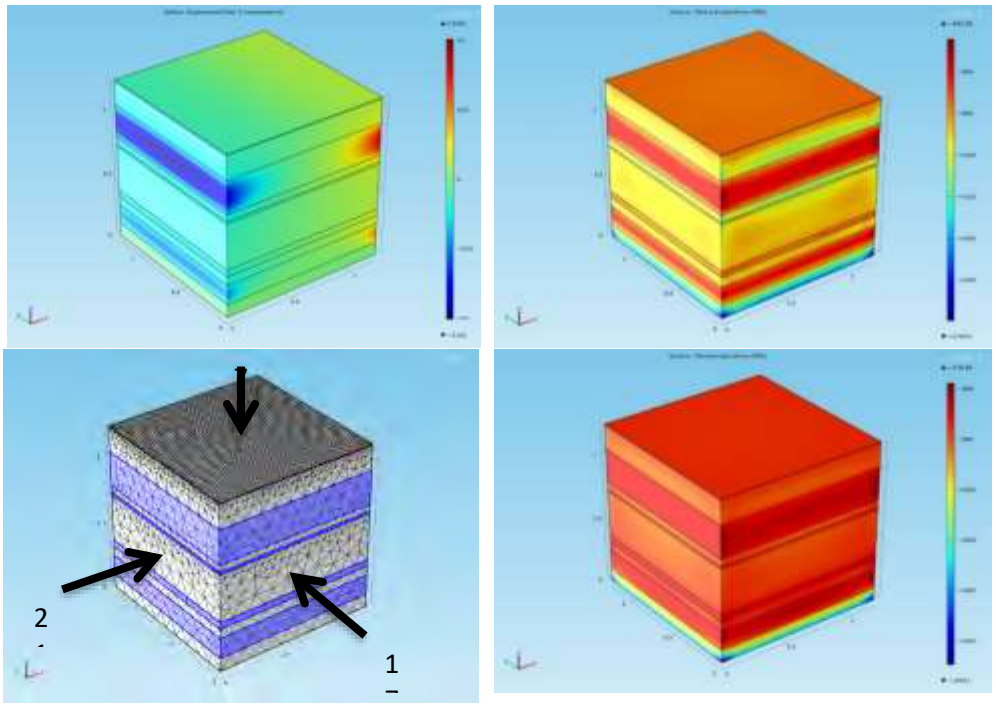

Figure 2.38: 3D model of limestone and shale layers based on Nash Point cliff (see in Fig 2.47). Young's Modulus values (GPa) of shale layers are displayed on each model. Results shown in terms of maximum principal stress, σ1.

I started with three dimensional ellipsoid and increase the horizontal (lateral) radius,

created oblate ellipsoid. Meanwhile if I start with prolate ellipsoid and increase the horizontal 'lateral' radius again, I am transforming magma chamber shape from prolate ellipsoid to sphere. (Figure 2.36) Shapes, relatively close to prolate ellipsoid we have formed down breaking on the surface of the model. While relatively close to oblate ellipsoid we have formed very sharp uplifting on the surface of the model (Figure 2.37) then shapes close to Sphere formed smooth uplifting surface model.

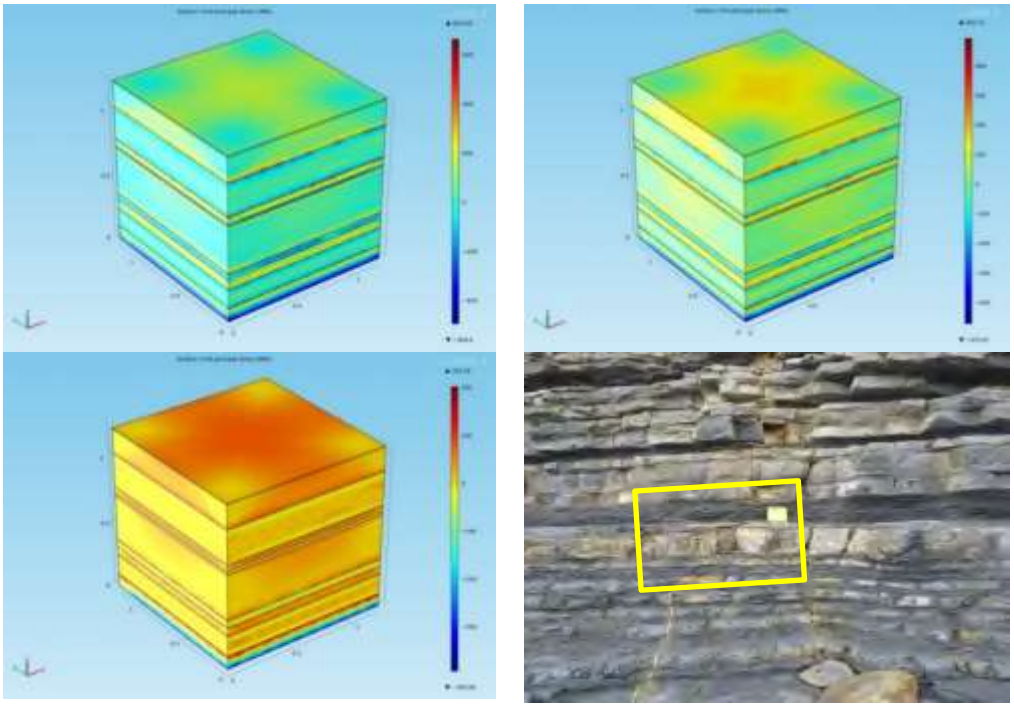

Figure 2.39 3D model of limestone and shale layers based on Nash Point cliff

This model is used to test illustrate the mechanical properties of rocks influence the concentration of tensile stresses and gravity effect in the rock mass. The model uses geometries from a cliff section at Nash Point formed by shale and limestone layers of various thickness (Fig 2.38). The limestone layers a Young's Modulus given 10GPa and the shale stiffness varied from 0.5GPa to 10GPa during the modelling. This variation simulates the stiffening of shale over time as burial and diagenesis occur. Presenting the maximum and minimum principal stresses (σ_1, σ_3 in geology) and displacement in x direction. The higher magnitude stresses found in the limestone layers. To create stress on the model, the overburden of 3000 meters of rock modelled based on the burial history of the area (Cornford, 1986). As the shale stiffens to have a more similar Young's modulus to the limestone (e.g. Fig 2.39 case 10GPa for shale), stress is almost equally distributed across all layers.

Contents lists available at ScienceDirect

Journal of Volcanology and Geothermal Research

journal homepage: www.elsevier.com

Dike-induced stresses and displacements in layered volcanic zones

Mohsen Bazargan , Agust Gudmundsson *

Department of Earth Sciences, Queen's Building, Royal Holloway University of London, Egham TW20 0EX, UK

ARTICLE INFO

Article history:
Received 8 November 2018
Received in revised form 5 July 2019
Accepted 12 July 2019
Available online xxx

Keywords:
Volcano deformation
Volcano stresses
Crustal displacements
Volcano unrest
Geodetic data
Numerical modelling

ABSTRACT

During a volcanic unrest period with dike injection, one of the main tasks is to assess the geometry and the propagation path of the dike and, in particular, the likelihood of the dike reaching the surface to erupt. Currently, the dike path and geometry (including depth and opening/aperture) are both partly determined from geodetic surface data using mostly dislocation models that assume the volcanic zone/volcano to be an elastic half space of uniform mechanical properties. By contrast, field observations of volcanic zones/volcanoes (active and extinct) show that they are composed of numerous layers whose mechanical properties (primarily Young's modulus) vary widely and whose contacts commonly arrest dikes. Here we provide field observations and numerical models on the effects of a typical variation in Young's modulus in an active volcanic zone on the internal and surface stresses and displacements induced by a dike whose tip is arrested at 0.5 km depth below the surface of the volcanic zone. Above the layer or unit hosting the dike are four layers of equal thickness. We vary the Young's modulus or stiffness of the fourth layer (the one adjacent to the layer or unit hosting the dike) from 10 GPa to 0.01 GPa, while all the other layers/units maintain their Young's moduli in the model runs. The results show that as the fourth layer becomes more compliant or soft (0.1–0.01 GPa) dike-induced stresses and displacements (lateral and vertical) above the layer, including those at the surface, become suppressed but the stresses and displacements of the layer/unit hosting the dike increase and their peaks do not coincide in location or magnitude with those of the other layers. Thus, the dike-induced internal deformation of the volcanic zone increases as the fourth layer becomes softer. Also, the tensile-and-shear stress peaks at the surface occur at locations widely different from those of maximum surface uplift. More specifically, for a comparatively stiff fourth layer (1–10 GPa), the surface tensile and shear stresses peak at lateral distances of 0.5–0.7 km from the projection of the dike to the surface. (Essentially no tensile/shear stresses reach the surface when the fourth layer is as soft as 0.1–0.01 GPa, so that there are no stress peaks). By contrast the maximum surface displacements (uplift) peak at lateral distances of 2.8–3.3 km from the dike projection to the surface. If tension fractures or faults – in particular the boundary faults of a graben – are induced by the dike, they should form at the tensile/shear stress peaks and not, as is commonly suggested, at the location of the surface displacement peaks. Our results thus suggest that any dike-induced graben is likely to be of a width about twice the depth to the tip/top of the arrested dike. The results demonstrate that elastic half-space models overestimate the dike-induced surface stresses, and thus the depth to the tip/top of the associated dike. In particular, the models presented here indicate that, for typical dikes little or no dike-induced surface deformation would be expected until the dike tip propagates to depths below the surface of less than a kilometre.

1. Introduction

Almost all eruptions, whether in volcanic zones/fields or central volcanoes (composite volcanoes/stratovolcanoes, collapse calderas, basaltic edifices), are supplied with magma through dikes or inclined sheets (cone sheets). The dikes/sheets, in turn, derive their magmas from a particular source, normally a shallow magma chamber or a deep-seated reservoir (Fig. 1). Thus most eruptions occur when a magma-filled fracture is able to propagate from its source chamber/reservoir to the surface. In central volcanoes the source is usually a shallow magma chamber with a roof at a depth of less than 5–6 km below the surrounding surface. The shallow chamber, in turn, is supplied by magma from a deeper reservoir or reservoirs (Fig. 1; Gudmundsson, 2017). In volcanic zones and volcanic fields outside central volcanoes, however, dikes commonly propagate directly from deep-seated reservoirs (Fig. 1). In volcanic rift zones the minimum compressive (maximum tensile) principal stress σ_3 is normally horizontal and parallel with the local spreading vector or rifting vector. Since magma-filled fractures generally form perpendicular to the σ_3, and thus follow the direction of the maximum principal compressive stress σ_1, most magma paths in rift zones tend to be vertical dikes (e.g., Pinel and Jaupart, 2004, 2005; Acocella and Neri, 2009; Kervyn et al., 2009). Inside central volcanoes, particularly close to magma chambers, however, the trajectories of σ_1 are commonly inclined because of local stress concentration around the shallow chamber – re-

* Corresponding author.
Email address: rock.fractures@googlemail.com (A. Gudmundsson)

https://doi.org/10.1016/j.jvolgeores.2019.07.010
0377-0273/

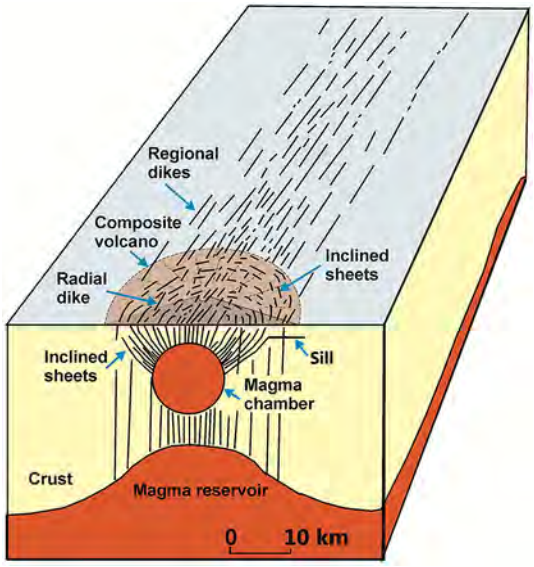

Fig. 1. Internal structure of a central volcano (composite volcano, stratovolcano, basaltic edifice) and the associated part of the volcanic zone/system to which it belongs. A shallow magma chamber supplies magma to the inclined (cone) sheets and most of the local radial dikes associated with the volcano itself. The magma chamber, in turn, is supplied with magma by a much larger deep-seated magma reservoir, which also supplies magma to many of the regional dikes. Thus eruptions within the composite/central volcano are mainly supplied with magma from thin inclined sheets and radial dikes injected from the shallow chamber, whereas the eruptions outside the central volcano are primarily supplied with magma through much thicker regional dikes. Most dikes and inclined sheets do not reach the surface to erupt but stop on their propagation paths, become arrested (Figs. 2–5), at contacts between mechanically dissimilar layers, some deflecting into sills at the contacts. Arrested dikes may induce deformation, particularly fractures, at the surface.

sulting in modification of the regional stress field – so that inclined (cone) sheets are common in the volcanoes (Fig. 1; Gautneb and Gudmundsson, 1992; Siler and Karson, 2009; Tibaldi et al., 2008, 2011, 2013). In this paper we focus on induced stresses and displacements by vertical dikes; inclined sheets will be treated in a separate publication.

Many recent studies show that most dikes do not reach the surface to erupt but rather become arrested or stall at various depths in the crust (Figs. 2–5; Gudmundsson et al., 1999; Gudmundsson and Brenner, 2001; Gudmundsson, 2002, 2003; Moran et al., 2011; Rivalta et al., 2015; Townsend et al., 2017). The conditions for dike arrest have been studied in the field (Figs. 2–5; Gudmundsson and Brenner, 2001; Gudmundsson, 2002, 2003; Gudmundsson and Philipp, 2006) and through analytical models (Gudmundsson, 2011a, 2011b). In recent years, there have also been many analogue (Kavanagh et al., 2006) and numerical (Gudmundsson and Philipp, 2006; Barnett and Gudmundsson, 2014; Rivalta et al., 2015; Townsend et al., 2017) studies of the conditions for dike arrest.

Understanding the conditions for dike arrest is of very great importance for assessing volcanic hazards during unrest periods; in particular, for forecasting likely dike paths following magma-chamber rupture and, thereby, the likelihood of a dike-fed eruption. Despite extensive instrumentation for volcano monitoring, we still cannot make reliable forecasts of dike-propagation paths. This is because there is a lack of well-founded theoretical tools for forecasting likely path of an injected dike during unrest period in a volcano. More specifically, we cannot provide reliable forecasts whether a dike injected during an unrest period is likely to reach the surface and erupt or, alternatively, become arrested at some depth in the volcano. Direct field studies of arrested, solidified or 'frozen' dikes (Figs. 2–4) as well as geodetic and seismic studies of dike arrest during unrest periods provide the data with which any reliable theories of dike propagation and dike-fed eruptions must fit.

One aim of this paper is to demonstrate how the internal stresses and displacements/deformation in a volcano/volcanic zone induced by a dike change as a function of changes in the mechanical properties (primarily Young's modulus) of the layers located between the tip of the dike and the surface. We present brief field data on arrested dike tips (Figs. 2–4), but the focus is on the results of numerical models on dike-induced stresses and displacements inside and at the surface of volcanoes/rift zones composed of layers with widely varying mechanical properties. We use the new results to propose likely – and in our view reliable – scenarios for expected internal and surface stresses and displacements/deformation during dike emplacement in central volcanoes and volcanic rift zones.

A second aim is to explain and discuss the implications these new results have for the interpretation of volcano deformation and, in general, for understanding volcanic unrest periods with dike injections. We explain how the results suggest that any dike-induced graben is likely to be of a width about twice the depth to the tip/top of the arrested dike or less. We discuss how this result differs from the common assumption that the width of a dike-induced graben is equal to the much greater distance between the associated surface-displacement peaks (Pollard et al., 1983; Rubin and Pollard, 1988). We also explain how the present results indicate that standard elastic half-space models tend to overestimate the dike-induced surface stresses, and thus the depth to the tip and the dimensions (and therefore the volume), particularly the thickness, of the associated dike. As regards hazards, we emphasise that the present models, in combination with other recent models (Al Shehri and Gudmundsson, 2018) indicate that little or no dike-induced surface deformation would normally be expected unless the dike tip propagates to depths below the surface of much less than a kilometre. This implies that when significant dike-induced deformation is seen at the surface, the dike is would be expected to be very close to the surface, indicating a high likelihood of its reaching the surface to erupt.

2. Volcanotectonic data

2.1. Arrested dikes – geophysical data

Many episodes of volcanic unrest with dike injection and arrest have been reported in recent decades. While some of the unrest episodes have eventually resulted in dike-fed eruptions, others have not. A well-documented episode of the former type was the unrest in the volcano Eyjafjallajökull in South Iceland. From 1993 to 2010 there were 4–5 dike injections from reservoir at great depth (perhaps as deep as 25 km; Tarasewicz et al., 2012). All these dikes became arrested at various crustal depths, some being deflected into sills. Then in March 2010 a new dike injection finally reached the surface and erupted (Sigmundsson et al., 2010). Many dikes and sills are exposed in the volcano, suggesting that episodes of this kind are common (Gudmundsson, 2017).

Some episodes of dike injection and propagation to shallow depths, however, eventually did not result in eruptions. These include the dike propagation at the depth of several kilometres in the volcanic complex of Teide-Pico Viejo in Tenerife, Canary Islands, in 2004 (Carracedo and Troll, 2006; Garcia et al., 2006; Gottsmann et al., 2006). No surface deformation was detected and the interpretation is debated.

A better documented recent dike injection and arrest occurred in Harrat Lunayyir in western Saudi Arabia in 2009 (Baer and Hamiel,

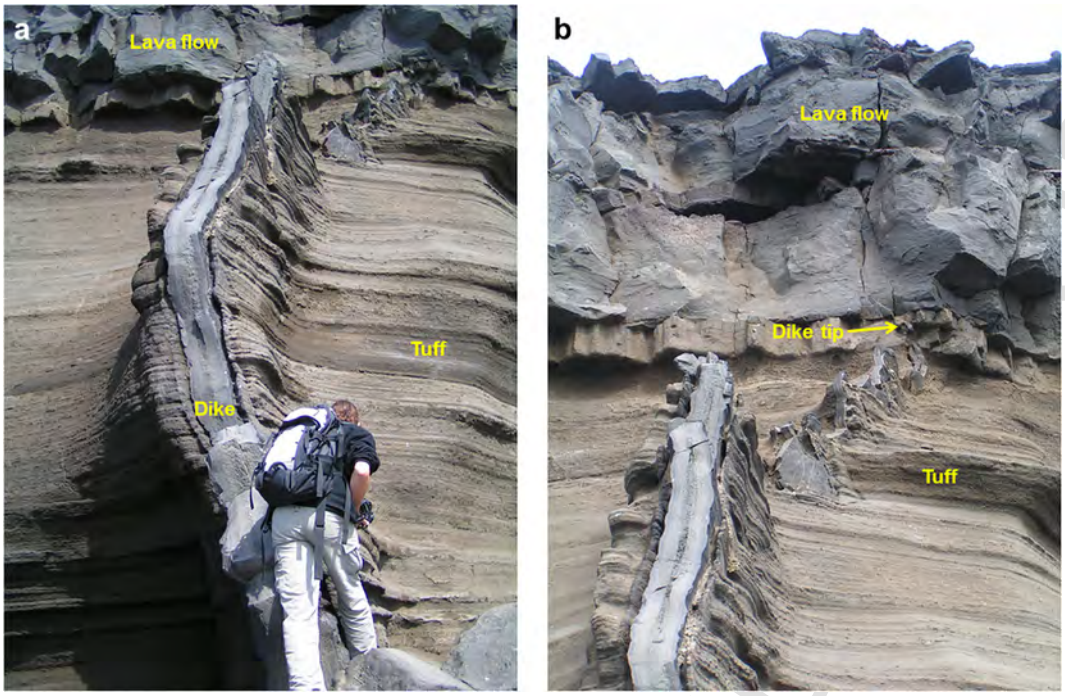

Fig. 2. Dike arrested at 5 m below the surface of the active Holocene volcanic zone of the Reykjanes Peninsula in Southwest Iceland. (a) View northwest, the dike became arrested at the contact between a soft tuff and the stiff basaltic lava flow. (b) Close-up of the contact and the dike tip as well as the entire thickness of the 800-year-old basaltic lava flow, showing that the dike became arrested, most likely around 800 years ago (soon after the eruption of the lava flow), just below the surface of the volcanic zone. No normal faults or grabens occur ahead of the arrested tip. In the lowermost exposed part the dike is about 35 cm thick but it gradually thins to a few centimetres at its arrested tip (cf. Gudmundsson, 2017).

2010; Pallister et al., 2010; Xu et al., 2016). The surface deformation associated with the episode was primarily in a zone 3–7 km wide composed of normal faults and tension fractures. Since there are no significant normal faults at the east margin of the zone – only tension fractures – the deformation does not constitute a real graben. Part of the surface fracturing, however, is likely to be induced by the dike. In order to do so, the shallowest tip of the dike may have had to be within 500 m of the surface (Al Shehri and Gudmundsson, 2018).

One of the difficulties in obtaining reliable information on injected dikes and assessing the hazards associated with episodes such as in Teide-Pico Viejo in 2004 and in Harrat Lunayyir in 2009 is that most current surface-deformation interpretations rely on standard dislocation models. These models normally assume the volcano/volcanic zone and the hosting crustal segment to be an elastic half space of uniform mechanical properties. As we show below, such models tend to overpredict the likely surface stresses and deformation, for a given dike-tip depth, associated with dikes typically injected into central volcanoes/volcanic zones. In particular, the models in the present paper indicate that, for typical dikes, little or no surface deformation would be expected unless the dike tip propagated to depths below the surface of much less than a kilometre.

One way to put constraints on the likely stresses and associated deformation, including fracture formation at the surface, induced by a dike is explore the geometry of and the deformation around the tips of arrested dikes. We shall therefore now describe briefly some typical arrested dike tips as seen in the field.

2.2. Arrested dikes – geological data

Arrested dikes are commonly observed during detailed field studies in well-exposed parts of active and inactive (eroded) volcanoes and volcanic zones. Studies in the past decades include those of Gudmundsson et al. (1999), Gudmundsson and Brenner (2001), Gudmundsson (2002, 2003, 2011a, 2011b), Geshi et al. (2010, 2012), Moran et al. (2011), and Browning et al. (2015). By contrast, feeder-dikes are much more rarely observed, although careful observations often allow such dikes to be identified in the field (Gudmundsson et al., 2008; Geshi et al., 2010, 2012; Galindo and Gudmundsson, 2012; Becerril et al., 2013; Geshi and Neri, 2014). Here the focus is on non-feeders since the surface stresses and deformation induced by dikes that fail to reach the surface are the main topic of the paper. Given the number of arrested dikes described in the papers cited above, we here present only a rather brief description of those indicated above (Figs. 2–5).

First, however, we provide a short overview of the main mechanical conditions for dike arrest, mostly at contacts between mechanically dissimilar layers as in Figs. 2–5. There are three main mechanical conditions that encourage dike arrest, namely: Cook-Gordon delamination, stress barrier, and elastic mismatch. These are discussed in detail elsewhere (Gudmundsson, 2011a, 2011b; Al Shehri and Gudmundsson, 2018), but a brief summary may be helpful here.

In the Cook-Gordon delamination mechanism the contact that arrests the dike opens up, that is, becomes delaminated. For this to happen the tensile strength of the contact (and, by implication, the shear strength also, because these strengths are related) must be low. For a propagating dike, the highest tensile stress is perpendicular to the dike and generates the dike-fracture. But there is also a high dike-parallel tensile stress which, for a low-tensile-strength, may open up the contact when the dike tip approaches the contact. When the dike tip eventually reaches the open contact, the tip may become deflected along the contact to form sill or, alternatively, become arrested.

Stress barrier is a layer or unit where the local stress field is unfavourable for a particular type of fracture propagation, here vertical dike propagation. Normally, a dike propagates along a path whose di-

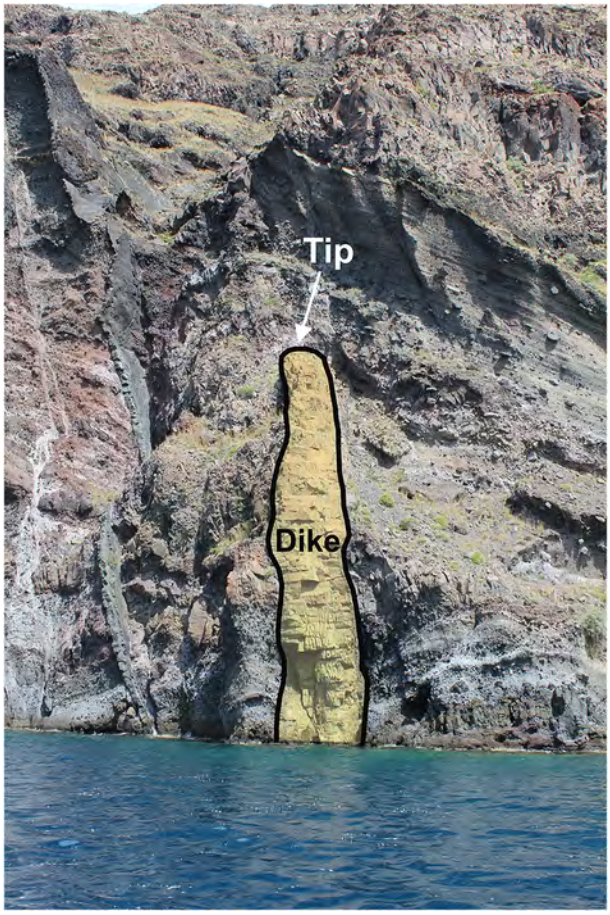

Fig. 3. Vertically arrested basaltic dike (highlighted) in the caldera wall of Santorini (Greece). The dike tip is rounded, partly because it is arrested in (hosted by) a comparatively compliant (soft) pyroclastic unit. More specifically, the tip arrest occurs at the contact between mechanically dissimilar layers, partly because their different grain size, within the pyroclastic unit. The maximum dike thickness is about 2 m.

Fig. 4. Vertically arrested somewhat curved thin basaltic dike in the caldera wall of Santorini (Greece). At the bottom of the outcrop, at sea level, the dike thickness is about 0.4 m gradually decreases upwards. The dike dissects lava flows and pyroclastic layers and ends vertically at the contact between a stiff lava flow and a comparatively soft scoria layer.

rection is parallel with σ_1 and σ_2 and perpendicular to the minimum compressive (maximum tensile) principal stress, σ_3. A stress barrier to dike propagation is thus a layer/unit where σ_1 and σ_2 are horizontal and σ_3 thus vertical. On meeting such a layer, the dike must either deflect into a sill or become arrested. In volcanic rift zones, stress barriers commonly form either when the overpressure of an earlier dike injections have resulted in a 90° flip of the principal stresses. Slip on the boundary faults of a graben may also generate stress barriers to dyke propagation (Gudmundsson, 2011a; Al Shehri and Gudmundsson, 2018).

In an elastic-mismatch mechanism deflection and arrest of a dike are primarily controlled by the contrast – the mismatch – in elastic properties (primarily Young's modulus) of the layers or units on either side of a contact, in relation to the elastic properties of the contact itself (He and Hutchison, 1989; Hutchinson, 1996; cf. Gudmundsson, 2011a, 2011b; Al Shehri and Gudmundsson, 2018). More specifically, when a dike (or any extension fracture) meets a contact between layers, its arrest or deflection is encouraged when the Young's modulus of the layer hosting the fracture (E_2) and below the contact is lower than that of the layer above the contact (E_1). The probability of dike arrest at a contact varies positively with increasing elastic mismatch or difference between E_1 and E_2, that is, with increasing Dundurs parameter (Gudmundsson, 2011a, 2011b). In particular, arrest of a dike or its deflection into a sill is more likely when

Fig. 5. Vertically arrested basaltic dike in Tenerife (Canary Islands). The dike is hosted by comparatively compliant or soft pyroclastic rock and becomes arrested where its tips comes into contact with much stiffer (higher Young's modulus) inclined basaltic sheet. The maximum thickness of the dike is about 0.8 m.

the layer above the contact (E_1) has a higher Young's modulus than the layer below the contact (E_2).

Let us now consider some typical arrested dikes as seen in the field (Figs. 2–5). The first one is remarkable in the sense that the dike became arrested at only 5 m below the surface of the rift zone of the Reykjanes Peninsula in Southwest Iceland (Fig. 2). The arrested dike, well-exposed in a sea cliff, and a nearby (25 m to the west) feeder-dike, both basaltic and about 800 year-old, are described in great detail by Gudmundsson (2017), so that only a brief description of the

arrested dike is given here. The top or tip of the non-feeder becomes arrested on meeting a contact between a stiff basaltic lava flow above and a compliant tuff layer below. The arrest therefore occurs where there is an abrupt increase in Young's modulus or stiffness from the layer below to the layer above the contact – a condition that, through the elastic-mismatch mechanism described above, encourages dike arrest. However, this dike is arrested at a very shallow depth, so that it is likely that the Cook-Gordon delamination discussed above may also have contributed to the arrest.

The overall strike of the dike is N25°E, but the individual segments vary in strike; for example, the top, arrested segment strikes N46°E. The dike is of basalt and with numerous phenocrysts of plagioclase as well as vesicles. The lowermost visible exposure of the dike is about 0.35 m thick, and from there it gradually thins to a few centimetres where it ends vertically at the contact with the lava flow. The lava flow was formed in the Reykjanes Fires, during the period from 1210 to 1240 CE. It follows that the lava flow had considerable time to solidify and become stiff before the non-feeder met it, even if the non-feeder most likely was injected sometime during the same period.

One of the main themes in this paper is the relation between surface deformation and dike-induced stresses and fractures. None of the arrested dikes discussed in this paper (Figs. 2–4) has induced any observed grabens or normal faults ahead of the dike tip. This is particularly remarkable for the present dike, since it is arrested only 5 m below the surface of the rift zone, yet is unable to generate surface tension fractures or normal faults. The same applies to the nearby feeder-dike – no surface faults or tension fractures (apart from the extension fracture which the dike itself occupies) were associated with its emplacement (Gudmundsson, 2017). While this may sound surprising, it is in fact a common observation. Most volcanic fissures worldwide are not associated with grabens that are likely to have been induced by the feeder-dikes of the fissures.

The two next arrested dikes are particularly well exposed in the caldera walls of Santorini, Greece (Figs. 3, 4). The first dike (highlighted) is vertical, with a maximum thickness of about 2 m, and arrested within a layered pyroclastic rock (Fig. 3). The tip is rounded and arrested at the contact between mechanically dissimilar layers – the dissimilarly being partly due to their different grain size - in the pyroclastic host rock unit. The tip is rounded because the layers that constitute the pyroclastic unit were comparatively soft or compliant at the time of dike emplacement. Thus, at the tip the host rock deforms in a quasi-ductile manner rather than in an entirely brittle manner. Very soft (compliant) pyroclastics and sediments normally have close to zero tensile strength, so that it is essentially impossible to propagate an extension fracture through such materials. They can, however, fail in shear, generating shear fractures or faults, while most dikes are extension fractures. All these factors contribute to dike arrest, many of which have rounded tips in compliant pyroclastic and sedimentary layers within stratovolcanoes and volcanic zones (Fig. 3) thereby making the volcanoes fracture resilient to dike propagation (Gudmundsson, 2009, 2011a, 2011b). Here either a stress barrier or an elastic mismatch, or both, are the most likely reasons for dike arrest.

The next dike, also basaltic and in Santorini, is arrested at a contact between compliant pyroclastic/scoria layer (below the contact) and stiff lava flow (Fig. 4). This is a very common type of arrest (Figs. 2, 4, 5; Gudmundsson, 2002, 2003), and can, again, be attributed either to elastic mismatch or a stress barrier, except at very shallow depths (Fig. 2) where the Cook-Gordon delamination or debonding may dominate as an arrest mechanism (Gudmundsson, 2011a, 2011b; Martí et al., 2016, 2017; Al Shehri and Gudmundsson, 2018). Here the bottom of the dike, at sea level, has a thickness of about 0.4 m thick but the dike becomes gradually thinner upwards (Fig. 4).

The final example presented here of an arrested basaltic dike is from Tenerife, one of the Canary Islands (Fig. 5). This vertically arrested dike is hosted by comparatively compliant pyroclastic rock and becomes arrested at its contact with much stiffer inclined basaltic sheet. The maximum thickness of the dike is about 0.8 m. The dike tip is blunt, as is common for dike tips arrested at contacts where the layer above the contact is stiff, such as a stiff lava flow or, as here, a sheet intrusion (Fig. 5). A very likely mechanism of dike arrest here is elastic mismatch.

These and other field examples show that dike arrest is particularly common at contacts between mechanically dissimilar layers. Perhaps the most favoured contacts for vertical dike arrest are those where the stiff layer (e.g., a lava flow or a sheet intrusion) is above the contact and the soft or compliant layer (e.g., pyroclastic, soil, or sedimentary) below the contact. This is in accordance with the three main mechanisms of dike arrest, namely the Cook-Gordon delamination/debonding, the stress barrier, and the elastic mismatch (Gudmundsson, 2011a, 2011b; Martí et al., 2016, 2017).

None of the arrested dikes described here (Figs. 2–5) induced fractures ahead of the dike tip. By implication, presumably none of these dikes generated fractures at the surface. This follows because the dike-induced stresses are normally largest at the dike tip. So if the dike is unable to induce fractures at or close to its tip, then the dike is unlikely to induce fractures at the surface far above the tip (cf. Gudmundsson, 2003; Geshi et al., 2010; Philipp et al., 2013). This applies particularly when there are soft (compliant) layers between the dike tip and the surface (Section 3; Al Shehri and Gudmundsson, 2018). Clearly, therefore, dike-induced fractures at the surface require special conditions which were presumably not satisfied by any of the dikes seen here. One of the aims of the present paper is to explore these conditions.

All these arrested dikes are rather thin, ranging in thickness from about 0.3 m to 2 m (Figs. 2–5). While many dikes are of thicknesses similar to these (e.g. Rickwood, 1990; Gudmundsson, 2002; Galindo and Gudmundsson, 2012; Becerril et al., 2013; Rivalta et al., 2015), it should be noted that non-feeder dikes tend to become thinner on approaching their tips/tops (Gudmundsson et al., 1999). This thinning is most noticeable in the uppermost few tens of metres below the arrested tip (Geshi et al., 2010, 2012). In fact, such a thinning is seen in the exposed parts of the dikes in Figs. 2–4. It follows that all the arrested dikes in Figs. 2–5 could be thicker at depths below the present exposures.

The dikes seen in Figs. 2–5, and in the field in general, are segments. The entire three-dimensional structures of dikes are, for obvious reasons, never seen exposed in the field. Many dikes, however, have been traced for tens of kilometres in essentially lateral sections, some for hundreds of kilometres, and others in vertical sections for tens to hundreds of metres (e.g., Delaney and Pollard, 1981; Rickwood, 1990; Ernst et al., 2001; Geshi et al., 2010, 2012; Kavanagh and Sparks, 2011), so that the general field geometries of dikes are well known. It is, for example, well established that dikes are normally segmented and propagate as segmented fractures – a conclusion also supported by observations of the development of dike-fed volcanic fissures (e.g. Gudmundsson, 2017) and seismic and geodetic studies of dike propagation (Gudmundsson et al., 2014; Sigmundsson et al., 2015).

In view of the segmentation, a question is sometimes raised to the effect that while individual dike segments may be seen arrested (Figs. 2–5), it does not follow that the entire dike became arrested. More specifically, the observations of arrested dike segments, such as those

in Figs. 2–5, does not preclude the possibility that other segments of the dike reached the surface to erupt - were feeders. That interpretation is correct in the sense that all the observations of arrested dikes as seen in the field refer to dike segments. But the same applies to all measurements of dikes in the field – and to those of other types of fractures (and most structures) as measured in specific outcrops. Namely, the measurements – say of an attitude (strike and dip) or opening/thickness - always refer to a given segment or part of the structure. The results of such measurements are statistical in nature, and the same applies to observed vertical ends of dikes. More specifically, most vertical ends of dike segments, as observed in numerous outcrops worldwide, are arrested rather than connected to eruptive materials (such as crater cones, lava flows, and pyroclastic flows). It then follows that most dike segments and - since individual dikes are simply collections of dike segments - most vertical ends or tips of entire dikes also become arrested.

3. Numerical modelling - framework

In the following numerical models, the finite-element-method (FEM) software Comsol Multiphysics (www.comsol.com) is used to analyse the local stresses and displacements induced by dikes in a mechanically layered crustal segment hosting a volcano/volcanic zone. Like other FEM software, Comsol divides or discretises the problem to be solved into an equivalent system of small units or 'elements' and solves simultaneous algebraic equations. The resulting numerical approximations for each element are then combined into solutions for the entire body. The solutions are approximate solutions for the differential equations that describe the problem. At the corners of the elements (and sometimes also along their outer lines), are the nodes that connect the elements. In calculations, loads (stresses, displacements, or, as here, magmatic overpressures) are applied to these nodes and the resulting displacements at each node calculated. From these displacements, the nodal stresses and the element stresses, strains, and displacements are derived using linear equations (cf. Deb, 2006; Liu and Quek, 2014).

The results are specific solutions to a particular set of conditions and, as indicated, provide solutions only for the specified points in the body. In the models presented here the layered crustal segment hosting the dike is divided or discretised using triangular elements (Fig. 6b). All the models are fastened in the corners, so as to avoid rigid-body rotation and translation. The dimensions of the computational domain are 20 km × 20 km. This is large enough so that the main displacements and stresses induced by the dike are unaffected by the boundary conditions of the models being fastened in the corners. More specifically, the main dike-induced stresses and displacement are within a few kilometres of the dike tip, and are negligible at distances of 10 km to either side of the tip (where the model is fastened).

The crustal segment hosting the dike, including all the layers of which it is composed, is assumed to behave as elastic. This assumption rests experimental physics results which show that solid rocks at crustal conditions and low strain normally behave as elastic (Gudmundsson, 2011b). But also on in-situ or field measurements of crustal deformation around fault zones prior to earthquake ruptures and at volcanoes during inflation and deflation periods, all of which suggest elastic behaviour to a first approximation (Scholz, 1990; Dzurisin, 2006; Segall, 2010). No failure criteria is used for the dikes, because in all the models the dikes are already emplaced with a tip at 500 m depth below the surface and propagate no further – that is, the tip becomes arrested at this depth. When estimating whether the dike-induced stresses and displacements would be large enough to cause tension fractures and/or faults, the normal criteria for the formation of

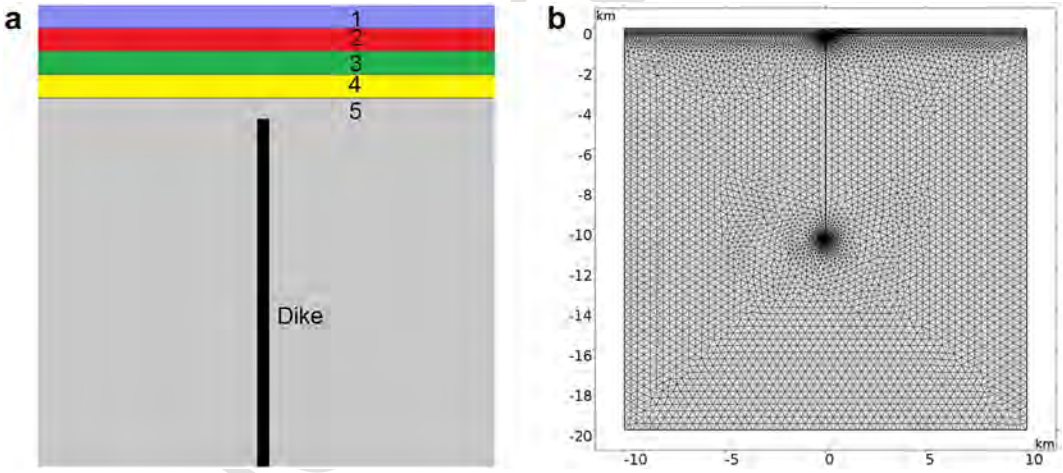

Fig. 6. Setup of the numerical models. (a) Schematic illustration of the modelled dike. The dike is vertical with a tip or top arrested at 0.5 km below the free surface of the volcanic zone/volcano within which the dike is emplaced. In all the models and figures the x-axis is the horizontal axis and the y-axis the vertical axis. The model itself is 20 km × 20 km in size. Each of the four layers above the dike tip (layers 1–4) is 100 m thick, whereas layer 5, the unit hosting the dike, extends to the lower tip of the dike (arbitrarily the dike dip dimension or height is set at 10 km). The indicated dike thickness is not to scale (it is far too thick in comparison with the thickness of the crustal layers). The actual dike thickness depends on the overpressure used, the dike dimensions, and the Young's modulus of the host rock (there is greater dike thickness for given overpressure and dimensions in more compliant layers or units). In the model the entire dike is located in the comparatively stiff unit/layer 5 (with a Young's modulus of 40 GPa). Simple fracture-mechanics models (Gudmundsson, 2011b; Becerril et al., 2013) indicate model-dike thickness of about 2.3 m for an overpressure of 5 MPa and a thickness of 6.9 m for an overpressure of 15 MP. This range is similar to common thicknesses of dikes as observed in the field (Rickwood, 1990; Delaney and Pollard, 1981; Gudmundsson, 2002; Geshi et al., 2010; Becerril et al., 2013). In most models, the Young's moduli are as follows: layer 1 modulus of 3 GPa, layer 2 modulus of 20 GPa, layer 3 modulus of 30 GPa, and layer or unit 5 modulus of 40 GPa. The modulus of layer 4 is varied between models, from 0.01 GPa (very soft) to 20 GPa (moderately stiff). All the layers, 1–5, have a Poisson's ratio of 0.25. We also tested some models with a very stiff surface layer 1, namely with a modulus of 20 GPa. In most models the magmatic overpressure of the dike (the only loading) is 5 MPa, but we also tested all the models with an overpressure of 15 MPa, and show two of them here. (b) Setup of the Comsol model with the 10 km tall dike in the central upper part (black, thick line) of the model (whose dimensions are 20 km × 20 km, as indicated above). The minimum element quality is 0.4534 m, the number of boundary triangular elements is 1100, and the total number of elements in the model is 12,981.

these fractures (based on tensile strength and shear strength) are used as a basis (Gudmundsson, 2011b).

In all the models the only loading is internal magmatic overpressure (driving or net magmatic pressure) defined as (Gudmundsson, 2011b):

$$p_o = p_e + (\rho_r - \rho_m)\, gh + \sigma_d \quad (1)$$

Here p_o is the overpressure, ρ_r the average host-rock density, ρ_m the average magma density, g the acceleration due to gravity, h the dip dimension of the dike, and σ_d the differential stress (the difference between the maximum and the minimum principal stress) - at the time of emplacement - in the host rock where the dike is studied. The dip dimension of a dike (and any rock fracture) is its dimension in the direction of dip, that is, the height (in seismology the width) of the dike. Similarly, strike dimension is the dike dimension in the direction of strike, that is, its outcrop length (Gudmundsson, 2011b).

The second term on the right-hand side of Eq. (1) is the buoyancy term. For almost all volcanoes and volcanic zones, the average density of the uppermost 1–3 km of the crust is 2500–2600 kg m^{-3}. By contrast, basaltic magma at depth may have density between 2650 and 2800 kg m^{-3} (e.g., Gudmundsson, 2011b). Consequently, in the uppermost part of the crust, buoyancy for basaltic magmas is commonly potentially negative. During ascent of magma, there is normally gas expansion which reduces the magma density. Gas expansion and density reduction is common in acid magmas to depths of many kilometres (Gonnermann and Manga, 2013). By contrast, much of the gas exsolution in basaltic magmas takes place at very shallow depths. Studies in Hawaii, for example, suggest that gas exsolution in basaltic magmas occurs primarily in the uppermost few hundred metres of the feeder-dike/conduit (Greenland et al., 1985, 1988). Field studies of basaltic dikes, sills, and inclined sheets in deeply eroded lava piles and central volcanoes show only small and rather infrequent gas-formed vesicles at depths exceeding several hundred below the original surface of the volcanic zone/central volcano, while large and small vesicles are common very close to the surface (Fig. 2), particularly in feeder-dikes (Galindo and Gudmundsson, 2012; Gudmundsson, 2017).

Density decrease of basaltic magma due to gas exsolution is thus unlikely to affect the potential negative buoyancy term in Eq. (1), except close to the surface. For basaltic dikes injected from shallow magma chambers the only driving pressure in Eq. (1) is therefore commonly the excess pressure p_e in the chamber at the time of its rupture. That pressure is roughly equal to the tensile strength of the walls or, normally, the roof of the magma chamber. The tensile strength of most rocks is between 0.5 and 9 MPa, the common values being 2–5 MPa. We use 5 MPa magmatic overpressure in most of the models. However, some basaltic dikes are injected directly from deep-seated reservoirs at 15–25 km depth, or deeper (Fig. 1), in which case the overall crustal density is higher than that of typical basaltic magma and the buoyancy term is positive. To take this into account, we also ran models where the dike overpressure is 15 MPa. Generally, the results are similar for the 5 MPa and the 15 MPa dike overpressure, except that the magnitudes of the dike-induced stresses and displacements are, of course, larger for the models with 15 MPa overpressure. This is as expected, since we use linear elastic material for the crustal layers, so that the stresses and deformation/displacements are proportional to the overpressure, for a given dike geometry and rock properties. Nevertheless, we show a few of the 15 MPa-overpressure models just to emphasise how the geometry and magnitudes of the stresses and displacement change proportionally with the overpressure.

In all the models the dike is vertical and with an upper tip at 500 m below the free surface of the volcano/volcanic zone (Fig. 6). The dike dip dimension is taken as 10 km, but is to a degree arbitrary. The indicated dike thickness in Fig. 6 is not to scale (it is far too thick in comparison with the thickness of the crustal layers). The actual dike thickness depends on the overpressure used, the dike dimensions, and the Young's modulus of the host rock (there is greater dike thickness for given overpressure and dimensions in more compliant layers or units). The entire dike is located in the comparatively stiff unit/layer 5 (with a Young's modulus of 40 GPa), in which case fracture-mechanics models (Gudmundsson, 2011b; Becerril et al., 2013) indicate model-dike thickness of about 2.3 m for an overpressure of 5 MPa (similar to that of the dike in Fig. 3) and 6.9 m for an overpressure of 15 MPa. These values cover a range similar to common thicknesses of dikes worldwide (Rickwood, 1990; Delaney and Pollard, 1981; Gudmundsson, 2002; Geshi et al., 2010; Becerril et al., 2013). For the present purpose the surface is taken as flat, so that it is more appropriate for a volcanic zone or a caldera will little topography than for a volcanic edifice that stands high above its surroundings. In all the models, there is one unit or layer hosting the dike, and then 4 layers of different mechanical properties above the dike tip. Each of these 4 layers has a thickness of 100 m, but their mechanical properties vary between model runs.

The main point of the layering used in the models is to study the effects of variation in Young's modulus or stiffness on the dike-induced stresses and displacements. For this purpose we vary the stiffnesses of the layers but not the thicknesses between model runs. By contrast, the thickness of the layers, here taken as 100 m, is somewhat arbitrary. Sedimentary layers with thicknesses of tens of metres or more are common in volcanic zones – such as late glacial sediments which underlie many Holocene lava flows in the volcanic zones of Iceland. Similarly, hyaloclastite (basaltic breccia) layers and units formed during the last glacial period reach thicknesses of hundreds of metres and are commonly compliant (Gudmundsson, 2017). Comparatively thick compliant sedimentary and hyaloclastite layers, as well as pyroclastic layers (Figs. 2 and 3), are common in volcanic zones and central volcanoes, thereby reflecting the thicknesses used in the models. More generally, however, the 100-m-thick layers may be regarded as 'seismic layers', that is, groups of layers with similar seismic/mechanical properties, in which case the thicknesses of the layers in the models would be interpreted as mechanical/seismic rather than lithological.

In most of the numerical models the overpressure of the dike is 5 MPa and layering is as follows (Fig. 6). The surface layer has a Young's of 3 GPa, the second layer from the top a Young's modulus of 20 GPa, the third layer from the top a Young's modulus of 30 GPa, the fourth layer from the top a variable Young's modulus, and the fifth layer from the top, that is, the unit hosting the dike, a Young's modulus of 40 GPa. These are all reasonable values for typical volcanic zones (e.g., Gudmundsson, 2011b). In particular, many Holocene lava flows have static Young's moduli of the order of several mega-pascals and young pyroclastic layer may be still lower. Older lava flows, such as layers 2 and 3 here, may have static Young's moduli of 20–30 MPa, while some would be lower. The stiffness of 40 GPa is similar to the estimated average static Young's modulus of the uppermost 10 km of the volcanic rift zones in Iceland (Gudmundsson, 2003, 2011b).

We also tested some models with stiffer surface layers, namely 10 GPa and 20 GPa, some of the results being indicated below. The main change between model runs, however, is the stiffness of the

fourth layer from the top. We vary the stiffness of layer 4 between model runs so as to explore the effects on dike-induced stresses and displacements. The Young's moduli used for layer 4 vary from 10 GPa, which is reasonably stiff, to 0.01 GPa, which is very compliant. However, it is likely that most or all active volcanic zones and central volcanoes contain layers as soft as 0.1–0.01 GPa. This follows because such zones normally contain many layers of unconsolidated pyroclastics, including tuff layers, and many contain unconsolidated soils and sediments. In addition, clays are common in some of the volcanoes, particularly in association with geothermal fields. As examples, the normal range of Young's moduli (measured in the laboratory) of unconsolidated sand is 0.01–0.1 GPa, that of clay is 0.003–0.5 GPa, and that of tuff 0.05–5 GPa (Gudmundsson, 2011b). The models discussed are presented in the order of gradually decreasing stiffness of layer 4.

4. Numerical modelling - results

4.1. Layer 4 with a stiffness of 10 GPa

In the first model layer 4 has a stiffness of 10 GPa, or similar to the in-situ stiffness of a lava flow, a welded pyroclastic layer, or a sedimentary rock. The results as regards stress (Fig. 7) show that layer 4, being of lower stiffness than the adjacent layers (40 GPa below and 30 GPa above), tends to suppress the tensile the minimum principal compressive or maximum tensile stress, σ_3 (Fig. 7a) as well as the von Mises shear stress (Fig. 7b). Yet considerable stresses pass through layer 4 up into layers 3 and 2. This is confirmed in the stress-magnitude curves plotted at the contacts between the layers (Fig. 7c). All the stress curves show the typical double-peak variation in σ_3, but the distance between the peaks is much smaller in layers 4 and 5 than in the other 3 layers. This is partly because these layers are closer to the surface, and partly because of the variation in the mechanical properties of the layers.

The white (Fig. 7a) and black (Fig. 7b) ticks show the direction of the trajectories of the maximum principal compressive stress, σ_1. Below about 2 km, that is, far from the free surface of the earth, the ticks are horizontal and perpendicular to the dike. They continue to be perpendicular to the dike down to its bottom (not shown here). This is as expected since the magmatic overpressure in the dike (here 5 MPa) induces horizontal compressive stress in the surrounding host rock. Close to the surface, however, there is rotation of σ_1 close to the dike, but further away from the dike the ticks are still horizontal and perpendicular to the dike. This rotation is presumably related to the

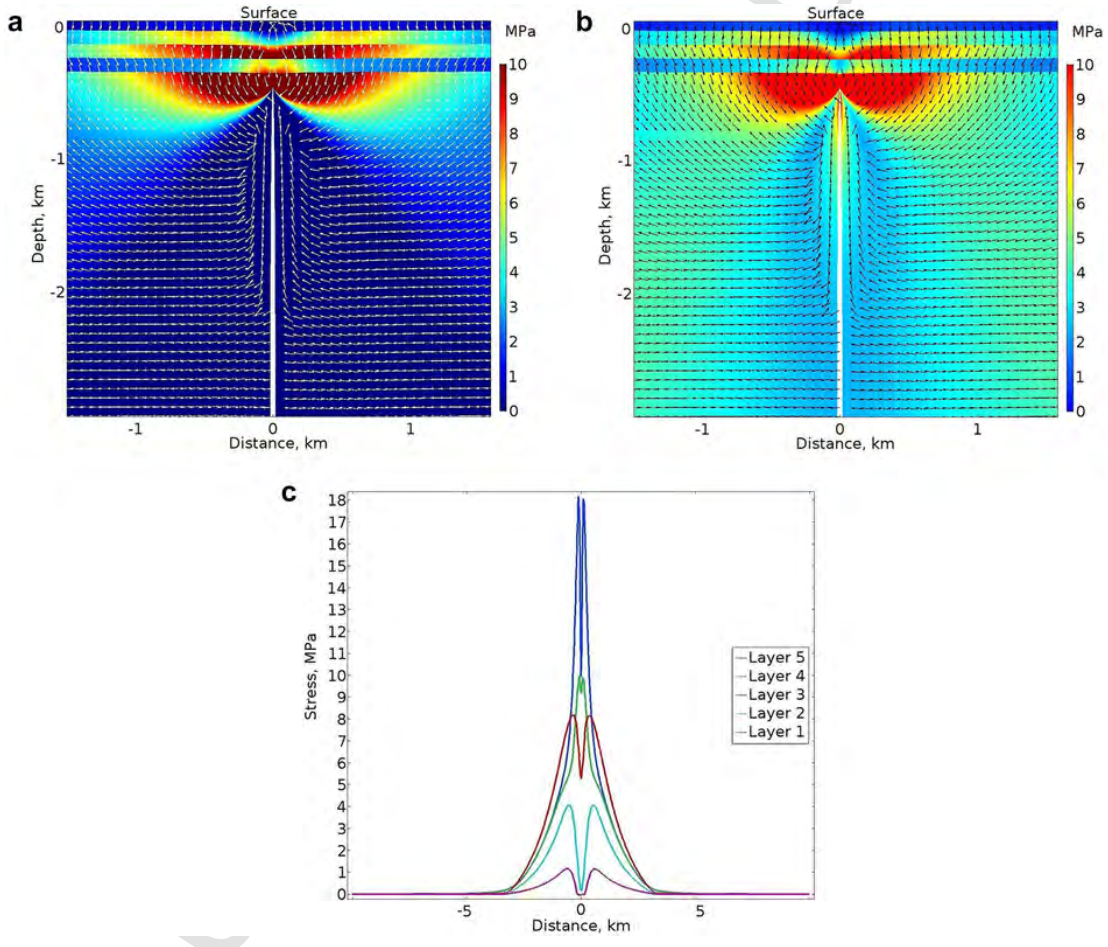

Fig. 7. Numerical model results with the following Young's moduli: 3 GPa (layer 1), 20 GPa (layer 2), 30 GPa (layer 3), 10 GPa (layer 4), and 40 GPa (layer 5). Overpressure of dike: 5 MPa. (a) Contours of the maximum tensile principal stress σ_3 in mega-pascals (red highest stress, blue lowest), with white arrows (ticks) indicating the direction or trajectories of the maximum principal compressive stress σ_1. (b) Contours of the von Mises shear stress in mega-pascals. (c) Plots of the variation in the magnitude of the maximum tensile principal stress σ_3 (in mega-pascals) at the contacts between the layers. Layer 5 denotes the contact between layer 5 and 4. Layer 4 denotes the contact between layer 4 and 3. Layer 3 denotes the contact between layer 3 and 2. Layer 2 denotes the contact between layer 3 and 2. Layer 1 denotes the contact between layer 1 and the atmosphere, that is, is the free surface of the volcanic zone/volcano. (For interpretation of the references to colour in this figure legend, the reader is referred to the web version of this article.)

free-surface effects, that is, the fact that the uppermost part of the dike is close to the free surface of the Earth.

The associated displacements are given for lateral and vertical directions (Fig. 8). For the present model, the lateral displacements at the surface (layer or contact 1) and all the contacts (layers 2–5) are similar and reach a maximum of about 44 cm (Fig. 8a) at a lateral distance of around 3 km from the dike (the dike is located at 0 km). The vertical displacements induced by the dike are also generally similar (Fig. 8b). The model predicts absolute subsidence or downward vertical displacement of the layers just above the dike tip, of a maximum of about 16 cm for layer 5 (the lowermost contact), but about 12 cm for the other layers. Similarly, there is a double-peak rise or upward vertical displacement on either side of the dike, reaching a maximum uplift of about 34 cm. The maximum upward vertical displacement occurs in two peaks at about 3 km to either side of the dike projection to the surface.

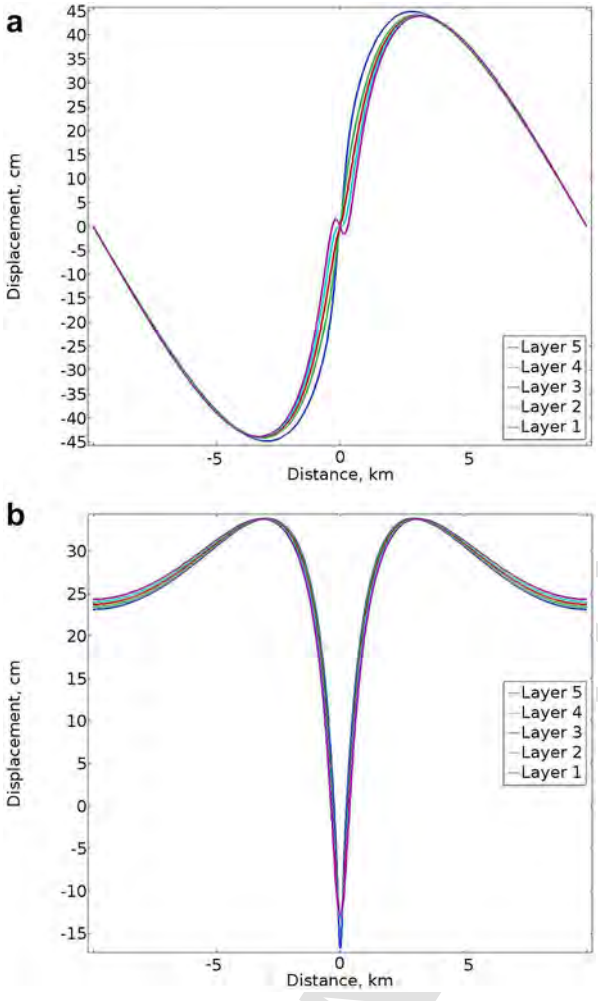

Fig. 8. Lateral and vertical displacement of the contacts between layers (denoted as layers 1–5) in the model in Fig. 7. (a) Here the lateral displacements at all the contacts, including the surface (layer 1), are similar and reach a maximum of 44 cm at a horizontal distance of about 3 km from the dike (the dike projection to the surface is located at 0 km). Displacements to the right of the dike are regarded arbitrarily as positive whereas those to the left of the dike as negative. (b) All the vertical displacements at the contacts are here also similar. The maximum uplift or vertical displacement of the contacts is about 34 cm and occurs at a horizontal distance of about 3 km on either side of the dike. Right above the tip of the dike there is a general subsidence of 12 cm for all the contacts except for the contact between layers 5 and 5 (denoted as layer 5), where the subsidence reaches 16 cm.

Comparison of Figs. 7c and 8b shows that while the peak of the surface tensile stress (layer or contact 1) is at about 0.5 km measured horizontally from the projection of the dike to the surface (Fig. 8b), the peak of the upward vertical displacement is at 3 km from the projection of the dike to the surface. Although not shown here, our results shown that the surface peak of the von Mises shear stress also coincides roughly with the peak of the tensile stress at the surface. The lateral distance from the projection of the dike tip to the surface to the peak on either side is roughly equal to the depth to the tip or top of the dike. This suggests that the maximum width of a dike-induced graben is roughly double the vertical distance to its bottom or the top (upper tip) of the dike. For this relation to hold in general, the boundary faults of the graben must have shallow dips between 40° and 50°. Such shallow dips on graben faults do occur, particularly in sedimentary basins, but are not common on grabens in volcanoes and volcanic zones, where normal-fault dips are mostly 60–80°, and some vertical close to the surface (e.g., Gudmundsson, 2005, 2017). In the latter case, the width of the induced graben would be less than twice the vertical distance to the top of the dike. Another exception to this relationship between the depth to the dike top and the lateral distance between the induced stress peaks at the surface is when there is an open contact between layers, usually at shallow depths, in which case the stress peaks occur above the lateral ends of the open contact (Gudmundsson, 2003). Thus, in the absence of open contacts that deflect the stress peaks laterally or vertical or steeply dipping normal faults, the above relationship holds (sometimes referred to as the 'graben rule'), as is confirmed by many numerical models (e.g., Al Shehri and Gudmundsson, 2018).

In the present model, and in the subsequent models, because the dike tip is arrested at 0.5 km depth, the lateral distance to the stress peaks on either side of the dike is about 0.5 km. Thus, the lateral distance between the peaks is about 1 km. As discussed further below, if any tension fractures and/or normal faults would be induced by an arrested dike, they would tend to form at the location of the tensile and shear stress peaks at the surface and not at the location of the maximum vertical upward displacement of the surface.

4.2. Layer 4 with a stiffness of 1 GPa

Certain aspects of the stress field remain very similar when the stiffness of layer 4 is reduced from 10 to 1 GPa (Figs. 7 and 9). For example, the direction of the trajectories of the maximum principal compressive stress, σ_1, is very similar, as they are in all the models. There are, however, clear differences. The first is that layer 4 with a stiffness of 1 GPa has much lower tensile and shear stresses than when its stiffness is 10 GPa. The zones of high stresses, tensile and shear, are also much more extensive in layer 3 when layer 4 has a stiffness of 10 GPa than when its stiffness is 1 GPa. This means that higher stresses 'pass through' the 10 GPa layer than through the 1 GPa layer to the shallower layers (Figs. 7a,b and 9a,b). By contrast, the area (volume in 3D) of high stress (red) in layer or unit 5 just under layer 4 is larger in Fig. 9a,b than in Fig. 7a,b, indicating that as less high stress passes through layer 4, more stress above the dike tip becomes concentrated at its contact with the stiff layer or unit 5.

As in the previous model (Fig. 8), the lateral and vertical displacements at the surface (layer or contact 1) and at the other layers/contacts are generally similar, except for layer 5, that is, the layer or unit hosting the dike (Fig. 10). The lateral displacements for most of the layers (layers 1–4) reach a maximum of about 40 cm at about 4 km from the dike (Fig. 10a). By contrast, the lateral displacement of layer 5 reaches a maximum of about 47 cm at a distance of about 2.7 km from the dike. We are here beginning to see the effect of softening of

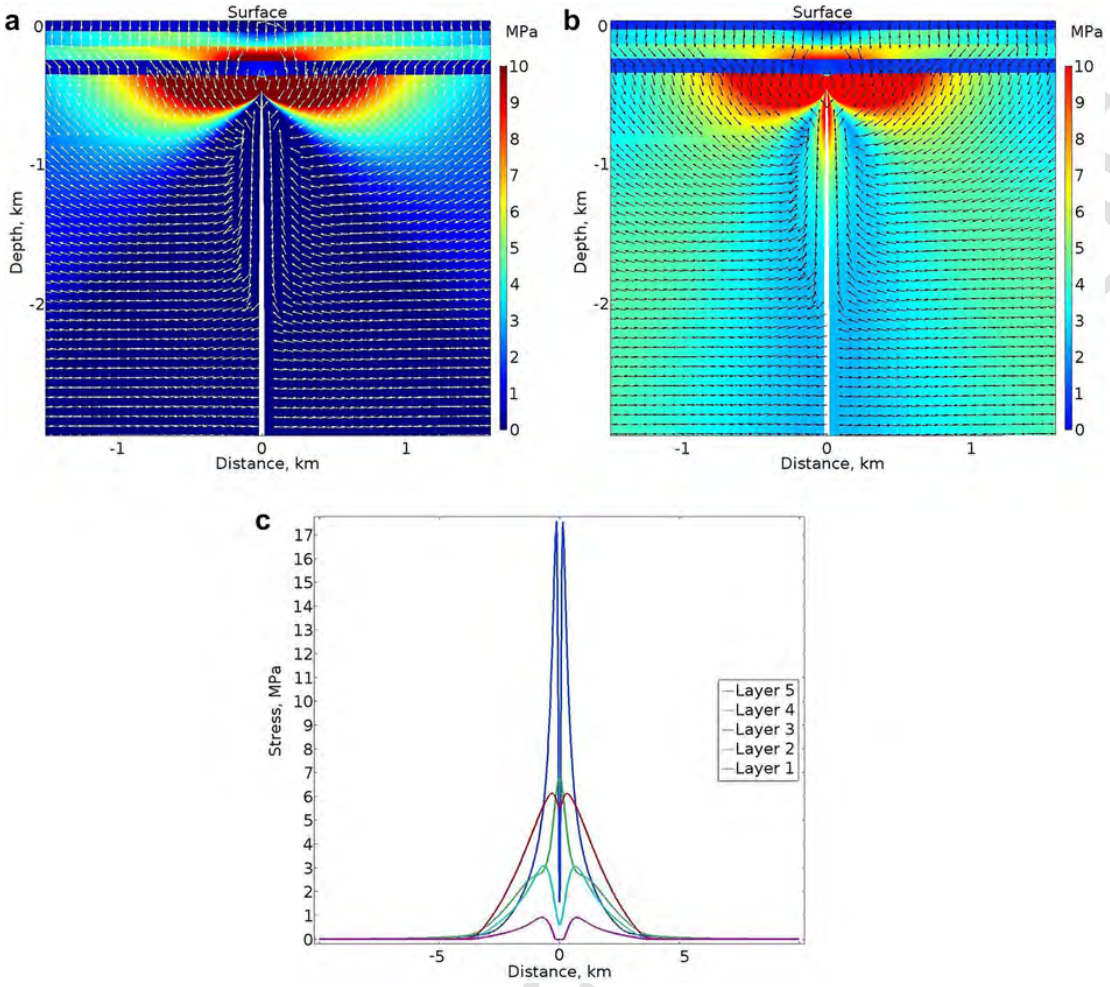

Fig. 9. The same model as in Fig. 7 except that layer 4 has here a Young's modulus of 1 GPa. (a) Contours of the maximum tensile principal stress σ_3 (red highest stress, blue lowest), with white arrows (ticks) indicating the direction or trajectories of the maximum principal compressive stress σ_1. (b) Contours of the von Mises shear stress. (c) Plots of the variation in the magnitude of the maximum tensile principal stress σ_3 at the contacts between the layers. Layer 5 denotes the contact between layer 5 and 4. Layer 4 denotes the contact between layer 4 and 3. Layer 3 denotes the contact between layer 3 and 2. Layer 2 denotes the contact between layer 3 and 2. Layer 1 denotes the contact between layer 1 and the atmosphere, that is, is the surface of the volcanic zone/volcano. (For interpretation of the references to colour in this figure legend, the reader is referred to the web version of this article.)

layer 4 in that the displacements below and above that layer are gradually more out of phase.

This difference between the displacement of layer 5 and the other layers is also seen in the vertical displacement (Fig. 10b). While the maximum upward displacements of all the layers roughly coincide and reach about 34 cm at a distance of about 3 km from the dike, the maximum downward displacements show differences between layer 5 and the other layers. In particular, while layers or contacts 1–4 show a maximum subsidence of about 7 cm below the surface in the centre above the dike tip, layer or unit 5 shows a displacement of as much as 14 cm at the same location.

4.3. Layer 4 with a stiffness of 0.1 GPa

At this low stiffness of layer 4, little stress passes through the layer. As a consequence, the stresses above layer 4, such as in layer 3, are very low (Fig. 11). At the same time the tensile and shear stress concentration in layer 5 increase (Fig. 11a,b). These results are confirmed by the stress-magnitude curves (Fig. 11c). These show that while the tensile stress in layer 5 peaks at about 19 MPa, hardly any stresses (fraction of a mega-pascal) reach the surface (layer or contact 1) and only about 1 MPa reach the contact between the surface layer and layer below (contact or layer 2).

Here the lateral and vertical displacements of the layers/contacts are increasingly different close to the dike – that is, close to zero (Fig. 12). The maximum lateral displacement however, is still similar for layers/contacts 1–4, as regards the magnitude, about 20 cm, and location - at about 4.3 km from the dike (Fig. 12a). By contrast, the maximum lateral displacement of layer 5, that is, the layer or unit hosting the dike, reaches a maximum of about 52 cm at 3 km from the dike.

While the maximum upward displacements of all the layers roughly coincide and reach about 34 cm at a distance of about 2.8 km from the dike, the maximum downward displacements show an increasing difference between layer 5 and the other layers. Here layers 1–4 do not show any absolute subsidence above the dike tip, in contract to that in previous models. There is still a clear trough or two-peak displacement, but the surface (layer 1, and contacts 2–4) is still at about 2 cm above the un-deformed surface. Layer 5, however, shows an absolute vertical subsidence of as much as 18 cm right above the dike tip (Fig. 12b).

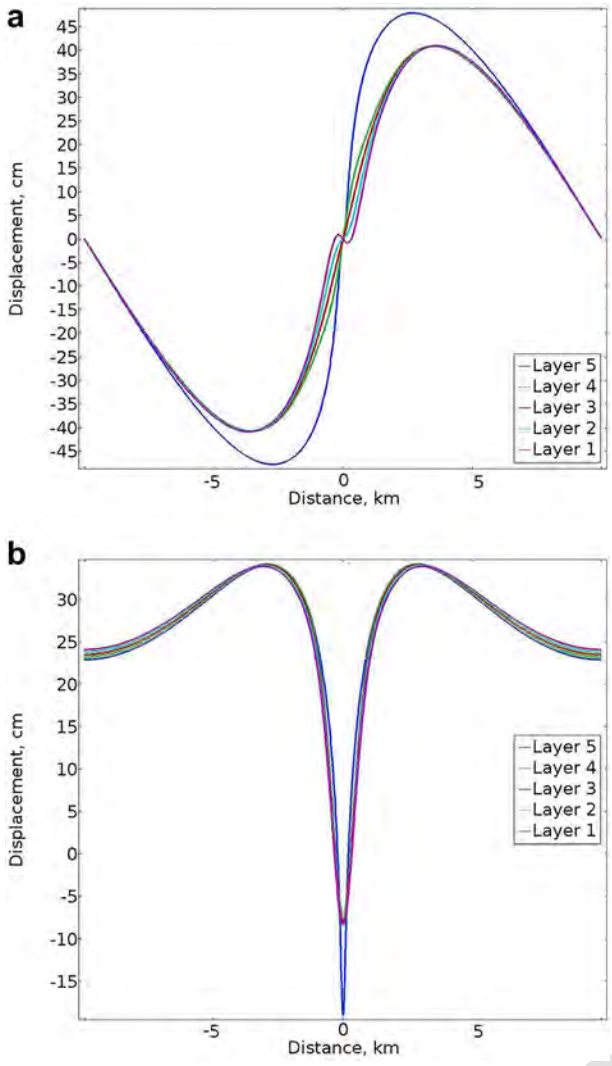

Fig. 10. Lateral and vertical displacement of the contacts between layers (denoted as layers 1–5) in the model in Fig. 9. (a) The lateral displacements at all the contacts, including the surface (layer 1), are similar except for layer 5 (contact 5/4) and reach a maximum of 40 cm at a horizontal distance of about 4 km from the dike (the dike is located at 0 km). By contrast, the lateral displacement of layer 5 (contact 5/4) reaches a maximum of about 47 cm at a distance of about 2.7 km from the dike. Displacements to the right of the dike are regarded arbitrarily as positive whereas those to the left of the dike as negative. (b) All the vertical displacements at the contacts are here also similar, except for layer 5 (contact 5/4). The maximum uplift or vertical displacement of the contacts is about 34 cm and occurs at a horizontal distance of about 3 km on either side of the dike. Right above the tip of the dike there is a general subsidence of 7 cm for all the contacts except for contact 5/4 (layer 5) where the subsidence reaches 14 cm.

4.4. Layer 4 with a stiffness of 0.01 GPa

Such a low-stiffness layer 4 effectively blocks or suppresses all the stress above layer 5. little stress passes through the layer. As a consequence, there are hardly any tensile or shear stresses in layers 1–4 while stresses in layer 5 above and around the dike tip up to the contact with layer 4 increase (Fig. 13a,b). These results are seen more clearly by the stress-magnitude curves (Fig. 13c). These show that while the tensile stress in layer 5 peaks at about close to 20 MPa, the surface stresses in layers/contacts 1 and 2 above the dike are essentially zero, and a fraction of a mega-pascal for layers/contacts 3 and 4.

Here the maximum lateral displacements of layers/contacts 1–4 are somewhat dissimilar close to the dike, but reach a maximum of only about 4 cm at a distance of about 5 km from the dike (Fig. 14a). The maximum lateral displacement of layer 5, that is, the layer or unit hosting the dike, however, reaches a maximum of about 54 cm at a distance of about 2.8 km from the dike.

With the exception of layer/contact 5, the maximum upward displacements of all the layers/contacts roughly coincide and reach about 35 cm at a distance of about 3.3 km from the dike (Fig. 14b). Layers/contacts 1–4 show a clear trough or two-peak displacement above the dike tip, but the surface (layer/contact 1) and layers/contacts 2–4 is still at about 13 cm above the un-deformed surface. By contrast, layer/contact 5 shows a maximum upward displacement of about 35 cm, but the location is different from that of the other layers/contacts, namely at a distance of about 2.6 km from the dike.

This model and the previous one (with layer 4 of stiffness 0.1 GPa) show that further softening of layer 4 makes the variation in internal stresses and displacements induced by the dike more complex than in the models where layer 4 had more similar stiffness to that of the adjacent layers. In particular, the results show that the differences in magnitudes and locations of the horizontal and vertical displacements increase as layer 4 becomes softer.

5. Discussion

Because of their role in assessing volcanic hazards and estimating geometries of dikes (including their volumes) injected from magma chambers/reservoirs during unrest periods, surface deformation studies in volcanoes/volcanic zones are of increasing importance in volcanology. In particular, geodetic studies together with seismic studies are of fundamental importance for assessing dike volumes, and thus the volume of magma supposed to flow out of the chamber/reservoir during the associated unrest period. In addition, deformation studies help determine the dike path and assess the likelihood of dike-fed eruptions.

There have been many numerical models on local stresses and surface deformation during inflation of magma chambers hosted by layered rocks. These include, for example, Gudmundsson (2002), Gudmundsson and Philipp (2006), Manconi et al. (2007), and Masterlark (2007). These provide information on local stresses and deformation inside volcanoes that can be of great use in making crude forecasts as to the likely paths of injected dikes, but do not address the stresses and displacements/deformation induced by the dikes themselves (or mode I cracks, extension fractures, in general), which is the main theme of the present paper.

Following earlier general analytical studies of the deformation and stresses at the surface of an elastic half-space above an elliptical crack (Isida, 1955; Tuschida and Nakahara, 1979) there have been many numerical fracture studies focusing on dikes in an elastic half-space. These include studies by Pollard et al. (1983), Davis (1983), Rubin and Pollard (1988), and Cayol and Cornet (1998). A very different approach is to model dikes as elastic dislocations. The models are applied to invert surface geodetic data to infer the opening or thickness, strike, dip, and depth of dikes, inclined sheets, and sills. The application of the dislocation theory volcano deformation is reviewed in detail by Okada (1985, 1992) and also by Dzurisin (2006) and Segall (2010).

All these numerical and dislocation models assume the volcanic zone/volcano hosting the dike to act as a homogeneous, isotropic, elastic half-space. This means that the models do not consider the ef-

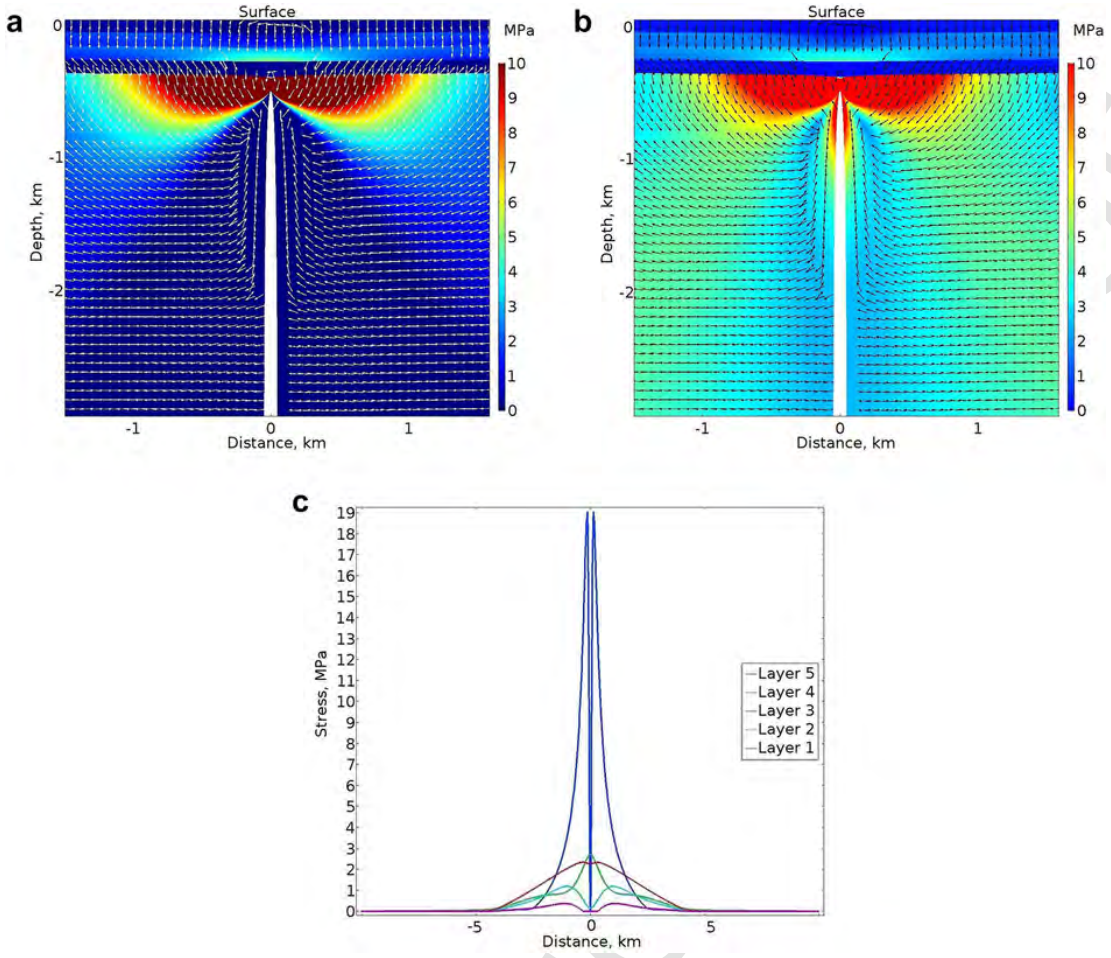

Fig. 11. The same model as in Fig. 7 except that layer 4 has here a Young's modulus of 0.1 GPa. (a) Contours of the maximum tensile principal stress σ_3 (red highest stress, blue lowest), with white arrows (ticks) indicating the direction or trajectories of the maximum principal compressive stress σ_1. (b) Contours of the von Mises shear stress. (c) Plots of the variation in the magnitude of the maximum tensile principal stress σ_3 at the contacts between the layers. Layer 5 denotes the contact between layer 5 and 4. Layer 4 denotes the contact between layer 4 and 3. Layer 3 denotes the contact between layer 3 and 2. Layer 2 denotes the contact between layer 3 and 2. Layer 1 denotes the contact between layer 1 and the atmosphere, that is, is the surface of the volcanic zone/volcano. (For interpretation of the references to colour in this figure legend, the reader is referred to the web version of this article.)

fects of mechanical layering or contacts between layers on the dike-induced stresses and deformation. Surface deformation in layered elastic host rocks, however, has been considered by Roth (1993) and by Bonafede and Rivalta (1999a, 1999b). Dislocation and numerical models of dike-induced deformation are reviewed by Rivalta et al. (2015) and by Townsend et al. (2017).

With a few exceptions, all these models focus on the surface displacement induced by the dike. Only a few studies have combined field observations of arrested dikes/hydrofractures in layered rocks with numerical models of the local stresses induced by the dike in the adjacent layers as well as at the surface. These studies include Gudmundsson and Brenner (2001), Gudmundsson (2003), Gudmundsson and Loetveit (2005), and Philipp et al. (2013). In contrast to the present study, none of these studies focuses on the changes in the dike-induced stresses and displacements/deformation inside the volcano/volcanic zone as a function of the variation in the elastic properties of the mechanical layering.

Since almost all the early models assume the rocks hosting the dike to be homogeneous and isotropic, and thus do not consider any layering, the most appropriate comparison as regards the present models is with the first models, namely where layer 4 has a stiffness of 10 GPa and thus rather similar to the stiffnesses of the adjacent layers. The present results are in good general agreement with the surface displacements obtained in the earlier elastic half-space models, such as summarised by Dzurisin (2006) and Segall (2010). In particular, for this model (layer 4 with stiffness of 10 GPa) the surface displacements and stresses show similarities to those obtained by Pollard et al. (1983) and Rubin and Pollard (1988).

The surface upward and downward displacements are of important for understanding better the location, geometry, and propagation paths of associated dikes. For understanding and forecasting dike-induced surface fracturing, however, the surface stresses are of main concern. This follows because tension fractures and faults form at the surface – or elsewhere – only if the local stresses reach certain magnitudes. These magnitudes are well known. For tension fractures, the local absolute tensile stress must normally reach at least 2–5 MPa, which is the most common tensile strength of rocks (Gudmundsson, 2011b). Similarly, for faults – here in particular dip-slip faults – the shear strength is normally about double the tensile strength, so commonly 4–8 MPa, which is, indeed, similar to common stress drops in earthquakes (Kanamori and Anderson, 1975; Scholz, 1990).

The present models (Figs. 7–14) show clearly that the location of the maximum surface uplift or vertical displacement does not coincide with the location of the maximum surface stress concentration.

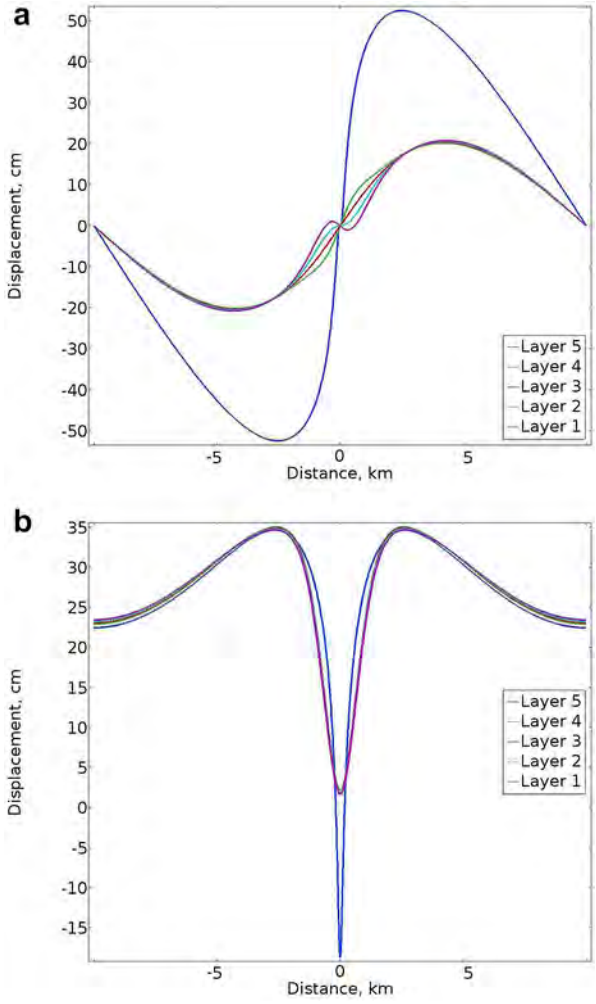

Fig. 12. Lateral and vertical displacement of the contacts between layers (denoted as layers 1–5) in the model in Fig. 11. Here the lateral and vertical displacements of the layers/contacts are increasingly different close to the dike. (a) The maximum lateral displacements are still similar for layers/contacts 1–4, about 20 cm at a distance of about 4.3 km from the dike. The maximum lateral displacement of layer 5 (contact 5/4), however, reaches a maximum of about 52 cm at about 3 km from the dike. Displacements to the right of the dike are regarded arbitrarily as positive whereas those to the left of the dike as negative. (b) The maximum upward displacements of all the layers roughly coincide and reach about 34 cm at a distance of about 2.8 km from the dike. Here, however, layers/contacts 1–4 do not show any absolute subsidence above the dike tip, while layer 5 (contact 4/5) shows an absolute maximum vertical subsidence of about 18 cm.

The maximum shear and tensile stress at the surface (as well as subsurface) roughly coincide and occur at locations widely different from those of maximum surface uplift. In particular, the lateral distance between the two peaks of the surface tensile (and shear) stresses is much less than that between the two peaks of the surface uplift. Thus, while the surface stresses peak at lateral distances of 0.5–0.7 km from the projection of the dike to the surface, the surface uplifts peak at 2.8–3.3 km from the project of the dike. The models clearly show that the maximum surface uplifts, the uplift peaks, do not show high tensile or shear stresses. This is understandable because the strain associated with uplift of a fraction of a metre over distances of kilometres to tens of kilometres is of the order of 10^{-4} to 10^{-5} and thus too small to result in high stress for the given Young's modulus of the surface layer of 3 GPa.

The maximum tensile and shear stress occurs at a lateral distance from the projection of the dike which is similar to the depth to the tip of the dike. The present results thus support other recent results on dike-induced stresses (Al Shehri and Gudmundsson, 2018) that any tension fractures or normal faults induced by arrested dikes would tend to form within a zone of a width similar to that of the depth to the tip of the dike. In particular, any dike-induced graben would be likely to be of a width similar to, or perhaps somewhat less than, the depth to the tip of the arrested dike. Our results thus do not lend any support to the common practice of interpreting the boundary faults of grabens as coinciding with the maximum uplift, the upward displacement peaks, at the surface above an arrested dike.

The only exceptions to the above relationship between the depth of the arrested dike tip (the dike top) and the location of the stress peaks at the surface occur when (1) the graben faults are steeply (sometimes vertically) dipping or (2) the contact arresting the dike also opens up through Cook-Gordon delamination or debonding (Gudmundsson, 2011a, 2011b). Contact delamination may happen at very shallow crustal depths, and has been modelled for arrested dikes (Gudmundsson, 2003, 2011b). The main result of the modelling is that for delamination the stresses at the surface normally peak above the lateral ends of the opened-up contact. It follows that the double-stress peak does not have any correlation with the depth to arrested tip of the dike (Gudmundsson, 2003). In the models in the present paper, however, the contacts are mechanically too strong to open up.

In all the models presented here the magmatic overpressure or driving pressure p_o is 5 MPa and the surface layer has a Young's modulus or stiffness of 3 GPa. We ran all the models also for the much higher magmatic overpressure of 15 MPa. The results are geometrically similar, while the absolute stresses induced by the dike are, as expected, higher. To test the maximum possible effects, we used the overpressure of 15 MPa combined with a surface layer with the very high stiffness of 20 GPa. This high stiffness in unrealistic but the models are intended to explore the greatest effects very stiff surface layers could have on the results (cf. Geyer and Gottsmann, 2010). We ran the models for the two cases of greatest importance, namely layer 4 with a stiffness of 0.1 GPa and stiffness of 0.01 GPa. The main aim was to see how great much the surface stresses would increase for high overpressure and very high surface stiffness in a volcanic zone/volcano with one or more soft layers (layer 4).

For layer 4 with stiffness of 0.1 the results show that the surface tensile and shear stresses reach about 5 MPa (Fig. 15). Thus tension-fracture and normal-fault formation (including graben formation) would be possible under these conditions. For this very great surface stiffness, the lateral distance between the stress peaks is about 2.2 km, rather than about 1.4 km so that the graben, if formed, would be somewhat wider than in the models with 3 GPa surface-layer stiffness. The results mean that for a dike with an arrested tip at 0.5 km below a very stiff surface of 20 GPa and with the high overpressure of 15 MPa, normal faulting and tension fracturing is just possible.

For layer 4 with stiffness of 0.01 GPa, an overpressure of 15 MPa, and a surface stiffness of 20 GPa, the results show that the surface tensile and shear stresses reach only a fraction of a mega-pascal (Fig. 16). Thus, even an unusually high surface-layer stiffness and overpressure for an arrested dike with a tip at the shallow depth of 0.5 km, the stresses at the surface are still far too small to generate either tension fractures or normal faults. The results thus underline the great effects of soft layers in reducing dike-inducing stresses and in suppressing surface stresses and fracture formation even for very high driving pressures and unusually stiff surface layers.

As regards the likelihood of dike-fed eruption, the models indicate that for 5 MPa overpressure little or no dike-induced surface defor-

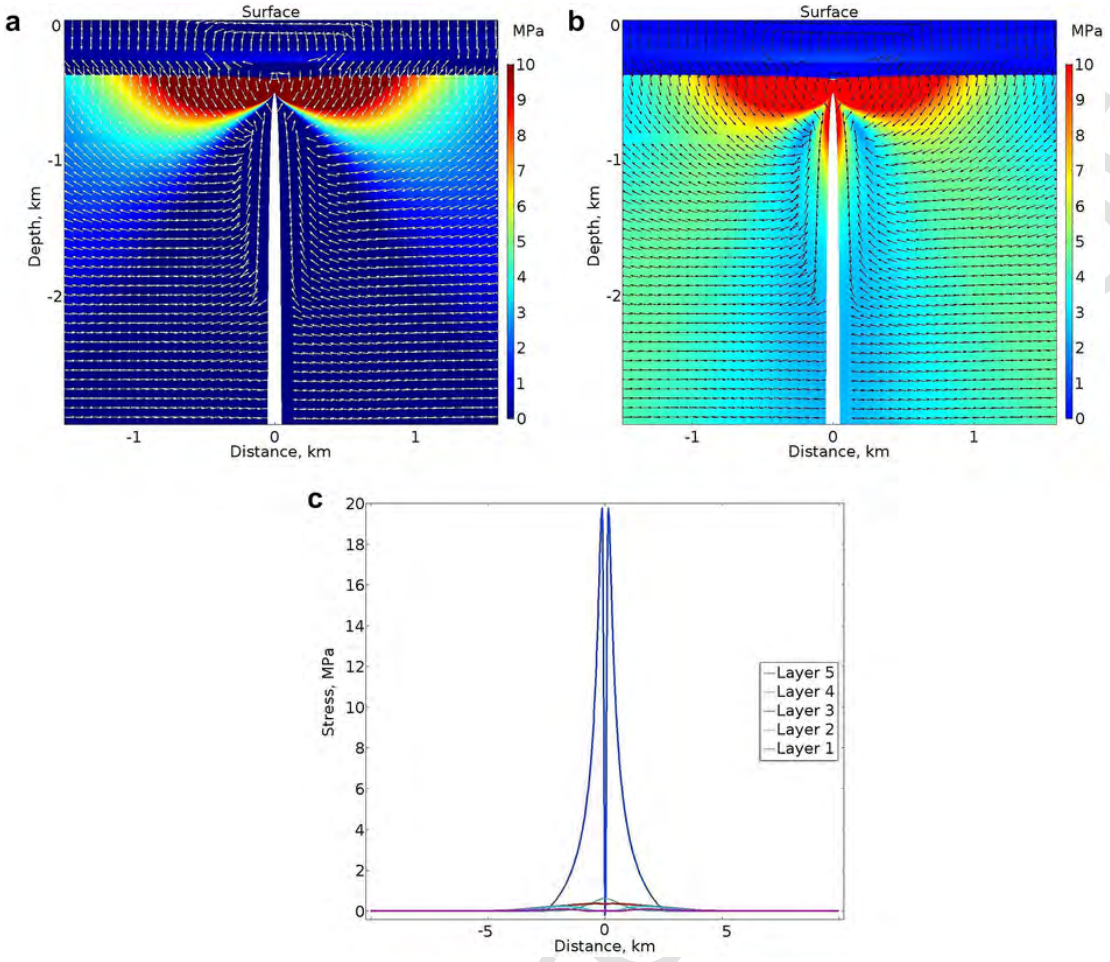

Fig. 13. The same model as in Fig. 7 except that layer 4 has here a Young's modulus of 0.01 GPa. (a) Contours of the maximum tensile principal stress σ_3 (red highest stress, blue lowest), with white arrows (ticks) indicating the direction or trajectories of the maximum principal compressive stress σ_1. (b) Contours of the von Mises shear stress. (c) Plots of the variation in the magnitude of the maximum tensile principal stress σ_3 at the contacts between the layers. Layer 5 denotes the contact between layer 5 and 4. Layer 4 denotes the contact between layer 4 and 3. Layer 3 denotes the contact between layer 3 and 2. Layer 2 denotes the contact between layer 3 and 2. Layer 1 denotes the contact between layer 1 and the atmosphere, that is, is the surface of the volcanic zone/volcano. (For interpretation of the references to colour in this figure legend, the reader is referred to the web version of this article.)

mation would be expected unless the dike tip propagates to depths below the surface of less than a kilometre, and commonly to depths of only several hundred metres. The model results thus suggest that when significant dike-induced deformation is seen at the surface, the dike is normally very close to the surface – within several hundred metres of the surface - indicating a high likelihood of the dike reaching the surface to erupt.

Elastic half-space models commonly overestimate the potential dike-induced surface stresses and, consequently, the depth of the tip of the associated dike below the surface. It also follows that half-space models commonly underestimate the dimensions – particularly the thickness – and therefore the volumes of the dike inducing a particular surface deformation during a volcanotectonic episode (e.g., Al Shehri and Gudmundsson, 2018). When the dike volumes are underestimated, then the flow of magma out of the source chamber during the episode is also underestimated. For an eruption, the combined intrusive and extrusive (erupted) volume of magma injected from the chamber is then also underestimated. Since this combined volume is one of the factors used to estimate the volume of the source magma chamber (Gudmundsson, 2016), that volume, and hence the likely dimensions, of the chamber will also be in error.

In summary, the results of all the models (Figs. 7–16) demonstrate the importance of the effects of mechanical layering in volcanic zones and volcanoes on dike-induced displacements and stresses. In particular, the results show that compliant layers make dike-induced surface fracturing unlikely until the dike is at a very shallow depth, or with a very high overpressure, or both. This is in agreement with the field observations of arrested dike tips, showing that many dikes arrested at shallow depths did not generate tension fractures or normal faults above their tips (Figs. 2–5). More specifically, the results suggest that the common use of homogeneous, elastic half-space dislocation models to infer dike geometries and dimensions thorough the inversion of surface-deformation data is likely to lead to highly unreliable results. Furthermore, the present models indicate that the common practice of associating the calculated the maximum theoretical surface displacements with graben formation is not justified.

6. Conclusions

The main conclusions of this paper may be summarised as follows:

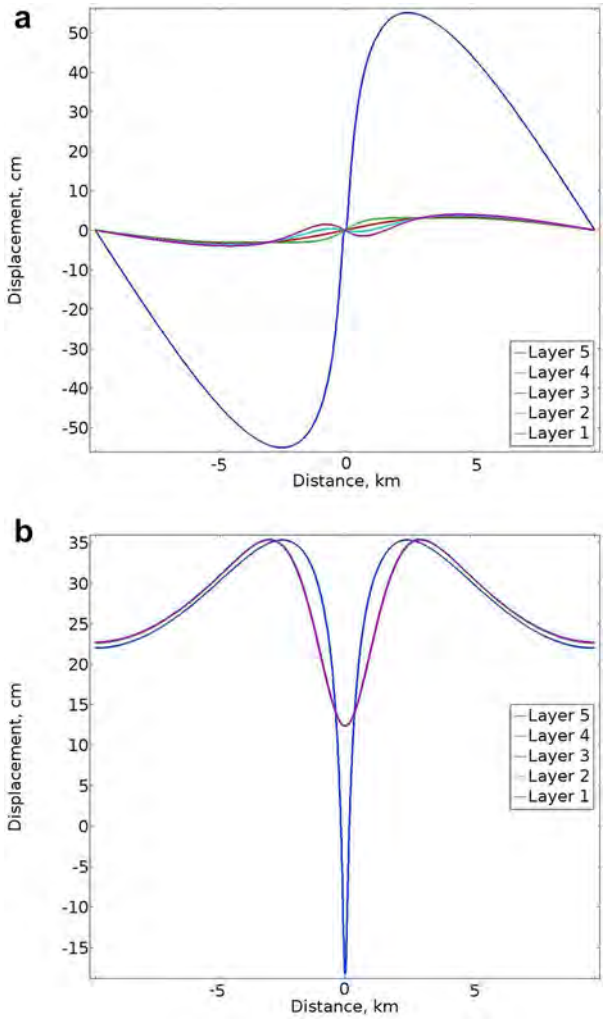

Fig. 14. Lateral and vertical displacement of the contacts between layers (denoted as layers 1–5) in the model in Fig. 13. (a) The lateral displacements of layers/contacts 1–4 are somewhat dissimilar close to the dike, but reach a maximum of about 4 cm at a distance of about 5 km from the dike. The maximum lateral displacement of layer 5 (contact 5/4), however, reaches a maximum of about 54 cm at a distance of about 2.8 km from the dike. (b) The vertical upward displacement of layers/contacts 1–4 roughly coincide and reach about 35 cm at a distance of about 3.3 km from the dike, showing a clear trough or two-peak displacement above the dike tip, but with the minimum displacement still at about 13 cm above the un-deformed surface (so no absolute subsidence). By contrast, layer 5 (contact 5/4) shows a maximum upward displacement of about 35 cm at a distance of about 2.6 km from the dike and an absolute subsidence right about the dike tip of about 17 cm.

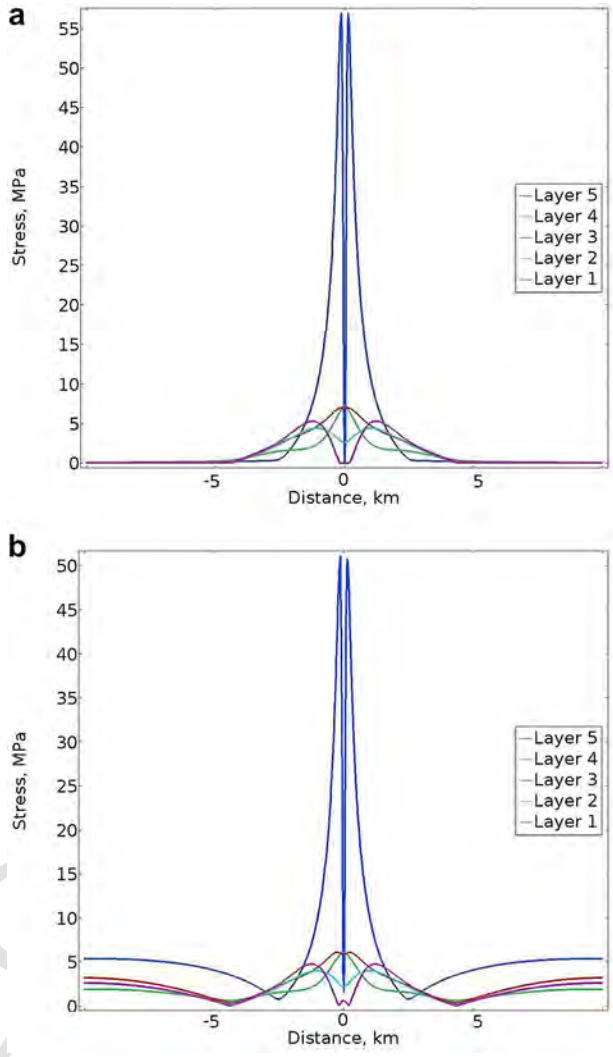

Fig. 15. The same basic model as in Fig. 7. The differences are (1) layer 4 has Young's modulus of 0.1 GPa, the surface layer 1 has a Young's modulus of 20 GPa, and the magmatic overpressure in the dike is 15 MPa. (a) Plots of the variation in the magnitude of the maximum tensile principal stress σ_3 at the contacts between the layers. (b) Plots of the variation in the magnitude of the von Mises shear stress (τ) at the contacts between the layers. Layer 5 denotes the contact between layer 5 and 4. Layer 4 denotes the contact between layer 4 and 3. Layer 3 denotes the contact between layer 3 and 2. Layer 2 denotes the contact between layer 3 and 2. Layer 1 denotes the contact between layer 1 and the atmosphere, that is, is the surface of the volcanic zone/volcano.

- Field observations show that although some dikes just thin out, or taper away in vertical sections, most dikes become arrested at contacts between mechanically dissimilar rock layers. The main mechanical property that varies across the contact is the stiffness or Young's modulus. The ideal condition for a dike (or any other mode I, extension, fracture) to become arrested at such a contact is when the layer above the contact is much stiffer than the layer below the contact (the one hosting the dike). However, for many arrested dikes the layer above may be more compliant than the one hosting the dike. This is because there are three processes that may contribute to dike arrest at any particular contact: Cook-Gordon delamination, stress barrier, and elastic mismatch.
- Field observations also show that many arrested dike tips do not generate any significant large-scale fracturing ahead of the dike tip. Even dikes that become arrested only several metres below the free surface of a rift zone may, for specific mechanical layering, be unable to generate fractures at the surface. There are, however, many well-documented cases of tension-fracture and normal-fault generation associated with dike emplacement during unrest periods.
- The new numerical results presented here use 5 layers with different mechanical properties, that is, different Young's moduli. In most models, the surface layer, layer 1, has a stiffness of 3 GPa, layer 2 a stiffness of 20 GPa, layer 3 a stiffness of 30 GPa, and layer or unit 5 a stiffness of 40 GPa. Layer or unit 5 is the one hosting the dike whose tip is arrested at 0.5 km below the surface. Between model runs, the stiffness of layer 4 is varied, from 10 GPa, and thus rather stiff, to 1 GPa, 0.1 GPa, and 0.01 GPa. The last stiffness, 0.01 GPa, is very compliant but layers of similar stiffness are likely to occur in most active volcanoes and volcanic zones.

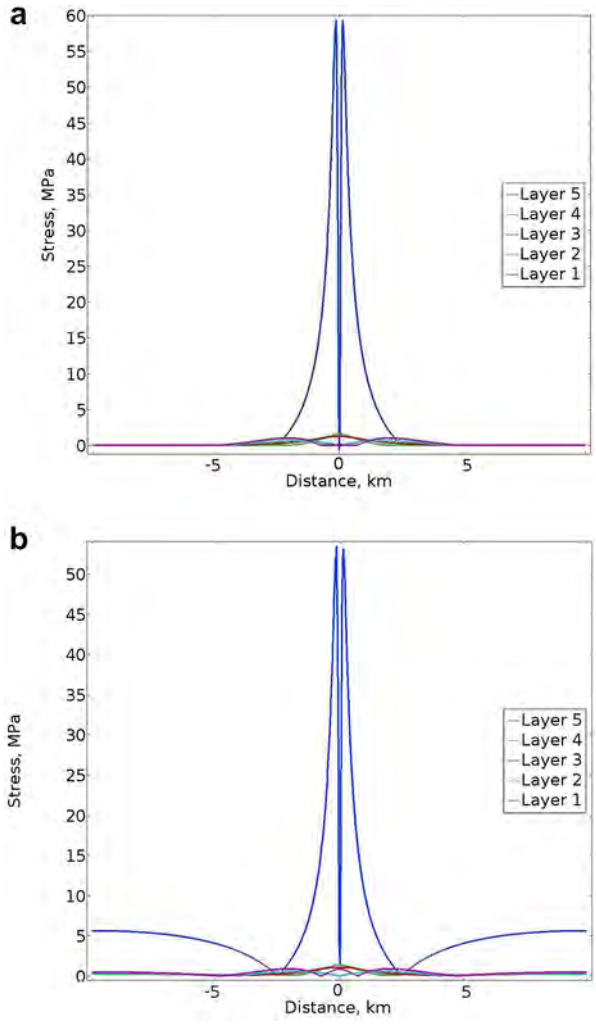

Fig. 16. The same model as in Fig. 15, except that layer 4 has here a Young's modulus of 0.01 GPa. (a) Plots of the variation in the magnitude of the maximum tensile principal stress σ_3 at the contacts between the layers. (b) Plots of the variation in the magnitude of the von Mises shear stress (τ) at the contacts between the layers. Layer 5 denotes the contact between layer 5 and 4. Layer 4 denotes the contact between layer 4 and 3. Layer 3 denotes the contact between layer 3 and 2. Layer 2 denotes the contact between layer 3 and 2. Layer 1 denotes the contact between layer 1 and the atmosphere, that is, is the surface of the volcanic zone/volcano.

- As for dike-induced stresses, the numerical results show very great effect of layering, in particular of the gradually more compliant layer 4. When its stiffness becomes as low as 0.1–0.01 GPa, layer 4 transports hardly any stresses to the shallower layers. The result is very low stress at shallower depth, including the surface. Generally, the location of the maximum tensile and shear stresses roughly coincide so that, when significant stresses are transported to the surface, the most likely initiation of tension fracture and shear fractures should occur in roughly the same areas at the surface.
- When the stiffness of layer 4 is gradually decreased from 10 GPa to 0.01 GPa, the internal deformation of the volcano/volcanic zone increases. This is reflected in the displacement fields. Thus, the horizontal displacement of all layers/contacts is generally similar while the stiffness of layer 4 is 10 GPa, but as the layer becomes softer, the difference in displacements between the layers/contacts increases and reaches a maximum when the stiffness of layer 4 is 0.01 GPa. At that stiffness the horizontal displacement of layer/contact 5 is totally different, in terms of magnitude and location of the peak, from that of the other layers/contacts. And similarly for the vertical displacement.
- The maximum tensile and shear stresses, that is, the stress peaks vary throughout the interior of the volcano/volcanic zone. They are highest in layer/contact 5, hosting the dike, and decrease towards the surface. As the stiffness of layer 4 decreases, so do the tensile and shear stresses inside and above that layer, including the surface. At the surface the tensile and shear stresses peak mostly at a lateral distances of 0.5–0.7 km from the projection of the dike to the surface. This implies that any dike-induced graben would be likely to be of a width about twice the depth to the tip of the arrested dike. Thus, in most of the present models, a graben, if formed at all, would tend to be between 1 km and 1.4 km wide at the surface.
- The maximum surface uplift or vertical displacement peaks at lateral distances of 2.8–3.3 km from the projection of the dike to the surface and have low stresses. We conclude that tension fractures and faults – in particular the boundary faults of grabens – are most likely to form, if at all, in the location of the tensile/shear stress peaks and not, as is commonly suggested, at the location of the surface uplift peaks. Our results thus do not lend any support to the common practice of interpreting the boundary faults of grabens as coinciding with the maximum uplift, the upward displacement peaks, at the surface above an arrested dike.
- The results suggest that failure to take typical and reasonable mechanical layering in volcanoes and volcanic zones into account, such as in using homogeneous, elastic half-space dislocation models, when inferring dike geometries and dimensions thorough the inversion of surface-deformation data is likely to lead to highly unreliable results. In particular, such models tend to overestimate the dike-induced surface stresses, and thus the depth to the tip of the associated dike. It also follows that half-space models commonly underestimate the dimensions – particularly the thickness – and therefore the volumes of the dike inducing the surface deformation. When the dike volumes are underestimated, then the flow of magma out of the source chamber during the volcanotectonic episode is also underestimated.
- As regards the likelihood of dike-fed eruption, the present models indicate that, normally, little or no dike-induced surface deformation would be expected unless the dike tip propagates to depths below the surface of less than a kilometre. This implies that when significant dike-induced deformation is seen at the surface, the dike is normally very close to the surface – within several hundred metres of the surface - indicating a high likelihood of the dike reaching the surface to erupt.

Acknowledgements

We thank Weld on Sweden for financial support. We also thank Adelina Geyer and Alessandro Tibaldi for very helpful review comments.

References

Acocella, V., Neri, M., 2009. Dike propagation in volcanic edifices: overview and possible developments. Tectonophysics 471, 67–77. https://doi.org/10.1016/j.tecto.2008.10.002.

Al Shehri, A., Gudmundsson, A., 2018. Modelling of surface stresses and fracturing during dyke emplacement: application to the 2009 episode at Harrat Lunayyir, Saudi Arabia. J. Volcanol. Geotherm. Res. 356, 278–303.

Baer, G., Hamiel, Y., 2010. Form and growth of an embryonic continental rift: InSAR observations and modelling of the 2009 western Arabia rifting episode. Geophysics. J. Int. 182, 155–167.

Barnett, Z.A., Gudmundsson, A., 2014. Numerical modelling of dykes deflected into sills to form a magma chamber. J. Volcanol. Geotherm. Res. 281, 1–11.
Becerril, L., Galindo, I., Gudmundsson, A., Morales, J.M., 2013. Depth of origin of magma in eruptions. Sci. Rep. 3, 2762https://doi.org/10.1038/srep02762.
Bonafede, M., Rivalta, E., 1999. The tensile dislocation problem in a layered elastic medium. Geophys. J. Int. 136, 341–356.
Bonafede, M., Rivalta, E., 1999. On tensile cracks close to and across the interface between two welded elastic half-spaces. Geophys. J. Int. 138, 410–434.
Browning, J., Drymoni, K., Gudmundsson, A., 2015. Forecasting magma-chamber rupture at Santorini volcano, Greece. Sci. Rep. 5, https://doi.org/10.1038/srep15785.
Carracedo, J.C., Troll, V.R., 2006. Seismicity and gas emissions on Tenerife: a real cause for alarm?. Geol. Today 22, 138–141.
Cayol, V., Cornet, F.H., 1998. Three-dimensional modelling of the 1983-1984 eruption of Piton de la Fournaise volcano, Reunion Island. J. Geophys. Res. 103, 18,025–18,037.
Davis, P.M., 1983. Surface deformation associated with a dipping hydrofracture. J. Geophys. Res. 88, 5826–5834.
Deb, D., 2006. Finite Element Method: Concepts and Applications in Geomechanics. Prentice-Hall, New Jersey.
Delaney, P.T., Pollard, D.D., 1981. Deformation of host rock and flow of magma during growth of minette dike and breccia-bearing intrusions near Ship Rock, New Mexico. In: U.S. Geol. Surv. Prof. Pap. vol. 1202, pp. 1–69.
Dzurisin, D., 2006. Volcano Deformation. Springer Verlag, New York.
Ernst, R.E., Grosfils, E.B., Mege, D., 2001. Giant dike swarms: Earth, Venus, and Mars. Annu. Rev. Earth Planet. Sci. 29, 489–534.
Galindo, I., Gudmundsson, A., 2012. Basaltic feeder-dykes in rift zones: geometry, emplacement, and effusion rates. Nat. Hazards Earth Syst. Sci. 12, 3683–3700.
Garcia, A. Ortiz, R., Marrero, J.M., Sanchez, N., Tarraga, M., Vila, J., Correig, Macia, R., Sleeman, R., 2006. Monitoring the reawakening of Canary Islands' Teide Volcano. Eos, 87, 61–72.
Gautneb, H., Gudmundsson, A., 1992. Effect of local and regional stress fields on sheet emplacement in West Iceland. J. Volcanol. Geotherm. Res. 51, 339–356.
Geshi, N., Neri, M., 2014. Dynamic feeder dyke systems in basaltic volcanoes: the exceptional example of the 1809 Etna eruption (Italy). Front. Earth Sci. 2, https://doi.org/10.3389/feart.2014.00013.
Geshi, N., Kusumoto, S., Gudmundsson, A., 2010. Geometric difference between non-feeder and feeder dikes. Geology 38, 195–198.
Geshi, N., Kusumoto, S., Gudmundsson, A., 2012. Effects of mechanical layering of host rocks on dike growth and arrest. J. Volcanol. Geotherm. Res. 223-224, 74–82.
Geyer, A., Gottsmann, J., 2010. The influence of mechanical stiffness on caldera deformation and implications for the 1971–1984 Rabaul uplift (Papua New Guinea). Tectonophysics 483, 399–412. https://doi.org/10.1016/j.tecto.2009.10.029.
Gonnermann, H.M., Manga, M., 2013. Dynamics of magma ascent in the volcanic conduit. In: Fagents, S.A., Gregg, T.K.P., Lopes, R.M.C. (Eds.), Modeling Volcanic Processes. Cambridge University Press, Cambridge, pp. 55–84.
Gottsmann, J., Wooller, L., Marti, J., Fernandez, J., Camacho, A.G., Gonzalez, P.J., Garcia, A., Rymer, H., 2006. New evidence for the reawakening of Teide volcano. Geophys. Res. Lett. 33, L20311https://doi.org/10.1029/2006GL027523.
Greenland, L.P., Rose, W.I., Stokes, J.B., 1985. An estimate of gas emissions and magmatic gas content from Kilauea volcano. Geochim. Cosmochim. Acta 49, 125–129.
Greenland, L. P., Okamura, A. T., Stokes, J. B., 1988. Constraints on the mechanics of the eruption. In: Wolfe, E. W (ed), The Puu Oo Eurption of Kilauea Volcano, Hawaii: Episodes through 20, January 3, 1983 through June 8, 1984, US Geol. Survey Professional Paper, vol. 1463, 155–164.
Gudmundsson, A., 2002. Emplacement and arrest of sheets and dykes in central volcanoes. J. Volcanol. Geotherm. Res. 116, 279–298.
Gudmundsson, A., 2003. Surface stresses associated with arrested dykes in rift zones. Bull. Volcanol. 65, 606–619.
Gudmundsson, A., 2005. Effects of mechanical layering on the development of normal faults and dykes in Iceland. Geodin. Acta 18, 11–30.
Gudmundsson, A., 2009. Toughness and failure of volcanic edifices. Tectonophysics 471, 27–35.
Gudmundsson, A., 2011. Deflection of dykes into sills at discontinuities and magma-chamber formation. Tectonophysics 500, 50–64.
Gudmundsson, A., 2011. Rock Fractures in Geological Processes, Cambridge University Press, Cambridge.
Gudmundsson, A., 2017. The Glorious Geology of Iceland's Golden Circle. Springer-Nature, Heidelberg.
Gudmundsson, A., Brenner, S.L., 2001. How hydrofractures become arrested. Terra Nova 13, 456–462.
Gudmundsson, A., Loetveit, I.F., 2005. Dyke emplacement in layered and faulted rift zone. J. Volcanol. Geotherm. Res. 144, 311–327.
Gudmundsson, A., Philipp, L., 2006. How local stress fields prevent volcanic eruptions. J. Volcanol. Geotherm. Res. 158, 257–268.
Gudmundsson, A., Marinoni, L., Marti, J., 1999. Injection and arrest of dykes: implications for volcanic hazards. J. Volcanol. Geotherm. Res. 88, 1–13.
Gudmundsson, A., Friese, N., Galindo, I., Philipp, S.L., 2008. Dike-induced reserve faulting in a graben. Geology 36, 123–126. https://doi.org/10.1130/G24185A.
Gudmundsson, A., Lecoeur, N., Mohajeri, N., Thordarson, T., 2014. Dike emplacement at Bardarbunga, Iceland, induces unusual stress changes, caldera deformation, and earthquakes. Bull. Volcanol. 76, 869https://doi.org/10.1007/s00445-014-0869-8.
He, M.Y., Hutchison, J.W., 1989. Crack deflection at an interface between dissimilar elastic materials. Int. J. Solids Struct. 25, 1053–1067.
Hutchinson, J.W., 1996. Stresses and Failure Modes in Thin Films and Multilayers. Notes for a Dcamm Course. Technical University of Denmark, Lyngby, 1–45.
Isida, M., 1955. On the tension of a semi-infinite plate with an elliptical hole. Sc. Pap. Fac. Engng. Tokushima Univ. 5, 75–95.
Kanamori, H., Anderson, D.L., 1975. Theoretical basis of some empirical relations in seismology. Bull. Seismol. Soc. Am. 65, 1074–1095.
Kavanagh, J., Menand, T., Sparks, R.S.J., 2006. An experimental investigation of sill formation and propagation in layered elastic media. Earth Planet. Sci. Lett. 245, 799–813.
Kavanagh, J.L., Sparks, R.S.J., 2011. Insights of dyke emplacement mechanics from detailed 3D dyke thickness datasets. J. Geol. Soc. Lond. 168, 965–978.
Kervyn, M., Ernst, G. G. J., van Wyk de Vries, B., Mathieu, L., Jacobs, P., 2009. Volcano load control on dyke propagation and vent distribution: insights from analogue modeling, J. Geophys. Res., 114(B3), B03401, doi:https://doi.org/10.1029/2008jb005653.
Liu, G.R., Quek, S.S., 2014. Finite Element Method, 2nd ed. Elsevier, Amsterdam.
Manconi, A., Walter, T.R., Amelung, F., 2007. Effects of mechanical layering on volcano deformation. Geophys. J. Int. 170, 952–958.
Martí, J., López, C., Bartolini, S., Becerril, L., Geyer, A., 2016. Stress controls of monogenetic volcanism: a review. Front. Earth Sci. 4 (106)https://doi.org/10.3389/feart.2016.00106.
Martí, J., Villaseñor, A., Geyer, A., López, C., Tryggvason, A., 2017. Stress barriers controlling lateral migration of magma revealed by seismic tomography. Sci. Reports 7, 40757https://doi.org/10.1038/srep40757.
Masterlark, T., 2007. Magma intrusion and deformation predictions: sensitivities to the Mogi assumptions. J. Geophys. Res. 112, https://doi.org/10.1029/2006JB004860.
Moran, S.C., Newhall, C., Roman, D.C., 2011. Failed magmatic eruptions: late-stage cessation of magma ascent. Bull. Volcanol. 73, 115–122. https://doi.org/10.1007/s00445-010-0444-x.
Okada, Y., 1985. Surface deformation due to shear and tensile faults in a half-space. Bull. Seismol. Soc. Am. 75, 1135–1154.
Okada, Y., 1992. Internal deformation due to shear and tensile faults in half space. Bull. Seismol. Soc. Am. 82, 1018–1040.
Pallister, J., McCausland, W., Jónsson, S., Lu, Z., Zahran, H., El-Hadidy, S., Aburukbah, A., Stewart, I., Lundgern, P., White, R., Moufti, M., 2010. Broad accommodation of rift-related extension recorded by dyke intrusion in Saudi Arabia. Nat. Geosci. 3, 705–712.
Philipp, S.L., Afsar, F., Gudmundsson, A., 2013. Effects of mechanical layering on hydrofracture emplacement and fluid transport in reservoirs. Front. Earth Sci. 1, https://doi.org/10.3389/feart.2013.00004.
Pinel, V., Jaupart, C., 2004. Magma storage and horizontal dyke injection beneath a volcanic edifice. Earth Planet. Sci. Lett. 221, 245–262.
Pinel, V., Jaupart, C., 2005. Some consequences of volcanic edifice destruction for eruption conditions. J. Volcanol. Geotherm. Res. 145, 68–80.
Pollard, D.D., Delaney, P.T., Duffield, W.A., Endo, E.T., Okamura, A.T., 1983. Surface deformation in volcanic rift zones. Tectonophysics 94, 541–584.
Rickwood, P.C., 1990. The anatomy of a dyke and the determination of propagation and flow directions. In: Parker, A.J., Rickwood, P.C., Tucker, D.H. (Eds.), Mafic Dykes and Emplacement Mechanisms. Balkema, Rotterdam, pp. 81–100.
Rivalta, E., Taisne, B., Bunger, P., Katz, F., 2015. A review of mechanical models of dyke propagation: Schools of thought, results and future directions. Tectonophysics 638, 1–42. https://doi.org/10.1016/j.tecto.2014.10.003.
Rubin, A.M., Pollard, D.D., 1988. Dike-induced faulting in rift zones of Iceland and Afar. Geology 16, 413–417.
Scholz, C.H., 1990. The Mechanics of Earthquakes and Faulting. Cambridge University Press, Cambridge.
Segall, P., 2010. Earthquake and Volcano Deformation. Princeton University Press, Princeton.
Sigmundsson, F., Hreinsdottir, S., Hooper, A., Arnadottir, T., Pedersen, R., Roberts, M.J., Oskarsson, N., Auriac, A., Decriem, J., Einarsson, P., Geirsson, H., Hench, M., Ofeigsson, B.G., Sturkell, E., Sveinbjörnsson, H., Feigl, K.L., 2010. Intrusion triggering of the 2010 Eyjafjallajökull explosive eruption. Nature 468, 426–430. https://doi.org/10.1038/nature09558.
Sigmundsson, F., Hooper, A., Hreinsdottir, S., Vogfjord, K.S., Ofeigsson, D.G., Heimisson, E.L., Dumont, S., Parks, M., Spaans, K., Gudmundsson, G.B., Drouin, V., Arnadottir, T., Jonsdottir, K., Gudmundsson, M.T., Hognadottir, T., Fridriksdottir, H.M., Hensch, M., Einarsson, P., Magnusson, E., Samsonov, S., Brandsdottir,

B., White, R.S., Agustsdottir, T., Greenfield, T., Green, R.G., Hjartardottir, A., Pedersen, R., Bennett, R., Geirsson, H., La Femina, P.C., Bjornsson, H., Palsson, F., Sturkell, E., Bean, C.J., Mollhoff, M., Braiden, A.K., Eibl, E., 2015. Segmented lateral dyke growth in a rifting event at Barðarbunga volcanic system. Iceland. Nature 517, 191–U158. https://doi.org/10.1038/nature14111.

Siler, D.L., Karson, J.A., 2009. Three-dimensional structure of inclined sheet swarms: implications for crustal thickening and subsidence in the volcanic rift zones of Iceland. J. Volcanol. Geotherm. Res. 18, 333–346.

Tarasewicz, J., White, R.S., Woods, A.W., Brandsdottir, B., Gudmundsson, M.T., 2012. Magma mobilization by downward-propagating decompression of the Eyjafjallajökull volcanic plumbing system. Geophys. Res. Lett. 39, https://doi.org/10.1029/2012GL053518.

Tibaldi, A., Vezzoli, I., Pasquare, F.A., Rust, D., 2008. Strike-slip fault tectonics and the emplacement of sheet-laccolith systems: the Thverfell case study (SW Iceland). J. Struct. Geol. 30, 274–290.

Tibaldi, A., Pasquare, F.A., Rust, D., 2011. New insights into the cone sheet structure of the Cuillin complex, Isle of Skye, Scotland. J. Geol. Soc. 168, 689–704.

Tibaldi, A., Bonali, F., Pasquare, F.A., Rust, D., Cavallo, A., D'Urso, A., 2013. Structure of regional dykes and local cone sheets in the Nidhyrna-Lysuskard area, Snaefellsnes Peninsula (NW Iceland). Bull. Volcanol. 75, 764https://doi.org/10.1007/s00445-013-0764-8.

Townsend, M.R., Pollard, D.D., Smith, R.P., 2017. Mechanical models for dikes: a third school of thought. Tectonophysics 703-704, 98–118.

Tuschida, E., Nakahara, I., 1979. Three-dimensional stress concentration around a spherical cavity in a semi-infinite elastic body. Japan Soc. Mech. Engng Bull. 13, 499–508.

Xu, W., Jonsson, S., Corbi, F., Rivalta, E., 2016. Graben formation and dike arrest during the 2009 Harrat Lunayyir dike intrusion in Saudi Arabia: insights from InSAR, stress calculations and analog experiments. J. Geophys. Res. 121, https://doi.org/10.1002/2015JB012505.

Stresses and displacements in layered rocks induced by inclined (cone) sheets

Mohsen Bazargan and Agust Gudmundsson

Department of Earth Sciences, Queen's Building, Royal Holloway University of London, Egham TW20 0EX, UK (rock.fractures@googlemail.com)

Abstract

Currently, the sheet-intrusion paths and geometry, including depth to tip and opening/thickness, are commonly determined from geodetic surface data using elastic dislocation models. These models assume the volcanic zone/volcano to be an elastic half space of uniform mechanical properties. Field observations, however, show that volcanic zones/volcanoes are composed of numerous layers whose mechanical properties (primarily Young's modulus) vary widely. Here we provide new numerical models on the effects of a typical variation in Young's modulus in an active volcanic zone/central volcano on the internal and surface stresses and displacements induced by a sheet-intrusion whose tip is arrested at a crustal depth (below the surface) of 100 m. The sheet has a dip dimension (height) of 2 km and an opening (aperture, thickness) of 2 m. The only loading is internal magmatic overpressure in the sheet of 5 MPa. The modelled crustal segment/volcano consists of 5 layers, all with the same Poisson's ratio (0.25). Each of the 4 uppermost layers is 10 m thick. Layer 1 (the top or surface layer) has a Young's modulus of 3 GPa, layer 2 a modulus of 20 GPa, layer 3 a modulus of 30 GPa, and layer or unit 5 a modulus of 40 GPa. We vary the Young's modulus or stiffness of the fourth layer from 10 GPa to 0.01 GPa, while the dip of the sheet takes the following values: 30°, 45°, 60° (for an inclined sheet) and 90° (for a dike). The resulting displacement and stresses are highly asymmetric across the sheet tip (except for the dike), with the main stresses and displacements being above the dipping sheet and highest for the 30°-dipping sheet. As the stiffness of layer 4 decreases the surface stresses gradually decrease while changes in vertical displacements are comparatively small but greater in horizontal displacements. In particular, as the stiffness of layer 4 decreases from 10 GPa to 0.01 GPa, for the 30°-dipping sheet the maximum surface shear stress decreases from about 6.6 MPa to 2.2 MPa and the maximum tensile stress from about 6.9 MPa to about 2.3 MPa. Thus, even a single comparatively thin (10 m) soft layer close to the surface of a central volcano/volcanic zone (where such layers are almost universal), there is a great change in the maximum sheet-induced stresses at the surface, and thereby in the likely sheet-induced fracture formation. Furthermore, the stress peaks do not coincide with the displacement peaks; fracture formation is most likely at the location of the stress peaks. The results have important implications for the correct interpretation of geodetic data and fracturing during unrest periods with magma-chamber rupture and sheet injection.

Keywords: volcano deformation, volcano stresses, crustal displacements, volcano unrest, geodetic data, numerical modelling

1. Introduction

One of the basic aims of volcanology is to understand the processes that happen inside a volcano during unrest periods. Some unrest periods do not result in magma-chamber rupture, but for those that do, forecasting the potential propagation path and geometry of the resulting sheet intrusion is of fundamental importance. This follows because most eruptions are supplied with magma through sheet intrusions. Thus, in most cases a volcanic eruption is simply the consequence of a sheet intrusion, propagating as a magma-filled fracture, is able to make a path from its magma source to the surface.

Sheet intrusions are of three main types: sills, dikes, and inclined (cone) sheets. Sills are concordant and thus close to horizontal in gently dipping or flat lava piles. Dikes are concordant and thus close to vertical in gently dipping or flat lava piles. Inclined sheets are, as the name implies, inclined that is neither vertical nor horizontal, and commonly with an average dip somewhere between 30° and 50°. While the deformation induced by dikes and sills has been widely studied, that induced by inclined sheets has received much less attention. This is unfortunate because inclined sheets are much more common in many central volcanoes (stratovolcanoes, basaltic edifices; polygenetic volcanoes) than either sills or dikes (Fig. 1). In fact, close to fossil shallow magma chambers, that is, plutons, inclined sheets may constitute 70-80% of the rock (Fig. 2).

When assessing the processes inside a volcano during an unrest period with magma-chamber rupture and sheet injection, it is important to be able to distinguish between the types of sheet-intrusions. Clearly, the displacements and stresses induced by a vertical dike are very different from those generated by a horizontal sill (e.g., Barnett and Gudmundsson, 2014). But the displacements and stresses induced by an inclined sheet are somewhere between those induced by dikes and sills. In order to forecast likely propagation paths and eventual eruptions, we must be able to distinguish the displacements and stresses due to an inclined sheet from those of either a dike or a sill.

The present paper focuses on the stresses and displacements induced by inclined sheets. The emphasis is on new numerical models as to the effects of mechanical layering in volcanoes and crustal segments on internal and surface stresses and displacements. We also provide a general overview of inclined sheets, using detailed studies of sheets in Iceland and Scotland as a basis.

2. Field observations

Inclined sheets were first described in connection with studies of the Tertiary volcanoes of Scotland (Harker 1904), such as on the island of Skye and the peninsula of Ardnamurchan. These were later referred to as cone sheets apparently on the assumption that the excess pressure the source chamber would generate conical fractures into which the magma would flow. On this view the sheets would be parts of cones, meeting at a focal point, which was supposed to be at the source. The sheets would then be concentric and inward-dipping at an

average angle of about 45º and all intersect at a certain point, the apex or summit of the chamber.

In the past decades, cone sheets have been studied in many eroded volcanoes. The results indicate that they do not, as a rule, form conical fractures, and their attitudes vary much, with many cross-cutting sheets (e.g., Gautneb et al., 1989; Gautneb and Gudmundsson, 1992; Gudmundsson, 1995, 1998; Klausen, 2004, 2006; Pasquare and Tibaldi, 2007; Siler and Karson, 2009; Tibaldi et al., 2011, 2013; Bistacchi et al., 2012). The term cone sheet is thus regarded as less appropriate than the general term inclined sheet, which is now more generally used. The main point in using the term inclined sheets is that the structures are sheet-like, and their dips are mostly much shallower than those of dikes, while being much steeper than those of sills.

2.1 Mechanical characteristics

The mechanical characteristics of geological structures such as sheet-intrusions can, of course, only be determined by field observations. This applies to their typical attitude (strike and dip), thickness, under what conditions they become arrested and, in particular, the type of fracture they are. Below we present some general results on the attitude and thickness of sheets, using primarily data from well-studied sheet swarms in Iceland. We also discuss the way that sheets are seen arrested in the field. To model sheets, however, we need to know what types of fractures they are; in particular, are they shear fractures (faults) or extension fractures? Field studies of thousands of cross-cutting relationships between inclined sheets and the host-rock layers, particularly lava flows (and sills) and pyroclastic layers, as well as among inclined sheets and between sheets and dikes provide clear evidence that the great majority of inclined sheets are extension fractures (Figs. 3 and 4). It follows that they can be modelled as mode I cracks, as is discussed below.

This is a very important conclusion, with wide implications for modelling and forecasting sheet-propagation paths and sheet-fed eruptions. It is therefore worthwhile to clarify this point. No modelling - analogue, analytical, numerical - can determine what mechanical type a rock fracture is: only direct observations of the fracture in the field make such a decision possible. Decades ago it was unclear what mechanical types of fracture inclined sheets are, and several authors (e.g., Phillips, 1974) speculated that they might be shear fractures, that is, faults. This was plausible at the time, since extensive datasets on cross-cutting relations did not exist. In the past decades, many thousand cross-cutting relationships have been observed, however, showing that the great majority of inclined sheets are extension fractures (e.g., Gautneb et al., 1989; Gautneb and Gudmundsson, 1992; Gudmundsson, 1995, 1998; Klausen, 2004, 2006; Pasquare and Tibaldi, 2007; Siler and Karson, 2009; Tibaldi et al., 2011, 2013; Bistacchi et al., 2012). The same applies to other sheet-like intrusions, such as dikes (e.g., Gudmundsson, 1995, 1998; Geshi et al., 2010; Galindo and Gudmundsson, 2012). Dikes and inclined sheets may, however, occasionally follow shear fracture, mostly existing faults along parts of their paths. This can happen under certain restricted conditions, all of which can be formulated and explained in terms of energy considerations (Gudmundsson, 2019).

Inclined sheets are best studied in three dimensions in deeply eroded volcanic edifices (Figs. 2-4). But many inclined sheets can been observed in active volcanoes. For example, some of the fissures associated with the Askja Central Volcano in Iceland are clear examples of inclined sheets (Gudmundsson, 1998). Generally, many flank eruptions in major volcanic edifices are likely to be fed by inclined sheets or radial dikes (Fig. 1).

2.2 Field characteristics

The main characteristics of inclined sheets, primarily based on data from Iceland and Scotland (Gautneb et al., 1989; Gautneb and Gudmundsson, 1992; Gudmundsson, 1995, 1998; Klausen, 2004, 2006; Pasquare and Tibaldi, 2007; Siler and Karson, 2009; Tibaldi et al., 2011, 2013; Bistacchi et al., 2012) may be summarised as follows:

- The sheets occur in swarms that are mostly confined to central volcanoes, that is, stratovolcanoes, basaltic edifices, and calderas. A typical swarm may contain many thousand sheets (Figs. 2 and 4), the swarm being circular or slightly elliptical in plan view, and commonly many kilometres in radius. In Iceland, the largest swarm is about 9 km in radius. At that distance from the centre of the source volcano there is an abrupt increase in dip and thickness of sheet-like intrusions, meaning that the regional dike swarm is taking over from the local sheet swarm (Fig. 5; Gautneb and Gudmundsson, 1992).
- In deeply eroded central volcanoes, the sheets can commonly be traced into the source shallow magma chamber (Fig. 2). The fossil magma chamber is currently exposed as a pluton, most commonly a mafic body (a gabbro body in Fig. 2). There is then no doubt about the source of the inclined sheets. Suggestions that the sheets originate somehow from dikes are not supported by any field data that we are aware of. In particular, such ideas are in contradiction with the fact that in the swarms sheets are many times more frequent than dikes and commonly more evolved chemically.
- The sheets commonly make up 60-100% of the rock in short traverses close to their sources, that is, close to the margins of the associated plutons that constitute the frozen magma chambers (Fig. 2). The percentage, however, declines rapidly with distance from the fossil source magma chamber and is only 6-8% in kilometre-long traverses.
- The attitude (strike and dip) of the sheets within a swarm varies widely. Some swarms show two peaks in the sheet dip distribution: steep-dipping sheets dip at 75-90º whereas shallow-dipping sheets dip at 20-50º. The steep-dipping sheets are mostly confined to the central part of the swarm, where many of them could be classified as dikes. The shallow-dipping sheets are mostly confined to the marginal parts of the swarm, where some of them could be classified as sills. The average dip in several swarms in Iceland is about 34° (Gudmundsson et al., 2018).
- The sheets range in thickness form a few centimetres to about ten metres, and occasionally more. The thickness of most sheets, however, is between 0.1 and 1 m.
- Like the regional dikes, the sheets are commonly segmented and offset, some of the offset parts being connected by thinner segments, or igneous veins. Individual

segments tend to be flat ellipses, both in plan views as well as in vertical sections. But many show irregularities in geometries and abrupt changes in propagation paths.

- While the great majority of the sheets are mafic (and intermediate at convergent boundaries), the sheets are, on average, somewhat more evolved in composition than the regional mafic dikes. This is understandable since the sheets are confined to shallow crustal magma chambers where crystal fractionation and anatexis are common whereas many of the regional dikes derive from deep-seated magma reservoirs hosting primitive melts. In addition to the mafic sheets, there are some felsic sheets in many swarms. These are generally thicker, on average, than the mafic sheets.

A comparison with the regional dikes suggests the following main differences. Inclined sheets are generally (1) shorter, (2) thinner, (3) more gently dipping, (4) of more evolved composition, and (5) with a much higher frequency (number per unit length of profile) than regional dikes. All these differences relate to most or all of the inclined sheets being derived from shallow crustal magma chambers whereas many of the regional dikes derive from deeper reservoirs with a more primitive magma. There are, of course, many dikes that are injected from the shallow magma chambers. These include, in particular, radial dikes (Fig. 1). However, these, as well as dikes within the swarms of inclined sheets, are commonly regarded as parts of the local sheet swarms rather than the regional dike swarms. This follows because the dikes of the sheet swarms are controlled as regards composition, attitude, and thickness by the local stress fields of the shallow magma chambers, rather than the regional stress fields that control the formation of the regional dikes.

3. Mechanics of emplacement

Before we discuss the numerical results on the sheets and the stresses and displacements that they induce, we first discuss briefly the conditions of shallow magma-chamber rupture and sheet injection followed by the mechanics of sheet emplacement.

3.1 *Magma-chamber rupture*

The three main processes that may result in magma-chamber rupture and sheet injection are:

- Magma is added to the chamber, usually from a deeper source reservoir below (Fig. 1) As the volume of magma in the chamber increases, local tensile stresses at the boundary of the chamber gradually reaches roughly the tensile strength of the host rock. Depending on the local stress field (Figs. 6 and 7), the resulting magma-filled fracture that is injected from the chamber is either a dike or an inclined sheet.
- Gradual extension of the crustal segment hosting the chamber, such as in continental rift zones or at divergent plate boundaries in general, results in the concentration of tensile stress at the boundary which, eventually, reaches the tensile strength of the host rock. Again, depending on the local stress field (Figs. 6 and 7), a dike or an inclined sheet (occasionally, a sill) is injected.
- Magma addition and extension commonly operate together, particularly at divergent plate boundaries.

The condition for rupture and sheet injection is given by (Gudmundsson, 2011a,b):

$$p_l + p_e = \sigma_3 + T_0 \quad (1)$$

where p_l denotes the lithostatic stress at the rupture site at the boundary of the magma chamber (normally the roof or the walls; rarely the floor), p_e is the excess magmatic pressure in the chamber (the pressure in excess of σ_3, the minimum compressive or maximum tensile principal stress), and T_0 the in situ tensile strength at the rupture site. Eq. (1) can also be written on the form:

$$p_t = \sigma_3 + T_0 \quad (2)$$

where $p_t = p_l + p_e$ is the total fluid pressure in the chamber at the time of rupture. Eqs. (1) and (2) imply that when the total fluid pressure in the chamber reaches the combined value of the minimum principal compressive (maximum tensile) stress and the in-situ tensile strength, the chamber (roof) ruptures and injects a magma-filled fracture. Depending on the local stress trajectories, this fracture may either be a vertical dike or an inclined sheet (Figs. 6 and 7).

It is important to realise that rupture and sheet/dike injection would always occur at some irregularities at the boundary of the chamber, where the local stress concentration is significantly higher than that around the magma chamber as a whole. Thus, it is the local stress concentration at an irregularity in the roof or the walls of the magma chamber (rarely the floor of the chamber) that results in rupture rather than the concentration around the chamber as a whole of a given general geometric shape. It follows that Eqs. (1) and (2) are generally appropriate as conditions for rupture irrespective of the overall approximate shape of the chamber (oblate ellipsoid or sill-like, spherical, or prolate ellipsoid, for example).

3.*2 Sheets form their own fractures*

The sheet-fracture is an extension fracture, a hydrofracture, to which Eqs. (1) and (2) apply. This is in accordance with the field results, discussed above, which show clearly that the great majority of inclined sheets and dikes are extension fractures. Eqs. (1) and (2) also imply that it is the magma itself that breaks or ruptures the rock, in a manner analogous to artificial hydraulic fracturing used to increase the permeability in reservoirs of various types. This conclusion rests on direct field observations as well as theoretical considerations. There are no wide-open extension fractures at many kilometres depth waiting to be filled with magma, neither in rift zones nor anywhere else in the Earth's crust. Griffith's fracture theory of explains why large tension fractures (formed by tensile forces/stresses and not by fluid pressure – the latter are hydrofractures) cannot form at greater depths than about 1 km, and do usually not extend from the surface to depths exceeding a few hundred metres (Gudmundsson, 2011a). Direct observations in caldera walls, erosional cliffs, and other sections into active and inactive volcanoes and rift zones show that large tension fractures only exist at very shallow depths. Furthermore, large inclined fractures, such as would be

suitable paths for inclined sheets, would normally be shear fractures, faults, and, as mentioned, most inclined sheets do not occupy faults.

During magma-chamber rupture and sheet injection, the host rock is assumed to fail in a brittle manner, that is, through fracture propagation. This is in agreement with field observations which show that even close to or at the contacts with the magma chambers, rock failure during magma-chamber rupture and dike or sheet injection is predominantly brittle (Fig. 2). Many have suggested viscoelastic, plastic, and viscoplastic behaviour of the host rocks of shallow magma chambers. However, where the ruptured margins between the chambers and their host rocks can be studied in detail, the observations confirm that the failure was normally in a brittle manner (Fig. 8). The strength that needs to be reached for the magma to form an inclined sheet is the in-situ tensile strength of the roof (Eqs. 1 and 2), which is between 0.5 and 9 MPa, and most commonly 2-4 MPa (Gudmundsson, 2011a,b). The in situ tensile strength is most commonly measured using small hydraulic fractures in drill-holes or wells, thereby providing a good analogy with magma-chamber rupture and sheet/dike injection.

3.3 The driving pressure (overpressure)

The total pressure p_t and the excess pressure p_e, (Eqs. 1 and 2) result from and include the combined pressure effects of all the fluids (gases and liquids) in the chamber as well as any contribution of buoyancy. When either of these equations is satisfied, the chamber ruptures and an inclined sheet (or a dike) is injected into its roof or walls. The magmatic driving pressure or overpressure p_o is given by (Gudmundsson, 2011a):

$$p_o = p_e + (\rho_r - \rho_m)gh + \sigma_d \tag{3}$$

where p_e is the excess magmatic pressure in the chamber, ρ_r is the average host-rock density, ρ_m is the average magma density, g is acceleration due to gravity, h is the dip dimension of the sheet at a particular time during its propagation, as measured from the chamber point of rupture. The term $\sigma_d = \sigma_1 - \sigma_3$ is the differential stress at the crustal level/layer which the propagating sheet has reached at that particular time (which, for an arrested sheet, is the layer/contact hosting the sheet tip). For a feeder, the dip dimension h is the vertical distance between the point of initiation at the boundary of the chamber and the Earth's surface where resulting fissure or crater cone forms.

Equation (3) can be used to estimate the magmatic overpressure of a sheet. For feeders, the overpressure follows, from the aspect (length/opening) ratio of a volcanic fissure it feeds (where the opening is normally determined from GPS or InSAR data). For a sheet exposed at the surface of eroded areas, the overpressure at the time of emplacement can be estimated from the length/thickness ratio of the sheet. The following points are relevant when considering the magmatic overpressure/driving pressure:

- At the time of magma-chamber rupture and sheet initiation the excess pressure p_e must be positive and roughly equal to the in-situ tensile strength of the host rock at the chamber boundary, that is, $p_e = T_0$. From Eq. (3) it follows that while h is small, say for the first hundreds of metres above the chamber roof, the overpressure available to drive the sheet propagation derives primarily from the excess pressure, p_e. This is because for small h the second term on the right-hand side of Eq. (3), the buoyancy term, does not contribute significantly to the overpressure. More specifically, for high-density basaltic sheets injected from shallow magma chambers, the buoyancy may be zero, when the magma and host-rock density equal, or negative, when the magma is denser than the host rock. In both cases, the only overpressure available to drive the sheet propagation all the way to the surface is the excess pressure.

- The differential stress $\sigma_d = \sigma_1 - \sigma_3$ must be either zero or positive; it cannot be negative because, by definition, σ_1 cannot be less than σ_3. By contrast, the density difference $\rho_r - \rho_m$ can be negative, zero, or positive. The average density of the roofs of many shallow chamber (the parts of the crustal segments above the chambers, including the volcanoes themselves) is commonly similar to, or somewhat less than, that of basaltic magmas. It follows that the density difference, and thus the buoyancy term in Eq. (3), is zero or negative, as indicated above.

- When calculating stresses around magma chambers and inclined sheets or dikes, the excess pressure (for the chamber) and the overpressure or driving pressure (for the sheet/dike) are the relevant ones and used. The total pressure is rarely used. Since excess pressure and overpressure are the pressures above σ_3 and, in the case of lithostatic state of stress, above all the principal stresses, it follows that the effect of gravity is automatically taken into account in such analyses.

3.4 Propagation paths

Once the initiated inclined sheet or dike begins to propagate, the local stress field will control its propagation path. Because sheets are primarily extension fractures, as indicated above, they must, by definition, follow paths that are perpendicular to σ_3 and thus parallel with the trajectories of the intermediate principal stress σ_2 and maximum principal compressive stress σ_1. For dikes propagating in a homogeneous, isotropic crustal segment, plotting the likely paths of dikes is thus easy (Fig. 6). However, all large crustal segments, such as occur above magma chambers, are to a degree layered, that is, anisotropic and commonly heterogeneous as well. In particular, in active volcanoes and volcanic zones the mechanical properties of the layers commonly vary abruptly across contacts.

The layering or anisotropy has important implications for dike propagation paths (Geshi et al., 2010, 2012; Gudmundsson, 2011b; Philipp et al., 2013; Marti et al., 2016, 2017). The trajectories of σ_1 commonly change abruptly at contacts between mechanically dissimilar layers, resulting in complex sheet paths and sheet arrest (Figs. 7 and 8). At some contacts the trajectories of σ_1 change from vertical to horizontal or inclined, resulting in inclined sheets or

dikes changing into sills/shallow-dipping sheets at contacts (Figs. 8 and 9), or becoming arrested altogether.

The layering and anisotropy to a degree thus controls the propagation paths of sheets (Figs. 7-9). But the layering has also great effects on the deformation and stresses induced by the sheets. How the mechanical layering affects sheet-induced stresses and displacement is of fundamental importance, because during unrest periods with sheet propagation we infer sheet dimensions and depth to top partly from geodetic data. Also, the likelihood of a propagating sheet reaching the surface to erupt is partly estimated from geodetic surface data. Here we present new numerical models on sheet-induced displacements and stresses, focusing on the surface effects, to which we turn now.

4. Model setup – software and boundary conditions

Here the finite-element-method (FEM) software Comsol Multiphysics (www.comsol.com) is used to analyse the sheet-induced displacements stresses and displacements in a mechanically layered crustal segment hosting a volcano/volcanic zone. The focus is on the surface effects (stresses and displacements) induced by inclined sheets. Since inclined sheets show a great range in dip, we provide models for sheets with widely different dips, as discussed below. First, however, we give a general overview of the Comsol software.

Comsol (like other finite-element-method (FEM) programs) discretises the problem into an equivalent system of small 'elements' and solves simultaneous algebraic equations (Fig. 10). Then the resulting numerical approximations for each element are combined into solutions for the entire body under consideration, here a crustal segment hosting an inclined sheet. The obtained results provide approximate solutions for the differential equations that describe the problem. In calculations, loads (stresses, displacements, forces or, as here, magmatic overpressures or driving pressures) are applied at specific nodes that are at the corners of the elements (and occasionally at the outer lines) and connect the element. From the calculated displacements at each node, the nodal stresses and the element stresses, strains, and displacements are derived using linear equations (cf. Deb, 2006; Liu and Quek, 2014).

The FEM modelling results are specific to a particular set of conditions and, therefore, give solutions only for the specified points in the body. But numerical solutions can be obtained for very complex geometries, such as anisotropic and fractured volcanoes. The FEM can additionally be applied to large strains, and heterogeneous and anisotropic mechanical properties, such as those related to the emplacement of inclined sheets in layered crustal segments and volcanoes. In the models presented here the layered crustal segment hosting the inclined sheet is discretised using triangular elements and the models are fastened in the corners, so as to avoid rigid-body rotation and translation (Fig. 10). Each model size is 20 km × 20 km and thus large enough to make the main displacements and stresses induced by the sheet unaffected by the models being fastened in the corners. More specifically, the main sheet-induced stresses and displacement are within a few kilometres of the sheet tip, and are negligible at distances of 10 km to either side of the tip (where the model is fastened).

In the models, all the layers of which the crustal segment and associated volcano are composed are assumed to behave as elastic. This assumption derives partly from

experimental physics results which show that solid rocks at crustal conditions and little strain normally behave as elastic (Gudmundsson, 2011a). Partly, however, the assumption derives from in-situ or field measurements of crustal deformation around fault zones prior to earthquake ruptures and at volcanoes during inflation and deflation periods, all of which suggest elastic behaviour to a first approximation (Scholz, 1990; Dzurisin, 2006; Segall, 2010). The general rock-failure criteria for the inclined sheet initiation are used (Eqs. 1 and 2), and for the propagation the condition (from Eq. 3) $p_o = T_0$ is assumed to apply. Apart from that, no specific failure criteria are used in the models because they all assume that the inclined sheet is already emplaced at the time of analysis. When estimating if the sheet-induced stresses and displacements would be large enough to cause tension fractures and/or faults, the normal shear-strength/tensile-strength criteria for the formation of these fractures are used as a basis (Gudmundsson, 2011a).

The sheet dip dimension or height is 2 km (Fig. 10). Its tip or top (where it is arrested at the time of the analysis) is constant at 100 m below the surface. The surface is here assumed flat, and is thus more appropriate for a volcanic zone/field or a collapse caldera than for a volcanic edifice that stands high above its surroundings. The tip propagates no further towards the surface in the models, that is, it becomes arrested at this depth. In all the models, the only loading is the magmatic overpressure in the sheet (Eq. 3). The tensile strength of most rocks is between 0.5 and 9 MPa, the common values being 2-5 MPa. We use 5 MPa magmatic overpressure in all the models. We ran all the models also for the much higher magmatic overpressure of 15 MPa. The results are geometrically similar, while the absolute stresses and displacements induced by the sheets are, as expected, higher.

The sheet thickness is 2 m. The entire sheet is located within the comparatively stiff unit/layer 5 (with a Young's modulus of 40 GPa and a Poisson's ratio of 0.25). For a dip dimension of 2 km and an overpressure of 5 MPa, the thickness would be around 0.5 m, a common thickness in swarms of inclined sheets in Iceland, as indicated above.

Above the unit/layer hosting the inclined sheet there are 4 layers of different mechanical properties. More specifically, the layers have different Young's moduli or stiffnesses, but have all the same Poisson's ratio of 0.25 – a common ratio for rocks (Gudmundsson, 2011a) The layers are located between the sheet tip and the surface. Each of these 4 layers has a thickness of 10 m, which remains the same in all the models. In most of the numerical models that we made, and all published here, the top 3 layers have constant mechanical properties. That is, their Young's moduli and Poisson's ratios do not change between the model runs. More specifically, the top layer (the surface layer) has a Young's modulus of 3 GPa, the second layer a Young's modulus of 20 GPa, and the third layer a Young's modulus of 30 GPa. By contrast, the Young's modulus of the fourth layer has the following values in the different runs: 0.01 GPa (very soft or compliant), 0.1 (compliant), 1 GPa (moderately stiff), and 10 GPa (stiff). Notice that the descriptions here of moderately stiff and stiff for 1 GPa and 10 GPa refer to near-surface in-situ layers. In laboratory measurements on small specimens, 1 GPa would be regarded as compliant and 10 GPa as moderately stiff (Gudmundsson, 2011a). As indicated, the unit or layer hosting the inclined sheet itself has a Young's modulus of 40 GPa.

These are all common stiffnesses for typical volcanic zones (Gudmundsson, 2011a). For example, many Holocene lava flows have static Young's moduli of the order of several mega-pascals and young pyroclastic layers may be more compliant. Older lava flows, such as might constitute the second and the third layer here, may have static Young's moduli of 20-30 MPa, while others might be more compliant. The stiffness of 40 GPa for the unit hosting the inclined sheet is similar to the estimated average static Young's modulus of the uppermost 10 km of the volcanic rift zones in Iceland (Gudmundsson, 2003, 2011a). The Young's moduli of the fourth layer is as low as 0.01 GPa, which is very compliant. It is, however, likely that most active volcanic zones and central volcanoes contain layers as soft as 0.1-0.01 GPa. Such zones normally include many layers of unconsolidated pyroclastics, such as tuff layers, and in addition many contain unconsolidated soils and sediments. Also, clays are common in some of the volcanoes, particularly in association with geothermal fields. The normal range of Young's moduli (measured in the laboratory) of unconsolidated sand, for instance, is 0.01-0.1 GPa, that of clay is 0.003-0.5 GPa, and that of tuff 0.05-5 GPa (Gudmundsson, 2011a).

Apart from testing the effect of mechanical layering, particularly variation in the stiffness of the fourth layer, on the surface stresses and displacement, the models also show the effects of variation in the dip of the inclined sheets. Based on the dip measurements in numerous sheet swarms (Fig. 1), discussed above, we tested the effects of the following dips: 30°, 45°, 60°, and 90°. The last one, 90°, is for a dike and is here shown as a comparison with the stresses and displacements induced by inclined sheets, most of which have dips between 30° and 60°.

In the model images presented here we zoom in on the important and relevant results. As indicated above the models are 20 km × 20 km in size, so that the model surface is 20 km wide. However, because the tip of the inclined sheet is so close to the surface, at 100 m, the significant stresses and displacements induced by the sheets are confined to a couple of kilometres to either side of the tip, or its projection to the surface. Thus, we show the stress and displacement results only for those parts, particularly at the surface, where there are significant sheet-induced stresses and displacements. The widths of the parts where there are significant changes vary somewhat between models, but are mostly 4-8 km. Outside the central 4-8-km-wide parts shown here the models show no significant sheet-induced changes.

5. Numerical modelling - results

5.1 Layer 4 with a stiffness of 10 GPa

In the first model layer 4 has a stiffness of 10 GPa, so similar to that of a Quaternary lava flow or a compact pyroclastic or sedimentary layer. As in all the models, and indicated above, the three layers above the fourth layer have stiffnesses of 30 GPa, 20 GPa, and 3 GPa (the surface layer) and the only loading is 5 MPa magmatic pressure in the inclined sheet. Here we first show the magnitude of minimum principal compressive or maximum tensile stress, σ_3, for the sheet dips 30°, 45°, and 60° (Fig. 11). For the surface stresses we also show the results for a sheet dipping 90°, that is, a dike, just for comparison, while more detailed dike

results are given by Al Shehri and Gudmundsson (2018) and by Bazargan and Gudmundsson (2019). The results show that even if layer 4 is reasonably stiff (10 GPa), it still suppresses the tensile stress, so that the stress is transferred instead to other layers – in particular, to layers 2 and 3. Furthermore, the tensile stress close to and at the contact between the unit/layer (40 GPa) hosting the sheet is raised (concentrated).

The theoretical tensile stress exceeds 40 MPa around the tip of the sheets for all sheet dips, but is as high as 80 MPa for the sheets dipping 45° and 30° (Fig. 11a,b). So high tensile stresses would not be reached in nature – the rock would fracture once the in-situ tensile strength was reached (normally several mega-pascals). The stress distribution is also highly asymmetric, the zone of high stress being primarily to the left of the tip of the sheet. This follows because the dip (inclination) of the sheet is to the left, so that the loaded crustal segment between the sheet and the bottom of layer 4 is much smaller and narrower, and thus takes on higher stress, than the segment to the right of the sheet. For the same reason, high tensile stress in layers 2 and 3 occurs only in the upper left part of the loaded crustal segment.

The ticks indicate the trajectories or orientation of the maximum principal compressive stress, σ_1. They give a crude indication of the likely orientation of the next propagation step that a sheet would take in case it propagated further. Notice that the ticks are just a crude indication of the orientation of such a step, and following the next step (if it happened, which is not the case here, given that the sheet is assumed arrested) the local stress field, hence the orientation of the σ_1, would change somewhat. In the present paper, we show the ticks of σ_1 so as to make the stress information more complete, but they are not very relevant to the main discussion, which focuses on the sheet-induced surface stresses and displacements.

The surface stresses and displacements associated with the sheet models in Fig. 11 are shown in Fig. 12. Here and elsewhere in the surface stress and displacement models the projection of the tip of the inclined sheet meets the surface at a distance of 10 km from either margin of the model, that is, in the centre of the model. Notice that the horizontal distances (along the horizontal or X-axis) is in all the figures given as a number multiplied by 10 (shown as 10^1). This means, for example, that the distance of 1 km corresponds to 1×10^1 km = 10 km, which is the centre of the model.

The largest surface von Mises shear and tensile (σ_3) stresses exceed 6 MPa (Fig. 12a,b) and are induced by the sheet dipping at 30°. Since the common in-situ tensile strength is 2-4 MPa and the shear strength 4-8 MPa, these stresses would result in fracture formation, particularly in the formation of tension fractures. All the surface stresses are asymmetric about the projection of the tip of the sheet to the surface (subsequently referred to as the 'tip of the sheet') except for the sheet dipping 90°, namely the dike. As expected, the shear stress (Fig. 12a) is somewhat less 'asymmetric' than the tensile stress (Fig. 12b). The tensile stress (σ_3) peaks to the left of the tip of the sheet (above the dipping sheet) are highest for the sheet dipping 30°, and then gradually diminish until they reach the lowest values for the vertical dike (Fig. 12b). By contrasts, to the right of the sheet tip, that is, in the direction opposite to the dip direction of the sheet, the tensile stress associated with the dike is the highest.

The variation in the shear stress magnitudes at the surface is generally more complex than those of the tensile stress magnitudes (Fig. 12a). This is partly because the shear stress is a function of both σ_3 and σ_1. The highest shear stress is, again, for the 30° dipping sheet, and peaks on both sides of the sheet tip. But the shear stress for the 45° dipping sheet is also

higher, on both sides, than that of the dike (90° dipping sheet). In addition, there is a small additional peak in the shear stress for the 30° dipping sheet to the left, in the down-dip direction of the sheet. This, 'peak', however, reaches only about 1 MPa and would normally not be high enough shear stress to induce faulting.

The horizontal (Fig. 12c) and vertical (Fig. 12d) displacements induced by the sheet are also highly asymmetric about the tip of the sheet. For the horizontal displacements, the negative values (to the left of the tip) simply mean displacements to the left, that is, in the dip direction of the sheet, whereas the positive values mean horizontal displacement to the right, that is, in the opposite direction. All the displacements are shown as fraction of metre, that is, as $10^{-1} = 0.1$ times the values in metres. Thus, -5 on the vertical scale is -5×10^{-1} m = 0.5 m = 50 cm. All the displacements are asymmetric across the sheet tip, except those induced by the dike (90° dipping sheet).

The maximum horizontal displacement is for the 30° dipping sheet, occurs about 1.2 km to the left of the sheet tip (down-dip direction) and reaches 0.8 m (Fig. 12 c). For comparison the maximum displacement induced by the 90° dipping sheet, the dike, is only about 0.2 m. All the displacements to the left of the sheet tip are much larger than those on to the right of the sheet tip (except for the dike, where the displacements are equal).

The maximum vertical displacement, also induced by the 30° dipping sheet, occurs about 0.6 km to the left of the sheet tip (down-dip direction) and reaches about 1.70 m. The sheet itself is 2 m thick, so here it generates space for itself primarily by uplift or doming of the surface above. This is to be expected when the sheet is very shallow (the tip is at the depth of only 100 m) and gently dipping (30°). For the other sheet dips the maximum uplift is much less, namely about 0.8 m (for 45° dipping sheet), about 0.4 m (for 60° dipping sheet), and 0.1 m (for 90° dipping sheet, a dike). These are somewhat larger than the maximum horizontal displacements, except for the dike where the horizontal displacement (about 0.2 m in each direction) is somewhat larger than the dike-induced vertical displacement. The lateral distance to the uplift peaks is also less for these than for the 30° dipping sheet. Apart from about 0.1 m uplift induced by the dike, there are no significant vertical displacements induced by the sheet to the right of its tip.

5.2 Layer 4 with a stiffness of 1 GPa

Here we show only the internal tensile magnitude of σ_3 and the trajectories of σ_1 for the sheet dipping 30° (Fig. 13). The trajectories of σ_1 are here similar to those in Fig. 11a. The main difference from Fig. 11a is that here there is less tensile stress concentrates in layers 2 and 3. This follows because layer 4 in the model in Fig. 11a has a stiffness of 10 GPa and therefore transmits stresses more easily to the layers above, layers 2 and 3, than in the present model where layer 4 has the much lower stiffness of 1 GPa. As a consequence, in the present model the tensile stress becomes more concentrated below the lower margin of layer 4, that is, in the top part of the unit hosting the sheet. In this top region above the sheet (to the left of the sheet tip) the theoretical tensile stress reaches 80 MP. This is higher than in the previous model (Fig. 11a) where the 80 MPa is reached only around the tip itself but not below the contact between layer 4 and the layer hosting the sheet. So high tensile stresses cannot be reached in nature; the rock fails commonly at tensile stresses of 2-4 MPa as discussed above.

The surface shear (Fig. 14a) and tensile (Fig. 14b) stresses are again highest for the sheet dipping 30°. The stress peaks, however, are somewhat lower than those in Figs. 12a and 12b. This is primarily because the comparatively compliant layer 4 of 1 GPa transmits less stresses to the surface that the stiffer layer 4 (10 GPa) in the model in Fig. 12. Nevertheless, for the 30° dipping sheet the peak shear stress is about 5.3 MPa (Fig. 14a) and the peak tensile stress around 5.8 MPa (Fig. 14b). Normally, so high surface stresses would result in fracture formation, or reactivation of existing fractures. In particular, the tensile stress (σ_3) is so high that it would almost certainly generate tension fractures. As before, all the stresses are asymmetric with the exception of those induced by the vertical sheet, the dike.

The maximum horizontal displacement is again for the 30° dipping sheet and reaches 0.81 m (Fig. 14c). It is noticeable that the horizontal displacements on to the left of the sheet tip are here somewhat larger, and those to the right of the sheet tip somewhat smaller, than those in the earlier model (Fig. 12c). Overall, however, the horizontal displacement values are similar for all the sheet dips to those in the earlier model (Fig. 12c).

The maximum vertical displacement is, as before, for the 30° dipping sheet and reaches about 1.76 m (Fig. 14d), or slightly larger than in the previous model (Fig. 12d). This very slight increase is due to layer 4 being more compliant (1 GPa) in this model than in the previous one (10 GPa). Similar slight increase is seen in the maximum displacements for the other dips of the sheet. As before, all the displacements are highly asymmetric about the tip of the sheet except for the vertical sheet, the dike.

5.3 Layer 4 with a stiffness of 0.1 GPa

The trajectories of σ_1 are again similar to those in the earlier models (Figs. 11a and 13), but there is much less tensile stress concentrates in layers 2 and 3 (Fig. 15). This is the result of layer 4 being soft (0.1 GPa) and thus transmitting little tensile stress to layers 2 and 3 (and to the surface, as discussed below). Consequently, the zone of high tensile stress concentration – in excess of 80 MPa – below the bottom of layer 4 is here much larger than in the model in Fig. 13. Tension fractures would be expected to develop in this zone.

As before, the surface shear (Fig. 16a) and tensile (Fig. 16b) stresses are highest for the sheet dipping 30°. The stress peaks, however, are much lower than those in Figs. 12a,b and 14a,b. The difference is primarily because of compliant layer of 0.1GPa which transmits little stress to the surface. For the 30° dipping sheet the peak shear stress is about 3.8MPa (Fig. 16a) and the peak tensile stress around 4.2MPa (Fig. 16b). Neither of these stresses does necessarily result in fracture formation, but both could reactivate existing fractures. The tensile stress (σ_3), at over 4 MPa, however, is so high that it could generate tension fractures. Again, all the stresses are asymmetric with the exception of those induced by the vertical sheet, the dike.

The maximum horizontal displacement for the 30° dipping sheet is about 0.74 m and occurs, as before, to the left of the sheet tip (Fig. 16c), whereas the displacement to the right of the tip is about 0.02 m (2 cm). Thus the trend continues with increasing compliance of layer 4 that the horizontal displacement on to the left of the sheet tip increases whereas the displacement to the right of the sheet tip decreases.

The maximum vertical displacement for the 30° dipping sheet reaches about 1.89 m (Fig. 16d), and thus significantly larger than in the previous models. Similar increases occur in the maximum displacements for the other dips of the sheet. All the displacements are highly asymmetric about the tip of the sheet except for the dike.

5.4 Layer 4 with a stiffness of 0.01 GPa

Again the trajectories of σ_1 are similar to those in the earlier models (Figs. 11a, 13, and 15), but very little tensile stress concentrates in layers 2 and 3 (Fig. 17), primarily because layer 4 is now so soft (0.01 GPa) that it transmits very little tensile stress to layers 2 and 3 and the surface. The zone of high tensile stress concentration – in excess of 80 MPa – below the bottom of layer 4 is here large and would be expected to develop tension fractures.

Again the surface shear (Fig. 18a) and tensile (Fig. 18b) stresses are highest for the sheet dipping 30°. The stress peaks, however, are much lower than those in Figs. 12a,b, 14a,b, and 16a,b. The difference is primarily because of the very compliant layer of 0.01GPa which transmits little stress to the surface. For the 30° dipping sheet the peak shear stress is about 2.2 MPa (Fig. 18a) and the peak tensile stress around 2.3MPa (Fig. 18b). Neither of these stresses is likely to generate fractures, but could possibly reactive some fractures. As before, all the stresses are asymmetric with the exception of those induced by the vertical sheet, the dike.

The maximum horizontal displacement for the 30° dipping sheet is about 0.49 m and occurs, as before, to the left of the sheet tip (Fig. 18c). The displacement to the right is now negative, about 0.01 m (1 cm), that is, is towards the left (towards the sheet tip rather than away from the tip as in earlier models). This displacement stays negative out to a distance of about 2 km to the right of the sheet tip, where it becomes positive (to the right and away from the tip) again. In fact, the horizontal displacements to the right of the sheet tip are all negative (are towards the tip) for a while except that of the vertical sheet, the dike. There were also some negative displacements in this sense in the model in Fig. 16.c, but of a much smaller magnitude and extension.

The maximum vertical displacement for the 30° dipping sheet reaches about 1.95 m (Fig. 18d), and thus the largest one in all the models. Similar increases occur in the maximum displacements for the other sheet dips. All the displacements are highly asymmetric about the tip of the sheet except for the dike.

6. Discussion

There have been very few analytical and numerical studies of the stress and displacement fields induced by inclined sheets. Those few that exist are mostly based on modelling the sheets as elastic dislocations. The models are applied to invert surface geodetic data to infer the opening or thickness, strike, dip, and depth of the inclined sheets, and can also be applied to dikes and sills. The elastic dislocation theory as applied to volcano deformation in general is reviewed in detail by Okada (1985, 1992), Dzurisin (2006), and Segall (2010). In the dislocation theory it is assumed that the volcano/crustal segment hosting the inclined sheet act as a homogeneous, isotropic, elastic half-space. It follows that the models do not consider

any effects of mechanical layering or contacts between layers on the sheet-induced stresses and deformation. Most models that consider layering are numerical and have, so far, generally been confined to the stresses and displacements induced by vertical dikes (e.g., Gudmundsson and Brenner, 2001; Gudmundsson, 2003; Gudmundsson and Loetveit, 2005; Al Shehri and Gudmundsson, 2018; Bazargan and Gudmundsson, 2018). Analytical and numerical dike models are reviewed by Rivalta et al. (2015) and by Townsend and Pollard (2017).

A representative example of inclined sheets (and dikes) modelled as elastic dislocations is provided by Dzurisin (2006). Here the dislocation models show the vertical (Fig. 19a) and the horizontal (Fig. 19b) displacement for a sheet dipping at 0° (a sill), 60° (an inclined sheet), and at 90° (a dike). In addition, the author shows the same for a classical Mogi model, that is, a nucleus of strain. The results are geometrically generally similar to those shown in the models in the present paper (Figs. 12, 14, 16, and 18). In particular, the following geometric similarities are noticeable:

- The vertical displacement induced by the dike (90° dip) has a clear 'valley' shape. That is, the displacement is zero or negative (subsidence) right above the dike (above its tip) and then forms positive peaks on either side (compare Figs. 12d, 14d, 16d, and 18d with Fig. 19a). More detailed results on the displacement associated with a dike in a layered crust are provided by Bazargan and Gudmundsson (2019).
- The vertical displacement induced by the 60° dipping sheet shows a steep downward slope above the tip of the sheet and becomes somewhat negative for a short while to the right of the tip and then close to zero (compare Figs. 12d, 14d, 16d, and 18d with Fig. 19a).
- The horizontal displacement induced by the dike is the same on either side of the vertical y-axis except for a change in sign. The displacement is zero right above the tip of the dike (compare Figs. 12c, 14c, 16c, and 18c with Fig. 19b).
- The horizontal displacement induced by the 60° dipping sheet shows a noticeable 'wave' immediately to the right of the vertical y-axis, that is, after crossing the tip of the sheet (compare Figs. 12c, 14c, 16c, and 18c with Fig. 19b). The absolute location of the 'wave', however, depends on the layering; in the present models on the stiffness of layer 4.

There are, however, many differences in detail between the models presented here - and in Al Shehri and Gudmundsson (2018) and Bazargan and Gudmundsson (2019) – and those presented in Fig. 19. The latter, being based on elastic half-space modelling, ignores the effects of layering in volcanoes/volcanic zones. The present models show that when layering is taken into account, the details of the magnitude (size) and the geometry of the displacement curves change. This is particularly clear for the horizontal displacement which decreases much as the stiffness of layer 4 decreases (Figs. 12c, 14c, 16c, and 18c). The uplift or vertical displacement is also affected, but to a lesser degree (Figs. 12d, 14d, 16d, and 18d).

In addition, the present models show that the stresses induced by the sheet depend strongly on the layering. This is clear from the distribution and magnitude of the maximum tensile stress inside the volcano/crustal segment (Figs. 11, 13, 15, and 17). Soft layers allow little stress to be transmitter to the layers above – here layers 2 and 3. And, most importantly,

soft layer 4 greatly reduces the shear and tensile stress that is transmitted to the surface (Figs. 12, 14, 16, and 18). As the stiffness of layer 4 decreases from 10 GPa to 0.01 GPa, the maximum shear stress at the surface decreases from about 6.6 MPa to 2.2 MPa (Figs. 12a and 18a) and the maximum tensile stress from about 6.9 MPa to about 2.3 MPa (Figs. 12b and 18b). This means that, even with only one comparatively thin (10 m) soft layer close to the surface of a volcano/volcanic zone (and such layers are very common, almost universal), there is a great reduction in the maximum sheet-induced stresses at the surface, and thereby in the likely fracture formation induced by the sheet.

Active volcanoes and volcanic zones/fields contain numerous compliant layers, particularly close to the surface. These are easily seen in the field in caldera walls, pit crater walls, landslide walls, fault walls, sea cliffs, and other erosional and tectonic sections into volcanoes, as well as in numerous drill holes into volcanoes worldwide. From such sections it is commonly easy to estimate roughly the mechanical layering in the upper parts of volcanoes/volcanic zones. Taking the layering into account in modelling sheet (and dike) injection – so as to estimate the likely dimensions, depth, and other geometric factors of the intrusions – are a necessary step in order to improve our understanding of unrest periods with sheet injections.

The present models (compare Figs. 12b, 14b, 16b, and 18b with 12d, 14d, 16d, and 18d) show that the locations of the maximum surface uplift or vertical displacement and the horizontal displacement do not coincide with the locations of the maximum (peak) surface tensile and shear stresses. More specifically, the maximum stresses are much closer to the sheet tips than the maximum horizontal or vertical displacements. For example, the maximum tensile stress for the 30° dipping sheet when layer 4 has a stiffness of 1 GPa is at about 0.17 km to the left of the tip of the sheet (Fig. 14b) whereas the maximum vertical displacement for the same model is at 0.6 km from the tip. Similar differences between displacement peaks and stress peaks occur for other sheet dips.

It is important to remember that the most likely fracture formation is normally not where the displacement peaks occur but rather where the stress peaks occur. These results are in agreement with earlier modelling and observational results (Al Shehri and Gudmundsson, 2018; Bazargan and Gudmundsson, 2019) and are particularly important when trying to understand surface deformation in relation to injected sheets during unrest periods in volcanoes.

The results of all the models (Figs. 11-18) indicate the importance of the effects of mechanical layering in volcanoes/volcanic zones on sheet-induced displacements and stresses. The models show that a single compliant layer may reduce the sheet-induced surface stresses so much as to make surface fracturing unlikely until the sheet has more or less reached the surface. This is in agreement with the field observations of arrested sheet (particularly dike) tips which show that sheets arrested at shallow depths commonly do not generate tension fractures or normal faults above their tips (Al Shehri and Gudmundsson, 2018; Bazargan and Gudmundsson, 2019).

7. Conclusions

The main conclusions of this paper may be summarised as follows:

- The new numerical results presented here focus on the effects of mechanical layering on sheet-induced stresses and displacements, primarily at the surfaces of central (polygenetic) volcanoes and volcanic zones. The models use 5 layers with different mechanical properties, that is, different stiffnesses or Young's modulis. In the models the surface layer, layer 1, has a stiffness of 3 GPa, the next layer below, layer 2, a stiffness of 20 GPa, and layer 3 a stiffness of 30 GPa. Each of these layers is 10 m thick. Below layer 4 is layer or unit 5, with a stiffness of 40 GPa, which hosts the inclined sheet. The sheet is 2 m thick, with a dip dimension 'length' (in a vertical section) of 2 km, and an arrested tip at 100 m below the surface.
- Between model runs, the stiffness of layer 4 is varied, from 10 GPa, and thus rather stiff, to 1 GPa, 0.1 GPa, and 0.01 GPa. The last stiffness, 0.01 GPa, is very compliant but layers of similar stiffness are likely to occur in most active central volcanoes and volcanic zones. The modelled sheets have four dips: 30°, 45°, 60°, and 90°, the last one being a vertical dike. These dips span the common dip range of sheets in sheet swarms, based on observations in Iceland, Scotland, and elsewhere.
- The internal stress shown as contours is the maximum tensile stress, σ_3 (Figs. 11, 13, 15, and 17). The results show clearly the importance of mechanical layering. In particularly, when layer 4 becomes more compliant, less and less stress is transmitted to the layers above (layers 2 and 3) and to the surface (layer 1). By contrast, the tensile stress concentrates at the top of layer 5, at its contact with layer 4, and is so high that fracturing would be expected.
- For the various dips of the sheets, the following sheet-induced surface results are provided. (a) The von Mises shear stress, (b) the principal tensile stress (σ_3), (c) the horizontal displacement, and (d) the vertical displacement.
- The sheet dipping 30° induces the greatest surface stresses and displacements. Both stresses and displacements are highly asymmetric across the tip of the sheet, except for the vertical sheet (the dike), where they are symmetric. When the stiffness of layer 4 decreases to 0.1 GPa and 0.01 GPa, little stress is transmitted to the surface, so that the surface stresses gradually decrease. For this decrease in stiffness, changes in vertical displacement, however, are comparatively small but greater for the horizontal displacement.
- In particular, when the stiffness of layer 4 decreases from 10 GPa to 0.01 GPa, the maximum shear stress at the surface decreases from about 6.6 MPa to 2.2 MPa (Figs. 12a and 18a) and the maximum tensile stress from about 6.9 MPa to about 2.3 MPa (Figs. 12b and 18b). Thus, even a single comparatively thin (10 m) soft layer close to the surface of a central volcano/volcanic zone (and such layers are almost universal), there is a great reduction in the maximum sheet-induced stresses at the surface, and thereby in the likelihood of fracture formation.
- The stress peaks and displacement peaks do not coincide. Tension fractures and faults – in particular the boundary faults of grabens – are most likely to form, if at all, at the location of the tensile/shear stress peaks and not, as is commonly suggested, at the location of the surface uplift peaks.

- Information on mechanical layering in active volcanoes is widely available, from eroded cliff sections, caldera walls, pit-crater walls, landslide walls, fault walls, and from drill holes. Reasonable estimates of the variation in stiffness of the layers can thus commonly be made for active volcanoes. The results suggest that failure to take typical and reasonable mechanical layering in central volcanoes and volcanic zones into account, such as by using homogeneous, elastic half-space dislocation models, when inferring sheet geometries and depths thorough the inversion of surface-deformation data is likely to lead to highly unreliable results. In particular, such models tend to overestimate the theoretical sheet-induced surface stresses, and thus the depth to the tip of the associated sheet – a topic of great importance during periods of volcanic unrest and when estimating the likelihood of sheet-fed eruption.

Acknowledgements

We thank Weld on Sweden for financial support.

References

Al Shehri, A., Gudmundsson, A., 2018. Modelling of surface stresses and fracturing during dyke emplacement: Application to the 2009 episode at Harrat Lunayyir, Saudi Arabia. J. Volcanol. Geotherm. Res., 356, 278-303.

Barnett, Z.A., Gudmundsson, A., 2014. Numerical modelling of dykes deflected into sills to form a magma chamber. J. Volcanol. Geotherm. Res., 281, 1-11.

Bazargan, M., Gudmundsson, A., 2019. Dike-induced stresses and displacements in layered volcanic zones. J. Volcanol. Geotherm. Res. (in press).

Becerril, L., Galindo, I., Gudmundsson, A., Morales, J.M., 2013. Depth of origin of magma in eruptions. Scientific Reports 3, 2762. doi: 10.1038/srep02762

Bistacchi, A., Tibaldi, A., Pasquarè, F..A., Rust, D., 2012. The association of cone–sheets and radial dykes: Data from the Isle of Skye (UK), numerical modelling, and implications for shallow magma chambers. Earth Planet. Sci. Lett., 339–340, 46-56.

Deb, D., 2006. Finite Element Method: Concepts and Applications in Geomechanics. Prentice-Hall, New Jersey.

Dzurisin, D., 2006. Volcano Deformation. Springer Verlag, New York.

Galindo, I., Gudmundsson, A., 2012 Basaltic feeder-dykes in rift zones: geometry, emplacement, and effusion rates. Natural Hazards and Earth System Sciences, 12, 3683–3700.

Gautneb, H., Gudmundsson, A., 1992. Effect of local and regional stress fields on sheet emplacement in West Iceland. J. Volcanol. Geoth. Res .51, 339-356.

Gautneb, H., Gudmundsson, A., Oskarsson, N., 1989. Structure, petrochemistry, and evolution of a sheet swarm in an Icelandic central volcano. Geol. Mag., 126, 659-673.

Geshi, N., Kusumoto, S., Gudmundsson, A., 2010. Geometric difference between non-feeder and feeder dikes. Geology, 38, 195–198.

Geshi, N., Kusumoto, S., Gudmundsson, A., 2012. Effects of mechanical layering of host rocks on dike growth and arrest. J. Volcanol. Geotherm. Res., 223-224, 74-82.

Gudmundsson, A., 1995. Infrastructure and mechanics of volcanic systems in Iceland. J. Volcanol. Geotherm. Res., 64, 1-22.

Gudmundsson, A., 1998. Magma chambers modeled as cavities explain the formation of rift zone central volcanoes and their eruption and intrusion statistics. J. Geophys. Res., 103, 7401-7412.

Gudmundsson, A., 2003. Surface stresses associated with arrested dykes in rift zones: Bull. Volcanol., 65, 606-619.

Gudmundsson, A., 2011a. Rock Fractures in Geological Processes. Cambridge University Press, Cambridge.

Gudmundsson, A., 2011b. Deflection of dykes into sills at discontinuities and magma-chamber formation. Tectonophysics, 500, 50-64.

Gudmundsson, A., 2019. Volcanotectonics. Understanding the Structure, Deformation, and Dynamics of Volcanoes. Cambridge University Press, Cambridge.

Gudmundsson, A., Brenner, S.L., 2001. How hydrofractures become arrested. Terra Nova, 13, 456-462.

Gudmundsson, A., Loetveit, I.F., 2005. Dyke emplacement in layered and faulted rift zone. Journal of Volcanology and Geothermal Research, 144, 311-327.

Gudmundsson, A., Pasquare, F.A., Tibaldi, A., 2018. Dykes, sills, laccoliths, and inclined sheets in Iceland. In: Breitkreuz, C., Rocchi, S. (eds), Physical Geology of Shallow Magmatic Systems: Dykes, Sills and Laccoliths. Berlin, Springer, pp. 363-376.

Harker, A., 1904. The Tertiary Igneous Rocks of Skye. UK Geological Surv. Mem., 481 pp.

Klausen, M.B., 2004. Geometry and mode of emplacement of the Thverartindur cone sheet swarm, SE Iceland. J. Volcanol. Geotherm. Res., 138, 185-204.

Klausen, M.B., 2006. Geometry and mode of emplacement of dike swarms around the Birnudalstindur igneous centre, SE Iceland. J. Volcanol. Geotherm. Res .,151, 340-356.

Liu, G.R. , Quek, S.S., 2014. Finite Element Method, 2nd ed. Elsevier, Amsterdam.

Martí, J., C. López, S. Bartolini, L. Becerril, Geyer , A., 2016. Stress controls of monogenetic volcanism: a review. Front. Earth Sci., 4(106), doi: 10.3389/feart.2016.00106.

Martí, J., A. Villaseñor, A. Geyer, C. López, Tryggvason, A., 2017. Stress barriers controlling lateral migration of magma revealed by seismic tomography. Sci. Reports, 7, 40757, doi: 10.1038/srep40757

Okada, Y., 1985. Surface deformation due to shear and tensile faults in a half-space. Bulletin of the Seismological Society of America, 75, 1135-1154.

Okada, Y., 1992. Internal deformation due to shear and tensile faults in half space. Bulletin of the Seismological Society of America, 82, 1018-1040.

Pasquarè., F, Tibaldi., A., 2007. Structure of a sheet-laccolith system revealing the interplay between tectonic and magma stresses at Stardalur Volcano, Iceland. J. Volcanol. Geotherm. Res., 161, 131-150.

Philipp, S.L., Afsar, F., Gudmundsson, A., 2013. Effects of mechanical layering on hydrofracture emplacement and fluid transport in reservoirs. Frontiers in Earth Science, 1, doi:10.3389/feart.2013.00004

Phillips, W.J., 1974. The dynamic emplacement of cone sheets. Tectonophysics, 24, 69-84.

Rivalta, E., Taisne, B., Bunger, P., Katz, F., 2015. A review of mechanical models of dyke propagation: Schools of thought,results and future directions. Science Direct ,Tectono physics. 638, 1-42, doi.org/10.1016/j.tecto.2014.10.003.

Scholz, C.H., 1990. The Mechanics of Earthquakes and Faulting. Cambridge, Cambridge University Press.

Segall, P., 2010. Earthquake and Volcano Deformation. Princeton University Press, Princeton.

Siler, D.L., Karson, J.A., 2009. Three-dimensional structure of inclined sheet swarms: Implications for crustal thickening and subsidence in the volcanic rift zones of Iceland. J. Volcanol. Geotherm. Res., 18, 333-346.

Tibaldi., A, Pasquarè, F.A., Rust, D., 2011. New insights into the cone sheet structure of the Cuillin Complex, Isle of Skye, Scotland. J. Geol. Soc., 168, 689-704.

Tibaldi, A., Bonali, F., Pasquaré, F.A., Rust, D., Cavallo, A., D'Urso, A., 2013. Structure of regional dykes and local cone sheets in the Midhyrna-Lysuskard area, Snaefellsnes Peninsula (NW Iceland). Bull. Volcanol., 75: 764, doi 10.1007/s00445-013-0764-8.

Townsend, M.R., Pollard, D.D., Smith, R.P., 2017. Mechanical models for dikes: A third school of thought. Tectonophysics, 703-704, 98-118.

Figure captions

Fig. 1 Internal structure of a typical rift-zone volcanic system fed by a deep-seated reservoir as well as a shallow magma chamber which supplies magma to the central (here composite) volcano. The composite volcano is mainly supplied with magma from thin inclined sheets and radial dikes injected from the shallow chamber, whereas the eruptions outside the central volcano are primarily supplied with magma through much thicker regional dikes. Most dikes and inclined sheets do not reach the surface to erupt but stop, become arrested, at contacts between dissimilar layers at some depth – some deflecting into sills at these contacts. The local swarm that forms above the shallow chamber is what is referred to as a sheet swarm, whereas the swarm outside the volcano is the regional dike swarm.

Fig. 2. Dense swarm of inclined sheets in the fossil central volcano Geitafell in Southeast Iceland. When the chamber was active (the fossil chamber is now a gabbro pluton) its roof was at about 2 km below the surface of the associated central volcano. Part of the local swarm of inclined sheets and radial dikes is seen here. The sheets constitute 80-100% of the rock close to the fossil magma chamber. Also indicated is the main contact between the chamber and the sheet swarm. The person provides a scale.

Fig. 3. Cross-cutting inclined sheets and basaltic dikes in lake sediments in South Iceland. The length of the hammer is about 30 cm. The cross-cutting relationship here and in thousands of other outcrops show that the great majority of inclined sheets and dikes are extension fractures (cf. Figs. 2 and 4).

Fig. 4. Dense sheet swarm showing numerous cross-cutting relationships (some indicated by the letter C) among inclined sheets. From the fossil Geitafell central volcano in Southeast Iceland (cf. Figs. 2 and 3).

Fig. 5. Abrupt increase in thickness and dip of inclined sheet at a distance of about 9 km from the centre of the caldera, located above the fossil shallow magma chamber of the central volcanoe of Reykjadalur in West Iceland. At this distance there is a change from a local sheet swarm to a regional dike swarm. Vertical error bars indicate the range in values at each measurement station (Gautneb and Gudmundsson, 1992).

Fig. 6. Inclined sheet paths follow the σ_1- trajectories, as indicated here for four sheets (marked 1-4), injected from a shallow magma chamber of a circular vertical cross-section. In this numerical model the crustal segment is homogeneous and isotropic and the only loading is internal chamber excess magmatic pressure p_e of 10 MPa. So long as the magma has any significant overpressure (Eq. 3) all sheets should reach the surface.

Fig. 7. Potential paths (parallel to the indicated σ_1 trajectories) of sheets (dikes, sills, and inclined sheets) injected from a shallow magma chamber of a circular cross-section subject to 5 MPa internal excess pressure as the only loading. The thin layers are compliant (soft, 1 GPa) whereas the thick layers stiff (100 GPa). Sheet path A becomes arrested at the contact where the σ_1- trajectories flip 90º while path B changes into a sill. At the contact, path C first changes into a sill and then into an inclined sheet.

Fig. 8. Part of the roof and the walls of a fossil shallow magma chamber in Southeast Iceland. Many sheets, primarily dikes, cut the roof. The granophyre pluton is hosted by a pile of basaltic lava flows. When it was active its roof was about 1.5 km below the surface of the associated volcanic zone. Many dikes cut the roof. The thick one to the left on the figure changes its path from vertical to inclined and then again to vertical.

Fig. 9. Propagation path of a basaltic inclined sheet, 0.5-1 m thick, in Southwest Iceland. The sheet deflects along a contact between a stiff basaltic lava flow and a compliant or soft scoria layer and then follows an inclined path through the lava flow.

Fig. 10. Setup of the Comsol model with the 2 km tall sheet (dip dimension) and 2 m thick in the central upper part (indicates as thick white line) of the model (whose dimensions are 20 km × 20 km). The complete mesh consists of 46,945 domain elements and 7434 boundary elements. The minimum element quality is 0.3985 m.

Fig. 11. The maximum principal tensile stress (σ_3) inside the model in mega-pascals (vertical colour scale to the right of the model shows the magnitude in MPa). Layer 4 has a stiffness of 10 GPa. (a) Sheet dipping 30°. (b) Sheet dipping 45°. (c) Sheet dipping 60°.

Fig. 12. Surface stresses and displacements induced by an inclined sheet with a dip dimension of 2 km and 5 MPa internal magmatic pressure as the only loading. Layer 4 has a stiffness of

10 GPa. (a) Von Mises shear stress. (b) Maximum principal tensile stress (σ_3). (c) Horizontal displacement. (d) Vertical displacement.

Fig. 13. The maximum principal tensile stress (σ_3) inside the model in mega-pascals (vertical colour scale to the right of the model shows the magnitude in MPa) for a sheet dipping 30°. Layer 4 has a stiffness of 1 GPa.

Fig. 14. Surface stresses and displacements induced by an inclined sheet with a dip dimension of 2 km and 5 MPa internal magmatic pressure as the only loading. Layer 4 has a stiffness of 1 GPa. (a) Von Mises shear stress. (b) Maximum principal tensile stress (σ_3). (c) Horizontal displacement. (d) Vertical displacement.

Fig. 15. The maximum principal tensile stress (σ_3) inside the model in mega-pascals (vertical colour scale to the right of the model shows the magnitude in MPa) for a sheet dipping 30°. Layer 4 has a stiffness of 0.1 GPa.

Fig. 16. Surface stresses and displacements induced by an inclined sheet with a dip dimension of 2 km and 5 MPa internal magmatic pressure as the only loading. Layer 4 has a stiffness of 0.1 GPa. (a) Von Mises shear stress. (b) Maximum principal tensile stress (σ_3). (c) Horizontal displacement. (d) Vertical displacement.

Fig. 17. The maximum principal tensile stress (σ_3) inside the model in mega-pascals (vertical colour scale to the right of the model shows the magnitude in MPa) for a sheet dipping 30°. Layer 4 has a stiffness of 0.01 GPa.

Fig. 18. Surface stresses and displacements induced by an inclined sheet with a dip dimension of 2 km and 5 MPa internal magmatic pressure as the only loading. Layer 4 has a stiffness of 0.01 GPa. (a) Von Mises shear stress. (b) Maximum principal tensile stress (σ_3). (c) Horizontal displacement. (d) Vertical displacement.

Fig. 19. Inclined sheets (and dikes) modelled as elastic dislocation and dipping at 0° (a sill), 60° (an inclined sheet), and at 90° (a dike). In addition, the author shows the same for a classical Mogi model, that is, a nucleus of strain (modified from Dzurisin, 2006).

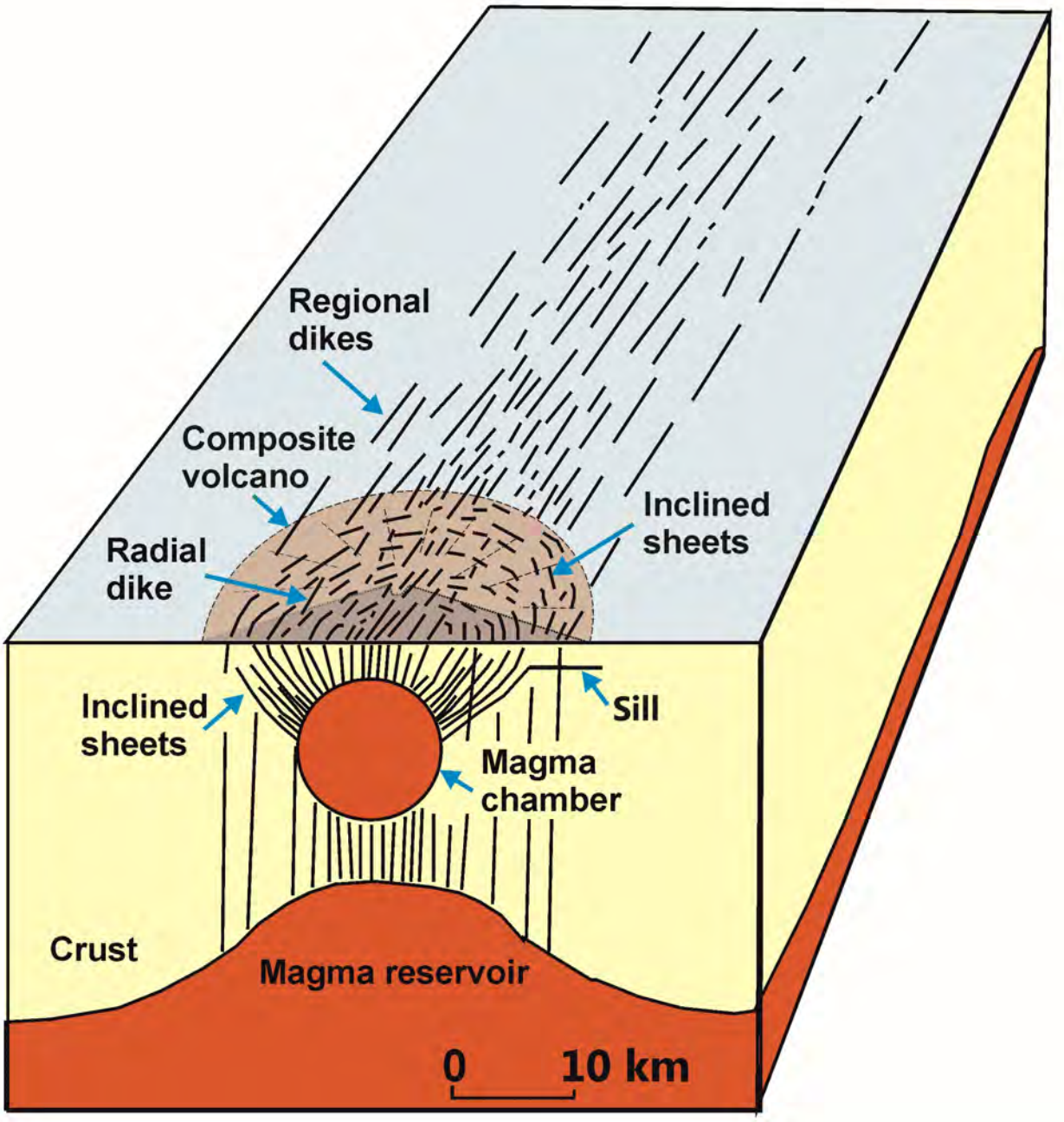
Regional dikes
Composite volcano
Radial dike
Inclined sheets
Inclined sheets
Sill
Magma chamber
Crust
Magma reservoir
0
10 km

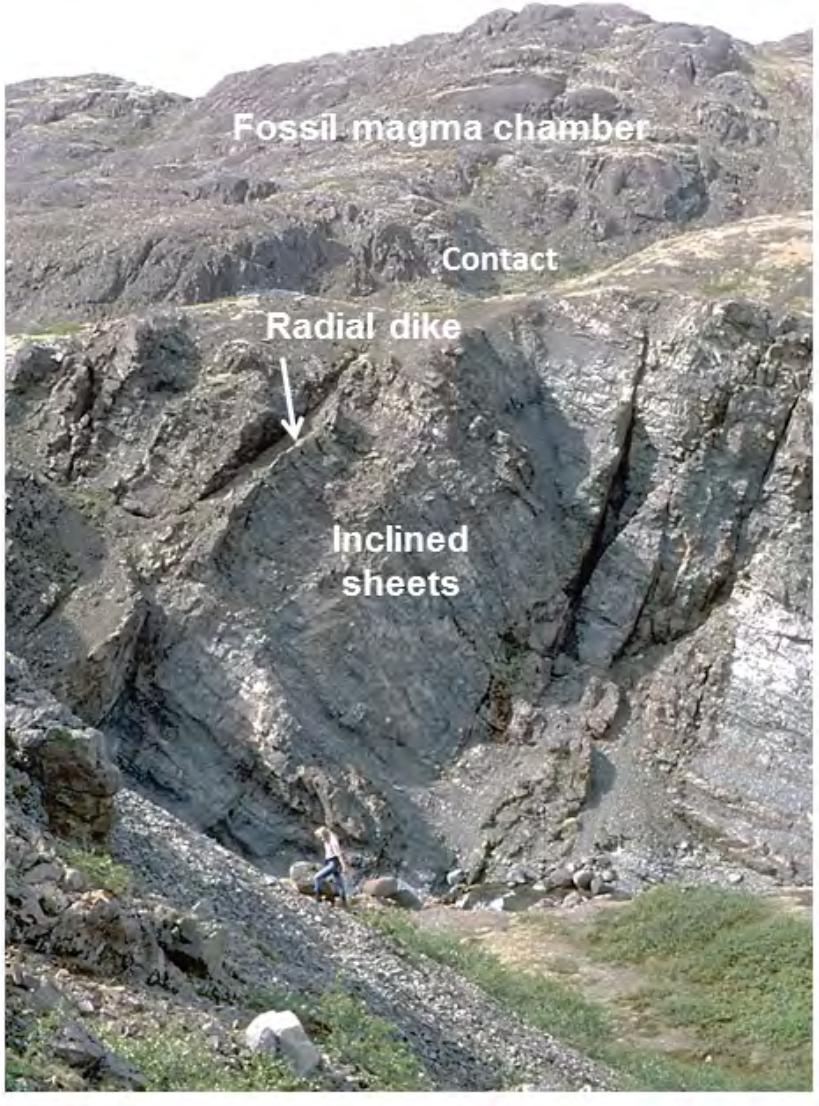
Fossil magma chamber
Contact
Radial dike
Inclined
sheets

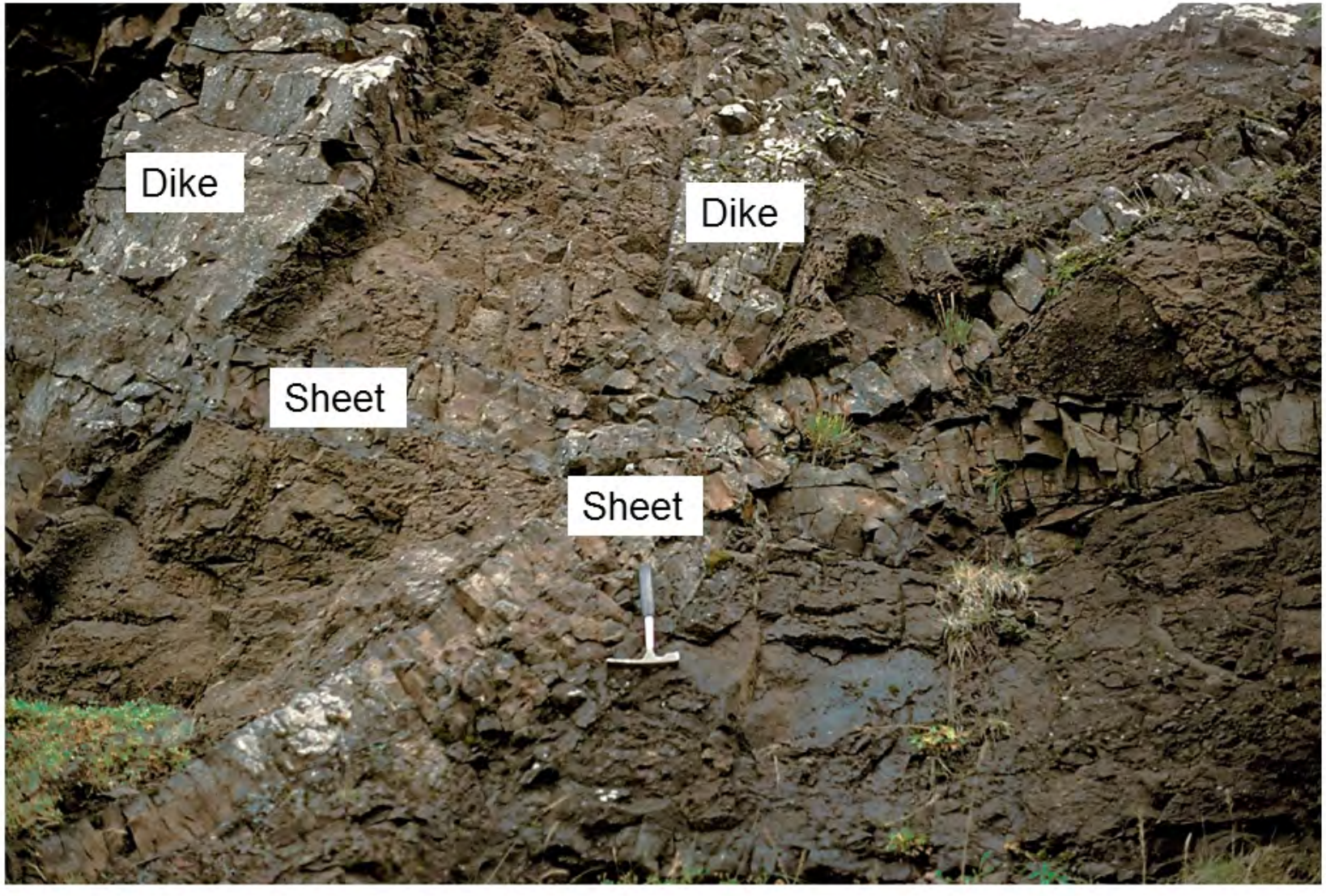
Dike
Dike
Sheet
Sheet


C
C
C

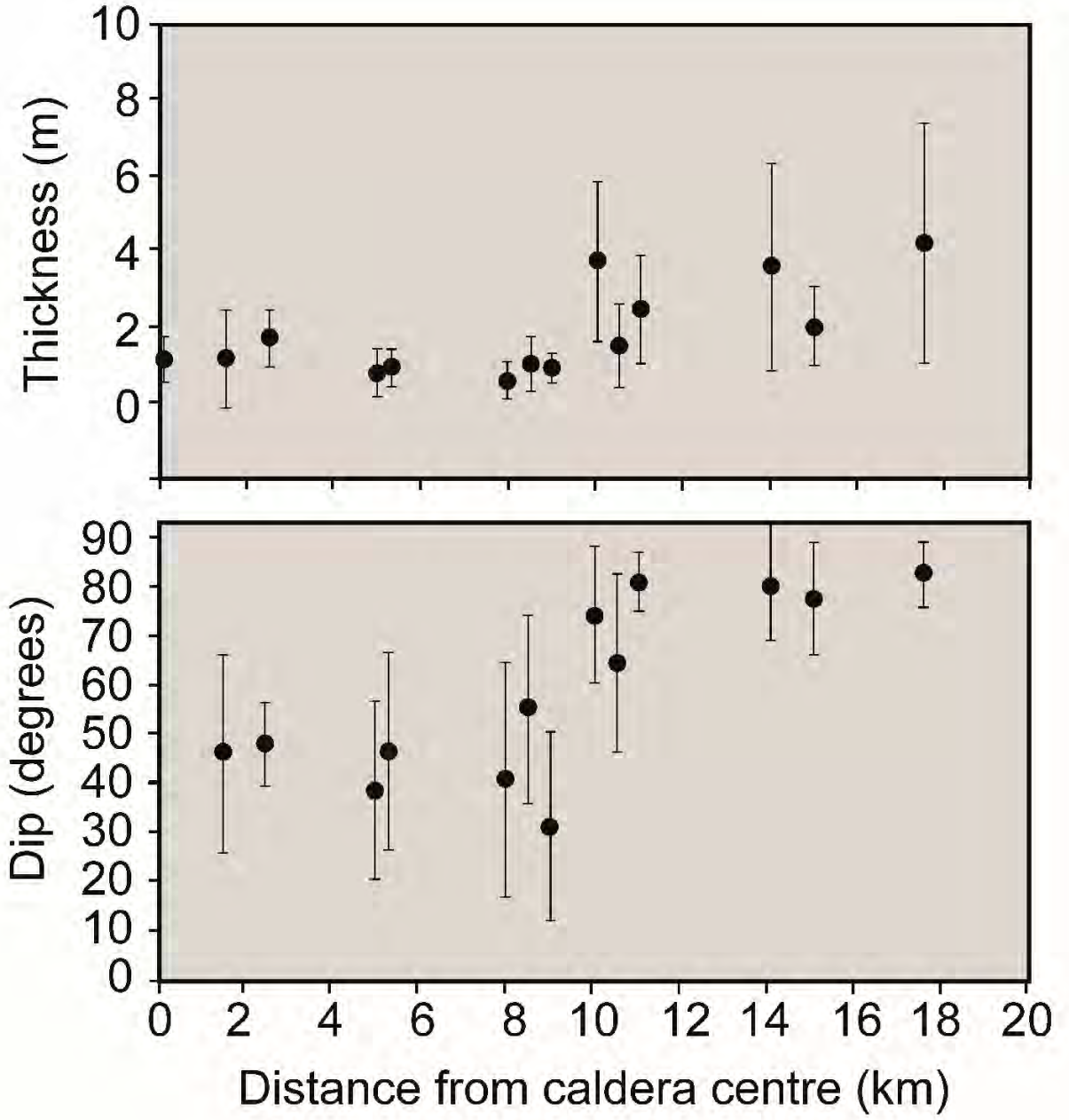
Thickness (m)
0
2
4
6
8
10
Dip (degrees)
0
10
20
30
40
50
60
70
80
90
0
2
4
6
8
10
12
14
16
18
20
Distance from caldera centre (km)

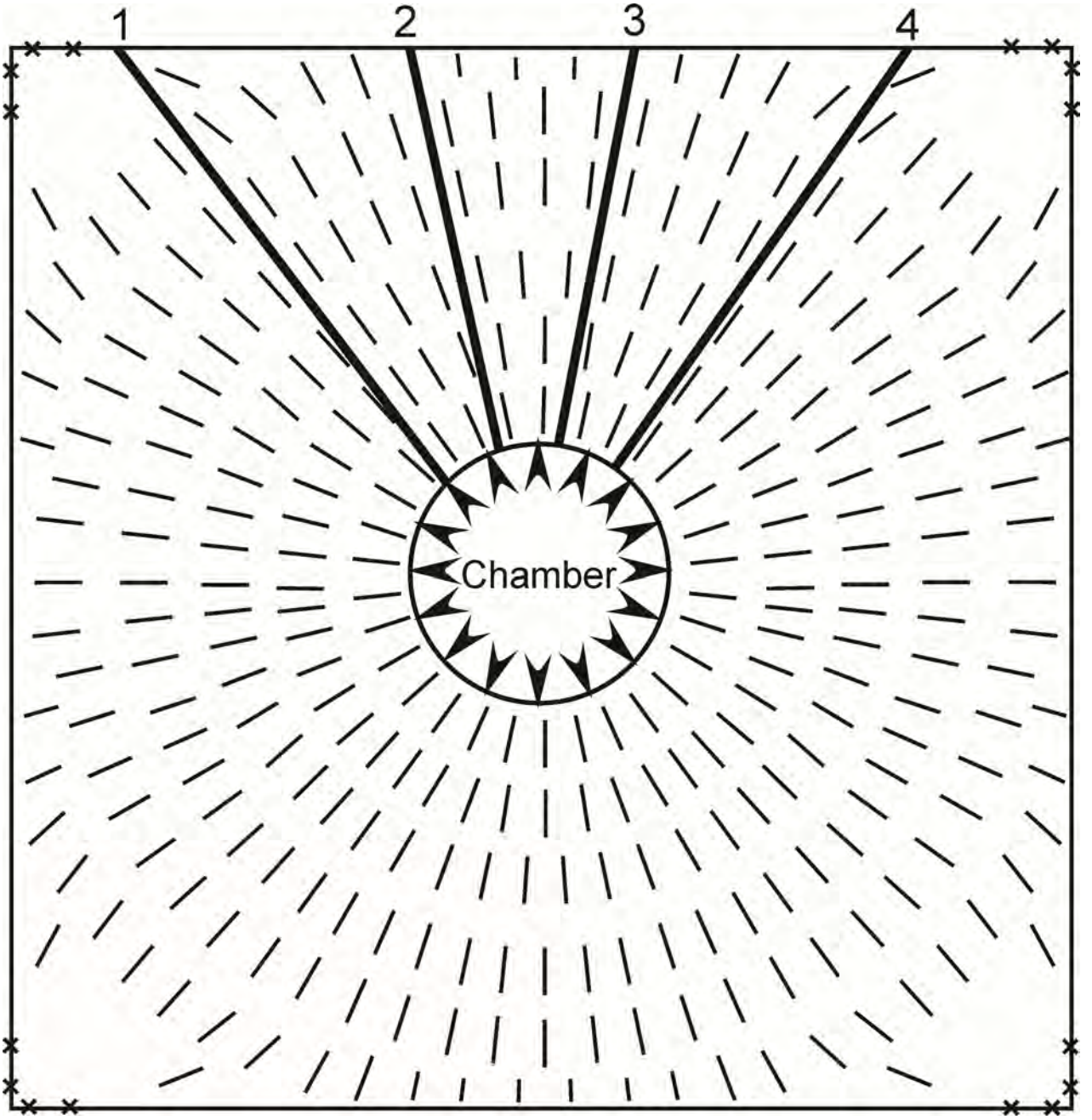
1
2
3
4
Chamber

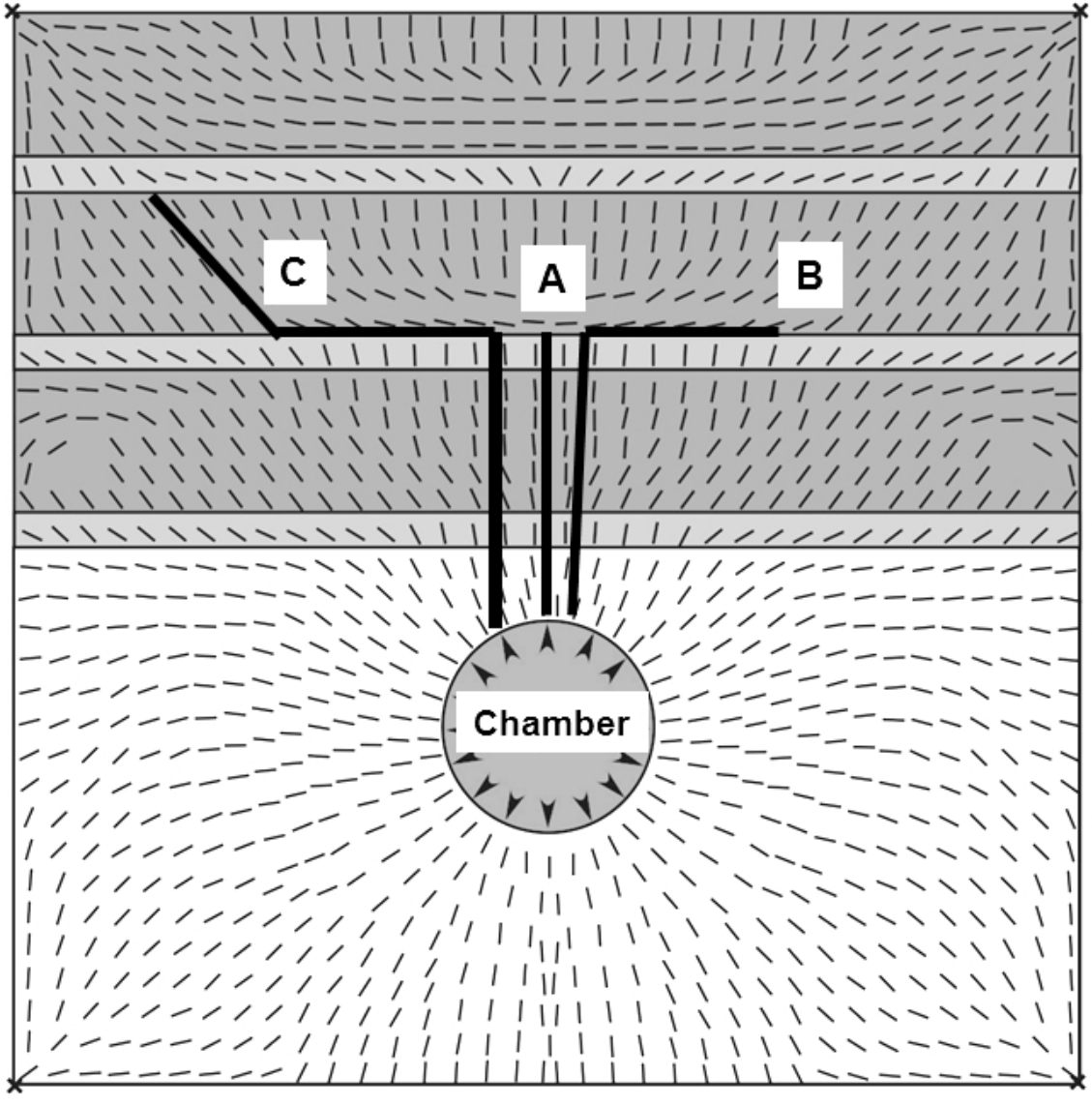
C
A
B
Chamber

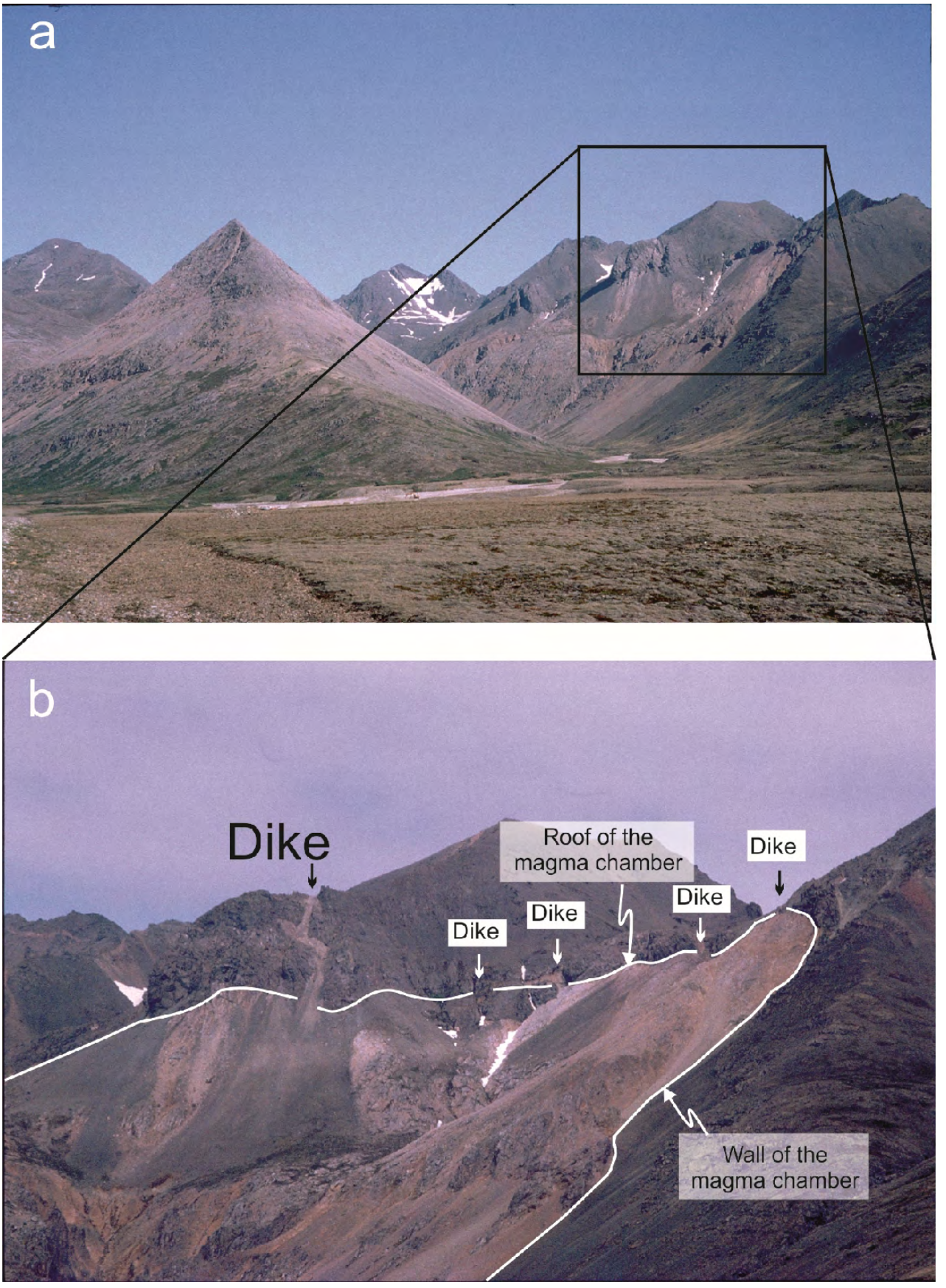
a
b
Dike
Roof of the magma chamber
Dike
Dike
Dike
Dike
Wall of the magma chamber

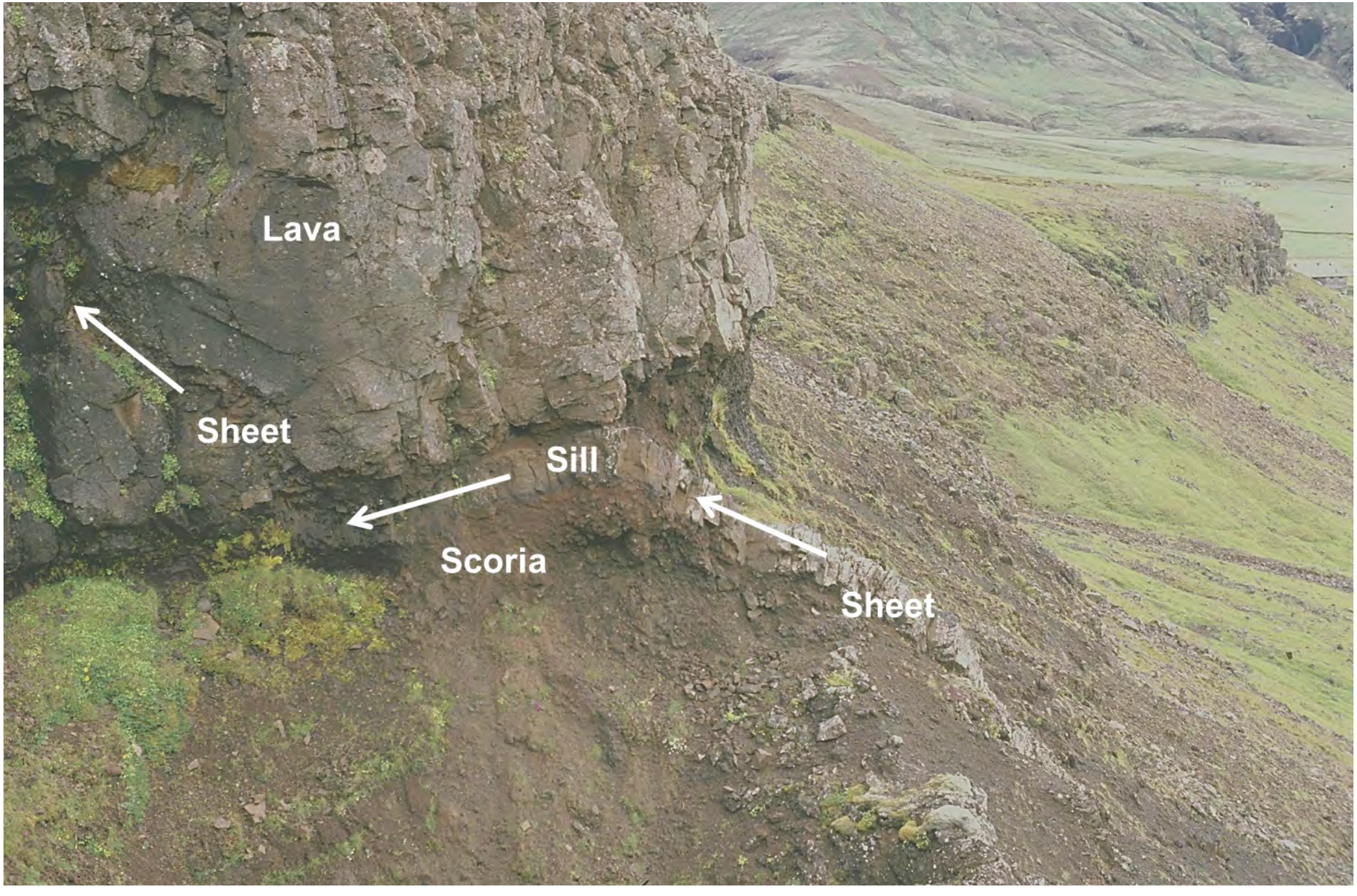
Lava
Sheet
Sill
Scoria
Sheet

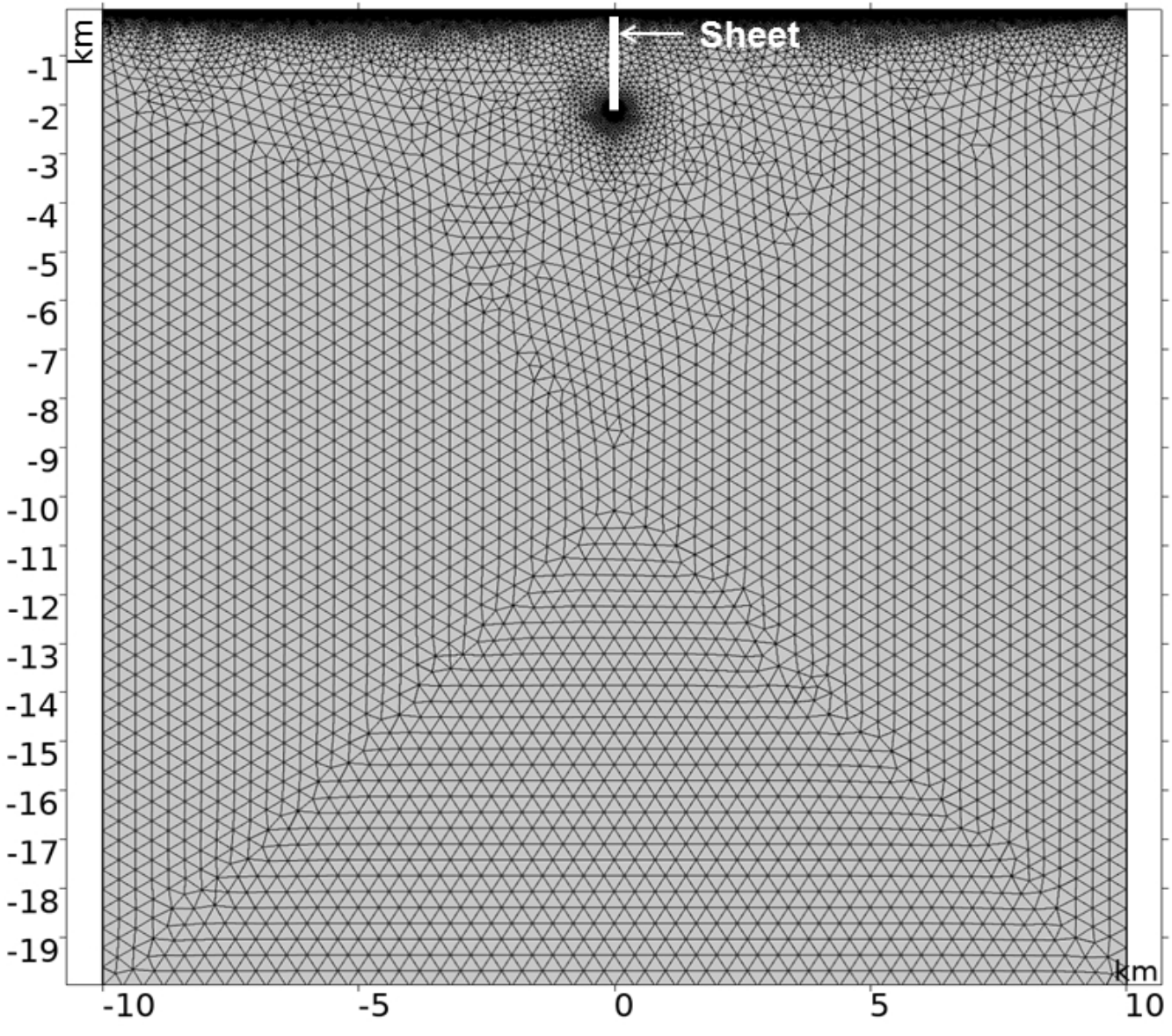
Sheet
km
-1
-2
-3
-4
-5
-6
-7
-8
-9
-10
-11
-12
-13
-14
-15
-16
-17
-18
-19
km
-10
-5
0
5
10

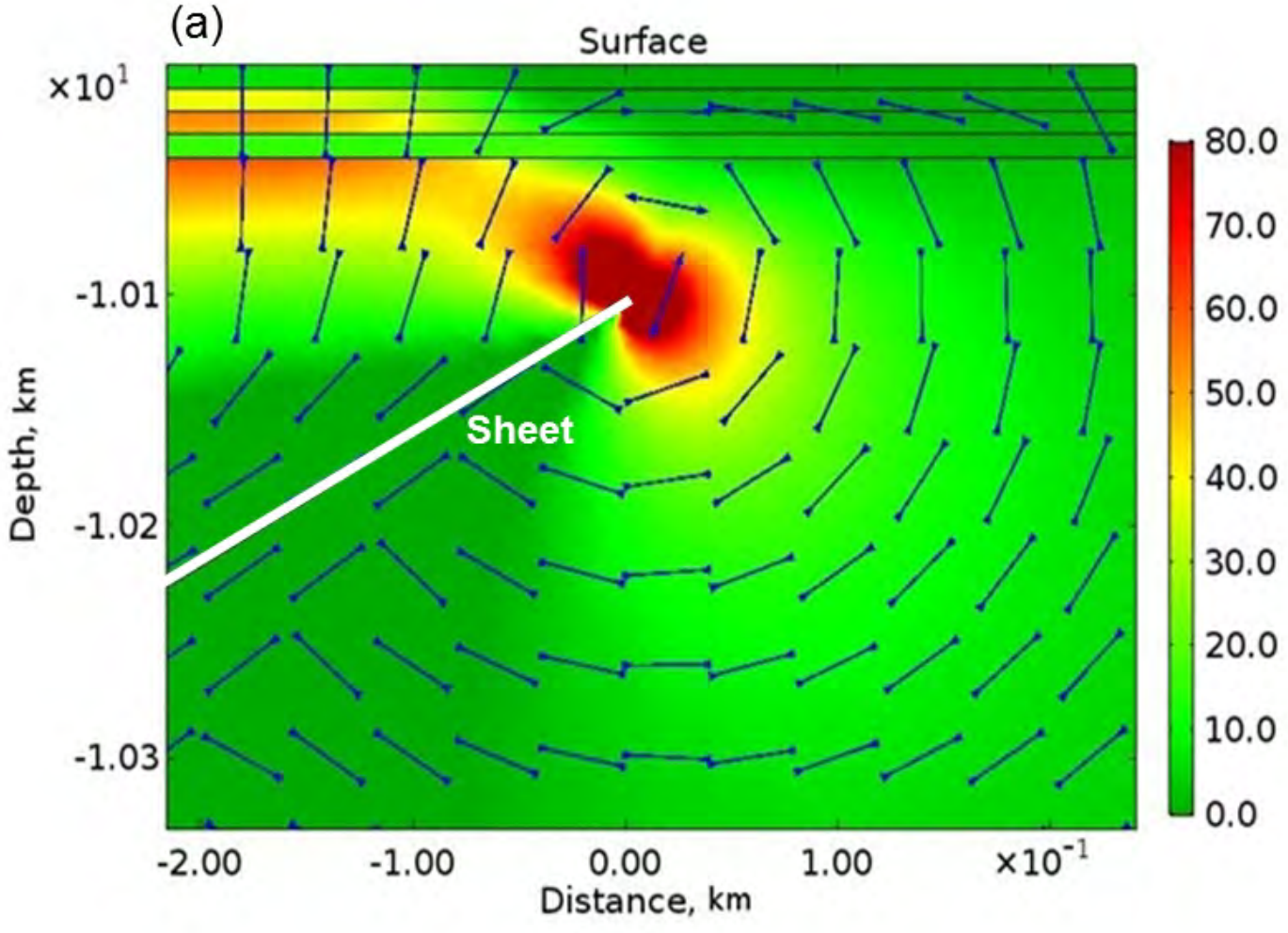
(a)
Surface
×10^1
-1.01
-1.02
-1.03
Depth, km
Sheet
-2.00
-1.00
0.00
1.00
×10^-1
Distance, km
80.0
70.0
60.0
50.0
40.0
30.0
20.0
10.0
0.0

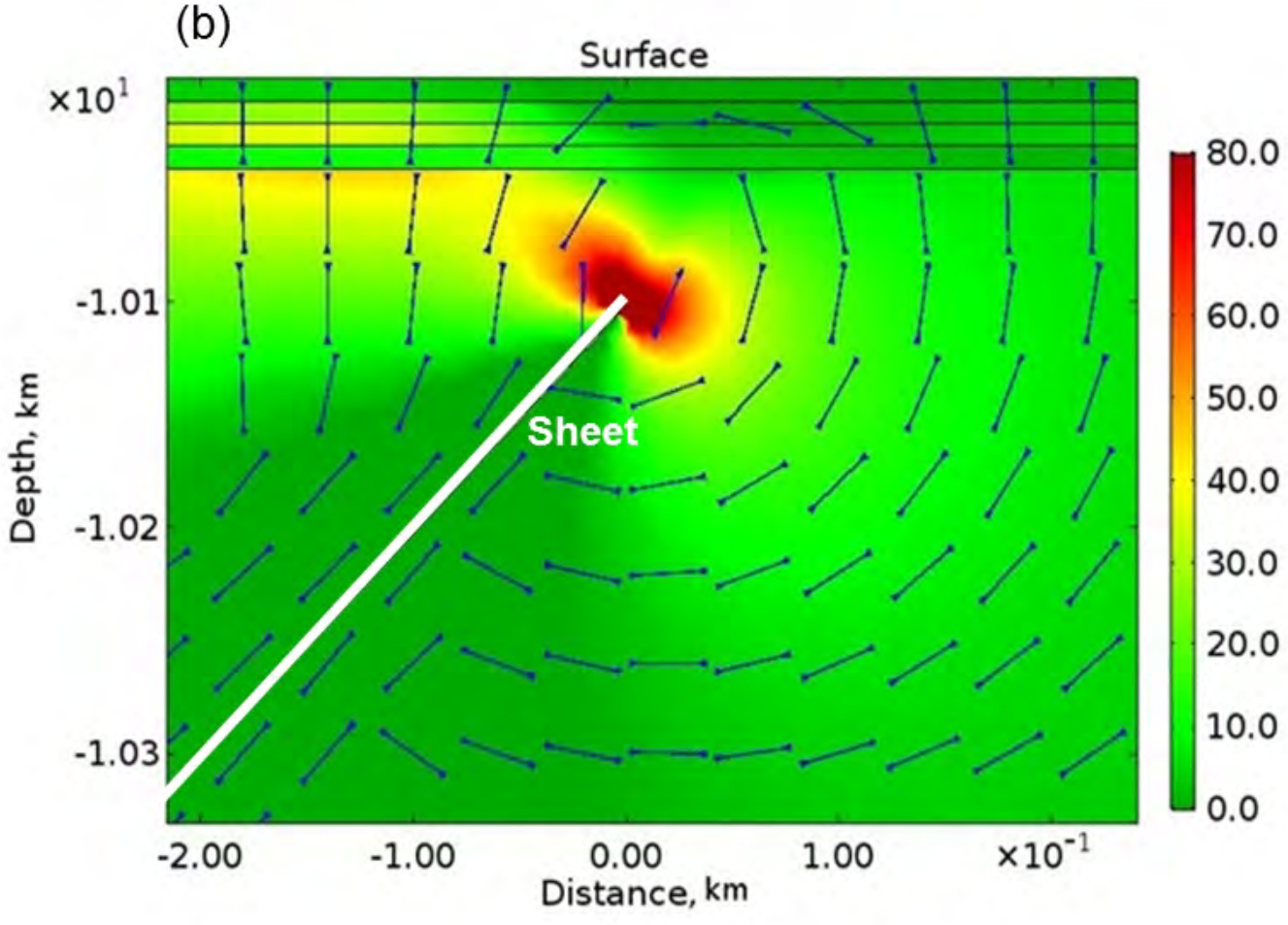
(b)
Surface
×10^1
-1.01
-1.02
-1.03
Depth, km
Sheet
-2.00
-1.00
0.00
1.00
×10^-1
Distance, km
80.0
70.0
60.0
50.0
40.0
30.0
20.0
10.0
0.0

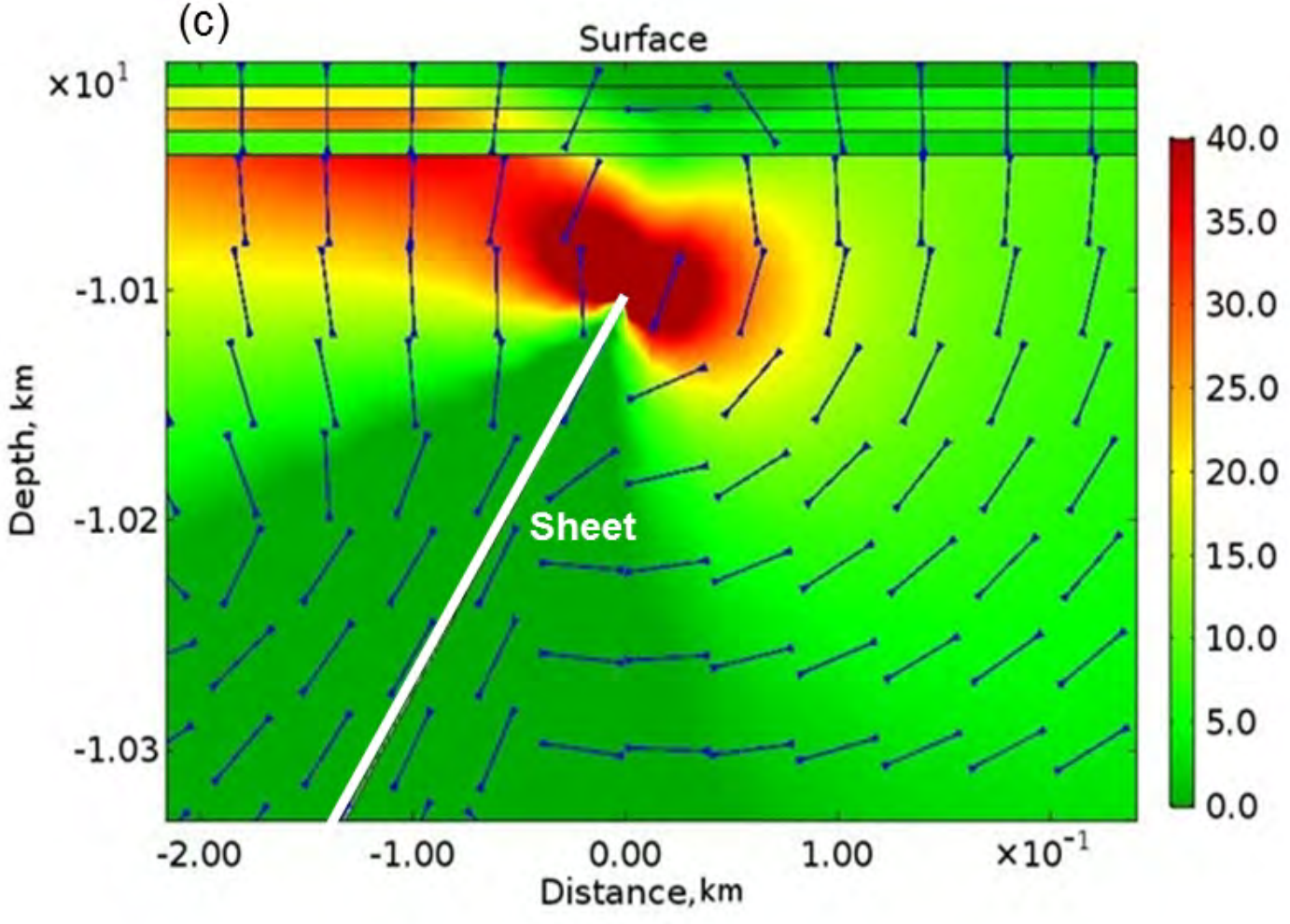
(c)
Surface
×10^1
-1.01
-1.02
-1.03
Depth, km
Sheet
-2.00
-1.00
0.00
1.00
×10^-1
Distance, km
40.0
35.0
30.0
25.0
20.0
15.0
10.0
5.0
0.0

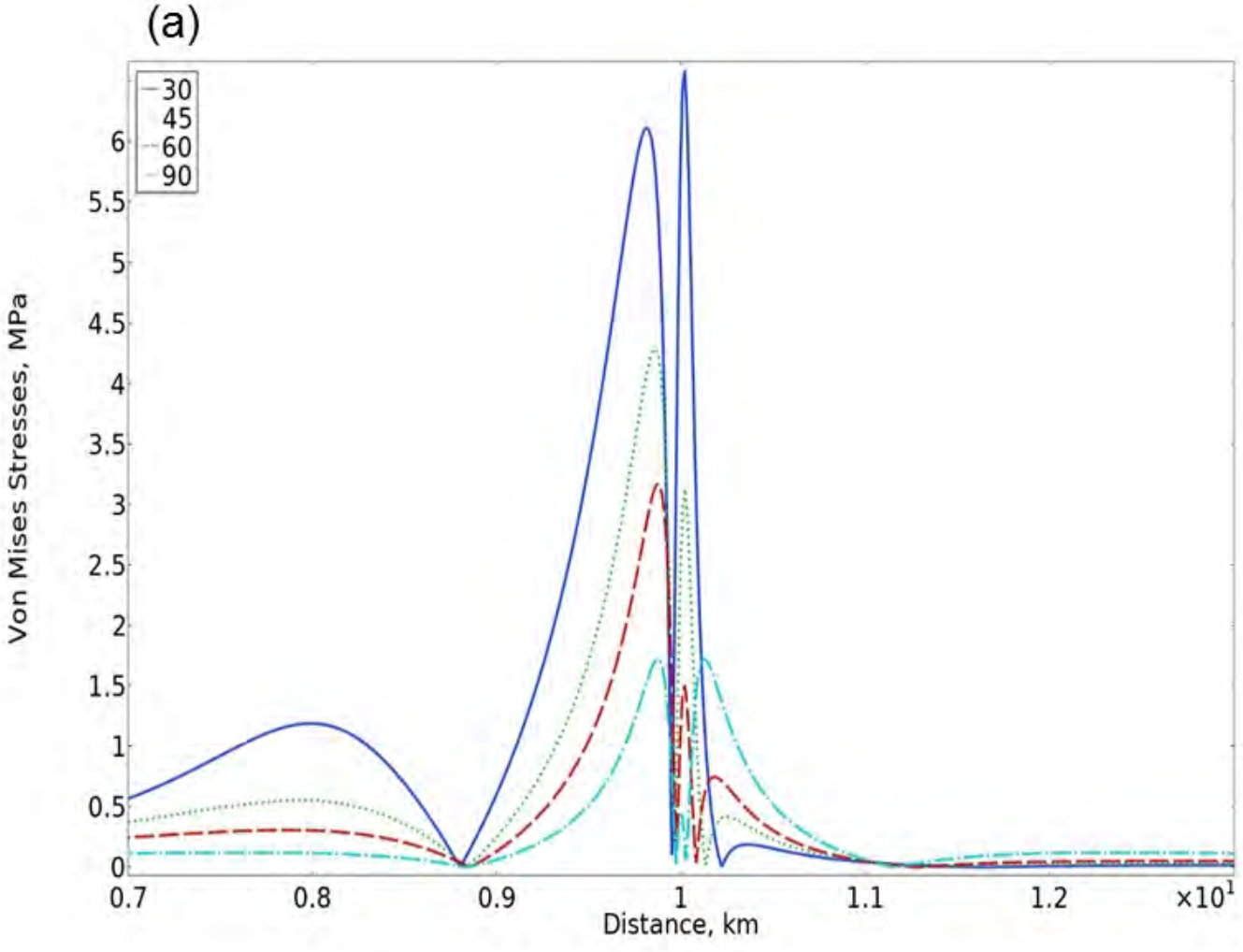
(a)
30
45
60
90
Von Mises Stresses, MPa
0
0.5
1
1.5
2
2.5
3
3.5
4
4.5
5
5.5
6
0.7
0.8
0.9
1
1.1
1.2
×10^1
Distance, km

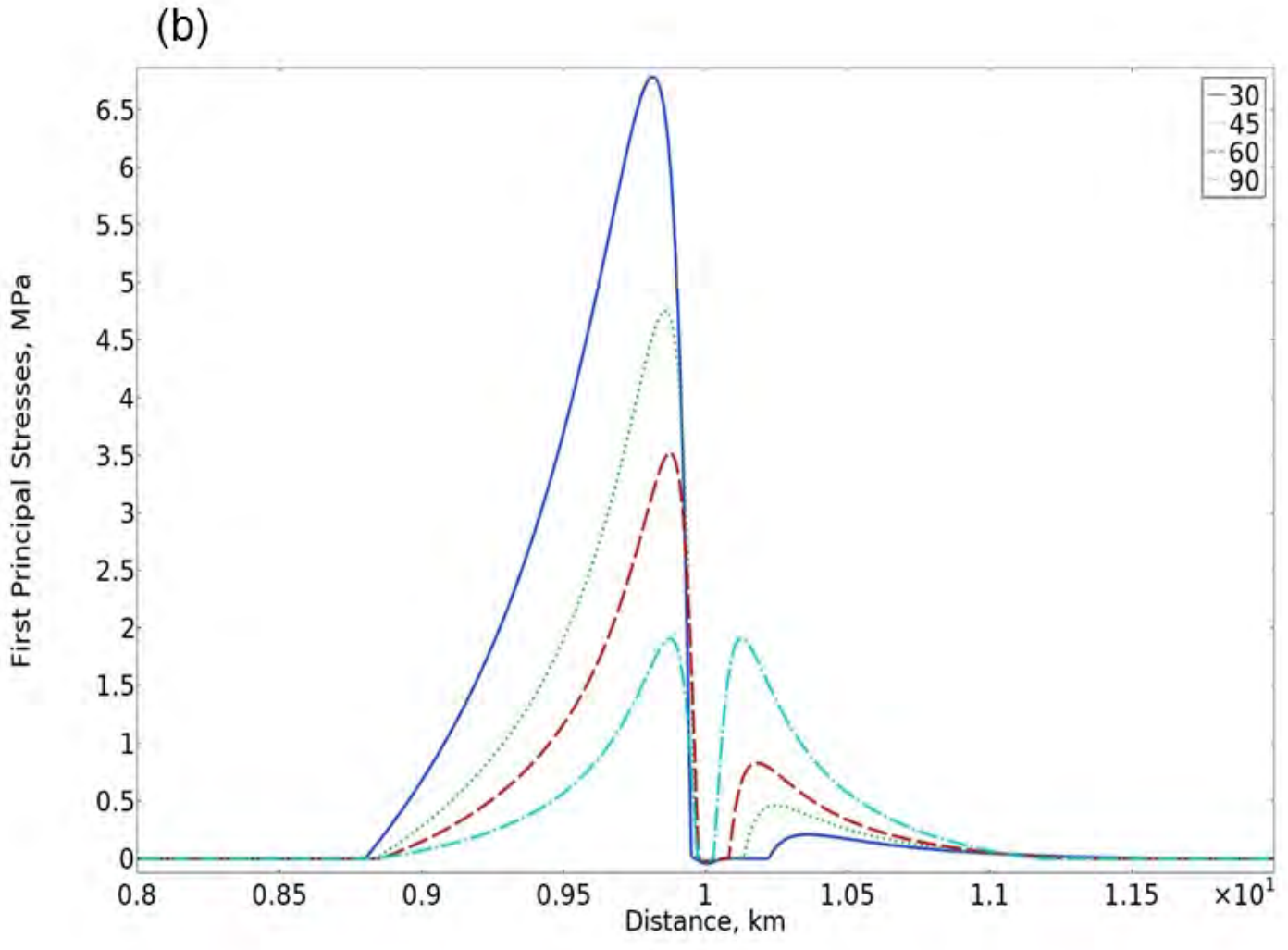
(b)
First Principal Stresses, MPa
Distance, km
×10^1
30
45
60
90
0
0.5
1
1.5
2
2.5
3
3.5
4
4.5
5
5.5
6
6.5
0.8
0.85
0.9
0.95
1
1.05
1.1
1.15

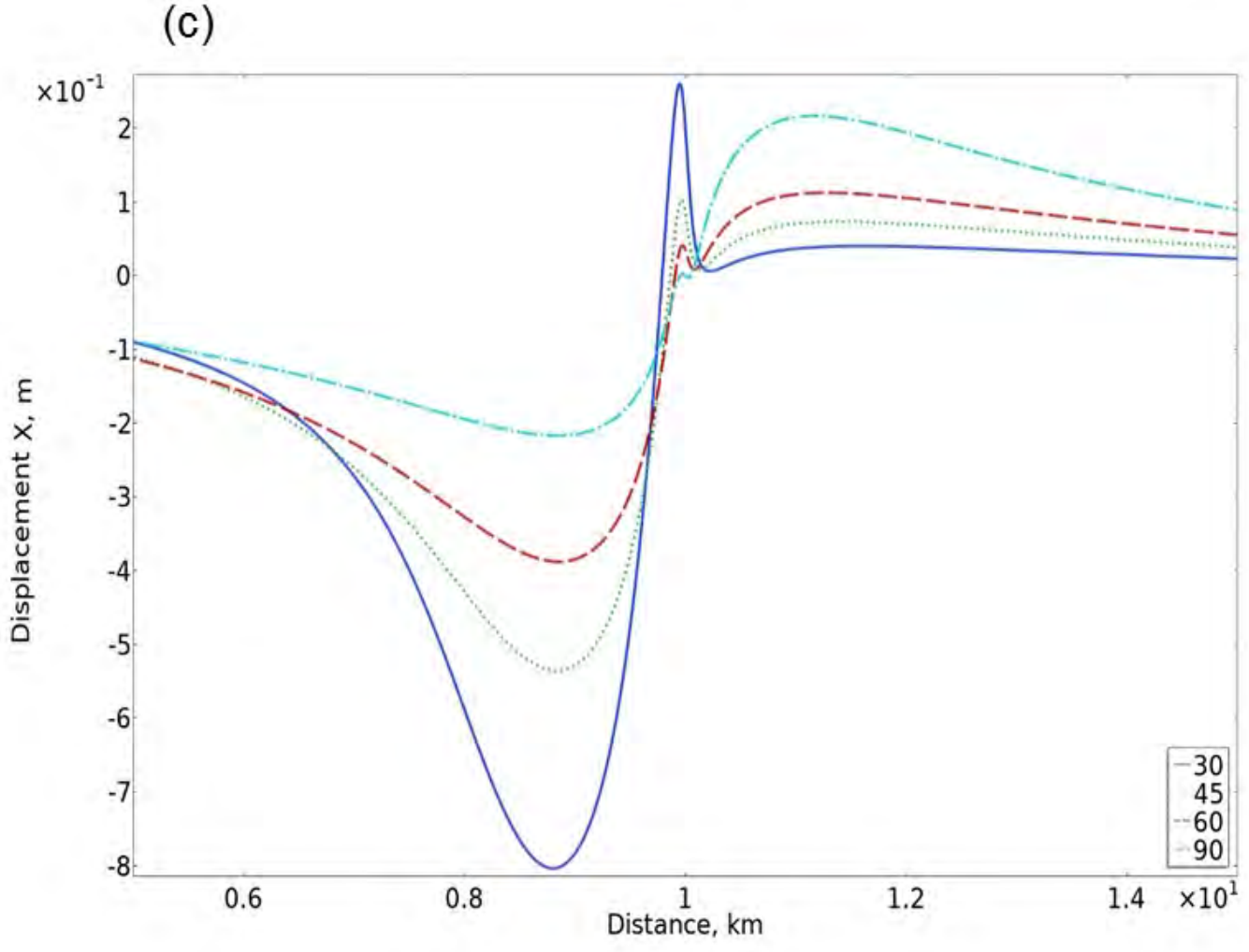
(c)
×10^-1
2
1
0
-1
-2
-3
-4
-5
-6
-7
-8
Displacement X, m
0.6
0.8
1
1.2
1.4
×10^1
Distance, km
30
45
60
90

(d)

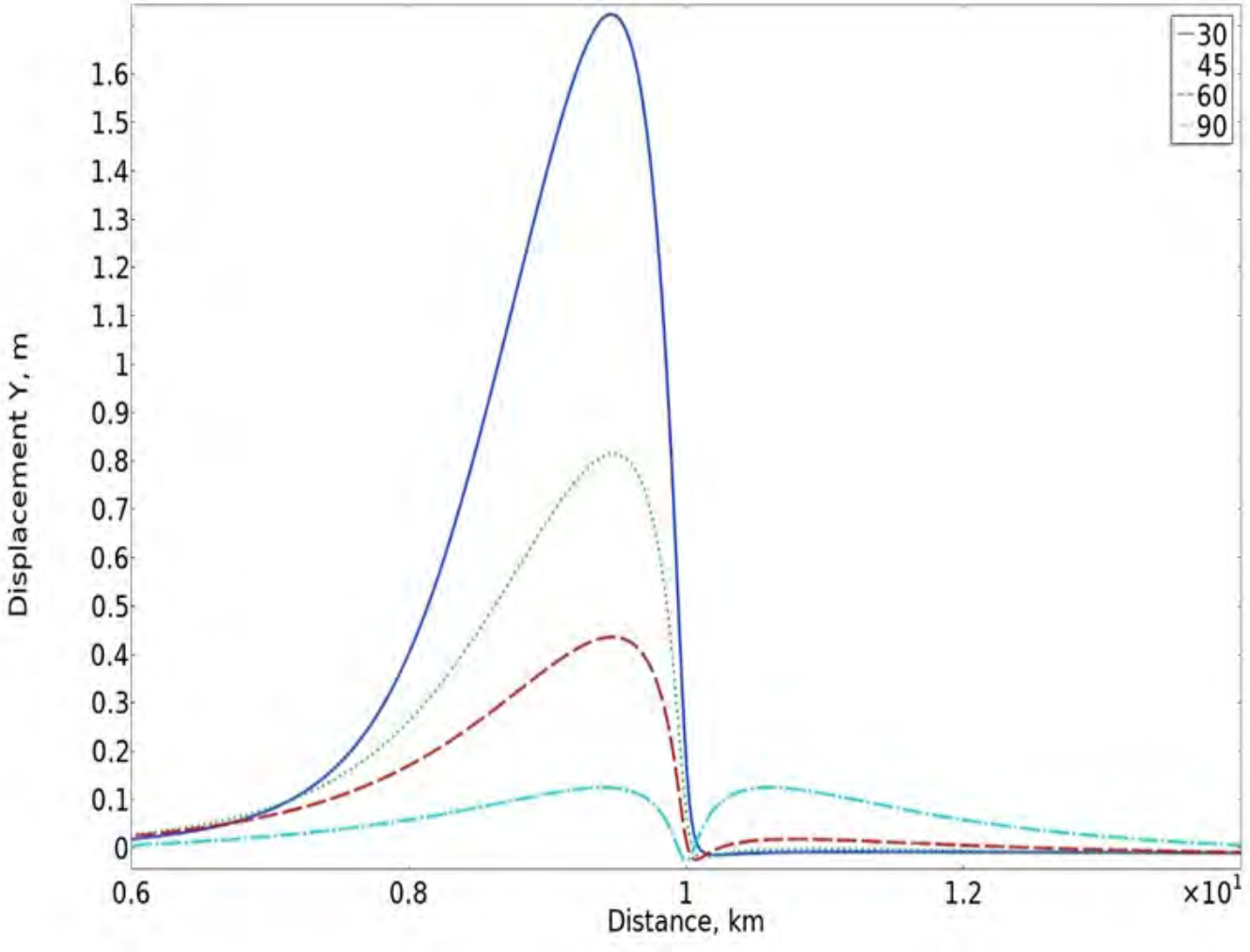
30
45
60
90
Displacement Y, m
1.6
1.5
1.4
1.3
1.2
1.1
1
0.9
0.8
0.7
0.6
0.5
0.4
0.3
0.2
0.1
0
0.6
0.8
1
1.2
×10^1
Distance, km

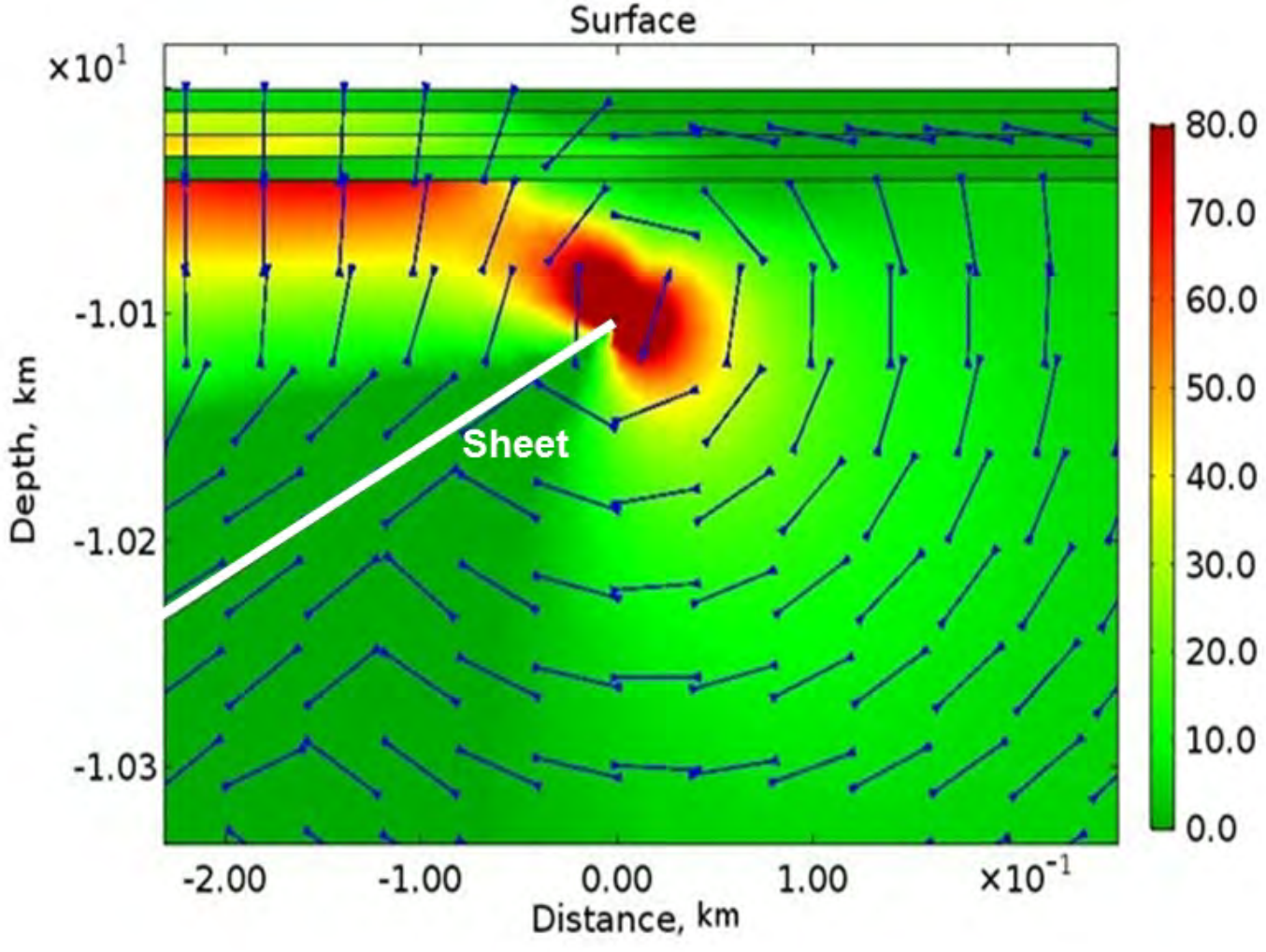
Surface
x10^1
-1.01
-1.02
-1.03
Depth, km
Sheet
-2.00
-1.00
0.00
1.00
x10^-1
Distance, km
80.0
70.0
60.0
50.0
40.0
30.0
20.0
10.0
0.0

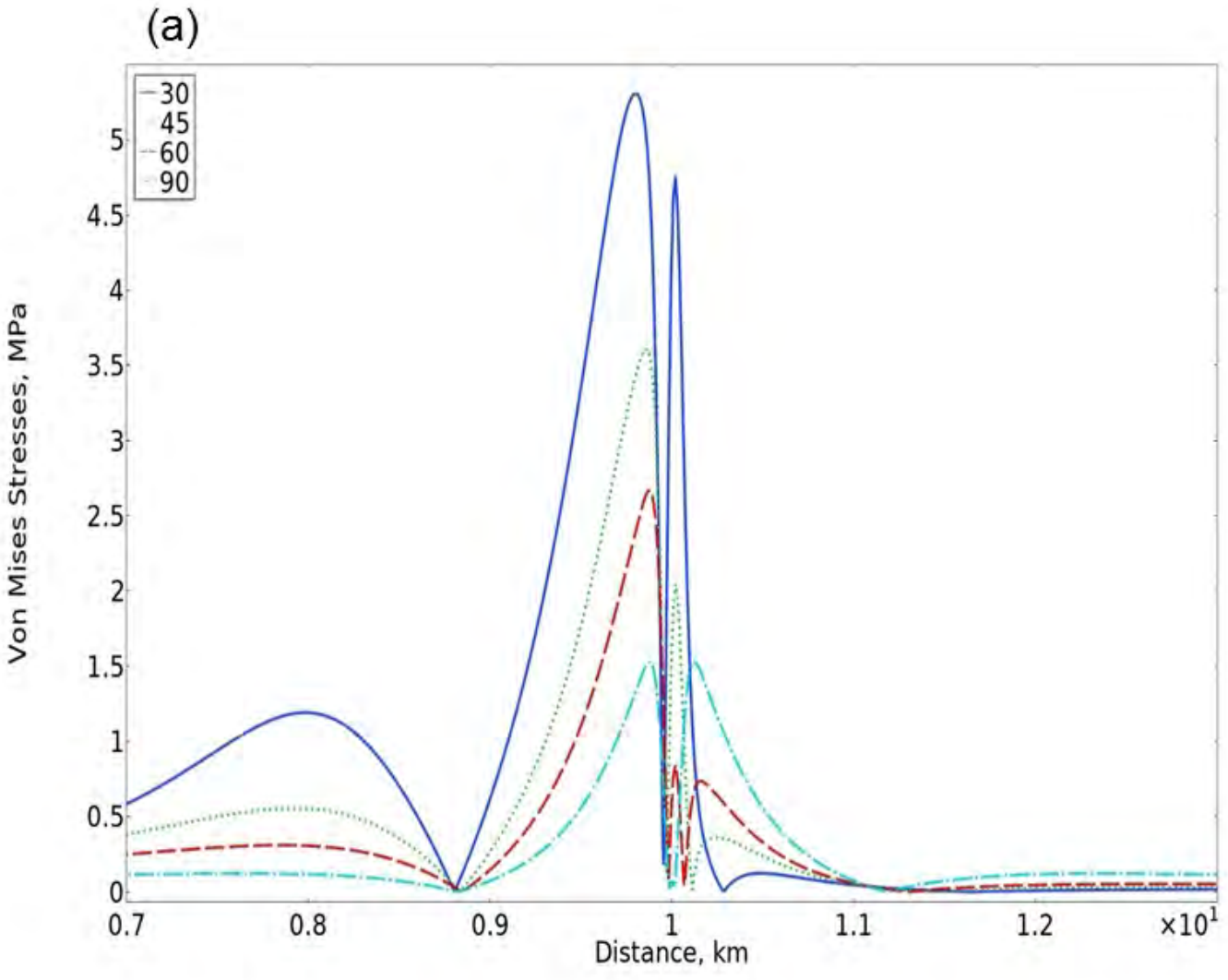
(a)
30
45
60
90
Von Mises Stresses, MPa
0
0.5
1
1.5
2
2.5
3
3.5
4
4.5
5
0.7
0.8
0.9
1
1.1
1.2
×10^1
Distance, km

(b)

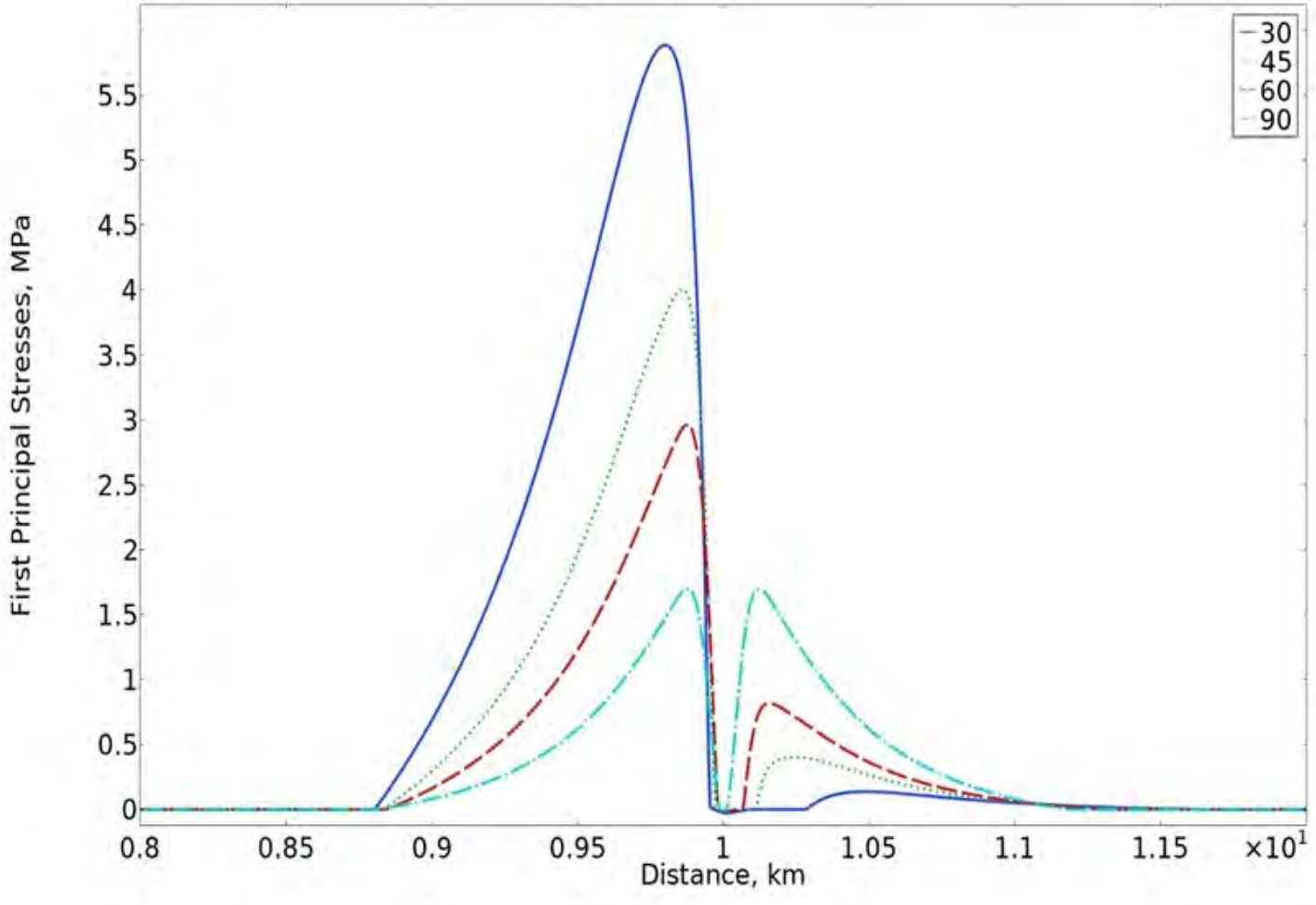
30
45
60
90
First Principal Stresses, MPa
5.5
5
4.5
4
3.5
3
2.5
2
1.5
1
0.5
0
0.8
0.85
0.9
0.95
1
1.05
1.1
1.15
×10^1
Distance, km

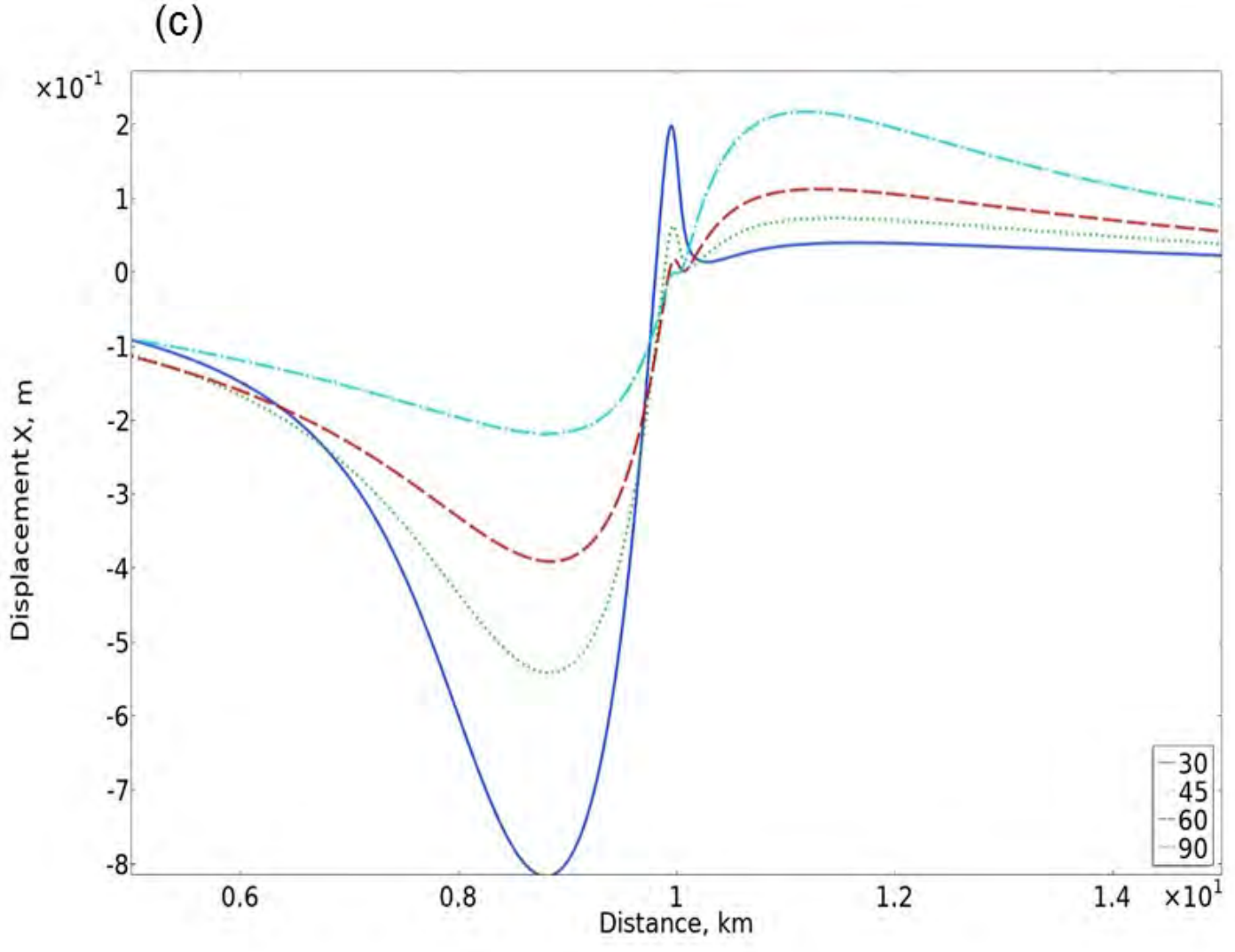
(c)
×10^-1
2
1
0
-1
-2
-3
-4
-5
-6
-7
-8
Displacement X, m
0.6
0.8
1
1.2
1.4
×10^1
Distance, km
30
45
60
90

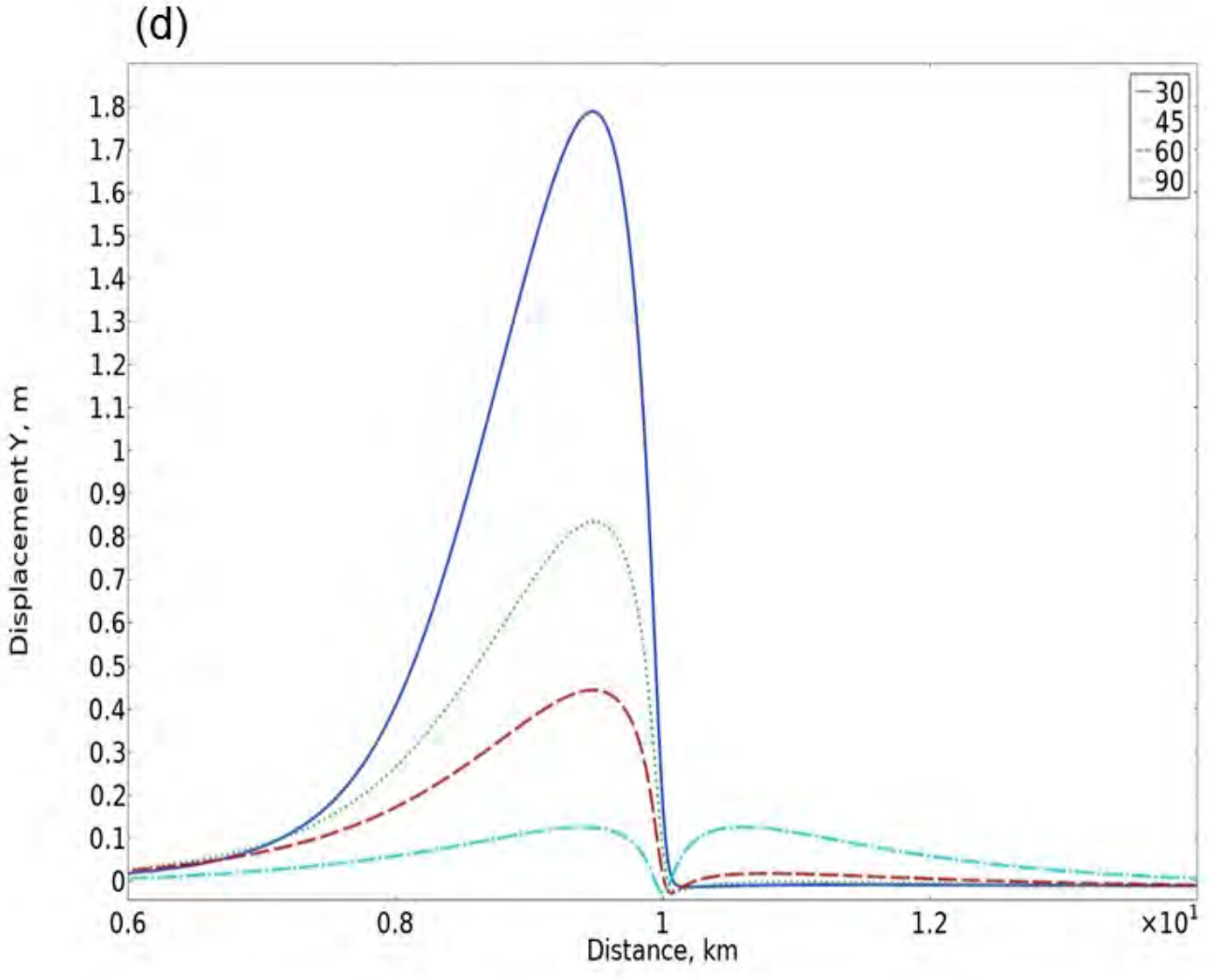
(d)
30
45
60
90
1.8
1.7
1.6
1.5
1.4
1.3
1.2
1.1
1
0.9
0.8
0.7
0.6
0.5
0.4
0.3
0.2
0.1
0
Displacement Y, m
0.6
0.8
1
1.2
×10^1
Distance, km

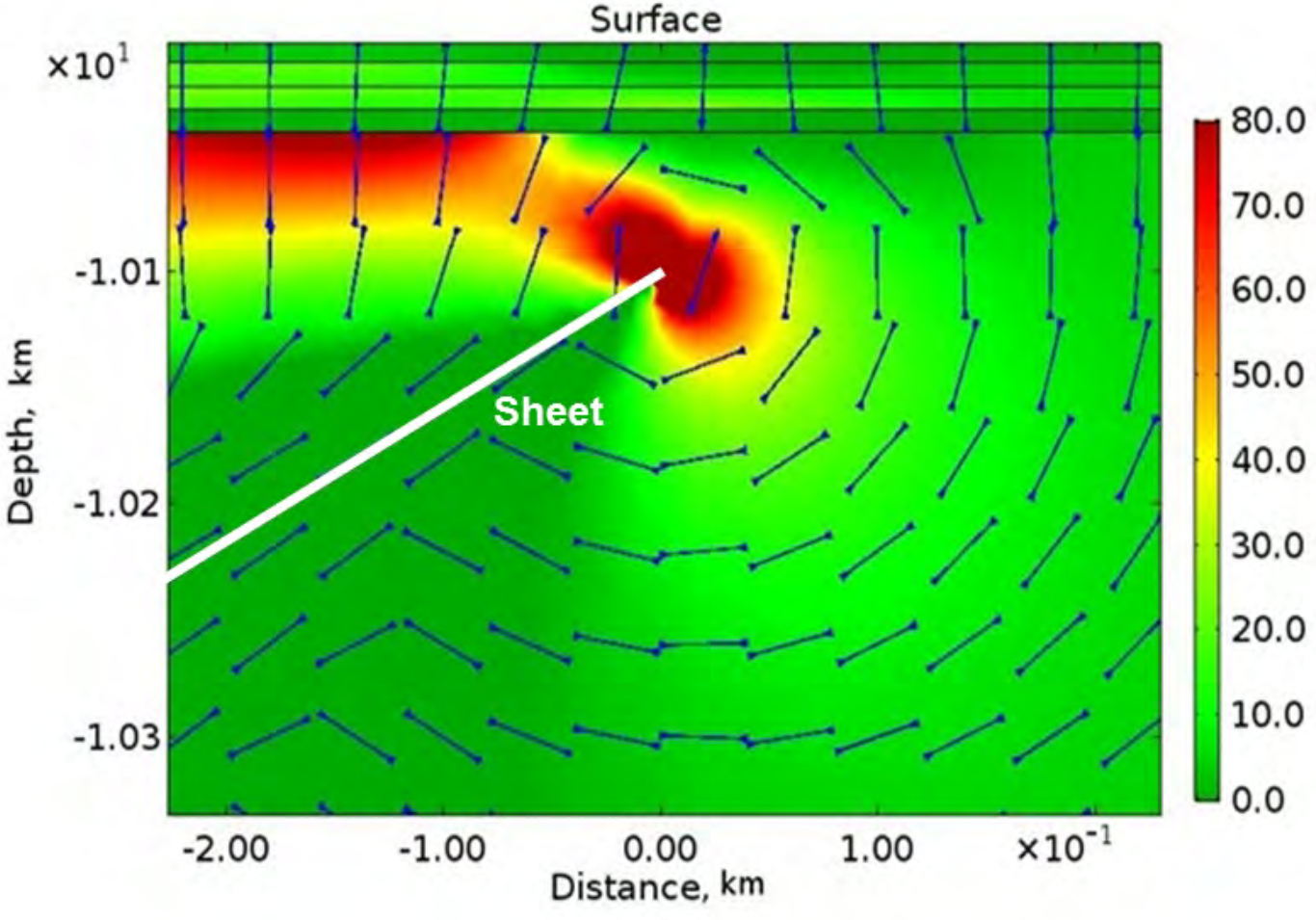
Surface
×10^1
-1.01
-1.02
-1.03
Depth, km
Sheet
-2.00
-1.00
0.00
1.00
×10^-1
Distance, km
80.0
70.0
60.0
50.0
40.0
30.0
20.0
10.0
0.0

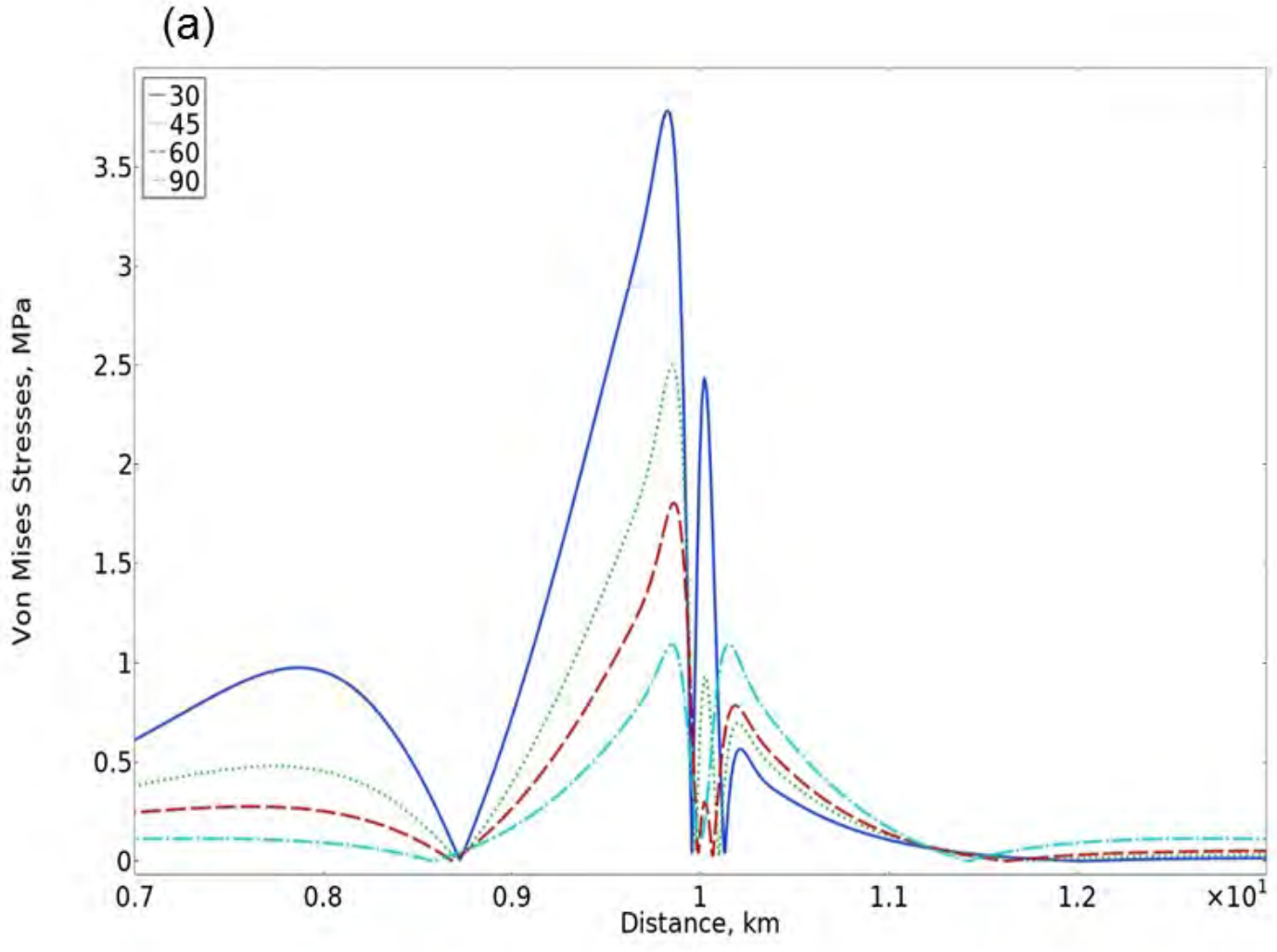
(a)
30
45
60
90
Von Mises Stresses, MPa
3.5
3
2.5
2
1.5
1
0.5
0
0.7
0.8
0.9
1
1.1
1.2
×10^1
Distance, km

(b)

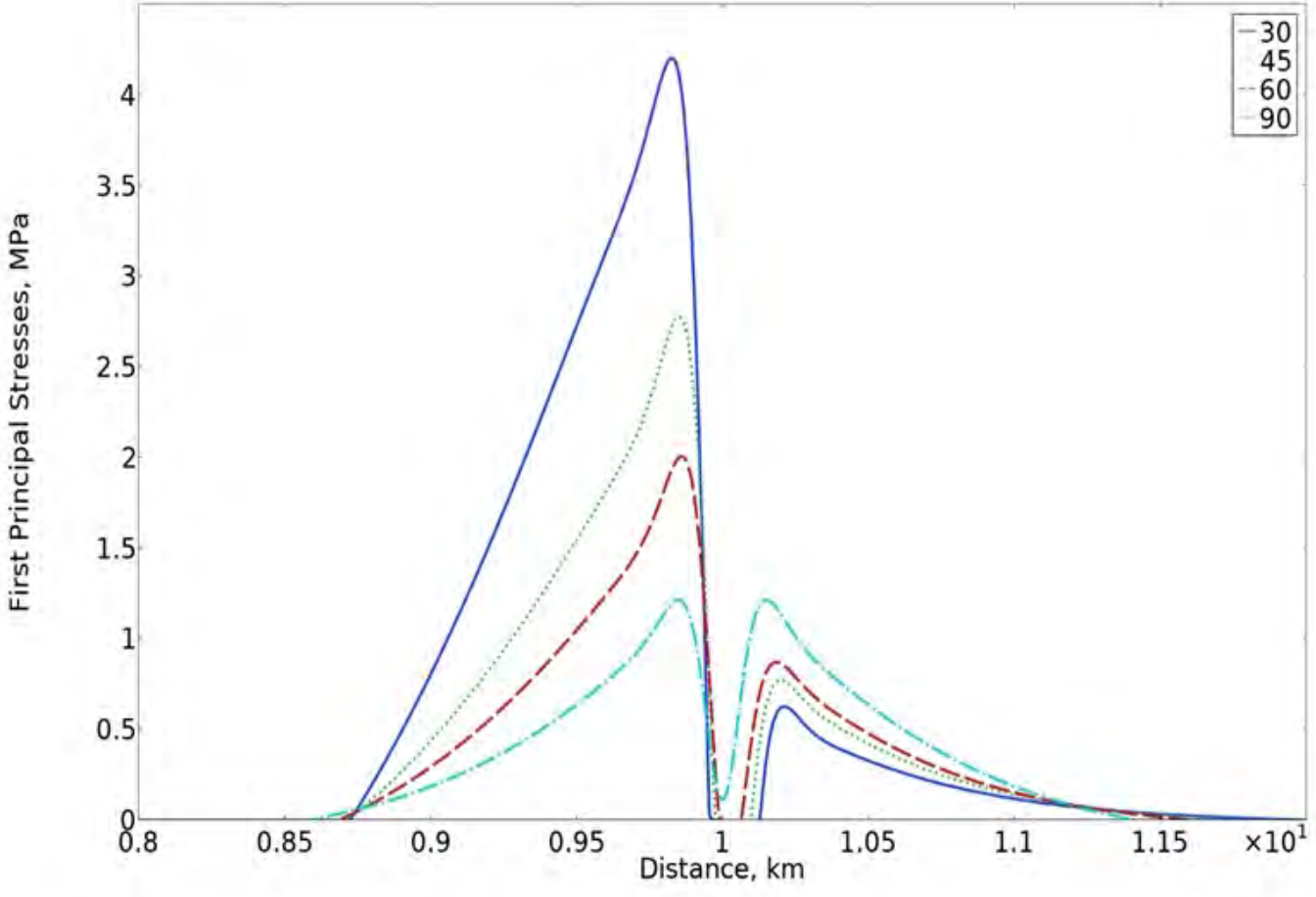
30
45
60
90
First Principal Stresses, MPa
0
0.5
1
1.5
2
2.5
3
3.5
4
0.8
0.85
0.9
0.95
1
1.05
1.1
1.15
×10^1
Distance, km

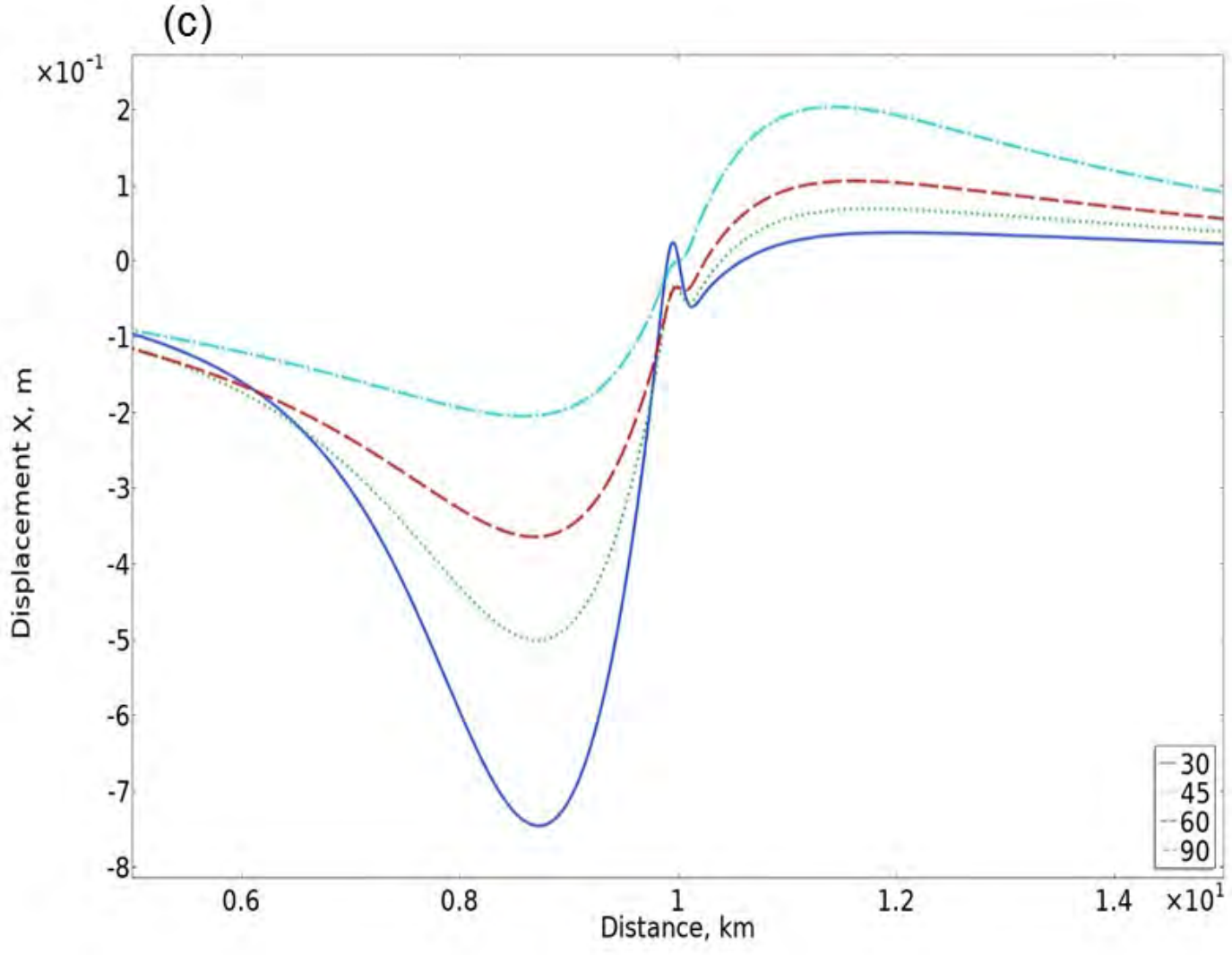
(c)
×10^-1
2
1
0
-1
-2
-3
-4
-5
-6
-7
-8
Displacement X, m
0.6
0.8
1
1.2
1.4
×10^1
Distance, km
30
45
60
90

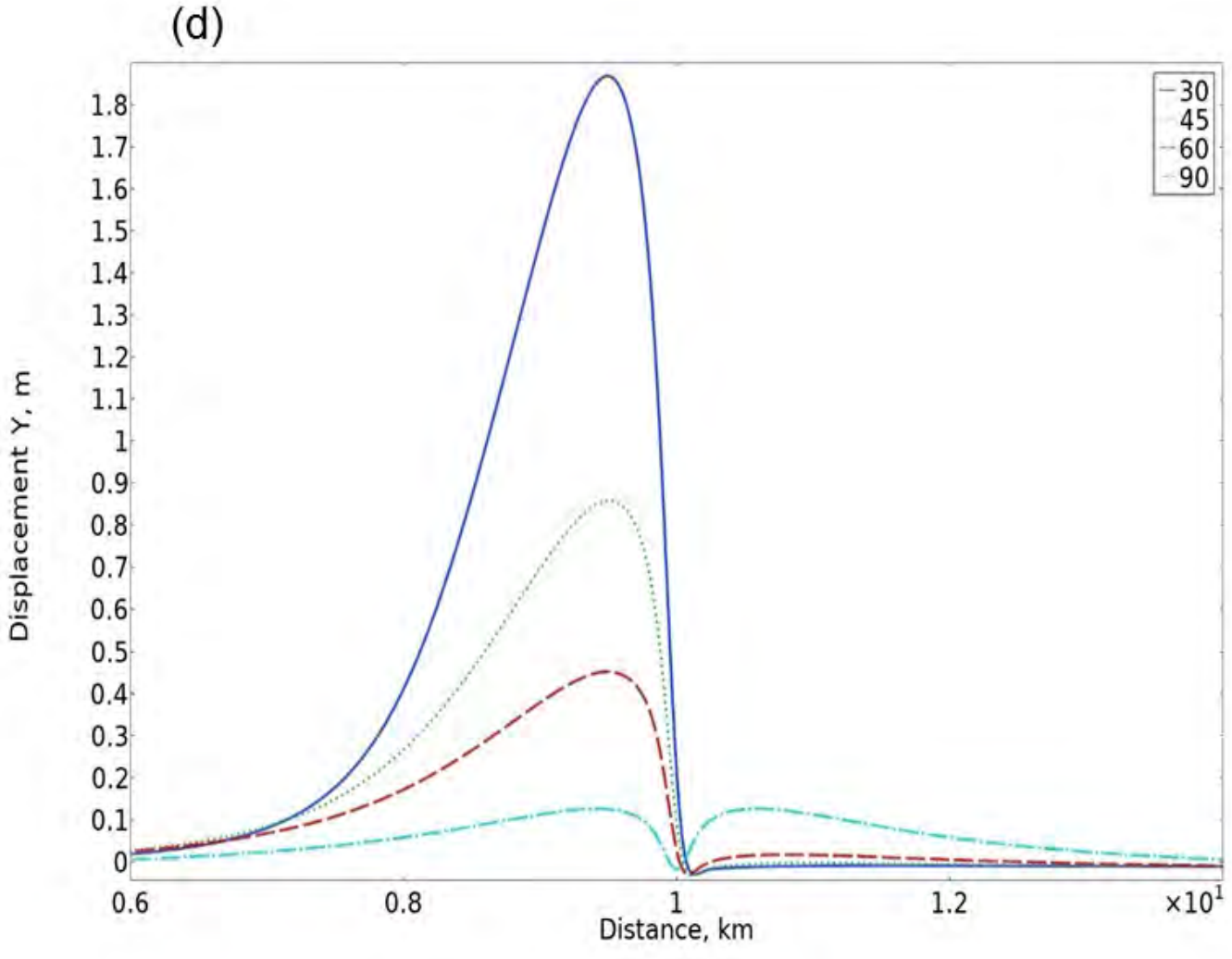
(d)
30
45
60
90
Displacement Y, m
1.8
1.7
1.6
1.5
1.4
1.3
1.2
1.1
1
0.9
0.8
0.7
0.6
0.5
0.4
0.3
0.2
0.1
0
0.6
0.8
1
1.2
×10^1
Distance, km

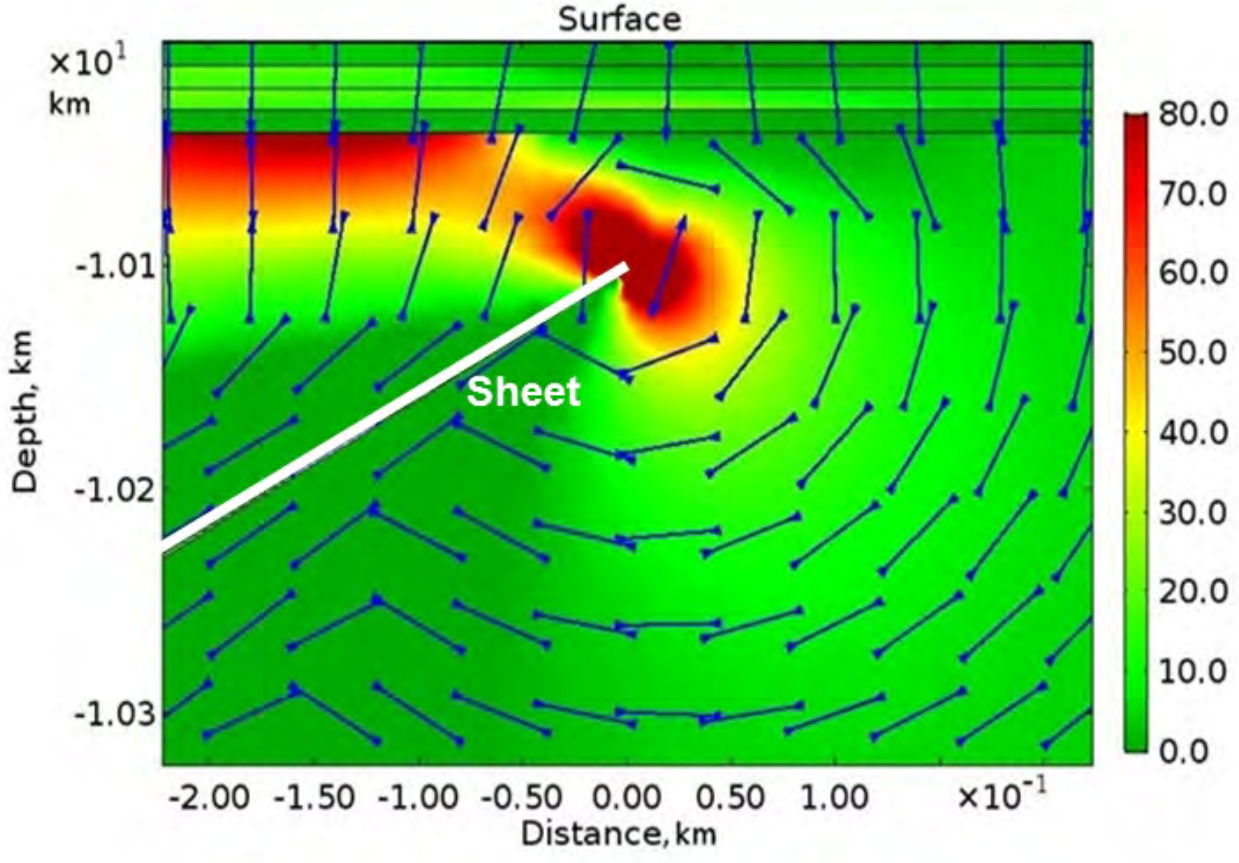
Surface
×10^1
km
-1.01
-1.02
-1.03
Depth, km
Sheet
-2.00 -1.50 -1.00 -0.50 0.00 0.50 1.00
×10^-1
Distance, km
80.0
70.0
60.0
50.0
40.0
30.0
20.0
10.0
0.0

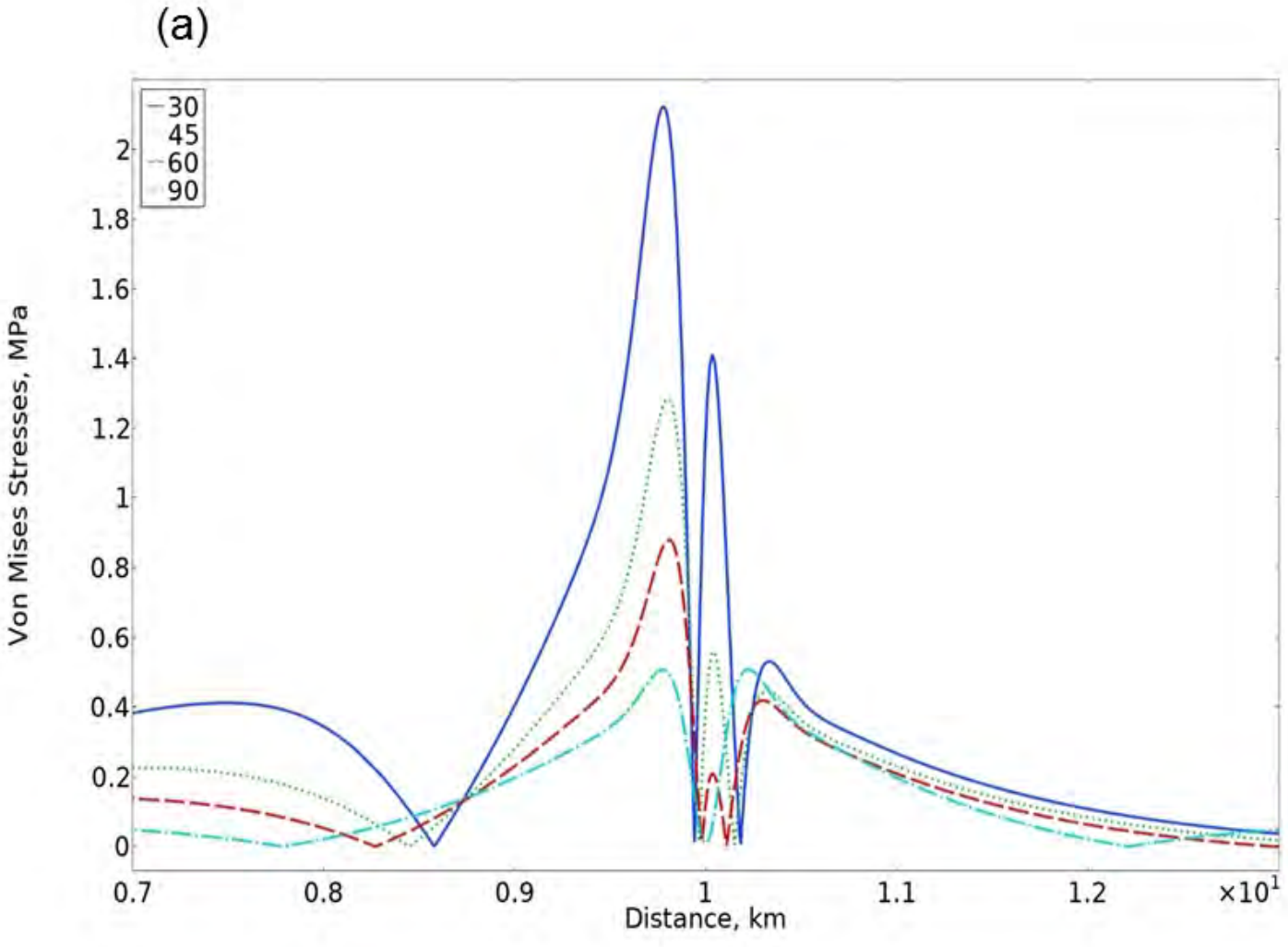
(a)
30
45
60
90
Von Mises Stresses, MPa
0
0.2
0.4
0.6
0.8
1
1.2
1.4
1.6
1.8
2
0.7
0.8
0.9
1
1.1
1.2
×10^1
Distance, km

(b)

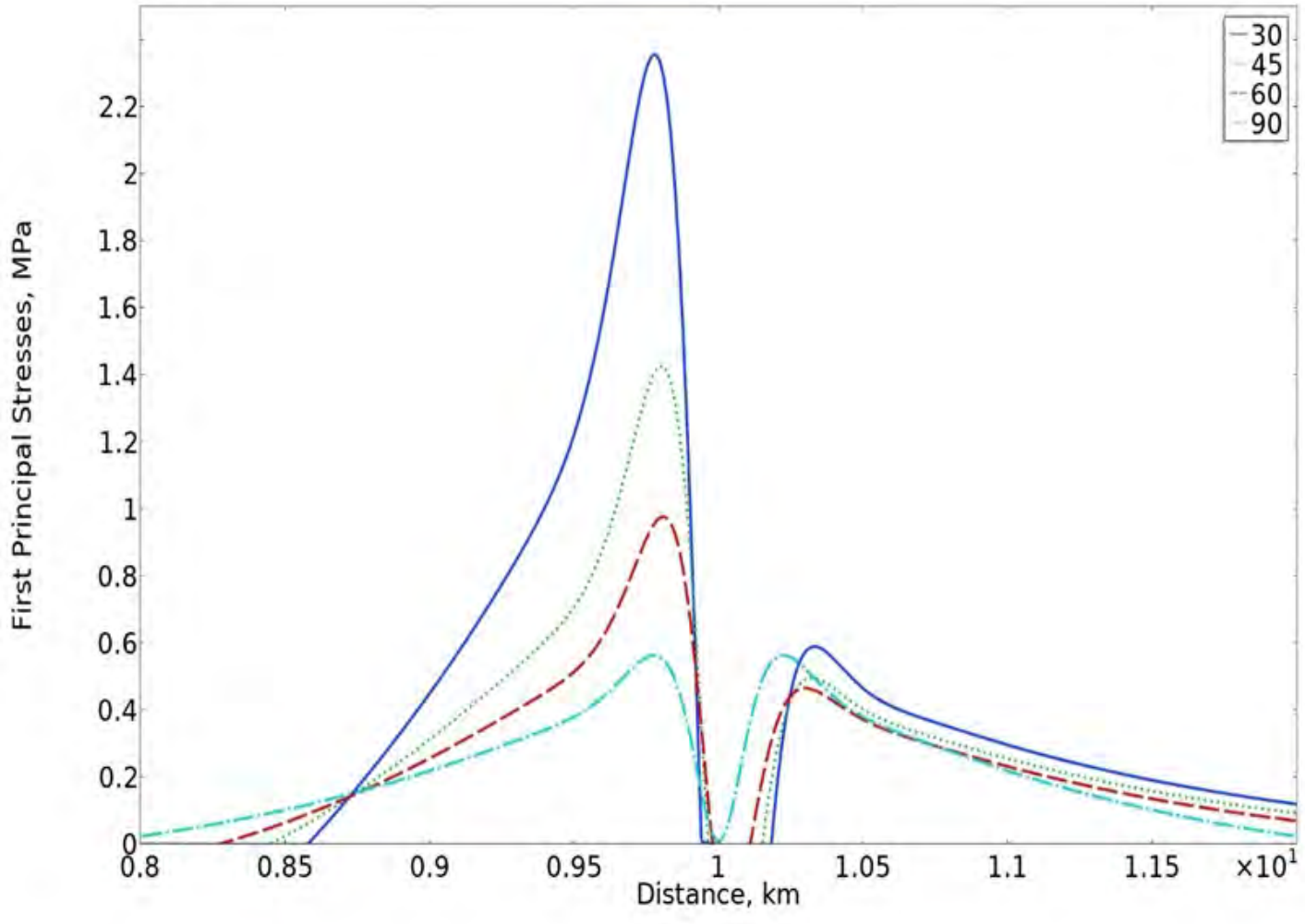
30
45
60
90
First Principal Stresses, MPa
2.2
2
1.8
1.6
1.4
1.2
1
0.8
0.6
0.4
0.2
0
0.8
0.85
0.9
0.95
1
1.05
1.1
1.15
×10^1
Distance, km

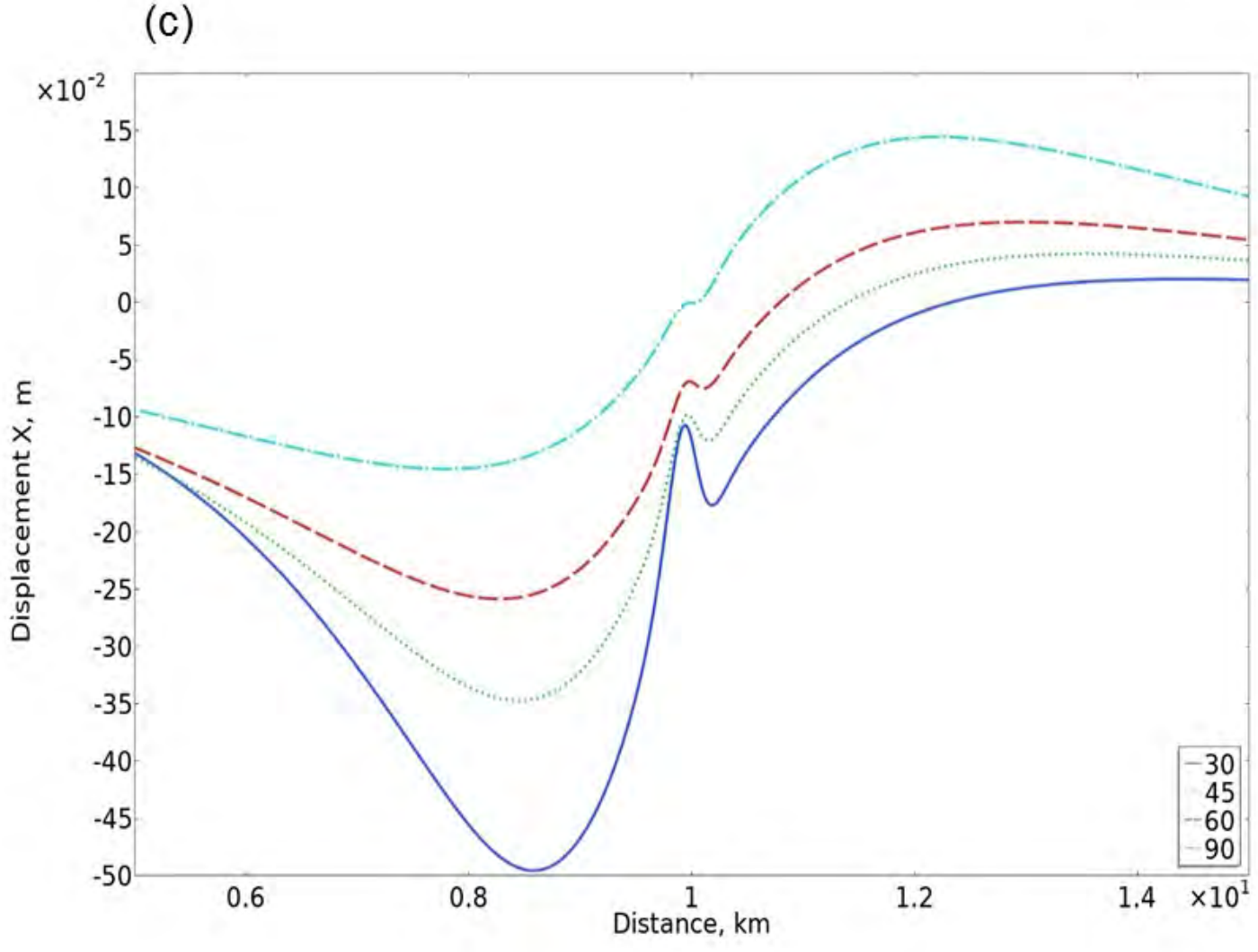
(c)
×10^-2
15
10
5
0
-5
-10
-15
-20
-25
-30
-35
-40
-45
-50
Displacement X, m
0.6
0.8
1
1.2
1.4
×10^1
Distance, km
30
45
60
90

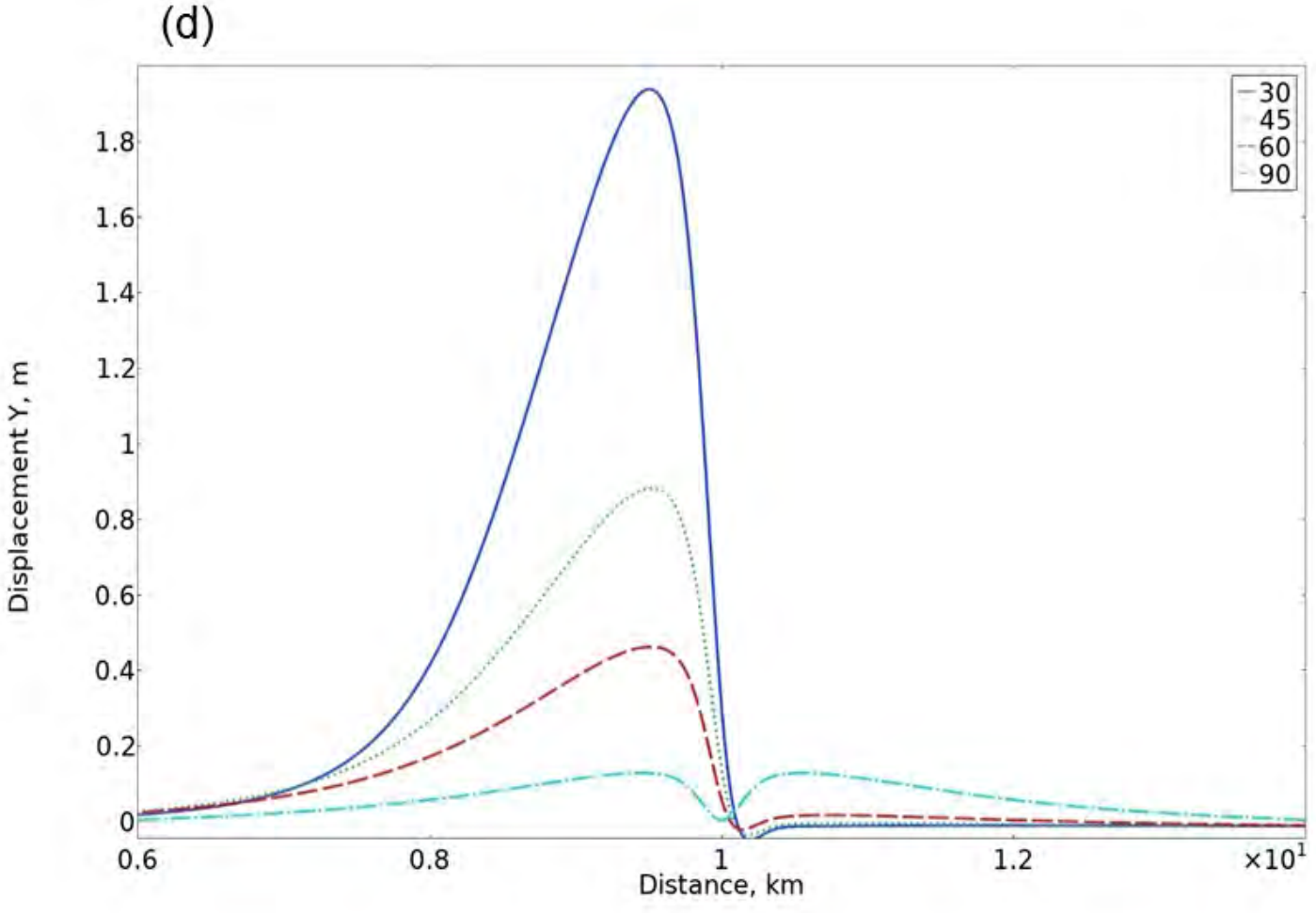
(d)
30
45
60
90
1.8
1.6
1.4
1.2
1
0.8
0.6
0.4
0.2
0
Displacement Y, m
0.6
0.8
1
1.2
×10^1
Distance, km

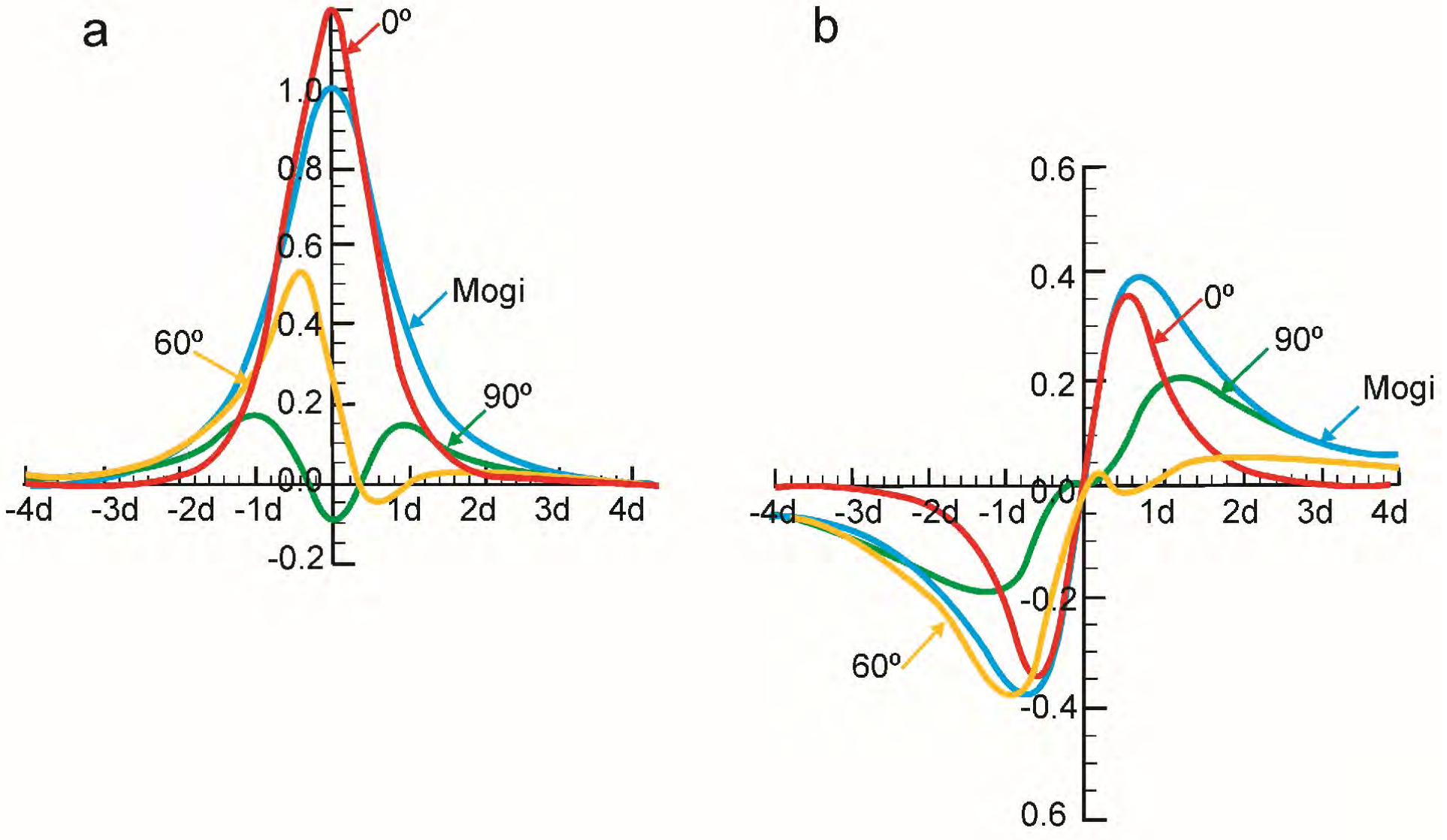
a
0º
1.0
0.8
0.6
Mogi
60º
0.4
90º
0.2
0.0
-4d
-3d
-2d
-1d
1d
2d
3d
4d
-0.2
b
0.6
0.4
0º
90º
0.2
Mogi
0.0
-4d
-3d
-2d
-1d
1d
2d
3d
4d
-0.2
60º
-0.4
0.6

Earth and Planetary Science Letters 452 (2016) 157–170

Contents lists available at ScienceDirect

Earth and Planetary Science Letters

www.elsevier.com/locate/epsl

Numerical modelling of triple-junction tectonics at Karlıova, Eastern Turkey, with implications for regional magma transport

Özgür Karaoğlu [a,b,*], John Browning [b,c], Mohsen Bazargan [b,c], Agust Gudmundsson [b]

[a] Eskişehir Osmangazi University, Department of Geological Engineering, 26040 Eskişehir, Turkey
[b] Department of Earth Sciences, Royal Holloway University of London, Egham, TW20 0EX, UK
[c] Department of Earth Sciences, University College London, Gower Street, London WC1E 6BT, UK

ARTICLE INFO

Article history:
Received 28 January 2016
Received in revised form 19 July 2016
Accepted 20 July 2016
Available online 16 August 2016
Editor: T.A. Mather

Keywords:
triple-junction tectonics
numerical modelling
dyke propagation
Eastern Turkey

ABSTRACT

Few places on Earth are as tectonically active as the Karlıova region of eastern Turkey. In this region, complex interactions between the Arabian, Eurasian and Anatolian plates occur at the Karlıova Triple Junction (KTJ). The relationship between tectonics and magma propagation in triple-junction tectonic settings is poorly understood. Here we present new field and numerical results on the mechanism of magma propagation at the KTJ. We explore the effects of crustal heterogeneity and anisotropy, in particular the geometry and mechanical properties of many faults and layers, on magma propagation paths under a variety of tectonic loadings. We propose that two major volcanic centres in the area, the Turnadağ volcano and the Varto caldera, are both fed by comparatively shallow magma chambers at depths of about 8 km, which, in turn, are fed by a single, much larger and deeper reservoir at about 15–18 km depth. By contrast, the nearby Özenç volcanic area is fed directly by the deeper reservoir. We present a series of two-dimensional and three-dimensional numerical models showing that the present tectonic stresses encourage magma-chamber rupture and dyke injection. The results show that inversion tectonics encourages the formation of magma paths as potential feeder dykes. Our three-dimensional models allow us to explore the local stresses induced by complex loading conditions at the Karlıova triple junction, using an approach that can in future be applied to other similar tectonic regions. The numerical results indicate a great complexity in the potential magma (dyke) paths, resulting from local stresses generated by interaction between mechanical layers, major faults, and magma chambers. In particular, the results suggest three main controls on magma path formation and eventual eruptions at KTJ: (1) the geometry and attitude of the associated faults; (2) the heterogeneity and anisotropy of the crust; and (3) mechanical (stress) interactions between deep and shallow magma chambers.

1. Introduction

One fundamental problem concerning convergent plate boundary tectonics is the nature of the interplay between deformation processes and magma transport (e.g. Hutton, 1988; Vigneresse, 1999). Networks of fractures (primarily extension fractures but also faults) and contacts play a crucial role in creating efficient paths through which magma is transported, stored and eventually erupted at the surface (e.g. Clemens and Mawer, 1992; Cembrana and Lara, 2009). Extrusion-block tectonic regimes may be characterised by triple-junction tectonics with significant components of mostly active strike-slip faulting. These regimes provide a good opportunity to understanding of the interplay between crustal stresses and magma propagation in strike-slip regimes.

A triple junction, defined as a boundary where three lithospheric plates meet, marks an important type of setting for extrusion tectonics, initiation of volcanism, and seismicity at active plate margins (cf. Jarosinski, 2012). Triple-junctions are the sites of abundant seismicity, high heat flow, and volcanism (e.g. Furlong and Schwartz, 2004). Although 16 types of possible triple junctions have been identified (McKenzie and Parker, 1967), the spatial and temporal relationships between magmatism and the extrusion tectonics of triple junctions remain poorly constrained. A Karlıova-type triple junction, the focus of this study, is a continental triple junction (Şengör et al., 2004) consisting of a non-subductable continental crust. Convergence is predominantly accommodated by strike-slip faults resulting in extrusion tectonics

* Corresponding author at: Eskişehir Osmangazi University, Department of Geological Engineering, 26040 Eskişehir, Turkey.
E-mail addresses: ozgur.karaoglu@rhul.ac.uk, ozgur.karaoglu@deu.edu.tr (Ö. Karaoğlu).

http://dx.doi.org/10.1016/j.epsl.2016.07.037
0012-821X/

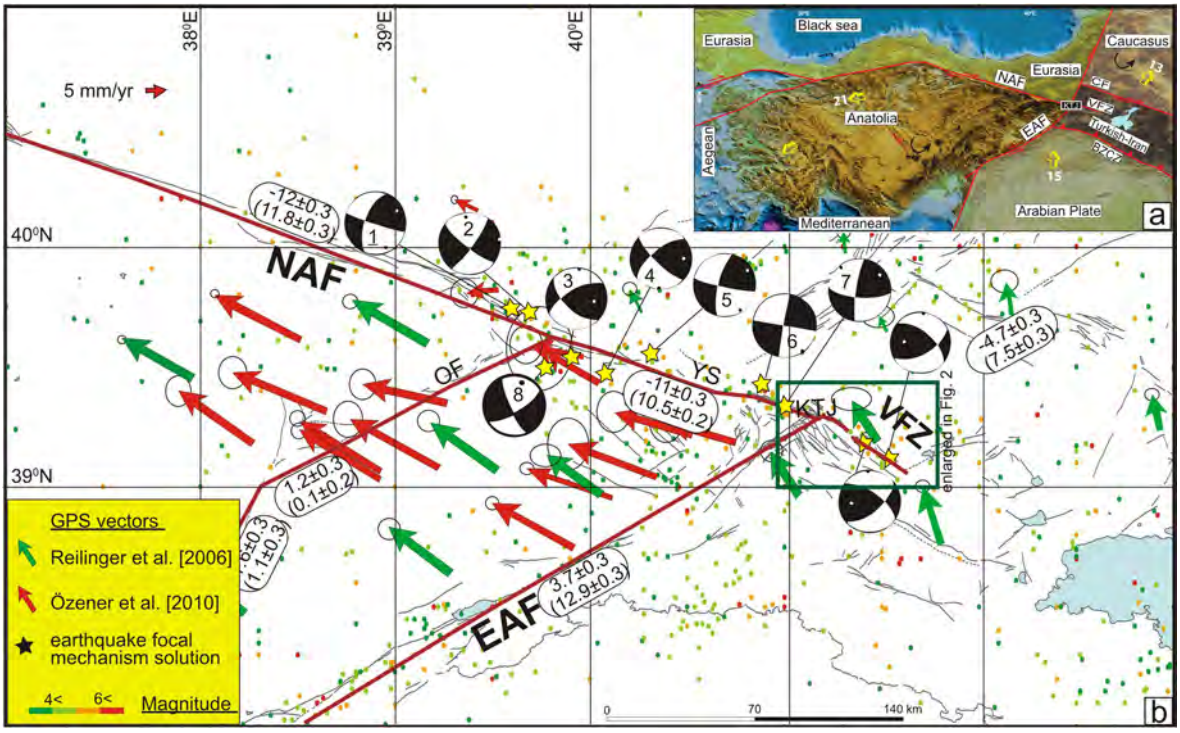

Fig. 1. a) Regional map showing crustal deformation in the eastern Mediterranean and Anatolia (Armijo et al., 1999). NAF: North Anatolian Fault, EAF: East Anatolian Fault, BZCZ: Bitlis–Zagros Collision Zone, CF: Çaldıran Fault, VFZ: Varto Fault Zone, YS: Yedisu Fault, KTJ: Karlıova Triple Junction; b) map showing GPS velocities with respect to Eurasia for 95% confidence ellipses (green vectors are Reilinger et al., 2006; red vectors are Ozener et al., 2010; and the focal mechanism solutions from Tan et al., 2008 for the study area). Numbers represent strike-slip component of the fault in mm/yr, numbers within parentheses represent normal component of the fault, red lines are block boundaries (Aktug et al., 2013). Seismic data are from KOERİ (http://udim.koeri.boun.edu.tr/zeqdb/). (For interpretation of the references to colour in this figure legend, the reader is referred to the web version of this article.)

(Şengör et al., 2004). The new data and numerical model results presented here offer excellent opportunities to clarify and constrain better the relationships between volcanism and tectonic activity at continental triple junctions.

Migration of an extruded block promotes crustal thinning of thickened accretionary complex crust composed of a variety of materials (e.g. Furlong and Schwartz, 2004). Suitably stressed crustal rocks of the extruded block on the Karlıova-type triple junctions are potential regions for magma ascent. Magma in the mantle and partly in the lower crust ascends by porous flow. At shallower crustal levels, magma ascends primarily through magma-driven fractures, mostly dykes. Dyke initiation and propagation is known to be partly controlled by regional stress fields (Tibaldi, 2015), particularly those induced by crustal extension (e.g. Gudmundsson, 1990; Hurwitz et al., 2009; Daniels et al., 2012; Le Corvec et al., 2013; Maccaferri et al., 2014).

Magma chambers are the main sources for major polygenetic volcanoes and, partly, for associated volcanic systems, that is, swarms or fields of volcanic (and in rift zones, also tectonic) fissures and basaltic lava flows. The depths of shallow or upper-crustal magma chambers are commonly between 1 km and 6 km, particularly at divergent plate boundaries (Gudmundsson, 2012). However, some chambers reach depths of 7–9 km, depending on the tectonic regime and crustal structure, and may also be regarded as comparatively shallow (Chaussard and Amelung, 2014). Chambers at greater depths are normally classified as deep-seated reservoirs, and these may reach depths of 20–30 km or more (Gudmundsson, 2012; Chaussard and Amelung, 2014; Le Corvec et al., 2015).

As is detailed below, we propose the existence of two comparatively shallow magma chambers at around 8 km depth and a deep-seated reservoir at around 15 km depth in the KTJ region (Figs. 1, 2). We relate these magma sources to likely magma paths, i.e. dykes. For an eruption to occur, the magma chamber must rupture (Browning et al., 2015) and propagate a dyke or an inclined sheet to the surface (Gudmundsson, 2012; Chestler and Grosfils, 2013; Le Corvec et al., 2013; Caricchi et al., 2014). The conditions for magma-chamber rupture and dyke injection have been analysed by many (e.g. Gudmundsson, 1990, 2006; Grosfils, 2007; Hurwitz et al., 2009; Gerbault, 2012; Le Corvec et al., 2015). Many of the basic ideas are reviewed and analysed by Gudmundsson (2012), with particular reference to direct observations of fossil magma chambers and the results of hydraulic fracture stress measurements in drill-holes worldwide down to crustal depths of about 9 km.

Generally, the critical stress required for magma-chamber rupture can be reached in two ways (Gudmundsson, 1990, 2006; Folch and Marti, 1998; Browning et al., 2015): (1) by increasing the total pressure inside the chamber (for example, by adding magma to the chamber or through gas exsolution from its magma), and (2) by external extension, such as in rift zones, where divergent plate movements gradually reduce the minimum principal compressive stress σ_3. Tensile fractures do not normally extend to depths greater than 0.5–1 km. If they try to propagate to greater depths they will change into closed normal faults, in accordance with Griffith criterion (Gudmundsson, 2011). There are thus no open tension fractures or open normal faults at the depth of many kilometres ready to be filled with magma to form dyke fractures. By contrast, dyke fractures are initiated when the excess pressure in the chamber reaches the host-rock tensile strength under either loading condition. Then the magma chamber ruptures and a dyke (or an inclined sheet) is injected (Gudmundsson, 1990; Gaffney et al., 2007). The mechanical layering and local state of stress inside the volcano, together with rate of magma solidification and other factors, ultimately determine whether the dyke propagates to the surface and erupts or, alternatively, becomes

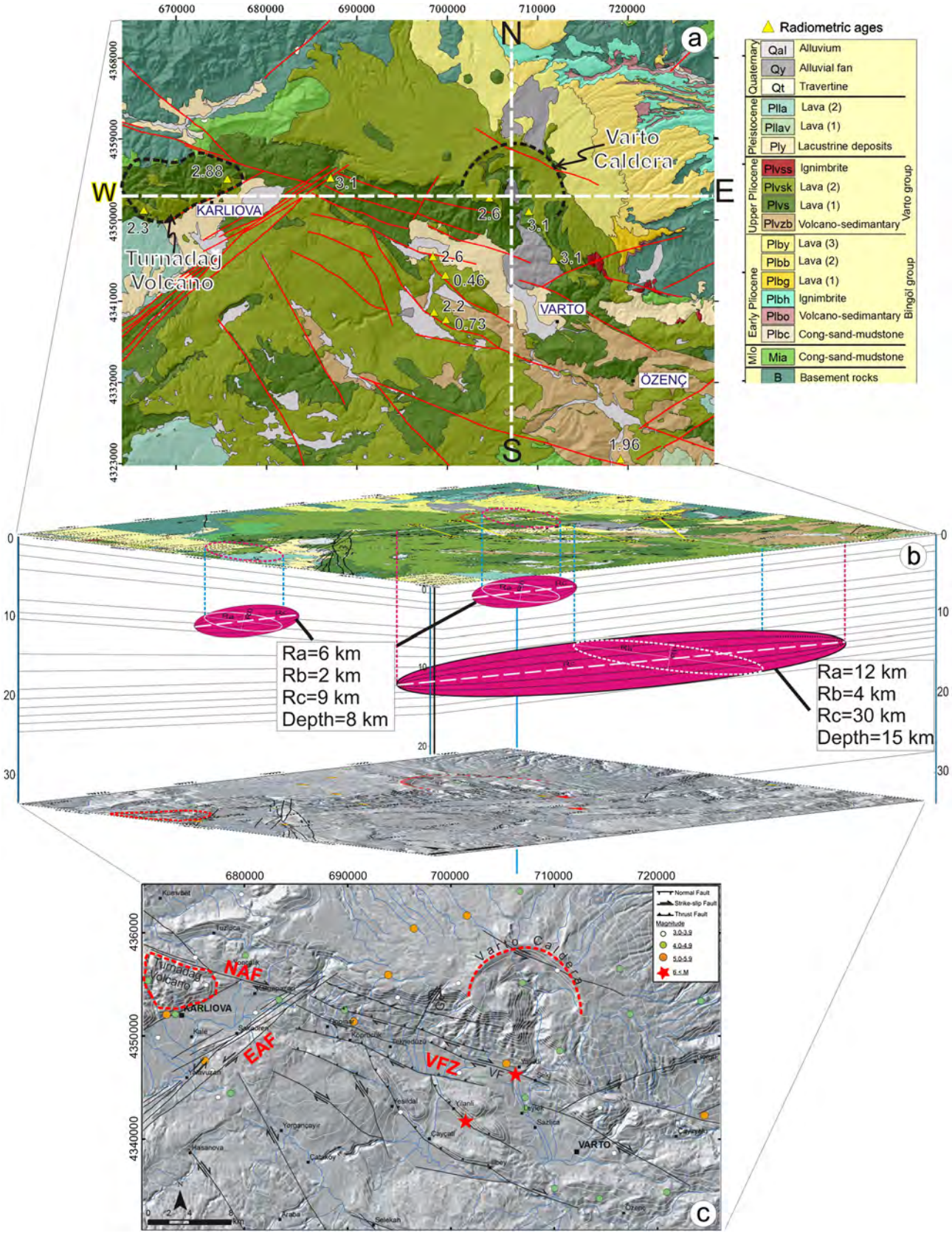

Fig. 2. a) Geological map showing the main faults and seismicity around the Karlıova and Varto regions. Radiometric ages are given in Ma. Active faults are modified from Herece (2008) and Sançar et al. (2015). b) Magma chambers on the block model using a geological cross-section through the region and the physical parameters of the stratigraphy (Ra, Rb and Rc); c) Shaded relief basis map showing the main faults and seismicity around the Karlıova and Varto regions. Active faults are modified from Herece (2008) and Sançar et al. (2015). Seismicity data from KOERİ. NAF: North Anatolian Fault, EAF: East Anatolian Fault, KTJ: Karlıova Triple Junction, VFZ: Varto Fault Zone, VF: Varto Fault; GF: Güzeldere Fault.

arrested at depth in the volcano (e.g. Spence et al., 1987; Gudmundsson, 1990, 2011; Acocella and Neri, 2009; Geshi and Neri, 2014).

Although the geometries of magma chambers vary, many and perhaps most crustal magma chambers are sill-like (Gudmundsson, 1990; Annen and Sparks, 2002; Kavanagh et al., 2006; Grosfils et al., 2015) as evidenced by seismic studies of volcanoes and rift zones (Sinton and Detrick, 1992) and field studies of fossil chambers, that is, plutons (Pasquarè and Tibaldi, 2007; Tibaldi et al., 2008; Gudmundsson, 2012). Numerical, analogue, and field studies indicate that piston-type calderas are often associated with a sill-like magma chambers (Geyer et al., 2006; Geyer and Marti, 2009; Gerbault, 2012; Gregg et al., 2012, 2015; Le Corvec et al., 2013; Gudmundsson, 2015). The size of an underlying shallow magma chamber is then thought to closely resemble the radius of associated collapse caldera, whereas the deeper reservoirs may be many times larger (Gudmundsson, 2012, 2015; Gerbault, 2012; Gregg et al., 2013; Grosfils, 2007; Grosfils et al., 2015; Browning and Gudmundsson, 2015). As indicated above, the depths of many magma chambers have been estimated using petrological, geochemical, and geophysical methods (Becerril et al., 2013; Chaussard and Amelung, 2014).

The emplacement of hot asthenospheric mantle to shallow levels beneath a Karlıova-type triple junction could be expected to generate melt and, likely, surface volcanism. Consistent with this expectation is the sequence of volcanic centres that have erupted in the wake of the triple junction within the Karlıova regime (e.g. Furlong and Schwartz, 2004; Gaffney et al., 2007).

This study focuses on the mechanism of magma propagation, primarily through dykes, in the Karlıova Triple Junction (KTJ) tectonic regime. We aim to demonstrate how fault geometry and mechanical properties may affect magma propagation under a variety of tectonic boundary loads. We discuss the geologic setting of the KTJ and the manifestations of shallow and deeper magma chambers within the crustal segment. Our numerical modelling aims to quantify the crustal response to various tectonic regimes in Eastern Turkey. The region is characterised by considerable lithological heterogeneity and anisotropy (cf. Jarosinski, 2012) which are taken into account in our numerical models. We present a series of two-dimensional and three-dimensional numerical models to help constrain evolving ideas regarding the tectonics of the KTJ. We also analyse a north–south striking profile that is subject to regional compression and local extensional tectonic phases which likely operated in the region ∼3 My. A general three-dimensional model is presented to show the local stress effects resulting from complex regional loading on crustal magma chambers.

2. Geologic and tectonic setting

Eastern Turkey is a part of the Mediterranean region which is characterised by the presence of major continental fragments and suture zones (Şengör et al., 2004). Propagation of the westward extrusion of the Anatolian block, just after the formation of the Northern Anatolian Fault Zone (NAFZ), started around 12 Ma from the pivot point of KTJ and triggered lithosphere-scale transtensional deformation (Barka, 1992; Şengör et al., 2004). The NAFZ, whose main fault is the active right-lateral North Anatolian Fault (NAF), is a nearly 2000 km long zone, extending from Karlıova in eastern Anatolia to the tip of the Corinth Rift in Greece (Armijo et al., 1999). The overall width of NAFZ increases from ∼10 km (Figs. 1, 2) in the east to ∼100 km in the west (Şengör et al., 2004).

Present-day earthquake focal-mechanism solutions indicate dextral transtensional movements (McKenzie, 1972; Ozener et al., 2010) on the Yedisu Fault at the western part of the KTJ (Fig. 1). GPS data show that the eastern part of the Anatolian plate (the western part of the KTJ) moves at a rate of ∼20 mm/yr with respect to the Eurasian plate (Fig. 1, McClusky et al., 2000; Reilinger et al., 2006). Solid-block modelling of the region and GPS velocity data (Fig. 1) show that eastern margin of the KTJ is undergoing crustal shortening, whereas in the west the prevailing tectonic stress and crustal deformation is transtensional (Barka, 1992; Aktug et al., 2013). The present geodetic average slip rate for Eastern Anatolian Fault Zone (EAFZ) is 5 mm/yr (Aktug et al., 2013). The EAFZ is around 30-km-wide at the eastern extremity near the KTJ. It is proposed that the fault zone has been active since the Pliocene (Tatar et al., 2004).

The NAFZ and EAFZ, which are two western branches of the KTJ, are characterised by transtensional tectonics (Şengör et al., 2004). The right-lateral Yedisu Fault (YS, Fig. 1), striking N105°E, represents the eastern branch of the NAFZ and extends for more than 30 km to the KTJ (Fig. 1). The VFZ (the Varto Fault Zone) extends for over 50 km, strikes N105°E–N120°E and can be subdivided into six fault segments (Sançar et al., 2015). The Varto Fault (VF, Fig. 2c) is seismically the most active segment of the VFZ; it is a N120°E-striking right-lateral strike-slip fault with a reverse component that offsets the southern part of the Varto caldera. Two destructive earthquakes (Mw = 6.8 and 6.2) occurred on the VFZ in 1966 (Fig. 2c, Ambraseys and Zatopek, 1968). Karaoğlu et al. (in press) suggest that the combined motions of NW-striking dextral, normal, oblique and thrust faults indicate a successive and reactive tectonic phase that caused incremental complex movement of numerous fault blocks during the deformation of the Karlıova and Varto region since 6 Ma.

Structural and stress data indicate a distinct kinematic behaviour of the KTJ during the past 12 Ma (Şengör et al., 2004). Following the formation of NAFZ and EAFZ, the western part of the triple junction has been subject to transtensional tectonics during which the east end of the KTJ has undergone incremental deformation accommodated by numerous faults during (i) ongoing shortening phases driven by the regional-scale thrust tectonic regime and (ii) transtensional phase caused by westward extrusion tectonics at a local-scale (Karaoğlu et al., in press). It has been suggested that a right-lateral motion developed under a NE–SW-trending extension associated with NW–SE contraction. The fault surface planes of the WNW–ESE-striking VFZ were reactivated at 3 Ma, which suggests that inversion tectonics occurred when transtensional faults reversed their movement during a subsequent compressional tectonic episode (e.g. Williams et al., 1989). Since 3 Ma, thrusting shifted further south, coupled with a component of dextral strike-slip motion (Karaoğlu et al., in press).

Volcanic activity commenced on the EAF with some eruptions producing acidic rocks whose ages are between 4.4 and 6.06 Ma (Poidevin, 1998). The earliest volcanism occurred at around 6 Ma and highlights the initiation of crustal deformation in the EAF. As for the deformation of Varto and Turnadağ volcanoes, the age of the basement volcanic rocks in the southern part of Varto is around 3 Ma (Fig. 2a). The lifespan of the Varto caldera volcanism is estimated at between 3 and 1 Ma (Hubert-Ferrari et al., 2009). This may be regarded as the second major volcanic episode in the area. The third event or activity in the area relates to some small-scale volcanism on the southern sector of the VFZ. The resulting domes are dated at approximately 0.73 Ma to 0.46 Ma (Fig. 2a). The most recent dyke-fed eruptive and effusive-type volcanism (1.96–2.67 Ma, based on K/Ar ages from Biggazi et al. 1997, 1998) occurred around the Özenç area, at the southern part of the Varto caldera (Fig. 2). The volcanism produced partly mafic lavas, mostly of the alkaline and, rarely, sub-alkaline series, including basaltic trachy-andesite and basaltic andesite (Buket and Temel, 1998; Hubert-Ferrari et al., 2009). The Varto caldera, the Turnadağ volcano, and the Özenç volcanic area (Fig. 2) show distinct volcanic facies, and also certain geochemical characteristics (e.g. Buket and Temel, 1998; Hubert-Ferrari et al., 2009; Sançar et al., 2015).

3. Magma-chamber geometry

In order to estimate the rough geometry and depth of the magma chamber feeding a polygenetic volcano, field and analytical data are required. There have not, however, been any petrological or geodetic studies on the geometry of the magma feeding systems in Eastern Turkey. Recent compilations, based on various methods, suggest that most magma-chamber or reservoir depths worldwide range from about 1 km to about 20 km below the volcanoes to which they supply magma (Middlemost, 1997; Gudmundsson, 2012; Chaussard and Amelung, 2014; Tibaldi, 2015). The exact depths of the magma chambers for the volcanoes Turnadağ and Varto (Fig. 2b), as well as for the Özenç volcanic area, are not known. The chemistry of the eruptive materials suggest that the source chamber for the Özenç volcanism is deeper and larger than the chambers beneath Turnadağ and Varto. All these areas, however, contain dykes whose aspect (length/thickness) ratios can be used to estimate the depths of the source chambers.

We use a method based on the principles of fracture mechanics and fluid-dynamics to constrain the depth of the magma chambers/reservoirs at Karlıova (e.g. Becerril et al., 2013). All dykes in the area are dominantly trachy-basaltic in composition. Magma overpressure (p_o) within a dyke during its formation can be estimated from the ratio of dyke strike dimension (L) and thickness (Δu_I). A total of 14 dyke measurements in the study area were used to estimate the depth of their source chamber/reservoir. The method is as follows. The opening displacement of an elastic mode I (tensile mode) crack, such as a dyke, subject to internal fluid or magma overpressure (driving pressure) p_o is given by:

$$\Delta u_I = \frac{2p_o(1-\nu^2)L}{E} \tag{1}$$

where L is the smaller of the strike and dip dimensions of the fracture, and E and ν are Young's modulus and Poisson's ratio, respectively, of the host rock. While Δu_I denotes the opening or aperture of the dyke at its time of emplacement it also corresponds roughly to the thickness of a solidified dyke as measured in the field (the error due to contraction as the magma as the dyke solidifies is about 10% – Becerril et al., 2013). Here we use 40 GPa as an average Young's modulus for the host rock and 0.25 for the Poisson's ratio. The overpressure in a dyke at the crustal level of exposure (at the surface for a feeder) is given by:

$$p_o = p_e + (\rho_r - \rho_m)gh + \sigma_d \tag{2}$$

where p_e is the fluid excess pressure in the source magma chamber, ρ_r is the average density of the host rock, ρ_m is the average density of the magma in the dyke, g is acceleration due to gravity, h is the dip-dimension or height of the dyke, and σ_d is the differential stress (the difference between the vertical stress and the minimum principal horizontal stress) at the depth in the crust where the dyke is measured or, for a feeder-dyke, the stress difference at the surface where the volcanic fissure forms. From equations (1) and (2) the depth to the intersection between the source magma chamber and the feeder dyke is:

$$h = \frac{\Delta u_I E}{2L(1-\nu^2)(\rho_r - \rho_m)g} - \frac{p_e + \sigma_d}{(\rho_r - \rho_m)} \tag{3}$$

Using Eq. (3), we calculated the depth to the source of the feeder-dykes exposed in the three volcanic regions under consideration (Fig. 1). We use the typical trachy-basaltic magma density (ρ_m) of 2730 kg m^{-3} (e.g. Middlemost, 1997). Since there are no detailed and accurate density data for the crust of the Eastern Anatolia Accretionary Complex, we have used a revised geological stratigraphy made of 18 lithologic units (Appendix 1), of the region (e.g. Tarhan, 1991). The crust is thought to be mostly composed of units of limestone, metamorphic rocks, massive gabbro and sandstone with estimated laboratory densities in the range from about 2000–3100 kg m^{-3} (e.g. Gudmundsson, 2011). We use an average density of 2650 kg m^{-3}. Note that excess magma pressure in the chamber/reservoir (p_e) is defined as pressure in excess of lithostatic stress or pressure and thus automatically takes into account the effects of gravitational loading (e.g. Gudmundsson, 2011, 2012).

The measured feeder-dyke thicknesses range from 0.8 to 3 m. The estimated overpressures from Eq. (1) are from 9 to 11 MPa for the Varto and Turnadağ volcanoes and from 15 to 18 MPa for the Özenç volcanic area (flood basalts). These are similar overpressures as estimated for dykes in many other areas (e.g., Becerril et al., 2013). Using these and the above values, Eq. (3) yields source-chamber depths of 8–10 km for Varto and Turnadağ volcanoes, and 15–18 km for the Özenç volcanic area (Appendix 2). In the numerical models we thus use an estimated depth of 8 km for the magma chambers feeding eruptions in volcanoes of Varto and Turnadağ and 15 km for the larger reservoir supplying magma to the flood basalts of the Özenç volcanic area.

4. Model set-up

All the numerical models are built and solved using the finite element program COMSOL (www.comsol.com; cf. Zienkiewicz, 1979; Deb, 2006; Tabatabaian, 2014). The models are based on the real geological setting of the KTJ as interpreted from field measurements and seismic data (e.g. Sandvol et al., 2003) as well as InSAR data (Cavalié and Jónsson, 2014). We differentiate between two predominant magma-chamber modelling techniques. The first uses 2-D geometry where magma chambers are modelled as holes with applied excess pressure (p_e) (Gudmundsson, 2006, 2011; Gerbault, 2012; Gerbault et al., 2012). The second set uses 3-D geometry where the chambers/reservoirs are modelled as ellipsoids or cavities of prescribed volume with applied excess pressure. We present two geometries of 2-D models based upon (1) a N–S striking profile through the Varto caldera (Fig. 2), and (2) an E–W striking profile that encompasses both the Turnadağ volcano to the west and the Varto caldera to the east.

Our models consider ellipsoidal magma chambers/reservoirs. While these are, in detail, simplifications of the actual shapes, the long-term stable geometries may be similar to these (e.g. Gudmundsson, 2012). Topography may affect near-surface stress fields. However, in the present models the primary focus is on the local stresses induced by the stress concentration around chambers/reservoirs subject to different boundary conditions, in which case topography normally plays a less prominent role (cf. Gaffney and Damianac, 2006; Gudmundsson, 2006). Thus, we assume a flat topography in all models. The 16 different mechanical layers used in our models are based on our direct geological observations. The values used to calculate magma chamber depth encompass all of these mechanical layers.

In Fig. 3 we show only the N–S model setup. In this model two magma chambers, one relatively shallow, at a depth of 8 km, and one deeper, at a depth of 15 km, are residing within a heterogeneous, anisotropic elastic half space with Young's modulus (E) varying between individual layers from 40 GPa to 0.1 GPa, as shown in Fig. 2. The shallower magma chamber has a maximum diameter of 9 km, whereas the deeper chamber or reservoir has a maximum diameter of 30 km. Poisson's ratio (ν) does not vary significantly between individual layers; thus, in the models we use a constant typical value for rocks of 0.25 (Gudmundsson, 2011). In the N–S striking profile all the layers dip gently to the north, whereas the E–W striking profile hosts predominantly horizontal layers. The softest (most compliant) layers are those comprising the fault cores/damage zones (E_{fault}), indicated by black polygons in Fig. 3. The faults are given Young's modulus values of 0.1 GPa,

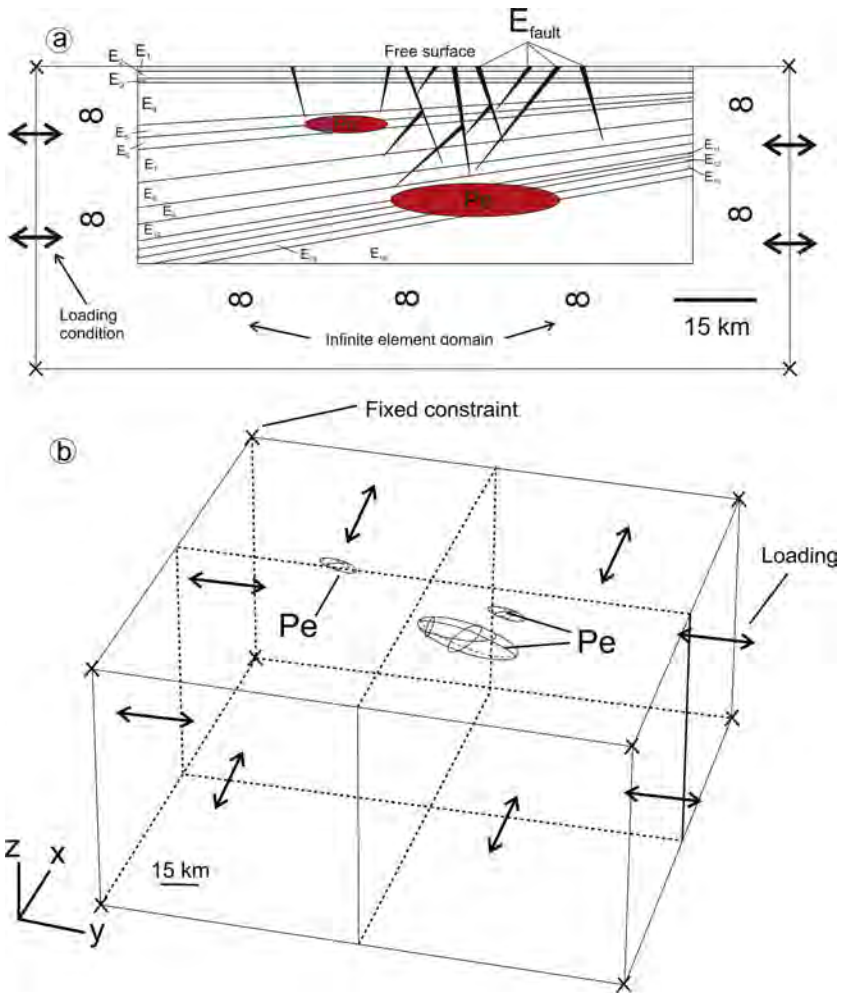

Fig. 3. (a) 2-D and (b) 3-D numerical model setups. The 2-D example shown represents the geology of a N–S striking profile through Varto caldera to the east of the KTJ. All 2-D models are layered $E_{(1-16)}$ with each unit assigned a different value of Young's modulus. The dips of individual layers are based on field measurements. Faults (E_{fault}), shown as black polygons, are represented by zones of low stiffness and assigned Young's modulus of 0.1 GPa. Magma chambers, represented by cavities, are given an excess pressure of 5 to 15 MPa. Finally, boundary conditions such as extension or compression are assigned to the model edges. All 3-D models assume a homogeneous crustal segment with a Young's modulus of 40 GPa.

as has been estimated for some active faults (Gaffney et al., 2007; Gudmundsson, 2011; Grosfils et al., 2015). The thicknesses of layers and fault cores/damage zones are taken from our geological measurements (Fig. 2) and given in Appendix 1. All 2-D models are fixed at the corners, with boundary loads applied at the left and right edges and a free surface (a region free from shear stress) prescribed on the upper edge. More specifically, the fixing of the models at the corners means that the model boundaries are free to move (be displaced) under loading, except for the corners themselves. This is a standard procedure in modelling magma chambers subject to various loading conditions (e.g. Gudmundsson, 2006, 2011).

Loading conditions applied are (1) internal magmatic excess pressure between 5 and 15 MPa, (2) regional extension (tension) of 5 MPa, (3) regional compression of 5 MPa, and (4) a combination of regional stress and magmatic excess pressure. Magma-chamber rupture and dyke injection is supposed to occur when the tensile strength is reached. Tensile strengths, mostly measured through hydraulic fracturing and down to crustal depths of about 9 km, are between 0.5 and 9 MPa, the most common values being 2–4 MPa (Gudmundsson, 2011). As indicated above, by using excess pressure in the chamber/reservoir, rather than total pressure, the effects of gravity are automatically considered (cf. Gudmundsson, 2012). We use a triangular mesh with a maximum element size of 4.02 km; minimum element size of 0.018 km for 2-D, and tetrahedral mesh with a maximum element size of 4.02 km; minimum element size of 1.8 km for 3-D models.

Due to the complex tectonic nature of a triple junction it is not possible to fully encompass the regional stress pattern in two dimensions. For this reason we made additional 3-D models that allow more boundary loading options. In contrast to the two-dimensional models, in these 3-D models results can be observed normal to the plane of interest. In the 3-D models, we impose three magma chambers of similar depths and sizes to those used in the 2-D models, i.e., two shallow chambers at 8 km depth and one deeper and larger reservoir at 15 km depth. The axes (diameters) of the ellipsoidal shallow chambers are 2 km, 6 km, and 9 km (Fig. 2b), similar in general dimensions to many shallow magma chambers (Gudmundsson, 2012). By contrast, the axes of the deep reservoir are 4 km, 12 km, and 30 km (Fig. 2b), and thus similar in geometry and dimensions to many inferred deep-seated reservoirs in rift zones (Gudmundsson, 1990, 2006). All 3-D models simulate an elastic half space with a Young's modulus of 40 GPa. In these models the focus is not on the mechanical contrast between individual layers but on the effect of regional stresses on spatial distribution of the local stresses around the magma chambers. The boundary loads prescribed in these 3-D models include (1) compression or extension various directions in relation to the axes of the magma chambers/reservoirs had (2) shear, that is, compression

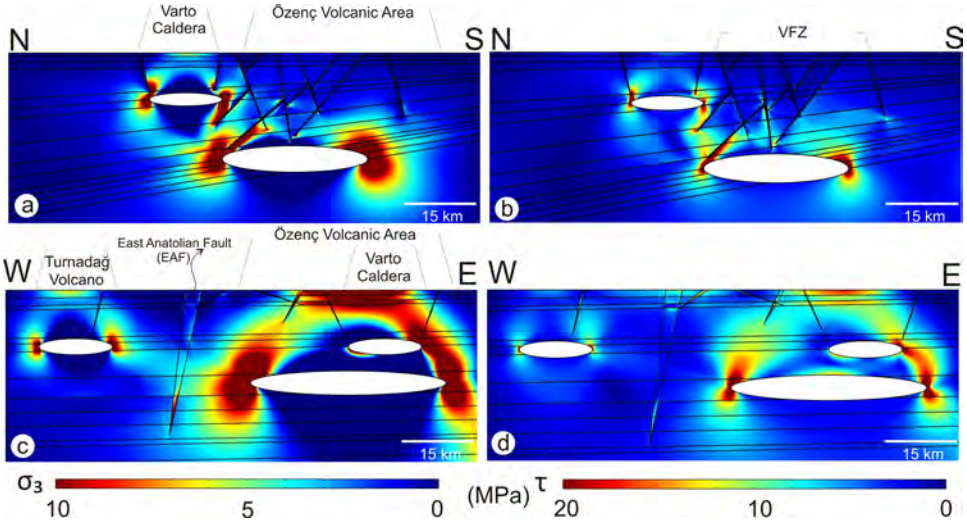

Fig. 4. Modelled stresses induced by excess magmatic pressure based on the geologic setting along the Northern Anatolian fault region. Left: Magnitudes of the minimum principal compressive (maximum tensile) stress (σ_3). Right: Magnitude of von Mises shear stresses (τ). The excess magmatic pressure in each chamber is 5 MPa and is the only loading (no regional tectonic loading is applied here).

or extension in opposing directions across a zone, thereby simulating strike-slip tectonics.

5. Results

In order to characterise the propagation path of dykes in the shallow crust at the KTJ it is first necessary to consider the stress required for magma chamber rupture. In the simplest terms, a magma chamber will rupture and inject a dyke or an inclined sheet when (Gudmundsson, 1990, 2011):

$$p_l + p_e = \sigma_3 + T_o \tag{4}$$

where p_l is lithostatic pressure and p_e is the excess pressure in the magma chamber, σ_3 is minimum principal compressive stress in the host rock, and T_o is the tensile strength of the host rock which, as indicated above, ranges from 0.5 to 9 MPa (cf. Amadei and Stephenson, 1997). When a chamber roof has failed in tension and a dyke is initiated then the magma follows the path or trajectories of maximum principal compressive stress, σ_1 (Gudmundsson, 2011).

5.1. Magma-chamber excess pressure

Here we present first the results on crustal stresses induced solely by magmatic excess pressure within each chamber, ignoring initially the potential effects of any regional tectonic loading. In Fig. 4 we show the magnitudes of the minimum principal compressive (maximum tensile), stress, σ_3, and von Mises shear stress, τ. In both the N–S and E–W profiles the maximum tensile and shear stresses concentrate at the lateral margins of each magma chamber and at the earth's surface above the magma chamber. Complex stress patterns and interactions occur at depth because of the attitude and mechanical properties of the imposed fault structures. In all models the soft or compliant material that comprises each fault zone inhibits stresses within the fault, but raises and concentrates stresses at the boundaries or contacts of the faults with the host rock. The effects are, for example, prominent in the steeply dipping East Anatolian Fault (EAF) segment that extends between the shallow and deep chambers along the E–W profile (Figs. 4a, b). At this location (Fig. 4a) high shear stresses concentrate where the fault zone intersects the surface and at depth high tensile stresses occur where the fault zone narrows (Fig. 4c). In the N–S profile, two shallow dipping faults concentrate both shear and tensile stress between the margins of the deep and shallow chambers, indicating that magma transfer between the two systems in this location is likely (Figs. 4a, b). Stress also concentrates at depth along the EAF in the E–W profile (Figs. 4c, d).

It should be noted that we did test excess magmatic pressure of 15 MPa (and 10 MPa as well) for the loading of the magma chambers/reservoirs. However, in the models presented here we used only 5 MPa as the loading, both as regards the magmatic excess pressure as well as for the external tension (in some of the models). This we did primarily because 5 MPa is similar to the in situ tensile strength of rocks. Increasing the excess magmatic pressure simply increases the stress concentration magnitudes (higher stresses close to the chamber, in particular) but does not markedly change the geometry of the concentration zones and their location – as is well known from numerical modelling in volcanology and other fields (e.g. Gudmundsson, 2011).

5.2. Regional tectonic stresses

In the second set of 2-D models the focus is on the effect of regional stresses induced by tectonic loading on the local stresses around the magma chambers. In Fig. 5 we show the tensile and shear stresses around overpressured magma chambers subjected to both regional compression and regional extension, as indicated by arrows in the Fig. 5. During E–W extension of 5 MPa, two stiff (high Young's modulus) near-surface units concentrate tensile stress, which may encourage dyke propagation (Gudmundsson, 2006). Focusing on the EAF (Figs. 5e–h), we note that shear stress concentrates at the surface during regional compression but dissipates during imposed regional extension in both strike directions (Figs. 5a, e). The N–S striking profile is dominated by a series of high angle faults (Fig. 5a) that during regional compression (Figs. 5a–d) suppress much of the shear stress surrounding the deeper chamber (Figs. 4b, 5d). The effect is similar during regional extension; however, the steepest central fault concentrates substantial shear stress directly above the central part of the deep chamber. Our models also show that caldera-related ring faults increase the maximum tensile stresses (Figs. 5a, c).

Regional tectonic loading gives different stresses which potentially affects magma paths. The effect is most clear in the E–W profile whereby tensile stresses are shifted to the west at the Turnadağ volcano during regional extension. Our findings also indicate

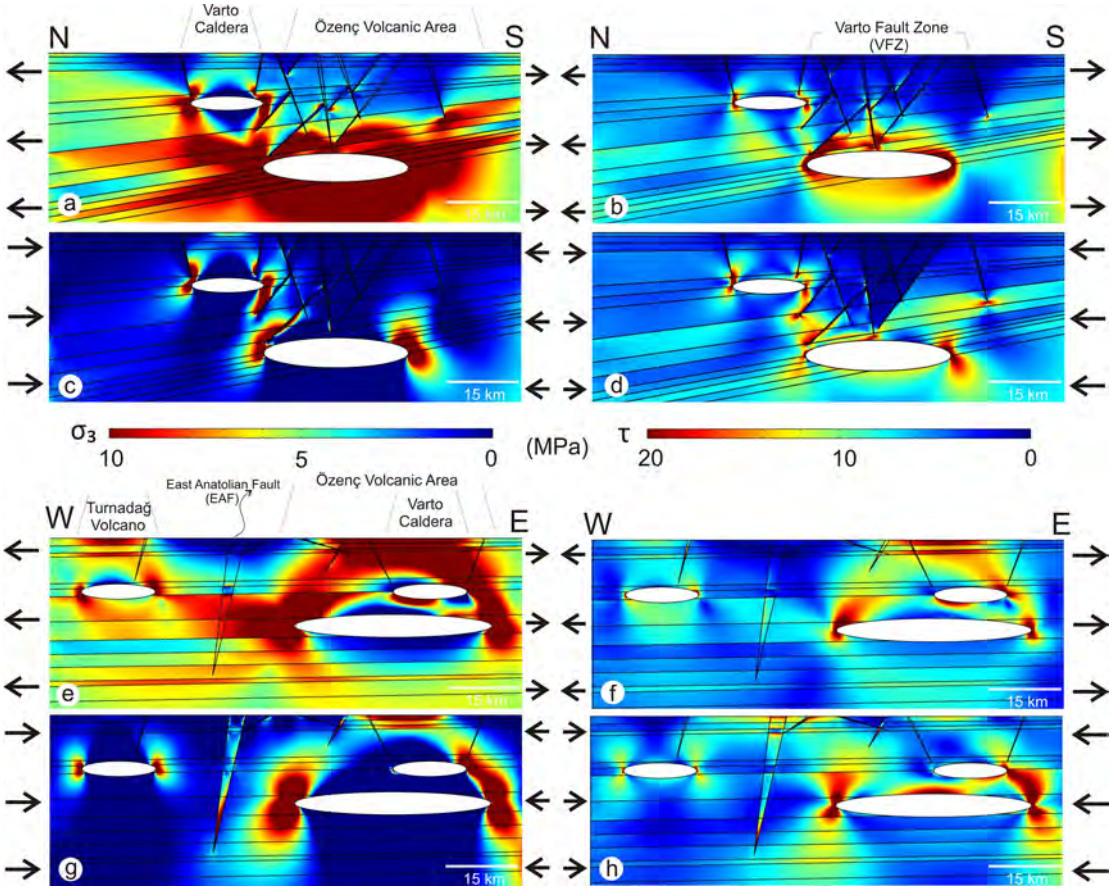

Fig. 5. Modelled stresses resulting from regional tectonic extension (a–b and e–f) and compression (c–d and g–h). Applied tensile and compressive boundary loadings are 5 MPa and excess magmatic pressure is 5 MPa in each chamber in all the models.

an increased likelihood of shallow chamber dyke injection from the deeper source during periods of regional extension.

5.3. Three-dimensional models

In order to better understand the geodynamic setting of the Karlıova Triple-Junction we present a series of simple three-dimensional (3-D) models (Figs. 6–10) exploring the local stresses in differential tectonic regimes. These models are homogeneous; the aim here is not to fully encompass the geological setting of Karlıova but instead to provide constraints on the location of volcanism as a function of different tectonic loading. In Figs. 6a, b in the E–W profile we apply a north–south directional extensional load of 5 MPa and observe the resultant tensile and shear stresses along E–W and N–S profiles. The deeper and shallower chambers concentrate shear stress at their margins. However, those shear stresses dissipate close to the surface, and then the stress state is dominated by the deeper chamber at Earth's free surface (Figs. 6a–d). Maximum tensile stresses concentrate at the lateral margins of all the chambers, which suggests that the chamber walls tend to rupture and dykes become injected at these locations (Figs. 5a–b).

In Figs. 7, 8 and 9 we model the loading effects of strike-slip faulting, using compressional load of 5 MPa on either side of the N–S-striking plane (Fig. 7). Such a regime cannot be represented fully in a two-dimensional model. As in previous models we show the magnitudes of tensile and shear stresses, although now in two directions (Figs. 7–9). We note stress concentrations and linkage between the deeper chamber and the shallow chamber directly above (Varto) (Fig. 7). Surface stresses are dominated by the larger reservoir, and no stress interaction occurs with either chamber or the shallow chamber to the west (Figs. 7b, d). There are tensile stress concentrations around, and particularly above and in-between, the chambers and reservoirs of Varto and Özenç (Fig. 7c). This stress concentration between the chamber and the reservoir may promote rupture at the upper margin (the roof) of the reservoir and encourage dyke propagation from the reservoir to the shallow chamber. Furthermore, from the shallow chamber there is a zone of tensile stress concentration all the way to the surface (Fig. 7a), suggesting that the local stress field encourages dyke propagation from the chamber to the surface. While these models only show the stress magnitudes, we also analysed the stress trajectories (the directions of the principal stresses) and these agree with the suggested dyke paths.

We also made a set of three-dimensional models to explore the effect of N–S and E–W directed regional extension. Even though these models do not accurately reflect the exact tectonic regime of the study area, the results are general and should broadly apply to triple junctions worldwide, even regions where biaxial tension might operate (Appendix 3). We note again that there is very little stress interaction between the eastern and western magmatic systems. Whilst magma propagation between the two systems is unlikely, it appears substantially more difficult to envisage linkage or interaction during a compressional regime where tensile stresses are lower in the area between the eastern and western chambers. In the eastern segment, our results indicate an increased likelihood of magma chamber rupture at the lateral margin of each chamber during extensional loading. We find that extensional loading favours central chamber roof rupture and vertical dyke propagation. As indicated in our earlier models (Figs. 5a, e), the precise direction of the dyke propagation path will depend on local stresses related to crustal heterogeneity and anisotropy (layering). How-

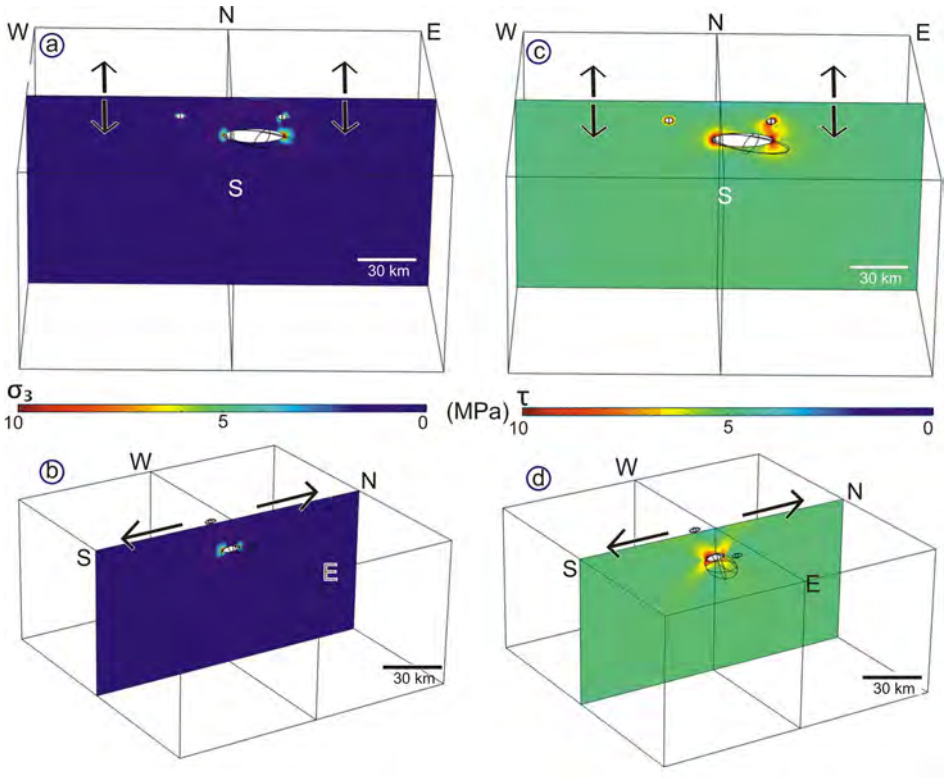

Fig. 6. 3-D model showing the stresses resulting from tectonic extension from north to south. Applied tensile and compressive boundary loads are 5 MPa and excess magma pressure is 5 MPa in each chamber in all the models. (a)–(b) Magnitudes of the minimum principal compressive (maximum tensile) stress (σ_3); (c)–(d) Magnitudes of von Mises shear stress (τ).

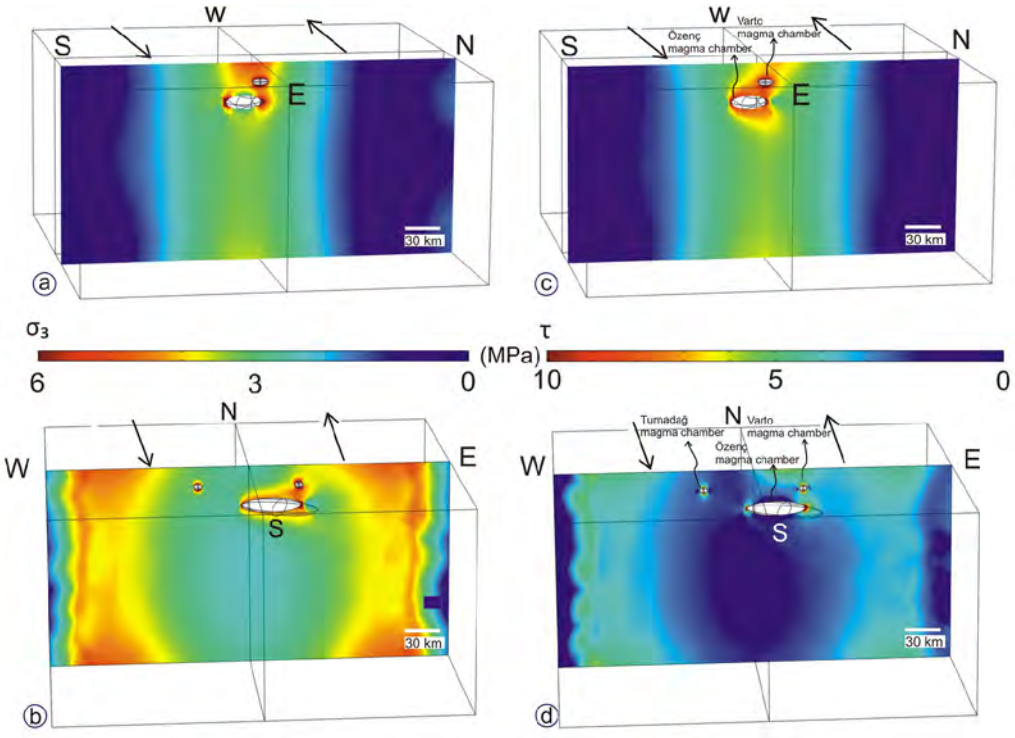

Fig. 7. 3-D model showing the stresses resulting from an opposing boundary load directions in a N–S direction. The eastern half of the model is subject to a 5 MPa load to the north, and the western half of the model subject to the same load to the south. Excess magmatic pressure is 5 MPa in each chamber in all models. (a)–(b) Magnitudes of the minimum principal compressive (maximum tensile) stress (σ_3). (c)–(d) Magnitudes of von Mises shear stress (τ).

ever, the extension appears to have shifted the principal stresses towards the north in comparison to the previous models that consider only extension or compression independently.

In Figs. 8 and 9 we compare the effects different types of shear, that is, left-lateral and right-lateral strike-slip faulting, on the local stresses, particularly around the magma chambers/reservoirs.

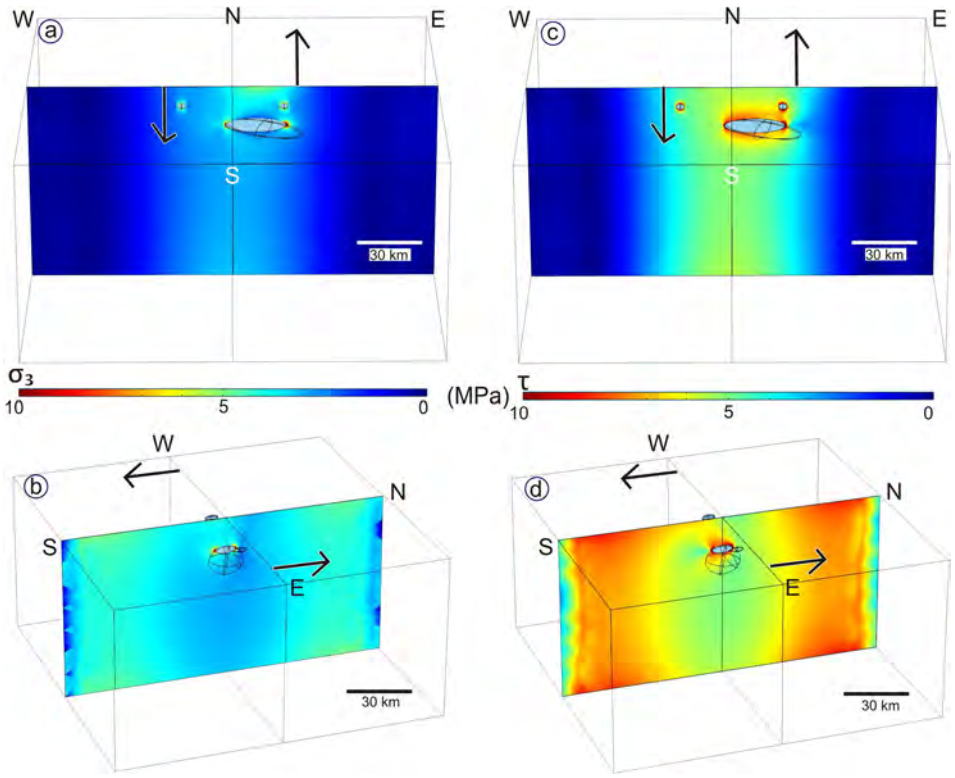

Fig. 8. 3-D modelled stresses resulting from N–S-directed left-lateral tectonic shear loading. Applied tensile and compressive boundary loads are 5 and excess magma pressure is 5 MPa in each chamber in all the models. (a)–(b) Magnitudes of the minimum principal compressive (maximum tensile) stress (σ_3). (c)–(d) Magnitudes of von Mises shear stress (τ).

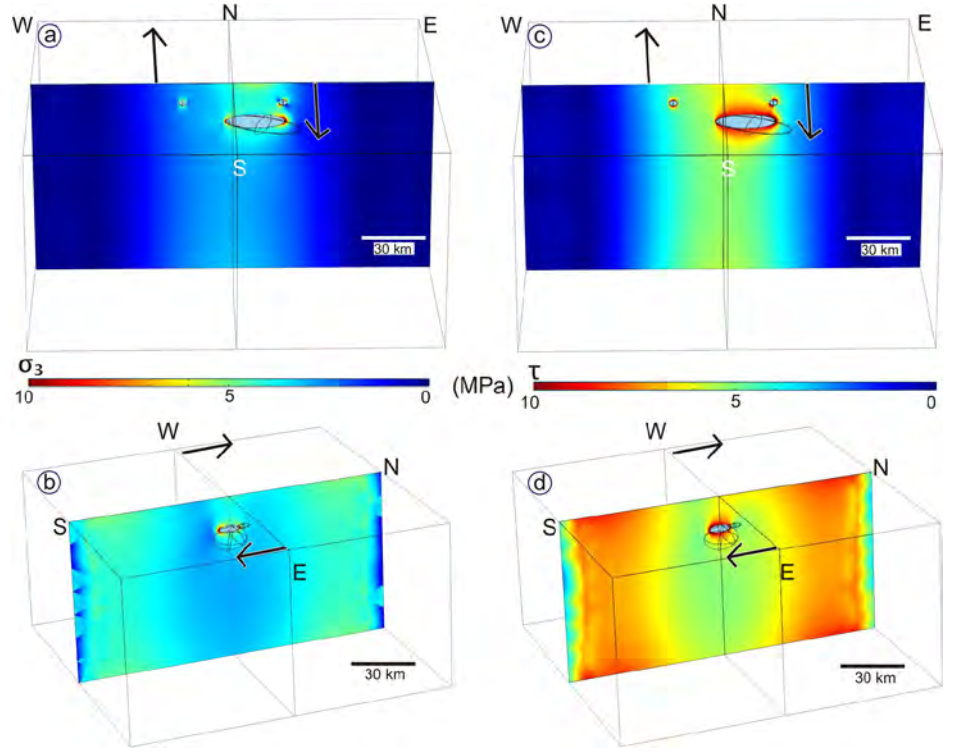

Fig. 9. 3-D modelled stresses resulting from N–S-directed right-lateral tectonic shear loading. Applied tensile and compressive boundary loads are 5 and excess magmatic pressure is 5 MPa in each chamber in all models. (a)–(b) Magnitudes of the minimum principal compressive (maximum tensile) stress (σ_3). (c)–(d) Magnitudes of von Mises shear stress (τ).

The main finding is that the shear and tensile stresses again concentrate around the chambers/reservoirs, but the stresses concentrated around the deep-seated chamber (reservoir) are greater at the surface in the right-lateral simulations than in the left-lateral simulations, shifting stresses slightly to the east (Fig. 9c). In Fig. 10 we simulate a N–S compressional regime which has the effect of

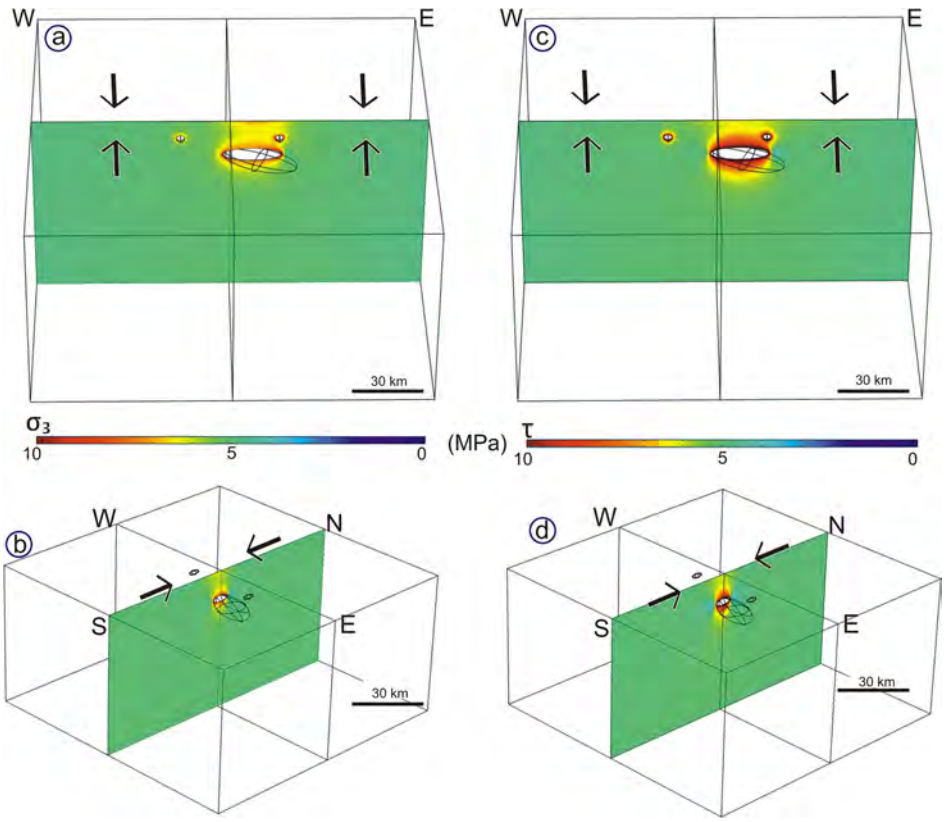

Fig. 10. 3-D modelled stresses resulting from tectonic compression from north to south. Applied tensile and compressive boundary loads are 5 and excess magmatic pressure is 5 MPa in each chamber in all the models. (a)–(b) Magnitudes of the minimum principal compressive (maximum tensile) stress (σ_3). (c)–(d) Magnitudes of von Mises shear stress, σ_1–σ_3.

increasing the symmetry of local stresses, and in doing so concentrating both tensile and shear stresses vertically above the deeper magma reservoir.

6. Discussion

Over the past decades many studies have focused on understanding better the mechanical principles that control dyke propagation paths through the Earth`s crust (e.g. Druitt and Sparks, 1984; Martí et al., 1994; Acocella et al., 2004; Geyer et al., 2006; Gudmundsson, 2006; Martí et al., 2008; Hurwitz et al., 2009; Gerbault, 2012; Gudmundsson, 2012; Le Corvec et al., 2013; Karaoğlu, 2014). Although some studies have attempted to understand how faults affect magma ascent (Magee et al., 2014; Browning and Gudmundsson, 2015; Gudmundsson, 2015) many aspects of fault-magma path interactions remain poorly understood. Our work focuses on the mechanism of dyke propagation through a highly heterogeneous, anisotropic, and intensely faulted crust of the KTJ. It is widely accepted that the region has experienced N–S directed crustal shortening. We have also taken into consideration the inversional tectonic regime, i.e., a successive N–S directed extension and compression during the past 3 Ma, an idea based on the results of recent field studies (Karaoğlu et al., in press). We further accounted for dyke propagation under either E–W compressional, or E–W extensional tectonic regimes (Fig. 4), as well as strike-slip regimes.

The numerical results presented demonstrate that the initiation of a dyke is influenced by the geometries and depths of magma chambers as well as the local stresses in the heterogeneous, anisotropic, and faulted crust. The overall process of dyke initiation and propagation may be affected by at least three distinct factors, namely (i) the geometry and attitude of the associated faults; (ii) the heterogeneity and anisotropy of the crust; and (iii) stress concentrations around, and stress (mechanical) interactions between, magma chambers. Here we discuss our numerical analysis of two different tectonic regimes, namely inversion tectonics using N–S and E–W-striking profiles in order to better understand dyke propagation under different stress conditions at the Karlıova-Varto region.

6.1. Magma transport in the absence of tectonic stresses

Our numerical models indicate that the mechanical properties of a heterogeneous and anisotropic crust substantially influence the local stresses and thus the potential dyke propagation paths (e.g. Chaussard and Amelung, 2014; Le Corvec et al., 2015) (Fig. 4). The initial stage of dyke propagation is magma-chamber roof rupture leading to the initiation of a dyke (e.g. Clements and Mawer, 1992; Gerbault, 2012). One of the most common reasons for the generation of excess pressure within a shallow magma chamber is likely recharge from parental magma at depth that has accumulated in a deeper reservoir or chamber (e.g. Chestler and Grosfils, 2013). It is only when a sufficient volume of magma accumulates within a shallow chamber that it can reach the conditions of likely rupture (Eq. (4); Browning et al., 2015). Dyke propagation at great depths requires suitable stress interactions between the shallower and the deeper magma chambers or reservoirs (Fig. 4a). Our numerical results show that layering affects local stresses and many aspects of fault-dyke path interactions (Figs. 4c, d). For all loadings considered (compression, extension, and shear), tensile and shear stresses concentrate around, and particularly at the margins of the deep magma chambers (Fig. 4).

While the 4 km wide EAF is one of the most remarkable structural elements along the E–W profile (Fig. 4c), the conditions for dyke propagation through and along a fault are only observed at the much smaller VFZ primarily due to the faults orientation and

position. However, we note some minor stress accumulation in the EAF (Figs. 4c, d). Tensile stress along the VFZ likely creates favourable conditions for dyke propagation along the previously dissected fault at the northern margin of the deeper reservoir. This result suggests that deep and shallow magma chamber stress interactions may play an important role in dyke propagation which is strongly influenced by faults and other crustal heterogeneities and layering (Fig. 4).

6.2. Magma transport under regional tectonic stresses

The magmatic systems in this part of Turkey evolve partly as a result of tectonic deformation, generally and in the context of processes associated with the KTJ. Recently, this area has experienced N–S directed compression and E–W directed extension (e.g. Aktug et al., 2013). In the E–W profile, shallow dyke injection, some reaching the surface to erupt, appears possible during both extensional and compressional tectonic loading in and around the Varto caldera (Figs. 5e, g). Deep and shallow magma chamber interactions may result in magmatism that becomes partly channelised through the EAF, thereby encouraging volcanic eruptions in the Varto region. Our results demonstrate that fault zones may facilitate magma transport during different tectonic loadings. The effects of these faults on potential magma paths is more prominent for compressional (Figs. 5g, h) than extensional loading (Figs. 5e, f).

While tensile and shear stresses concentrate mostly at the margins of the shallow magma chambers, shear stresses concentrate also above the central parts of the deeper chambers/reservoirs (Fig. 5h), as well as at caldera ring-faults (e.g. Annen and Sparks, 2002; Marti et al., 1994). Our models indicate how magma transport and regional tectonics may interact in an intensely fragmented and mechanically layered crust (e.g. Spence et al., 1987; Tibaldi et al., 2008), in particular through the cross faults of the VFZ (Figs. 5b, d). The vertical stress patterns between the two magma chambers observed in the N–S profile support the view that fault zones can act as magmatic paths (Fig. 5d). Even during a N–S compressional phase the results suggest that dykes may be injected, resulting in possible dyke propagation from the deeper source to the shallow magma chamber (Fig. 5d). In the case of N–S extension (Fig. 6), the youngest fault, which is a normal fault as shown in Fig. 2a, plays a crucial role for shear stress concentration (Figs. 5a–d and Fig. 6). We show that the interaction between these fault systems, of various ages, encourages dyke injection from the central part of a deeper magma reservoir, and therefore acts as a potential vertical dyke path (Fig. 5b).

6.3. Numerical models in the Karlıova geological context

In the 2-D models, Varto caldera is represented by steeply dipping inward zones of soft material, as is commonly observed in eroded ring-faults of calderas (e.g. Martíet al., 2008; Browning and Gudmundsson, 2015). The Varto caldera is 8 km in diameter and with a semi-circular shape. The Varto fault is the most seismically active segment of the VFZ, a N70°W-striking fault that offsets the southern part of the Varto caldera (Fig. 1). Several distinct dyke locations have previously been reported, the dykes being primarily composed of trachy-basalt, both inside and around the Varto caldera. Those dykes mostly display NW–SE, and rarely NE–SW, orientations. Strike orientation values range from 205° to 300° with some indicating the presence of cross-cutting (polyphase) dykes. Our numerical results indicate the potential for multi-stage dyke injections during transtensional to compressional tectonic phases (e.g. inversion tectonic regime) resulting principal stress rotation (Fig. 5). Although radiometric data of Varto caldera yields ages from 3.1 to 2.6 Ma (Hubert-Ferrari et al., 2009), which might represent the duration of the volcanism, magma propagation in the crust has probably continued up to the latest eruptions, based on our numerical results (Fig. 5). Recent block rotations around the KTJ based on GPS data (Fig. 1) indicate an intense crustal deformation via successive extensional and shear loading (e.g., Le Corvec et al., 2013; 2015). Long-lived volcanic activity is possible at Varto caldera and in the KTJ in general.

Zones of tensile stress concentration indicate potential magma propagation paths from the shallow magma chambers to the surface of Turnadağ volcano (Fig. 5e). Magma transfer under E–W-oriented compression is unlikely (Figs. 5g, h). Dyke-fed eruptions at Turnadağ volcano are most likely when the magma chamber feeding the volcano is subject to an E–W-directed extension (Fig. 5e). On account of the westward extrusion of the Anatolian plate since 12 Ma, an E–W-directed tectonic regime seems most favourable for eruptions in the Turnadağ volcano (Figs. 1, 5e).

In the Özenç volcanic area our numerical models suggest that volcanic activity is more likely under E–W-directed extension than N–S-directed extension, and may occur under E–W-directed compression as well. We suggest that some, perhaps most, of the feeder dykes may have originated from the deeper magma chamber (Figs. 5c, d). In particular, 3-D modelling results suggest that the deeper magma chamber largely controls the local stress field and, thereby, dyke propagation and resultant eruptions (Figs. 7, 8, 9).

Our 3-D models show the potential for subtle changes in magma propagation paths and eventual eruption resulting from the differences in the boundary loads. While all-round extension has the likely effect of shifting volcanism to the south-east (Appendix 3), strike-slip type loading can either concentrate volcanism directly above a deep magma system or extend the zone of volcanism substantially to the east, depending on the loading direction (Figs. 7, 8, 9). All results show that the most likely paths for dyke propagation to the surface are from the eastern margin of either the deeper chamber or, possibly, the eastern margin of the shallow (Varto) chamber.

6.4. Relationships between local stress fields in Karlıova and volcanic eruptions

Studies indicate that most volcanic unrest periods do not culminate in an eruption (Dzurisin, 2006). Only during comparatively rare periods do dykes propagate all the way to the surface and erupt. For eruptions to occur, the local stresses between the source and the surface along the potential dyke path must be uniform, that is, homogenised (Gudmundsson and Philipp, 2006).

Crustal heterogeneity and anisotropy as well as fault attitude and mechanical properties are the main parameters which influence the local stresses and thereby the magma paths (e.g. Gudmundsson and Philipp, 2006; Browning and Gudmundsson, 2015). Our models suggest that, for many loadings, regional tectonic stresses encourage dyke propagation to the surface.

Since the development of the NAFZ and EAFZ, at around 6 Ma, a strike-slip tectonic regime has dominated the province. Westward extrusion of the Anatolian plate led to a stress field suitable for magmatism at the extremity of the KTJ. The wedge extrusion accommodated by high strain encouraged magmatic paths as feeders for the volcanism. The period represented the initiation of the minor volcanic activity caused by major extension at a local scale. The first volcanic activity commenced with regional stress induced by KTJ tectonics at around 3 Ma. The swarm of parallel dykes in the southern part of KTJ, particularly Özenç volcanic area (Fig. 2), show a stress field with σ_1 in a N–S direction and σ_3 in the E–W direction (Karaoğlu et al., in press). The strain direction associated with this dyke emplacement confirms that volcanism was controlled by a NEE–SWW-trending zone of weakness, particularly in the Özenç volcanic area and at the Turnadağ volcano.

7. Conclusions

We document numerical results on the mechanism of magma propagation paths under a variety of tectonic loadings in the crust. We particularly explore the relationship between tectonics and magma propagation in the tectonic settings at the Karlıova Triple Junction (KTJ) of Eastern Turkey. The interpretation of our numerical models suggests that Turnadağ volcanism at the western part of the KTJ has been fed by a shallow magma chamber located at about 8 km depth during E–W extension. Also, that the Varto caldera is fed by a shallow magma chamber at a similar depth. More specifically, the numerical results show that if the region was subject to an E–W-oriented compressional stress (σ_1), then magma propagation and associated volcanic eruptions would most likely come to an end. Magma transfer between the magma chambers of Varto volcano and Özenç volcanic area exhibits complex stress interactions (Figs. 4, 5). The pattern of local stress changes from the eastern part of the triple junction to the western part. Even though the Özenç volcanic area has experienced N–S-directed compression, inversion tectonics encourage magma propagation through the crust. Hence, loading during inversion tectonics dramatically changes the orientation of σ_1 and affects magma propagation more than the individual extension or compression regimes. Local stresses are dominated by a deep reservoir located at 15–18 km depth. It is this reservoir that largely controls the potential of injected dykes reaching the surface and, additionally, the locations of the eventual eruptions. Our three-dimensional models, simulating the complex loading conditions at the KTJ triple junction, can be used (with suitable modifications) to advance our understanding of triple junctions worldwide.

Acknowledgements

This study was supported by funds of the Yüzüncü Yıl Üniversitesi (Project No. 2014-MİM-B062). Özgür Karaoğlu is supported by The Scientific and Technological Research Council of Turkey (TUBITAK) International Postdoctoral Research Fellowship Programme. Thanks to the Editor, Tamsin Mather, and to the reviewers, Alessandro Tibaldi and Nicolas Le Corvec, for very helpful comments which greatly improved the paper.

Appendix A. Supplementary material

Supplementary material related to this article can be found online at http://dx.doi.org/10.1016/j.epsl.2016.07.037.

References

Acocella, V., Funiciello, R., Marotta, E., Orsi, G., de Vita, S., 2004. The role of extensional structures on experimental calderas and resurgence. J. Volcanol. Geotherm. Res. 129 (1–3), 199–217.

Acocella, V., Neri, M., 2009. Dike propagation in volcanic edifices: overview and possible developments. Tectonophysics 471 (1), 67–77.

Aktug, B., Dikmen, Ü., Dogru, A., Ozener, H., 2013. Seismicity and strain accumulation around Karlıova Triple Junction (Turkey). J. Geodyn. 67, 21–29.

Amadei, B., Stephansson, O., 1997. Rock Stress and Its Measurement. Chapman Hall, New York.

Ambraseys, N.N., Zatopek, A., 1968. The Varto Ustukran earthquake of 19 August 1966. Bull. Seismol. Soc. Am. 58, 47–102.

Annen, C., Sparks, R.S.J., 2002. Effects of repetitive emplacement of basaltic intrusions on the thermal evolution and melt generation in the crust. Earth Planet. Sci. Lett. 203, 937–955.

Armijo, R., Meyer, B., Hubert-Ferrari, A., Barka, A.A., 1999. Propagation of the North Anatolian fault into the Northern Aegean: timing and kinematics. Geology 27, 267–270.

Barka, A.A., 1992. The North Anatolian fault zone. Ann. Tecton. 6, 164–195.

Becerril, L., Galindo, I., Gudmundsson, A., Morales, J.M., 2013. Depth of origin of magma in eruptions. Sci. Rep. 3, 2762. http://doi.org/10.1038/srep02762.

Bigazzi, G., Yegingil, Z., Ercan, T., Oddone, M., Ozdogan, M., 1997. Age determination of obsidian bearing volcanics in Eastern Anatolia using the fission track dating method. Geol. Bull. Turkey 40, 57–72.

Bigazzi, G., Poupeau, G., Yeğingil, Z., Bellotgurlet, L., 1998. Provenance studies of obsidian artefacts in Anatolia using the fission track dating method. An overview. In: Gourgaud, A., Gratuze, B., Poupeau, G., Poidevin, J.L., Cauvin, M.C. (Eds.), L'Obsidienne au Proche et Moyen Orient, du Volcan à l'Outil. In: BAR International Series, vol. 738. Hadrian Books, pp. 69–89.

Browning, J., Gudmundsson, A., 2015. Caldera faults capture and deflect inclined sheets: an alternative mechanism of ring dike formation. Bull. Volcanol. 77 (1), 1–13.

Browning, J., Drymoni, K., Gudmundsson, A., 2015. Forecasting magma-chamber rupture at Santorini Volcano, Greece. Sci. Rep. 5, 15785. http://doi.org/10.1038/srep15785.

Buket, E., Temel, A., 1998. Major-element, trace element, and Sr–Nd isotopic geochemistry and genesis of Varto (Muş) volcanic rocks, Eastern Turkey. J. Volcanol. Geotherm. Res. 85, 405–422.

Caricchi, L., Annen, C., Blundy, J., Simpson, G., Pinel, V., 2014. Frequency and magnitude of volcanic eruptions controlled by magma injection and buoyancy. Nat. Geosci. 7 (2), 126–130.

Cavalié, O., Jónsson, S., 2014. Block-like plate movements in eastern Anatolia observed by InSAR. Geophys. Res. Lett. 41, 26–31.

Cembrano, J., Lara, L., 2009. The link between volcanism and tectonics in the southern volcanic zone of the Chilean Andes: a review. Tectonophysics 471 (1), 96–113.

Chaussard, E., Amelung, F., 2014. Regional controls on magma ascent and storage in volcanic arcs. Geochem. Geophys. Geosyst. 15. http://dx.doi.org/10.1002/2013GC005216.

Chestler, S.R., Grosfils, E.B., 2013. Using numerical modeling to explore the origin of intrusion patterns on Fernandina volcano, Galápagos Islands, Ecuador. Geophys. Res. Lett. 40 (17), 4565–4569.

Clemens, J.C., Mawer, C.K., 1992. Granitic magma transport by fracture propagation. Tectonophysics 204, 339–360.

Daniels, K.A., Kavanagh, J.L., Menand, T., Stephen, J.S.R., 2012. The shapes of dikes: evidence for the influence of cooling and inelastic deformation. Geol. Soc. Am. Bull. 124 (7–8), 1102–1112.

Deb, D., 2006. Finite Element Method, Concepts and Applications in Geomechanics. PHI Learning Private Limited, New Delhi.

Druitt, T.H., Sparks, R.S.J., 1984. On the formation of calderas during ignimbrite eruptions. Nature 310, 679–681.

Dzurisin, D., 2006. Volcano Deformation: New Geodetic Monitoring Techniques. Springer Verlag, Berlin.

Folch, A., Marti, J., 1998. The generation of overpressure in felsic magma chambers by replenishment. Earth Planet. Sci. Lett. 163 (1), 301–314.

Furlong, K.P., Schwartz, S.Y., 2004. Influence of the Mendocino triple junction on the tectonics of coastal California. Annu. Rev. Earth Planet. Sci. 32, 403–433.

Gaffney, E.S., Damjanac, B., 2006. Localization of volcanic activity: topographic effects on dike propagation, eruption and conduit formation. Geophys. Res. Lett. 33, L14313. http://dx.doi.org/10.1029/2006GL026852.

Gaffney, E.S., Damjanac, B., Valentine, G.A., 2007. Localization of volcanic activity, 2: effects of pre-existing structure. Earth Planet. Sci. Lett. 263 (3), 323–338.

Gerbault, M., 2012. Pressure conditions for shear and tensile failure around a circular magma chamber, insight from elasto-plastic modelling. Geol. Soc. (Lond.) Spec. Publ. 367 (1), 111–130.

Gerbault, M., Cappa, F., Hassani, R., 2012. Elasto-plastic and hydromechanical models of failure around an infinitely long magma chamber. Geochem. Geophys. Geosyst. 13 (3).

Geshi, N., Neri, M., 2014. Dynamic feeder dyke systems in basaltic volcanoes: the exceptional example of the 1809 Etna eruption (Italy). Earth Sci. Front. 2, 13. http://dx.doi.org/10.3389/feart.2014.00013.

Geyer, A., Marti, J., 2009. Stress fields controlling the formation of nested and overlapping calderas: implications for the understanding of caldera unrest. J. Volcanol. Geotherm. Res. 181, 185–195.

Geyer, A., Folch, A., Martí, J., 2006. Relationship between caldera collapse and magma chamber withdrawal: an experimental approach. J. Volcanol. Geotherm. Res. 157 (4), 375–386.

Gregg, P.M., De Silva, S.L., Grosfils, E.B., Parmigiani, J.P., 2012. Catastrophic caldera-forming eruptions: thermomechanics and implications for eruption triggering and maximum caldera dimensions on Earth. J. Volcanol. Geotherm. Res. 241, 1–12.

Gregg, P.M., de Silva, S.L., Grosfils, E.B., 2013. Thermomechanics of shallow magma chamber pressurization: implications for the assessment of ground deformation data at active volcanoes. Earth Planet. Sci. Lett. 384, 100–108.

Gregg, P.M., Grosfils, E.B., de Silva, S.L., 2015. Catastrophic caldera-forming eruptions II: the subordinate role of magma buoyancy as an eruption trigger. J. Volcanol. Geotherm. Res. 305, 100–113.

Grosfils, E.B., 2007. Magma reservoir failure on the terrestrial planets: assessing the importance of gravitational loading in simple elastic models. J. Volcanol. Geotherm. Res. 166 (2), 47–75.

Grosfils, E.B., McGovern, P.J., Gregg, P.M., Galgana, G.A., Hurwitz, D.M., Long, S.M., Chestler, S.R., 2015. Elastic models of magma reservoir mechanics: a key tool for investigating planetary volcanism. Geol. Soc. (Lond.) Spec. Publ. 401 (1), 239–267.

Gudmundsson, A., 1990. Emplacement of dikes, sills and crustal magma chambers at divergent plate boundaries. Tectonophysics 176, 257–275.
Gudmundsson, A., 2006. How local stresses control magma-chamber ruptures, dyke injections, and eruptions in composite volcanoes. Earth-Sci. Rev. 79, 1–31.
Gudmundsson, A., 2011. Rock Fractures in Geological Processes. Cambridge University Press, Cambridge.
Gudmundsson, A., 2012. Magma chambers: formation, local stresses, excess pressures, and compartments. J. Volcanol. Geotherm. Res. 237–238, 19–41.
Gudmundsson, A., 2015. Collapse-driven large eruptions. J. Volcanol. Geotherm. Res. 304, 1–10.
Gudmundsson, A., Philipp, S.L., 2006. How local stress fields prevent volcanic eruptions. J. Volcanol. Geotherm. Res. 158, 257–268.
Herece, E., 2008. Atlas of East Anatolian Fault. Special Publication Series. General Directorate of Mineral Research and Exploration, Ankara, Turkey.
Hubert-Ferrari, A., King, G., Woerd, J., Van der Villa, I., Altunel, E., Armijo, R., 2009. Long-term evolution of the North Anatolian Fault: new constraints from its eastern termination. Geol. Soc. (Lond.) Spec. Publ. 311 (1), 133–154.
Hurwitz, D.M., Long, S.M., Grosfils, E.B., 2009. The characteristics of magma reservoir failure beneath a volcanic edifice. J. Volcanol. Geotherm. Res. 188 (4), 379–394.
Hutton, D.H., 1988. Granite emplacement mechanisms and tectonic controls: inferences from deformation studies. Trans. R. Soc. Edinb. Earth Sci. 79 (2–3), 245–255.
Jarosinski, M., 2012. Compressive deformations and stress propagation in intracontinental lithosphere: finite element modelling along the Dinarides–East European Craton profile. Tectonophysics 526–529, 24–41.
Karaoğlu, O., 2014. Tectonic controls on the Yamanlar volcano and Yuntdagi volcanic region, western Turkey: implications for an incremental deformation. J. Volcanol. Geotherm. Res. 274, 16–33.
Karaoğlu, Ö., Sağlam-Selçuk, A., Gudmundsson, A., in press. Tectonic controls on the Karlıova Triple Junction (Turkey): implications for tectonic inversion and the initiation of volcanism. Tectonophysics.
Kavanagh, J.L., Menand, T., Sparks, R.S.J., 2006. An experimental investigation of sill formation and propagation in layered elastic media. Earth Planet. Sci. Lett. 245, 799–813.
Le Corvec, N., Menand, T., Lindsay, J., 2013. Interaction of ascending magma with pre-existing crustal fractures in monogenetic basaltic volcanism: an experimental approach. J. Geophys. Res., Solid Earth 118 (3), 968–984.
Le Corvec, N., McGovern, P.J., Grosfils, E.B., Galgana, G., 2015. Effects of crustal-scale mechanical layering on magma chamber failure and magma propagation within the Venusian lithosphere. J. Geophys. Res. 120 (7), 1279–1297.
Maccaferri, F., Rivalta, E., Keir, D., Acocella, V., 2014. Off-rift volcanism in rift zones determined by crustal unloading. Nat. Geosci. 7 (4), 297–300.
Magee, C., McDermott, K.G., Stevenson, C.T., Jackson, C.A.L., 2014. Influence of crystallised igneous intrusions on fault nucleation and reactivation during continental extension. J. Struct. Geol. 62, 183–193.
Martí, J., Ablay, G.J., Redshaw, L.T., Sparks, R.S.J., 1994. Experimental studies of collapse calderas. Q. J. Geol. Soc. Lond. 151, 919–929.
Martí, J., Geyer, A., Folch, A., Gottsmann, J., 2008. A review on collapse caldera modelling. In: Gottsmann, J., Martí, J. (Eds.), Caldera Volcanism: Analysis, Modelling and Response. In: Development in Volcanology, vol. 10. Elsevier, Amsterdam, pp. 233–283.
McClusky, S., et al., 2000. GPS constraints on plate motion and deformation in the eastern Mediterranean: implication for plate dynamics. J. Geophys. Res. 105, 5695–5719.
McKenzie, D., 1972. Active tectonics of the Mediterranean region. Geophys. J. R. Astron. Soc. 30, 109–185.
McKenzie, D.P., Parker, R.L., 1967. The North Pacific: an example of tectonics on a sphere. Nature 216, 1276–1280.
Middlemost, E.A., 1997. Magmas, Rocks and Planetary Development: A Survey of Magma/Igneous Rock Systems. Routledge, Oxford.
Ozener, H., Arpat, E., Ergintav, S., Dogru, A., Cakmak, R., Turgut, B., Dogan, U., 2010. Kinematics of the eastern part of the North Anatolian Fault Zone. J. Geodyn. 49 (3–4), 141–150.
Pasquarè, F., Tibaldi, A., 2007. Structure of a sheet–laccolith system revealing the interplay between tectonic and magma stresses at Stardalur Volcano, Iceland. J. Volcanol. Geotherm. Res. 161, 131–150.
Poidevin, J.L., 1998. Provenance studies of obsidian artefacts in Anatolia using the fission track dating method, an overview. In: Gourgaud, A., Gratuze, B., Poupeau, G., Poidevin, J.L., Cauvin, M.C. (Eds.), L'Obsidienne au Proche et Moyen Orient, du Volcan a` l'Outil. In: BAR International Series Hadrian Books, vol. 738, pp. 105–156.
Reilinger, R., et al., 2006. GPS constraints on continental deformation in the Africa–Arabia–Eurasia continental collision zone and implications for the dynamics of plate interactions. J. Geophys. Res. 111, B05411.
Sançar, C., Zabcı, C., Akyüz, H.S., Sunal, G., Villa, I.M., 2015. Distributed transpressive continental deformation: the Varto Fault Zone, eastern Turkey. Tectonophysics 661, 99–111.
Sandvol, E., Turkelli, N., Zor, E., Gok, R., Bekler, T., Gurbuz, C., Seber, D., Barazangi, M., 2003. Shear wave splitting in a young continent–continent collision: an example from eastern Turkey. Geophys. Res. Lett. 30 (24), 8041–8059.
Sinton, J.M., Detrick, R.S., 1992. Mid-ocean magma chambers. J. Geophys. Res. 97, 197–216.
Spence, D.A., Sharp, P.W., Turcotte, D.L., 1987. Buoyancy-driven crack propagation: a mechanism for magma migration. J. Fluid Mech. 174, 135–153.
Şengör, A.M.C., Tüysüz, O., Imren, C., Sakınç, M., Eyidogan, H., Görür, N., Le Pichon, X., Rangin, C., 2004. The North Anatolian Fault: a new look. Annu. Rev. Earth Planet. Sci. 33, 37–112.
Tabatabaian, M., 2014. COMSOL for Engineers. Mercury Learning and Information, Boston.
Tan, O., Tapırdamaz, M.C., Yörük, A., 2008. The earthquake catalogues for Turkey. Turk. J. Earth Sci. 17 (2), 405–418.
Tarhan, N., 1991. Hınıs–Varto–Karlıova (Erzurum–Muş–Bingöl) dolayındaki neojen volkanitlerinin jeolojisi ve petrolojisi. MTA Dergisi 113, 1–15 (in Turkish).
Tatar, O., Piper, J.D.A., Gürsoy, H., Heimann, A., Koçbulut, F., 2004. Neotectonic deformation in the transition zone between the Dead Sea Transform and the East Anatolian Fault Zone, southern Turkey: a palaeomagnetic study of the Karasu Rift Volcanism. Tectonophysics 385, 17–43.
Tibaldi, A., 2015. Structure of volcano plumbing systems: a review of multiparametric effects. J. Volcanol. Geotherm. Res. 298, 85–135.
Tibaldi, A., Vezzoli, L., Pasquarè, F.A., Rust, D., 2008. Strike-slip fault tectonics and the emplacement of sheet–laccolith systems: the Thverfell case study (SW Iceland). J. Struct. Geol. 30, 274–290.
Vigneresse, J.L., 1999. Intrusion level of granitic massifs along the Hercynian belt: balancing the eroded crust. Tectonophysics 307, 277–295.
Williams, G.D., Powell, C.M., Cooper, M.A., 1989. Geometry and kinematics of inversion tectonics. In: Cooper, M.A., Williams, G.D. (Eds.), Geol. Soc. (Lond.) Spec. Publ., vol. 44, pp. 3–15.
Zienkiewicz, O.C., 1979. The Finite Element Method. McGraw–Hill, New York, p. 787.

Geothermics 81 (2019) 168–184

Contents lists available at ScienceDirect

Geothermics

journal homepage: www.elsevier.com/locate/geothermics

Thermal fluid circulation around the Karliova triple junction: Geochemical features and volcano-tectonic implications (Eastern Turkey)

Özgür Karaoğlu[a,*], Mohsen Bazargan[b,c], Alper Baba[d], John Browning[e]

[a] Eskişehir Osmangazi University, Department of Geological Engineering, 26040, Eskişehir, Turkey
[b] Department of Earth Sciences, Royal Holloway University of London, Egham, TW20 0EX, UK
[c] Department of Research and Development, Weld On Sweden, Vaxjo, Sweden
[d] Izmir Institute of Technology, Engineering Faculty, 35430, Urla, Izmir, Turkey
[e] Department of Mining Engineering and Department of Structural and Geotechnical Engineering, Pontificia Universidad Católica de Chile, Santiago, Chile

ARTICLE INFO

Keywords:
Fluid circulation
Thermal water
Karliova triple junction
Caldera
Tectonic

ABSTRACT

The Karlıova triple junction (KTJ) in eastern Turkey has been subjected to incremental deformation resulting in complex kinematic and mechanical interactions throughout the upper crust. These interactions have generated tectonic inversions and uplift, extensive seismicity and volcanism. The regional tectonics generate local stresses, some of which are favorable to magma transport and thermal water circulation throughout the lithosphere. Here we evalauate hydrogeochemical, geological and numerical results relating to the mechanism of thermal fluid circulation around the KTJ. Hydrogeochemistry of the samples indicates that the thermal water springs are probably heated by steam. Volcanic rocks at the site appear to be the host rock owing to the enrichment of Na^+ and Cl^- ions in water and the abundance of these elements in minerals of the volcanic rocks. In addition, it is clear that the thermal fluids are sourced from depth and migrate through permeable networks of faults. The effects of crustal heterogeneities, in particular the geometry and mechanical properties of many faults and layers, on thermal fluid circulation in relation to active magma chambers were investigated under a variety of different mechanical conditions. The numerical results indicate very close relationships between the stress field causing faulting and thermal fluid movement in the KTJ. The effect of thermal transfer was modeled with depth throughout the crust and along the the crustal surface. The models show that some faults encourage thermal fluid circulation below the Varto and Özenç volcanoes. Hydrogeochemical, geological and numerical results suggest that magmas residing beneath both the Varto caldera and the Özenç volcano are the main heat source for thermal fluid in the Varto region. Fluid-solid interactions and fluid circulation models show that the permeable faults are important factors affecting heat transport and fluid circulation. In a series of thermal fluid flow models we probe the mechanism for fluid and gas transport from the 900 °C 'hot' zone around the deep magma chambers and investigate how heat is lost throughout the crust on the way to the surface and so eventually creates water channels of temperatures between 50 to 60 °C.

1. Introduction

Faults and fractures which accommodate the deformation of large sections of the upper crust have a significant impact on the physical processes controlling heat transfer and fluid motion in the subsurface. This is because they disturb the conformal succession of geological layers (Press and Siever, 1995). In addition, the mechanical properties of the rocks, the hydraulic characteristics of the rocks, and the geologic and also geodynamic relations provide useful information about thermal fluid circulation through the fractured upper crust. Numerical modeling provides one approach to estimate the structural setting of the subsurface and the mechanical processes controlling fluid and heat transfer (e.g., Cherubini et al., 2013).

The emplacement of hot asthenospheric mantle into shallow levels beneath the crustal materials of the Karlıova-type triple junction could be expected to generate magmatism and possibly thermal water potential. Consistent with this expectation, sequences of volcanic centers have historically erupted along the triple junction within Karlıova (e.g., Furlong and Schwartz, 2004).

Geothermal systems are linked to magmatism in a variety of geodynamic contexts in volcanic environments (i.e., island arcs, hot-spots, middle oceanic ridges, sea-mounts, intraplate volcanism and intrusions)

* Corresponding author.
E-mail address: ozgur.karaoglu@deu.edu.tr (Ö. Karaoğlu).

https://doi.org/10.1016/j.geothermics.2019.05.003
Received 18 October 2017; Received in revised form 15 February 2019; Accepted 7 May 2019

(Caracausi et al., 2005). Thermal fluid circulation is affected by both temporal variations in degassing and in the activity level of the magmatic systems supplying fluids and energy to the geothermal reservoirs (Baker, 1995; Von Damm et al., 1995; Baker and Urabe, 1996; Giggenbach, 1996; Caracausi et al., 2005). Active tectonics and very recent volcanic activity have a strong impact on the geochemistry of the circulating fluids (e.g., Italiano et al., 2013).

A triple junction that deforms the upper crust in a complex manner is a site of special interest in which to study thermal and cold water transportation. Geometric consequences of the motions of three plates, following a collision between convergent plates, mostly result in extrusion through crustal-scale transtensive faults. Triple junction tectonics can produce surface uplift and crustal deformation, abundant seismic activity, high heat flow, and the eruption of volcanoes on the Earth's surface (e.g., Furlong and Schwartz, 2004).

In order to better understand the source and thermo-mechanical constraints on hydrothermal systems, the detailed geologic background and geochemical analysis of the fluids, which in turn form a numerical modeling approach, must first be evaluated. The young Karlıova-Varto volcanic terrain provides an excellent opportunity to explore the relationships between magmatic heat sources (i.e., magma chambers, magma storage, magma plumes, hot spots) and geothermal fluids throughout the upper crust.

The aim of the study is to demonstrate how hydrothermal systems follow paths with different dimensions along these faults, and also how a fluid behaves in this intensely deformed crust. The hydrogeochemistry of geothermal springs around the Varto volcanic province is documented in order to link geochemical constraints with thermo-mechanical controls on fluids in the crust.

2. Tectonic and geologic setting

Eastern Turkey represents a particular part of the Mediterranean region which is characterized by the presence of major continental fragments and suture zones (e.g., Isik et al., 2014). The closure of the Neotethyan Ocean along the BZSZ during the Cretaceous-early Paleogene led to the formation of the Eastern Anatolian Accretionary Complex (EAAC), which has subsequently acted as one of the major tectonic units during the subsequent tectonic evolution of the region (Barka, 1992; Okay and Tüysüz, 1999; Bozkurt, 2001).

The Karlıova triple junction area is one of the best examples of an active continental collision zone in the world (Fig. 1). The location, timing and geochemical characteristics of volcanism result from the complex interaction of the colliding Eurasian and Afro-Arabian plates. Escape tectonics of the Anatolian plate to the west gave rise to strike-slip motion along the North Anatolian Fault Zone (NAFZ) and East Anatolian Fault Zone (EAFZ) after the closure of the Neotethyan Ocean as a result of Arabia-Eurasian convergence (Barka, 1992; Okay and Tüysüz, 1999; Bozkurt, 2001). The Varto Fault Zone (VFZ) presents a structural continuation of the NAFZ starting from the KTJ (Fig. 2). The VFZ is composed of sets of discontinuous faults with differential kinematics and associated sets of striae (Karaoğlu et al., 2017). The VFZ extends for over 50 km and can be subdivided into six segments (Fig. 1b). Fault planes from the VFZ commonly exhibit multiple sets of striations, highlighting incremental and complex deformation of the KTJ region since ~6 Ma (Karaoğlu et al., 2017).

The northernmost segment of the VFZ, called the Tuzla Fault, is mainly a thrust fault (Karaoğlu et al., 2017). The western part of these faults is offset laterally by the EAFZ (Fig. 1b). The Varto fault is the most seismically active segment of the VFZ, a N70 °W-trending-normal fault that offsets the southern part of the Varto caldera (Fig. 1b) (or the Bingöl caldera; Hubert-Ferrari et al., 2009), and was introduced for the first time by Karaoğlu et al. (2017). Several destructive earthquakes (Mw = 6.8) shifting further south took place on the Varto fault in 1966 and on the Leylek Fault (Mw = 6.2), and there was also a small earthquake (Mw ≥ 3) on the Çayçatı Fault (Wallace, 1968; Ambraseys and Zatopek, 1968).

The first volcanic activity began with high-silica obsidian flows at Çatak on the EAFZ reflecting the southern branch of the triple junction, and started at 6.06 Ma (Poidevin, 1998). Two composite volcanoes were emplaced in the area at around 3 My ago. The Turnadağ volcano located in the western part of KTJ was formed 2.3–2.8 Ma ago, but the Varto caldera was active 2.6–3.1 Ma ago (Fig. 2) (see Pearce et al., 1990; Hubert-Ferrari et al., 2009 for details about K/Ar whole rock and $^{40}Ar/^{39}Ar$ groundmass dating of the rocks). The two volcanic domes are 0.46 Ma and 0.73 Ma old (Hubert-Ferrari et al., 2009, see Fig. 2). Recent tomographic image data shows the presence of active magma reservoirs throughout the crust around the Karlıova region (Salah et al., 2011; Karaoğlu et al., 2018).

The Varto and Turnadağ volcanoes exhibit quite similar major or trace element compositions. Volcanic rocks from the two volcanoes are composed of high-K and shoshonitic series rocks including trachy-andesite to rhyolite with a small amount of basaltic trachy-andesite (Buket and Temel, 1998; Hubert-Ferrari et al., 2009).

Italiano et al. (2013) stated that the release of volcanic fluids is a common feature along the main active faults in Turkey, however the local geological setting is responsible for the uprising of deep fluids through tectonic discontinuities and the occurrence of shallow processes affecting the original characteristics of the circulating fluids. Moreover, the presence of carbonatic rocks, travertine deposits, metamorphic rocks and old volcanic rocks (Fig. 2) accounts for the different nature of the circulating fluids and different fluid–rock interactions (Italiano et al., 2013). Across the Karlıova-Varto area, a volcano-sedimentary package, around 45 m thick, interfingers with the effusive and explosive-type volcanic rocks of the Bingöl group (Fig. 2). The former volcano-sedimentary deposits display a well preserved subaqueous-subaerial transition in a fluvio-lacustrine setting generated after some volcanic eruptions. The deposits are composed of mud-poor sandstone, sand-filled pebbles intercalated with the mudstone, which in turn are exposed in restricted plains dissected by braided rivers in the western part of the Varto caldera (Karaoğlu et al., 2017). Most of these volcaniclastic successions have experienced an intense deformation particularly since 6 Ma. These deposits are overlain by lava stacks and ignimbrite veneers of the Varto group. The Pleistocene lacustrine sediments are mainly composed of marl, limestone, and tuff. Tectonic activity has created a faint deformation within these deposits on the plain near Teknedüzü and Yayıklı villages (Fig. 2). Fault complexity is observed in strongly folded lacustrine sediments at a meter-scale, with nearly horizontal axial planes, whose strikes are scattered around an NNE-SSW direction (Fig. 1b). The youngest effusive and extrusive volcanism conformably overlies these sediments. A massive-type travertine is exposed in the northern part of Karlıova, on a continuation of the EAF to the northeast.

3. Fault kinematics

KTJ is a key area for understanding the deformation of Neogene volcanoes in eastern Turkey because of their progressive inversion tectonics. Structural analysis suggests that this volcano has undergone incremental tectonic controls in eastern Turkey since the Upper Miocene. Karaoğlu et al. (2017) documented 128-slip data points from 16 locations of two transpressional and transtensional deformational fields which were collected for palaeostress analysis (Fig. 3). The fault surfaces document that inversion tectonics dominated the area when both extensional and transtensional deformational phases progresively reversed over the past 3 My (Karaoğlu et al., 2017). Structural data across the Varto Fault Zone (VFZ), obtained from six faults for which kinematics indicate a range of shortening and extensional deformation for 3 Ma (Fig. 3). Many fault surfaces show evidence of reactivation. Particularly, the splays of the VFZ and the other segmented faults have thrust to strike-slip fault components, indicating multiple reactivation events. To establish the surface expressions of the deformation process,

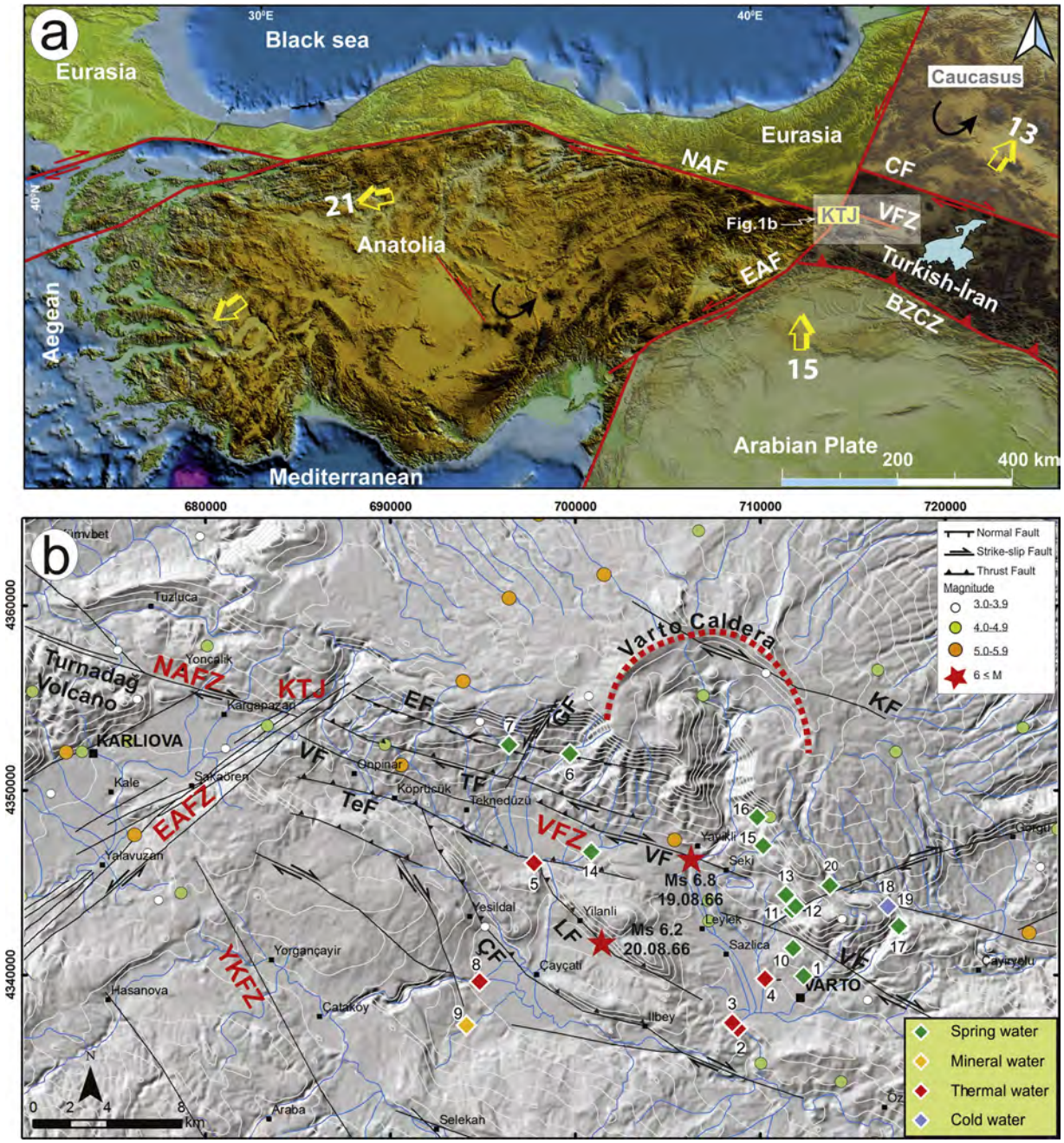

Fig. 1. a) Regional map showing crustal deformation in the eastern Mediterranean and Anatolia (Armijo et al., 1999). NAFZ: North Anatolian Fault Zone, EAFZ: East Anatolian Fault Zone, BZCZ: Bitlis–Zagros Collision Zone, CF: Çaldıran Fault, VFZ: Varto Fault Zone, YS: Yedisu Fault, KTJ: Karlıova Triple Junction; b) Shaded relief basis map showing locations of water sampling in the Varto region. The main faults and seismicity around the Karlıova and Varto regions are modified from Herece (2008); Karaoğlu et al. (2017). Seismicity data is obtained from KOERI.

we present the kinematic data, which was previously published by Karaoğlu et al. (2017), on each fault segment around the Varto region (Fig. 3). The episodic deformation, which took place at Eryurdu, Tuzlu, Varto, Teknedüzü, Leylekdağ, and Çayçatı faults, dominate the southern part of the Varto Caldera (Fig. 3).

The Eryurdu Fault terminates the southern flank of the Varto Caldera resulting in fault-related volcanic breccia deposits. This fault is offset by the sinistral strike-slip Geyiksuyu Fault (GF) on the southern margin of the Varto Caldera (Fig. 3). The Eryurdu Fault strikes N85 °W-and is around 18 km long with mostly high-angle and oblique-slip segments. This fault displays typical high-angle normal fault slickenlines (Fig. 3). Measurements indicate a well-preserved NNE–SSW-trending extension which formed from deformation of the southern part of the Varto caldera (Karaoğlu et al., 2017).

The Tuzla Fault is reported by Karaoğlu et al. (2017) as an active fault due to recorded seismic activities on this fault (Fig. 3). This fault is a thrust fault with a right-lateral component which extends laterally for over 20 km (Fig. 3). Fault kinematics suggest that it underwent a NW-SE directed compression with a maximum stress axis and that this compression has dominated for circa 6 Ma. The Pliocene deposits have been deformed by Tuzla Fault (Karaoğlu et al., 2017).

The N75 °W-striking Varto Fault is composed of three sub-parallel segments which extend for 20 km (Fig. 3). A zone of distributed compression affects Pleistocene lacustrine sediments, which accommodate the deformation between the dextral faults. The easternmost segment of the Varto Fault shows dextral offsets for around 1.5 km in the valleys.

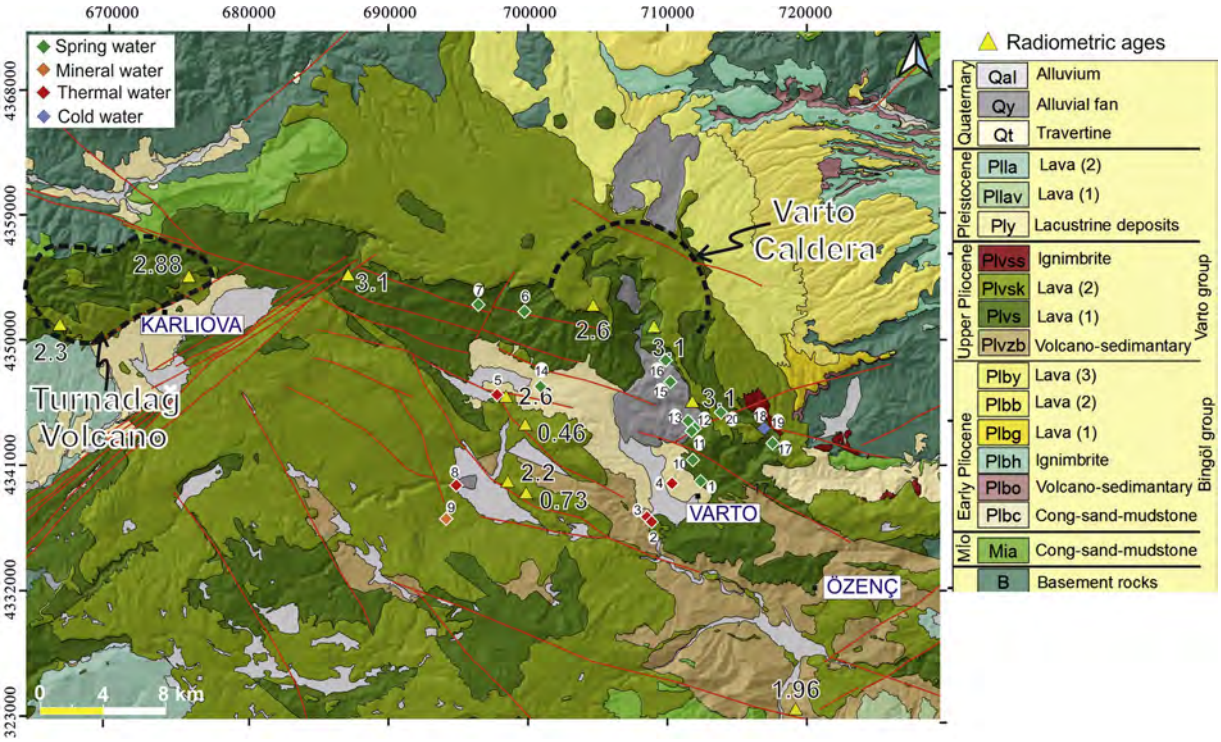

Fig. 2. Geological map showing the main faults and seismicity around the Karlıova and Varto regions. Radiometric ages are given in Ma. Active faults are modified from Herece (2008) and Karaoğlu et al. (2017). Thermal water signifies hot fluids that contain a variety and concentration of dissolved particles consistent with a thermal origin. The surface temperature of thermal water is higher than 20 °C. Mineral water means that which contains various minerals such as salts and sulfur compounds. These waters have temperatures lower than 20 °C. Spring water is defined as natural water that was collected from underground sources.

Westernmost segments display some releasing step-over structures. Kinematic data for this fault poses oblique-slip normal fault surfaces dipping 55 °S and with rakes of 35 °E (Fig. 3).

The Teknedüzü Fault exhibits typical thrust fault constraints of N75 °W-striking in different curved strands. The horsetail shape branches deformed up to 20 km in length of the fault (Fig. 3). This fault is regarded as one of the youngest faults because it cuts Pleistocene lava flows as well as recent lacustrine and alluvial deposits (Karaoğlu et al., 2017). The Teknedüzü Fault is represented by two main strands of The Leylekdağ and Çaydağ reverse faults, both have minor dextral strike-slip components (Fig. 3). The central part of the Leylekdağ Fault was ruptured by an earthquake (Mw 6.2) 20 August 1966.

The Varto region, where the thermal and non-thermal springs are most visible, has been subjected to intense deformation due to those reactivated faults. Fault planes of F9 and F10 record a NE–SW-directed contraction associated with a NW–SE extension, whilst a coeval phase of F11 developed under NE–SW extension (Fig. 3; Karaoğlu et al., 2017).

The Çayçatı Fault, which displays thrust fault kinematic morphological constraints, consists of two main segments. The western segment shows a N70E°-striking thrust component on a 7-km-long transpressional fault (Fig. 3). Evidence for the earthquake faulting scarps and related deformation generated by the 1966 earthquake can still be observed in this area. The kinematic data from F12 indicate that a NW–SE-trending extension is associated with the NE–SW contraction (Fig. 3; Karaoğlu et al., 2017).

Both extensional and transtensional dominated fault motions have been documented on the extruded Anatolian block (Karaoğlu et al., 2017) (Fig. 3). Measurements of stress tensors on the western part of the KTJ indicate E–W-trending extension which is compatible with the westward motion of the Anatolian block (Fig. 3). However, measurements from point F14 on Fig. 3 indicate a NE–SW-trending extension (Karaoğlu et al., 2017), point F13 on Fig. 3 indicates a sinistral strike-slip fault motion with at least two phases of movement. Both fault scarps suggest extensional tectonics along the East Anatolian Fault (Fig. 3) (Karaoğlu et al., 2017).

4. Governing equations

We present three sets of governing equations used to create models in COMSOL Multiphysics. They are mass balance, momentum and heat transfer.

The momentum and mass balance equations are as follows:

$$-\nabla\cdot\eta\left(\nabla\mathbf{u}+(\nabla\mathbf{u})^{T}\right)+\frac{\eta}{k}\mathbf{u}+\nabla p=\mathbf{g}\beta_{T}\left(T-T_{c}\right) \tag{1}$$

$$\nabla\cdot\mathbf{u}=0 \tag{2}$$

where p is pressure, u is a vector of directional velocities, h is dynamic viscosity, k is permeability, r is fluid density, g is gravity, β_T is thermal expansion coefficient, T is temperature from the heat transfer application, and Tc is the initial temperature.

A buoyant lifting term links flow and heat:

$$\nabla\cdot(-k\nabla T+c_{p}\rho T\mathbf{u})=0 \tag{3}$$

where, T is temperature, K_e is effective thermal conductivity of the fluid and solid medium, C_L is fluid volumetric heat capacity, $C_L = c_p$ r, c_p is fluid specific heat capacity, and u is a vector of directional fluid velocities from the flow application (Versteeg and Malalasekera, 1995).

The heat transport in this paper is described by the heat transport equation:

$$(\rho C_{p})_{eq}\partial T/\partial t+\rho C_{p}u.\ \nabla=\nabla.\ (k_{eq}\nabla T)+Q+Q_{geo} \tag{4}$$

Heat is balanced generally and it is transported by both conduction and convection processes within a fault zone. Heat can be generated or lost, which can be defined in the source term, Q. One special feature of heat transfer at the porous medium interface is the hydrothermal heatingfeature implemented, represented as a domain condition: Q_{geo}. It is also possible to implement an average representation of rock thermal

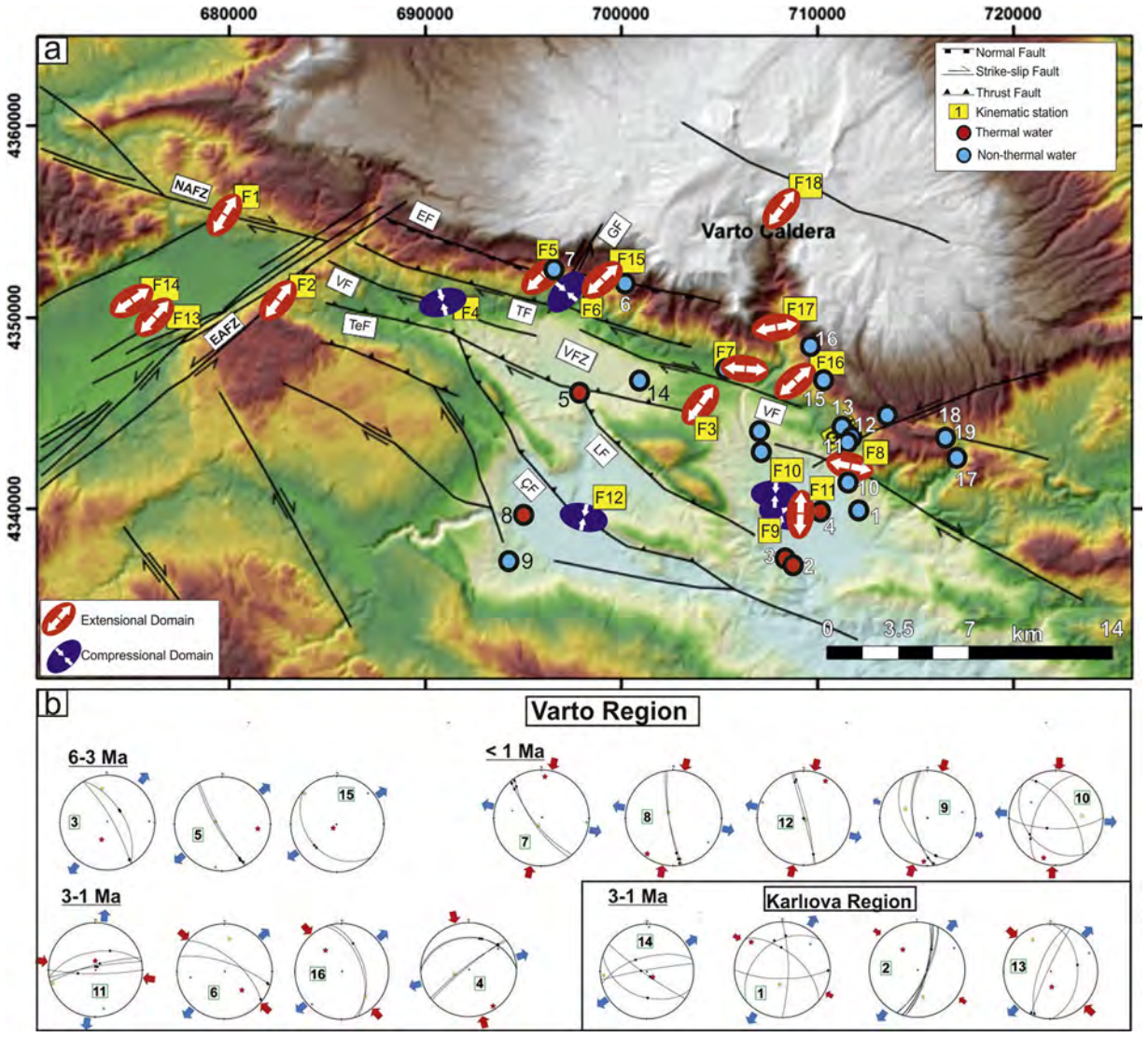

Fig. 3. a) Map showing dominant stress orientations. b) Lower hemisphere equal area projections and striations on the main faults around the Varto-Karlıova region (data from Karaoğlu et al., 2017). Locations of the fluid measurement sites and kinematic stations are given in the map.

parameters, comprising the rock structure and the underground water using the matrix volume fraction, Θ, as a weighting factor (for further details see the COMSOL website, www.comsol.com).

In the case of volume averaging, the volumetric heat capacity in the heat transport equation becomes:

$$(\rho C_p)_{eq} = \sum_i (\theta_{pi} p_{pi} C_{p.pi}) + (1 - \sum_i \theta_{pi})\rho C_p \quad (5)$$

and the thermal conductivity becomes:

$$k_{eq} = \sum_i (\theta_{pi} k_{pi}) + (1 - \sum_i \theta_{pi})\rho C_p \quad (6)$$

Solving the heat transport properly generally requires incorporation of a flow field. There are various situations in the subsurface which require different approaches to describe the fluid flow mathematically (Durbin, 1986). In this paper we focus on the macro-scale and also take into consideration resolution of flow in pores. However, fully-saturated and mainly pressure-driven flow in deep geothermal strata are sufficiently described by Darcy's law:

$$u = -\frac{k}{\mu}\nabla p \quad (7)$$

where the velocity field, u, depends on the permeability, κ, the fluid's dynamic viscosity, μ and is driven by a pressure gradient, P. Darcy's law is then combined with the continuity equation:

$$\frac{\partial}{\partial t}(p\varepsilon_p) + \nabla.\,(pu) = Q_m \quad (8)$$

as our scenario concerns geothermal time scales, the time dependence is due to storage effects on the flow and heat transfer from the fluid to solid and vice versa. Therefore, the first term on the left-hand side of the equation above vanishes because the density, ρ, and the porosity, ε_p, can be assumed to be constant. Usually, the temperature dependencies of the hydraulic properties are also negligible. In some of our models, especially if the number of degrees of freedom is large, it can make sense to utilize independence by splitting the problem into a few time dependant and stationary sections for solution. In the following models, heat transfer from the fluid into solids is only due to conduction (Taler and Duda, 2006). Fourier's law also describes how to define the conductive heat flux, q. This shall be proportional to the temperature gradient:

$$q = -k\nabla T \quad (9)$$

$$(\rho C_p)_{eq}\frac{\partial T}{\partial t} = \nabla.\,(k_{eq}\nabla T) + Q \quad (10)$$

5. Methods

5.1. Field investigations

To explore the thermo-mechanical relationships of the fault activity, hydrogeology, thermal and fluid circulation we carried out an extensive field study around the Varto-Karlıova region (Fig. 1b). The sampling strategy was developed based on the geological map, cross sections, and also fault surfaces.

The sampling study was performed on five hot fluids and two mineral water springs, together with cold waters in November 2008 in the region shown in Fig. 1b. During the field surveys, some physical parameters of water, including pH, electrical conductivity (EC as μS/cm), temperature (T as °C), redox potential (Eh as mV) and flow rate (Q as L/s), were measured in–situ with a WTW Multi 340i/SETS. For water-quality monitoring, four sets of samples were collected from each point: a 500 mL sample for major anions and cations; a 1000 mL sample for tritium isotopes; a 100 mL sample for oxygen-18 (^{18}O) and deuterium (^{2}H), and a 100 mL sample for heavy metals and trace elements. To prevent the complex formation of trace elements with oxygen, samples were filtered with 0.45 μm filter paper, transferred to 50-mL polyethylene bottles and stored at 4 °C.

5.2. Analytical methods

The heavy metals and trace elements were acidified to pH < 2 conditions by adding 0.5 ml HNO_3 to prevent the complex formation of trace elements with oxygen and then analyzed by inductively coupled plasma–mass spectroscopy (ICP-MS) at the ACME Laboratories in Canada. Chlorine and HCO_3^- were determined volumetrically and SO_4^{2-} by a gravimetric method in the Hacettepe University in Ankara, Turkey.

The concentrations of $\delta^{2}H$, $\delta^{3}H$ and $\delta^{18}O$ isotopes in water samples were determined in the isotope laboratories of the Hacettepe University in Ankara, Turkey. The analysis was carried out in accordance with the standards defined by the International Atomic Energy Agency (Attendorn and Bowen, 1997). $\delta^{18}O$ and $\delta^{2}H$ analyses were conducted using an MS technique that had an uncertainty of ± 0.05% and ± 1.0%, respectively. These values are expressed conventionally in delta notation as a per-mil deviation from the V-SMOW (Vienna Standard Mean Ocean Water) (Verhagen et al., 1991). Tritium ($\delta^{3}H$) analysis was conducted with a liquid scintillation counter after electrolytic enrichment of the water samples with an error of ± 0.8 tritium units (TU) (Attendorn and Bowen, 1997).

The data handling was performed by the descriptive manner of specifying water types (facies), their origins and average reservoir (host) rock temperature calculation. Piper and Schoeller diagrams are used to emphasize differences and similarities in terms of water types. Isotope signatures of samples indicate their origins. Solute geothermometer equations were applied to calculate average reservoir rock temperatures.

5.3. Hydrogeochemical properties of water resources

The preliminary evaluation of geological conditions at the site provides some information regarding depths of water circulation, bearing potential of the rocks and their influence on spring water chemistry. To represent the chemistry of the site, twenty water points were sampled, including five hot water springs, two mineral water springs, and twelve spring water and surface water (cold water) (Fig. 1b).

The average discharge of thermal springs ranges from 1 to 5 L/sec in the study area (Fig. 1b) (Table 1). Surface temperatures of these springs range from 22.5–32 °C, with electrical conductivity (EC) values from 2100 to 5775 μS/cm. The average discharges of mineral waters at that site are between 0.5 and 2 L/sec. Surface temperatures were measured as 13.2 and 14.8 °C. Their electrical conductivity values are also in the range of 719–751 μS/cm. The average discharges of cold water springs in the study area are between 1 and 150 L/sec. Surface temperatures of these springs vary between 4.9 and 11.7 °C and electrical conductivity values range from 51 to 199 μS/cm. Regarding pH values, water samples belonging to the site are entirely in the pH range of ˜5.4 - ˜6.2 for hot and mineral waters, and ˜6.2 to ˜7.7 for cold waters. Thermal springs have acid character, whereas pH values for cold water springs change from slightly acid, neutral to slightly basic. The ranges of physical parameters measured are affected by outcropping rocks and structural features of the site allow different circulation depths.

Volcanic and sedimentary rocks outcrop in the vicinity of the study area and the groundwater flow in the volcanic rocks appears to be controlled by the presence of structural features. The information indicating the circulation depth only arises from alignments of the springs. Thermal, mineral and cold water springs discharge from rocks of Upper Miocene and Upper Pliocene age (Yolüstü Formation of Upper Pliocene, Kohkale Lava and Zırnak Formation of Upper Miocene in Fig. 2).

These rocks include both volcanic rocks and intercalated volcanic rocks with continental deposits such as sandstone; therefore, they are water-bearing formations. In addition to this, the NAF in Upper Miocene rocks which can outcrop in the study area controls groundwater transport (see Fig. 1b). Shallow and deep flow paths for the groundwater are reflected in the chemistry of the springs (Table 2). The deep flow paths of groundwater resources consist of more ions than the shallow flow groundwater paths.

On the basis of major ion chemistry, the Piper and Schoeller diagrams for the study area are shown in Fig. 4. Both diagrams give not only information about different water types at the site but also their evolution. According to the Schoeller diagram, cold waters can be distinguished easily with low major cations and chloride when compared with geothermal and mineral waters. According to the Piper diagram and water type classification (Deutsch and Siegel, 1997), thermal springs are of Na-HCO_3-Cl and Mg-Na-HCO_3 types; while mineral and cold waters are of Ca-HCO_3 type. To compare the thermal waters with mineral and cold waters, a Cl-SO_4-HCO_3 a ternary plot was used (Fig. 5). This diagram covers the entire spectrum of naturally occurring waters from virtually pure chloride, over mixed chloride-sulfate, to bicarbonate (Giggenbach, 1988; Nicholson, 1993). For the hydrogeochemical data, relative portions of Cl-SO_4-HCO_3 cluster into steam-condensates and dilute Cl-HCO_3 sectors (Fig. 5); see the data labeled 2. According to the scatter diagram each thermal fluid has different concentration of SO_4^{2-} ions (Fig. 6). Sample 2 has a high SO_4^{2-} concentration which comes from volcanic units.

The hydrogeochemical facies map of the area is shown in Fig. 7. As seen in Fig. 7, the lower altitudes contain geothermal waters and the zone of Na-HCO_3-Cl. Cold waters discharge at higher altitudes and they represent the zone of Ca-HCO_3.

When taking account of the linear arrangement of plotted data in Fig. 4 and the processes of steam condensates and dilution with chloride acting upon them, water types change from dominant Ca^{2+} and HCO_3^- ions to dominant Na^+ and Cl^- ions as expressed in Eq. (11).

$$\text{Ca-HCO}_3 \rightarrow \text{Ca-Na-HCO}_3 \rightarrow \text{Na-HCO}_3\text{-Cl} \quad (11)$$

Na^+ and Cl^- ions are obtained from the altered volcanic rocks. Consequently, volcanic rocks at the site appear to be the likely host rock owing to enrichment of Na^+ and Cl^- ions in the water and abundance of those elements in minerals in the volcanic rocks. In addition, it is clear that thermal waters have relatively deeper circulation routes than cold water under the assumption that they are fluids ascending due to deep processes (water-rock interaction, boiling, and steam heating; see Nicholson, 1993 for details) which do not affect their isotope compositions and originate in descending cold waters.

Table 1
Physical properties of water resources around the study area.

No	Easting	Northing	Elevation (m)	Location	T (°C)	Q (l/s)	Ec (μS/cm)	pH	Salinity (%)	Type
1	712506	4339901	1573	Tas Cesme	11.6	3	187	6.22	0	Spring
2	708927	4337029	1465	Alagoztepe Kaplicasi	29.0	3–5	5775	6.04	3.3	Hot water
3	708625	4337352	1434	Alagoztepe Dere Kaplicasi	26.8	5	2100	6.09	1	Hot water
4	710407	4339752	1497	Dipsiz Gol Kaynagi	22.5	1-2	2845	6.19	1.4	Hot water
5	697835	4346054	1520	Guzelkent Koyu	28.2	1	2155	5.75	1	Hot water
6	699782	4352013	2072	TasliYayla	8.9	2	77	7.72	0	Spring
7	696479	4352499	2050	Hizir Cesme	8.6	50	61	7.09	0	Spring
8	694874	4339601	1472	Baskan Kaplicasi	32.0		2334	6.06	1.1	Hot water
9	694153	4337217	1524	Baskan Koyu Maden suyu	14.8	2	751	6.16	0.1	Mineral Water
10	711941	4341403	1659	Acarkent Koyu Kaynagi	11.0	1-2	136	6.50	0	Spring
11	711876	4343505	1848	Oglakci Koyu iki goze 1	10.3	2.5	115	6.54	0	Spring
12	712072	4343678	1910	Soguk Gol Kaynagi	7.2		60	6.68	0	Spring
13	711587	4344202	1857	Yali Golu- Oglakci Koyu	9.2	1	105	6.73	0	Spring
14	700947	4346658	1936	Seki Koyu Kaynagi	9.2	1.8	90	6.93	0	Spring
15	710297	4346997	2089	Cadir Baba Kaynagi	6.7	1	63	7.09	0	Spring
16	709989	4348552	2147	Seki Koyu Seker Kaynagi	4.9		51	7.34	0	Spring
17	717689	4342614	1940	Deregolluk Kaynaklari	7.5	1.5	87	7.11	0	Spring
18	717105	4343680	1901	Kamerkomu Maden suyu	13.2	0.5	719	5.41	0.1	Mineral Water
19	717105	4343680	1901	Hotan Deresi	6.0	150	63	7.30	0	Surface Water
20	713930	4344827	2120	Hotan Kaynagi	5.4	1.5	52	6.42	0	Spring

5.3.1. Isotope composition of water samples

$\delta^{18}O$ (‰) and $\delta^{2}H$ (‰) composition of the selected samples is essential to explore whether or not they are meteoric or processed waters. Craig (1961) demonstrated that the δ18O (‰) and δ2H (‰) ratios of meteoric waters (precipitation, river and lake samples from various countries) fit to a line known as the global meteoric water line (GMWL) represented by the formula in Eq. (12).

$$\delta D = 8\delta^{18}O + 10 \quad (12)$$

However, $\delta^{18}O$ and δD values at any locality are strongly dependent upon distance from the ocean (continental effect), latitude and altitude (Nicholson, 1993). Thereby, regional (RMWL) and especially local meteoric water lines (LMWL) are convenient references for understanding local groundwater isotope variations with reference to local meteoric waters (Mazor, 2004). Isotope signatures of groundwater can shift from meteoric water lines to schematic trends designating processes; each process represents a shift in isotopic composition to the extent that $\delta^{2}H$ as well as $\delta^{18}O$ enriched. Isotope processes can be separated as surficial and deep processes including surface evaporation for the former; and water-rock interaction, steam heating and boiling for the latter respectively. Groundwater influenced by these processes is defined as processed water mentioned in the first line of this section. To explore whether the selected samples are processed or not, selected RMWLs (Gat, 1983; Eisenlohr, 1995) and LMWLs (Sayın and Eyüpoğlu, 2005) are used (Eq. (13)) and the site data given in Table 3 are plotted (Fig. 8).

$$\delta D = 8\delta^{18}O + 22.00 \text{ (Eastern Mediterranean)}$$

$$\delta D = 8\delta^{18}O + 16.00 \text{ (Marmara)}$$

$$\delta D = 8\delta^{18}O + 10.00 \text{ (Global \& Central Anatolia)}$$

$$\delta D = 8\delta^{18}O + 11.36 \text{ (Dalbahçe-Erzurum)}$$

$$\delta D = 8\delta^{18}O + 14.87 \text{ (Şenyurt-Erzurum)} \quad (13)$$

The data are separated as thermal and cold waters in the diagram and clustered between the RMWL of Eastern Mediterranean and Marmara. Isotope signatures of the site data do not show any trend indicating processes.

The activity of $\delta^{3}H$ indicates groundwater circulation time consumed from recharge to discharge and can be simply stated that as the

Table 2
Major anion and cations in water resources around the study area.

NO	Na^+ mg/L	K^+ mg/L	Mg^{2+} mg/L	Ca^{2+} mg/L	Cl^- mg/L	NO_2^- mg/L	NO_3^- mg/L	PO_4^{3-} mg/L	$SO_4^{=}$ mg/L	CO_3^- mg/L	HCO_3^- mg/L	Li^+ mg/L	F^- mg/L	Br^- mg/L
1	6.34	2.44	7.82	25.03	2.55	0.00	6.56	0.00	4.40	0.00	110.91	0.00	0.05	0.00
2	970.00	77.15	177.38	218.69	1076.99	0.00	4.22	0.00	38.70	0.00	1971.72	1.26	0.13	0.91
3	335.25	30.35	83.48	100.42	208.93	0.16	0.49	0.00	15.26	0.00	1139.04	0.50	0.38	0.12
4	269.07	25.78	182.74	189.52	77.31	0.00	0.51	0.00	0.86	0.00	2069.68	0.75	0.17	0.07
5	269.04	30.99	118.06	115.20	102.94	0.00	0.39	0.00	11.89	0.00	1391.91	0.60	0.21	0.16
6	3.85	0.84	2.67	26.49	0.55	0.01	6.02	0.00	1.56	0.00	89.34	0.00	0.06	0.00
7	2.64	1.14	2.10	7.08	0.27	0.00	2.06	0.03	0.86	0.00	33.89	0.00	0.04	0.00
8	225.05	34.00	131.36	200.65	37.44	0.00	0.00	0.00	20.09	0.00	1688.28	0.40	0.15	0.00
9	22.13	6.07	50.52	90.75	3.53	0.09	0.29	0.00	9.54	0.00	532.98	0.02	0.19	0.00
10	5.66	1.89	5.57	15.72	0.75	0.00	4.82	0.12	1.50	0.00	77.02	0.00	0.09	0.00
11	4.12	2.30	4.47	14.87	1.06	0.00	5.20	0.14	2.00	0.00	73.94	0.00	0.04	0.00
12	2.68	1.23	2.47	13.22	0.28	0.00	1.99	0.00	0.83	0.00	58.60	0.00	0.04	0.00
13	4.08	1.29	4.38	13.28	0.53	0.00	5.33	0.04	1.49	0.00	70.92	0.00	0.04	0.01
14	3.68	1.36	3.58	16.07	0.63	0.00	5.83	0.02	1.67	0.00	67.78	0.00	0.03	0.00
15	2.63	1.55	2.41	8.45	0.51	0.00	3.19	0.02	2.03	0.00	36.91	0.00	0.02	0.00
16	2.35	1.06	2.08	7.06	0.23	0.00	3.14	0.00	0.78	0.00	33.83	0.00	0.01	0.00
17	4.78	0.97	2.60	12.69	0.44	0.00	2.13	0.00	1.55	0.00	58.54	0.00	0.05	0.00
18	52.80	18.58	27.47	84.29	4.05	0.00	0.00	0.00	6.44	0.00	499.09	0.06	0.21	0.00
19	3.24	1.38	2.08	7.53	0.29	0.04	1.33	0.00	0.85	0.00	36.91	0.00	0.05	0.00
20	2.59	1.34	1.61	8.08	0.29	0.00	3.01	0.00	0.99	0.00	33.89	0.00	0.04	0.00

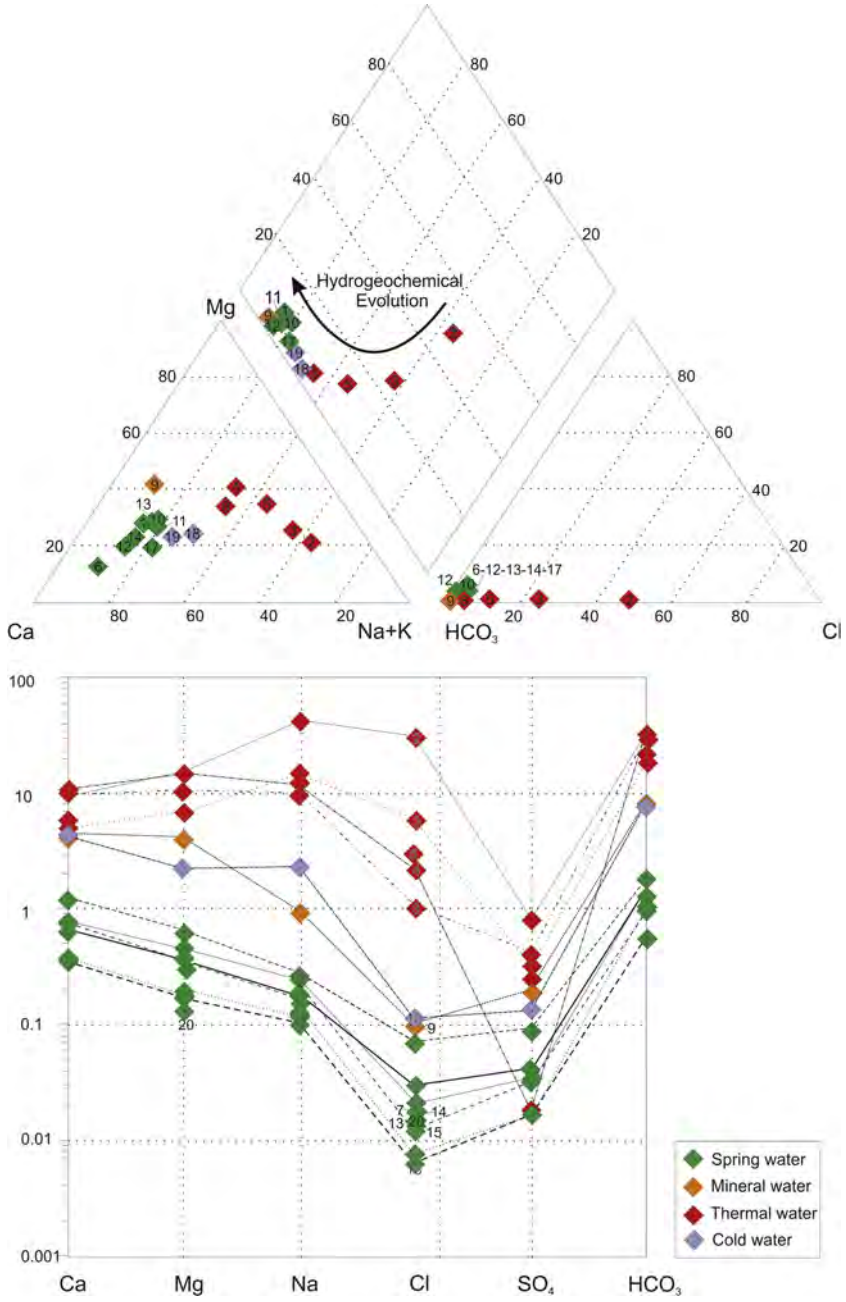

Fig. 4. a) Piper and b) Schoeller diagrams for the water resources in the study area. The red dots: thermal water, green dots: spring water, yellow dots: mineral water and blue dots: cold water (For interpretation of the references to colour in this figure legend, the reader is referred to the web version of this article.).

lower the δ^3H activity in groundwater, the older it is or it has taken a longer route. This statement is applicable under the assumption of the piston flow model (no dispersion or mixing between different aged flow paths; see Kazemi et al., 2006 for details). In this model, the passage of time through which the activity of ^3H decreases can be calculated by the decay law in Eq. (14) (Kresic, 2007).

$$^3H_s = {}^3H_o e^{-\lambda t} \quad (14)$$

where ^3H_s is the amount of ^3H in the sample, ^3H_o is the activity of ^3H in precipitation, and λ is the decay constant of tritium of 0.056 year^{-1}. In this equation, the most important point is to determine the δ^3H activity in precipitation, essentially needed for the use of δ^3H as a tracer of groundwater circulation time. Therefore, the activity of δ^3H atoms in precipitation water should be measured to determine peak values of natural δ^3H activity. These types of measurements are related to thermonuclear testing begun in 1952 (Kazemi et al., 2006). During the tests, large quantities of tritium were released into the atmosphere; hence, natural δ^3H in precipitation between 5 and 20 tritium units (TU) stated by Kaufmann and Libby (1954) reached up to several thousand TU in precipitation (Mazor, 2004). To sum up, in the year 1952 the start of thermonuclear tests provided an indicator to determine pre and post-1952 recharge entering into aquifers. To estimate pre and post-1952 recharge at the site, δ^3H values in Table 3 are used.

The results indicate that δ^3H values lower than 6 TU indicate mixing of pre and post-1952 recharges, whereasvalues higher than 6 TU are a sign of post-1952 recharge. Except for the spring labeled 1 which indicates cold water (post-1952), all thermal waters are mixed with cold waters. In conclusion, although thermal water samples cluster in steam-heated/condensates and dilute Cl-HCO_3 sectors on the Cl-SO_4-HCO_3 ternary plot (Fig. 9) they do not shift from meteoric water lines.

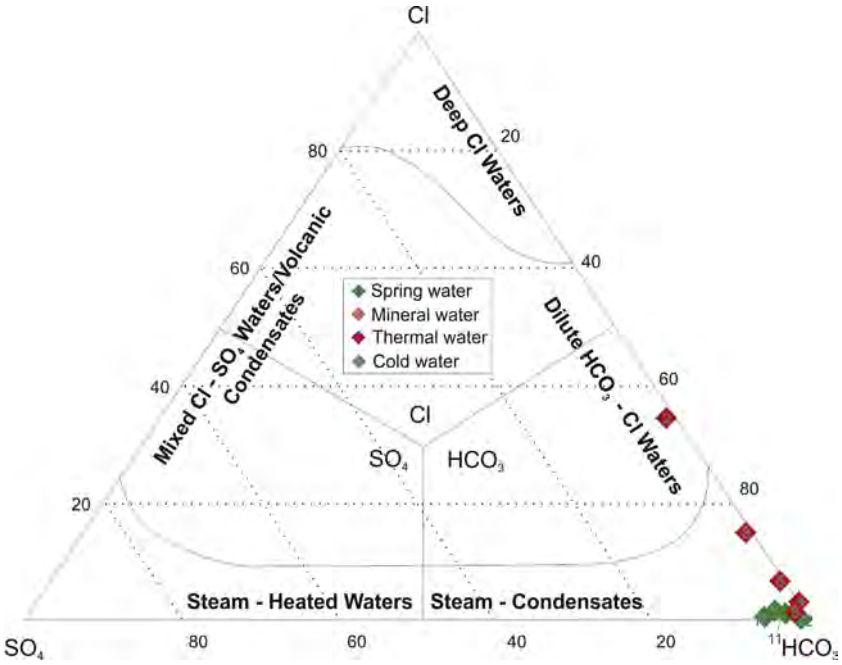

Fig. 5. Cl-SO_4-HCO_3 Ternary diagram for the water resources in the study area.

Therefore, steam-heated conditions are available for the site but for robust checking, solute geothermometers were used. It was expected that the host rock temperature is lower than that at steam condensate conditions.

5.3.2. Application of geothermometers to the site data

Chemical analyses of geothermal fluids can be used to estimate subsurface reservoir temperature. The results are given in Table 4. For robust checking, appropriate solution geothermometers given are explained by providing Giggenbach (1988) and SI diagrams (Reed and Spycher, 1984). The ternary plot of Na/1000–K/100–$Mg^{1/2}$ of

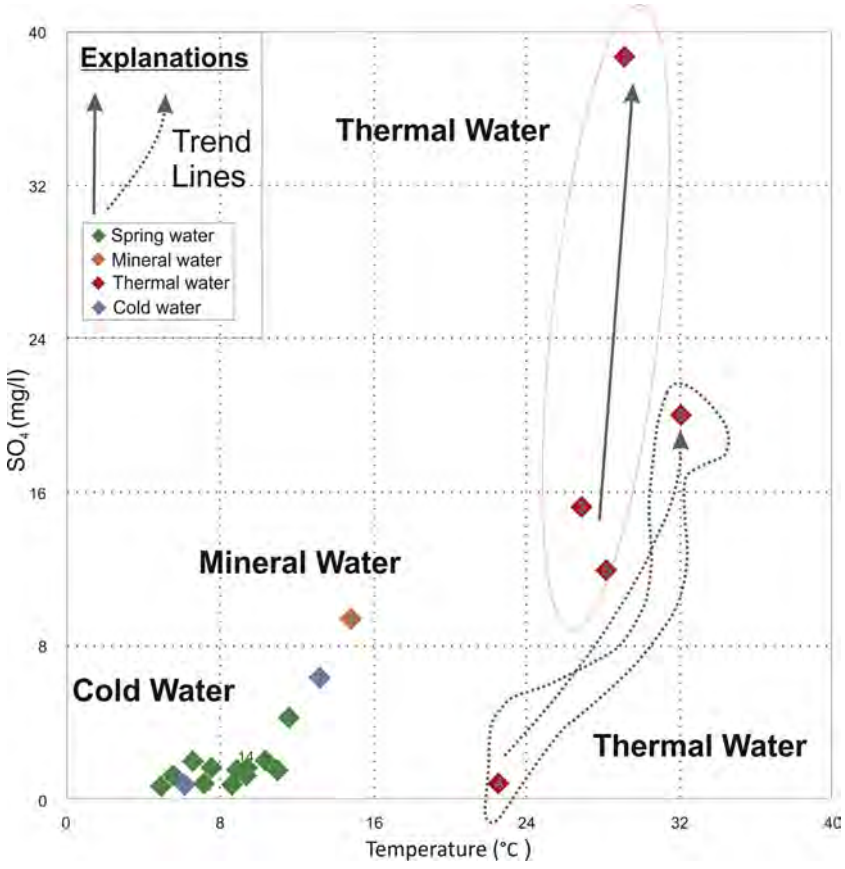

Fig. 6. Scatter diagram and trend lines for the water resources in the study area.

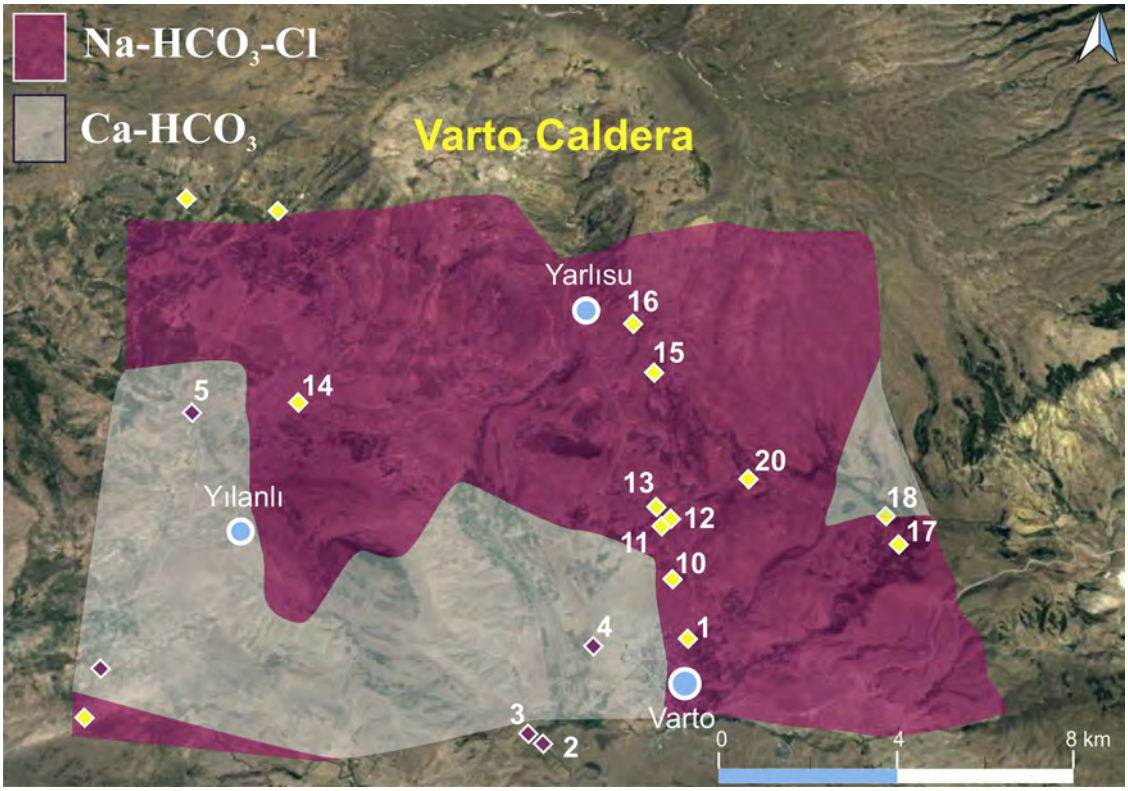

Fig. 7. Hydrogeochemical facies map of the site.

Table 3
Isotope values of the selected samples.

Sample No	$\delta^{18}O$ (‰)	$\delta^{2}H$ (‰)	$\delta^{3}H$ Values (TU)
1	−10.59	−65.86	6.40
3	−12.51	−82.50	0.40
4	−12.48	−78.47	0.00
5	−12.17	−79.81	0.95
8	−12.50	−80.41	0.20

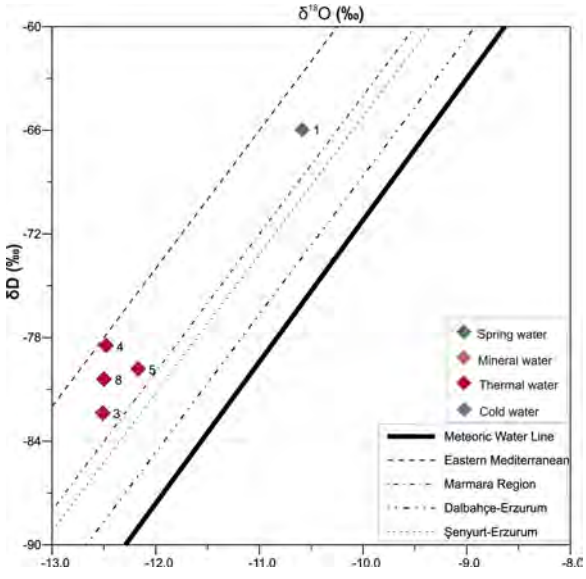

Fig. 8. $\delta^{18}O$ versus δD diagram for the thermal waters in the study area.

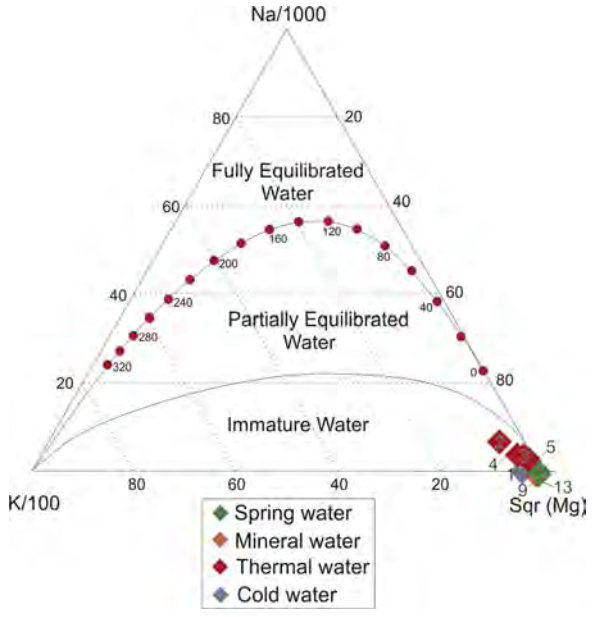

Fig. 9. Thermal waters on Na-K-Mg Triangle diagram for the study area.

Table 4
Reliable solute geothermometers results.

Geothermometers	Reference	*2	*3	*4	*5	*8
Silica (β-Cristobalite)	Fournier (1991)	54	55	55	70	80
Li-Mg	Kharaka and Mariner (1989)	66	54	54	54	44

* All calculated values are in °C.

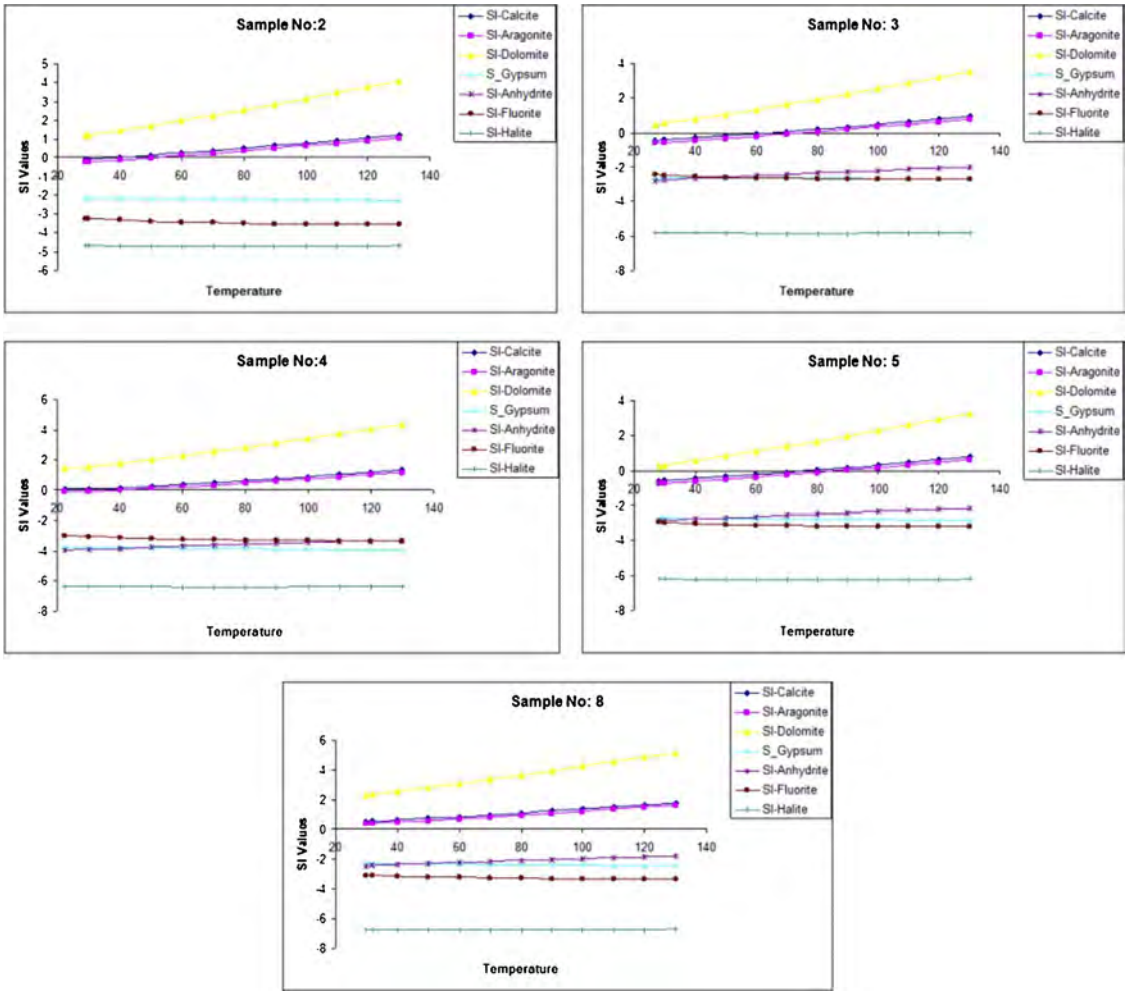

Fig. 10. Changes in the selected mineral saturations of thermal waters at different temperatures in the Varto Geothermal Region.

Giggenbach (1988) is a method to discriminate mature waters which have attained equilibrium with relevant hydrothermal minerals from immature waters and waters affected by mixing and/or re-equilibration at low temperatures during their circulation (Fig. 9). All samples plotted in the immature water zone in Fig. 9. Reservoir temperature values estimated by this method are invalid because thermal waters mix with some proportions of both cold and mineral waters. Na-K geothermometers thus provide unacceptable results for groundwater samples from this site.

A different approach to geothermometry (Reed and Spycher, 1984) is illustrated in Fig. 10, where SI (Saturation Indices) are computed as a function of temperature. In the calculation of the mineral saturation indices, the PhreeqC code (Parkhurst and Appelo, 1999) was used. It is easy to note that thermal waters are saturated with respect to dolomite, calcite and aragonite between 50 °C and 80 °C, thus suggesting this range of temperature as reliable for the deep geothermal reservoir temperature (Baba et al., 2010).

5.4. Thermal numerical modeling setup

In order to investigate magma heat transfer and fluid circulation a series of models is created that replicate the heat from a crustal shallow magma chamber which is overlain by a series of faults. The geometry of the models is based, as closely as possible, on the geology of the region. The various mechanical properties that are input into the models are investigated to obtain the most realistic outputs in terms of surface water temperatures. In the first set of models, shown in Fig. 11, vertical fault zones are simulated, each with a different permeability (k). The fault connects a magma chamber with an internal temperature of 900 °C to the surface, the geometry of the magma chamber is not generated and so we simply assign a 'hot' boundary. The surface temperature in this model is defined as with atmospheric conditions and so is 25 °C. The bottom of the model is defined with magma chamber conditions and so the given pressure and temperature conditions in this area are 10 MPa and 900 °C respectively, based on an intermediate magma composition (Murase and McBirney, 1973). The lower boundary is fixed, and both the left and right boundaries have no additional load but they are allowed to deform. The upper boundary is a free surface (a region free from shear stress). We present four models of this type (Fig. 11 a,b,c and d) to show the effect of permeability which varies across a narrow range (from 1×10^{-15} in part a to 4.3×10^{-15} in part d) of fluid velocities. Fluid rises in this model as we impose a temperature gradient of 25 °C / km. As such the body temperature in the model varies over distance according to the equation T = (D.x) + 25.

In Fig. 12 we extend the results from Fig. 11 to investigate the effects of both fault width and fault permeability on heat transfer within the fault. In total we present 18 models, with six different permeabilities (1.0×10^{-15} m^2 – 4.3×10^{-15} m^2) and three different fault widths (1 m, 5 m and 10 m). The models are designed with permeability steps of 0.1×10^{-15} m^2 and fault width steps of 0.1 m between the minimum and maximum ranges. In total, 430 different permeabilities over 100 different fault widths were investigated, here we present 18 representative model results from the full suite of model runs. We run the models to obtain a surface temperature of around 50 °C so as to

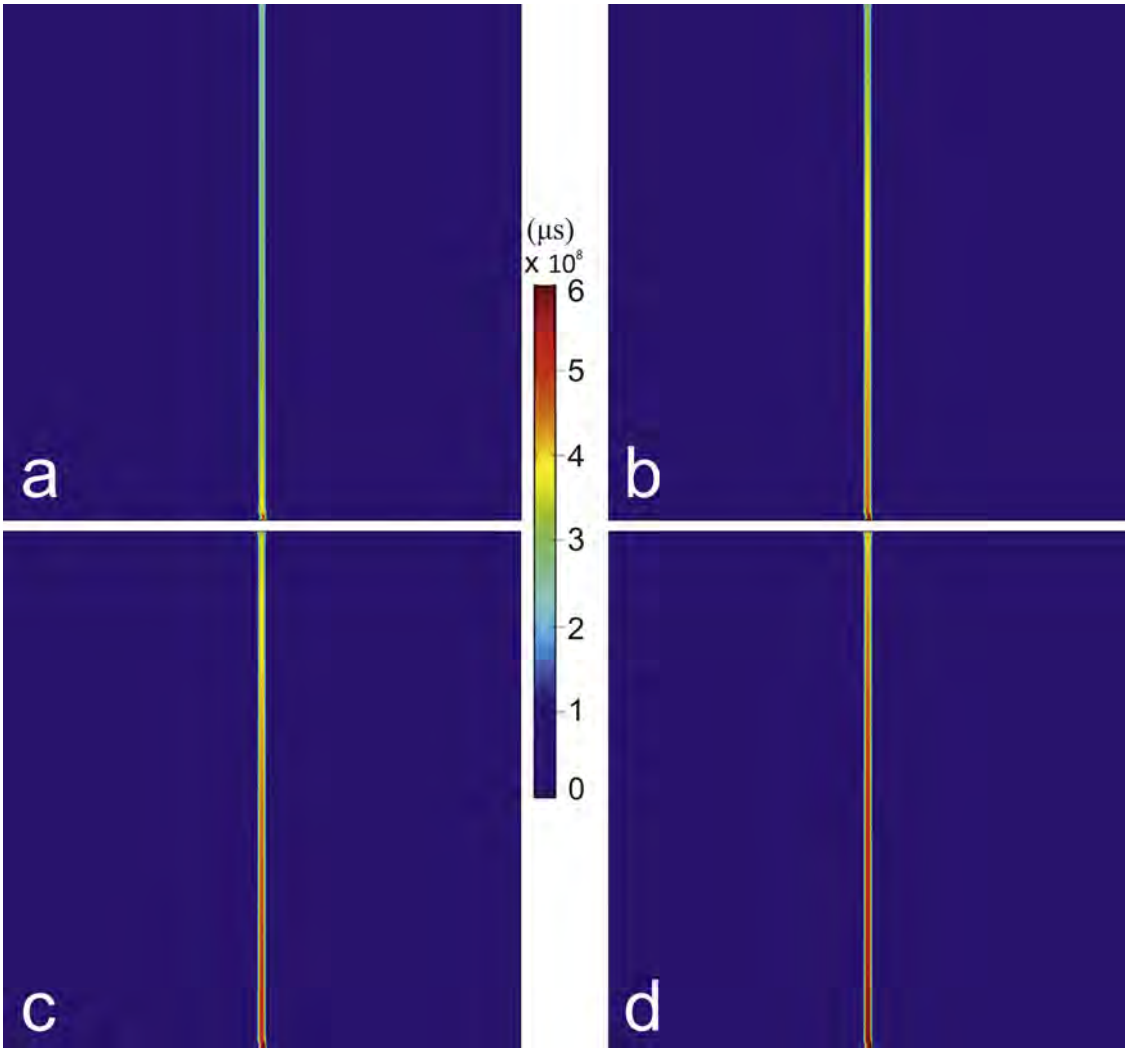

Fig. 11. Fluid velocities as a function of permeability change. The fault in a) has a permeability of 1.0×10^{-15} m^2 in part b) has a permeability of 2.1×10^{-15} m^2, in part c) has a permeability of 3.2×10^{-15} m^2 and in part d) has a permeability of 4.3×10^{-15} m^2. In the model we also impose a temperature gradient from 900 °C at the base of the model to 25 °C at the surface. The maximum velocity field is found in the fault with the largest permeability as expected.

compare with the field results.

In Fig. 13 we present a series of linear elastic stress models. These models consider the effects of regional tectonic loading on the fault zones of the KTJ. We imported a surface plan view of the faults from geological maps (Karaoğlu et al., 2016) (Fig. 12a), and then assigned a boundary horizontal extension (Fig. 13b) or compression (Fig. 13c) of 5 MPa. The resulting models (Figs. 13b and 13c) show the concentration and linkage of tensile stresses around the faults.

In the next set of models (Figs. 14,15) we use the results from the baseline models presented in Figs. 11–12 and combine these with the geological setting of the Karliova region (Fig. 13). The faults in plan view (Fig. 13) are extrapolated throughout the crust based on a contant dip, and interactions are inferred (Karaoğlu et al., 2016). The boundary conditions in Fig. 15 are fixed with a constraint on the horizontal edges, a set pressure and temperature on the lower boundary and a free surface on the upper boundary. The deepest fault inferred is around 10 km, and so we set a pressure gradient of 10 MPa/km, and a temperature gradient of 25 °C/km. A porous medium with a very low permeability was defined as the host rock in order to prevent fluid leakage from the fault to the host rock. The system cannot model fluid losses and so heat transfer takes place only from the fluid to the solid. This happens while the fluid is passing within the fault as the model edges are fixed for any Y direction movements. For this reason, this model will not be affected by the fault zone to the right or left side of the model or by any effect from these two sides of the medium.

In Fig. 15, we plot the fluid velocity field in several orientations although the fracture network that creates the permeability is assumed to be isotropic. This is a limitation that we seek to investigate further in the future as it is well known that fault zones in complex tectonic regimes may be overprinted with anisotropic fracture networks (e.g., Browning et al., 2018).

6. Results

6.1. Fluid and solid interactions

In order to better understand fluid and heat transport throughout crustal structures such as permeable faults, we created models to investigate the effects of fluid and heat transfer (Figs. 11 and 12). In Fig. 11 we show how fluid velocity changes within the fault zones as a function of permeability. These models represent fluid at pressures of 10 MPa injected into the fault (Fig. 11). The fault zone has a fixed size but the permeability varies by a factor of four. Permeability values are 1×10^{-15} m^2 to 4.3×10^{-15} m^2. In all the models the fastest velocities are found in the centre of the fault (assuming a homogenous fracture network), simulating a Poisuelle like flow. In the faults with the lowest

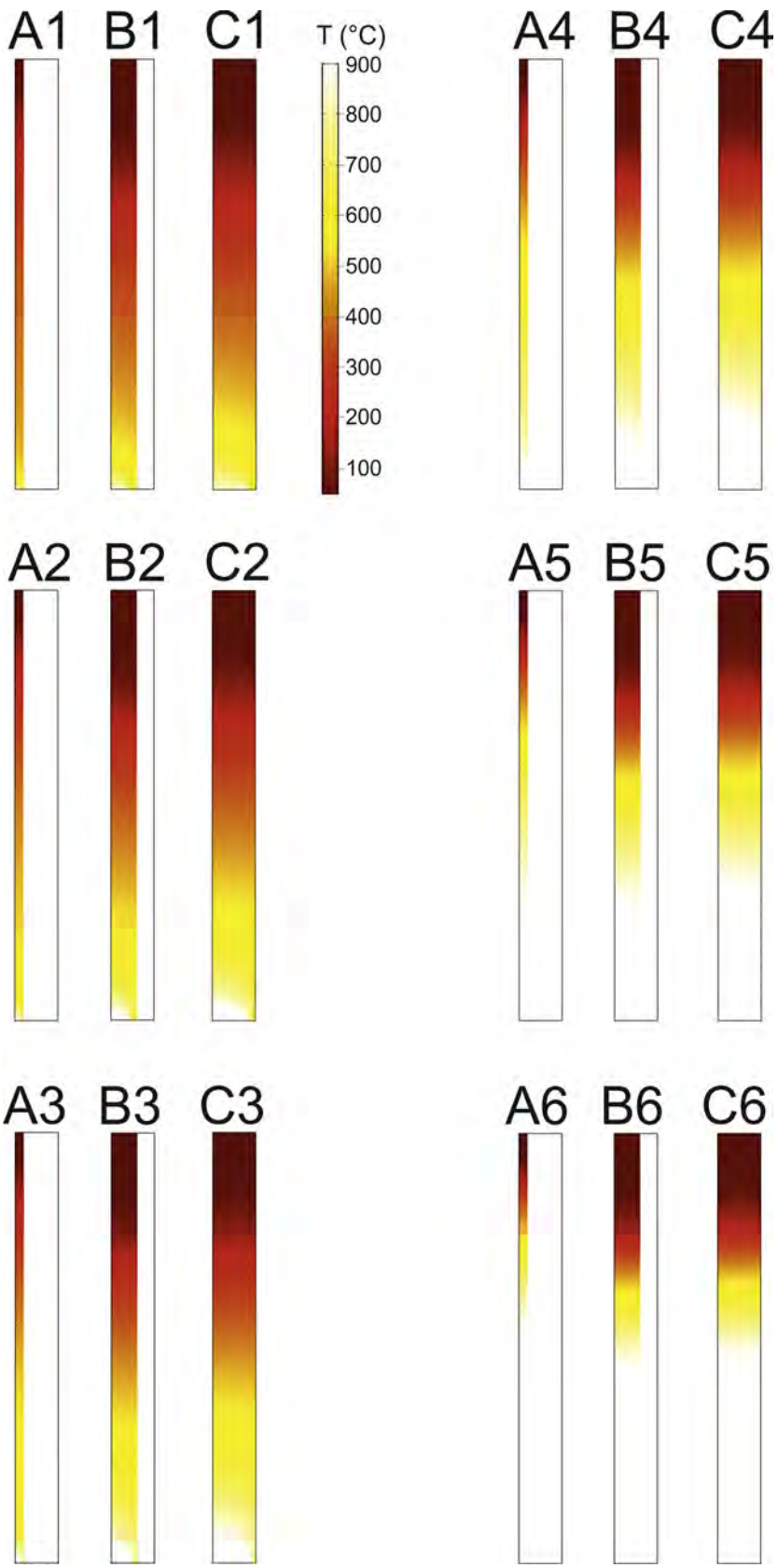

Fig. 12. Fluid heat loss in the modelled fault as a function of fault width (L), and permeability (k). The three different fault widths shown are 1 m, 5 m and 10 m. The six different permeabilities (k) shown are 1) $1.0 \times 10^{-15}\,m^2$, 2) $1.5 \times 10^{-15}\,m^2$, 3) $2.1 \times 10^{-15}\,m^2$ 4) $2.7 \times 10^{-15}\,m^2$, 5) $3.2 \times 10^{-15}\,m^2$, and 6) $4.3 \times 10^{-15}\,m^2$.

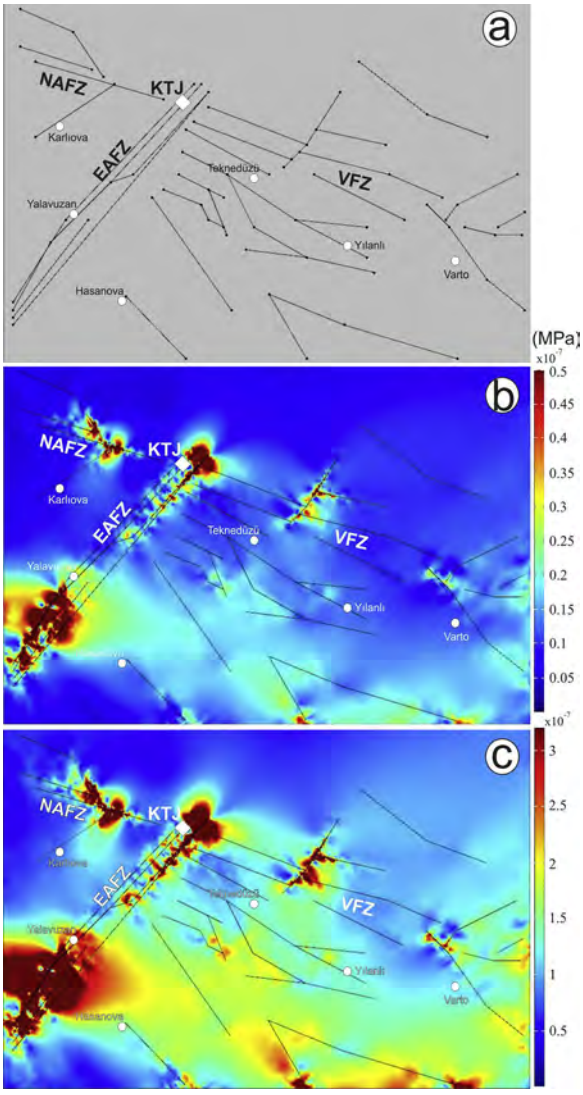

Fig. 13. a) Surface view of the model setup where the lineations simulate faults based on the geological setting along the Karlıova Triple Junction region. The only loading in these models is regional horizontal extension or compression. b) Modelled minimum principal compressive stresses induced from regional horizontal extension of 5 MPa. c) Modelled minimum principal compressive stresses induced regional horizontal compression of 5 MPa. NAFZ: North Anatolian Fault Zone, EAFZ: East Anatolian Fault Zone, VFZ: Varto Fault Zone, KTJ: Karlıova Triple Junction.

Fig. 14. A two dimensional vertical cross-section through a N–S striking profile of the faulted region around Varto caldera. The fault geometry is used as the model setup where each fault is assigned a different permeability. In all cases the top surface is unconstrained, whereas the x and lower y boundaries are fixed. The lower boundary of the model is assigned a starting temperature of 900 °C and the upper surface (free surface) is set at an atmospheric temperature of 25 °C.

permeabilities (Fig. 11a and b) the initial fluid velocity decreases almost immediately after fluid injection and is sustained for a maximum of 40% of the fault length. However, when the permeability is increased (even if only by a factor of 4) the initial injection fluid velocity is sustained for almost the entire length of the fault (Fig. 11c and d).

The rate at which fluids can pass through the fault network obviously has impllications for how quickly heat within the fluid and/or gas is transferred to the surrounding rocks. Essentially when a fluid or a gas is flowing with a high velocity, there will be less interactions with the rock body so less heat is transferred to the porous medium. In Fig. 12 we consider this problem by presenting models that investigate how the temperature of the fluid with an initial magma temperature of 900 °C interacts with the body (crustal rocks) while it moves vertically through the fault to the surface (Fig. 12). Over the 10 km of the fault the fluid loses almost allit's heat, around 875 °C depending on the permeability of the fault. We find, in all cases, that fault width has little effect in changing the temperature distribution. It is clear that the hot zone in part A5 (Fig. 12) is 4 times higher than A1 (Fig. 12). In A1 (Fig. 12), the temperature decreases rapidly to 700 °C (within a few tens of metres). In Fig. 12, part A6, the fluid remains with a temperature of 900 °C for almost 50% of the fault length. The body (crust) of the model medium uses the elastic parameters of Young Modulus (E) 40 GPa, Poisson's ratio 0.25 and a density of 3300 kg/m^3. The fluid thermal conductivity is 6[W/(m*K)], the fluid ratio of specific heat is 1, and the fluid heat capacity at constant pressure is 4200[J/(kg*K)]. The heat transfer coefficient, heat convection and heat conduction will all affect the fluid flow in the fault.

Both these models show that the properties of the material within the fault and their respective damage characteristics have significant effects on controlling the movement of both fluid and heat.

6.2. Stress intensity around the Karlıova triple junction

In order to better understand the mechanical relations between stress intensity and thermal fluid discharge to the surface, a series of stress models were created (Fig. 13). These models are very important in terms of identifying the location of thermal fluid outflow points as tensile stress intensity may indicate areas of fracture and fault dilation and hence increased permeability. The stress concentration models show that the main faults (e.g. NAF, EAF and VFZ) are zones of maximum stress concentration and are thereby likely to control the majority of fluid flow within the region (Fig. 13). During periods of regional extension associated to extrusion of the Anatolian plate we find that the main result is that a NE-SW strike is dominant for the main crustal strain deformation (e.g., Karaoğlu et al., 2017, Fig. 3 and b). During periods of regional compression we find a N–S compressional deformation is the main driving deformation process in the Karlıova Triple Junction (e.g., Karaoğlu et al., 2017, Fig. 3 and c).

6.3. Fluid circulation models in the KTJ

To investigate fluid circulation throughout the upper crust for the specific case of the KTJ, some additional models were developed (based on heat transfer and velocity considering the geological setting around the KTJ, Figs. 14 and 15). In this model, velocity changes were observed in the fault zone based on permeability changes. The velocity changes in each fault show how it is possible to have fluid flowing inside that fault. It is very important to determine why hot fluid concentrates in some areas and not in others. Rivers are fed by both hot and cold waters sourced from underground but the situation is even more complex as some of the rivers are relatively close to each other. This is one of the challenges that we attempt to deal with using geomechanical rationale which highlights why both hot and cold fluids can form over very narrow areas (Fig. 2). The origin of hot waters can then be discussed but for this discussion it is necessary to return and use model setups from the model series A–C (A1-6) (Fig. 12).

In Fig. 15 we present the pressure changes within the faults (Fig. 15 A1-B1), the resulting fluid velocities (Fig. 15 A2-B4), and the temperature field (Fig. 15 A5-B5). In Fig. 15 A1-B1 we note that pressure concentrations around the faults increase from this deformative fault zone at outer province. This pressure value reaches to 6 MPa through the upper crust where the western part of the KTJ is (Fig. 13 A1-B1).

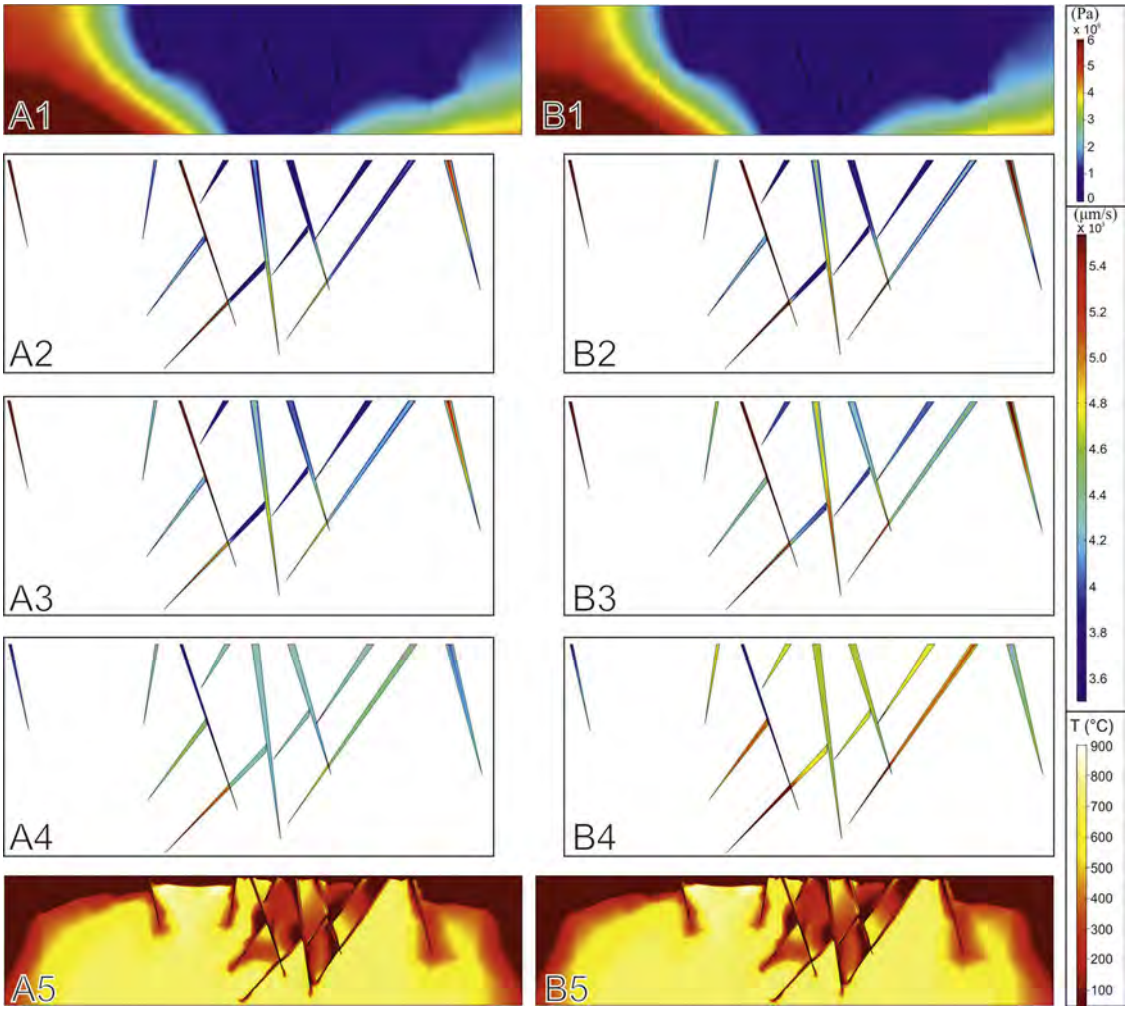

Fig. 15. Fluid circulation in the fault zones around the Karlıova region. A1) regional pressure at permeability 1×10^{-15} m^2, B1) regional pressure at permeability 4.3×10^{-15} m^2, A2) Fluid velocity within a fault of permeability 1×10^{-15} m^2, B2) Fluid velocity within a fault of permeability 4.3×10^{-15} m^2, displaying the total velocity field in both cases. A3) Fluid velocity within a fault of permeability 1×10^{-15} m^2, B3) Fluid velocity within a fault of permeability 4.3×10^{-15} m^2, displaying only the x direction (horizontal) flow in both cases. A4) fluid velocity within a fault of 1×10^{-15} m^2, B4) fluid velocity within a fault of permeability 4.3×10^{-15} m^2, displaying only the fluid velocity in the y direction (vertical) in both cases. A5) temperature field at permeability of 1×10^{-15} m^2, B5) temperature field at permeability of 4.3×10^{-15} m^2.

The minimum pressure value of 1 MPa (maximum) is characteristic for the fault zone (Fig. 13 A1-B1).

In Fig. 15 A2-B4 we compare the effects of different permability values on fluid velocity. The main finding is that increasing the permeability increases the fluid velocity at faults (Fig. 15 B2-B4). Applying a value of the 4.3×10^{-15} m^2 rather than 1×10^{-15} m^2, which is in the total velocity field, clearly demonstrates the effect of the fluid velocity within these faults. We note that a fault placed at the eastern side of the section show a value from 5.0 to 5.6 $\times 10^3$ μm/s (Fig. 15 A2-B2). Such an effect can be observed in all faults (Fig. 15 A2-B2). In Fig. 15 A3-B5 in the E–W profile we apply vertical and horizontal fluid velocity cases. We note again that there is a substantial incremental change between vertical (Fig. 15 A3-B3) and horizontal cases (Fig. 15 A4-B4). While this fluid velocity value is around 5.4 $\times 10^3$ μm/s (Fig. 15 B3), the values around 4.4 $\times 10^3$ μm/s (Fig. 15 B4).

Our numerical model indicate that the temperature field show markedly greater values around the fault zone (Fig. 15 A5-B5). These value reach to 900 °C particularly in the deeper zone, whilst the temperature show a decrease (between 100–300 °C) where the cross faults interact to each other (Fig. 15 A5-B5). We note that there is no substantial effect of the changing of permability values on temperature field (Fig. 15 A5-B5).

In this model, it can be observed that pressure is relatively constant at different permeabilities and so the temperature does not change dramatically. The temperature inside the fault zone changes similar to the model in Fig. 15 (A5 and B5). The model also displays how permeability in the fault zone affects fluid circulation, while there is no substantial impact on the solid porous matrix.

7. Discussion and conclusions

Kinematic data is a very useful tool to better understand the episodic deformational fields and fluid circulation interactions throughout the crust underneath the KTJ region (Fig. 3). Field studies coordinated with kinematic data show that the complexity of these fault deformations indicate variations in the local stress field following initial activity of a westward extrusion of the Anatolian plate since 6 Ma. The direction of the compressive principal stress (σ_1) has been shifted during this deformational period. This direction and local stress fields imply major controls of both magmatic fluids on magma propagation as an individual volcano, or fluid circulation throughout the crust in the region (Fig. 3).

Since Late Miocene, deformation of the KTJ has been controlled by the combined effects of continuing compressional tectonics due to a

regional shortening of Eastern Anatolia. This shortening is represented by a local stress field, and the westward displacement of Anatolia, which has kinematically responded through a local extensional stress field and coincides with transtensional tectonics (Fig. 3). In this framework, a successive and reactive tectonic motion has caused the incremental complex movement of numerous fault blocks which have resulted in mostly non-thermal but rarely thermal fluid circulation within intensely-deformed crustal materials. This is illustrated by the local stress fields and thermal and non-thermal spring points (Fig. 3). We note that non-thermal fluids are likely concentrated around zones of high minimum principal compressive (maximum tensile) stress (σ_3) (Fig. 3). Although these zones are expected as sources for thermal waters, the non-thermal waters like thermal waters tend to also circulate within the upper crust. These non-thermal waters may therefore be circulating in open fractures and faults in the upper level of the crust, but have not yet been subject to heating processes. Thus, these non-thermal waters may be temporally younger than other thermal water sources.

The fault stations of F3, 5, 8, 11, 15 and 16 show that an extensional regime agrees well with the location of non-thermal waters (Fig. 3). However, both non-thermal and thermal waters are found to circulate not only in extensional but also in compressional regimes (Fig. 3). So, the combined field and numerical studies show that crustal heterogeneity in the form of faults, as well as fault attitude and mechanical properties of both the crust and crustal faults, below the KTJ encourage fluid circulation in the region.

Field data and results from a suite of numerical modeling tests indicate that thermal water transport is influenced by the depth of intruded magmas and the permeability of crustal faults in the upper crust.

Magma chamber location plays a prominent role in the surface discharge of hot water around the Varto region (Fig. 1b). The thermal water discharge points are located just between the Varto caldera to the north, and the Özenç volcano to the east (Fig. 2). Numerical models indicate that maximum tensile and shear stresses concentrate at the lateral margins of magma chambers and at the Earth's surface above the magma chamber (see Karaoğlu et al., 2016). These stress accumulation zones are directly associated with thermal water circulation through the crust (Fig. 13). So, these thermal water locations in the region might be related to this stress intensity and fluid interaction. In volcanoes worldwide, the thermal water cycle might be used to indicate the lateral margins of magma chambers as zones of increased faulting and fracturing.

Hydrogeochemistry of the samples indicates that thermal water springs are likely heated by steam. Field studies, hydrogeochemical data and numerical models suggest that the magma systems beneath both the Varto caldera and the Özenç volcanoes are the main heat source for thermal water in the Varto region.

The results reveal that most water in the study area comes from the outcropping volcanic rocks in the Varto Region. The rocks demonstrate typical characteristics of water resources which originate in highly fractured volcanic formations where water seeps through cracks and faults and flows to the surface at lower elevations. On the basis of major ion chemistry, the Piper and Schoeller diagrams (Fig. 4) show that the majority of the cold water resources are of the Ca-HCO_3 type and the thermal water of the Na-HCO_3-Cl type. As the fractures allow a deep circulation of groundwater and a dominant NA–Cl component, we infer that the waters have a volcanic origin. However, the hot waters have the same recharge area as the cold waters. Reliable reservoir temperature ranges for hot waters were obtained with Li-Mg and β-Cristobalite geothermometers as 44–66 °C and 54–80 °C, respectively. These values were also checked with Saturation Indices (SI) vs T diagrams. Results of SI vs T diagrams indicate equilibration with calcite and aragonite. The result shows that jointed volcanic rocks are a reservoir for the geothermal system and that the heat source for the geothermal fluid is the magma chamber.

Fluid and solid interactions and fluid circulation models show the role of fault permeability on heat loss during fluid circulation. Also Fig. 12 illustrates what happens to fluid heat loss when the fault permeability and fault width changes. The main boundary condition is the constant injection pressure of 10 MPa. As the pressure is constant and dependent on the injecting boundary, fault width has no obvious effect. The permeability ranged from 1×10^{-15} to 4.3×10^{-15} m^2. When the fault permeability increases, heat loss from 900 °C to 50 °C takes place over a longer distance. In Fig. 15, the model is a combination of two previous models. The same effect of changing permeability of the fault was investigated in a porous medium. The model illustrated that increasing permeability from 1×10^{-15} to 4.3×10^{-15} m^2 can significantly affect the fluid pressure drop. Fluid injected at pressure declines from 10 MPa to atmospheric pressure over a smaller distance when the permeability is very low. The additional physical parameters added to Fig. 15 is the porous medium body temperature, and also the effects of stress and strain on fluid circulation in the porous medium where observed. These effects usually have little or no impact. However, those effects are very substantial and visible near the boundary area of the fault zone and the porous medium. In these models the detailed structural geology and fault zone are presented to illustrate how a relatively small permeability variation from 1×10^{-15} to 4.3×10^{-15} m^2 can significantly affect fluid circulation in fault zones. The result is important as the permeability of fault zones can be heterogeneous (Mitchell and Faulkner, 2009) and so for a proper understanding of geothermal resources and hot water fluid circulation this must be considered.

Acknowledgements

This study was supported by funds from Eskisehir Osmangazi Üniversitesi (Project Numbers: 201715031 and 201715A215). Özgür Karaoğlu was supported by The Scientific and Technological Research Council of Turkey (TÜBİTAK) International Postdoctoral Research Fellowship Programme. Mohsen Bazargan was supported by Weld On Sweden for European Doctoral research programme. We are grateful to the editor Eva Schill and three anonymous reviewers, for comments which improved this work.

Appendix A. Supplementary data

Supplementary material related to this article can be found, in the online version, at doi:https://doi.org/10.1016/j.geothermics.2019.05.003.

References

Ambraseys, N., Zatopek, A., 1968. The Varto Ustukran earthquake of 19 August 1966. B. Seismol. Soc. Am. 58, 47–102.
Armijo, R., Meyer, B., Hubert-Ferrari, A., Barka, A.A., 1999. Propagation of the North Anatolian fault into the Northern Aegean: timing and kinematics. Geology 27, 267–270.
Attendorn, H.G., Bowen, R., 1997. Radioactive and Stable Isotope Geology. Chapman and Hall, London, pp. 519.
Baba, A., Yiğitbaş, E., Ertekin, C., 2010. Hydrogeochemistry of geothermal resources of eastern part of turkey: a case study, Varto Region. World Geothermal Congress 2010 1–8.
Baker, E., 1995. Characteristics of hydrothermal discharge following a magmatic intrusion. Geol. Soc. (Lond.) Spec. Publ. 87, 65–76.
Baker, E.T., Urabe, T., 1996. Extensive distribution of hydrothermal plumes along the superfast spreading East Pacific Rise, 13 30′–18 40′ S. J. Geophys. Res-Sol. EA 101 (B4), 8685–8695.
Barka, A.A., 1992. The North Anatolian fault zone. Ann. Tecton. 6, 164–195.
Bozkurt, E., 2001. Neotectonics of Turkey-a synthesis. Geodin. Acta 14, 3–30.
Browning, J., Meredith, P.G., Stuart, C., Harland, S., Healy, D., Mitchell, T.M., 2018. A directional crack damage memory effect in Sandstone under true triaxial loading. Geophys. Res. Lett. 45, 6878–6886.
Buket, E., Temel, A., 1998. Major-element, trace element, and Sr-Nd isotopic geochemistry and genesis of Varto (Muş) volcanic rocks, Eastern Turkey. J. Volcanol. Geotherm. Res. 85, 405–422.
Caracausi, A., Ditta, M., Italiano, F., Longo, M., Nuccio, P.M., Paonita, A., Rizzo, A., 2005. Changes in fluid geochemistry and physico-chemical conditions of geothermal

systems caused by magmatic input: The recent abrupt outgassing off the island of Panarea (Aeolian Islands, Italy). Geochim. Cosmochim. Ac. 69 (12), 3045–3059.
Cherubini, C., Giasi, C.I., Pastore, N., 2013. Evidence of non-Darcy flow and non-Fickian transport in fractured media at laboratory scale. Hydrol. Earth Syst. Sci. 17 (7), 2599–2611.
Craig, H., 1961. Isotopic variations in meteoric waters. Science 133, 1702–1703.
Deutsch, W., Siegel, R., 1997. Groundwater Geochemistry: Fundamentals and Applications to Contamination. Lewis Publishers, New York.
Durbin, A., 1986. On the k-ε stagnation point anomality. Int. J. Heat Fluid Flow 17, 89–90.
Eisenlohr, T., 1995. Die Thermalwässer der Armutlu-Halbinsel (NW-Türkei) und deren Beziehung zu Geologie und Aktiver Tektonik, PhD. Dissertation, ETH-Zürich, Nr.11340.
Fournier, R.O., 1991. Water geothermometers applied to geothermal energy. In: D'Amore, F. (Ed.), Application of Geochemistry in Geothermal Reservoir Development. UNITAR, Rome, Italy, pp. 37–65.
Furlong, K.P., Schwartz, S.Y., 2004. Influence of the Mendocino triple junction on the tectonics of coastal California. Annu. Rev. Earth Planet. Sci. 32, 403–433.
Gat, J.R., 1983. Precipitation, groundwater and surface waters: control of climate parameters on their isotopic composition and their utilisation as palaeo climatological tools. Proceedings, Palaeoclimates and Palaeowaters: A Collection of Environmental Isotope Studies (Proc. Advisory Group Mtg Vienna, 1980) 3–12.
Giggenbach, W.F., 1988. Geothermal Solute Equilibria. Derivation of Na-K-Mg-Ca Geoindicators. Geochim. Cosmochim. Ac. 52, 2749–2765.
Giggenbach, W.F., 1996. Chemical Composition of Volcanic Gases. In Monitoring and Mitigation of Volcano Hazards. Springer, Berlin Heidelberg, pp. 221–256.
Herece, E., 2008. Atlas of East Anatolian Fault. General Directorate of Mineral Research and Exploration. Special Publication Series, Ankara, Turkey.
Hubert-Ferrari, A., King, G., van der Woerd, J., Villa, I., Altunel, E., Armijo, R., 2009. Long-term evolution of the North Anatolian Fault: new constraints from its eastern termination. In: van Hinsbergen, D.J.J., Edwards, M.A., Govers, R. (Eds.), Collision and Collapse at the Africa-Arabia-Eurasia Subduction Zone, pp. 133–154 Geol. Soc. Spec. Publ. 311.
Isik, V., Uysal, I.T., Caglayan, A., Seyitoglu, G., 2014. The evolution of intraplate fault systems in central Turkey: Structural evidence and Ar-Ar and Rb-Sr age constraints for the Savcili Fault Zone. Tectonics 33 (10), 1875–1899.
Italiano, F., Sasmaz, A., Yuce, G., Okan, O.O., 2013. Thermal fluids along the East Anatolian Fault Zone (EAFZ): geochemical features and relationships with the tectonic setting. Chem. Geol. 339, 103–114.
Karaoğlu, Ö., Browning, J., Bazargan, M., Gudmundsson, A., 2016. Numerical modelling of triple-junction tectonics at Karlıova, Eastern Turkey, with implications for regional magma transport. Earth Planet. Sc. Lett. 452, 152–170.
Karaoğlu, Ö., Sağlam-Selçuk, A., Gudmundsson, A., 2017. Tectonic controls on the Karlıova Triple Junction (Turkey): implications for tectonic inversion and the initiation of volcanism. Tectonophysics 694, 368–384.
Karaoğlu, Ö., Browning, J., Salah, M.K., Elshaafi, A., Gudmundsson, A., 2018. Depths of magma chambers at three volcanic provinces in the Karlıova region of Eastern Turkey. B.Volcanol. 80 (9), 69.
Kaufmann, S., Libby, W.F., 1954. The natural distribution of tritium. Phys. Rev. 93 (6), 1337–1344.
Kazemi, G.A., Lehr, J.H., Perrochet, P., 2006. Groundwater Age. Wiley-Interscience, New Jersey, USA.
Kharaka, Y.K., Mariner, R.H., 1989. Chemical geothermometers and their application to formation waters from sedimentary basins. In: Naeser, N.D., McCulloh, T.H. (Eds.), Thermal History of Sedimentary Basins. Springer-Verlag, New York, NY, USA, pp. 99–117.
Kresic, N., 2007. Hydrogeology and Groundwater Modeling, 2nd edition. CRC Press, Taylor & Francis Group, USA.
Mazor, E., 2004. Applied Chemical and Isotopic Groundwater Hydrology, 3rd edition. Marcel Dekker, Inc, New York.
Mitchell, T.M., Faulkner, D.R., 2009. The nature and origin of off-fault damage surrounding strike-slip fault zones with a wide range of displacements: a field study from the Atacama fault system, northern Chile. J. Struct. Geol. 31 (8), 802–816.
Nicholson, K., 1993. Geothermal Fluids Chemistry and Exploration Techniques. Springer-Verlag, Berlin.
Okay, A.I., Tüysüz, O., 1999. Tethyan sutures of northern Turkey. Geol. Soc. Spec. Publ. 156, 475–515.
Parkhurst, D.L., Appelo, C.A.J., 1999. User's guide to PHREEQC (Version 2) –a computer program for speciation batch-reaction, one-dimensional transport, and inverse geochemical calculations. Pearce, J.A., Bender, J.F., De Long, S.E., Kidd, W.S.F., Low, P.J., Güner, Y., Saroglu, F., Yilmaz, Y., Moorbath, S., Mitchell, J.G., 1990. Genesis of collision volcanism in Eastern Anatolia, Turkey. J. Volcanol. Geotherm. Res. 44, 189–229.
Poidevin, J.L., 1998. Provenance studies of obsidian artefacts in Anatolia using the fission track dating method, an overview. In: Gourgaud, A., Gratuze, B., Poupeau, G., Poidevin, J.L., Cauvin, M.C. (Eds.), L'Obsidienne au Proche et Moyen Orient, du Volcan a` l'Outil. BAR International Series Hadrian Books 738, pp. 105–156.
Press, F., Siever, R., 1995. Allgemeine Geologie. Spektrum Akademischer Verlag, Heidelberg Berlin, Oxford.
Reed, M., Spycher, N., 1984. Calculation of pH and mineral equilibria in hydrothermal waters with application to geothermometry and studies of boiling and dilution. Geochim. Cosmochim. Ac. 48, 1479–1492.
Salah, M.K., Sahin, S., Aydin, U., 2011. Seismic velocity and Poisson's ratio tomography of the crust beneath east Anatolia. J. Asian Earth Sci. 40, 746–761.
Sayın, M., Eyüpoğlu, S.Ö., 2005. Determination of the Local Meteoric Water Lines Using Stable Isotope Contents of Precipitation In Turkey (in Turkish). Proceedings, II. National Symposium of Isotopic Methods in Hydrology, General Directorate of State Hydraulic Works, İzmir. pp. 323–344.
Taler, J., Duda, P., 2006. Solving Direct and Inverse Heat Conduction Problems. Springer.
Verhagen, B.T., Geyh, M.A., Fröhlich, K., With, K., 1991. Isotope hydrological methods for the quantitative evaluation of groundwater resources in arid and semi-arid areas. Research Reports of the Federal Ministry for Economic Cooperation of the Federal Republic of Germany, Bonn, Germany, 7–122.Versteeg, H.K., Malalasekera, W., 1995. An Introduction to Computational Fluid Dynamics. Prentice Hall 1995.
Wallace, R.E., 1968. Earthquake of August 19, 1966. Varto Area, Eastern Turkey. B. Seismol. Soc. Am. 58, 11–45.

7 Over view of critical evaluation, limitations and future directions

7.1 Finite elements for cohesive cracks

Moës and Belytschko (2002a, b) presented first implementation of cohesive cracks in XFEM. This method was applied for modeling of arbitrary cohesive cracks propagation, whereas propagation of the cohesive zone was dependent to the amount of stress intensity factors at the tip of the crack. Crisfield and Alfano (2002) described a method for modelling delamination in fibre-reinforced composite structures with the aid of a decohesive zone model and interface elements. In this study, the elements around the softening process zone were enriched with hierarchical polynomial functions. Zi and Belytschko (2003) developed an extended finite element method scheme for a static cohesive crack with a new formulation for elements containing crack tips. All cracked elements were enriched by the sign function so that no blending of the local partition of unity would be required. A methodology for the simulation of quasi-static cohesive crack propagation in quasi-brittle materials was presented by Mariani and Perego (2003), where a cubic displacement discontinuity, able to reproduce the typical cusp-like shape of the process zone at the tip of a cohesive crack can propagate without any need to modify the background finite element mesh. Belytschko et al. (2003a) developed a methodology for switching from a continuum to a discrete discontinuity where the governing partial differential equation loses hyperbolicity. Larsson and Fagerström (2005) presented a theoretical and computational framework, which covers both linear and non-linear fracture behaviors. Analysis of three-dimensional crack initiation and propagation for the quasi-static cases has been the issue for a study by Areias and Belytschko (2005a). Xiao et al. (2007) illustrated modulus iteration scheme which is an incremental secant using the extended or generalized finite element method. This method was used to simulating of crack propagation and initiation process in only quasibrittleness materials. Asferg et al. (2007) also employed a new method by partly cracking the XFEM element for cohesive crack propagation with extra enrichments to the cracked elements. This part work with the extra enrichments, therefore the element include the crack-tip becomes capable to model the anisotropy of displacement field on each sides.

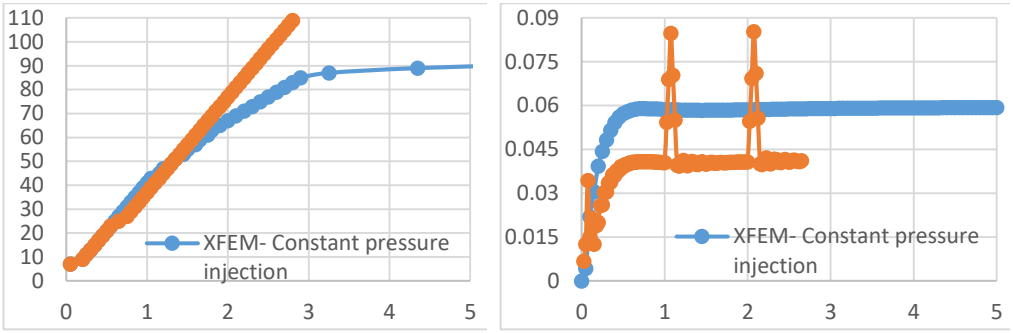

Crack length CMOD

Figure 7.1 crack opening and crack mouth opening relation during dynamic fluid driven fracture propagation

Hence also capable enough to model when symmetric stresses are present on the side of the crack wing. Bordas et al. (2007) had present a library for XFEM , which provides a tool for computations in geomechanical and geoscience system. Benvenuti et al. (2008) introduced continuous to discontinuous displacements just by regularizing XFEM model for the transition form. the regularized solution is defined in a layer where the mechanical work spent within it can be interpreted as an interface work provided that a spring-like constitutive law is adopted. Later Benvenuti (2008) employed this approach specifically for embedded cohesive interfaces. Deb and Das (2010) represented an XFEM model for the analysis of discontinuities in rock masses, where strong discontinuities in 3 and 6 nodded triangular elements are investigated with single and multiple discontinuities. In a study by Xu and Yuan (2011), the cohesive zone model with a threshold is introducing and applying this method for simulating different mixed-mode cracks in combining with XFEM.

Constant Variable

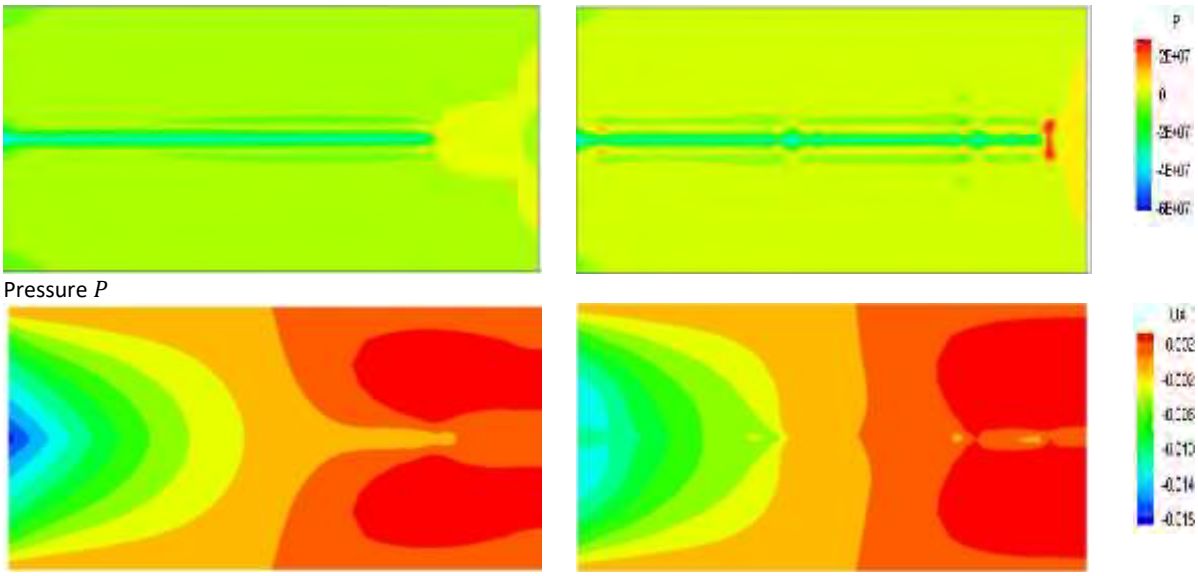

Pressure P

Deformation U_x

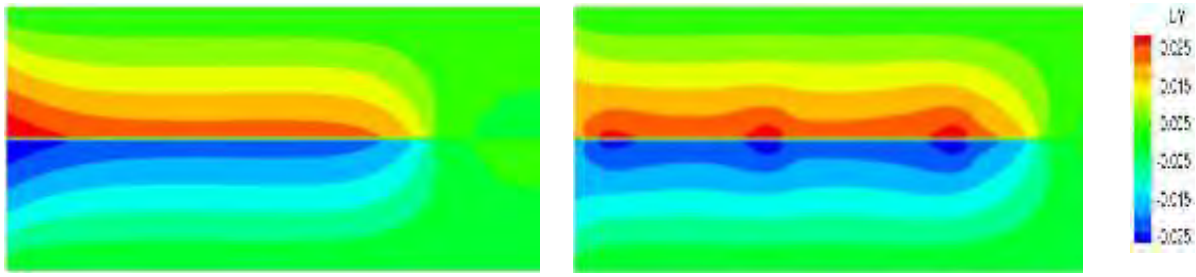

Deformation U_y

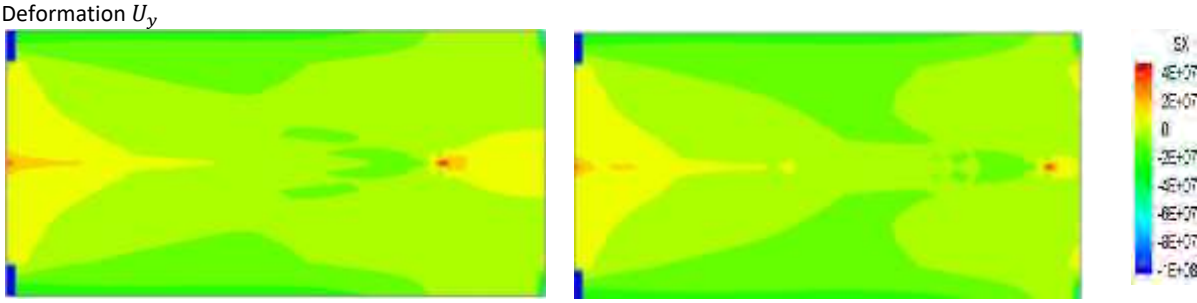

Stress S_x

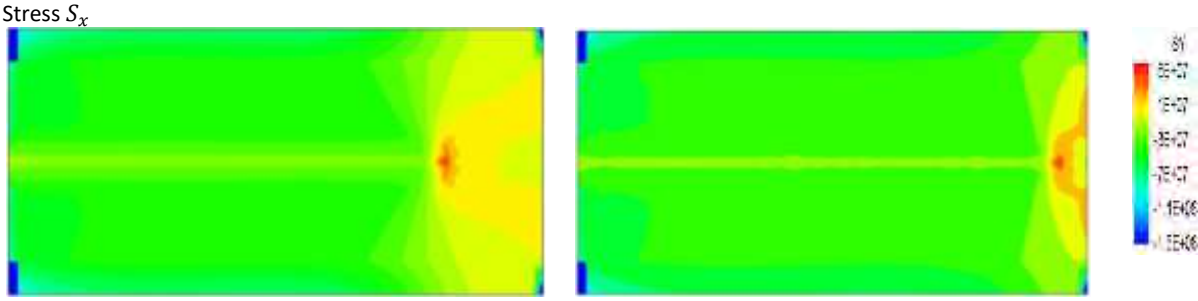

Stress S_y

Figure 7.2. Stresses, pressure and displacement of hydraulic fracturing

Campilho et al. (2011b) preformed a study on strength prediction of single- and double-lap joints. Campilho et al. (2011a) studied fracture characterization of adhesive joints in pure mode I. In this work XFEM is used to predict the fracture behavior of a thin layer of adhesive between stiff and compliant adherends. Mougaard et al. Zamani et al. (2012) performed a comprehensive study on the use of higher-order terms of the crack tip asymptotic fields as enriching functions for XFEM for both cohesive and traction-free cracks. Zhang et al. (2013) performed seismic cracking analysis of concrete gravity dams with initial faults by using the XFEM. In this study the cracking process and final crack profile of Koyna dam during the 1967 Koyna earthquake are simulated. Mougaard et al. (2013) introduced a complete tangent stiffness for XFEM by including crack growth parameters, which is based on the virtual work together with the constitutive conditions at the crack tip.

7.2 Finite elements for composite materials and material inclusions

Composite structures have been of great concern for possessing advantages of multiple materials resulting in substantial economic benefits. Material inhomogeneities result in discontinuous displacement gradient which is referred to as weak discontinuities. Sukumar et al. (2001) studied this issue in the context of XFEM for the first time and proposed a methodology to model arbitrary holes and inclusions without meshing the internal boundaries. The introduced method couples the XFEM to the level set method, which is used for representing the location of holes and material interfaces. Chessa et al. (2003) developed an enhanced strain formulation which leads to good performance, in which the optimal rate of convergence is achieved. Yvonnet et al. (2008) presented an efficient numerical approach to dealing with the interface effects described by the coherent interface model and to determining the size-dependent effective elastic moduli of nanocomposites. Ventura (2008) developed a new technique, based on mapping the enrichment functions onto polynomials with applications to cracks and dislocations, in which the location of the singularity/discontinuity is accounted for via the equivalent polynomial coefficients. Gracie et al. (2008a) developed a new method for modeling of dislocations, which is improved by adding enrichments about the dislocation core. Zhang and Li (2009) studied the mechanical responses of viscoelastic materials with inclusions. In this research the full integration scheme is used for the low Poisson ratio problem and the selective integration scheme treating the volumetric locking for problem high Poisson ratio often encountered in viscoelastic materials. Dréau et al. (2010) studied XFEM enrichment to handle material interfaces with higher orders, which is used to improve the geometrical representation of surfaces. Aragon et al. (2009) presented new enrichment functions which allow solving problems with multiple intersecting discontinuity lines, such as those found at triple junctions in polycrystalline materials and in actively cooled microvascular materials with complex embedded networks. Nouy and Clement (2010) proposed an extended stochastic finite element method for the numerical simulation of heterogeneous materials with random material Interfaces, which is based on a marriage between the XFEM and spectral stochastic methods. Oswald et al. (2009) represented a model for dislocations based on the XFEM, which is developed for thin shells such as carbon nanotubes and thin films. In this study singular enrichments are proposed which allow the Peach-Koehler force to be computed directly from the stress field along the dislocation line. Later, Oswald et al. (2011) introduced a higher-order formulation for dislocation energetics in strained layers and epitaxial islands.

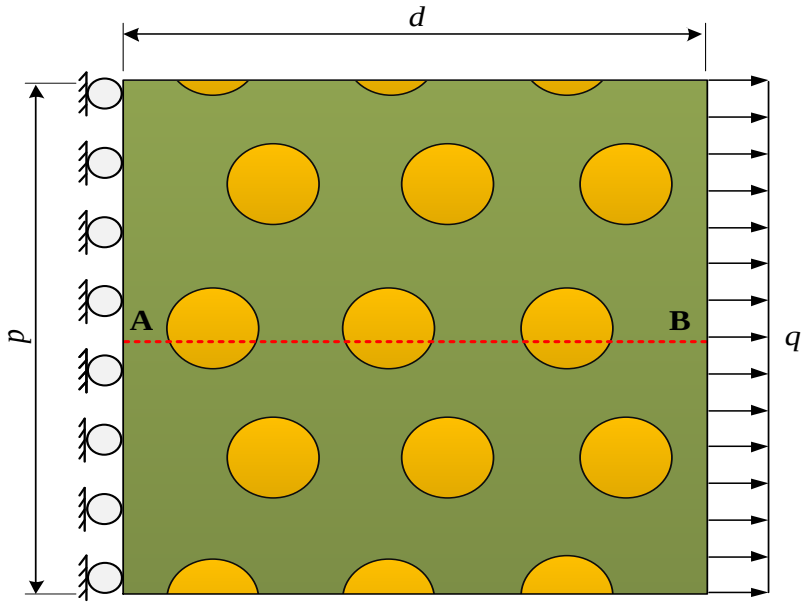

Figure 7.3. A uniformly reinforced plate with circular fibers.

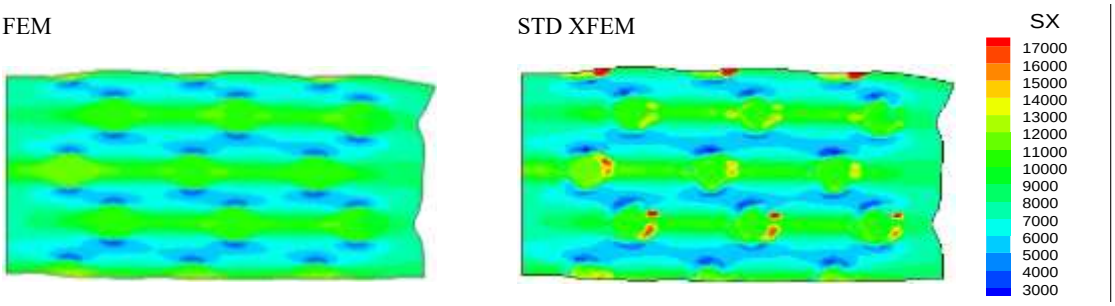

Figure 7.4. Normal stresses σ_x contours of a composite material with circular fibers example

Hiriyur et al. (2011) represented an extended finite element method coupled with a Monte Carlo approach to quantify the uncertainty in the homogenized effective elastic properties of multiphase materials. (2011) developed a multiple level set strategy to prevent numerical artefacts in complex microstructures with nearby inclusions within XFEM. According to this research work, whenever the distance between two inclusions is small enough to be comparable with the mesh size, an improved algorithm will be activated which improves convergence and accuracy of the numerical solution. Curiel Sosa and Karapurath (2012) presented an application of the XFEM for simulation of delamination in fibre metal laminates. An important issue in practical application has been crack initiation/propagation phenomenon occurring in composite Medias. Sukumar et al. (2003b) presented a numerical model of microstructural effects in brittle fracture, with an aim towards the understanding of toughening mechanisms in polycrystalline materials such as ceramics. Later Sukumar et al. (2004) extended this study for bimaterial interface cracks.

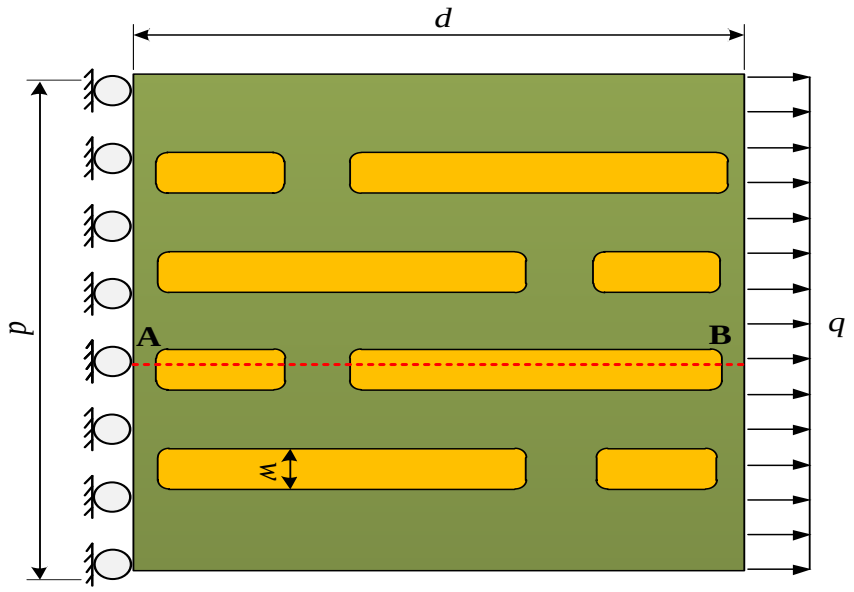

Figure 7.5. A composite material with unidirectional longitudinal fibers: Problem definition.

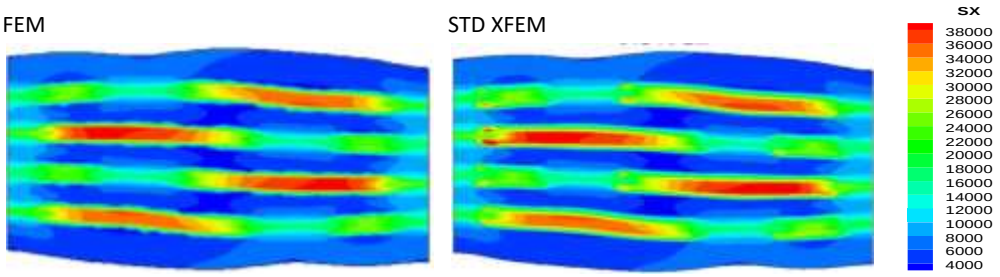

Figure 7.6. Normal stresses σ_x contours of a reinforced plate with unidirectional longitudinal fibers.

In this study, new crack-tip enrichment functions are chosen as those that span the asymptotic displacement fields for an interfacial crack. Liu et al. (2004) developed a XFEM formulation to directly evaluate mixed mode stress intensity factors (SIFs) without extra post-processing for homogeneous materials as well as for bimaterials. Ventura (2006) proposed an algorithm to eliminate quadrature subcells for discontinuous functions in the XFEM. Hettich and Ramm (2006) investigated a detailed geometric modeling of multi-phase materials, as well as at a local mechanical modeling of material interfaces and interfacial failure. Yan and Park (2008) applied the extended finite element method for the simulation of near-interfacial crack propagation in a metal-ceramic layered structure. Huynh and Belytschko (2009) represented methods for treating fracture in composite material by XFEM, where both full 12 function enrichments and approximate enrichments for bimaterial crack tips are employed. Singh et al. (2011) represented the numerical simulation of inhomogeneities/discontinuities (cracks, holes and inclusions) in functionally graded materials (FGMs) using extended finite element method. Menk and Bordas (2011) described a procedure to obtain stiffness matrices whose condition number is close to

the one of the finite element matrices without any enrichment. This is of great importance since the resulting stiffness matrices from XFEM can become ill-conditioned, which ends in iterative solvers need a large number of iterations to obtain an acceptable solution. Pathak et al. (2012) simulated bi-material interfacial cracks by using element free Galerkin method (EFGM) and XFEM under mode-I and mixed mode loading conditions. Wang et al. (2012) presented a numerical simulation of crack growth in brittle matrix of particle reinforced composites. Jiang et al.

7.3 Thermal effect of magmatic intrusions

The thermal effect of sills on a sedimentary basin is a complex topic, with many factors to consider, for example, how the sill diffuses heat can be different depending on the type of material the sill is formed of. Also how well the host rock absorbs the heat from the sill may impact whether source rock is matured or over-matured. The COMSOL models show how the heat diffuses out from the sill body as the sill is solidifying. The temperature is naturally lower, the further away from the sill. The quicker the solidification rate, the quicker the cooling rate, inferring that diffusion of heat to the surrounding rock happens quickly.

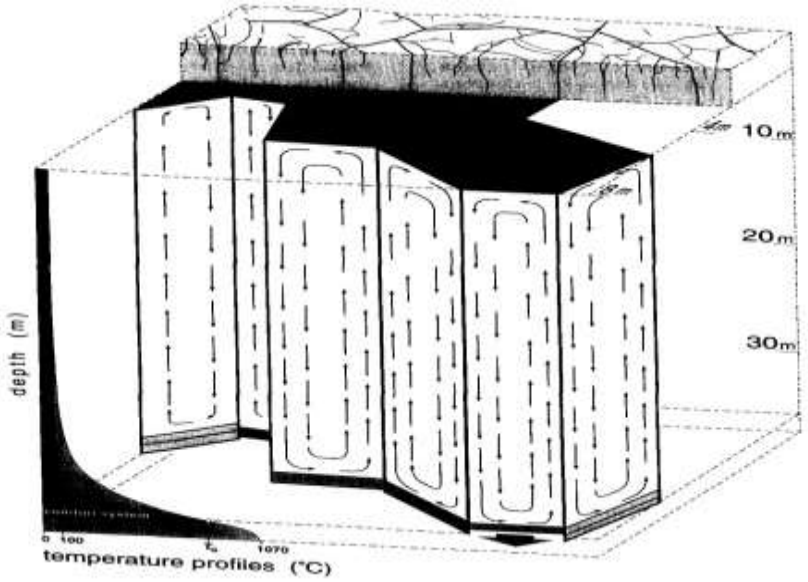

Figure 7.7 - Schematic representing convective heat flow in columns in a sill (Source: Budkewitsch and Robin, 1994).

A longer solidification may result in the sill not cooling down, increasing the likelihood that the sill will evolve into a shallow magma chamber. Thus, learning about how sills

evolve and cool has wider implications, in that information can be learnt about shallow magma chamber formation and consequently help in volcanic eruption prediction (Gudmundsson, 2012). This is a very basic model. There are several other factors which have not been considered, such as thermal conductivity, magma heat capacity, magma density, crystallisation heat, density of host rock and sill composition. Also, the host rock temperature and sill temperature will vary, which will change cooling times. How well the surrounding host rock absorbs the heat and how it impacts the potential organic matter can be judged on vitrinite reflectance (VR) data. VR is a method of measuring how much organic matter is in a material. This process can be done when solidification is complete (Fjeldskaar et al, 2008). Fjeldskaar et al (2008) suggest that a 120m thick-sill produces a theoretical VR value 0.8% 100m away from the sill. Representing how these thick sills play an important role in influencing the organic matter. Hence, why the sills collected in this study have positive associations with maturation of the basin. For instance, the Faroe- Shetland basin, Vøring basin, Bight basin, and Greenland basin to name a few have all reported sills increasing the maturation of organic matter with associated higher VR values (Eide et al, 2016; Rateau et al 2013; Schofield and Totterdell, 2008). The sill itself can also be broken down further. From published literature, we know that the sill is broken into segments. These segments in the field can be seen as cooling joints. The sill will be split into columns and these will be perpendicular to the direction of maximum tensile stress (Budkewitsch and Robin, 1994). Heat loss will occur in both conductive and convective ways (Budkewitsch and Robin, 1994).

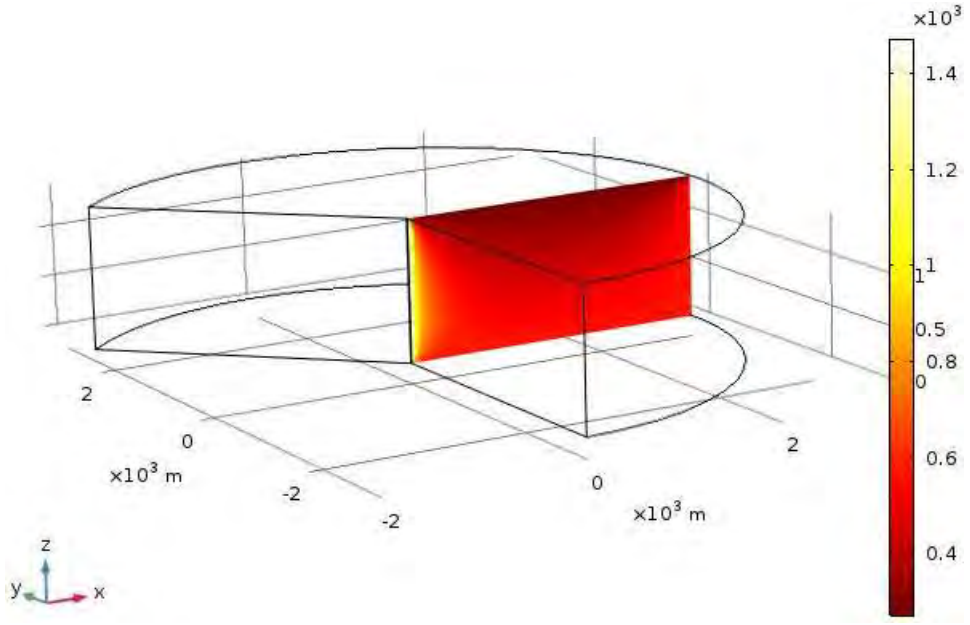

Figure 7.8. Thermal effect of vertical intrusions (Dike) during solidification process

The solidification times suggest that the larger the sill, the longer it will take the sill to cool. This study has only really concentrated on sills as individuals, but they can occur in clusters and as a cluster, they can create a higher ambient temperature too, as indicated by the COMSOL models. Sills also have a local thermal impact (Fjeldskaar et al, 2008). Around the sill is an aureole and depending on the size of the sill, it will have varying impacts. Fjeldskaar et al (2008) implies the thermal maturity effect 30-50% of the sill thickness. Temperatures generated by the sills are extremely high, as the initial temperature of the sill can be between 1000-1200°C (Gudmundsson, 1990). In addition, the COMSOL models suggest that multiple sills will create a higher temperature profile (Fig 8.7). To produce oil from organic matter the temperature needs to be raised to above 60°C and for gas up to 225°C (Stonely, 1995). Over this temperature will cause over-maturation. Therefore, it is clear how sills can cause over-maturation of source rock because of the intense initial temperature.

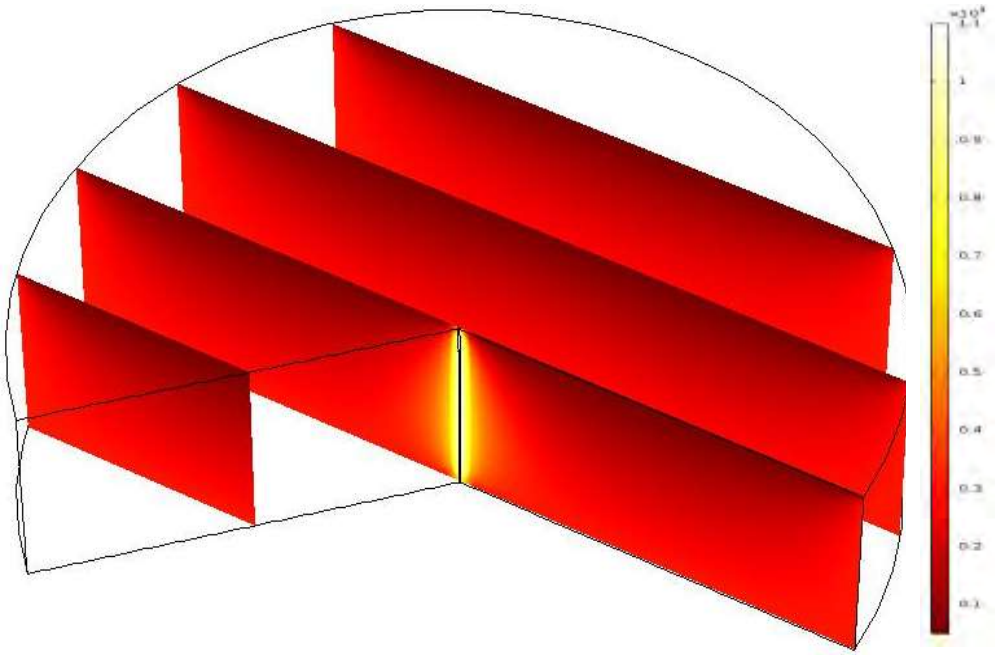

Figure7.9. Heat transfer between dike and host rock and investigating the phase change

However, it would depend on how quickly the sill cools (thus size of sill) and how far away the source rock is, as well as the timing of events in the basin. If vertical displacement increases with the size of the sill, as is suggested by the collected data, then this would increase the likelihood of fractures developing in the overlying strata. However, these measurements are based on a diameter that considers the sill does not have a complex structure and does not consider the different shapes of the sill. For instance, a sill may taper towards its end. If this sill tapers gently from a maximum

thickness in the middle to a very thin outer rim, the monocline created will also be gentle. Iceland relies significantly on geothermal systems for energy, it is vital to study them from every possible angle to maximize the efficiency and sustainability of the energy production. Important components of the geothermal systems to study are the shallow magmatic intrusions that are the driving forces of high-temperature systems (Arnórsson, Axelsson & Sæmundsson, 2008). They are however inaccessible for direct studies in active systems but, eroded intrusions can give important information to enhance our understanding of heat sources in geothermal systems. Studying the details of solidified intrusions, which are directly accessible, can improve interpretations of data from geothermal exploration. Data that is collected at the surface to reconstruct the sub-surface formations in geothermal systems is generally collected with geophysical and geochemical methods (Van der Meer et al., 2014).

Results from the methods are then of great use as input parameters when it comes to evaluating production capacities or forecasting the behavior of geothermal systems with numerical models (Franco & Vaccaro, 2014). Numerical models have been used by the geothermal industry for reservoir modeling since the 1980s and the most common software used is TOUGH2 (O'Sullivan, Pruess & Lippmann, 2001). Geothermal areas in Iceland have been modeled with this software to simulate the behavior of the systems under production (e.g. Björnsson, 1999; Björnsson et al., 2003; Gunnarsson, Arnaldsson & Oddsdóttir, 2011). However, models like that do not include the heat source of the geothermal fields, the solidifying intrusions. They are assumed to be out of the depth range of the models and are compensated by setting the boundary conditions of the bottom layer according to that.

Events confirming this have occurred in geothermal areas at Krafla. Magma reached the depth of production wells during the Krafla fires and even erupted from one borehole (Larsen, Grönvold & Thorarinsson, 1979) and magma has been intersected during drilling in the area (Elders et al., 2011). It is therefore important to include the geometry of the magmatic heat source in geothermal models. Studies performing numerical modeling of fluid flow around magma bodies were first published in the late 1970s (Norton & Knight, 1977; Cathles, 1977). Most studies model plutons geometries on a kilometer scale (e.g. Hayba & Ingebritsen, 1997; Eldursi et al., 2009), which is not representative for shallow geothermal systems where most of intrusions are dikes and sills (e.g. Kennedy et al., 2018). Therefore, there is a gap in research that needs to be bridged by modeling shallow geothermal systems including the geometry of their heat sources (Gunnarsson & Aradóttir, 2015). There has been a lot of research on the

thermal effects of sills in sedimentary basins. There appears to be an overall theme that sills can enhance the geothermal gradient and thus improve petroleum prospectivity within a sedimentary basin (Eide et al., 2016; Gressier et al., 2010; Schofield and Totterdell, 2008). As mentioned previously, sills typically emplace within organic shale formations, which, when heated, produces hydrocarbons (Spacapan et al., 2018). The heat transfer from the sill to the surrounding host rock depends on the thickness and temperature of the sill and whether the cooling is convective or conductive (Barnett, 2015; Lee et al, 2006). Syndes et al (2018) explain that after sill emplacement, thermal effect is initially located in the immediate vicinity of the sill but with time, the heat is dissipated and will therefore affect a larger area around the sill.

7.4 Four dimensional modeling

Solidification times have been calculated. However, numerical modeling of dike solidification or sill solidification in non-homogeneous area is one of the areas that I have already made my numerical modeling for and it will be on our table to go ahead for publishing. This shows that larger sills will take longer to cool, meaning that large sills may affect a basins geothermal profile for a longer period. This leading to either maturation or over-maturation, depending on source rock distance from sill. Further data collection on timing and depth could be added to the catalogue. COMSOL modelling and one-dimensional thermal models could be developed to improve this study. An increase data collection on intrusion dimensions and fracture frequency is needed. There have been a few assumptions made throughout this study and there are there a range of associated uncertainties. Such as crack wings, contacts, friction, cohesion and heat transfer related parameters. If I try to change this assumption to the real-life modeling, this will need a fast computer but also there are lot to learn from them. I have already mage fair bit of 3D models which our plan is to publish and get them all out as soon as possible. To receive some ideas of reviewers on our new method of verifying the surface measurement with the movement of faults and magma chamber inflation/deflation and their shapes.

Later working on three dimensional problems and cases with layering that comes from Fourier law can be very useful and very realistic, this direction with addition to the dynamic propagation of intrusions in layers geometry can be very useful to predict and

investigate the magma eruptions. This is still one of them mail unknown problems in the field of volcanotectonics. Finally, I believe that the fate of the eruption can only get closer to estimation with better understanding of 3D model and fully implementing the layering and their contacts.

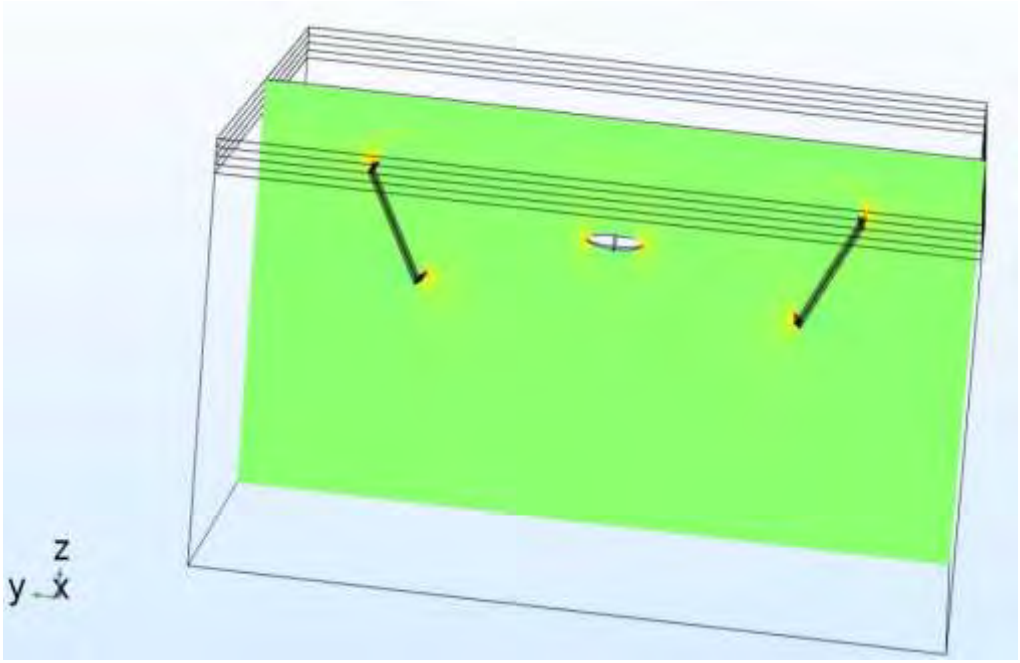

Figure 7.10. Three-dimensional time dependent of faults and magma chamber combination, fully single-phase solid mechanic model

7.5 Limitations and uncertainty in field data and COMSOL modeling

Compiling this new catalogue was difficult in terms of gathering as much data from individual published authors. There are limitations in collecting this data through inaccuracy of seismic and fieldwork collection. Therefore, many sills might be missed off which could potentially affect results. The data set could potentially be larger and that would decrease uncertainty. Furthermore, sills do not necessarily occur as individual bodies, the can form a complex system (Hansen, 2015) and the catalogue has not taken this into account either. In addition, the time and depth of emplacement has not been recorded. These two parameters can also play key role in determining how sills affects a basin (Senger et al, 2017).

When it goes to the modeling part of work, we had software such as MATLAB, COMSOL, Mathematica, and FORTRAN in hand to play with. One boundary element

software BEASY unfortunately got out of access in the very early stage of my PhD. Plus, as my source code in fluid drive fracture was still incapable of modeling the non-homogeneous zones. Then most of the geological features could have been ignored by using that type of models. However, luckily COMSOL 5.1 was available for me. The COMSOL results has its own uncertainties, such as some of the features of this software is look like lack box unless you open it up and try to add your own code and equations with mathematical physics that is already included.

COMSOL has difficulties, which are opening the source of it and make your own codding inside of it. It does need its own regulations and definitions to understand your ideas. After that, this software is very big with many graphical features; when we want more resolution in some areas, this make the model very heavy and the running process very long and very expensive. Sometimes some of the idea you have it been not that easy to implement in to COMSOL, it requires loads of reading to make sure your new feature is not going to interact with other physics and present confusing results. Sometimes I wished I could have just been able to open the COMSOL, write one-line code in MATLAB format, and make it work. Another limitation I had during my PhD was having a slow computer for numerical modeling over the first two years of my study. This really pulled me back for using COMSOL in geologically realistic models and three-dimensional modeling.

Bibliography

Abbas S, Alizada A, Fries TP. The XFEM for high-gradient solutions in convection-dominated problems. International journal for numerical methods in engineering 2010; 82:1044-1072.

Abgrall R, Krust A. An adaptive enrichment algorithm for advection-dominated problems. Informatics mathematics 2012; 72:359-374.

Acocella, V., Neri, M., 2009. Dike propagation in volcanic edifices: overview and pos- sible developments. Tectonophysics 471, 67–77. https://doi.org/10.1016/j.tecto.2008.10.002.

Al Shehri, A., Gudmundsson, A., 2018. Modelling of surface stresses and fracturing during dyke emplacement: application to the 2009 episode at Harrat Lunayyir, Saudi Arabia. J. Volcanol. Geotherm. Res. 356, 278–303.

Ahyan AO. Stress intensity factors for three-dimensional cracks in functionally graded materials using enriched finite elements. Solids and structures 2007; 44:8579-8599.

Acocella, V., Neri, M., 2009. Dike propagation in volcanic edifices: overview and pos- sible developments. Tectonophysics 471 (1), 67–77.

Ambraseys, N., Zatopek, A., 1968. The Varto Ustukran earthquake of 19 August 1966. B. Seismol. Soc. Am. 58, 47–102.

Armijo, R., Meyer, B., Hubert-Ferrari, A., Barka, A.A., 1999. Propagation of the North Anatolian fault into the Northern Aegean: timing and kinematics. Geology 27, 267–270.

Attendorn, H.G., Bowen, R., 1997. Radioactive and Stable Isotope Geology. Chapman and Hall, London, pp. 519.

Deutsch, W., Siegel, R., 1997. Groundwater Geochemistry: Fundamentals and Applications to Contamination. Lewis Publishers, New York.

Aktug, B., Dikmen, Ü., Dogru, A., Ozener, H., 2013. Seismicity and strain accumula- tion around Karlıova Triple Junction (Turkey). J. Geodyn. 67, 21–29.

Amadei, B., Stephansson, O., 1997. Rock Stress and Its Measurement. Chapman Hall, New York.

Ambraseys, N.N., Zatopek, A., 1968. The Varto Ustukran earthquake of 19 August 1966. Bull. Seismol. Soc. Am. 58, 47–102.

Annen, C., Sparks, R.S.J., 2002. Effects of repetitive emplacement of basaltic intru- sions on the thermal evolution and melt generation in the crust. Earth Planet. Sci. Lett. 203, 937–955.

Armijo, R., Meyer, B., Hubert-Ferrari, A., Barka, A.A., 1999. Propagation of the North Anatolian fault into the Northern Aegean: timing and kinematics. Geology 27, 267–270.

Amiri F, Anitescu C, Arroyo M, Bordas SPA, Rabczuk T. XLME interpolants, a seamless bridge between XFEM and enriched meshless methods. Computational mechanics 2013. DOI 10.1007/s00466-013-0891.

Anahid M, Khoei AR. New development in extended finite element modeling of large elasto-plastic deformations. International journal or numerical methods in engineering 2008b; 75:1133-1171.

Aragon AM, Duarte CA, Geubelle PH. Generalized finite element enrichment functions for discontinuous gradient fields. International journal for numerical methods in engineering 2010; 82:242-268.

Areias PM, Belytschko T. Two-scale shear band evolution by local partition of unity. International journal for numerical methods in engineering 2006; 66:878-910.

Areias PMA, Belytschko T. Analysis of three-dimensional crack initiation and propagation using the extended finite element method. International journal for numerical methods in engineering 2005a; 63:760-788.

Areias PMA, Belytschko T. Non-linear analysis of shells with arbitrary evolving cracks using XFEM. International journal for numerical methods in engineering 2005b; 62:384-415.

Asadpoure A Mohammadi S. Developing new enrichment functions for crack simulation in orthotropic media by the extended finite element method. International journal for numerical methods in engineering 2007; 69:2150-2172

Asadpoure A, Mohammadi S, Vafai A. Crack analysis in orthotropic media using the extended finite element method. Thin walled structures 2006; 44:1031-1038.

Asferg JL, Poulsen PN, Nielsen Lo. A consistent partly cracked XFEM element for cohesive crack growth. International journal for numerical methods in engineering 2007; 72:464-485.

Aubertin P, Rethore J, de'Borst R. A coupled molecular dynamics and extended finite element method for dynamic crack propagation. International journal for numerical methods in engineering 2010; 81:72-88

Ayhan AO. Simulation of three-dimensional fatigue crack propagation using enriched finite elements. Computers and structures 2011; 89:801-812.

Aarnes, I., et al. 2010. How contact metamorphism can trigger global climate changes: Modelling gas generation around igneous sills in sedimentary basins. Geochimica et Cosmochimica Acta, 74 (24), 7179-7195. doi: 10.1016/j.gca.2010.09.011

Aarnes, I., et al. 2011. Contact metamorphism devolatilization of shales in the Karoo Basin, South Africa, and the

effects of multiple sill intrusions. Chemical Geology, 281, 181-194. doi: 10.1016/j.chemgeo.2010.12.007
Alalade, B. & Tyson, R.V. 2013. Influence of igneous intrusions on thermal maturity of Late Cretaceous shales in the Tuma well, Chad Basin, NE Nigeria. Journal of African Earth Sciences, 77, 59-66. doi: 10.1016/j.jafrearsci.2012.09.006
Australian Government. 2018. Bass basin regional geology. [Online]. Available at: https://2017-petroleumacreage.industry.slicedtech.com.au/2017/geology/bass-basin/bass- basin-regional-geology (Accessed: 27th May, 2018).
Al Shehri, A., Gudmundsson, A., 2018. Modelling of surface stresses and fracturing during dyke emplacement: Application to the 2009 episode at Harrat Lunayyir, Saudi Arabia. J. Volcanol. Geotherm. Res., 356, 278-303.
Aarnes, I., et al. 2010. How contact metamorphism can trigger global climate changes: Modelling gas generation around igneous sills in sedimentary basins. Geochimica et Cosmochimica Acta, 74 (24), 7179-7195. doi: 10.1016/j.gca.2010.09.011
Aarnes, I., et al. 2011. Contact metamorphism devolatilization of shales in the Karoo Basin, South Africa, and the effects of multiple sill intrusions. Chemical Geology, 281, 181-194. doi: 10.1016/j.chemgeo.2010.12.007
Alalade, B. & Tyson, R.V. 2013. Influence of igneous intrusions on thermal maturity of Late Cretaceous shales in the Tuma well, Chad Basin, NE Nigeria. Journal of African Earth Sciences, 77, 59-66. doi: 10.1016/j.jafrearsci.2012.09.006
Australian Government. 2018. Bass basin regional geology. [Online]. Available at: https://2017-petroleumacreage.industry.slicedtech.com.au/2017/geology/bass-basin/bass- basin-regional-geology (Accessed: 27th May, 2018).
Barnett, Z. 2014. Emplacement and evolution of sills into shallow magma chambers and hydrocarbon reservoirs. Unpublished Ph.D. thesis, Royal Holloway, University of London, London, 404 pp.
Bell, B. & Butcher, H. 2002. On the emplacement of sill complexes: evidence from the Faroe- Shetland Basin. Geological Society, London, 197, 307-329. doi: 10.1144/GSL.SP.2002.197.01.12
Bermúdez, A. & Delpino, D. 2015. Concentric and radial joint systems within basic sills and their associated porosity enhancement, Neuquén basin, Argentina. Geological Society, London, 302 (1), 185-198. doi: 10.1144/SP302.13
Birch, F. & Schairer, J.F. & Spicer, H.C. 1942. Handbook of physical constants. Geological Society of America. Special papers, 36
Boudreau, A. & Simon, A. 2007. Crystallization and Degassing in the Basement Sill, McMurdo Dry Valleys, Antarctica. Journal of Petrology, 48 (7), 1369-1386. doi: 10.1093/petrology/egm022
Bradley, J. 1965. Intrusion of major dolerite sills. Trans Royal Soc NZ 3, 27–55
Brown, R. & Gallagher, K. & Duane, M. 1994. A quantitative assessment of the effects of magmatism on the thermal history of the Karoo sedimentary sequence. Journal of African Earth Sciences, 18 (3), 227-243. doi: 10.1016/0899-5362(94)90007-8
Budkewitsch, P. & Robin, P.Y. 1994. Modelling the evolution of columnar joints. Journal of Volcanology and Geothermal Research, 59 (3), 219-239. doi: 10.1016/0377-0273(94)90092-2
Burchardt, S. 2008. New insights into the mechanics of sill emplacement provided by field observations of the Njardvik Sill, Northeast Iceland. Journal of Volcanology and Geothermal Research, 173, 280-288. doi: 10.1016/j.jvolgeores.2008.02.009
Burchardt, S. 2018. Volcanic and igneous plumbing systems. Elsevier, Amsterdam, Netherlands. 341pp.
Byran, S.E. & Ferrari, L. 2013. Large igneous provinces and silicic large igneous provinces: Progress in our understanding over the last 125 years. GSA Bulletin, 125 (7-8), 1053-1078. doi: 10.1130/B30820.1
Barnett, Z.A., Gudmundsson, A., 2014. Numerical modelling of dykes deflected into sills to form a magma chamber. J. Volcanol. Geotherm. Res., 281, 1-11.
Bazargan, M., Gudmundsson, A., 2019. Dike-induced stresses and displacements in layered volcanic zones. J. Volcanol. Geotherm. Res. (in press).
Becerril, L., Galindo, I., Gudmundsson, A., Morales, J.M., 2013. Depth of origin of magma in eruptions. Scientific Reports 3, 2762. doi: 10.1038/srep02762
Bistacchi, A., Tibaldi, A., Pasquarè, F..A., Rust, D., 2012. The association of cone–sheets and radial dykes: Data from the Isle of Skye (UK), numerical modelling, and implications for shallow magma chambers. Earth Planet. Sci. Lett., 339–340, 46-56.
Barnett, Z. 2014. Emplacement and evolution of sills into shallow magma chambers and hydrocarbon reservoirs. Unpublished Ph.D. thesis, Royal Holloway, University of London, London, 404 pp.
Bell, B. & Butcher, H. 2002. On the emplacement of sill complexes: evidence from the Faroe- Shetland Basin. Geological Society, London, 197, 307-329. doi: 10.1144/GSL.SP.2002.197.01.12
Bermúdez, A. & Delpino, D. 2015. Concentric and radial joint systems within basic sills and their associated porosity enhancement, Neuquén basin, Argentina. Geological Society, London, 302 (1), 185-198. doi: 10.1144/SP302.13
Birch, F. & Schairer, J.F. & Spicer, H.C. 1942. Handbook of physical constants. Geological Society of America. Special

papers, 36
Bachene M, Tiberkak R, Rechak S, Maurice G, Hachi BK. Enriched finite element for modal analysis of cracked plates. Damage and fracture mechanics: Failure analysis of engineering materials and structures 2009a: 463-471.
Bachene M, Tiberkak R, Rechak S. Vibration analysis of cracked plates using the extended finite element method. Archive of applied mechanics 2009b; 79:249-262.
Baietto MC, Pierres E, Gravouil A, Berthel B, Fouvry S, Trolle B. Fretting fatigue crack growth simulation based on a combined experimental and XFEM strategy. International journal of fatigue 2013; 47:31-43.
Baydoun M, Fries TP. Crack propagation criteria in three dimensions using the XFEM and an explicit-implicit crack description. International journal of fracture 2012; 178:51-70.
Bayesteh H, Mohammadi S. XFEM fracture analysis of shells: The effect of crack tip enrichments. Computational materials science 2011; 50:2793-2813.
Bechet E, Moës N, Wohlmuth B. A stable Lagrange multiplier space for stiff interface conditions within the extended finite element method. International journal for numerical methods in engineering 2009a; 78:931-954.
Bechet E, Scherzer M, Kuna M. Application of the x-fem to the fracture of piezoelectric materials. International journal for numerical methods in engineering 2009b; 77:1535-1565.
Barka, A.A., 1992. The North Anatolian fault zone. Ann. Tecton. 6, 164–195.
Becerril, L., Galindo, I., Gudmundsson, A., Morales, J.M., 2013. Depth of origin of magma in eruptions. Sci. Rep. 3, 2762. http://doi.org/10.1038/srep02762.
Bigazzi, G., Yegingil, Z., Ercan, T., Oddone, M., Ozdogan, M., 1997. Age determination of obsidian bearing volcanics in Eastern Anatolia using the fission track dating method. Geol. Bull. Turkey 40, 57–72.
Bigazzi, G., Poupeau, G., Yeğingil, Z., Bellotgurlet, L., 1998. Provenance studies of ob- sidian artefacts in Anatolia using the fission track dating method. An overview. In: Gourgaud, A., Gratuze, B., Poupeau, G., Poidevin, J.L., Cauvin, M.C. (Eds.), L'Ob- sidienne au Proche et Moyen Orient, du Volcan à l'Outil. In: BAR International Series, vol. 738. Hadrian Books, pp. 69–89.
Browning, J., Gudmundsson, A., 2015. Caldera faults capture and deflect inclined sheets: an alternative mechanism of ring dike formation. Bull. Volcanol. 77 (1), 1–13.
Browning, J., Drymoni, K., Gudmundsson, A., 2015. Forecasting magma-chamber rupture at Santorini Volcano, Greece. Sci. Rep. 5, 15785. http://doi.org/10.1038/ srep15785.
Buket, E., Temel, A., 1998. Major-element, trace element, and Sr–Nd isotopic geo- chemistry and genesis of Varto (Muş) volcanic rocks, Eastern Turkey. J. Volcanol. Geotherm. Res. 85, 405–422.
Becker R, Burman E, Hansbo P. A Nitsche extended finite element method for incompressible elasticity with discontinuous modulus of elasticity. Computer methods in applied mechanics and engineering 2009; 198:3352-3360.
Belytschko T, Black T. Elastic crack growth in finite elements with minimal remeshing. International journal of fracture mechanics 1999; 45:601-620.
Belytschko T, Chen H, Xu J, Zi G. Dynamic crack propagation based on loss of hyperbolicity and a new discontinuous enrichment. International journal for numerical methods in engineering 2003a; 58:1873-1905.
Belytschko T, Gracie R, Ventura G. A review of extended/generalized finite element methods for material modeling. Modeling and simulations in material science and engineering 2009; 17: ??? DOI:10.1088/0965-0393/17/4/043001.
Belytschko T, Xiao SP, Parimi C. Topology optimization with implicit functions and regularization. International journal for numerical methods in engineering 2003b; 57:1177-1196.
Benvenuti E, Tralli A, Ventura G. A regularized XFEM model for the transition from continuous to discontinuous displacements. International journal for numerical methods in engineering 2008; 74:911-944.
Benvenuti E, Tralli A. Simulation of finite-width process zone in concrete-like materials by means of a regularized extended finite element model. Computational mechanics 2012; 50:479-497.
Benvenuti E, Ventura G, Ponara N. Finite element quadrature of regularized discontinuous and singular level set functions in 3D problems. Algorithms 2012a; 5:529-544.
Benvenuti E, Vitarelli O, Tralli A. Delamination of FRP-reinforced concrete by means of an extended finite element formulation. Composites: part B 2012b; 43:3258-3269.
Benvenuti E. A regularized XFEM framework for embedded cohesive interfaces. Computer methods in applied mechanical engineering 2008; 197:4367-4378.
Baer, G., Hamiel, Y., 2010. Form and growth of an embryonic continental rift: InSAR observations and modelling of the 2009 western Arabia rifting episode. Geo- physics. J. Int. 182, 155–167.
Barnett, Z.A., Gudmundsson, A., 2014. Numerical modelling of dykes deflected into sills to form a magma chamber. J. Volcanol. Geotherm. Res. 281, 1–11.

Becerril, L., Galindo, I., Gudmundsson, A., Morales, J.M., 2013. Depth of origin of magma in eruptions. Sci. Rep. 3, 2762https://doi.org/10.1038/srep02762.
Bonafede, M., Rivalta, E., 1999. The tensile dislocation problem in a layered elastic medium. Geophys. J. Int. 136, 341–356.
Bonafede, M., Rivalta, E., 1999. On tensile cracks close to and across the interface be- tween two welded elastic half-spaces. Geophys. J. Int. 138, 410–434.
Browning, J., Drymoni, K., Gudmundsson, A., 2015. Forecasting magma-chamber rupture at Santorini volcano, Greece. Sci. Rep. 5, https://doi.org/10.1038/ srep15785.
Bhargava RR, Sharma K. Generalized crack-tip enrichment functions for X-FEM simulation in piezoelectric media. Journal of information and operations management 2012; 3:166-169.
Bhargava RR, Sharma K. A study of finite size effects on cracked 2-D piezoelectric media using extended finite element method. Computational materials science 2011; 50:1834-1845.
Bhattacharya S, Singh IV, Mishra BK, Bui TQ. Fatigue crack growth simulations of interfacial cracks in bi-layered FGMs using XFEM. Computational mechanics 2013; 52:799-814.
Bhattacharya S, Singh IV, Mishra BK. Fatigue-life estimation of functionally graded materials using XFEM. Engineering with computers 2012; 29:427-448.
Bonfils N, Chevaugeon N, Moës N. Treating volumetric inequality constraint in a continuum media with a coupled X-FEM/level-set strategy. Computer methods in applied mechanics and engineering 2012; 205:16-28.
Bordas S, Legay A. X-FEM mini-course. EPFL, Lausanne, Switzerland, 2005.
Bordas S, Moran B. Enriched finite elements and level sets for damage tolerance assessment of complex structures. Engineering fracture mechanics 2006; 73:1176-1201.
Bordas S, Nguyen PV, Dunant C, Guidoum A, Nguyen-Dang H. An extended finite element library. International journal for numerical methods in engineering 2007; 71:703-732.
Bordas SPA, Natarajan S, Kerfriden P, Augarde CH , Mahapatra DR, Rabczuk T, Pont SD. On the performance of strain smoothing for quadratic and enriched finite element approximations (XFEM/GFEM/PUFEM). International journal for numerical methods in engineering 2011; 86:637-666.
Bordas SPA, Rabczuk T, Hung NX, Nguyen VP, Natarajan S, Bog T, Quan DM, Hiep NV. Strain smoothing in FEM and XFEM. Computers and structures 2010; 88:1419-1443.
Budyn E, Zi G, Moës N, Belytschko T. A method for multiple crack growth in brittle materials without remeshing. International journal for numerical methods in engineering 2004; 61:1741-1770.
Bui TQ, Zhang C. Extended finite element simulation of stationary dynamic cracks in piezoelectric solids under impact loading. Computational materials science 2012; 62:243-257.
Byfut A, Schröder A. hp-adaptive extended finite element method. International journal for numerical methods in engineering 2012; 89:1392-1418.
Boudreau, A. & Simon, A. 2007. Crystallization and Degassing in the Basement Sill, McMurdo Dry Valleys, Antarctica. Journal of Petrology, 48 (7), 1369-1386. doi: 10.1093/petrology/egm022
Bradley, J. 1965. Intrusion of major dolerite sills. Trans Royal Soc NZ 3, 27–55
Brown, R. & Gallagher, K. & Duane, M. 1994. A quantitative assessment of the effects of magmatism on the thermal history of the Karoo sedimentary sequence. Journal of African Earth Sciences, 18 (3), 227-243. doi: 10.1016/0899-5362(94)90007-8
Budkewitsch, P. & Robin, P.Y. 1994. Modelling the evolution of columnar joints. Journal of Volcanology and Geothermal Research, 59 (3), 219-239. doi: 10.1016/0377-0273(94)90092-2
Burchardt, S. 2008. New insights into the mechanics of sill emplacement provided by field observations of the Njardvik Sill, Northeast Iceland. Journal of Volcanology and Geothermal Research, 173, 280-288. doi: 10.1016/j.jvolgeores.2008.02.009
Burchardt, S. 2018. Volcanic and igneous plumbing systems. Elsevier, Amsterdam, Netherlands. 341pp.
Byran, S.E. & Ferrari, L. 2013. Large igneous provinces and silicic large igneous provinces: Progress in our understanding over the last 125 years. GSA Bulletin, 125 (7-8), 1053-1078. doi: 10.1130/B30820.1
Baer, G., Hamiel, Y., 2010. Form and growth of an embryonic continental rift: InSAR observations and modelling of the 2009 western Arabia rifting episode. Geophysics. J.Int. 182, 155-167.
Barnett, Z.A., Gudmundsson, A., 2014. Numerical modelling of dykes deflected into sills to form a magma chamber. J. Volcanol. Geotherm. Res., 281, 1-11.
Becerril, L., Galindo, I., Gudmundsson, A., Morales, J.M., 2013. Depth of origin of magma in eruptions. Scientific Reports 3, 2762. doi: 10.1038/srep02762
Bonafede, M., Rivalta, E., 1999a. The tensile dislocation problem in a layered elastic medium. Geophys. J. Int., 136, 341-356.
Bonafede, M., Rivalta, E., 1999b. On tensile cracks close to and across the interface between two welded elastic half-spaces. Geophys. J. Int., 138, 410-434.

Browning, J., Drymoni, K., Gudmundsson, A., 2015. Forecasting magma-chamber rupture at Santorini volcano, Greece. Scientific Reports, 5, doi: 10.1038/srep15785.
Baba, A., Yiğitbaş, E., Ertekin, C., 2010. Hydrogeochemistry of geothermal resources of eastern part of turkey: a case study, Varto Region. World Geothermal Congress 2010 1–8.
Baker, E., 1995. Characteristics of hydrothermal discharge following a magmatic intru- sion. Geol. Soc. (Lond.) Spec. Publ. 87, 65–76.
Baker, E.T., Urabe, T., 1996. Extensive distribution of hydrothermal plumes along the superfast spreading East Pacific Rise, 13 30'–18 40' S. J. Geophys. Res-Sol. EA 101 (B4), 8685–8695.
Barka, A.A., 1992. The North Anatolian fault zone. Ann. Tecton. 6, 164–195. Bozkurt, E., 2001. Neotectonics of Turkey-a synthesis. Geodin. Acta 14, 3–30.
Browning, J., Meredith, P.G., Stuart, C., Harland, S., Healy, D., Mitchell, T.M., 2018. A directional crack damage memory effect in Sandstone under true triaxial loading. Geophys. Res. Lett. 45, 6878–6886.
Buket, E., Temel, A., 1998. Major-element, trace element, and Sr-Nd isotopic geochem- istry and genesis of Varto (Muş) volcanic rocks, Eastern Turkey. J. Volcanol.
BALEN, R. T., and SKAR, T., 2000. The influence of faults anintraplate stress on the overpressure evolution of the Halten Terrace, mid-Norwegian margin: Tectonophysics, v. 320, no. 3–4p. 331–345.
Bell, R. E., L. Jackson, C., Elliott, G. M., Gawthorpe, R. L., Sharp, I. R., and Michelsen, L. 2014.Insights into the development of major rift-related unconformities from geologically constrained subsidence modelling: Halten Terrace, offshore mid Norway. Basin Research, 26(1):203–224.
Blystad, P., Brekke, H., Færseth, R.B., Larsen, B.T., Skogseid, J., and Tørudbakken, B. 1995. Structural elements of the Norwegian continental shelf, part II: the Norwegian Sea region. Norwegian Petroleum Directorate Bulletin, 6, Stavanger, pp. 45
Bolas, H. M., and C. Hermanrud .2003. Hydrocarbon leakage processes and trap retention capacities offshore Norway,Pet. Geosci.,9,321–332.
Brekke, H. and Riis, F. 1987. Tectonics and basin evolution of the Norwegian shelf between 62°N and 72 N. Norsk Geologisk Tidsskrift, 67, 295-322.
Brekke, H. 2000. The tectonic evolution of the Norwegian Sea continental margin with emphasis on the Vøring and Møre basins. Geological Society of London Special Publication 136, 327–378.
Brekke, H., Sjulstad, H.I., Magnus, C. & Williams, R.W. 2001. Sedimentary environments offshore Norway – an overview. Norwegian Petroleum Society Special Publication 10, 7–37.
Broberg, K. B.1999. Cracks and Fracture, 752 pp., Elsevier, New York.
Caine, J.S., Evans, J.P., Forster, C.B .1996. Fault zone architecture and permeability structure. Geology 24, 1025±1028.
Caracausi, A., Ditta, M., Italiano, F., Longo, M., Nuccio, P.M., Paonita, A., Rizzo, A., 2005.
Changes in fluid geochemistry and physico-chemical conditions of geothermal systems caused by magmatic input: The recent abrupt outgassing off the island of Panarea (Aeolian Islands, Italy). Geochim. Cosmochim. Ac. 69 (12), 3045–3059.
Cherubini, C., Giasi, C.I., Pastore, N., 2013. Evidence of non-Darcy flow and non-Fickian transport in fractured media at laboratory scale. Hydrol. Earth Syst. Sci. 17 (7), 2599–2611.
Craig, H., 1961. Isotopic variations in meteoric waters. Science 133, 1702–1703.
Carracedo, J.C., Troll, V.R., 2006. Seismicity and gas emissions on Tenerife: a real cause for alarm? Geology Today, 22, 138-141.
Cayol, V., Cornet, F.H., 1998. Three-dimensional modelling of the 1983-1984 eruption of Piton de la Fournaise volcano, Reunion Island. J. Geophys. Res., 103, 18,025-18,037.
Carslaw, S. & Jaeger, J. C. 1959. Conduction of Heat in Solids (2nd eds).Clarendon, Oxford, UK. Cannat, M., et al. 1995. Proceedings of the ocean drilling program. Initial reports, 153
Clarke, J.D.A & Alley, N.F. 1993. Petrologic data on the evolution of the Great Australian Bight. Proceedings of the Gondwana Eight Symposium: International Gondwana Symposium, 8, 585-596.
Clark, S.P. 1966. Handbook of physical constants. Geological Society of America. Memoir 97, Washington, DC.
Coetzee, A. & Kisters, A.F.M. 2016. The 3D geometry of regional-scale dolerite saucer complexes and their feeders in the Secunda Complex, Karoo Basin. Journal of Volcanology and Geothermal Research, 317. doi: 10.1016/j.jvolgeores.2016.04.001
Costa, D.F.B., et al. 2016. Analysis of the geometry of diabase sills of the Serra Geral magmatism, by 2D seismic interpretation, in Guareì region, São Paulo, Paraná Basin, Brazil. Brazilian Journal of Geolog, 46 (4), 605-615. doi: 10.1590/2317-4889201620160078
Cooper, J.R., et al. 2007. Coal metamorphism by igneous intrusion in the Raton Basin, CO and NM: Implications for generation of volatiles. International Journal of Coal Geology, 71 (1), 15-27. doi: 10.1016/j.coal.2006.05.007
Campilho RDSG, Banea MD, Chaves FJP, da Silva LFM. eXtended finite element method for fracture characterization

of adhesive joints in pure mode I. Computational material science 2011a; 50:1543-1549.
Campilho RDSG, Banea MD, Pinto AMG, da Silva LFM, de Jesus AMP. Strength prediction of single- and double-lap joints by standard and extended finite element modelling. International journal of adhesion & adhesives 2011b; 31:363-372.
Chahine E, Laborde P, Renard Y. A non-conformal extended finite element approach: Integral matching Xfem. Applied numerical mathematics 2011; 61:322-343.
Chahine E, Laborde P, Renard Y. A quasi-optimal convergence result for fracture mechanics with XFEM. Comptes rendus mathematique 2006; 342:527-532.
Chatzi EN, Hiriyur B, Waisman H, Smyth AW. Experimental application and enhancement of the XFEM-GA algorithm for the detection of flaws in structures. Computers and structures 2011; 89:556-570.
Chen L, Rabczuk T, Bordas SPA, Liu GR, Zeng KY, Kerfriden P. Extended finite element method with edge-based strain smoothing (ESm-XFEM) for linear elastic crack growth. Computer methods in applied mechanics and engineering 2012; 209:250-265.
Cheng KW, Fries TP. XFEM with hanging nodes for two-phase incompressible flow. Computer methods in applied mechanics and engineering 2012; 245-246:290-312.
Chessa J, Belytschko T. An enriched finite element method and level sets for axisymetric two-phase flow with surface tension. International journal for numerical methods in engineering 2003a; 58:2041-2064.
Chessa J, Belytschko T. An extended finite element method for two-phase fluids. Journal of applied mechanics 2003b; 70:10-17.
Chessa J, Belytschko T. Arbitrary discontinuities in space-time finite elements by level sets and X-FEM. International journal for numerical methods in engineering 2004; 61:2595-2614.
Chessa J, Smolinski P, Belytschko T. The extended finite element method (XFEM) for solidification problems. International journal for numerical methods in engineering 2002; 53:1959-1977.
Chessa J, Wang H, Belytschko T. On the construction of blending elements for local partition of unity enriched finite elements. International journal for numerical methods in engineering 2003; 57:1015-1038.
Choi YJ, Hulsen MA, Meijer HEH. An extended finite element method for the simulation of particulate viscoelastic flows. Journal of non-Newtonian fluid mechanics 2010; 165:607-624.
Choi YJ, Hulsen MA, Meijer HEH. Simulation of the flow of a viscoelastic fluid around a stationary cylinder using an extended finite element method. Computers & fluids 2012; 57:183-194.
Chopp DL, Sukumar N. Fatigue crack propagation of multiple coplanar cracks with the coupled extended finite element/fast marching method. International journal of engineering science 2003; 41:845-869.
Cosimo A, Fachinotti V, Cardona A. An enrichment scheme for solidification problems. Computational mechanics 2013; 52:17-35.
Court S, Fournié M, Lozinski A. A fictitious domain approach for the Stokes problem based on the extended finite element method. International journal for numerical methods in fluids 2013. DOI: 10.1002/fld.3839.
Crisfield MA, Alfano G. Adaptive hierarchical enrichment for delamination fracture using a decohesive zone model. International journal for numerical methods in engineering 2002; 54:1369-1390.
Curiel Sosa JL, Karapurath N. Delamination modelling of GLARE using the extended finite element method. Composites science and technology 2012; 72:788-791.
Carracedo, J.C., Troll, V.R., 2006. Seismicity and gas emissions on Tenerife: a real cause for alarm?. Geol. Today 22, 138–141.
Cayol, V., Cornet, F.H., 1998. Three-dimensional modelling of the 1983-1984 eruption of Piton de la Fournaise volcano, Reunion Island. J. Geophys. Res. 103, 18,025–18,037.
Caricchi, L., Annen, C., Blundy, J., Simpson, G., Pinel, V., 2014. Frequency and mag- nitude of volcanic eruptions controlled by magma injection and buoyancy. Nat. Geosci. 7 (2), 126–130.
Cavalié, O., Jónsson, S., 2014. Block-like plate movements in eastern Anatolia ob- served by InSAR. Geophys. Res. Lett. 41, 26–31.
Cembrano, J., Lara, L., 2009. The link between volcanism and tectonics in the south- ern volcanic zone of the Chilean Andes: a review. Tectonophysics 471 (1), 96–113.
Chaussard, E., Amelung, F., 2014. Regional controls on magma ascent and stor- age in volcanic arcs. Geochem. Geophys. Geosyst. 15. http://dx.doi.org/10.1002/ 2013GC005216.
Chestler, S.R., Grosfils, E.B., 2013. Using numerical modeling to explore the origin of intrusion patterns on Fernandina volcano, Galápagos Islands, Ecuador. Geophys. Res. Lett. 40 (17), 4565–4569.
Clemens, J.C., Mawer, C.K., 1992. Granitic magma transport by fracture propagation. Tectonophysics 204, 339–360.
Carslaw, S. & Jaeger, J. C. 1959. Conduction of Heat in Solids (2nd eds).Clarendon, Oxford, UK.
Cannat, M., et al. 1995. Proceedings of the ocean drilling program. Initial reports, 153

Clarke, J.D.A & Alley, N.F. 1993. Petrologic data on the evolution of the Great Australian Bight. Proceedings of the Gondwana Eight Symposium: International Gondwana Symposium, 8, 585-596.
Clark, S.P. 1966. Handbook of physical constants. Geological Society of America. Memoir 97, Washington, DC.
Coetzee, A. & Kisters, A.F.M. 2016. The 3D geometry of regional-scale dolerite saucer complexes and their feeders in the Secunda Complex, Karoo Basin. Journal of Volcanology and Geothermal Research, 317. doi: 10.1016/j.jvolgeores.2016.04.001
Costa, D.F.B., et al. 2016. Analysis of the geometry of diabase sills of the Serra Geral magmatism, by 2D seismic interpretation, in Guareì region, São Paulo, Paraná Basin, Brazil. Brazilian Journal of Geolog, 46 (4), 605-615. doi: 10.1590/2317-4889201620160078
Cooper, J.R., et al. 2007. Coal metamorphism by igneous intrusion in the Raton Basin, CO and NM: Implications for generation of volatiles. International Journal of Coal Geology, 71 (1), 15-27. doi: 10.1016/j.coal.2006.05.007
Davison, I., et al. 2010. Sub-basalt hydrocarbon prospectivity in the Rockall, Faroe-Shetland and Møre basins, NE Atlantic. Geological Society, London, 7, 1025-1032. doi: 10.1144/0071025
Delpino, D.H. and Bermúdez, A.M. 2009. Petroleum systems including unconventional reservoirs in intrusive igneous rocks (sills and laccoliths). The Leading Edge, 28 (7), 804-811. doi: 10.1190/1.3167782
De Kock, et al., 2017. Deflating the shale gas potential of South Africa's Main Karoo Basin.
South African Journals, 113, 1-12. doi: 10.17159/sajs.2017/20160331
Daw, W.G. 1977. Kerogen studies and geological interpretations. Journal of Geochemical Exploration, 7, 79-99. doi: 10.1016/0375-6742(77)90078-4
Drits, V.A., et al. 2007. Formation and transformation of mixed-layer minerals by Tertiary intrusives in Cretaceous mudstones, West Greenland. Clays and Clay Minerals, 55 (3). doi: 10.1346/CCMN.2007.0550304
Daniels, K.A., Kavanagh, J.L., Menand, T., Stephen, J.S.R., 2012. The shapes of dikes: evidence for the influence of cooling and inelastic deformation. Geol. Soc. Am. Bull. 124 (7–8), 1102–1112.
Deb, D., 2006. Finite Element Method, Concepts and Applications in Geomechanics.
PHI Learning Private Limited, New Delhi.
Druitt, T.H., Sparks, R.S.J., 1984. On the formation of calderas during ignimbrite eruptions. Nature 310, 679–681.
Dzurisin, D., 2006. Volcano Deformation: New Geodetic Monitoring Techniques.
Springer Verlag, Berlin.
Davis, P.M., 1983. Surface deformation associated with a dipping hydrofracture. J. Geophys. Res. 88, 5826–5834.
Deb, D., 2006. Finite Element Method: Concepts and Applications in Geomechanics.
Prentice-Hall, New Jersey.
Delaney, P.T., Pollard, D.D., 1981. Deformation of host rock and flow of magma dur- ing growth of minette dike and breccia-bearing intrusions near Ship Rock, New Mexico. In: U.S. Geol. Surv. Prof. Pap. vol. 1202, pp. 1–69.
Dzurisin, D., 2006. Volcano Deformation. Springer Verlag, New York.
Daneshyar A, Mohammadi S. Strong tangential discontinuity modeling of shear bands using the extended finite element method. Computational mechanics 2013; 52:1023-1038.
Daux C, Moës N, Dolbow J, Sukumar N, Belytschko T. Arbitrary branched and intersecting cracks with the extended finite element method. International journal for numerical methods in engineering 2000; 48:1741-1760.
De'Borst R, Réthoré J, Abellan MA. A numerical approach for arbitrary cracks in a fluid-saturated medium. Archive of applied mechanics 2006; 75:595-606.
Deb D, Das KC. Extended finite element method for the analysis of discontinuities in rock masses. Geotechnical and geological engineering 2010; 28:643-659.
Davis, P.M., 1983. Surface deformation associated with a dipping hydrofracture. J. Geophys. Res., 88, 5826-5834.
Deb, D., 2006. Finite Element Method: Concepts and Applications in Geomechanics. Prentice-Hall, New Jersey.
Delaney, P.T., Pollard, D.D., 1981. Deformation of host rock and flow of magma during growth of minette dike and breccia-bearing intrusions near Ship Rock, New Mexico. U.S. Geol. Surv. Prof. Pap. 1202, 1-69.
Dzurisin, D., 2006. Volcano Deformation. Springer Verlag, New York. Ernst, R.E., Grosfils, E.B., Mege, D., 2001. Giant dike swarms: Earth, Venus, and Mars. Annu. Rev. Earth Planet. Sci., 29, 489-534.
Dhia HB, Jamond O. On the use of XFEM within the Arlequin framework for the simulation of crack propagation. Computer methods in applied mechanics and engineering 2010; 199:1403-1414.
Dolbow J, Moës N, Belytschko T. An extended finite element method for modeling crack growth with frictional contact. Computer methods in applied mechanics and engineering 2001; 190:6825-6846.
Dolbow J, Moës N, Belytschko T. Modeling fracture in Mindlin-Reissner plates with the extended finite element method. International journal of solids and structures 2000b; 37:7161-7183.
Dolbow J, Moës N, Belytschko, T. Discontinuous enrichment in finite elements with a partition of unity method.

Finite elements in analysis and design 2000a; 36:235-260.
Deb, D., 2006. Finite Element Method: Concepts and Applications in Geomechanics. Prentice-Hall, New Jersey.
Dzurisin, D., 2006. Volcano Deformation. Springer Verlag, New York.
Dolbow J, Mosso S, Robbins J, Voth T. Coupling volume-of-fluid based interface reconstructions with the extended finite element method. Computer methods in applied mechanics and engineering 2008; 197:439-447.
Dolbow JE, Devan A. Enrichment of enhanced assumed strain approximations for representing strong discontinuities: addressing volumetric incompressibility and the discontinuous patch test. International journal for numerical methods in engineering 2004; 59:47-67.
Dolbow JE. An extended finite element method with discontinuous enrichment for applied mechanics. PhD dissertation, Theoretical and applied mechanics, Northwestern university, USA, 1999.
Dréau K, Chevaugeon N, Moës N. Studied X-FEM enrichment to handle material interfaces with higher order finite element. Computer methods in applied mechanics and engineering 2010; 199:1922-1936.
Duddu R, Chopp DL, Voorhees P, Moran B. Diffusional evolution of precipitates in elastic media using the extended finite element and the level set methods. Journal of computational physics 2011; 230:1249-1264.
Duflot M. The extended finite element method in thermoelastic fracture mechanics. International journal for numerical methods in engineering 2008; 74:827-847.
Davison, I., et al. 2010. Sub-basalt hydrocarbon prospectivity in the Rockall, Faroe-Shetland and Møre basins, NE Atlantic. Geological Society, London, 7, 1025-1032. doi: 10.1144/0071025
Delpino, D.H. and Bermúdez, A.M. 2009. Petroleum systems including unconventional reservoirs in intrusive igneous rocks (sills and laccoliths). The Leading Edge, 28 (7), 804-811. doi: 10.1190/1.3167782
De Kock, et al., 2017. Deflating the shale gas potential of South Africa's Main Karoo Basin. South African Journals, 113, 1-12. doi: 10.17159/sajs.2017/20160331
Daw, W.G. 1977. Kerogen studies and geological interpretations. Journal of Geochemical Exploration, 7, 79-99. doi: 10.1016/0375-6742(77)90078-4
Drits, V.A., et al. 2007. Formation and transformation of mixed-layer minerals by Tertiary intrusives in Cretaceous mudstones, West Greenland. Clays and Clay Minerals, 55 (3). doi: 10.1346/CCMN.2007.0550304
Davis, G. H., and Reynolds, S. J. 1996. Structural geology of rocks and regions (second edition): John Wiley & Sons, Inc., New York, 776 p.
Deb, D. 2006. Finite element method- concepts and applications in geomechanics.
Prentice Hall of India, New Delhi
Doré, A.G., Lundin, E.R., Jensen, L.N., Birkeland, Ø., Eliassen, P.E. & Fichler, C. 1999. Principal tectonic events in the evolution of the northwest European Atlantic margins. In Fleet, A.J. & Boldy, S.A.R. (eds.): Petroleum Geology of Northwest Europe: Proceedings of the 5th Conference. Geological Society of London, pp. 41– 61.
Evans, D., Graham, C., Armour, A. Bathurst, P. (eds). 2003. The Millennium Atlas: petroleum geology of the central and northern North Sea. Geological Society, London, 235-259.
Eide, C.H., et al. 2016. Basinscale architecture of deeply emplaced sill complexes: Jameson Land, East Greenland. Journal of the Geological Society. doi: 10.1144/jgs2016-018
Ebrahimi SH, Mohammadi S, Asadpoure A. An extended finite element (XFEM) approach for crack analysis in composite media. International journal of civil engineering 2008; 6:198-207.
Edke MS, Chang KH. Shape optimization for 2-D mixed-mode fracture using Extended FEM (XFEM) and Level Set Method (LSM). Structural and multidisciplinary optimization 2011; 44:165-181.
Elguedj T, Gravouil A, Combescure A. A mixed augmented Lagrangian-extended finite element method for modelling elastic-plastic fatigue crack growth with unilateral contact. International journal or numerical methods in engineering 2007; 71:1569-1597.
Elguedj T, Gravouil A, Combescure A. Appropriate extended functions for X-FEM simulation of plastic fracture mechanics. Computational methods in applied mechanical engineering 2006; 195:501-515.
Elguedj T, Gravouil A, Maigre H. An explicit dynamics extended finite element method. Part 1: mass lumping for arbitrary enrichment functions. Computer methods in applied mechanics and engineering 2009; 198:2297-2317.
Esna Ashari S, Mohammadi S. Fracture analysis of FRP-reinforced beams by orthotropic XFEM. Journal of composite materials 2012; 46:1367-1389.
Esser P, Grande J, Reusken A. An extended finite element method applied to levitated droplet problems. International journal for numerical methods in engineering 2010; 84:757-773
Eppelbaum, L. & Kutasov, I. & Pilchin, A. 2014. Applied Geothermics. Springer. Canada. 52pp.
Elders, W.A. & Fridleifsson, G.O. & Saito, S. 2003. The Iceland deep drilling project: Its global significance. International Geothermal Conference, Reykjavik, 6
Ernst, R.E., Grosfils, E.B., Mege, D., 2001. Giant dike swarms: Earth, Venus, and Mars. Annu. Rev. Earth Planet. Sci. 29, 489–534.

Eisenlohr, T., 1995. Die Thermalwässer der Armutlu-Halbinsel (NW-Türkei) und deren Beziehung zu Geologie und Aktiver Tektonik, PhD. Dissertation, ETH-Zürich, Nr.11340.

Eide, C.H., et al. 2016. Basinscale architecture of deeply emplaced sill complexes: Jameson Land, East Greenland. *Journal of the Geological Society.* doi: 10.1144/jgs2016-018

Eppelbaum, L. & Kutasov, I. & Pilchin, A. 2014. Applied Geothermics. Springer. Canada. 52pp.

Elders, W.A. & Fridleifsson, G.O. & Saito, S. 2003. The Iceland deep drilling project: Its global significance. *International Geothermal Conference, Reykjavik,* **6**

Farooqui, M., et al. 2009. Evaluating volcanic reservoirs. *Oilfield Review*, **21** (1), 36-47.

Francis, T.J.G. 1982. Thermal expansion effects in deep-sea sediments. *Nature.* **299**, 334-336

Fjeldskaar, W. et al., 2008. Thermal modelling of magmatic intrusions in the Gjallar Ridge, Norwegian Sea: implications for vitrinite reflectance and hydrocarbon maturation. *Basin Research,* **8** (1), 143-159. , doi: 10.1111/j.1365-2117.2007.00347

Fournier, R.O., 1991. Water geothermometers applied to geothermal energy. In: D'Amore,

F. (Ed.), Application of Geochemistry in Geothermal Reservoir Development. UNITAR, Rome, Italy, pp. 37–65.

Furlong, K.P., Schwartz, S.Y., 2004. Influence of the Mendocino triple junction on the tectonics of coastal California. Annu. Rev. Earth Planet. Sci. 32, 403–433.

Farooqui, M., et al. 2009. Evaluating volcanic reservoirs. Oilfield Review, 21 (1), 36-47.

Francis, T.J.G. 1982. Thermal expansion effects in deep-sea sediments. Nature. 299, 334-336

Fjeldskaar, W. et al., 2008. Thermal modelling of magmatic intrusions in the Gjallar Ridge, Norwegian Sea: implications for vitrinite reflectance and hydrocarbon maturation. Basin Research, 8 (1), 143-159. , doi: 10.1111/j.1365-2117.2007.00347

Fagerstorm M, Larsson R. A thermo-mechanical cohesive zone formulation for ductile fracture. Journal of the mechanics and physics of solids 2008; 56:3037-3058.

Fan X, Zhang W, Wang T, Liu G, Zhang J. Investigation on periodic cracking of elastic film/substrate system by the extended finite element method. Applied surface science 2011; 257:6718-6724.

Fan XL, Zhang WX, Wang TJ, Sun Q. The effect of thermally grown oxide on multiple surface cracking in air plasma sprayed thermal barrier coating system. Surface & coatings technology 2012; 208:7-13.

Ferrie E, Buffiere JY, Ludwig W, Gravouil A, Edwards L. Fatigue crack propagation: In situ visualization using X-ray microtomography and 3D simulation using the extended finite element method. Acta materialia 2006; 54:1111-1122.

Fries T, Belytschko T. The intrinsic XFEM: a method for arbitrary discontinuities without additional unknowns. International journal for numerical methods in engineering 2006; 68:1358-1385.

Fries T. A corrected XFEM approximation without problems in blending elements. International journal for numerical methods in engineering 2008; 75:503-532.

Fries TP, Baydoun M. Crack propagation with the extended finite element method and a hybrid explicit-implicit crack description. International journal for numerical methods in engineering 2012; 89:1527-1558.

Fries TP, Belytschko T. The extended/generalized finite element method: An overview of the method and its applications. International journal for numerical methods in engineering 2010; 84:253-304.

Fries TP, Zilian A. On time integration in the XFEM. International journal for numerical methods in engineering 2009; 79:69-93.

Fries TP. The intrinsic XFEM for two-fluid flows. International journal for numerical methods in engineering 2009; 60:437-471.

Folch, A., Marti, J., 1998. The generation of overpressure in felsic magma chambers by replenishment. Earth Planet. Sci. Lett. 163 (1), 301–314.

Furlong, K.P., Schwartz, S.Y., 2004. Influence of the Mendocino triple junction on the tectonics of coastal California. Annu. Rev. Earth Planet. Sci. 32, 403–433.

Faleide, J.I., Tsikalas, F., Breivik, A.J., Mjelde, R., Ritzmann, O., Engen, O., Wilson, J. & Eldholm, O. 2008. Structure and evolution of the continental margin off Norway and Barents Sea. Episodes 31, 82–91.

Fejerskov, M. and Lindholm, C.D. 2000. Crustal stress in and around Norway; an evaluation of stress-generating mechanisms. In Nøttvedt. A. (ed.) Dynamics of the Norwegian margin, Geological Society, London, Special Publications, 167, 451– 467.

Fossen, H. 2010. Structural Geology. Cambridge University Press, Cambridge, UK, p. 154.

Fjeldskaar, W., Lindholm, C., Dehls, J.F. and Fjeldskaar, I. 2000. Post- glacial uplift, neotectonics and seismicity in Fennoscandia. Quaternary Science Reviews, 19, 1413–1422.

Gabrielsen. R.H., Braathen, A, Dehls, J. & Roberts, D. 2002. Tectonic Lineaments of Norway. Norsk Geologisk Tidsskrift, Vol. 82,pp. 153 – 174 Trondheim ISSN 029- 196X

Gabrielsen, R.H. and Doré, A.G. 1995. The history of tectonic models on the Norwegian Continental Shelf. In Hanslien, S. (ed.) Petroleum Exploration and Exploitation in Norway. Norwegian Petroleum Society (NPF) Special Publication 4, Elsevier, Amsterdam. 333-368.

Gabrielsen, R.H., Odinsen, T. & Grunnaleite, l. 1999. Structuring of the Northern Viking Graben and the Møre Basin; the influence of basement structural grain, and the particular role of the MøreTrøndelag Fault Complex. Marine and Petroleum Geology 16,443- 465.

Ganerød, M. 2003. Lineamenter, brudd og seismisitet: I relasjon til grunnvann på Bømlo, Vestlandet, MSc thesis, University of Bergen.

Grünthal G., Wahlström R., Stromeyer D. 2009. The unified catalogue of earthquakes in central, northern, and northwestern Europe (CENEC)—updated and expanded to the last millennium. Journal of Seismology 13, 517–541.

Galland, O., et al. 2009. Experimental modelling of shallow magma emplacement: Application to saucer-shaped intrusions. Earth and Planetary Science Letters, 277, 373-383. doi: 10.1016/j.epsl.2008.11.003

Galushkin, Y.I. 1997. Thermal effects of igneous intrusions on maturity of organic matter: a possible mechanism of intrusion. Org. Geochem, 26 (11-12), 645-658. doi: 10.1016/S0146- 6380(97)00030-2

Galerne, C.Y., & Neumann, E.R. & Planke, S. 2008. Emplacement mechanism of sill complexes: Information from the geochemical architecture of the Golden Valley Sill Complex, South Africa. Journal of Volcanology and Geothermal Research, 177, 425-440. doi: 10.1016/j.jvolgeores.2008.06.004

Gressier J-B., et al. 2010. Control of pore fluid pressure on depth of emplacement of magmatic sills: An experimental approach. Tectonophysics, 489, 1-13. doi: 10.1016/j.tecto.2010.03.004

Guo, L. & Jia, C. & Konhauser, K.O. 2016. Depositional system and hydrocarbon accumulation in Gubei slope zone, Zhanhua Depression, Bohai Bay Basin, eastern China. Energy and Exploration, 34 (6), 810-827. doi: 10.1177/0144598716665015

Gaffney, E.S., Damjanac, B., 2006. Localization of volcanic activity: topographic effects on dike propagation, eruption and conduit formation. Geophys. Res. Lett. 33, L14313. http://dx.doi.org/10.1029/2006GL026852.

Gaffney, E.S., Damjanac, B., Valentine, G.A., 2007. Localization of volcanic activity, 2: effects of pre-existing structure. Earth Planet. Sci. Lett. 263 (3), 323–338.

Gerbault, M., 2012. Pressure conditions for shear and tensile failure around a cir- cular magma chamber, insight from elasto-plastic modelling. Geol. Soc. (Lond.) Spec. Publ. 367 (1), 111–130.

Gerbault, M., Cappa, F., Hassani, R., 2012. Elasto-plastic and hydromechanical mod- els of failure around an infinitely long magma chamber. Geochem. Geophys. Geosyst. 13 (3).

Geshi, N., Neri, M., 2014. Dynamic feeder dyke systems in basaltic volcanoes: the exceptional example of the 1809 Etna eruption (Italy). Earth Sci. Front. 2, 13. http://dx.doi.org/10.3389/feart.2014.00013.

Geyer, A., Marti, J., 2009. Stress fields controlling the formation of nested and over- lapping calderas: implications for the understanding of caldera unrest. J. Vol- canol. Geotherm. Res. 181, 185–195.

Geyer, A., Folch, A., Martí, J., 2006. Relationship between caldera collapse and magma chamber withdrawal: an experimental approach. J. Volcanol. Geotherm. Res. 157 (4), 375–386.

Gregg, P.M., De Silva, S.L., Grosfils, E.B., Parmigiani, J.P., 2012. Catastrophic caldera- forming eruptions: thermomechanics and implications for eruption triggering and maximum caldera dimensions on Earth. J. Volcanol. Geotherm. Res. 241, 1–12.

Gregg, P.M., de Silva, S.L., Grosfils, E.B., 2013. Thermomechanics of shallow magma chamber pressurization: implications for the assessment of ground deformation data at active volcanoes. Earth Planet. Sci. Lett. 384, 100–108.

Gregg, P.M., Grosfils, E.B., de Silva, S.L., 2015. Catastrophic caldera-forming eruptions II: the subordinate role of magma buoyancy as an eruption trigger. J. Volcanol. Geotherm. Res. 305, 100–113.

Grosfils, E.B., 2007. Magma reservoir failure on the terrestrial planets: assessing the importance of gravitational loading in simple elastic models. J. Volcanol. Geotherm. Res. 166 (2), 47–75.

Grosfils, E.B., McGovern, P.J., Gregg, P.M., Galgana, G.A., Hurwitz, D.M., Long, S.M., Chestler, S.R., 2015. Elastic models of magma reservoir mechanics: a key tool for investigating planetary volcanism. Geol. Soc. (Lond.) Spec. Publ. 401 (1), 239–267.

Galindo, I., Gudmundsson, A., 2012 Basaltic feeder-dykes in rift zones: geometry, emplacement, and effusion rates. Natural Hazards and Earth System Sciences, 12, 3683–3700.

Garcia, A. Ortiz, R., Marrero, J.M., Sanchez, N., Tarraga, M., Vila, J., Correig, Macia, R., Sleeman, R., 2006. Monitoring the reawakening of Canary Islands' Teide Volcano. Eos, 87, 61-72.

Geshi, N., Kusumoto, S., Gudmundsson, A., 2010. Geometric difference between non-feeder and feeder dikes. Geology, 38, 195–198.
Geshi, N., Kusumoto, S., Gudmundsson, A., 2012. Effects of mechanical layering of host rocks on dike growth and arrest. J. Volcanol. Geotherm. Res., 223-224, 74-82.
Geshi, N., Neri, M., 2014. Dynamic feeder dyke systems in basaltic volcanoes: the exceptional example of the 1809 Etna eruption (Italy). Frontiers in Earth Science, 2, doi: 10.3389/feart.2014.00013.
Gonnermann, H.M., Manga, M., 2013. Dynamics of magma ascent in the volcanic conduit. In: Fagents, S.A., Gregg, T.K.P., Lopes, R.M.C. (eds), Modeling Volcanic Processes. Cambridge University Press, Cambridge, pp. 55-84.
Gottsmann, J., Wooller, L., Marti, J., Fernandez, J., Camacho, A.G., Gonzalez, P.J., Garcia, A., Rymer, H., 2006. New evidence for the reawakening of Teide volcano. Geophys. Res. Lett., 33, L20311, doi:10.1029/2006GL027523.
Greenland, L.P., Rose, W.I., Stokes, J.B., 1985. An estimate of gas emissions and magmatic gas content from Kilauea volcano. Geochim. Cosmochim. Acta, 49, 125-129.
Greenland, L. P., Okamura, A. T., Stokes, J. B., 1988. Constraints on the mechanics of the eruption. In: Wolfe, E. W (ed), The Puu Oo Eurption of Kilauea Volcano, Hawaii: Episodes Through 20, January 3, 1983 Through June 8, 1984, US Geol. Survey Professional Paper, 1463, 155–164.
Gudmundsson, A., 2002. Emplacement and arrest of sheets and dykes in central volcanoes. J. Volcanol. Geotherm. Res., 116, 279-298.
Gudmundsson, A., 2003. Surface stresses associated with arrested dykes in rift zones: Bull. Volcanol., 65, 606-619.
Gudmundsson, A., 2009. Toughness and failure of volcanic edifices. Tectonophysics, 471, 27-35.
Gudmundsson, A., 2011a. Deflection of dykes into sills at discontinuities and magma-chamber formation. Tectonophysics, 500, 50-64.
Gudmundsson, A., 2011b. Rock Fractures in Geological Processes. Cambridge University Press, Cambridge.
Gudmundsson, A., 2017. The Glorious Geology of Iceland's Golden Circle. Springer-Nature, Heidelberg.
Gudmundsson, A., Brenner, S.L., 2001. How hydrofractures become arrested. Terra Nova, 13, 456-462.
Gudmundsson, A., Friese, N., Galindo, I., Philipp, S.L., 2008. Dike-induced reserve faulting in a graben. Geology, 36, 123-126, doi: 10.1130/G24185A
Gudmundsson, A., Lecoeur, N., Mohajeri, N., Thordarson, T., 2014. Dike emplacement at Bardarbunga, Iceland, induces unusual stress changes, caldera deformation, and earthquakes. Bulletin of Volcanology, 76, 869, doi: 10.1007/s00445-014-0869-8
Gudmundsson, A., Loetveit, I.F., 2005. Dyke emplacement in layered and faulted rift zone. Journal of Volcanology and Geothermal Research, 144, 311-327.
Gudmundsson, A., Marinoni, L., Marti, J., 1999. Injection and arrest of dykes: implications for volcanic hazards. Journal of Volcanology and Geothermal Research, 88, 1-13.
Gudmundsson, A., Philipp, L., 2006. How local stress fields prevent volcanic eruptions. J. Volcanol. Geotherm. Res . 158, 257-268.
Gerstenberger A, Wall WA. An eXtended Finite Element Method/Lagrange multiplier based approach for fluid-structure interaction. Computer methods in applied mechanics and engineering 2008a; 197:1699-1714.
Gerstenberger A, Wall WA. Enhancement of fixed-grid methods towards complex fluid-structure interaction applications. International journal for numerical methods in fluids 2008b; 57:1227-1248.
Ghoneim A, Hunedy J, Ojo OA. An interface-enriched extended finite element-level set simulation of solutal melting of additive powder particles during transient liquid phase bonding. Metallurgical and materials transactions A 2013; 44:1139-1151.
Giner E, Navarro C, Sabsabi M, Tur M, Dominguez J, Fuenmayor FJ. Fretting fatigue life prediction using the extended finite element method. International journal of mechanical sciences 2011; 53: 217-225.
Giner E, Sukumar N, Denia FD, Fuenmayor FJ. Extended finite element method for fretting fatigue crack propagation. International journal of solids and structures 2008a; 45: 5675-5687.
Giner E, Sukumar N, Fuenmayor FJ, Vercher A. Singularity enrichment for complete sliding contact using the partition of unity finite element method. International journal for numerical methods in engineering 2008b; 76:1402-1418.
Golewski GL, Golewski P, Sadowski T. Numerical modelling crack propagation under Mode II fracture in plain concretes containing siliceous fly-ash additive using XFEM method. Computational materials science 2012; 62:75-78.
Gonzalez-Albuixech VF, Giner E, Tarancon JE, Fuenmayor FJ, Gravouil A. Domain integral formulation for 3-D curved and non-planar cracks with the extended finite element method. Computer methods in applied mechanics and engineering 2013a; 264:129-144.
González-Albuixech VF, Giner E, Tarancón JE, FuenmayorFJ, Gravouil A. Convergence of domain integrals for stress intensity factor extraction in 2-D curved cracks problems with the extended finite element method. International journal for numerical methods in engineering 2013b; 94:740-757.

Gordeliy E, Peirce A. Coupling schemes for modeling hydraulic fracture propagation using the XFEM. Computer methods in applied mechanics and engineering 2013; 253:305-322.
Gracie R, Belytschko T. Concurrently coupled atomistic and XFEM models for dislocations and cracks. International journal for numerical methods in engineering 2009; 78:354-378.
Gracie R, Craig JR. Modelling well leakage in multilayer aquifer systems using the extended finite element method. Finite elements in analysis and design 2010; 46:504-513.
Gracie R, Oswald J, Belytschko T. On a new extended finite element method for dislocations: Core enrichment and nonlinear formulation. Journal of the mechanics and physics of solids 2008a; 56:200-214.
Gracie R, Wang H, Belytschko T. Blending in the extended finite element method by discontinuous Galerkin and assumed strain methods. International journal for numerical methods in engineering 2008b; 74:1645-1669.
Gravouil A, Elguedj T, Maigre H. An explicit dynamics extended finite element method. Part 2: Element-by-element stable-explicit/explicit dynamic scheme. Computer methods in applied mechanics and engineering 2009; 198:2318-2328.
Gravouil A, Moës N, Belytschko T. Non-planar 3D crack growth by the extended finite element and level sets-Part II: Level set update. International journal for numerical methods in engineering 2002; 53:2569-2586.
Groß S, Reusken A. An extended pressure finite element space for two-phase incompressible flows with surface tension. Journal of computational physics 2007; 224:40-58.
Guidault PA, Allix O, Champaney L, Cornuault C. A multiscale extended finite element method for crack propagation. Computer methods in applied mechanics and engineering 2008; 197:381-399.
Galland, O., et al. 2009. Experimental modelling of shallow magma emplacement: Application to saucer-shaped intrusions. Earth and Planetary Science Letters, 277, 373-383. doi: 10.1016/j.epsl.2008.11.003
Galushkin, Y.I. 1997. Thermal effects of igneous intrusions on maturity of organic matter: a possible mechanism of intrusion. Org. Geochem, 26 (11-12), 645-658. doi: 10.1016/S0146- 6380(97)00030-2
Galerne, C.Y., & Neumann, E.R. & Planke, S. 2008. Emplacement mechanism of sill complexes: Information from the geochemical architecture of the Golden Valley Sill Complex, South Africa. Journal of Volcanology and Geothermal Research, 177, 425-440. doi: 10.1016/j.jvolgeores.2008.06.004
Gressier J-B., et al. 2010. Control of pore fluid pressure on depth of emplacement of magmatic sills: An experimental approach. Tectonophysics, 489, 1-13. doi: 10.1016/j.tecto.2010.03.004
Gudmundsson, A. 1990. Emplacement of dykes, sills and crustal magma chambers at divergent plate boundaries. Tectonophysics, 176, 257-275.
Galindo, I., Gudmundsson, A., 2012. Basaltic feeder-dykes in rift zones: geometry, emplacement, and effusion rates. Nat. Hazards Earth Syst. Sci. 12, 3683–3700.
Garcia, A. Ortiz, R., Marrero, J.M., Sanchez, N., Tarraga, M., Vila, J., Correig, Macia, R., Sleeman, R., 2006. Monitoring the reawakening of Canary Islands' Teide Vol- cano. Eos, 87, 61–72.
Gautneb, H., Gudmundsson, A., 1992. Effect of local and regional stress fields on sheet emplacement in West Iceland. J. Volcanol. Geotherm. Res. 51, 339–356.
Geshi, N., Neri, M., 2014. Dynamic feeder dyke systems in basaltic volcanoes: the ex- ceptional example of the 1809 Etna eruption (Italy). Front. Earth Sci. 2, https://doi. org/10.3389/feart.2014.00013.
Geshi, N., Kusumoto, S., Gudmundsson, A., 2010. Geometric difference between non-feeder and feeder dikes. Geology 38, 195–198.
Geshi, N., Kusumoto, S., Gudmundsson, A., 2012. Effects of mechanical layering of host rocks on dike growth and arrest. J. Volcanol. Geotherm. Res. 223-224, 74–82.
Geyer, A., Gottsmann, J., 2010. The influence of mechanical stiffness on caldera de- formation and implications for the 1971–1984 Rabaul uplift (Papua New Guinea). Tectonophysics 483, 399–412. https://doi.org/10.1016/j.tecto.2009.10.029.
Gonnermann, H.M., Manga, M., 2013. Dynamics of magma ascent in the volcanic con- duit. In: Fagents, S.A., Gregg, T.K.P., Lopes, R.M.C. (Eds.), Modeling Volcanic Processes. Cambridge University Press, Cambridge, pp. 55–84.
Gottsmann, J., Wooller, L., Marti, J., Fernandez, J., Camacho, A.G., Gonzalez, P.J., Garcia, A., Rymer, H., 2006. New evidence for the reawakening of Teide volcano. Geophys. Res. Lett. 33, L20311https://doi.org/10.1029/2006GL027523.
Greenland, L.P., Rose, W.I., Stokes, J.B., 1985. An estimate of gas emissions and mag- matic gas content from Kilauea volcano. Geochim. Cosmochim. Acta 49, 125–129.
Greenland, L. P., Okamura, A. T., Stokes, J. B., 1988. Constraints on the mechanics of the eruption. In: Wolfe, E. W (ed), The Puu Oo Eurption of Kilauea Volcano, Hawaii: Episodes through 20, January 3, 1983 through June 8, 1984, US Geol.
Survey Professional Paper, vol. 1463, 155–164.

Gudmundsson, A., 2002. Emplacement and arrest of sheets and dykes in central volca- noes. J. Volcanol. Geotherm. Res. 116, 279–298.
Gudmundsson, A., 2003. Surface stresses associated with arrested dykes in rift zones.
Bull. Volcanol. 65, 606–619.
Gudmundsson, A., 2005. Effects of mechanical layering on the development of normal faults and dykes in Iceland. Geodin. Acta 18, 11–30.
Gudmundsson, A., 2009. Toughness and failure of volcanic edifices. Tectonophysics 471, 27–35.
Gudmundsson, A., 2011. Deflection of dykes into sills at discontinuities and magma-chamber formation. Tectonophysics 500, 50–64.
Gudmundsson, A., 2011. Rock Fractures in Geological Processes, Cambridge Univer- sity Press, Cambridge.
Gudmundsson, A., 2017. The Glorious Geology of Iceland's Golden Circle.
Springer-Nature, Heidelberg.
Gudmundsson, A., Brenner, S.L., 2001. How hydrofractures become arrested. Terra Nova 13, 456–462.
Gudmundsson, A., Loetveit, I.F., 2005. Dyke emplacement in layered and faulted rift zone. J. Volcanol. Geotherm. Res. 144, 311–327.
Gudmundsson, A., Philipp, L., 2006. How local stress fields prevent volcanic erup- tions. J. Volcanol. Geotherm. Res. 158, 257–268.
Gudmundsson, A., Marinoni, L., Marti, J., 1999. Injection and arrest of dykes: implica- tions for volcanic hazards. J. Volcanol. Geotherm. Res. 88, 1–13.
Gudmundsson, A., Friese, N., Galindo, I., Philipp, S.L., 2008. Dike-induced reserve faulting in a graben. Geology 36, 123–126. https://doi.org/10.1130/G24185A.
Gudmundsson, A., Lecoeur, N., Mohajeri, N., Thordarson, T., 2014. Dike emplace- ment at Bardarbunga, Iceland, induces unusual stress changes, caldera deforma- tion, and earthquakes. Bull. Volcanol. 76, 869https://doi.org/10.1007/s00445-014- 0869-8.
Gudmundsson, A. 2011. Rock fractures in Geological Processes. Cambridge University Press, Cambridge, U.K. 578pp.
Gudmundsson, A. 2012. Magma chambers: Formation, local stresses, excess pressures, and compartments. Journal of Volcanology and Geothermal Research, 237-238, 19-41. doi: 10.1016/j.jvolgeores.2012.05.015
Gudmundsson, A. & Løtveit I.F. 2012. Sills as fractured hydrocarbon reservoirs: examples and models. Geological Society of London, 374, 251-271. doi: 10.1144/SP374.5
Galindo, I., Gudmundsson, A., 2012 Basaltic feeder-dykes in rift zones: geometry, emplacement, and effusion rates. Natural Hazards and Earth System Sciences, 12, 3683–3700.
Gautneb, H., Gudmundsson, A., 1992. Effect of local and regional stress fields on sheet emplacement in West Iceland. J. Volcanol. Geoth. Res .51, 339-356.
Gautneb, H., Gudmundsson, A., Oskarsson, N., 1989. Structure, petrochemistry, and evolution of a sheet swarm in an Icelandic central volcano. Geol. Mag., 126, 659-673.
Geshi, N., Kusumoto, S., Gudmundsson, A., 2010. Geometric difference between non-feeder and feeder dikes. Geology, 38, 195–198.
Geshi, N., Kusumoto, S., Gudmundsson, A., 2012. Effects of mechanical layering of host rocks on dike growth and arrest. J. Volcanol. Geotherm. Res., 223-224, 74-82.
Gudmundsson, A., 1995. Infrastructure and mechanics of volcanic systems in Iceland. J. Volcanol. Geotherm. Res., 64, 1-22.
Gudmundsson, A., 1998. Magma chambers modeled as cavities explain the formation of rift zone central volcanoes and their eruption and intrusion statistics. J. Geophys. Res., 103, 7401-7412.
Gudmundsson, A., 2003. Surface stresses associated with arrested dykes in rift zones: Bull. Volcanol., 65, 606-619.
Gudmundsson, A., 2011a. Rock Fractures in Geological Processes. Cambridge University Press, Cambridge.
Gudmundsson, A., 2011b. Deflection of dykes into sills at discontinuities and magma-chamber formation. Tectonophysics, 500, 50-64.
Gudmundsson, A., 2019. Volcanotectonics. Cambridge University Press, Cambridge.
Gudmundsson, A., Brenner, S.L., 2001. How hydrofractures become arrested. Terra Nova, 13, 456-462.
Gudmundsson, A., Loetveit, I.F., 2005. Dyke emplacement in layered and faulted rift zone. Journal of Volcanology and Geothermal Research, 144, 311-327.
Gudmundsson, A., Pasquare, F.A., Tibaldi, A., 2018. Dykes, sills, laccoliths, and inclined sheets in Iceland. In: Breitkreuz, C., Rocchi, S. (eds), Physical Geology of Shallow Magmatic Systems: Dykes, Sills and Laccoliths. Berlin, Springer, pp. 363-376.
Guo, L. & Jia, C. & Konhauser, K.O. 2016. Depositional system and hydrocarbon accumulation in Gubei slope zone, Zhanhua Depression, Bohai Bay Basin, eastern China. Energy and Exploration, 34 (6), 810-827. doi: 10.1177/0144598716665015

Gudmundsson, A., 1990. Emplacement of dikes, sills and crustal magma chambers at divergent plate boundaries. Tectonophysics 176, 257–275.
Gudmundsson, A., 2006. How local stresses control magma-chamber ruptures, dyke injections, and eruptions in composite volcanoes. Earth-Sci. Rev. 79, 1–31.
Gudmundsson, A., 2011. Rock Fractures in Geological Processes. Cambridge Univer- sity Press, Cambridge.
Gudmundsson, A., 2012. Magma chambers: formation, local stresses, excess pres- sures, and compartments. J. Volcanol. Geotherm. Res. 237–238, 19–41.
Gudmundsson, A., 2015. Collapse-driven large eruptions. J. Volcanol. Geotherm.
Res. 304, 1–10.
Gudmundsson, A., Philipp, S.L., 2006. How local stress fields prevent volcanic erup- tions. J. Volcanol. Geotherm. Res. 158, 257–268.
Herece, E., 2008. Atlas of East Anatolian Fault. Special Publication Series. General Directorate of Mineral Research and Exploration, Ankara, Turkey.
Hubert-Ferrari, A., King, G., Woerd, J., Van der Villa, I., Altunel, E., Armijo, R., 2009. Long-term evolution of the North Anatolian Fault: new constraints from its east- ern termination. Geol. Soc. (Lond.) Spec. Publ. 311 (1), 133–154.
Hurwitz, D.M., Long, S.M., Grosfils, E.B., 2009. The characteristics of magma reservoir failure beneath a volcanic edifice. J. Volcanol. Geotherm. Res. 188 (4), 379–394. Hutton, D.H., 1988. Granite emplacement mechanisms and tectonic controls: in- ferences from deformation studies. Trans. R. Soc. Edinb. Earth Sci. 79 (2–3),245–255.
Hansen, D.M. & Cartwright, J. 2006. Saucer-shaped sill with lobate morphology revealed by 3D seismic data: implications for resolving a shallow-level sill emplacement mechanism. Journal of the Geological Society, 163 (3), 509-523.
Hansen, D.M. et al. 2011. Early Cenozoic saucer-shaped sills of the Faroe Islands: an example of intrusive styles in basaltic lava piles. Journal of the Geological Society, 168, 159-178. doi: 10.1144/0016-76492010-012
Hattori G, Rojas-Díaz R, Sáez A, Sukumar N, García-Sánchez F. New anisotropic crack-tip enrichment functions for the extended finite element method. Computational mechanics 2012; 50:591-601.
Hettich T, Ramm E. Interface material failure modeled by the extended finite-element method and level sets. Computer methods in applied mechanics and engineering 2006; 195:4753-4767.
Hiriyur B, Waisman H, Deodatis G. Uncertainty quantification in homogenization of heterogeneous microstructures modeled by XFEM. International journal for numerical methods in engineering 2011; 88:257-278.
Holl M, Rogge T, Loehnert S, Wriggers P, Rolfes R. 3D multiscale crack propagation using the XFEM applied to a gas turbine blade. Compuational mechanics 2013. DOI 10.1007/s00466-013-0900-5
Hosseini SS, Bayesteh H, Mohammad S. Thermo-mechanical XFEM crack propagation analysis of functionally graded materials. Materials science & engineering A 2013; 561:285-302.
Huang H, Long TA, Wan J, Brown WP. On the use of enriched finite element method to model subsurface features in porous media flow problems. Computational geosciences 2011; 15:721-736.
Huang R, Prevost JH, Huang ZY, Suo Z. Channel-cracking of thin films with the extended finite element method. Engineering fracture mechanics 2003a; 70:2513-2526.
Huang R, Sukumar N, Prevost JH. Modeling quasi-static crack growth with the extended finite element method Part II: Numerical applications. International journal of solids and structures 2003b; 40:7539-7552.
Huynh DBP, Belytschko T. The extended finite element method for fracture in composite materials. International journal for numerical methods in engineering 2009; 77:214-239.
Holford, S.P., et al. 2012. Seismic analysis of igneous systems in sedimentary basins and their impacts on hydrocarbon prospectivity: Examples from the southern Australian margin. APPEA Journal, 52, 229-252. doi: 10.1071/AJ11017
Mitigation of Volcano Hazards. Springer, Berlin Heidelberg, pp. 221–256.
He, M.Y., Hutchison, J.W., 1989. Crack deflection at an interface between dissimilar elastic materials. Int. J. Solids Struct. 25, 1053–1067.
Hutchinson, J.W., 1996. Stresses and Failure Modes in Thin Films and Multilayers. Notes for a Dcamm Course. Technical University of Denmark, Lyngby, 1–45.
Herece, E., 2008. Atlas of East Anatolian Fault. General Directorate of Mineral Research and Exploration. Special Publication Series, Ankara, Turkey.
Hermanrud, C. & Nordgård Bolås, H.M. 2002. Leakage from overpressured hydrocarbon reservoirs at Haltenbanken and in the northern North Sea. In: 14 A. W. Martinius et al. Koestler, A.G. & Hunsdale, R. (eds) Hydrocarbon Seal Quantification. Norwegian Petroleum Society, Special Publications, 11, 221–23

Hermanrud, C., Wensaas, L., Teige, G.M.G., Nordgard, H.M., Hansen, S.& Vik, E. 1998. Shale porosities from well logs on Haltenbanken (Offshore Mid-Norway) show no influence of overpressuring, in B.E. Law, G.F. Ulmishek, and V.I. Slavin (eds.) Abnormal Pressures in Hydrocarbon environments: AAPG Memoir 70, p. 65-85.

Hansen, D.M. & Cartwright, J. 2006. Saucer-shaped sill with lobate morphology revealed by 3D seismic data: implications for resolving a shallow-level sill emplacement mechanism. Journal of the Geological Society, 163 (3), 509-523.

Hansen, D.M. et al. 2011. Early Cenozoic saucer-shaped sills of the Faroe Islands: an example of intrusive styles in basaltic lava piles. Journal of the Geological Society, 168, 159-178. doi: 10.1144/0016-76492010-012

Holford, S.P., et al. 2012. Seismic analysis of igneous systems in sedimentary basins and their impacts on hydrocarbon prospectivity: Examples from the southern Australian margin. APPEA Journal, 52, 229-252. doi: 10.1071/AJ11017

Hubert-Ferrari, A., King, G., van der Woerd, J., Villa, I., Altunel, E., Armijo, R., 2009. Long-term evolution of the North Anatolian Fault: new constraints from its eastern termination. In: van Hinsbergen, D.J.J., Edwards, M.A., Govers, R. (Eds.), Collision and Collapse at the Africa-Arabia-Eurasia Subduction Zone, pp. 133–154 Geol. Soc. Spec. Publ. 311.

Harker, A., 1904. The Tertiary Igneous Rocks of Skye. UK Geological Surv. Mem., 481 pp.

Isida, M., 1955. On the tension of a semi-infinite plate with an elliptical hole. Sc. Pap.

Isik, V., Uysal, I.T., Caglayan, A., Seyitoglu, G., 2014. The evolution of intraplate fault systems in central Turkey: Structural evidence and Ar-Ar and Rb-Sr age constraints for the Savcili Fault Zone. Tectonics 33 (10), 1875–1899.

Iyer, K., et al. 2017. Modelling hydrothermal venting in volcanic sedimentary basins: Impact on hydrocarbon maturation and paleoclimate. *Earth and Planetary Science Letters,* **467**, 30- 42. doi: 10.1016/j.epsl.2017.03.023

Italiano, F., Sasmaz, A., Yuce, G., Okan, O.O., 2013. Thermal fluids along the East Anatolian Fault Zone (EAFZ): geochemical features and relationships with the tec- tonic setting. Chem. Geol. 339, 103–114

Iyer, K., et al. 2017. Modelling hydrothermal venting in volcanic sedimentary basins: Impact on hydrocarbon maturation and paleoclimate. Earth and Planetary Science Letters, 467, 30- 42. doi: 10.1016/j.epsl.2017.03.023

Jaeger, J. C. 1968. Cooling and solidification of igneous rocks. In: H. H. Hess and A. Poldervaart (editors), Basalts, Interscience, New York, N.Y., 2, 503-536.

Jackson, C.A-L. & Schofield, N. & Golenkov, B. 2013. Geometry and controls on the development of igneous-sill-related forced folds: A 2-D seismic reflection case study from offshore southern Australia. Geological Society of America, 11/12, 1874-1890. doi: 10.1130/B30833.1

Jerram, D.A. 2015. Hot Rocks and Oil: Are Volcanic Margins the New Frontier? Elsevier R&D Solutions.

Jinghong, W., et al. 2011. Characteristics and controlling factors of fractures in igneous rock reservoirs. Petroleum Exploration and Development, 38 (6), 708-715.

Jones, M.T., et al. 2016. The effects of large igneous provinces on the global carbon and sulphur cycles. Palaeogeography, Palaeoclimatology, Paleoecology, 441 (1) 4-21. doi: 10.1016/j.palaeo.2015.06.042

Jones, S.F., et al. 2007. Impact of magmatism on petroleum systems in the Sverdrup basin, Canadian Arctic islands, Nunavut: a numerical modelling study. Journal of Petroleum Geology, 30 (3), 237-256. doi: 10.1111/j.1747-5457.2007.00237

Jha, M., et al. 2015. Study of temperature effect on thermal conductivity of Jhiri shale from Upper Vindhyan, India. Bulletin of Engineering Geology and the Environment, 75 (4). doi: 10.1007/s10064-015-0829-3

Ji H, Chopp D, Dolbow JE. A hybrid extended finite element level set method for modeling phase transformations. International journal for numerical methods in engineering 2002; 54:1209-1233.

Ji H, Dolbow JE. On strategies for enforcing interfacial constraints and evaluating jump conditions with the extended finite element method. International journal for numerical methods in engineering 2004; 61:2508-2535.

Jiang Y, Tay TE, Chen L, Sun XS. An edge-based smoothed XFEM for fracture in composite materials. International journal of fracture 2013; 179:179-199.

Ji-ming Z, Le-hua Q. Treatment of discontinuous interface in liquid-solid forming with extended finite element method. Transactions of nonferrous metals society of China 2010; 20:911-915.

Jung J, Jeong C, Taciroglu E. Identification of a scatterer embedded in elastic heterogeneous media using dynamic XFEM. Computer methods in applied mechanics and engineering 2013; 259:50-63.

Jarosinski, M., 2012. Compressive deformations and stress propagation in intraconti- nental lithosphere: finite element modelling along the Dinarides–East European Craton profile. Tectonophysics 526–529, 24–41.

Jaeger, J. C. 1968. Cooling and solidification of igneous rocks. In: H. H. Hess and A. Poldervaart (editors), Basalts, Interscience, New York, N.Y., 2, 503-536.

Jackson, C.A-L. & Schofield, N. & Golenkov, B. 2013. Geometry and controls on the development of igneous-sill-related forced folds: A 2-D seismic reflection case study from offshore southern Australia. Geological Society of America, 11/12, 1874-1890. doi: 10.1130/B30833.1

Jerram, D.A. 2015. Hot Rocks and Oil: Are Volcanic Margins the New Frontier? Elsevier R&D Solutions.

Jinghong, W., et al. 2011. Characteristics and controlling factors of fractures in igneous rock reservoirs. Petroleum Exploration and Development, 38 (6), 708-715.

Jones, M.T., et al. 2016. The effects of large igneous provinces on the global carbon and sulphur cycles. Palaeogeography, Palaeoclimatology, Paleoecology, 441 (1) 4-21. doi: 10.1016/j.palaeo.2015.06.042

Jones, S.F., et al. 2007. Impact of magmatism on petroleum systems in the Sverdrup basin, Canadian Arctic islands, Nunavut: a numerical modelling study. Journal of Petroleum Geology, 30 (3), 237-256. doi: 10.1111/j.1747-5457.2007.00237

Jha, M., et al. 2015. Study of temperature effect on thermal conductivity of Jhiri shale from Upper Vindhyan, India. Bulletin of Engineering Geology and the Environment, 75 (4). doi: 10.1007/s10064-015-0829-3

Jing, L. & Hudson, J.A. 2002. Numerical methods in rock mechanics. International Journal of Rock Mechanics and Mining Sciences, 39(4): 409–427

Koch J. O., Heum O. R. 1995. Petroleum Exploration and Exploitation in Norway, Exploration trends of the Halten Terrace, Norsk Petroleumsforening Special Publications, ed Hanslien S. 4, pp 235–251

Karlsen, D., Skeie, J., Backer-Owe, K., Bjø rlykke, K., Olstad, R., Berge, K., Cecchi, M., Vik, E., and Schaefer, R. 2004. Petroleum Migration, faults and overpressure. Part

II. Case History: The Haltenbanken Petroleum Province, offshore Norway. Geological Society of London, Special Publications, v. 237.Pg305–372

Kvamen, O.A. 2004. Postkaledonske brotstrukturar og ekstensjonstektonikk I Lindås, Vest- Noreg, MSc thesis, University of Bergen.

Kavanagh, J.L., et al. 2017. Controls on sill and dyke-sill hybrid geometry and propagation in the crust: The role of fracture toughness. Tectonophysics, 698, 109-120. doi: 10.1016/j.tecto.2016.12.027

Kontorovitch, A.E., et al. 1997. Intense basic magmatism in the Tunguska petroleum basin, eastern Siberia Russia. Petroleum Geoscience, 3, 359-369. doi: 10.1144/petgeo.3.4.359

Karaoğlu, O., 2014. Tectonic controls on the Yamanlar volcano and Yuntdagi volcanic region, western Turkey: implications for an incremental deformation. J. Volcanol. Geotherm. Res. 274, 16–33.

Karaoğlu, Ö., Sağlam-Selçuk, A., Gudmundsson, A., in press. Tectonic controls on the Karlıova Triple Junction (Turkey): implications for tectonic inversion and the ini- tiation of volcanism. Tectonophysics.

Kavanagh, J.L., Menand, T., Sparks, R.S.J., 2006. An experimental investigation of sill formation and propagation in layered elastic media. Earth Planet. Sci. Lett. 245, 799–813.

Kavanagh, J.L., et al. 2017. Controls on sill and dyke-sill hybrid geometry and propagation in the crust: The role of fracture toughness. Tectonophysics, 698, 109-120. doi: 10.1016/j.tecto.2016.12.027

Kontorovitch, A.E., et al. 1997. Intense basic magmatism in the Tunguska petroleum basin, eastern Siberia Russia. Petroleum Geoscience, 3, 359-369. doi: 10.1144/petgeo.3.4.359

Karihaloo BL, Xiao QZ. Modeling of stationary and growing cracks in FE framework without remeshing: a state-of-the-art review. Computers and structures 2003; 81:119-129.

Kastner M, Muller S, Goldmann J, Spieler C, Brummund J, Ulbricht V. Higher-order extended FEM for weak discontinuities - level set representation, quadrature and application to magneto-mechanical problems. International journal for numerical methods in engineering 2013; 93:1403-1424.

Khoei AR, Anahid M, Shahim K. An extended arbitrary Lagrangian-Eulerian finite element method for large deformation of solid mechanics. Finite elements in analysis and design 2008a; 44: 401-416.

Khoei AR, Biabanaki SOR, Anahid M. A Lagrangian-extended finite-element method in modeling large-plasticity deformations and contact problems. International journal of mechanical sciences 2009; 51:384-401.

Khoei AR, Biabanaki SOR, Anahid M. Extended finite element method for three-dimensional large plasticity deformations on arbitrary interfaces. Computer methods in applied mechanics and engineering 2008b; 197:1100-1114.

Khoei AR, Haghighat E. Extended finite element modeling of deformable porous media with arbitrary interfaces. Applied mathematical modelling 2011; 35:5426-5441.

Khoei AR, Karimi K. An enriched-FEM model for simulation of localization phenomenon in Cosserat continuum theory. Computational materials science 2008; 44:733-749.

Khoei AR, Moallemi S, Haghighat E. Thermo-hydro-mechanical modeling of impermeable discontinuity in saturated porous media with X-FEM technique. Engineering fracture mechanics 2012; 96:701-723.

Khoei AR, Nikbakht M. Contact friction modeling with the extended finite element method (X-FEM). Journal of

materials processing technology 2006; 177:58-62.
Khoei AR, Shamloo A, Azami AR. Extended finite element method in plasticity forming of powder compaction with contact friction. International journal of solids and structures 2006; 43:5421-5448.
Kreissl S, Maute K. Level set based fluid topology optimization using the extended finite element method. Structural and multidisciplinary optimization 2012; 46:311-326.
Karaoğlu, Ö., Browning, J., Bazargan, M., Gudmundsson, A., 2016. Numerical modelling of triple-junction tectonics at Karlıova, Eastern Turkey, with implications for regional magma transport. Earth Planet. Sc. Lett. 452, 152–170.
Karaoğlu, Ö., Sağlam-Selçuk, A., Gudmundsson, A., 2017. Tectonic controls on the Karlıova Triple Junction (Turkey): implications for tectonic inversion and the in- itiation of volcanism. Tectonophysics 694, 368–384.
Karaoğlu, Ö., Browning, J., Salah, M.K., Elshaafi, A., Gudmundsson, A., 2018. Depths of magma chambers at three volcanic provinces in the Karlıova region of Eastern Turkey. B.Volcanol. 80 (9), 69.
Kaufmann, S., Libby, W.F., 1954. The natural distribution of tritium. Phys. Rev. 93 (6), 1337–1344.
Kazemi, G.A., Lehr, J.H., Perrochet, P., 2006. Groundwater Age. Wiley-Interscience, New Jersey, USA.
Kharaka, Y.K., Mariner, R.H., 1989. Chemical geothermometers and their application to formation waters from sedimentary basins. In: Naeser, N.D., McCulloh, T.H. (Eds.), Thermal History of Sedimentary Basins. Springer-Verlag, New York, NY, USA, pp. 99–117.
Kresic, N., 2007. Hydrogeology and Groundwater Modeling, 2nd edition. CRC Press, Taylor & Francis Group, USA.
Kanamori, H., Anderson, D.L., 1975. Theoretical basis of some empirical relations in seismology. Bulletin of the Seismological Society of America, 65, 1074-1095.
Kavanagh, J.L., Sparks, R.S.J., 2011. Insights of dyke emplacement mechanics from detailed 3D dyke thickness datasets. Journal of the Geological Society of London. 168, 965-978.
Kroon M. Dynamic steady-state analysis of crack propagation in rubber-like solids using an extended finite element method. Computational mechanics 2012; 49:73-86.
Kanamori, H., Anderson, D.L., 1975. Theoretical basis of some empirical relations in seismology. Bull. Seismol. Soc. Am. 65, 1074–1095.
Kavanagh, J., Menand, T., Sparks, R.S.J., 2006. An experimental investigation of sill formation and propagation in layered elastic media. Earth Planet. Sci. Lett. 245, 799–813.
Kavanagh, J.L., Sparks, R.S.J., 2011. Insights of dyke emplacement mechanics from detailed 3D dyke thickness datasets. J. Geol. Soc. Lond. 168, 965–978.
Kervyn, M., Ernst, G. G. J., van Wyk de Vries, B., Mathieu, L., Jacobs, P., 2009. Vol- cano load control on dyke propagation and vent distribution: insights from ana- logue modeling, J. Geophys. Res., 114(B3), B03401, doi:https://doi.org/10.1029/ 2008jb005653.
Liu, G.R., Quek, S.S., 2014. Finite Element Method, 2nd ed. Elsevier, Amsterdam. Manconi, A., Walter, T.R., Amelung, F., 2007. Effects of mechanical layering on vol- cano deformation. Geophys. J. Int. 170, 952–958.
Liu, G.R. , Quek, S.S., 2014. Finite Element Method, 2nd ed. Elsevier, Amsterdam.
Le Corvec, N., Menand, T., Lindsay, J., 2013. Interaction of ascending magma with pre-existing crustal fractures in monogenetic basaltic volcanism: an experimen- tal approach. J. Geophys. Res., Solid Earth 118 (3), 968–984.
Le Corvec, N., McGovern, P.J., Grosfils, E.B., Galgana, G., 2015. Effects of crustal-scale mechanical layering on magma chamber failure and magma propagation within the Venusian lithosphere. J. Geophys. Res. 120 (7), 1279–1297.
Lee, G.W., et al. 2006. Igneous complexes in the eastern Northern South Yellow Sea Basin and their implications for hydrocarbons systems. Marine and Petroleum Geology. 23, 631- 645. doi: 10.1016/j.marpetgeo.2006.06.001
Ledevin, M., et al. 2011. Intrusion history of the Portrush Sill, County Antrim, Northern Ireland: evidence for rapid emplacement and high-temperature contact metamorphism' Geological Magazine, 149 (1), 67-79
Larsson R, Fagerström M. A framework for fracture modelling based on the material forces concept with XFEM kinematics. International journal for numerical methods in engineering 2005; 62:1763-1788.
Larsson R, Mediavilla J, Fagerström M. Dynamic fracture modeling in shell structures based on XFEM. International journal for numerical methods in engineering 2011; 86:499-527
Lasry J, Pommier J, Renard Y, Salaun M. eXtended finite element methods for thin cracked plates with Kirchhoff-Love theory. International journal for numerical methods in engineering 2010; 84:1115-1138.
Lasry J, Renard Y, Salaun M. Stress intensity factors computation for bending plates with extended finite element method. International journal for numerical methods in engineering 2012; 91:909-928.
Laursen TA, Puso MA, Sanders J. Mortar contact formulations for deformable-deformable contact: Past

contributions and new extensions for enriched and embedded interface formulations. Computer methods in applied mechanics and engineering 2012; 205-208:3-15.
Lecampion B. An extended finite element method for hydraulic fracture problems. Communications in numerical methods in engineering 2009; 25:121-133.
Lee P, Yang R, Maute K. An Extended finite element method for the analysis of submicron heat transfer phenomena. Multiscale methods in computational mechanics 2011; 55:195-212.
Lee SH, Song JH, Yoon YC, Zi G, Belytschko T. Combined extended and superimposed finite element method for cracks. International journal for numerical methods in engineering 2004; 59:1119-1136.
Legay A, Chessa J, Belytschko T. An Eulerian-Lagrangian method for fluid-structure interaction based on level sets. Computer methods in applied mechanics and engineering 2006; 195: 2070-2087.
Legay A. An extended finite element method approach for structural-acoustic problems involving immersed structures at arbitrary positions. International journal for numerical methods in engineering 2013; 93:376-399.
Legrain G, Allais R, Cartraud P. On the use of the extended finite element method with quadtree/octree meshes. International journal for numerical methods in engineering 2011; 86:717-743.
Legrain G, Moës N, Verron E. Stress analysis around crack tips in finite strain problems using the eXtended finite element method. International journal for numerical methods in engineering 2005; 63:290-314.
Legrain G. A NURBS enhanced extended finite element approach for unfitted CAD analysis. Computational mechanics 2013; 52:913-929.
Lee, G.W., et al. 2006. Igneous complexes in the eastern Northern South Yellow Sea Basin and their implications for hydrocarbons systems. *Marine and Petroleum Geology.* **23**, 631- 645. doi: 10.1016/j.marpetgeo.2006.06.001
Larsen, B. 2002. Bruddsystemer, active forkastninger og grunnvannspotensial på Bømlo, Vestlandet. MSc thesis, University of Bergen
Lundin, E.R. and Doré, A.G. 1997. A tectonic model for the Norwegian passive margin with implications for the NE Atlantic: Early Cretaceous to break-up. Journal of the Geological Society, 154, 545-550
Lundin, E. & Doré, A.G. 2002. Mid-Cenozoic post-breakup deformation in the "passive" margins bordering the Norwegian-Greenland Sea. Marine and Petroleum Geology, 19, 79-93.
Ledevin, M., et al. 2011. Intrusion history of the Portrush Sill, County Antrim, Northern Ireland: evidence for rapid emplacement and high-temperature contact metamorphism' *Geological Magazine,* **149** (1), 67-79
Liang J, Huang R, Prevost JH, Suo Z. Evolving crack patterns in thin films with the extended finite element method. International journal of solids and structures 2003; 40:2343-2354.
Liao JH, Zhuang Z. A consistent projection-based SUPG/PSPG XFEM for incompressible two-phase flows. Acta mechanica sinica 2012; 28:1309-1322.
Liu F, Borja RI. A contact algorithm for frictional crack propagation with the extended finite element method. International journal for numerical methods in engineering 2008; 76:1489-1512.
Liu F, Borja RI. An extended finite element framework for slow-rate frictional faulting with bulk plasticity and variable friction. International journal for numerical and analytical methods in geomechanics 2009; 33:1535-1560.
Liu F, Borja RI. Extended finite element framework for fault rupture dynamics including bulk plasticity. International journal for numerical and analytical methods in geomechanics 2013; 37:3087-3111.
Liu F, Borja RI. Stabilized low-order finite elements for frictional contact with the extended finite element method. Computer methods in applied mechanics and engineering 2010; 199:2456-2471.
Liu PF, Zhang BJ, Zheng JY. Finite element analysis of plastic collapse and crack behavior of steel pressure vessels and piping using XFEM. Journal of failure analysis and prevention 2012; 12:707-718.
Liu XY, Xiao QZ, Karihaloo BL. XFEM for direct evaluation of mixed mode SIFs in homogeneous and bi-materials. International journal for numerical methods in engineering 2004; 59:1103-1118.
Liu ZL, Menouillard T, Belytschko T. An XFEM/Spectral element method for dynamic crack propagation. International journal of fracture 2011; 169:183-198.
Loehnert S, Belytschko T. Crack shielding and amplification due to multiple microcracks interacting with a macrocrack. International journal of fracture 2007; 145:1-8.
Loehnert S, Mueller-Hoeppe DS, Wriggers P. 3D corrected XFEM approach and extension to finite deformation theory. International journal or numerical methods in engineering 2011; 86:431-452..
Magee, C., et al. 2016. Lateral magma flow in mafic sill complexes. Geosphere, 12 (3), 809- 841. doi: 10.1130/GES01256.1
Magee, C., Jackson, C.A. L. and Schofield, N. 2013. The influence of normal fault geometry on igneous sill emplacement and morphology. Geology, 41(4), 407-410. doi: 10.1130/G33824.1
Magoon L.B. & Dow W.G. 1994. The petroleum system: from source to trap. In: American Association of Petroleum Geologists Memoir, 60, 3-24

Matter, J.M., et al. 2006. Contact zone permeability at intrusion boundaries: New results from hydraulic testing and geophysical logging in the Newark Basin, New York, USA. Hydrogeology Journal, 14, 689–699. doi: 10.1007/s10040-005-0456-3

Mark, N.J., et al. 2018. Igneous intrusions in the Faroe Shetland basins and their implications for hydrocarbon exploration; new insights from well and seismic data. Marine and Petroleum Geology, 92, 733-753. doi: 10.1016/j.marpetgeo.2017.12.005

Maresh, J., et al. 2006. Seismic attenuation of Atlantic margin basalts: Observations and modelling. Geophysics, 71 (6), 211-221.

Malthe-Sørenssen et al., 2004. Formation of saucer-shaped sills. Physical Geology of High- Level Magmatic Systems. Geological Society, London, 234, 215-227

McCaffrey, K.J.W. & Petford, N. 1997. Are granitic intrusions scale invariant? Journal of the Geological Society, 154, 1-4. doi: 10.1144/gsjgs.154.1.0001

Menand, T. 2011. Physical controls and depth of emplacement of igneous bodies: A review. [Online]. Available at: https://hal.archives-ouvertes.fr/hal-00682291/file/Menand-2011- preprint.pdf (Accessed: 19 February 2018)

Meyers, P.A. & Simoneit, B.R.T. 1999. Effects of extreme heating on the elemental and isotopic compositions of an Upper Cretaceous coal. Organic Geochemistry, 30 (5), 299-305. doi: 10.1016/S0146-6380(99)00015-7

Mørk, A. and Bjorøy, M. 1984. Mesozoic source rocks on Svalbard. Petroleum geology of the north European margin, 371-382.

Macri M, Littlefield A. Enrichment based multiscale modeling for thermo-stress analysis of heterogeneous material. International journal for numerical methods in engineering 2013; 93:1147-1169.

Mariani S, Perego U. Extended finite element method for quasi-brittle fracture. International journal for numerical methods in engineering 2003; 58:103-126.

Massimi P, Tezaur R, Farhat C. A discontinuous enrichment method for three-dimensional multiscale harmonic wave propagation problems in multi-fluid and fluid-solid media. International journal for numerical methods in engineering 2008; 76:400-425.

Mayer UM, Gerstenberger A, Wall WA. Interface handling for three-dimensional higher-order XFEM-computations in fluid-structure interaction. International journal for numerical methods in engineering 2009; 79:846-869.

Mayer UM, Popp A, Gerstenberger A, Wall WA. 3D fluid-structure-contact interaction based on a combined XFEM FSI and dual mortar contact approach. Computational mechanics 2010; 46:53-67.

Melenk JM, Babuska I. The partition of unity finite element method: basic theory and applications. Seminar fur angewandte mathematik, eidgenossische technische hochschule, research report No. 96-01, January, CH-8092 Zurich, Switzerland, 1996.

Menk A, Bordas SPA. A robust preconditioning technique for the extended finite element method. International journal for numerical methods in engineering 2011; 85:1609-1632.

Menouillard T, Belytschko T. Dynamic fracture with meshfree enriched XFEM. Acta mechanica 2010a; 213:53-69.

Menouillard T, Belytschko T. Smoothed nodal forces for improved dynamic crack propagation modeling in XFEM. International journal for numerical methods in engineering 2010b; 84:47-72.

Menouillard T, Réthoré J, Combescure A, Bung H. Efficient explicit time stepping for the eXtended Finite Element Method (X-FEM). International journal for numerical methods in engineering 2006; 68:911-939.

Menouillard T, Song JH, Duan Q, Belytschko T. Time dependent crack tip enrichment for dynamic crack propagation. International journal of fracture 2010; 162:33-49.

Merle R, Dolbow J. Solving thermal and phase change problems with the extended finite element method. Computational mechanics 2002; 28:339-350.

Michlik P, Berndt C. Image-based extended finite element modeling of thermal barrier coatings. Surface & coatings technology 2006; 201:2369-2380.

Mitchell, T. M., and Faulkner, D. R. 2009. The nature and origin of off-fault damage surrounding strike-slip fault zones with a wide range of displacements: A field study from the Atacama fault system, northern Chile, J. Struct. Geol., 31(8), 802–816, doi:10.1016/j. jsg.2009.05.002.

Mosar, J., Lewis, G. & Torsvik, T. H. 2002. North Atlantic sea-floor spreading rates: implications for the Tertiary development of inversion structures of the Norwegian- Greenland Sea. Journal of the Geological Society, London 159, 503-515

Minnebo H. Three-dimensional integration strategies of singular functions introduced by the XFEM in the LEFM. International journal for numerical methods in engineering 2012; 92:1117-1138.

Moës N, Béchet E, Tourbier M. Imposing Dirichlet boundary conditions in the extended finite element method. International journal for numerical methods in engineering 2006; 67:1641-1669.

Moës N, Belytschko T. Extended finite element method for cohesive crack growth. Engineering fracture mechanics 2002a; 69:813-833.

Manconi, A., Walter, T.R., Amelung, F., 2007. Effects of mechanical layering on volcano deformation. Geophysical Journal International, 170, 952-958.
Maccaferri, F., Rivalta, E., Keir, D., Acocella, V., 2014. Off-rift volcanism in rift zones determined by crustal unloading. Nat. Geosci. 7 (4), 297–300.
Magee, C., McDermott, K.G., Stevenson, C.T., Jackson, C.A.L., 2014. Influence of crys- tallised igneous intrusions on fault nucleation and reactivation during continen- tal extension. J. Struct. Geol. 62, 183–193.
Martí, J., Ablay, G.J., Redshaw, L.T., Sparks, R.S.J., 1994. Experimental studies of col- lapse calderas. Q. J. Geol. Soc. Lond. 151, 919–929.
Martí, J., Geyer, A., Folch, A., Gottsmann, J., 2008. A review on collapse caldera mod- elling. In: Gottsmann, J., Martí, J. (Eds.), Caldera Volcanism: Analysis, Modelling and Response. In: Development in Volcanology, vol. 10. Elsevier, Amsterdam, pp. 233–283.
McClusky, S., et al., 2000. GPS constraints on plate motion and deformation in the eastern Mediterranean: implication for plate dynamics. J. Geophys. Res. 105, 5695–5719.
McKenzie, D., 1972. Active tectonics of the Mediterranean region. Geophys. J. R. As- tron. Soc. 30, 109–185.
McKenzie, D.P., Parker, R.L., 1967. The North Pacific: an example of tectonics on a sphere. Nature 216, 1276–1280.
Middlemost, E.A., 1997. Magmas, Rocks and Planetary Development: A Survey of Magma/Igneous Rock Systems. Routledge, Oxford.
Martí, J., C. López, S. Bartolini, L. Becerril, Geyer , A., 2016. Stress controls of monogenetic volcanism: a review. Front. Earth Sci., 4(106), doi: 10.3389/feart.2016.00106.
Martí, J., A. Villaseñor, A. Geyer, C. López, Tryggvason, A., 2017. Stress barriers controlling lateral migration of magma revealed by seismic tomography. Sci. Reports, 7, 40757, doi: 10.1038/srep40757
Masterlark, T., 2007. Magma intrusion and deformation predictions: sensitivities to the Mogi assumptions. Journal of Geophysical Research, 112, doi.org/10.1029/2006JB004860.
Moran, S.C., Newhall, C., Roman, D.C., 2011. Failed magmatic eruptions: late-stage cessation of magma ascent. Bull. Volcanol., 73, 115-122, doi: 10.1007/s00445-010-0444-x.
Moës N, Belytschko T. X-FEM: De nouvelles frontières pour les éléments finis. Revue européenne des eléments finis 2002b; 11:305-318.
Moës N, Dolbow J, Belytschko T. A finite element method for crack growth without remeshing. International journal for numerical methods in engineering 1999; 46:131-150.
Moës N, Gravouil A, Belytschko T. Non-planar 3D crack growth by the extended finite element and level sets-Part I: Mechanical model. International journal for numerical methods in engineering 2002; 53:2549-2568.
Mohammadi S. Extended finite element method for fracture analysis of structures. Black well publishing, 2008.
Mohammadi S. XFEM: fracture analysis of composites. Wiley, 2012.
Mohammadnejad T, Khoei AR. An extended finite element method for fluid flow in partially saturated porous media with weak discontinuities; the convergence analysis of local enrichment strategies. Computational mechanics 2013a; 51:327-345.
Mohammadnejad T, Khoei AR. An extended finite element method for hydraulic fracture propagation in deformable porous media with the cohesive crack model. Finite elements in analysis and design 2013b; 73:77-95.
Mohammadnejad T, Khoei AR. Hydro-mechanical modeling of cohesive crack propagation in multiphase porous media using the extended finite element method. International journal for numerical and analytical methods in geomechanics 2012; 37:1247-1279.
Motamedi D, Mohammadi S. Dynamic analysis of fixed cracks in composites by the extended finite element method. Engineering fracture mechanics 2010a; 77:3373-3393.
Motamedi D, Mohammadi S. Dynamic crack propagation analysis of orthotropic media by the extended finite element method. International journal of fracture 2010b; 161:21-39.
Motamedi D, Mohammadi S. Fracture analysis of composites by time independent moving-crack orthotropic XFEM. International journal of mechanical sciences 2012; 54:20-37.
Mougaard JF, Poulsen PN, Nielsen LO. A partly and fully cracked triangular XFEM element for modeling cohesive fracture. International journal for numerical methods in engineering 2011; 85:1667-1686.
Mougaard JF, Poulsen PN, Nielsen LO. Complete tangent stiffness for extended finite element method by including crack growth parameters. International journal for numerical methods in engineering 2013; 95:33-45.
Mousavi SE, Grinspun E and Sukumar N. Harmonic enrichment functions: A unified treatment of multiple, intersecting and branched cracks in the extended finite element method. International journal for numerical methods in engineering. 2011a; 85:1306-1322.

Mousavi SE, Grinspun E, Sukumar N. Higher-order extended finite elements with harmonic enrichment functions for complex crack problems. International journal for numerical methods in engineering 2011b; 86:560-574

Mousavi SE, Sukumar N. Generalized Gaussian quadrature rules for discontinuities and crack singularities in the extended finite element method. Computer methods in applied mechanics and engineering 2010; 199:3237-3249.

Mueller-Hoeppe DS, Wriggers P, Loehnert S. Crack face contact for a hexahedral-based XFEM formulation. Computational mechanics 2012; 49:725-734.

Monaghan, A.A. 2014. The Carboniferous shales of the Midland Valley of Scotland: geology and resource estimation. British Geological Survey for Department of Energy and Climate Change, London, UK.

Monreal, F.R., et al. 2009. Modelling an atypical petroleum system: A case study of hydrocarbon generation, migration and accumulation related to igneous intrusions in the Neuquén Basin, Argentina. Marine and Petroleum Geology, 26, 590-605. doi: 10.1016/j.marpetgeo.2009.01.005

Murchison, D.G, & Raymond, A.C. 1989. Igneous activity and organic maturation in the Midland Valley of Scotland. International Journal of Coal Geology, 14, 47-82. doi: 10.1016/0166-5162(89)90078-5

Martí, J., López, C., Bartolini, S., Becerril, L., Geyer, A., 2016. Stress controls of monogenetic volcanism: a review. Front. Earth Sci. 4 (106)https://doi.org/10.3389/ feart.2016.00106.

Martí, J., Villaseñor, A., Geyer, A., López, C., Tryggvason, A., 2017. Stress barriers controlling lateral migration of magma revealed by seismic tomography. Sci. Re- ports 7, 0757https://doi.org/10.1038/srep40757.

Masterlark, T., 2007. Magma intrusion and deformation predictions: sensitivities to the Mogi assumptions. J. Geophys. Res. 112, https://doi.org/10.1029/2006JB004860.

Moran, S.C., Newhall, C., Roman, D.C., 2011. Failed magmatic eruptions: late-stage cessation of magma ascent. Bull. Volcanol. 73, 115–122. https://doi.org/10.1007/ s00445-010-0444-x.

Mazor, E., 2004. Applied Chemical and Isotopic Groundwater Hydrology, 3rd edition.

Marcel Dekker, Inc, New York.

Mitchell, T.M., Faulkner, D.R., 2009. The nature and origin of off-fault damage sur- rounding strike-slip fault zones with a wide range of displacements: a field study from the Atacama fault system, northern Chile. J. Struct. Geol. 31 (8), 802–816.

Magee, C., et al. 2016. Lateral magma flow in mafic sill complexes. Geosphere, 12 (3), 809- 841. doi: 10.1130/GES01256.1

Magee, C., Jackson, C.A. L. and Schofield, N. 2013. The influence of normal fault geometry on igneous sill emplacement and morphology. Geology, 41(4), 407-410. doi: 10.1130/G33824.1

Magoon L.B. & Dow W.G. 1994. The petroleum system: from source to trap. In: American Association of Petroleum Geologists Memoir, 60, 3-24

Matter, J.M., et al. 2006. Contact zone permeability at intrusion boundaries: New results from hydraulic test-ing and geophysical logging in the Newark Basin, New York, USA. Hydrogeology Journal, 14, 689–699. doi: 10.1007/s10040-005-0456-3

Mark, N.J., et al. 2018. Igneous intrusions in the Faroe Shetland basins and their implications for hydrocarbon exploration; new insights from well and seismic data. Marine and Petroleum Geology, 92, 733-753. doi: 10.1016/j.marpetgeo.2017.12.005

Maresh, J., et al. 2006. Seismic attenuation of Atlantic margin basalts: Observations and modelling. Geophysics, 71 (6), 211-221.

Malthe-Sørenssen et al., 2004. Formation of saucer-shaped sills. Physical Geology of High- Level Magmatic Systems. Geological Society, London, 234, 215-227

McCaffrey, K.J.W. & Petford, N. 1997. Are granitic intrusions scale invariant? Journal of the Geological Society, 154, 1-4. doi: 10.1144/gsjgs.154.1.0001

Menand, T. 2011. Physical controls and depth of emplacement of igneous bodies: A review. [Online]. Available at: https://hal.archives-ouvertes.fr/hal-00682291/file/Menand-2011- preprint.pdf (Accessed: 19 February 2018)

Meyers, P.A. & Simoneit, B.R.T. 1999. Effects of extreme heating on the elemental and isotopic compositions of an Upper Cretaceous coal. Organic Geochemistry, 30 (5), 299-305. doi: 10.1016/S0146-6380(99)00015-7

Mørk, A. and Bjorøy, M. 1984. Mesozoic source rocks on Svalbard. Petroleum geology of the north European margin, 371-382.

Monaghan, A.A. 2014. The Carboniferous shales of the Midland Valley of Scotland: geology and resource estimation. British Geological Survey for Department of Energy and Climate Change, London, UK.

Monreal, F.R., et al. 2009. Modelling an atypical petroleum system: A case study of hydrocarbon generation, migration and accumulation related to igneous intrusions in the Neuquén Basin, Argentina. Marine and Petroleum Geology, 26, 590-605. doi: 10.1016/j.marpetgeo.2009.01.005

Murchison, D.G, & Raymond, A.C. 1989. Igneous activity and organic maturation in the Midland Valley of Scotland. International Journal of Coal Geology, 14, 47-82. doi: 10.1016/0166-5162(89)90078-5

Nakashima K. 2004. Petroleum Potential in the East Siberian Region. Institute of Energy Economics, Japan.
Nesse, O. 2004. Oppbygging av bruddnettverksmodeller og permeabilitetanalyser med anvendelse påveg Vest transéct sørlige del, MSc thesis, University of Bergen
Nicholson, K., 1993. Geothermal Fluids Chemistry and Exploration Techniques. Springer- Verlag, Berlin.
Nakashima K. 2004. Petroleum Potential in the East Siberian Region. Institute of Energy Economics, Japan.
Natarajan S, Baiz PM, Bordas S, Rabczuk T, Kerfriden P. Natural frequencies of cracked functionally graded material plates by the extended finite element method. Composite structures 2011; 93:3082-3092.
Natarjan S. Enriched finite element methods: advances & applications. PhD thesis, Institute of mechanics and advanced materials theoretical and computational mechanics, Cardiff university, Wales, UK, 2011.
Nguyen-Vinh H, Bakar I, Msekh MA, Song JH, Muthu J, Zi G, Le P, Bordas S, Simpson R, Natararajan S, Lahmer T, Rabczuk T. Extended finite element method for dynamic fracture of piezo-electric materials. Engineering fracture mechanics 2012; 92:19-31.
Nicaise S, Renard Y, Chahine E. Optimal convergence analysis for the extended finite element method. International journal for numerical methods in engineering 2011; 86:528-548.
Nistor I, Pantale O, Caperaa S. Numerical implementation of the eXtended Finite Element Method for dynamic crack analysis. Advances in engineering software 2008; 39:573-587.
Nouy A, Clement A. Extended stochastic finite element method for the numerical simulation of heterogeneous materials with random material Interfaces. International journal for numerical methods in engineering 2010; 83:1312-1344.
Olesen JF, Poulsen PN. An embedded crack in a constant strain triangle utilizing extended finite element concepts. Computers and structures 2013; 117:1-9.
Osher S, Sethian JA. Fronts propagating with curvature dependent speed: algorithms Based on Hamilton-Jacobi formulations. Journal of computational physics 1988; 79:12-49.
Oswald J, Gracie R, Khare R, Belytschko T. An extended finite element method for dislocations in complex geometries: Thin films and nanotubes. Computer methods in applied mechanics and engineering 2009; 198:1872-1886.
Oswald J, Wintersberger E, Bauer G, Belytschko T. A higher-order extended finite element method for dislocation energetics in strained layers and epitaxial islands. International journal for numerical methods in engineering 2011; 85:920-938.
Olesen, O., Brönner, M., Dehls, J.F., Kierulf, H.P., Lindholm, C. and Rise, L. 2012. Onshore-offshore neotectonics in Nordland, northern Norway. In Hendriks, B. and Haukdal, G.K. (eds.) Onshore-offshore relationships on the North Atlantic Margin. Abstracts and Proceedings of the Geological Society of Norway, 2, 54–56
Osmundsen, P.T. & Ebbing, J. 2008. Styles of extension offshore mid- Norway and implications for mechanisms of crustal thinning at passive margins. Tectonics 27, DOI:10.1029/2007TC002242.
Osmundsen, P.T., Sommaruga, A., Skilbrei, J.R. & Olesen, O. 2002. Deep structure of the Mid Norway rifted margin. Norwegian Journal of Geology 82, 205–224
Odonkor, C. 2017. Timing and magmatic sill emplacement in the Vøring Basin, Norwegian Sea. Unpublished Ph.D. thesis, Norwegian University of Science and Technology. Norway.
Omosanya K.O., et al. 2017. Forced folding and complex overburden deformation associated with magmatic intrusion in the Vøring Basin, offshore Norway. *Tectonophysics,* **706-707**, 14- 34. doi: 10.1016/j.tecto.2017.03.026
Oxburgh, E. R. 1980. Heat flow and magma genesis. In: R.B. Hargraves (editor), *Physics of Magmatic Processes,* Princeton University Press, Princeton, N. J. 161-199.
Odonkor, C. 2017. Timing and magmatic sill emplacement in the Vøring Basin, Norwegian Sea. Unpublished Ph.D. thesis, Norwegian University of Science and Technology. Norway.
Omosanya K.O., et al. 2017. Forced folding and complex overburden deformation associated with magmatic intrusion in the Vøring Basin, offshore Norway. Tectonophysics, 706-707, 14- 34. doi: 10.1016/j.tecto.2017.03.026
Oxburgh, E. R. 1980. Heat flow and magma genesis. In: R.B. Hargraves (editor), Physics of Magmatic Processes, Princeton University Press, Princeton, N. J. 161-199.
Okay, A.I., Tüysüz, O., 1999. Tethyan sutures of northern Turkey. Geol. Soc. Spec. Publ. 156, 475–515.
Okada, Y., 1985. Surface deformation due to shear and tensile faults in a half-space. Bulletin of the Seismological Society of America, 75, 1135-1154.
Okada, Y., 1992. Internal deformation due to shear and tensile faults in half space. Bulletin of the Seismological Society of America, 82, 1018-1040.
Okada, Y., 1985. Surface deformation due to shear and tensile faults in a half-space. Bulletin of the Seismological Society of America, 75, 1135-1154.

Okada, Y., 1985. Surface deformation due to shear and tensile faults in a half-space. Bull. Seismol. Soc. Am. 75, 1135–1154.
Okada, Y., 1992. Internal deformation due to shear and tensile faults in half space. Bull. Seismol. Soc. Am. 82, 1018–1040.
Ozener, H., Arpat, E., Ergintav, S., Dogru, A., Cakmak, R., Turgut, B., Dogan, U., 2010. Kinematics of the eastern part of the North Anatolian Fault Zone. J. Geodyn. 49 (3–4), 141–150.
Okada, Y., 1992. Internal deformation due to shear and tensile faults in half space. Bulletin of the Seismological Society of America, 82, 1018-1040.
Parkhurst, D.L., Appelo, C.A.J., 1999. User's guide to PHREEQC (Version 2) –a computer program for speciation batch-reaction, one-dimensional transport, and inverse geo- chemical calculations. Pearce, J.A., Bender, J.F., De Long, S.E., Kidd, W.S.F., Low, P.J., Güner, Y., Saroglu, F., Yilmaz, Y., Moorbath, S., Mitchell, J.G., 1990. Genesis of collision volcanism in Eastern Anatolia, Turkey. J. Volcanol. Geotherm. Res. 44, 189–229.
Poidevin, J.L., 1998. Provenance studies of obsidian artefacts in Anatolia using the fission track dating method, an overview. In: Gourgaud, A., Gratuze, B., Poupeau, G., Poidevin, J.L., Cauvin, M.C. (Eds.), L'Obsidienne au Proche et Moyen Orient, du Volcan a` l'Outil. BAR International Series Hadrian Books 738, pp. 105–156.
Press, F., Siever, R., 1995. Allgemeine Geologie. Spektrum Akademischer Verlag, Heidelberg Berlin, Oxford.
Parfitt, E.A & Wilson, L. 2008. Fundamentals of Physical Volcanology. Blackwell Publishing Ltd, Oxford, U.K
Planke, S., et al. 2005. Seismic characteristics and distribution of volcanic intrusions and hydrothermal vent complexes in the Vøring and Møre basins. Petroleum Geology: North- West Europe and Global Perspectives—Proceedings of the 6th Petroleum Geology Conference, 833-844.
Polyansky, O.P, & Reverdatto, V.V. 2006. Contact metamorphism and metasomatism near the Talnakh intrusion: fluid convection and heat transfer modelling on the basis of the finite–difference method. Doklady Earth Sciences, 114 (9), 803-807. doi: 10.1134/S1028334X06090339
Polteau S., et al. 2008. Saucer-shaped intrusions: occurrences, emplacement and implications. Earth Planet, 266, 195-204. doi: 10.1016/j.epsl.2007.11.015
Panetier J, Ladeveze P, Chamoin L. Strict and effective bounds in goal-oriented error estimation applied to fracture mechanics problems solved with XFEM. International journal for numerical methods in engineering. 2010; 81:671-700.
Park K, Pereira JP, Duarte CA, Paulino GH. Integration of singular enrichment functions in the generalized/extended finite element method for three-dimensional problems. International journal for numerical methods in engineering 2009; 78:1220-1257.
Pathak H, Singh A, Singh IV, Yadav SK. A simple and efficient XFEM approach for 3-D cracks simulations. International journal of fracture 2013; 181:189-208.
Pathak H, Singh A, Singh IV. Numerical simulation of bi-material interfacial cracks using EFGM and XFEM. International journal of mechanics and materials in design 2012; 8:9-36.
Pierrès E, Baietto MC, Gravouil A. A two-scale extended finite element method for modelling 3D crack growth with interfacial contact. Computer methods in applied mechanics and engineering 2010; 199:1165-1177.
Prabel B, Combescure A, Gravouil A, Marie S. Level set X-FEM non-matching meshes: application to dynamic crack propagation in elastic-plastic media. International journal for numerical methods in engineering 2007; 69:1553-1569.
Prange C, Loehnert S, Wriggers P. Error estimation for crack simulations using the XFEM. International journal for numerical methods in engineering 2012; 91:1459-1474.
Pallister, J., McCausland, W., Jónsson, S., Lu, Z., Zahran, H., El-Hadidy, S., Aburukbah, A., Stewart, I., Lundgern, P., White, R., Moufti, M., 2010. Broad accommodation of rift- related extension recorded by dyke intrusion in Saudi Arabia. Nat. Geosci . 3, 705-712.
Philipp, S.L., Afsar, F., Gudmundsson, A., 2013. Effects of mechanical layering on hydrofracture emplacement and fluid transport in reservoirs. Frontiers in Earth Science, 1, doi:10.3389/feart.2013.00004
Pollard, D.D., Delaney, P.T., Duffield, W.A., Endo, E.T., Okamura, A.T., 1983. Surface deformation in volcanic rift zones. Tectonophysics, 94, 541-584.
Pasquarè., F, Tibaldi., A., 2007. Structure of a sheet-laccolith system revealing the interplay between tectonic and magma stresses at Stardalur Volcano, Iceland. J. Volcanol. Geotherm. Res., 161, 131-150.
Philipp, S.L., Afsar, F., Gudmundsson, A., 2013. Effects of mechanical layering on hydrofracture emplacement and fluid transport in reservoirs. Frontiers in Earth Science, 1, doi:10.3389/feart.2013.00004
Phillips, W.J., 1974. The dynamic emplacement of cone sheets. Tectonophysics, 24, 69-84.

Pallister, J., McCausland, W., Jónsson, S., Lu, Z., Zahran, H., El-Hadidy, S., Aburuk- bah, A., Stewart, I., Lundgern, P., White, R., Moufti, M., 2010. Broad accommo- dation of rift-related extension recorded by dyke intrusion in Saudi Arabia. Nat. Geosci. 3, 705–712.

Philipp, S.L., Afsar, F., Gudmundsson, A., 2013. Effects of mechanical layering on hy- drofracture emplacement and fluid transport in reservoirs. Front. Earth Sci. 1, https://doi.org/10.3389/feart.2013.00004

Pasquarè, F., Tibaldi, A., 2007. Structure of a sheet–laccolith system revealing the interplay between tectonic and magma stresses at Stardalur Volcano, Iceland. J. Volcanol. Geotherm. Res. 161, 131–150.

Poidevin, J.L., 1998. Provenance studies of obsidian artefacts in Anatolia using the fission track dating method, an overview. In: Gourgaud, A., Gratuze, B., Pou- peau, G., Poidevin, J.L., Cauvin, M.C. (Eds.), L'Obsidienne au Proche et Moyen Orient, du Volcan a` l'Outil. In: BAR International Series Hadrian Books, vol. 738, pp. 105–156.

Pinel, V., Jaupart, C., 2004. Magma storage and horizontal dyke injection beneath a volcanic edifice. Earth Planet. Sci. Lett. 221, 245–262.

Pinel, V., Jaupart, C., 2005. Some consequences of volcanic edifice destruction for eruption conditions. J. Volcanol. Geotherm. Res. 145, 68–80.

Pollard, D.D., Delaney, P.T., Duffield, W.A., Endo, E.T., Okamura, A.T., 1983. Sur- face deformation in volcanic rift zones. Tectonophysics 94, 541–584.

Rickwood, P.C., 1990. The anatomy of a dyke and the determination of propagation and flow directions. In: Parker, A.J., Rickwood, P.C., Tucker, D.H. (Eds.), Mafic Dykes and Emplacement Mechanisms. Balkema, Rotterdam, pp. 81–100.

Parfitt, E.A & Wilson, L. 2008. Fundamentals of Physical Volcanology. Blackwell Publishing Ltd, Oxford, U.K

Planke, S., et al. 2005. Seismic characteristics and distribution of volcanic intrusions and hydrothermal vent complexes in the Vøring and Møre basins. Petroleum Geology: North- West Europe and Global Perspectives—Proceedings of the 6th Petroleum Geology Conference, 833-844.

Polyansky, O.P, & Reverdatto, V.V. 2006. Contact metamorphism and metasomatism near the Talnakh intrusion: fluid convection and heat transfer modelling on the basis of the finite–difference method. Doklady Earth Sciences, 114 (9), 803-807. doi: 10.1134/S1028334X06090339

Polteau S., et al. 2008. Saucer-shaped intrusions: occurrences, emplacement and implications. Earth Planet, 266, 195-204. doi: 10.1016/j.epsl.2007.11.015

Peacock, D., Knipe, R., Sanderson, D. 2000. Glossary of normal faults. J. Struct. Geol. 22, 291–305.

Pollard, D. D., and Segall, P. 1986. Theoretical displacements and stresses near fractures in rock with applications to faults, joints, veins, dikes and solution surfaces, in Rock Fracture Mechanics, edited by B. Atkinson, Academic, Orlando

Priest, S.D., 1993. Discontinuity Analysis for Rock Engineering. Chapman and Hall, London.

Reinecker, J., Heidbach, O., Tingay, M., Sperner, B., Müller, M., 2005. The 2005 release of the World Stress Map. Res. Group of the Heidelberg Acad. Of Sc. And Humanities, Heidelberg, Germany. www.world-stress-map.org.

Ray, R. R. 1989. Seismic expressions of igneous sills in San Juan Sag, south-central Colorado. American Association of Petroleum Geologists, Bulletin, 73, 1159.

Rateau, R. & Schofield, N. & Smith, M. 2013. The potential role of igneous intrusions on hydrocarbon migration, West of Shetland. Petroleum Geoscience, 19, 259-272. doi: 10.1144/petgeo2012-035

Robertson, C. 1988. Thermal properties of rocks, U.S.G.S. Open file report, U.S Geological Society, 88, 106.

Rui, G., et al. 2013. Fingered Intrusion of Shallow Saucer-shaped Igneous Sills: Insights from the Jiaojiang Sag, East China Sea. Acta Geologica Sinica. 87, 1306-1318. doi: 10.1111/1755- 6724.12130

Reilinger, R., et al., 2006. GPS constraints on continental deformation in the Africa– Arabia–Eurasia continental collision zone and implications for the dynamics of plate interactions. J. Geophys. Res. 111, B05411.

Rivalta, E., Taisne, B., Bunger, P., Katz, F., 2015. A review of mechanical models of dyke propagation: Schools of thought, results and future directions. Tectono- physics 638,1–42. https://doi.org/10.1016/j.tecto.2014.10.003.

Rubin, A.M., Pollard, D.D., 1988. Dike-induced faulting in rift zones of Iceland and Afar. Geology 16, 413–417.

Reed, M., Spycher, N., 1984. Calculation of pH and mineral equilibria in hydrothermal waters with application to geothermometry and studies of boiling and dilution. Geochim. Cosmochim. Ac. 48, 1479–1492.

Rivalta, E., Taisne, B., Bunger, P., Katz, F., 2015. A review of mechanical models of dyke propagation: Schools of thought,results and future directions. Science Direct,Tectono physics. 638, 1-42, doi.org/10.1016/j.tecto.2014.10.003.

Rickwood, P.C., 1990. The anatomy of a dyke and the determination of propagation and flow directions. In: Parker, A.J., Rickwood, P.C., Tucker, D.H. (eds), Mafic Dykes and Emplacement Mechanisms. Balkema, Rotterdam, 81-100.

Rivalta, E., Taisne, B., Bunger, P., Katz, F., 2015. A review of mechanical models of dyke propagation: Schools of thought,results and future directions. Science Direct, Tectono physics. 638, 1-42, doi.org/10.1016/j.tecto.2014.10.003.

Rubin, A.M., Pollard, D.D., 1988. Dike-induced faulting in rift zones of Iceland and Afar. Geology, 16, 413-417.

Rabczuk T, Samaniego E, Belytschko T. Simplified model for predicting impulsive loads on submerged structures to account for fluid-structure interaction. International journal of impact engineering 2007; 34:163-177.

Rabczuk T, Wall WA. Extended finite element and meshfree methods. Technical university of Munich, Germany, WS200/2007, 2006.

Rabinovich D, Givoli D, Vigdergauz S. XFEM-based crack detection scheme using a genetic algorithm. International journal for numerical methods in engineering 2007; 71:1051-1080.

Rabinovich D, Givoli D,Vigdergauz S. Crack identification by 'arrival time' using XFEM and a genetic algorithm. International journal for numerical methods in engineering 2009; 77:337-359.

Rethore J, De'Borst R and Abellan MA. A two-scale approach for fluid flow in fractured porous media. International journal for numerical methods in engineering 2007; 71:780-800.

Réthoré J, Gravouil A, Combescure A. An energy-conserving scheme for dynamic crack growth using the eXtended finite element method. International journal for numerical methods in engineering 2005; 63:631-659

Rethore J, Hild F, Roux S. Shear-band capturing using a multiscale extended digital image correlation technique. Computer methods in applied mechanics and engineering 2007; 196:5016 - 5030.

Richardson CL, Hegemann J, Sifakis E, Hellrung J, Teran JM. An XFEM method for modeling geometrically elaborate crack propagation in brittle materials. International journal for numerical methods in engineering 2011; 88:1042-1065.

Rochus V, Van Miegroet L, Rixen DJ, Duysinx P. Electrostatic simulation using XFEM for conductor and dielectric interfaces. International journal for numerical methods in engineering 2011; 85:1207-1226.

Ródenas JJ, González-Estrada OA, Díez P, Fuenmayor P. Accurate recovery-based upper error bounds for the extended finite element framework. Computer methods in applied mechanics and engineering 2010; 199:2607-2621.

Ródenas JJ, González-Estrada OA, Fuenmayor FJ, Chinesta F. Enhanced error estimator based on a nearly equilibrated moving least squares recovery technique for FEM and XFEM. Computational mechanics 2013; 52:321-344.

Rodenas JJ, Gonzalez-Estrada OA, Tarancon JE, Fuenmayor FJ. A recovery-type error estimator for the extended finite element method based on singular+smooth stress field splitting. International journal for numerical methods in engineering 2008; 76:545-571.

Rojas-Diaz R, Sukumar N, Saez A, García-Sánchez F. Fracture in magnetoelectroelastic materials using the extended finite element method. International journal for numerical methods in engineering 2011; 88:1238-1259.

Rüter M, Gerasimov T, Stein E. Goal-oriented explicit residual-type error estimates in XFEM. Computational mechanics 2013; 52:361-376.

Ray, R. R. 1989. Seismic expressions of igneous sills in San Juan Sag, south-central Colorado. American Association of Petroleum Geologists, Bulletin, 73, 1159.

Rateau, R. & Schofield, N. & Smith, M. 2013. The potential role of igneous intrusions on hydrocarbon migration, West of Shetland. Petroleum Geoscience, 19, 259-272. doi: 10.1144/petgeo2012-035

Robertson, C. 1988. Thermal properties of rocks, U.S.G.S. Open file report, U.S Geological Society, 88, 106.

Rui, G., et al. 2013. Fingered Intrusion of Shallow Saucer-shaped Igneous Sills: Insights from the Jiaojiang Sag, East China Sea. Acta Geologica Sinica. 87, 1306-1318. doi: 10.1111/1755- 6724.12130

Santos, R.V., et al. 2009. Geochemical and thermal effects of a basic sill on black shales and limestones of the Permian Irati Formation. Journal of South American Earth Sciences, 28 (1), 14-24. doi: 10.1016/j.jsames.2008.12.002

Saxby, J.D. & Stephenson, L.C. 1987. Effect of an igneous intrusion on oil shale at Rundle (Australia). Chemical Geology, 63 (1-2), 1-16.

Schofield, N., et al. 2017. Regional magma plumbing and emplacement mechanisms of the Faroe-Shetland Sill Complex: implications for magma transport and petroleum systems within sedimentary basins. Basin Research, 29, (1), 41-63. doi: 10.1111/bre.12164

Schofield, N. & Totterdell, J. 2008. Distribution, timing, and origin of magmatism in the Bight and Eucla basins. Geoscience Australia.

Schofield, N. & Jerram, D.A. 2016. Sills in sedimentary basins and petroleum systems. Advances in Volcanology. doi: 10.1007/11157_2015_17.

Samaniego E, Belytschko T. Continuum-discontinuum modelling of shear bands. International journal for numerical methods in engineering 2005; 62:1857-1872.

Sanborn SE, Prévost H. Frictional slip plane growth by localization detection and the extended finite element method (XFEM). International journal for numerical and analytical methods in geomechanics 2011; 35:1278-1298.

Scholz, C.H., 1990. The Mechanics of Earthquakes and Faulting. Cambridge Univer- sity Press, Cambridge.

Segall, P., 2010. Earthquake and Volcano Deformation. Princeton University Press, Princeton.

Sigmundsson, F., Hreinsdottir, S., Hooper, A., Arnadottir, T., Pedersen, R., Roberts, M.J., Oskarsson, N., Auriac, A., Decriem, J., Einarsson, P., Geirsson, H., Hench, M., Ofeigsson, B.G., Sturkell, E., Sveinbjörnsson, H., Feigl, K.L., 2010. Intrusion triggering of the 2010 Eyjafjallajökull explosive eruption. Nature 468, 426–430. https://doi.org/10.1038/nature09558.

Sigmundsson, F., Hooper, A., Hreinsdottir, S., Vogfjord, K.S., Ofeigsson, D.G., Heimisson, E.L., Dumont, S., Parks, M., Spaans, K., Gudmundsson, G.B., Drouin, V., Arnadottir, T., Jonsdottir, K., Gudmundsson, M.T., Hognadottir, T., Fridriks- dottir, H.M., Hensch, M., Einarsson, P., Magnusson, E., Samsonov, S., Brandsdot-tir,

B., White, R.S., Agustsdottir, T., Greenfield, T., Green, R.G., Hjartardottir, A., Pedersen, R., Bennett, R., Geirsson, H., La Femina, P.C., Bjornsson, H., Palsson, F., Sturkell, E., Bean, C.J., Mollhoff, M., Braiden, A.K., Eibl, E., 2015. Segmented lateral dyke growth in a rifting event at Barðarbunga volcanic system. Iceland. Na-ture 517, 191–U158. https://doi.org/10.1038/nature14111.

Siler, D.L., Karson, J.A., 2009. Three-dimensional structure of inclined sheet swarms: implications for crustal thickening and subsidence in the volcanic rift zones of Ice- land. J. Volcanol. Geotherm. Res. 18, 333–346.

Sarhangi Fard A, Hulsen MA, Anderson PD. Extended finite element method for viscous flow inside complex three-dimensional geometries with moving internal boundaries. International journal for numerical methods in fluids 2012a; 70:775-792.

Sarhangi Fard A, Hulsen MA, Meijer HEH, Famili NMH, Anderson PD. Adaptive non-conformal mesh refinement and extended finite element method for viscous flow inside complex moving geometries. International journal for numerical methods in fluids 2012b; 68:1031-1052.

Sauerland H, Fries TP. The extended finite element method for two-phase and free-surface flows: A systematic study. Journal of computational physics 2011; 230: 3369-3390.

Sauerland H, Fries TP. The stable XFEM for two-phase flows. Computers & fluids 2013; 87:41-49.

Seabra MRR, Sustaric P, Cesar de Sa JMA, Rodic T. Damage driven crack initiation and propagation in ductile metals using XFEM. Computational mechanics 2013; 52:161-179.

Sethian JA. A marching level set method for monotonically advancing fronts. Proceeding of the national academy of sciences 1996; 93:1591-1595.

Shamloo A, Azami AR, Khoei AR. Modeling of pressure-sensitive materials using a cap plasticity theory in extended finite element method. Journal of materials processing technology 2005; 164:1248-1257.

Shen Y, Lew A. An optimally convergent discontinuous Galerkin-based extended finite element method for fracture mechanics. International journal for numerical methods in engineering 2010a; 82:716-755.

Shen Y, Lew A. Stability and convergence proofs for a discontinuous-Galerkin-based extended finite element method for fracture mechanics. Computer methods in applied mechanics and engineering 2010b; 199: 2360-2382.

Shi J, Chopp D, Lua J, Sukumar N, Belytschko T. Abaqus implementation of extended finite element method using a level set representation for three-dimensional fatigue crack growth and life predictions. Engineering fracture mechanics 2010; 77:2840-2863.

Shibanuma K, Utsunomiya T. Evaluation on reproduction of priori knowledge in XFEM. Finite element in analysis and design 2011; 47:424-433.

Shibanuma K, Utsunomiya T. Reformulation of XFEM based on PUFEM for solving problem caused by blending elements. Finite elements in analysis and design 2009; 45:806-816

Singh IV, Mishra BK, Bhattacharya S, Patil RU. The numerical simulation of fatigue crack growth using extended finite element method. International journal of fatigue 2012; 36:109-119.

Singh IV, Mishra BK, Bhattacharya S. XFEM simulation of cracks, holes and inclusions in functionally graded materials. International journal of mechanics and materials in design 2011; 7:199-218.

Skrzypczak T. Sharp interface numerical modeling of solidification process of pure metals. Archives of metallurgy and metals 2012; 57:1189-1199.

Song JH, Areias PMA, Belytschko T. A method for dynamic crack and shear band propagation with phantom nodes. International journal for numerical methods in engineering 2006; 67:868-893.

Stazi FL, Budyn E, Chessa J, Belytschko T. An extended finite element method with higher-order elements for curved cracks. Computational mechanics 2003; 31:38-48.

Stolarska M, Chopp DL, Moës N, Belytschko T. Modeling of crack growth by level sets in the extended finite element method. Journal of numerical methods in engineering 2001; 51:943-960.
Stolarska M, Chopp DL. Modeling thermal fatigue cracking in integrated circuits by level sets and the extended finite element method. International journal of engineering science 2003; 41:2381-2410.
Sukumar N, Chop DL, Moës N, Belytschko T. Modeling of holes and inclusions by level sets in the extended finite element method. Computer methods in applied mechanics and engineering 2001; 190:6183-6200.
Sukumar N, Chopp DL, Bechet EB and Moës N. Three-dimensional non-planar crack growth by a coupled extended finite element and fast marching method. International journal for numerical methods in engineering 2008; 76:727-748.
Sukumar N, Chopp DL, Moran B. Extended finite element method and fast marching method for three-dimensional fatigue crack propagation. Engineering fracture mechanics 2003a; 70:29-48.
Sukumar N, Huang ZY, Prévost JH, Suo Z. Partition of unity enrichment for bimaterial interface cracks. International journal for numerical methods in engineering 2004; 59:1075-1102.
Sukumar N, Moës N, Moran B, Belytschko T. Extended finite element method for three-dimensional crack modeling. International journal for numerical methods in engineering 2000; 48:1549-1570.
Sukumar N, Prevost JH. Modeling quasi-static crack growth with the extended finite element method. Part I: Computer implementation. International journal of solids and structures 2003b; 40:7513-7537.
Sukumar N, Srolovitz DJ, Baker TJ, Prevost H. Brittle fracture in polycrystalline microstructures with the extended finite element method. International journal for numerical methods in engineering 2003b; 56:2015-2037.
Sy A, Renard Y. A fictitious domain approach for structural optimization with a coupling between shape and topological gradient. Far East journal of mathematical sciences 2010; 47:33-50.
Senger, K., et al. 2015. Fracturing of doleritic intrusions and associated contact zones: Implications for fluid flow in volcanic basins. Journal of African Earth Sciences, 102, 70-85. doi: 10.1016/j.jafrearsci.2014.10.019.
Senger K., et al. 2017. Effects of igneous intrusions on the petroleum system: a review. Volcanic Basin Petroleum Research, Norway. 35
Shutter, S.R. 2003. Occurrences of hydrocarbons in and around igneous rocks. Geological Societ, 214, 35-68. doi: 10.1144/GSL.SP.2003.214.01.03.
Simoneit, B.R. 1994. Organic matter alteration and fluid migration in hydrothermal systems. Geological Society, London, Special Publications, 78 (1), 261-274. doi: 10.1144/GSL.SP.1994.078.01.18
Spacapan, J.B., et al. 2018. Thermal impact of igneous sill-complexes on organic-rich formations and implications for petroleum systems: A case study in the northern Neuquén Basin, Argentina. Marine and Petroleum Geology, 91, 519-531. doi: 10.1016/j.marpetgeo.2018.01.018
Sloane, D.J., 1991. Some Physical Properties of Dolerite. Tasmania Department of Resources and Energy: Division of Mines and Mineral Resources.
Sruoga, P. & Rubinstein, N. 2007. Processes controlling porosity and permeability in volcanic reservoirs from the Austral and Neuquén basins, Argentina. AAPG Bulletin, 91, 115-129. doi: 10.1306/08290605173
Stemmerik, L. et al., 1993. Depositional history and petroleum geology of the Carboniferous to Cretaceous sediments in the northern part of East Greenland. Norwegian Petroleum Society Special Publications, 2, 67-87. doi: 10.1016/B978-0-444-88943-0.50009-5
Stephens T.L., et al. 2017. Igneous sills record far-field and near-field stress interactions during volcano construction: Isle of Mull, Scotland. Earth and Planetary Sciences Letter, 478, 159-174. doi: 10.1016/j.epsl.2017.09.003
Stoneley, R. 1995. An introduction to petroleum exploration for non-geologists. Oxford University Press, Oxford, U.K. pp 119.
Sydnes, M., et al. 2018. The importance of sill thickness and timing of sill emplacement on hydrocarbon maturation. Marine and Petroleum Geology, 89 (2), 500-514. doi: 10.1016/j.marpetgeo.2017.10.017.
Svensen, H. & Jamtveit, B. 2010. Metamorphic Fluids and Global Environmental Changes. Elements, 6 (3), 179-182. doi: 10.2113/gselements.6.3.179.
Svensen, H., et al. 2010. Sandstone dikes in dolerite sills: Evidence for high-pressure gradients and sediment mobilization during solidification of magmatic sheet intrusions in sedimentary basins. Geosphere. 6 (3), 211-224. doi: 10.1130/GES00506.1
Sançar, C., Zabcı, C., Akyüz, H.S., Sunal, G., Villa, I.M., 2015. Distributed transpres- sive continental deformation: the Varto Fault Zone, eastern Turkey. Tectono- physics 661, 99–111.
Sandvol, E., Turkelli, N., Zor, E., Gok, R., Bekler, T., Gurbuz, C., Seber, D., Barazangi, M., 2003. Shear wave splitting in a young continent–continent collision: an example from eastern Turkey. Geophys. Res. Lett. 30 (24), 8041–8059.
Sinton, J.M., Detrick, R.S., 1992. Mid-ocean magma chambers. J. Geophys. Res. 97, 197–216.
Spence, D.A., Sharp, P.W., Turcotte, D.L., 1987. Buoyancy-driven crack propagation: a mechanism

for magma migration. J. Fluid Mech. 174, 135–153.
Şengör, A.M.C., Tüysüz, O., Imren, C., Sakınç, M., Eyidogan, H., Görür, N., Le Pichon, X., Rangin, C., 2004. The North Anatolian Fault: a new look. Annu. Rev. Earth Planet. Sci. 33, 37–112.
Salah, M.K., Sahin, S., Aydin, U., 2011. Seismic velocity and Poisson's ratio tomography of the crust beneath east Anatolia. J. Asian Earth Sci. 40, 746–761.
Sayın, M., Eyüpoğlu, S.Ö., 2005. Determination of the Local Meteoric Water Lines Using Stable Isotope Contents of Precipitation In Turkey (in Turkish). Proceedings, II. National Symposium of Isotopic Methods in Hydrology, General Directorate of State Hydraulic Works, İzmir. pp. 323–344.
Scholz, C.H., 1990. The Mechanics of Earthquakes and Faulting. Cambridge, Cambridge University Press.
Segall, P., 2010. Earthquake and Volcano Deformation. Princeton University Press, Princeton.
Siler, D.L., Karson, J.A., 2009. Three-dimensional structure of inclined sheet swarms: Implications for crustal thickening and subsidence in the volcanic rift zones of Iceland. J. Volcanol. Geotherm. Res., 18, 333-346.
Scholz, C.H., 1990. The Mechanics of Earthquakes and Faulting. Cambridge, Cambridge University Press.
Segall, P., 2010. Earthquake and Volcano Deformation. Princeton University Press, Princeton.
Sigmundsson, F., Hreinsdottir, S., Hooper, A., Arnadottir, T., Pedersen, R., Roberts, M.J., Oskarsson, N., Auriac, A., Decriem, J., Einarsson, P., Geirsson, H., Hench, M., Ofeigsson, B.G., Sturkell, E., Sveinbjörnsson, H., and Feigl, K.L., 2010. Intrusion triggering of the 2010 Eyjafjallajökull explosive eruption. Nature, 468, 426-430, doi:10.1038/nature09558.
Sigmundsson, F., Hooper, A., Hreinsdottir, S., Vogfjord, K.S., Ofeigsson, D.G., Heimisson, E.L., Dumont, S., Parks, M., Spaans, K., Gudmundsson, G.B., Drouin, V., Arnadottir, T., Jonsdottir, K., Gudmundsson, M.T., Hognadottir, T., Fridriksdottir, H.M., Hensch, M., Einarsson, P., Magnusson, E., Samsonov, S., Brandsdottir, B., White, R.S., Agustsdottir, T., Greenfield, T., Green, R.G., Hjartardottir, A., Pedersen, R., Bennett, R., Geirsson, H., La Femina, P.C., Bjornsson, H., Palsson, F., Sturkell, E., Bean, C.J. , Mollhoff, M., Braiden, A.K., and Eibl, E., 2015. Segmented lateral dyke growth in a rifting event at Barðarbunga volcanic system, Iceland. Nature, 517, 191-U158, doi:10.1038/nature14111.
Santos, R.V., et al. 2009. Geochemical and thermal effects of a basic sill on black shales and limestones of the Permian Irati Formation. Journal of South American Earth Sciences, 28 (1), 14-24. doi: 10.1016/j.jsames.2008.12.002
Saxby, J.D. & Stephenson, L.C. 1987. Effect of an igneous intrusion on oil shale at Rundle (Australia). Chemical Geology, 63 (1-2), 1-16.
Schofield, N., et al. 2017. Regional magma plumbing and emplacement mechanisms of the Faroe-Shetland Sill Complex: implications for magma transport and petroleum systems within sedimentary basins. Basin Research, 29, (1), 41-63. doi: 10.1111/bre.12164
Schofield, N. & Totterdell, J. 2008. Distribution, timing, and origin of magmatism in the Bight and Eucla basins. Geoscience Australia.
Schofield, N. & Jerram, D.A. 2016. Sills in sedimentary basins and petroleum systems.
Advances in Volcanology. doi: 10.1007/11157_2015_17.
Senger, K., et al. 2015. Fracturing of doleritic intrusions and associated contact zones: Implications for fluid flow in volcanic basins. Journal of African Earth Sciences, 102, 70-85. doi: 10.1016/j.jafrearsci.2014.10.019.
Senger K., et al. 2017. Effects of igneous intrusions on the petroleum system: a review.
Volcanic Basin Petroleum Research, Norway. 35
Shutter, S.R. 2003. Occurrences of hydrocarbons in and around igneous rocks. Geological Societ, 214, 35-68. doi: 10.1144/GSL.SP.2003.214.01.03.
Simoneit, B.R. 1994. Organic matter alteration and fluid migration in hydrothermal systems. Geological Society, London, Special Publications, 78 (1), 261-274. doi: 10.1144/GSL.SP.1994.078.01.18
Spacapan, J.B., et al. 2018. Thermal impact of igneous sill-complexes on organic-rich formations and implications for petroleum systems: A case study in the northern Neuquén Basin, Argentina. Marine and Petroleum Geology, 91, 519-531. doi: 10.1016/j.marpetgeo.2018.01.018
Sloane, D.J., 1991. Some Physical Properties of Dolerite. Tasmania Department of Resources and Energy: Division of Mines and Mineral Resources.
Sruoga, P. & Rubinstein, N. 2007. Processes controlling porosity and permeability in volcanic reservoirs from the Austral and Neuquén basins, Argentina. AAPG Bulletin, 91, 115-129. doi: 10.1306/08290605173
Stemmerik, L. et al., 1993. Depositional history and petroleum geology of the Carboniferous to Cretaceous sediments in the northern part of East Greenland. Norwegian Petroleum Society Special Publications, 2, 67-87. doi: 10.1016/B978-0-444-88943-0.50009-5
Stephens T.L., et al. 2017. Igneous sills record far-field and near-field stress interactions during volcano construction: Isle of Mull, Scotland. Earth and Planetary Sciences Letter, 478, 159-174. doi: 10.1016/j.epsl.2017.09.003

Stoneley, R. 1995. An introduction to petroleum exploration for non-geologists. Oxford University Press, Oxford, U.K. pp 119.
Sydnes, M., et al. 2018. The importance of sill thickness and timing of sill emplacement on hydrocarbon maturation. Marine and Petroleum Geology, 89 (2), 500-514. doi: 10.1016/j.marpetgeo.2017.10.017.
Svensen, H. & Jamtveit, B. 2010. Metamorphic Fluids and Global Environmental Changes.
Elements, 6 (3), 179-182. doi: 10.2113/gselements.6.3.179.
Svensen, H., et al. 2010. Sandstone dikes in dolerite sills: Evidence for high-pressure gradients and sediment mobilization during solidification of magmatic sheet intrusions in sedimentary basins. Geosphere. 6 (3), 211-224. doi: 10.1130/GES00506.1
Scholz, C. H. 1990. The Mechanics of Earthquakes and Faulting, Cambridge University Press, Cambridge, UK
Sibson, R.H., Robert, F., and Poulsen, K.H. 1988. High-angle reverse faults, fluidpressure cycling, and mesothermal gold-quartz deposits: Geology, v. 16, p. 551–555, doi:10.1130/0091-7613(1988)0162.3.CO;2
Simmenes ,T. H. 2002. Fracture systems, fault development and fluid transport in Vaksdal, West Norway. MSc thesis, University of Bergen.
Skar, T., Beekman, F.2003. Modelling the Influence of Tectonic Compression on the In-Situ Stress Field with Implications for Seal Integrity; the Haltenbanken Area, Offshore Mid-Norway. Geological Society, London, Special Publication 212, pp. 295–311.
Skogseid, J., Planke, S., Faleide, J.I., Pedersen, T., Eldholm, O., and Neverdal, F. 2000. NE Atlantic continental rifting and volcanic margin formation: Geological Society, London, Special Publications, v. 167, pp. 295–326.
Stein, R. and Yeats, R. 1989. Hidden earthquakes, Sci. Am., 260, 48-57
Torabi, A., Berg, S.S. 2011. Scaling of fault attributes: a review. Mar. Pet. Geol. 28, 1444– 1460.
Townsend, J., and M. D. Zoback .2000. How faulting keeps the crust strong, Geology, 28, 399 – 402.
Thorey, C. & Michaut, C. 2016. Elastic-plated gravity currents with a temperature-dependent viscosity. Journal of Fluid Mechanics, 805, 88-117. doi: 10.1017/jfm.2016.538
Trosdtorf, I., et al. 2018. Phanerozoic magmatism in the Parnaìba Basin: characterization of igneous bodies (well logs and 2D seismic sections), geometry, distribution and sill emplacement patterns. Geological Society, London. doi: 10.1144/SP472.10
Tarasewicz, J., White, R.S., Woods, A.W., Brandsdottir, B., Gudmundsson, M.T., 2012. Magma mobilization by downward-propagating decompression of the Eyjafjallajökull volcanic plumbing system. Geophys. Res. Lett., 39, doi:10.1029/2012GL053518.
Townsend, M.R., Pollard, D.D., Smith, R.P., 2017. Mechanical models for dikes: A third school of thought. Tectonophysics, 703-704, 98-118.
Tuschida, E., Nakahara, I., 1979. Three-dimensional stress concentration around a spherical cavity in a semi-infinite elastic body. Japan Soc. Mech. Engng Bull., 13, 499-508.
Tibaldi., A, Pasquarè, F.A., Rust, D., 2011. New insights into the cone sheet structure of the Cuillin Complex, Isle of Skye, Scotland. J. Geol. Soc., 168, 689-704.
Tibaldi, A., Bonali, F., Pasquaré, F.A., Rust, D., Cavallo, A., D'Urso, A., 2013. Structure of regional dykes and local cone sheets in the Midhyrna-Lysuskard area, Snaefellsnes Peninsula (NW Iceland). Bull. Volcanol., 75: 764, doi 10.1007/s00445-013-0764-8.
Townsend, M.R., Pollard, D.D., Smith, R.P., 2017. Mechanical models for dikes: A third school of thought. Tectonophysics, 703-704, 98-118.
Taler, J., Duda, P., 2006. Solving Direct and Inverse Heat Conduction Problems. Springer.
Tabatabaian, M., 2014. COMSOL for Engineers. Mercury Learning and Information, Boston.
Tan, O., Tapırdamaz, M.C., Yörük, A., 2008. The earthquake catalogues for Turkey. Turk. J. Earth Sci. 17 (2), 405–418.
Tarhan, N., 1991. Hınıs–Varto–Karlıova (Erzurum–Muş–Bingöl) dolayındaki neojen volkanitlerinin jeolojisi ve petrolojisi. MTA Dergisi 113, 1–15 (in Turkish).
Tatar, O., Piper, J.D.A., Gürsoy, H., Heimann, A., Koçbulut, F., 2004. Neotectonic de- formation in the transition zone between the Dead Sea Transform and the East Anatolian Fault Zone, southern Turkey: a palaeomagnetic study of the Karasu Rift Volcanism. Tectonophysics 385, 17–43.
Tibaldi, A., 2015. Structure of volcano plumbing systems: a review of multi- parametric effects. J. Volcanol. Geotherm. Res. 298, 85–135.
Tibaldi, A., Vezzoli, L., Pasquarè, F.A., Rust, D., 2008. Strike-slip fault tectonics and the emplacement of sheet–laccolith systems: the Thverfell case study (SW Ice- land). J. Struct. Geol. 30, 274–290.
Thorey, C. & Michaut, C. 2016. Elastic-plated gravity currents with a temperature-dependent viscosity. Journal of Fluid Mechanics, 805, 88-117. doi: 10.1017/jfm.2016.538
Trosdtorf, I., et al. 2018. Phanerozoic magmatism in the Parnaìba Basin: characterization of igneous bodies (well logs and 2D seismic sections), geometry, distribution and sill emplacement patterns. Geological Society,

London. doi: 10.1144/SP472.10
Tabarraei A, Sukumar N. Extended finite element method on polygonal and quadtree meshes. Computer methods in applied mechanics and engineering 2008; 197:425-438.
Tarancon JE, Vercher A, Giner E, Fuenmayor FJ. Enhanced blending elements for XFEM applied to linear elastic fracture mechanics. International journal for numerical methods in engineering. 2009; 77:126-148.
Tran AB, Yvonnet J, He Q-C, Toulemonde C, Sanahuja J. A multiple level set approach to prevent numerical artefacts in complex microstructures with nearby inclusions within XFEM. International journal for numerical methods in engineering 2011; 85:1436-1459.
Tarasewicz, J., White, R.S., Woods, A.W., Brandsdottir, B., Gudmundsson, M.T., 2012. Magma mobilization by downward-propagating decompression of the Eyjaf- jallajökull volcanic plumbing system. Geophys. Res. Lett. 39, https://doi.org/10. 1029/2012GL053518.
Tibaldi, A., Vezzoli, I., Pasquare, F.A., Rust, D., 2008. Strike-slip fault tectonics and the emplacement of sheet-laccolith systems: the Thverfell case study (SW Ice- land). J. Struct. Geol. 30, 274–290.
Tibaldi, A., Pasquare, F.A., Rust, D., 2011. New insights into the cone sheet structure of the Cuillin complex, Isle of Skye, Scotland. J. Geol. Soc. 168, 689–704.
Tibaldi, A., Bonali, F., Pasquare, F.A., Rust, D., Cavallo, A., D'Urso, A., 2013. Struc- ture of regional dykes and local cone sheets in the Nidhyrna-Lysuskard area, Snae- fellsnes Peninsula (NW Iceland). Bull. Volcanol. 75, 764https://doi.org/10.1007/ s00445-013-0764-8.
Townsend, M.R., Pollard, D.D., Smith, R.P., 2017. Mechanical models for dikes: a third school of thought. Tectonophysics 703-704, 98–118.
Tuschida, E., Nakahara, I., 1979. Three-dimensional stress concentration around a spherical cavity in a semi-infinite elastic body. Japan Soc. Mech. Engng Bull. 13, 499–508.
Tran TQN, Lee HP, Lim SP. Modelling porous structures by penalty approach in the extended finite element method. Computer methods in biomechanics and biomedical engineering 2013; 16:347-357.
Uchibori A, Ohshima H. Numerical analysis of melting/solidification phenomena using a moving boundary analysis method X-FEM. Nuclear technology 2009; 167:83.
Unger JF, Eckardt S, Konke C. Modelling of cohesive crack growth in concrete structures with the extended finite element method. Computer methods in applied mechanical engineering 2007; 196:4087-4100
Vajragupta N, Uthaisangsuk V, Schmaling B, Münstermann S, Hartmaier A, Bleck W. A micromechanical damage simulation of dual phase steels using XFEM. Computational materials science 2012; 54: 271-279.
Van der Bos F, Gravemeier V. Numerical simulation of premixed combustion using an enriched finite element method. Journal of computational physics 2009; 228:3605-3624.
Ventura G, Gracie R, Belytschko T. Fast integration and weight function blending in the extended finite element method. International journal for numerical methods in engineering 2009; 77:1-29.
Ventura G, Xu JX, Belytschko T. A vector level set method and new discontinuity approximations for crack growth by EFG. International journal for numerical methods in engineering 2002; 54:923-944.
Ventura G. Domain and boundary quadrature for enrichment functions in the extended finite element method. International journal of material forming 2008; 1:1135-1138.
Ventura G. On the elimination of quadrature subcells for discontinuous functions in the extended finite-element method. International journal for numerical methods in engineering 2006; 66:761-795.
Verhoosel CV, Remmers JJC, Gutirrez MA. A partition of unity-based multiscale approach for modeling fracture in piezoelectric ceramics. International journal for numerical methods in engineering 2010; 82:966-994.
Vitali E, Benson D. Kinetic friction for multi-material arbitrary Lagrangian Eulerian extended finite element formulations. Computational mechanics 2009; 43:847-857.
Vitali E, Benson DJ. An extended finite element formulation for contact in multi-material arbitrary Lagrangian-Eulerian calculations. International journal for numerical methods in engineering 2006; 67:1420-1444.
Wagner GJ, Moës N, Liu WK, Belytschko T. The extended finite element method for rigid particles in Stokes flow. International journal for numerical methods in engineering 2001; 51:293-313.
Wall WA, Gerstenberger A, Kuttler A, Mayer UM. An XFEM based fixed-grid approach for 3D fluid-structure interaction. Fluid structure interaction II 2010; 73:327-349.
Wang, K., et al. 2012. Numerical modelling of the hydrocarbon generation of Tertiary source rocks intruded by doleritic sills in the Zhanhua depression, Bohai Bay Basin, China. *Basin Research,* **24,** 234-247. doi: 10.1111/j.1365-2117.2011.00518
Wenzhi, Z., et al. 2009. Comparative study on volcanic hydrocarbon accumulation in western and eastern China and its significance. *Petroleum Exploration and Development,* **36** (1) 1-11. doi: 10.1016/S1876-3804(09)60106-3
Wu, C., et al. 2006. Formation mechanisms of hydrocarbon reservoirs associated with volcanic and subvolcanic intrusive rocks: Examples in Mesozoic-Cenozoic basins of eastern China. *AAPG Bulletin*, **90** (1), 137-147. doi:

10.1306/04070505004
Wibberley, C.A.J., Yielding, G., Di Toro, G. 2008. Recent advances in the under- standing of fault zone internal structure; a review. In: Wibberley, C.A.J., Kurz, W., Imber, J., Holdsworth, R.E., Collettini, C. (Eds.), Structure of Fault Zones: Implications for Mechanical and Fluid-flow Properties. Geological Society of London Special Publication, vol. 299, pp. 5e33.
Wang H, Belytschko T. Fluid-structure interaction by the discontinuous-Galerkin method for large deformations. International journal for numerical methods in engineering 2009; 77:30-49.
Wang H, Chessa J, Liu WK, Belytschko T. The immersed/fictitious element method for fluid-structure interaction: Volumetric consistency, compressibility and thin members. International journal for numerical methods in engineering 2008; 74:32-55.
Wang H, Zhang C, Yang L, You Z. Study on the rubber-modified asphalt mixtures' cracking propagation using the extended finite element method. Construction and building materials 2013; 47: 223-230.
Wang Z, Ma L, Wu L, Yu H. Numerical simulation of crack growth in brittle matrix of particle reinforced composites using the XFEM technique. Acta mechanical solida sinica 2012; 25:9-21.
Watanabe N, Wang W, Taron J, Görke UJ, Kolditz O. Lower-dimensional interface elements with local enrichment: application to coupled hydro-mechanical problems in discretely fractured porous media. International journal for numerical methods in engineering 2012; 90:1010-1034.
Wyart E, Coulon D, Pardoen T, Remacle JF, Lani F. Application of the substructured finite element/extended finite element method (S-FE/XFE) to the analysis of cracks in aircraft thin walled structures. Engineering fracture mechanics 2009; 76:44-58.
Wang, K., et al. 2012. Numerical modelling of the hydrocarbon generation of Tertiary source rocks intruded by doleritic sills in the Zhanhua depression, Bohai Bay Basin, China. Basin Research, 24, 234-247. doi: 10.1111/j.1365-2117.2011.00518
Wenzhi, Z., et al. 2009. Comparative study on volcanic hydrocarbon accumulation in western and eastern China and its significance. Petroleum Exploration and Development, 36 (1) 1-11. doi: 10.1016/S1876-3804(09)60106-3
Wu, C., et al. 2006. Formation mechanisms of hydrocarbon reservoirs associated with volcanic and subvolcanic intrusive rocks: Examples in Mesozoic-Cenozoic basins of eastern China. AAPG Bulletin, 90 (1), 137-147. doi: 10.1306/04070505004
Wallace, R.E., 1968. Earthquake of August 19, 1966. Varto Area, Eastern Turkey. B. Seismol. Soc. Am. 58, 11–45.
Williams, G.D., Powell, C.M., Cooper, M.A., 1989. Geometry and kinematics of inver- sion tectonics. In: Cooper, M.A., Williams, G.D. (Eds.), Geol. Soc. (Lond.) Spec. Publ., vol. 44, pp. 3–15.
Xu, W., Jonsson, S., Corbi, F., Rivalta, E., 2016. Graben formation and dike arrest dur- ing the 2009 Harrat Lunayyir dike intrusion in Saudi Arabia: insights from InSAR, stress calculations and analog
Xiao QZ, Karihaloo BL, Liu XY. Incremental-secant modulus iteration scheme and stress recovery for simulating cracking process in quasi-brittle materials using XFEM. International journal for numerical methods in engineering 2007; 69:2606-2635.
Xiao QZ, Karihaloo BL. Implementation of hybrid crack element on a general finite element mesh and in combination with XFEM. Computer methods in applied mechanics and engineering 2007; 196:1864-1873.
Xu J, Lee CK, Tan HK. An XFEM plate element for high gradient zones resulted from yield lines. International journal for numerical methods in engineering 2013a; 93:1314-1344.
Xu, W., Jonsson, S., Corbi, F., Rivalta, E., 2016. Graben formation and dike arrest during the 2009 Harrat Lunayyir dike intrusion in Saudi Arabia: insights from InSAR, stress calculations and analog experiments. J. Geophys. Res., 121, doi:10.1002/2015JB012505.
Xu J, Lee CK, Tan KH. A two-dimensional co-rotational Timoshenko beam element with XFEM formulation. Computational mechanics 2012; 49:667-683.
Xu J, Lee CK, Tan KH. An XFEM frame for plate elements in yield line analyses. International journal for numerical methods in engineering 2013b; 96:150-175.
Xu J, Li Y, Chen X, Yan Y, Ge D, Zhu M, Liu B. Characteristics of windshield cracking upon low-speed impact: Numerical simulation based on the extended finite element method. Computational materials science 2010; 48:582-588.
Xu Y, Yuan H. Applications of normal stress dominated cohesive zone models for mixed-mode crack simulation based on extended finite element methods. Engineering fracture mechanics 2011; 78:544-558.
Xu Y, Yuan H. Computational analysis of mixed-mode fatigue crack growth in quasi-brittle materials using extended finite element methods. Engineering fracture mechanics 2009; 76:165-181.
Yan Y, Park SH. An extended finite element method for modeling near-interfacial crack propagation in a layered structure. International journal of solids and structures 2008; 45:4756-4765.

Ye C, Shi J, Cheng GJ. An eXtended Finite Element Method (XFEM) study on the effect of reinforcing particles on the crack propagation behavior in a metal-matrix composite. International journal of fatigue 2012; 44:151-156.
Yu TT, Gong ZW. Numerical simulation of temperature field in heterogeneous material with the XFEM. Archives of civil and mechanical engineering 2013; 13:199-208.
Yvonnet J, He QC, Zhu QZ, Shao JF. A general and efficient computational procedure for modelling the Kapitza thermal resistance based on XFEM. Computational materials science 2011; 50:1220-1224.
Yvonnet J, Le Quang H, He QC. An XFEM/level set approach to modelling surface/interface effects and to computing the size-dependent effective properties of nanocomposites. Computational mechanics 2008; 42:119-131.
Zabaras N, Ganapathysubramanian B, Tan L. Modelling dendritic solidification with melt convection using the extended finite element method. Journal of computational physics 2006; 218:200-227.
Zamani A, Eslami MR. Implementation of the extended finite element method for dynamic thermoelastic fracture initiation. International Journal of solids and structures 2010; 47:1392-1404.
Zamani A, Gracie R, Eslami MR. Cohesive and non-cohesive fracture by higher-order enrichment of XFEM. International journal for numerical methods in engineering 2012; 90:452-483.
Zamani A, Gracie R, Eslami MR. Higher order tip enrichment of eXtended Finite Element Method in thermoelasticity. Computational mechanics 2010; 46:851-866.
Zhang HH, Li LX. Modeling inclusion problems in viscoelastic materials with the extended finite element method. Finite elements in analysis and design 2009; 45:721-729.
Zhang HH, Rong G, Li LX. Numerical study on deformations in a cracked viscoelastic body with the extended finite element method. Engineering analysis with boundary elements 2010; 34:619-624.
Zhang S, Wang G, Yu X. Seismic cracking analysis of concrete gravity dams with initial cracks using the extended finite element method. Engineering structures 2013; 56:528-543.
Zhao X, Bordas SPA, Qu J. A hybrid smoothed extended finite element/level set method for modeling equilibrium shapes of nano-inhomogeneities. Computational mechanics 2012. DOI arXiv preprint arXiv:1210.5430
Zi G, Belytschko T. New crack-tip elements for XFEM and applications to cohesive cracks. International journal for numerical methods in engineering 2003; 57:2221-2240.
Zi G, Song JH, Budyn E, Lee SH, Belytschko T. A method for growing multiple cracks without remeshing and its application to fatigue crack growth. Modeling and simulation in materials science and engineering 2004; 12: 901-915.
Zilian A, Fries TP. A localized mixed-hybrid method for imposing interfacial constraints in the extended finite element method (XFEM). International journal for numerical methods in engineering 2009; 79:733-752.
Zilian A, Legay A. The enriched space-time finite element method (EST) for simultaneous solution of fluid-structure interaction. International journal for numerical methods in engineering 2008; 75:305-334.
Zilian A, Netuzhylov H. Hybridized enriched space-time finite element method for analysis of thin-walled structures immersed in generalized Newtonian fluids. Computers and structures 2010; 88:1265-1277.
Zunino P. Analysis of backward Euler/extended finite element discretization of parabolic problems with moving
Zienkiewicz, O.C., 1979. The Finite Element Method. McGraw–Hill, New York, p. 787.
Zhu D., et al. 2007. Effect of igneous activity on hydrocarbon source rocks in Jiyang sub- basin, eastern China. *Journal of Petroleum Science and Engineering,* **59**, 309-320. doi:10.1016/j.petrol.2007.05.002
Zeig, M.J & Marsh, B.D. 2002. Crystal size distributions and scaling laws in the quantification of igneous textures. *Journal of Petrology,* **43**, 85-101.
Zinger, A.S. & Kotrovsky, V.V. 1979. Hydro-geothermal conditions of water systems of western part of Pre-Caspian depression. Saratov University, Saratov Russia.
Ziegler, P. A., Doery, R. & Scott, J. 1986. Tectonic habitat of Norwegian oil and gas. In Spencer, A. M. (ed.): Habitat of Hydrocarbons on the Norwegian Continental Shelf. Norwegian Petroleum Society (Graham & Trotman), 3-19.
Ziegler, P. A. 1988. Evolution of the Artic-North Atlantic and the Western Thethys, AAPG Mem., 43, 1–198.

Appendix 2:

Here, I am presenting my conference papers which I presented them or plan to present them until end of this accademic year. In all these extended abstracts for conferences, my main job was to handle more than 70% of all modeling results and more than 80% of all experiments but very few involved with collecting field data. I managed to have this opportunity in presenting my works as oral or poster presentation in number of British, European or International events. Most of these works have already been presented mostly in London then Paris, Texas, San Fransisco, Vienna, Manchester, Cambridge, Egham, Strasbourg, Malmo, Minnesota and Edinburgh. And few works are going to be presented in Oklahoma, Hauge, Uppsala and Vienna later this year.

- Shahram Chamankhah, Mohsen Bazargan, Mahdi Habibpour Fatideh: Managed Pressure Drilling Application to Solve Laser Assist Drilling Fracturing Issues. SPE - Oklahoma city oil and gas symposium, Oklahoma; 04/2019

- Mohsen Bazargan: NUMERICAL COMPARISON OF IMPROVED OIL RECOVERY FROM CHALK RESERVOIRS WITH SEA WATER AND SMART WATER. European symposium of improved oil recovery, France; 11/2018

- Pooyan Broumand, Mohsen Bazargan, Mehdi Fahandezh Saadi, Agust Gudmundsson: Experimental Investigation of Nitrogen Assisted Enhanced Oil Recovery of an Iranian Fractured Oil Reservoir. 80th EAGE Conference and Exhibition 2018, Denmark; 06/2018, DOI:10.3997/2214-4609.201801563

- Mohsen Bazargan, Pooyan Broumand, Agust Gudmundsson: Modelling Nitrogen Gas-Assisted Gravity Drainage for Enhanced Oil Recovery in a Fractured Media. 80th EAGE Conference and Exhibition 2018, Denmark; 06/2018, DOI:10.3997/2214-4609.201801526

- Mohsen Bazargan: Comparison of Pore-Scale and Darcy-Scale Simulation of Acid Injection in Carbonate Formations. Saint Petersburg 2018, Russia; 04/2018

- Azizah al shehri, Mohsen Bazargan, Agust Gudmundsson: Numerical modelling of dike-induced surface stresses and fractures. EGU, Vienna; 04/2018

- Mohsen Bazargan, Agust Gudmundsson: Deformation of mechanically layered volcanic zone induced by an arrested dike. EGU, Vienna; 04/2018

- Mohsen Bazargan, Shahram Chamankhah: Feasibility of Using Pressurized Mud Cap Drilling for Geothermal Wells. EAGE 2017, mälmö; 09/2017, DOI:10.3997/2214-4609.201702133

- Mohsen Bazargan, Shahram Chamankhah: Feasibility Study of Operating Managed Pressure Drilling in Geothermal Well Using CBHP. EAGE 2017, mälmö; 09/2017, DOI:10.3997/2214-4609.201702135

- Mohsen Bazargan, Agust Gudmundsson, Philip Meredith: Feasibility of Using Plasma Assisted Drilling in Geothermal Wells. EAGE 2017, mälmö; 09/2017, DOI:10.3997/2214-4609.201702130

- Mohsen Bazargan, Agust Gudmundsson, Philip Meredith, Pooyan Broumand: Investigating the Role of Temperature on Thermal Stress and Fracture Propagation in Geothermal Systems. ARMA 2017, San Francisco, California, USA; 06/2017

- Mohsen Bazargan, Agust Gudmundsson, Philip Meredith: Hydraulic Fracturing in Oil and Gas Resources and its Risks and Hazards While it's Interacting with Natural Faults. 79th EAGE Conference & Exhibition 2017, Paris; 06/2017

- Mohsen Bazargan, Agust Gudmundsson, Philip Meredith, Mahdi Habibpour Fatideh: Experimental and numerical analysis of using laser for perforation operation in sedimentary rock reservoirs. PETEX 2016, London; 11/2016

- Mohsen Bazargan, Agust Gudmundsson, Philip Meredith, Reza Mohammadi: Hydraulic Fracturing in Oil and Gas Resources and its Risks and Hazards While its Interacting with Natural Faults. Petex 2016, London; 11/2016, DOI:10.3997/2214-4609.201701323

- Mohsen Bazargan, Agust Gudmundsson, Philip Meredith, Reza Mohammadi, Isaac Kenyon: Developing

Geothermal Energy from Hydrothermal and EGS Sources while Minimizing Risks and hazards. European Geothermal Congress 2016, France; 09/2016

- Mohsen Bazargan, Agust Gudmundsson, Philip Meredith: Using Laser-Assisted Drilling Method with MPD and UBD Condition In Case Of Geothermal Resources. European Geothermal Congress 2016, France; 09/2016

- Alex Harper, Mohsen Bazargan, Agust Gudmundsson: Nemerical modelling and statistical Analysing of the geometrical properties of fracture populations. The Heat - Royal Holloway University of London, Egham, Surrey, United Kingdom; 06/2016

- Mohsen Bazargan, Alberto Striolo, Tom Mitchell, Agust gudmundsson, Philip Meredith: Multi Physics Modeling Of Hydraulic Fracturing and Fluid Transfer in Fractured Porous Medium to Monitoring Enhanced Oil Recovery and Engineering Geothermal System. Tectonic Studies Group Annual Meeting - London 2016, London; 01/2016

- Özgür Karaoğlu, John Browning, Mohsen Bazargan, Agust Gudmundsson: Numerical modelling of Triple Junction Tectonics at Karlıova, Eastern Turkey: implications for the mechanism of magma transport. EGU2016; 01/2016

- Mehdi Fahandezh, Emily Crowder, Mohsen Bazargan, Agust Gudmundsson, Philip Meredith: Numerical modeling and experimental investigation of enhanced oil recovery; nitrogen injection. Burlington House, London; 10/2015

- Mohsen Bazargan, Agust Gudmundsson, Philip Meredith, Nathaniel Forbes Inskip, Mohamed Soliman, Mahdi Habibpour, Ali Rezaee, John Browning: Wellbore instability during plasma torch drilling in geothermal reservoirs. ARMA 2015, San Francois - USA; 07/2015, DOI:10.13140/RG.2.1.3829.1284

- Mohsen Bazargan, Agust Gudmundsson, Nathaniel Forbes Inskip, Reza Mohammadi, Philip Meredith, Mahdi Habibpour: Experimental and numerical 2D analysis of hydraulic fracturing using high-power electric discharge. ARMA 2015, San Francois - USA; 06/2015, DOI:10.13140/RG.2.1.1731.9763

- Mohsen Bazargan: thermal assisted drilling in geothermal resources. ARMA 2015, USA - San Francisco; 06/2015

- Mohsen Bazargan: experimental and numerical analysis of 2D novel hydraulic fracturing process in shale reservoirs. ARMA, USA - San Francisco; 06/2015

- Mohsen Bazargan, Agust Gudmundsson, Philip Meredith, Nathaniel Forbes Inskip: Developing Geothermal Energy from Both Hydrothermal and EGS Sources with Considering On Decreasing Risks. Fire & ICE, Cambridge University; 03/2015